

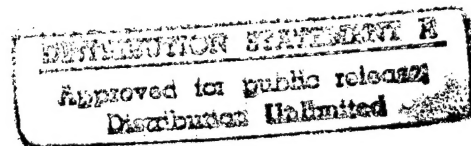
# Development of the Microstructure Based Stochastic Life Prediction Models

## *Final Report*

ONR Grant No: N00014-91-J-1299

### Submitted to:

Dr. A. K. Vasudevan  
Code 332  
Office of Naval Research  
800 North Quincy Street  
Arlington, VA 22217-5660



### Prepared by:

Professor Marek A. Przystupa  
Department of Materials Science and Engineering  
University of California  
Los Angeles, CA 90024  
Tel.: (310) 825-5669  
FAX: (310) 206-7353

DTIC QUALITY INSPECTED 3

July 1997

19970912 013

# REPORT DOCUMENTATION PAGE

Form Approved  
OMB No. 0704-0188

Public reporting burden for this collection of information is estimated to average 1 hour per response, including the time for reviewing instructions, searching existing data sources, gathering and maintaining the data needed, and completing and reviewing the collection of information. Send comments regarding this burden estimate or any other aspect of this collection of information, including suggestions for reducing this burden, to Washington Headquarters Services, Directorate for Information Operations and Reports, 1215 Jefferson Davis Highway, Suite 1204, Arlington, VA 22202-4302, and to the Office of Management and Budget, Paperwork Reduction Project (0704-0188), Washington, DC 20503.

1. AGENCY USE ONLY (Leave blank)		2. REPORT DATE 7/18/97	3. REPORT TYPE AND DATES COVERED Final Technical, 12/15/90 - 12/31/96	
4. TITLE AND SUBTITLE  Development of the Microstructure Based Stochastic Life Predictions Models			5. FUNDING NUMBERS  G N00014-91-J-1299	
6. AUTHOR(S)  Marek Przystupa				
7. PERFORMING ORGANIZATION NAME(S) AND ADDRESS(ES)  University of California, Los Angeles Department of Materials Science and Engineering 405 Hilgard Avenue Los Angeles, CA 90095			8. PERFORMING ORGANIZATION REPORT NUMBER  910878-00-A12	
9. SPONSORING/MONITORING AGENCY NAME(S) AND ADDRESS(ES)  Office of Naval Research Ballston Centre Tower One 800 North Quincy Street Arlington, VA 22217-5660			10. SPONSORING/MONITORING AGENCY REPORT NUMBER	
11. SUPPLEMENTARY NOTES				
12a. DISTRIBUTION/AVAILABILITY STATEMENT  Approved for public release. Distribution is unlimited.			12b. DISTRIBUTION CODE	
13. ABSTRACT (Maximum 200 words) The goal of this program was to develop a methodology for predicting fatigue lives of structural alloys based on their microstructural characteristics and mechanical properties. Such methodology has been successfully implemented and verified by predicting fatigue lives of the four different variants of the aluminum airframe 7050-T7451 plate alloy and, with modifications, of the butt welds of the ship hull HSLA-80 steels. The key features of the method is the assumption that the incipient fatigue crack size distribution is related to the size distribution of the bulk material flaws through the statistics of extreme. When combined with the Monte-Carlo (MC) crack growth model the extreme value estimates of the initial crack sizes gave excellent predictions of the fatigue lives of the 7050-T7451 alloy for samples both with and without stress concentrators. The specially for this purpose developed MC model utilized initial crack size distribution, crack location, crystallographic texture on the crack path and crack deflections as the random variables. A modified, closed-form three-parameter version of the model has been proposed for the butt welds of the HSLA-80 steels. This version, with parameters obtained based on the constant amplitude data, showed outstanding predictive capabilities for the samples with welds subjected to the variable amplitude loading conditions. Both versions of the model represent very useful and economical alternative to the lengthy fatigue testing programs. They allow for rapid differentiation between fatigue qualities of different material variants and on the parametric studies of the effects of the microstructural variables on fatigue lives. The methodology should instrumental in aiding alloy designers and process engineers in optimizing alloy microstructures for fatigue performance. Additional benefits of the program included development of the first ever detailed data-base on the 7050-T7451 alloy which contains information on (1) particle, pore, grain, subgrain and precipitate sizes, shapes, volume fraction, spatial distributions and their gradients, (2) complete fractographic data on the crack path characteristics of the 7050 alloys including types and size distributions of the fatigue crack initiating features and (3) a set of composite forty fractographs documenting types of fatigue failures in the HSLA-80 steel weldments subjected to both constant and variable amplitude loading conditions.				
14. SUBJECT TERMS Fatigue life prediction, 7050 Alloy, HSLA steels, crack growth, crack initiation, fatigue cracks, probabilistic fracture mechanics, microstructure, statistics of extreme, quantitative metallography, fractography, airframe alloys, steel welds			15. NUMBER OF PAGES 427	
			16. PRICE CODE	
17. SECURITY CLASSIFICATION OF REPORT Unclassified	18. SECURITY CLASSIFICATION OF THIS PAGE Unclassified	19. SECURITY CLASSIFICATION OF ABSTRACT Unclassified	20. LIMITATION OF ABSTRACT	

### ***Abstract***

The goal of this program was to develop a methodology for predicting fatigue lives of structural alloys based on their microstructural characteristics and mechanical properties. Such methodology has been successfully implemented and verified by predicting fatigue lives of the four different variants of the aluminum airframe 7050-T7451 plate alloy and, with modifications, of the butt welds of the ship hull HSLA-80 steels. The key features of the method is the assumption that the incipient fatigue crack size distribution is related to the size distribution of the bulk material flaws through the statistics of extreme. When combined with the Monte-Carlo (MC) crack growth model the extreme value estimates of the initial crack sizes gave excellent predictions of the fatigue lives of the 7050-T7451 alloy for samples both with and without stress concentrators. The specially for this purpose developed MC model utilized initial crack size distribution, crack location, crystallographic texture on the crack path and crack deflections as the random variables. A modified, closed-form three-parameter version of the model has been proposed for the butt welds of the HSLA-80 steels. This version, with parameters obtained based on the constant amplitude data, showed outstanding predictive capabilities for the samples with welds subjected to the variable amplitude loading conditions. Both versions of the model represent very useful and economical alternative to the lengthy fatigue testing programs. They allow for rapid differentiation between fatigue qualities of different material variants and on the parametric studies of the effects of the microstructural variables on fatigue lives. The methodology should be instrumental in aiding alloy designers and process engineers in optimizing alloy microstructures for fatigue performance. Additional benefits of the program included development of the first ever detailed data-base on the 7050-T7451 alloy which contains information on (1) particle, pore, grain, subgrain and precipitate sizes, shapes, volume fraction, spatial distributions and their gradients, (2) complete fractographic data on the crack path characteristics of the 7050 alloys including types and size distributions of the fatigue crack initiating features and (3) a set of composite forty fractographs documenting types of fatigue failures in the HSLA-80 steel weldments subjected to both constant and variable amplitude loading conditions.

## Table of Content

ABSTRACT .....	II
TABLE OF CONTENT .....	III
INTRODUCTION .....	1
<b>PART I: FATIGUE OF 7050 ALLOYS</b> .....	<b>3</b>
CHARACTERIZATIONS OF BULK MATERIAL .....	4
<i>Metallography</i> .....	4
Methodologies .....	4
Results .....	18
Discussion .....	31
Summary .....	33
<i>TEM</i> .....	35
Methodologies .....	35
Results .....	36
Summary .....	38
FRACTOGRAPHY .....	39
<i>Crack Nucleation Sites</i> .....	39
Methodology .....	39
Results and Discussion .....	40
Summary .....	42
<i>Fracture Surface and Crack Path</i> .....	44
Methodologies .....	47
Results and Discussion .....	50
Summary .....	57
MODELING .....	59
<i>Size Distributions of Fatigue Crack Initiating Features</i> .....	59
Extreme value statistic .....	59
Smooth Fatigue Samples .....	64
Open Hole Fatigue Samples .....	67
Summary .....	69
<i>Life predictions</i> .....	71
Introduction .....	71
Crack Nucleation .....	73
Magnitudes of Microstructural Effects .....	75
Monte-Carlo Simulations .....	80

Markov Chain Model .....	89
Summary .....	92
<b>PART II: FATIGUE OF HSLA-80 WELDMENTS .....</b>	<b>94</b>
<i>Introduction</i> .....	94
<i>Fatigue Results</i> .....	95
S-N Testing .....	95
Fractography .....	97
<i>Modeling</i> .....	99
Constant Average Stress .....	103
Constant Amplitude .....	104
<i>Verifications and Predictions</i> .....	105
<i>Summary</i> .....	108
OVERALL SUMMARY .....	110
ACKNOWLEDGMENTS .....	111
LIST OF PUBLICATIONS AND PRESENTATIONS .....	112
REFERENCES .....	116
LIST OF TABLES .....	128
TABLES .....	132
LIST OF FIGURES .....	164
FIGURES .....	179
APPENDIX A. Fracture Surfaces of the Fatigue Failures of the HSLA-80 Steel Butt Weldments .....	297
APPENDIX B. Quantitative Analysis of Heterogeneous Grain Structures on Plane Sections .....	338
APPENDIX C. Microstructural Models for Quantitative Analysis of Grains and Second- Phase Particles .....	345
APPENDIX D. Characterizations of Pore and Constituent Particle Populations in 7050- T7451 Aluminum Plate Alloys .....	357
APPENDIX E. Estimation of True Size Distribution of Partially Aligned Same-Shape Ellipsoidal Particles .....	396
APPENDIX F. Accumulation of Microstructural Damage Due to Fatigue of High-Strength Aluminum Alloys .....	403

APPENDIX G. Microstructure Based Fatigue Life Predictions for Thick Plate 7050-	
T7451 Airframe Alloys.....	412

## ***Introduction***

The demands for reliable estimates of both average fatigue lives and life distributions of metallic structures is very pressing in many areas. The most apparent ones are design of the new and maintenance of the old and aging aircraft [1,2,3]. Dependable estimates of fatigue lives of the airplane structures can significantly lower structures weight and lessen the economic burden associated with the maintenance costs. In spite of these needs, the microstructure based models which have potential to offer the most accurate predictions of life expectancy variations, instead of only average lives, are still in the infancy stage [4,5]. The models which are currently used are mostly phenomenological in nature and their predictive capabilities depend on several parameters that have to be determined through testing [6,7]. The microstructure either does not explicitly enter those descriptions or it is accounted for through phenomenological quantities such as characteristic length or scaling parameters. As a result, substitution of a new alloy for the old one, or modifications of the alloy microstructure through processing, requires series of expensive tests to determine new values of all parameters.

The goal of this program was to develop a microstructure based stochastic fatigue life predictions model for the materials used in the naval airframe applications and explore the possibility of using this model for predicting fatigue lives of the ship hull steels. The airframe material selected for this work was aluminum 7050-T7451 plate alloy. This alloy has been recently intensively studied with the focus on the improvement of its fatigue durability [8,9,10]. Results showed that although most of the mechanical properties of the slightly different alloy variants are practically the same, there are large differences in fatigue lives and fatigue cracks initiation sites between the variants [11,12]. This suggests that microstructural differences may be responsible for differences in fatigue performance. 7050-T7451 alloy indeed contains small volume fractions of micropores and constituent particles which are detrimental to its fracture response and fatigue life. In addition, when made as a plate, it is known to have microstructural gradients. The sizes and/or spacing of

the micropores and constituent particles are then not only non-uniform but also change with the position within the plate. Any attempt to obtain meaningful correlation of the microfeatures dimensional characteristics with mechanical properties requires then quantification of not only their average sizes, but also their size and spatial distributions, shapes, orientations and volume fractions. The 7050-T7451 plate alloy is then an ideal material to test the capabilities of the microstructure characterization techniques for life prediction models and the models themselves. Consequently, the main technical goals of the program were:

1. Ascertain microstructural features relevant to fatigue in aluminum 7050-T7451 plate alloys and develop quantitative techniques for their characterizations.
2. Characterize initial microstructures and accumulation of microstructural fatigue damage in aluminum 7050-T7451 plate alloys.
3. Formulate and test scaling relationships and models relating relevant microstructural characteristics with the accumulation of fatigue damage and reliability of aluminum 7050 alloys.
4. Expand predictive capabilities of the life prediction and microstructural characterizations methodologies developed for aluminum alloys to HSLA ship hull steels.

Since the developed models would be directly linked to the microstructural characteristics controlling fatigue performance, they would have impact in the two important areas. First, they would allow for the prediction of the fatigue life variations from microstructural characteristics of the starting material and from its mechanical properties. This opens the possibility of eliminating the need for fatigue tests for similar alloys. Secondly, they will provide ranking of microstructural features responsible for the deterioration of the alloy fatigue quality, therefore will be instrumental for the development of more reliable microstructure based material acceptance criteria.

## ***Part I: Fatigue of 7050 Alloys***

The materials investigated in this program included four variants of the 7050-T7451 aluminum plate alloy which is an airframe alloy used in the Navy fighter planes. This alloy contains nominally 6.2 w/o Zn, 2.3 w/o Cu, 2.2 w/o Mg and 0.12 w/o Zr. It is primarily used in the overaged and partially recrystallized conditions. The first two investigated variants were manufactured as 6" plates and designated as the old and new alloys (or pedigrees). Their microstructural characterizations have been performed earlier in the program. The two remaining variants were designated as the low porosity and thin plate alloys. The low porosity alloy was also manufactured as 6" plate but had reduced pore volume fractions and sizes. The thin plate alloy was made as a 1" plate. The reason for using these particular four alloy variants was to facilitate tests of fatigue life predictions methodologies on the same bulk matrix material with different types of the crack nucleation sites. In the old alloy the fatigue failures were expected to initiate predominantly from large pores while in the new one from constituent particles. In the thin plate and low porosity plate alloys, it was anticipated that the fatigue cracks would nucleate either at constituent particles or as the Stage I failures. Basic mechanical properties of the alloys are summarized in Table I.

All fatigue testing of the alloys were performed at Alcoa Laboratories. The tests were run on the two types of samples shown in Figure 1. The smooth samples were used to obtain the data compatible with the standard fatigue S-N tests, while the open-hole specimens were to simulate loading condition similar to those of the bolt holes in aircraft parts. All samples were cut from plate centers, had LT orientation and were tested under constant amplitude loading with R- value of 0.1 and frequency of 10 Hz for smooth and 30 Hz for the open hole samples. For smooth samples the maximum stresses were between 50 to 70% of the yield strength (equal 455 MPa) and for the open hole ones they were between 20 to 50% of the yield strength. The maximum stress levels and the

number of samples tested at each level are listed in Table II. Details on the fatigue testing procedure can be found in Alcoa team reports [13].

### ***Characterizations of Bulk Material***

Our material characterizations involved (1) metallographic study of the bulk material and (2) fractographic examinations of broken fatigued samples. The metallography included measurements of the size and spatial characteristics of pores, constituent particles, grains, subgrains and grain boundary precipitates on planes and locations indicated in Table III and Figure 2. The fractographic examinations were used to identify the fatigue nucleation sites, determine the types and sizes of the fatigue crack nucleating features and to find the distributions of microstructural features along the crack path.

#### **Metallography**

#### ***Methodologies***

#### ***Grains and Subgrains***

The grain structures were characterized in the old and new alloys. All measurements were made on all three planes shown in Figure 2 and at the plates surface, quarter depth and center locations. The characterizations included estimations of the grain (1) shapes, (2) orientations, (3) recrystallization levels and (4) size distributions. The magnification used was 100x and the averages were based on the data for at least 290 grains for each section. Characterizations of subgrains were limited to the TL plane at the center of the plate in the new alloy.

The grain sizes, shapes and orientations were quantified using a new version of the linear intercept method developed by us during the first two years of the program. The details of the method can be found in our previous reports [14,15] and in two papers

[16,17] attached as Appendix B and C. The key element of this method is the measurement of the grains average intercept lengths,  $L_2(\alpha)$ , at a scan angle  $\alpha$ .  $L_2(\alpha)$  is defined as[16]:

$$L_2(\alpha) = \frac{A}{H_2(\alpha)} \quad \text{eq. 1}$$

where  $A$  is the grain cross-section area and  $H_2(\alpha)$  its tangent height, equal to the grain projected length on the direction perpendicular to the scan lines. The grain size,  $L_H$  or  $D$ , is defined as the average  $L_2(\alpha)$  for scan angles from 0 to  $180^\circ$ :

$$D \equiv L_H = \frac{\pi A}{\frac{1}{\pi} \int_0^\pi H_2(\alpha) d\alpha} = \frac{\pi A}{L_p} \quad \text{eq. 2}$$

The same size definition were used later for pores and constituent particles.

The grain shapes were characterized using the aspect ratios and a dimensionless shape factor  $SI$  [16]. In this case it was necessary to use a normalized average intercept length,  $d$ , defined as:

$$d = \frac{L_2(\alpha)}{\max_{0 < \alpha < 180} L_2(\alpha)} \quad \text{eq. 3}$$

The shape factor was subsequently defined as the area under the  $d$  vs.  $\alpha$  curve :

$$SI = \frac{1}{\alpha_p} \int_0^{\alpha_p} d(\alpha) d\alpha \quad \text{eq. 4}$$

where  $\alpha_p$  is the curve period. Such defined  $SI$  is equal to one for a circle, it decreases with increasing object aspect ratio and is independent of both the object size and its orientation with respect to the scan lines. The expressions for  $SI$  for regular and elongated polygons, circles and ellipses can be found in Appendix C. The  $d$  vs. scan angle curves were also used in an attempt to describe grain shapes with spherical harmonics functions [18,19,20].

Grain alignment was quantified using two ancillary shape factors [21,16]. The first of them, called global or  $SI_g$ , was equal to the area under the  $d-\alpha$  curve obtained using standard scanning method. The second shape index, called the average or  $SI_{avg}$ , was defined as the area under the  $d-\alpha$  plot obtained by artificially aligning all grain major axes, hence eliminating orientation effect. To illustrate the difference let's assume that two elliptical grain sections are rotated with respect to each other. Their individual  $d-\alpha$  curves will have a phase difference, hence their average will reflect both the shapes and the relative orientations of both grains. The area under that curve, which is the global shape index,  $SI_g$ , increase with increasing particle misalignment and approaches one for a statistically random structure of several elliptical grains. The true average shape index for all grains can be obtained by constructing an average  $d-\alpha$  curve for grains aligned along their maximum  $L_2(\alpha)$  directions. We defined the area under such curve as  $SI_{avg}$ . Since  $SI_{avg}$  does not contain the information about particle orientation, comparing it to  $SI_g$  allows separation of the shape and orientation effects through the orientation factor,  $\Omega$ , defined by us as:

$$\Omega = \frac{1 - SI_g}{1 - SI_{avg}} \quad \text{eq. 5}$$

Hence,  $\Omega$  increases from zero to one when the grain structures changes from random to perfectly aligned [16]. Similar parameter used to describe the degree of alignment is the ratio of the total length of oriented lines in the microstructure to the total length of all lines,  $\Omega_{1,2}$  [21]. This ratio was introduced by Saltykov and for our case it is equal to [21]:

$$\Omega_{1,2} = \frac{L_2(a=0) - L_2(a=90)}{L_2(a=0) + 0.571 L_2(a=90)} \quad \text{eq. 6}$$

The  $\Omega_{1,2}$  is zero for a random structure and approaches one for structure with highly oriented and elongated grains. However, it is not guaranteed that the structure is random when  $\Omega_{1,2}$  is zero because eq. 6 is strictly valid only for the partially oriented straight lines and not curves. We therefore prefer  $\Omega$  defined by eq. 5, as a more precise measure of the particle alignment.

Since old and new alloys were partially recrystallized, their recrystallization levels were assumed to be equivalent to the area fractions of the recrystallized grains. The recrystallized grains were identified as the ones which were (1) elongated and positioned along the grain boundaries of the equiaxed ones, (2) appeared lighter under the optical microscope due to the absence of the subgrain networks and (3) contained more constituent particles.

### *Particles and Pores*

Both particles and pores were measured at the center plate locations on the TL, ST and LS planes in all alloy variants and, additionally, at the surface and quarter depth location for the old and new alloys, Table III. All characterizations included quantifications of the global descriptors such as volume fractions, spatial distributions and alignments and the measurements of the characteristics of the individual features, such as sizes, shapes and orientations.

All metallographic samples were prepared by mechanical grinding to a surface finish of 600 grit using wet SiC paper, followed by polishing on a felt wheel with 1  $\mu\text{m}$  and then 0.25  $\mu\text{m}$  diamond pastes mixed with ethanol. This procedure provided a clean surface with little or no particle pull-outs. Measurements of porosity and constituent particles were made from the optical micrographs taken from as-polished specimens to avoid distortions of shapes and number-densities by etching. A few SEM micrographs were also taken and used in characterizing particle shapes.

The magnifications used was 900X for the old and new alloys and 100X for the low porosity and thin plate variants. The 900X was chosen as a compromise between efficiency and accuracy. It gave resolution limit in the order of 0.5  $\mu\text{m}$ , and allowed for detection of about 2000 constituent particles on a scan area of the order of 1.2  $\text{mm}^2$  for each of the nine test planes. The number of pores detected at 900X in the alloys was

about 190, which corresponds to a search area of  $\sim 2.5 \text{ mm}^2$  for each plane. The area examined for pores in the old and new alloys was twice that for the constituents because of the pores' lower volume fractions. The magnification used for the low porosity and thin plate alloys was changed to 100X to improve statistical accuracy of the results. Lower magnification assures (1) increased size of the search area, (2) detection of ample number of large particles and pores and (3) improvement of the accuracy at the right tail of the particle and pore size distributions. The resolution limit was in this case about  $5 \mu\text{m}$  for each of the three characterized plane sections in the low porosity and thin plates the scan area was in the range of  $20 \text{ mm}^2$  which resulted in the detection of from 20 to 90 pores and from 200 to 1200 particles per section. As will be discussed later in the report, the change in the resolution limit did not adversely affect the fatigue relevant region of the size distribution.

The micrographs obtained from the metallographic examinations were digitized and saved as image files for subsequent analysis using our custom-made image analysis program. The program measured linear intercepts, determined individual and average pore and particle shapes, orientation indices, aspect ratios and volume fractions. It also estimated parameters of the normal and lognormal approximations of the size distributions[22], constructed tessellation cell networks (described in sections dealing with spatial distributions) and analyzed particle spatial distributions. The particle and pore sizes and shapes on plane sections were measured using the same methods as for the grains [16, 23, 24, 25, 26]. Size differences between the alloys have been quantified using the standard one-factor analysis of variance (ANOVA).

### *True Three-Dimensional Size Distributions*

Complete characterization of the second phase features requires estimation of their true three-dimensional (3-D) size and spatial distributions. There are number of techniques suitable for this purpose with the earliest dating back to 1925 [27]. Exhaustive review of all pre-1970s methods have been given by Underwood [23]. Among the proposed methods the DeHoff's approach [28] allows for the estimation of the size

distribution of cylindrical ellipsoids and DeHoff and Bousquet [29] method for the estimation of size distribution of triaxial ellipsoids from their linear intercepts. However, the use of both methods is not always justified because they require that all ellipsoids have the same shape. Since particles in the engineering materials are not always ellipsoidal and do not always have identical shapes, these method should be used with caution.

In the 1980s, a number of stereological methods for obtaining 3-D distributions for arbitrary oriented particles with different shapes have been proposed [30,31,32,33,34,35]. The point-sampled intercept method (PSIM), which gives only the average value and not the distribution, was one of them [36,37,38]. Its advantage was that it did not required assumption about particle shapes[30]. The basic averaging formula used by PSIM has the form:

$$\bar{v}_v = \frac{\pi}{3} l_o^3 \quad \text{eq. 7}$$

which relates  $\bar{v}_v$ , the volume-weighted average particle volume, to  $l_o$ , the point-sampled intercept length. Although eq. 7 gives an unbiased estimate of the average particle volume, it is important to emphasize that  $\bar{v}_v$  is not a conventional number average  $\bar{v}_n$ , but a volume weighted average calculated as:

$$\bar{v}_v = \frac{[\bar{v}^2]}{\bar{v}_n} = \frac{\sum_{i=1}^n v_i^2}{\sum_{i=1}^n v_i} \quad \text{eq. 8}$$

where  $\bar{v}_i$ 's are volumes of individual particles. Although PSIM method needs no assumption about the particle shapes it requires isotropic structure[37]. A very general method for estimating 3-D distributions of sizes and shapes from size measurements made on plane sections has been recently proposed by T. -S. Liu *et al.*[39]. The features were modeled in this case as prolates or oblates with variable aspect ratios and orientations (the method reduces to that of DeHoff [28] for particles with identical shapes). Karlsson and Sandstrom [40] proposed similar method for evaluating 3-D size distribution of inclusions

from their 2-D sections. They assumed that all inclusions were ellipsoidal, had non-cylindrical symmetry and that they were aligned and had identical shape factors .

We have implemented two procedures for transforming 2-D particle and pore measurements into their 3-D size distributions. The first procedure assumed that all measured features were ellipsoidal, had identical aspect ratios but varied in sizes. A program developed for this purpose generated a 3-D model microstructure with the ellipsoids randomly placed in space. The program then sectioned the model sample along TL, LS and ST planes, estimated the ellipsoid intercept lengths for each plane and compared result with the experimental data for the 7050 alloys. The mean and the standard deviation of the ellipsoids size distribution was then adjusted to minimize the normalized error,  $R_e$ , defined as:

$$R_e = \frac{1}{6} \sqrt{\sum_{i=1}^3 \left( \left( \frac{\Delta\mu_{LII,i}}{\mu_{LII,exp,i}} \right)^2 + \left( \frac{\Delta\sigma_{LII,i}}{\sigma_{LII,exp,i}} \right)^2 \right)} \quad \text{eq. 9}$$

where  $\Delta\mu_{LII}$  and  $\Delta\sigma_{LII}$  are the differences between the means and standard deviations of  $L_{II}$  for the experimental and simulated microstructures and  $\mu_{LII,exp,i}$  and  $\sigma_{LII,exp,i}$  are the mean and standard deviation of the experimental  $L_{II}$ . The  $i = 1, 2$  and  $3$  correspond to the ST, LS and TL planes respectively. The ellipsoids in the model were assumed to be the best approximation for the particles or pores in the real alloy for the minimum  $R_e$ . We note that the expression for  $R_e$  is not unique and other forms could be also be used.

The input to the 3-D numerical model includes ellipsoid (1) size distribution, (2) spatial distribution and (3) alignment. Each ellipsoid is described by the largest samiaxes,  $A$ , and two aspect ratios  $A/B$  and  $A/C$  where  $B$  and  $C$  are ellipsoid minor semiaxes. The  $A$  values are generated according to either normal or lognormal distribution, depending which gives the better fit [41]. The aspect ratios are adjusted from 1 to  $\infty$  to accommodate the shapes varying from a sphere to a line. To generate random spatial dispersion of ellipsoids, the coordinates of the center of each ellipsoid are independently and randomly selected within the specimen volume. Each location is then checked for

overlapping and if overlapping takes place, the location is rejected and a new random location generated again. The spatial distribution of the ellipsoids is therefore not exactly random but pseudo or non-intersecting random. The orientations of ellipsoids are also independently and randomly chosen and they can be varied from 100% aligned to random. The degree of alignment is assumed to be known a priori, and treated as an input parameter. The randomness of the generated microstructures has been tested by comparing characteristics of the simulated microstructure consisting of 1,000 identical spheres with the theoretical expectations. In particular, the theoretical average intercept length  $L_3$  is for spheres equal [23]:

$$L_3 = \frac{4V}{S} = \frac{4r}{3} \quad \text{eq. 10}$$

where  $V$ ,  $S$  and  $r$  are sphere volume, surface area and radius respectively. The difference between  $L_3$  obtained from eq. 10 and the one obtained for our model microstructures differed be no more than 2.9%.

The second procedure for the 2-D to 3-D size conversions was based on the DeHoff's two-parameter distribution method [23,42]. This particular methodology, and its extension, are described in details in Appendix D and E. It was selected because it is compatible with the fatigue models demand for the continuous flaw size distribution functions[43]. The pores and particles were again assumed as the same-shape triaxial ellipsoids and their 3-D size distributions were assumed *a priori* as lognormal, as supported by numerous experimental evidences [44]. It was also expected that they could have either random orientations or be partially aligned with one major axes parallel to the rolling plane normal, Appendix D Figure 1a. Since each of these cases require slightly different formulas for 2-D to 3-D conversions, they will be dealt with separately below.

For the same-shape particles or pores randomly orientated in space the procedure for estimating moments of their lognormal size distributions is well known. It was developed by DeHoff [44] and it requires measurement of the three standard microstructural characteristics, namely

$N_A$  - the number of particles per unit area,

$N_L$  - the number of particle intercepts per unit length of a random test line,

$P_P$  - the fraction of random points within the phase of interest.

Knowing  $N_A$ ,  $N_L$  and  $P_P$  for particles or pores allows for the estimation of the parameters of the true 3-D lognormal size distributions from expressions:

$$\ln \mu_{D_a} = -2.5 \ln N_A + 4 \ln N_L - 1.5 \ln P_P + \ln \left( \frac{16 k_1^{2.5} k_3^{1.5}}{k_2^4} \right) \quad \text{eq. 11}$$

$$\ln^2 \sigma_{D_a} = \ln N_A - 2 \ln N_L + \ln P_P + \ln \left( \frac{2 k_2^2}{4 k_1 k_3} \right) \quad \text{eq. 12}$$

where  $\mu_{D_a}$  and  $\sigma_{D_a}$  are the geometric mean and geometric standard deviation of the 3-D maximum diameters and  $k_1$ ,  $k_2$  and  $k_3$  are the unitless shape factors, dependent on the feature shape. The shape factors represent proportionality constants in the relations [44]:

$$D_V = k_1 a \quad \text{eq. 13}$$

$$S = k_2 a^2 \quad \text{eq. 14}$$

$$V = k_3 a^3 \quad \text{eq. 15}$$

where  $D_V$ ,  $S$  and  $V$  are the average feature caliper diameter, surface area and volume, respectively and  $a$  is a measure of feature size. To find these shape factors for triaxial ellipsoids one needs explicit forms of relations 13 to 15. From the three, only the ellipsoid volume can be expressed in a close form as:

$$V = \frac{\pi}{6} D_a D_b D_c = \frac{\pi}{6} \frac{D_a^3}{q_{ab} q_{ac}} \quad \text{eq. 16}$$

where  $D_a$ ,  $D_b$  and  $D_c$ , are ellipsoid diameters, Appendix D Figure 1a, and  $q_{ab}$  and  $q_{ac}$  are aspect ratios

$$q_{ab} = \frac{D_a}{D_b} \quad \text{eq. 17}$$

$$q_{ac} = \frac{D_a}{D_c} \quad \text{eq. 18}$$

Comparing equations 15 and 16, assuming  $a \equiv D_a$ , gives:

$$k_3 = \frac{\pi}{6q_{ab}q_{bc}} \quad \text{eq. 19}$$

The caliper diameter,  $D_V$ , can be calculated precisely only from the integral form.

However, a good approximation of that integral is a formula [45, 46]:

$$D_V \cong \frac{1}{3}(D_a + D_b + D_c) = \frac{D_a}{3} \left( 1 + \frac{1}{q_{ab}} + \frac{1}{q_{ac}} \right) \quad \text{eq. 20}$$

which gives an error of the order of only 3%. Consequently,

$$k_1 \cong \frac{1}{3} \left( 1 + \frac{1}{q_{ab}} + \frac{1}{q_{ac}} \right) \quad \text{eq. 21}$$

The expression for the triaxial ellipsoid surface area is also implicit, but the following formula:

$$S \cong \pi \left( \frac{D_a + D_b + D_c}{3} \right)^2 = \frac{\pi D_a^2}{9} \left( 1 + \frac{1}{q_{ab}} + \frac{1}{q_{ac}} \right)^2 \quad \text{eq. 22}$$

is recommend by us as an adequate approximation. The last shape factor is then equal to:

$$k_2 \cong \frac{\pi}{9} \left( 1 + \frac{1}{q_{ab}} + \frac{1}{q_{ac}} \right)^2 \quad \text{eq. 23}$$

Knowing  $k_i$ 's, the geometric mean and standard deviation of ellipsoid diameters can be obtained from eqs. 11 and 12. Subsequently, the average maximum diameter  $\bar{D}_a$ , volume density  $N_V$ , and volume fraction  $f$ , can be estimated from expressions[44]:

$$\bar{D}_a = \mu_{D_a} \exp \left( \frac{1}{2} \ln^2 \sigma_{D_a} \right) \quad \text{eq. 24}$$

$$N_V = \frac{N_A^3 P_P}{N_L^3} \frac{k_2^3}{8k_1^3 k_3} \quad \text{eq. 25}$$

$$f = P_P \quad \text{eq. 26}$$

All that is required to find the characteristics of the randomly oriented same-shape triaxial ellipsoids are then the values of  $N_A$ ,  $N_L$  and  $P_P$  and the aspect ratios  $q_{ab}$  and  $q_{ac}$ . The first three quantities are readily available from the measurements on the random planes. The same holds for aspect ratio  $q_{ab}$ , equal to the largest aspect ratio observed for the plane sections. The second aspect ratio,  $q_{ac}$ , is not accessible directly from the plane section data. Possible ways to proceed have been discussed by DeHoff *et al* [29].

The conversion procedure is slightly different for ellipsoidal features aligned parallel to the rolling plane but with random rotations about the rolling plane normal, see Appendix E. Considering the nature of the rolling deformation, it is expected that for each ellipsoid its largest two diameters,  $D_a$  and  $D_b$ , will be parallel to the rolling plane. The TL test planes will cut such ellipsoids parallel to the  $D_a - D_b$  plane and all obtained ellipsoidal cross-sections will have aspect ratios  $q_{ab}$ . As shown in the Appendix E, mathematically this case is equivalent to the one of the polydisperse spheres [47]. The first two moments of the maximum diameters of the ellipsoids, the parameters of their lognormal size distributions and their volume fraction are therefore given by relationships[48]:

$$\overline{D_a} = \frac{\pi}{2} \left( \overline{\frac{1}{d_{aTS}}} \right)^{-1} \quad \text{eq. 27}$$

$$\overline{(D_a^2)} = 2 \overline{d_{aTS}} \left( \overline{\frac{1}{d_{aTS}}} \right)^{-1} \quad \text{eq. 28}$$

$$\ln \mu_{D_a} = 2 \ln \overline{D_a} - \frac{1}{2} \ln \overline{(D_a^2)} \quad \text{eq. 29}$$

$$\ln^2 \sigma_{D_a} = \ln \overline{(D_a^2)} - 2 \ln \overline{D_a} \quad \text{eq. 30}$$

$$f = \frac{\pi N_{A-TS}}{4q_{ab}} \overline{(d_{aTS}^2)} \quad \text{eq. 31}$$

where  $\overline{d_{aTS}}$  is the average maximum diameter of the ellipsoidal cross-sections,  $\overline{(d_{aTS}^2)}$  average of their squares,  $\overline{(1/d_{aTS})}$  their harmonic mean and  $N_{A-TS}$  the number of cross-sections per unit area, all for the TS planes. This means that size distribution of the ellipsoids, their volume fraction and one of the aspect ratio can be obtained just from the measurements on the TS planes alone. Estimations of the volume density,  $N_V$ , and the second aspect ratio,  $q_{ac}$ , require additional measurements of the diameters  $d_{ci}$  on any of the planes perpendicular to the rolling plane, such as LS or TS. The average size  $\overline{D_c}$  is then estimated using relation identical to eq. 27 [47, 48]:

$$\overline{D_c} = \frac{\pi}{2} \overline{\left(\frac{1}{d_c}\right)}^{-1} \quad \text{eq. 32}$$

The aspect ratio,  $q_{ac}$ , and  $N_V$  can be subsequently obtained from relations, Appendix E:

$$q_{ac} = \frac{\overline{D_a}}{\overline{D_c}} \quad \text{eq. 33}$$

$$N_V = \frac{N_{A-TS}}{\overline{D_c}} \quad \text{eq. 34}$$

Characterization of the same-shape triaxial ellipsoids with one of the axes parallel to the rolling plane normal requires then measurements of:

- (1) major diameters, aspect ratios and area densities of the ellipsoidal cross-sections on the TS-planes,
- (2) diameters parallel to the rolling plane normal on the planes normal to the rolling plane.

Because of the difficulty of obtaining aspect ratio of the randomly orientated ellipsoids from the direct measurements, we have developed an alternative numerical procedure. The basic steps of the method are (1) generation of a model 3-D specimen with identical ellipsoids randomly oriented and distributed in volume, (2) cutting the model specimen with random planes to obtain aspect ratios of ellipses on 2-D sections, and (3) comparing

the obtained distributions of aspect ratios with those for the real particles or pores. The shape of the model ellipsoids is then adjusted until the difference between the model and experimental aspect ratios is minimum. The final aspect ratios of the model are then assumed as the true 3-D averages. The model specimen is set to contain 800 particles or pores and during each trial the computer generates ninety 2-D sections. The minimization procedure is moderately fast and it takes about 10 to 15 minutes on the IBM RS/600 model 560 computer to obtain conversion.

### *Spatial Distributions*

Characterizations of the particle and pore populations for fatigue modeling purposes should always provide some information about the patterns describing their 3-D spatial distributions. Although such determinations are not possible without knowing the 3-D spatial coordinates of object centers, adequate information can be inferred from the plane section data.

The spatial distributions can be usually classified as regular, random, clustered and random with clusters. The regular distribution is easy to recognize as the features are arranged in a distinct pattern. To specify its character it is only necessary to specify the features point density and to identify the pattern. The random spatial distributions can be characterized by the features' area density and the parameters of the Poisson distribution describing their spacing. Clusters are the most difficult to ascertain. The available methods have been recently reviewed by Vander Voort [49]. Among them the number density [50], nearest neighbor spacing [51,52,53], Voronoi (Dirichlet) tessellation [50,54,55,56,57] and image amendment techniques [58,49] are the most frequently used. In the number density approach, the mean number of particles per unit area,  $N_A$ , and its standard deviation are found in successive fields. An increase in the standard deviation for a given field indicates clustering. In the image amendment method, all particles separated by a distance less than or equal to a critical spacing are fused together. The number of fused aggregates represents then a measure of clustering. In the nearest neighbor method, the ratio of the means and variances of the nearest-neighbor distances for the real and the

equivalent random microstructures are used [51]. Similarly, in the Voronoi tessellation method the distribution of the 2-D tessellation cell areas, and the cells' area variances are used to identify the particle arrangement. The last two methods are related because near-neighbors can be uniquely identify after constructing Voronoi tessellation -- they have been used in this study and will be discussed in details below. There have been also attempts to use 3-D tessellation to characterize particle spatial distribution [59,60,61]. In this case the cells form space-filling ensemble of irregular polyhedra [62,63,64,65]. The utility of this last method is however limited because it requires knowledge of the spatial coordinates of particle centers.

In this study we used the Voronoi tessellation constructions to quantify the spatial distributions of the second phase features[50-57]. The 2-D Voronoi cells are plane-filling polygons, with the sides constructed as the bisectors of the lines connecting centers of the neighboring features. Each polygon contains then one feature and the ratio of the feature area to its polygon area is defined as the "local area fraction". With the help of tessellations the spatial distribution of particles and pores can be analyzed by studying their local area fractions, averages and standard deviations of cell sides or cell areas, etc.\* [50-57]. From that group of methods we selected the nearest neighbor spacing method for our spatial distribution characterizations [51]. This method utilizes two indexes, Q and R, defined as follows:

$$Q = \frac{\text{Observed Nearest Neighbor Distance}}{\text{Expected Nearest Neighbor Distance}} \quad \text{eq. 35}$$

$$R = \frac{\text{Observed Nearest Neighbor Distance Standard Deviation}}{\text{Expected Nearest Neighbor Distance Standard Deviation}} \quad \text{eq. 36}$$

where the expected values are calculated by assuming a random structure with the same point density as the experimental one. To identify different types of spatial distribution the following guidelines are used:

---

\* It should be kept in mind that the obtained results are approximations, as ideally only three dimensional Voronoi tessellations should be used for spatial characterizations.

- 1) for the clustered distribution,  $Q < 1$  and  $R < 1$ ;
- 2) for regular distribution  $Q > 1$  and  $R > 1$ ;
- 3) for random distribution with clusters  $Q < 1$  and  $R > 1$ ;
- 4) for totally random distribution  $Q = 1$  and  $R = 1$ .

In addition to Q - R method, we also evaluated the utility of the tessellation cell shape method to identify spatial distribution patterns. In this method, the sizes and shapes of the tessellation cells are analyzed using the same methods as for the second phase objects.

The advantage of this approach, originally suggested by Wary et al. [52], is that it is sensitive to the fluctuations in the cell orientations. The tessellation cell shape method is also useful for analyzing the orientations of the second phase clusters. This is because in an ideal clustered structure the change of the cluster location and /or orientation does not affect the nearest neighbor spacing, hence Q and R remain unchanged. The shapes of tessellation cells are on the other hand sensitive to the changes in the anisotropy of the cluster orientations and spacing and the cells'  $d-\alpha$  curves and  $SI_g$  indexes can be used to analyze those changes. The information on the spatial distributions provided by the cell shape and the Q-R method are then complementary: the former gives information about spatial isotropy while the latter characterizes the spatial distribution type.

## Results

### *Grains and Subgrains*

Typical microstructures of the 7050-T7451 alloys are shown in Figure 3. The alloys are partially recrystallized with grains aligned parallel to the rolling direction. The recrystallized grains appear light and elongated while the unrecrystallized ones are equiaxed with fine subgrain structure inside. The dark spots are constituent particles.

Results of the characterizations of the grain structures are summarized in Table IV through Table VII (grains were characterized only in new and old alloys). Figure 4 shows change of the recrystallization levels from the plate surface to the center in both alloys. Distributions of grain sizes are in Figure 5 and 6 while Figure 7 and 8 show average grain shapes. The recrystallization levels, Figure 4, were similar in both alloys. They varied

from 1 to 3.5 % at the plate surface to nearly 20% at the center. In the new alloy the maximum recrystallization, about 22%, was at the quarter depth. The old alloy was less recrystallized, with maximum at the center. The differences in the recrystallization levels between the alloys can be attributed to the proprietary changes in the thermo-mechanical processing and compositions.

The average sizes of the recrystallized grains, Table IV, Figure 5 and 7, were from 20 to 55  $\mu\text{m}$ . They were slightly larger in the new alloy and always the largest at the plate center as a result of higher recrystallization level in that region. Figure 5 shows size distributions of recrystallized grains obtained by scanning each grain with 1000 random intercepts. The changes of the grain intercept lengths with orientation are in Figure 7. It is apparent that recrystallized grains had pancake shapes which change very little with location.

The data for unrecrystallized grains are in Table V, Figure 6 and 8. The largest grains were in the old alloy at the quarter depth and in the new alloy at the center region. The new alloy had finer overall grain structure with the sizes ranging from 40 to 160  $\mu\text{m}$ . For the old alloy the grain sizes were between 70 to 220  $\mu\text{m}$ . Cumulative size distributions of unrecrystallized grains are in Figure 6. Figure 8 shows that the grains had high aspect ratios with large through-thickness size and shape gradients.

Since both old and new alloys were almost unrecrystallized at the surface, the grains at that location can be considered as the representatives of the original unrecrystallized structure. During recrystallization the size of the unrecrystallized grains decreases and it reflect both the original sizes and the percent recrystallization. The relation describing that interdependence has following form [18]:

$$D = D_o \sqrt{1 - f} \quad \text{eq. 37}$$

where  $D$  is the observed unrecrystallized grain size,  $f$  is percent recrystallization and  $D_o$  is the starting, i.e. true unrecrystallized grain size. Comparing the sizes of surface grain in

the old and new alloys suggests finer initial grain structure in the new alloy. The same holds for the quarter depth and the center if the grain sizes are corrected using eq. 37.

To determine the type of the grain size distributions, the data were fitted with normal and lognormal distributions using the correlation coefficient,  $R^2$ , as the discriminating factor [66]. For both alloys the size distributions turned out to be better described by the normal approximation. For example, the distribution for the unrecrystallized grains in the new alloy (LS plane, quarter depth) had  $R^2$  of 0.949 for the normal fit and only 0.848 for the lognormal one. Results of the normal fit are summarized in Table VI and Table VII. Note that the averages obtained from the fit are different from those in Table IV and Table V because of the differences in the calculation procedures. The normal nature of the grain size distributions is unexpected, as these distributions are usually lognormal. We have no explanation for that result.

The grain shapes were quantified using aspect ratios and shape indices,  $SI$ . Typical normalized intercept length  $\bar{d}$  vs scan angle plots used in those measurements can be found in ref. 16 and 16. The obtained aspect ratios were between 1.8 and 4.3 for the unrecrystallized and from 1.7 to 3.9 for the recrystallized grains. The average shape indexes,  $SI$ , were 0.66 and 0.65 for the recrystallized grains, and 0.62 and 0.61 for unrecrystallized grains in the new and old alloys respectively. The results for all test planes and location have been compiled in Table IV and Table V. They suggests that the grains have pancake shapes which is consistent with the average shapes shown in Figure 7 and 8.

Micrographs of the typical grain structures of the thin and the low porosity plate alloys can be found in ref [15]. These alloy variants were also partially recrystallized. As for the old and new alloys the unrecrystallized grains were flat, elongated in the rolling direction with fine subgrain structure inside. The unrecrystallized grains were smaller and more equiaxed. The grain sizes were not measured because they were not required for our life predictions models.

The unrecrystallized grains in all alloy variants had fine subgrain structures. These subgrains were similar in all alloys hence they were measured only on the TL planes in the new alloy. The subgrain average size was  $6.2\text{ }\mu\text{m}$  and their size distributions can be found in Appendix B and C and refs. 16 and 16. The subgrain aspect ratios were about 1.05, which means that they can be considered as equiaxed. However, as detailed in Appendix B and C, their morphology can be best represented by an arrays of elongated octagons with the aspect ratios of  $\sim 1.10$ . The subgrains did not have preferential orientations and their orientation parameter,  $\Omega$ , was only 3.3%.

We have also evaluated the utility of spherical harmonics for characterizing grain structures. In this method the grains are assumed to be ellipsoidal with semiaxes obtained from the plots in Figure 7 and 8. Results from this method have been reported in ref. 14. We did not proceed beyond the preliminary stage because the obtained information were incompatible with the input data required by the life prediction models.

### *Pores*

Pores were characterized on all planes and at all locations for the old and new alloys and on all planes at the center location for the low porosity and thin plates Table III. The results of the measurements, including the numbers of detected pores and the area scanned, are compiled in Table VIII. The obtained pore volume fractions were 0.16% for the old, 0.11% for the new alloys and 0.035% and 0.018% for the low porosity and thin plate respectively (the observed order of magnitude decrease was partially a result of the change of the magnification used in the measurements). The through-thickness volume fraction gradients for the old and new alloys are shown in Figure 9, with each point representing the average for TL, LS and ST planes. As expected, the volume fractions are the highest at the center and decrease towards the surface. The porosity levels are practically the same at the surface and quarter-depth locations, which means that the reduction of the porosity levels came mainly from the elimination of pores at the center-plate region.

Typical collection of the pore sections obtained from the metallographic sections is shown in Figure 10. These particular pores were found on the ST planes at the center of the old alloy. Results of the quantitative characterizations of pores for all alloys and planes are summarized in Table VIII with the sizes represented by the average intercept lengths,  $L_{II}$ . The change of the intercept lengths with directions,  $L_2(\alpha)$ , are in Figure 11 and 12. These curves are ellipsoidal and illustrate pore 3-D profiles. Note that information provided by  $L_{II}$  and  $L_2(\alpha)$  plots are complimentary:  $L_{II}$  represents the overall average size while  $L_2(\alpha)$  provides information about size variation with orientation and location.

Since the magnifications used in characterizing old and new alloys were different from those for the low porosity and thin plates, the results for each group of alloys need to be first considered separately. For the old and new alloys (magnification 900X) the average  $L_{II}$  values were 3.4  $\mu\text{m}$  and 3.5  $\mu\text{m}$  respectively. The  $L_{II}$  through-thickness gradients for these alloys are in Figure 13. For the old alloy the pores are the smallest near the plate surface and their size increases with the distance from surface. For the new alloy, the smallest pores are also near the plate surface but there is almost no size difference between quarter-depth and the center location. Considering the variation of pore volume fractions, Figure 9, it appears that both alloys have strong morphology gradients with the largest pores and volume fractions at the plate center. Cumulative 2-D pore size distributions for the old and new alloys are in Figure 14. The size measure used there was the average intercept length,  $L_{II}$ . Comparing pore sizes and size ranges for both alloys it seems that in the new alloy the pores are not only smaller but also have narrower distribution. To quantify the differences the size distributions were fitted with both normal and lognormal distributions, using appropriate probability plots. The lognormal distribution gave always better fit with  $R^2$  close to one. The fitting results are in Table IX and typical frequency distribution and the lognormal fit curves are in Figure 15.

The differences between the pore average intercept lengths,  $L_{II}$ , in the new and the old alloy have been evaluated using the one factor ANOVA. It was determined that the null hypothesis that the pore sizes for both alloys have the same mean could not be rejected, and that the average pore sizes in the two alloys were statistically the same at 95% probability. However, the tails of the size distributions were very different, especially at the larger pore sizes. For example, the old alloy had 23 pores with diameters larger than 10  $\mu\text{m}$  while the new one had only 9. Since the fatigue crack initiate from the largest pores, it is the upper tail of the size distribution, not the average value, that controls fatigue behavior. The tail differences explain then the differences in the fatigue behaviors of the old and new alloys and illustrate the need to perform a complete quantitative microstructural analysis to detect them.

Results of the characterizations of pores in the thin and low porosity plate alloys (magnification 100X) are also in Table VIII. The average sizes for the LS, LT and ST planes were for both materials about 11 to 12  $\mu\text{m}$ . It should be however kept in mind that those are the averages for the pores which are grater than the resolution limit of 5  $\mu\text{m}$ . The pore area fractions were 0.018 and 0.035 % for the thin and low porosity plates respectively and their area densities varied from 2.0  $\text{mm}^{-2}$  for the thin to 3.3  $\text{mm}^{-2}$  for the low porosity plates. In both materials the pores cross-sections were elliptical with an average aspect ratio of about 1.3. Their shape indexes were consistent with those for the ellipses.

The average pore shapes and size distributions for the low porosity and thin plates are shown in Figure 12 and 16. For both materials the 5  $\mu\text{m}$  resolution limit appears as an imaginary vertical asymptote in Figure 16. Some percentage of small pores was then undetected which means that the average sizes in Table VIII are overestimations. However, the number of detected large pores increased, improving the accuracy of the right tail of the size distribution. This tail will be used later in the report for predicting size distributions of the fatigue crack initiating pores using extreme value approach. The accuracy of the data in the right tail is then critical to the accuracy of the predictions,

which justifies use of the lower magnifications. It is also important to point out that despite the error in the average due to the resolution limits<sup>1</sup>, the right tails of the censored and true distributions converge. The expression for correcting the data for left censoring is well known and it is given by relation [67]:

$$F(D) = F_{cen}(D, D_{min})[1 - F(D_{min})] + F(D_{min}) \quad \text{eq. 38}$$

where  $F(D)$  - true or corrected cumulative distribution

$F(D, D_{min})$  - measured or censored cumulative distribution

$D_{min}$  - resolution limit

$F(D_{min})$  - cumulative fraction of censored or not detected features.

Examples of the corrections using eq. 38 are shown in Figure 17. Since the fractions of undetected pores were not known, they were set to the expected values to illustrate the directions and magnitudes of the trends. Results show that even with the large percentages of missing data the right distribution tail, and particularly its slope, closely follows that of the real data.

Comparison of the pore size distributions for the low porosity and thin plates suggests, Figure 16, that although the thin plate has less pores it contains more large ones. In the thin plate the pores with the largest cross-sections were observed on the LS plane while in the low porosity variant the largest pores were seen on the TL section. Shapes of the size distributions on different sections suggests that the pores can be approximated as prolate spheroids. The major axes of the spheroids are however not completely aligned with the rolling direction. In the thin plate they deviate from the perfect alignment by random rotations about transverse direction while for the low porosity plate these rotations are about the plate normal. This is the reason why in Figure 12 these particular pore sections are the most circular. For the thin plate alloy the pore true average aspect ratio can be therefore obtained from the data for the LS plane, and it is equal 1.43. For

---

<sup>1</sup> Such limit is also referred to as left censoring.

the low porosity alloy the pore cross-sections on the LT plane are the most representative giving the pore aspect ratio of 1.49.

The pore 2-D to 3-D size conversion were only performed for the old and new alloys. They were not done for low porosity and thin plates because these conversions turned out to be not critical for the fatigue modeling purposes. Before performing the transformations it was necessary to quantify pore average shapes and orientations. The shapes were characterized using the aforementioned  $d$ - $\alpha$  plots [16]. Figure 18 shows typical  $d_g$  and  $d_{avg}$  vs. scan angle curves used in the analysis. The average shape indexes for pores on all test planes were 0.815 and 0.831 for the new and old alloys respectively conforming their ellipsoidal shapes. The corresponding average pore aspect ratios, equal to the harmonic mean of the  $d$ -values at  $90^\circ$ , were 1.45 for the old and 1.51 for the new alloy. These values are in agreement with aspect ratios obtained from the direct measurement listed in Table VIII, again supporting assumption of the ellipsoidal shapes. The through-thickness average shape index  $SI$  gradients are in Figure 19. The changes were small and the shape factors were slightly smaller for the new alloy, suggesting more elongated pore shapes.

The orientation factors,  $\Omega$ , for pores on different test planes, Table VIII, varied from 0.11, which corresponds to almost random structure, to 0.65 which indicates slight alignment. The average values were 0.40 for the new and 0.34 for the old alloy. Since  $\Omega$  increases to one as the pores become more and more elongated and aligned, pore orientations in the studied alloys can be considered as random. Examples of the change of the average orientation factor  $\Omega$  with location are shown in Figure 20. Alternatively, the pore orientations can be determine from the pore orientation distribution plots, Figure 21. Analysis of such plots for all sections in both alloys conformed random distribution of pore axes.

Results of the 3-D pore size estimations using numerical method are shown, together with the original experimental data, in Figure 22. The 3-D size measures used

are the maximum intercept lengths,  $L_{II,max}$ , obtained from the planes containing 3-D ellipsoid centers and the major axes. Table X lists the calculated means, standard deviations and aspect ratios of the 3-D lognormal size distributions for both alloy. As expected, the maximum average intercept lengths for the 3-D ellipsoids are larger than those for their 2-D experimental sections. This is because the diameter of any 2-D section is either smaller or equal to the maximum 3-D diameter. The experimental 2-D data should then approach the 3-D values at larger pore sizes, as it is indeed the case in Figure 22. The goodness of fit of the estimated 3-D size distributions were evaluated using normalized errors,  $R_e$ , defined earlier. Alternatively, the error can be assessed by comparing the 2-D experimental size distributions with those obtained by sectioning model 3-D microstructure. Results of such comparisons are in Table X, showing that the experimental and simulated distributions are similar over the entire size range, proving validity of the model. We again emphasize here that the expression for the normalized error  $R_e$  used in the calculations is not unique. However, the obtained approximations of the 3-D pore sizes have sufficient accuracy for the mechanical behavior models.

Random orientations of pore axes also justified the use of the DeHoff's 3-D conversion method to find pore true size distributions. Since the required average aspect ratios were in this case inaccessible from direct measurements, they were estimated using our 3-D microstructural computer model. The results from that model are in Table XI and Table XII, showing small differences in aspect ratios between different locations. The parameters of the 3-D pore size distributions were estimated using eqs. 11 and 12 with average  $N_v$ ,  $N_L$  and  $P_p$  obtained from the TL, LS and ST planes ( $N_L$  was averaged for scan angles from 0 to 90 °). The resulting  $\mu_a$  (average  $A$ ) and  $\sigma_a$  (standard deviation), and the two calculated aspect ratios, are listed in Table XII. Additional analysis of the results, including comparisons of the obtained lognormal size distributions can be found in Appendix D.

To verify the results from the DeHoff's method, the average 3-D intercept lengths,  $L_3$ , for pore true 3-D size distributions were compared with the 2-D experimental

values of  $L_{II}$ . The theoretical ratio  $L_3/L_{II}$  is 1.03 for the spheres randomly distributed in volume. For the ellipsoids with aspect ratios in the ranges similar to those for the old and new alloys, this ratio should be slightly less than one. To obtain the  $L_3/L_{II}$  ratio, the 3-D average intercept lengths were calculated from relation [23]:

$$L_3 = \frac{4V}{S} \quad \text{eq. 39}$$

which combined with eqs (16) and (22) gives:

$$L_3 = \frac{12D_a}{q_{ab}q_{ac}\left(1 + \frac{1}{q_{ab}} + \frac{1}{q_{ac}}\right)^2} \quad \text{eq. 40}$$

This expression was used to calculate the values of  $L_3$  for the  $D_a$ -values generated according to the true size distributions  $\mu_a$ - $\sigma_a$ . Results are in Table XIII together with the  $L_{II}$  values obtained experimentally. Figure 23 shows typical plots of the generated  $L_3$  distributions and the measured  $L_{II}$  distributions for pores in the new alloy. Inspection of the results revealed that only in few cases the values of  $L_3$  are smaller than  $L_{II}$ . The  $L_3/L_{II}$  ratios are in most cases larger than one, contrary to the expectations. This discrepancy illustrates the approximate nature of the 2-D to 3-D conversions; the 3-D results are sensitive to the assumptions about the shapes of the measured features, assumed size distributions and to the scatter in the experimental data. The errors are cumulative and there is no direct method for their estimation.

### *Constituent Particles*

The 7050-7451 plate alloys have two types of constituent particles:  $\text{Al}_7\text{Cu}_2\text{Fe}$  and  $\text{Mg}_2\text{Si}$ . Since both types were found at the fatigue crack initiation sites they were characterized without distinction to their chemical compositions using the same methods as for pores. For the old and new alloys the particles were measured at 900X for all three through-thickness locations. For the low porosity and thin plates they were measured only at plate centers at 100X. The obtained average volume fractions, numbers of detected particles and the number of fields used in the measurements are listed in Table XIV. The

average particle area fractions were 0.64% for the new and 0.70% and 0.75% and 0.24% for the low porosity and thin plates respectively. The volume fraction results and their through-thickness gradients are in Figure 9.

Because of the differences in the magnifications used during measurements, the particle data for the new and old alloys will be analyzed separately from those for the low porosity and thin plates. The representative collection of the constituent particles sections found on the ST plane at the center of the old plate alloy is shown in Figure 24. The average sizes of such cross-sections, measured on all nine test planes, were  $4.02\text{ }\mu\text{m}$  for the new and  $4.77\text{ }\mu\text{m}$  for the old alloy, Table XIV. The changes of the average intercept lengths with direction are in Figure 25 and 26. The sizes are the smallest on the ST planes which can be attributed to particle elongated shapes resulting from rolling. A null hypothesis that the constituent sizes in the new and old alloy were the same had to be rejected for 5% significance level. The size of particles in the old alloy is, at 95% probability level, larger than that in the new one. The through-thickness size gradients are shown in Figure 13. The sizes increase with the distance from the surface and the particles are in general greater than the pores. The size fluctuations are most likely due to the compositional gradients and temperature variations during the thermal-mechanical processing. The cumulative 2-D size distributions are shown in Figure 27 and 28. As for pores, these size distributions were also lognormal with  $R^2$  close to one. The best fit lognormal distribution parameters are listed in Table XV.

Estimations of particle true sizes required assessments of their shapes and orientations. The  $d-\alpha$  plots used for this purpose were similar to those shown in Figure 18. They showed that for the old alloy the particles had average shape index,  $SI$ , of 0.74 and the aspect ratio 1.86. For the new alloy these values were 0.68 and 2.28 respectively, Table XIV. The through-thickness shape index gradients are shown in Figure 19 and examples of the changes of the shape indexes with test plane orientation can be found in Appendix D, Figure 4a. All obtained  $SI$  values clearly support ellipsoidal approximation of the particle shapes. These values were lower than those for pores suggesting that particles

had more elongated shapes. The average orientation factors,  $\Omega$ , for the constituents were 0.52 for the new and 0.43 for the old alloy, Table XIV. Changes of  $\Omega$  from the surface to the center are in Figure 20 and in Appendix D, Figure 4b. Note that for the surface and quarter depth locations they are similar to those for pores. The particle orientations at those locations can be then assumed as random. For the plate center region, the orientation factors were high for the LS and ST planes and low for the TL sections. This means the particles were aligned parallel to the rolling plane, but had random rotations about the rolling plane normal. In other words, one of the particles axes was parallel to the rolling plane normal. Based on the  $\Omega$ -values in Table XIV, the same type of particle alignment has been present throughout the new plate.

Results of the estimations of particle 3-D true size distributions using numerical method are summarized in Table X. These estimates utilized information about particle major axis orientations summarized in Figure 21. Results from the conversions using DeHoff's approach are in Table XII and in Appendix D. In this case for the surface and the quarter depth regions in the old alloy the procedure was the same as for pores. For the new alloy and for the center-plate location of the old one the particle sizes were estimated using described earlier procedure for one axis perpendicular to the TL plane. As for pores, the particle sizes were the largest at the plate centers and the smallest at the surface, Table XII and Table XIII. The volume fractions for the old alloy were practically the same for all locations. In the new alloy they were the smallest at the quarter depth and the largest at the center, Appendix D Figure 5b. The cumulative size distributions, Appendix D Figure 6, show that the largest particles would be always expected at the plate center. At that region the average particle sizes were smaller for the old alloy which is the opposite to what was observed for the pores. However, the size distribution for the new alloy was much tighter, resulting in the higher probability of the larger particles in the old alloy.

Results of the characterizations of the constituent particles for the low porosity and thin plate alloys are summarized in Table XIV and in Figure 28. As for pores the

results show evidences of the truncations of the left tails of the distributions resulting from the resolution limit. The average particle size listed in the Table XIV should be therefore treated as overestimations. The remaining results in Table XIV are however not affected by the resolution limit. Accordingly, the low porosity plate has about three times larger particle area fractions and about two times larger particle area densities than the thin plate alloy. The same trend holds for the percentages of the largest particles: there are more large particles in the low porosity alloy.

The shapes of the constituent particles in the low porosity and thin plate alloys can be characterized as prolate spheroids. They are only slightly elongated, with aspect ratios not exceeding 1.35. Analysis of the particle size distributions on different planes suggests that they were parallel to rolling plane with major axes randomly rotated about rolling plane normal. The true particle aspect ratios are then those on the LT planes. For both thin plate and low porosity alloys these ratios were both 1.35 which means that the particles were more equiaxed than pores.

### *Spacing and Clustering of Pores and Particles*

The particle and pore spatial distributions were quantified in the old and new alloys. Figure 29 shows an example of the Voronoi tessellation cell construction used in the analysis. This particular tessellations are for pores on the ST plane at the center plate location of the old alloy. Table XVI lists examples of the microstructural characteristics that has been obtained using the tessellations from Figure 29. The most important ones are local volume fractions and near and nearest neighbor distances -- these quantities can be obtained unambiguously only from the tessellations. The observed nearest neighbor distance for pores in Figure 29 is 48.2  $\mu\text{m}$  with standard deviation of 33.2  $\mu\text{m}$ . The expected values for the random structure with the same point density are 51.86 and 27.18  $\mu\text{m}$  respectively. This gives  $Q = 0.929$  and  $R = 1.224$  (see eqs. 35 and 36 for definitions) which corresponds to the spatial distribution that can be classified as random with clusters. For the constituent particles at the same location the observed nearest neighbor distance

was  $25.2\ \mu\text{m}$  with standard deviation  $19.2\ \mu\text{m}$  while expected values for random case were  $27.64$  and  $14.45\ \mu\text{m}$  respectively. This gives  $Q = 0.879$  and  $R = 1.281$  which again suggests random distribution with clusters. The Q-R values and the second phase spatial distribution types for all sections at the old and new plates centers have been compiled in Table XVII. In all cases the spatial distributions are random with clusters, Figure 30. We emphasize that ideally one should use 3-D tessellations to study the spatial distribution. However, as pointed out earlier, the main difficulty in this case is acquisition of 3-D data on particle locations.

Example of the results which could be obtained by analysing tessellation cell shapes are shown in Figure 31. The cells used were those from Figure 29 and the methodology was the same as the one for analyzing shapes of pores and particles. Figure 31 shows comparison of  $d-\alpha$  curve for the cells with a curves for the rectangular point pattern. The global shape  $SI_g$  for the tessellation is  $0.963$  while it is  $1$  for the random and  $0.760$  for the rectangular cells. The average shape index,  $SI_{avg}$ , for cells in Figure 29 is  $0.736$ , giving orientation factor  $\Omega$  of  $0.138$  and aspect ratio of  $1.872$ . Combination of high aspect ratio with low  $SI_{avg}$  indicates elongated and ellipsoidal cells. Since for random structure the cells should be equiaxed, this suggests some degree of clustering. On the other hand high value of  $SI_g$  combined with low  $\Omega$  suggests semi-isotropic overall cell structure. Both results combined give then random structure with clusters which is consistent with the results from the Q-R method. However, the advantage of the Q-R methods is that it allows for the quantification of the results.

### *Discussion*

Comparing results of the quantitative characterizations of the pores and constituent particle it appears that the particles always have higher volume fractions, larger number densities and that they are more elongated and aligned than pores. For volume fractions the only exception was the center of the old alloy where pore and particle volume fractions were similar. The particles are also usually slightly larger than pores. However, since data for different alloys were obtained under different magnifications, the results

could not be compared without corrections. Results of corrections using eq. 38 for the data for old and new alloys are in Table XVIII. Obtained sizes are about half of those for the low porosity and thin plates which is clearly incorrect. Apparently additional correction for larger number of big features detected at lower magnification is also in order. Although such corrections are possible, they were not attempted because of the approximate nature of the obtained results.

Because of the problems associated with differences in the apparent pore and particle sizes obtained under different magnifications and with the 2-D to 3-D conversions, it was necessary to find an alternative way of obtaining the true size distributions for fatigue modeling purposes. Since in this case only the right tail of the distribution matters, it is not necessary to know the entire 3-D size distribution but only its large size region. Considering the sizes of the largest pore or particle found on the metallographic sections it is evident that they must also represent the sizes of the largest particles and pores in the sample. This is because the largest 2-D sections represent the largest particles and pores that happen to be cut through the center by the test plane, Figure 32. The 2-D and 3-D size distributions must then converge at the large size limit. The lognormal probability plot in Figure 32 shows that this is indeed the case. The 2-D data used there were for pores at the center of the old plate alloy and the 3-D conversions are from the using Saltykov matrix method[23]. To improve accuracy, the data were divided into thirty intervals and all pores were assumed to have the same aspect ratios. Results show that the 2-D and 3-D distributions indeed converge and can be considered as equivalent for large pore sizes. The right tail of the pore true 3-D size distributions can be then adequately approximated, without loss of accuracy, by the 2-D metallographic data.

Despite particle higher volume fraction and larger sizes, in all studied alloys the fatigue cracks had tendency to nucleate from pores. This apparent inconsistency can be attributed to the differences in the fatigue crack nucleation periods associated with each feature type. It has been observed that pores can act as cracks from the very first fatigue cycle, while formation of a crack at the particles require long nucleation times [13]. As a

consequence, a crack associated with pore can grow to a critical size and cause fatigue failure before particle has enough time to start a crack. As will be discussed later in the report, this trend can be reversed in the presence of stress concentrators, as for instance for the 7050 fatigue samples with holes [13].

### *Summary*

- The volume fractions, sizes, shapes and orientations of pores, constituent particles and grains in the old, new, low porosity and thin plate variants of the 7050-T7451 Al plate alloys have been quantified. The characterizations included measurements of both the average values and the distributions of all microstructural descriptors for the TL, ST and LS planes at the surface, quarter depth and at the center-plate locations. This is the first ever such exhaustive microstructural characterization of the 7050-T7451 plate alloys which was made possible by the implementation of the to number of quantitative analysis programs developed specially for this purpose.
- All alloys were partially recrystallized. The grain structure was quantified in the old and new alloys on all planes throughout the plate. The recrystallization levels varied from 0.1% at the surface to 24% in the plates center regions. The unrecrystallized grain sizes were from 44 to 220  $\mu\text{m}$ , while recrystallized grains were 22 to 54  $\mu\text{m}$ . The new pedigree alloy had finer grain structure with average unrecrystallized grain size of 87  $\mu\text{m}$ . Recrystallized grains in the new alloy were 38  $\mu\text{m}$  in size. The sizes of unrecrystallized and recrystallized grains in the old alloy were 138 and 34  $\mu\text{m}$  respectively. In both alloys the unrecrystallized grains were elongated with average aspect ratios of 2.6. Both unrecrystallized and recrystallized grains had normal size distributions.
- The volume fractions, sizes and spatial distributions of the constituent particles and pores have been measured at the center-plate locations for all alloys and, in addition, at

the surface and quarter depth regions for the new and old plates. The average sizes of the pores were from 3 to 12  $\mu\text{m}$  with the area fractions from 0.02% to 0.16%. The constituent particles were 4 to 11  $\mu\text{m}$  in size with area fractions from 0.24% to 0.75%. The old alloy had the largest number of particles and pores followed by the new, low porosity and thin plate variants. The size distributions of pores and constituent particles were lognormal and their spatial distributions random with clusters.

- Two procedures for estimating the true 3-D size distributions from the experimental 2-D measurements made on plane sections have been developed. The methods assume that particles can be modeled as triaxial ellipsoids which are either randomly or partially or completely aligned. The methods have been used to obtain 3-D size distributions of pores and constituent particles in the old and new 7050-T7451 Al plate alloys.
- The effect of magnification used in the measurement on the obtained results has been studied. It was determined that although the apparent average size of the measured features is inversely proportional to magnification, use of low magnification is recommended for fatigue modeling purposes. A method of correcting the data for magnification effect has been proposed.

## TEM

### *Methodologies*

Samples for the transmission electron microscopy (TEM) were taken from the surface and center sections of the new and old alloy plates. They were thinned to approximately 250  $\mu\text{m}$  and used to make 3 mm TEM disk samples. The disks were dimpled at a room temperature using solution of 10 % nitric acid and 90 % water at a voltage of 25 V. Final chemical polish and perforation were done using a solution of 30 % nitric acid and 70 % methanol at a temperature of -30  $^{\circ}\text{C}$  and a voltage of 15-18 V. The samples were examined in a 100 KeV JEOL transmission electron microscope.

The precipitates were measured on a digitizer from enlarged bright and dark-field TEM images. In addition to measuring sizes and size distributions, we also determined the area fractions ( $A_f$ ) and spacings (center-to-center and surface-to-surface) of the grain boundary precipitates. The area fractions have been calculated using equation:

$$\text{eq. 41} \quad A_f = \frac{\frac{\pi}{4} \langle d \rangle^2 N_p}{l \cdot w}$$

where  $N_p$  is the number of precipitates observed on the boundary,  $d$  is their average size, and  $l$  and  $w$  are the grain boundary length and width. The grain boundary lengths were measured directly from the photographs. The width was obtained from foil thickness measurements using the convergent beam method [68].

The precipitates center-to-center spacing,  $L_{c-c}$ , was calculated using equation[69]:

$$L_{c-c} = 1.2 \cdot N_a^{-1/2} \quad \text{eq. 42}$$

where:

$$N_a = \frac{N_p}{l \cdot w} \quad \text{eq. 43}$$

is the number of precipitates per unit grain boundary area. Surface-to-surface spacing was calculated as  $L_{c-c}$  minus the precipitate average diameter. Although the above equations are strictly valid for identical and evenly spaced precipitates, they give an adequate approximation in the considered case.

## Results

To identify the precipitate phases present in the alloy the obtained diffraction patterns were compared with those found in the literature on 7075 and 7050 alloys. The patterns of the studied alloy were identical to those obtained by Park and Ardell for overaged 7075 [70]. Since the predominate phases in the 7050 alloys have been identified as  $\eta'$ ,  $\eta_1$ ,  $\eta_2$ , and  $\eta_4$ , the same phases are expected to be present in the studied alloy. The grain boundaries contained one or more of the  $\eta$  phase variants with  $\eta_2$  and  $\eta_4$  predominantly on low angle boundaries. All grain boundary precipitates appeared as thin hexagonal plates varying in size for different boundaries, Figure 33. The only exceptions have been found in the center section where some boundaries contained a multiple of precipitate variants that were not all hexagonal, Figure 34.

Although the average size and density of the grain boundary precipitates are effected by the boundary type [71,72], this distinction ( in particular high versus low angle) was not taken into account in this study. This is because the material was partially recrystallized thus it contained a large number of subgrains. In such a material high angle grain boundaries are difficult to locate hence a high percentage of the boundaries examined were low angle. However, even though most of the boundaries were low angle, they did exhibit a wide range of precipitate sizes. We also observed instances where low angle boundaries contained large precipitates. For example, the precipitates in Figure 35 have an average size of 150 nm, while shift in the diffraction patterns on either side of their boundary is only  $2.7^\circ$ . The wide range of precipitates sizes on low angle boundaries is contrary to what has been observed in the 7xxx alloys. It has been reported who reported that the low angle boundaries usually contain small precipitates while the high

angle boundaries were expected to have large precipitates[72]. The exceptions in our alloys can be attributed to the differences in the aging treatment.

Results of the quantitative evaluation of the grain boundary precipitate size distributions can be seen in Figure 36. The surface sections of both alloys exhibit lognormal distributions of the precipitate sizes while for the center sections the distribution is bimodal. The bimodal distribution is not unusual. It has been reported in alloys that are doubly aged, which is the condition of the investigated alloys. The larger precipitates nucleate during quench hence they have more time to grow to the large size. The smaller precipitates form during regular aging process thus contributing to the low size peak [71]. Due to the slowest quenching rate at the center of the plate, the precipitate size ranges in that region are greater than for the surface sections.

To determine whether the distributions of the precipitates on the boundaries are governed by the coarsening law, their size distributions were compared with the theoretical distribution for coarsening [73]. It appears that the experimental distributions are best approximated by the theoretical coarsening distribution for volume fraction equal to one. This agreement should be considered as very good because the effect of volume fraction on theoretical distributions is non-linear and the theoretical distribution changes very little for volume fractions from 0.05 and 1 [73], i.e. for the range of precipitates volume fractions in the studied boundaries. The discrepancies can be attributed to the fact that the theoretical equations were derived assuming high angle grain boundaries while all boundaries investigated in this study were low angle [73]. Details of the analysis can be found in our '93 Report.

The average values of the area fractions and spacing of the grain boundary precipitates for surface and center sections of old and new alloys can be seen in Table XIX. Most of the boundaries examined contained single variants of the  $\eta$  phase with only a few with multiple variants. As can be seen from Table XIX, there was a large variation in precipitate area fractions and spacings for the boundaries from the same location (see

ref. 11 for the individual boundary data). The average precipitate sizes were in the 35 - 45 nm range in the surface sections and between 120 and 140 nm at the plate centers. The area fractions varied from 10 to 20 % at surface to 25 to 30 % in the interior. The precipitate spacings were in the order of 100 nm at the surface and 260 nm at the center of both examined plates.

### *Summary*

- The precipitate structures have been characterized at the surface and at the center-plate locations of the old and new alloy variants. The most common precipitating phases present were  $\eta'$ ,  $\eta_1$ ,  $\eta_2$  and  $\eta_4$ -variants of the  $\eta$  phase ( $\text{MgZn}_2$ ). The precipitates inside the grains were small, ranging from 5 to 45 nm in diameters, while those on the grain boundaries were generally larger with sizes between 20 - 250 nm.
- There was no significant difference in the character of the grain boundary precipitates between the old and new lots of 7050 aluminum alloy. The only gradients in the precipitate structure were in the sizes and size distributions between the surface and center sections of the alloys.
- Approximately 90 % of all boundaries contained thin, hexagonal  $\eta$  plate precipitates. The precipitate sizes on low angle boundaries had wide range which is contrary to previous reports that associate low angle boundaries with small and large angle with large precipitates.
- No significant precipitate free zones were observed at the grain boundaries

## ***Fractography***

### **Crack Nucleation Sites**

All fatigue testing were performed at Alcoa Laboratories. The tests were run on the two types of samples shown in Figure 1. The smooth samples were used to obtain the data compatible with the standard S-N fatigue tests, while the two-hole specimens were design to simulate loading condition similar to those of bolt holes in aircraft parts. All samples were cut from plate centers, had LT orientation and were tested under constant amplitude loading. The R- value was kept at 0.1 and frequency at 10 Hz for smooth and 30 Hz for the open-hole samples. For smooth samples the maximum stresses were between 50 to 70% and for the open hole ones between 20 to 50% of the yield strength. The maximum stress levels and the number of samples run for each level are listed in Table II. Details on fatigue testing can be found in Alcoa team reports [13].

A total of eighty eight broken fatigue samples have been analyzed in our laboratory. The analyzed set contained mixture of smooth and open hole specimens from all four alloy variants. We have identified and quantified crack nucleation sites in:

1. four smooth samples from the old alloy
2. four smooth samples from the new alloy
3. five smooth samples from the thin plate alloy
4. twenty nine open hole samples from the old alloy
5. thirteen open hole samples from the new alloy
6. twelve open hole samples from the low porosity plate
7. twenty one open hole samples from the thin plate alloy

Our fractographic studies complement work done by Alcoa team on the same materials reported in [13].

## ***Methodology***

All fractured fatigue samples were examined in the SEM to identify the fracture nucleation sites using both backscattered and secondary electron modes. In all cases it

was determined if the fracture originated from the pore, constituent particle or if it started crystallographically as the Stage I failure. The crack initiating features were photographed, measured and characterized by their length and width. For open hole samples also the position of the nucleation sites with respect to the sample corner and the hole edge were measured.

### *Results and Discussion*

Information obtained from the fractographic analysis and from the fatigue testing are summarized in Table XX for the smooth samples and in Table XXI to Table XXIV for the open hole ones. All smooth samples from the old and new alloys failed from the cracks originating from pores, Figure 37<sup>2</sup>. For the low porosity plate most of the cracks in smooth samples started either from the pores or from the pores with adjacent constituent particles. Large fraction of failures could be also traced back to either particles or particles with pore. For the thin plate none of the failures in smooth samples initiated at pore, and only a small portion of them started from particles. In the majority of samples fatigue cracks started in a Stage I mode. Similar trends have been observed in the open hole samples, Figure 38. The transitions between nucleation sites was in this case more gradual as failures from constituent particles were observed already in the old and new alloys. There was also a small percentage of low porosity plate samples with Stage I crack nucleation sites. For the new, low porosity and thin plates it was also necessary to de-burr the holes to prevent failures from the machining flaws. In the old alloy, despite rough hole surfaces, only one samples failed from the burr. A number of the open-hole samples had more than one nucleation sites. The largest percentage of these sites was observed in the old and thin plate alloys. In the low porosity and thin plate alloys the multiple crack origins were always associated with the presence of constituent particles.

---

<sup>2</sup> All figures include results obtained by both UCLA and Alcoa groups.

The relations between the types of the crack nucleation sites and fatigue lives are shown in Figure 39 to 44. For the smooth samples only the results for low porosity and thin plates are relevant because in the old and new alloys cracks always originated from pores, Figure 39. The trend seen in Figure 39 is towards increased fatigue life when initiation site changes from pore or particle to the crystallographic Stage I type. As shown in Figure 40 these transitions result in a significant increase in fatigue life. The improvement in fatigue performance has been accomplished through processing, by decreasing both the sizes and the volume fractions of the potential fatigue crack initiating features.

The S-N results for the open hole fatigue samples are summarized in Figure 41 to 44 with different markers for different types of the nucleation sites. The trends are similar to those for the smooth samples with a significant improvement in fatigue life when crack initiation change from pores to particles and finally to Stage I. Multiple nucleation sites always led to the deterioration of the fatigue life and the frequency of those sites increased with increasing maximum stress. On the other hand the scatter in fatigue lives was inversely proportional to the maximum stress. Additional details of the observed trends can be found in our earlier reports.

For the open hole samples from the old and new alloys it was possible to establish the relationship between the maximum stress level on the average size of the fatigue crack initiating pore. The relevant distributions of the crack initiating pore largest dimensions are shown in Figure 45 and 46. It appears that for both materials the average crack initiating pore size initially increases and then decreases with stress as the largest size is for  $\sigma_{\max}$  of about 25 ksi (172.5 MPa), Figure 47. This unexpected relationship can be rationalized by considering the volume of the material exposed to the high stress as the larger volume will always contain larger pore. Since increase in stress results in an increase of the high stressed volume, the size of the fatigue initiating pore should be proportional to the maximum stress. However, for the high stress levels the smaller pores closer to the hole may have the same or even larger growth rate than the largest pores

further away from the hole edge. This effect can result in a decrease in the average size of the fatigue crack initiating pore, as it is indeed observed in Figure 47. Since the stress concentration factor at the hole is about 3, this transition seems to coincide with the onset of the plasticity at the hole surface.

Figure 44 and 46 also compare actual sizes of the crack initiating pores for the smooth and open hole samples with the sizes of pores obtained from the metallographic analysis. As expected, the crack nucleating pores are always bigger, because they represent the largest pores in the sample surface or stress concentration regions. Since the surface region of the smooth sample is larger than the highly stressed volume around the hole, there is a higher probability of finding there a larger pore. The sizes of the crack initiating pores in the smooth samples may be then considered as the upper limit for the size - stress curves for the open hole samples, Figure 48. The average pore sizes obtained from the metallographic sections should be on the other hand always the smallest, because the test area has the smallest size. As described later in report all three size distributions from Figure 45 and 46 are related and can be obtained from each other using the statistics of extremes.

### *Summary*

- Fatigue crack nucleation sites have been identified, characterized and measured in the smooth and open hole fatigue samples from the old, new, low porosity and thin plate variants of the 7050-T7451 aluminum alloys. All samples were fatigue tested at Alcoa Laboratories at constant stress amplitudes from 102 MPa (14.8 ksi) to (310 MPa (45 ksi) and  $R=0.1$ .
- The fatigue crack initiating features we photographed and quantified in thirty three samples from the old alloy, seventeen from the new, five from the low porosity plate and twenty-six from the thin plate alloy.

- Results suggest transition of the crack initiation sites from pores in the old alloy to constituent particles in the new one and to constituent particles and grains in the low porosity and thin plate alloy variants. It was also found that in open hole samples the size of the fatigue crack initiating pore initially increases and then decreases with the maximum stress level.

## Fracture Surface and Crack Path

The purpose of this part of the study was to investigate the correlation between characteristics of the fatigue fracture surfaces and fatigue lives. The materials used were old and new alloy variants and of particular interest were changes of the surface roughness, fractal dimension and microstructural features along fatigue crack path. Both destructive and optical sectioning methods were used. For the new alloy the characterization also included use of a recently proposed trisector method [74].

Exploring fatigue fracture surfaces is important because it provides information about both the microstructural features on the crack path and on the accumulation of damage proceeding final fracture event. Information about surface morphologies can then help in identify the mechanisms of crack propagation and suggest strategies for improvement of the fatigue behavior. Traditionally, fractography has been used for descriptive characterizations of fracture surfaces. Modern quantitative fractography took advantage of the new advanced image analysis techniques and introduced several quantitative fracture surface descriptors. These new parameters enable one to correlate fracture surface morphology with mechanical properties as well as to identify fracture mechanisms and microstructural features involved in failures [75-85]. The two most important current issues in quantitative fractography are (1) how to obtain the information about the fracture surface in the most efficient and practical way and (2) how to describe the fracture surface using the obtained information.

Fracture surfaces are very complex and contain numerous unusual three dimensional features. They are difficult to describe and to compare even if they appear to be simple and regular. A practical alternative to overcome those difficulties is to define simple parameters which would quantify the surfaces and use them in correlations with mechanical properties. The most common of such parameters are roughness and fractal dimension. The surface roughness,  $R_s$ , is defined as the ratio of the fracture surface true area to the area projected on the mean or average topographic crack plane. Hence, the

larger the  $R_s$ , the rougher the surface. The values of the surface roughness are however not unique as they are the same for the morphologically different surfaces. Despite this limitation, the roughness parameter is very useful for comparing fracture characteristics of different materials. The surface roughness parameter is often approximated by its two dimensional counterpart, the profile roughness,  $R_L$  [74,86,87]. Although the measurement of  $R_L$  is less involved, there are number of methods that allow for the estimation of  $R_s$  without much effort [85, 88].

The estimation of the fractal dimension has been based on the principle that the number of ruler lengths,  $N$ , required to measure the length of a curve depends on the size of the ruler,  $\rho$ , used in the measurement [89]. A small ruler resolves finer details than a large one, but at the same time requires a greater number of steps to cover the analyzed curve. For a fractal curve a plot of  $\log(N)$  vs.  $\log(1/\rho)$  yields a straight line which can be described by the relation

$$N = k \left( \frac{1}{\rho} \right)^d \quad \text{eq. 44}$$

where  $d$  is referred to as the fractal dimension and  $k$  is a constant. Such defined fractal dimension gives an indication of the curve roughness: the closer the number is to 1, the smoother the curve. For a three dimensional case the measuring unit is an area  $A$ . The  $\log$  plot of the total number of areas  $A$  required to cover a surface versus  $1/A$  has a slope equal to the fractal dimension  $d$ . As with the surface roughness parameter, the values of fractal dimensions are not unique. They have been nevertheless successfully used in correlating mechanical properties with fracture surface characteristics for various engineering materials such as metallic alloys[79,80,87], ceramics materials[82], rubber[84] and intermetallic compounds[83].

To obtain the data for calculating surface characteristics, a number of experimental fracture surface 'sectioning' techniques can be employed[90,91,92]. The most straightforward is the vertical sectioning method. In this method the samples are sectioned with cuts perpendicular to the fracture surface. Obtained line profiles allow for measurement of

the profile roughness parameters,  $R_L$ , which in turn are used in calculating the surface roughness  $R_s$ . It is important to protect fracture surfaces during sectioning and measurements from plastic deformation; this is usually accomplished by coating. The work involved in the vertical sectioning method, both in sample preparation and in either digital or manual profile tracing, is then considerable.

In the slit-island method the fracture surface is cut with a series of sections parallel to the nominal fracture surface. The surface is first plated with a contrast medium and then polished in a series of steps. At each step, the islands' boundaries are either digitized or traced to obtain contours of the iso-elevation lines. The major drawback of this method is the difficulty of obtaining small and equally spaced polishing surfaces. Uniform polishing over the entire section and proper alignment of sections after each tracing are also difficult. The work in resolving fine details, particularly if the height of the fracture surface is large, can be in this case enormous.

To circumvent the destructive nature the vertical sectioning and the slit-island methods an optical sectioning technique has been developed[85, 88]. This method is an optical version of the slit-island method utilizing a confocal scanning microscopes with either laser or broad-band light source. During each measuring step the focus is set on a different height and only the regions on the same levels are in-focus, hence visible, while the rest of the area remains black. By assembling obtained series of equal-level sections, a 3-D image of the fracture surface can be recreated with the aids of a computer. The measurements of the fracture surface parameters are then simplified with concurrent improvements in precision. This technique is still relatively new but it has shown great potential for application in fracture surface characterizations [85].

Other non-destructive techniques include stereographic pairs, atomic force microscopy (AFM) and profilometry. The biggest limitation of the stereographic pair technique is huge amount of computations required in processing the data[93]. The AFM method is suited for resolving fine details in the nanometer range but is less efficient for

fracture surface where details are in 1 to 1,000  $\mu\text{m}$  in size. The use of the profilometry in fracture surface characterization has been restricted because of the discrete nature of the obtained data[85].

The information obtained from any of the described techniques allow for the calculation of only the 2-D surface parameters such as  $R_L$ . To obtain 3-D parameters these results need to be converted using appropriate equations [74, 94-98]. An extensive review of such formulae can be found on ref [91] and the most relevant ones are listed in Table XXV.

It is also important to point out that the results of the up to date studies on the relationships between the quantitative fracture surface characteristic and mechanical properties are so far inconclusive. It has been for instant observed that the fractal dimension is proportional to the fracture toughness of ceramics[82] and intermetallics[83], and that it scales well with the wear properties of rubber[84]. In metallic alloys however both strong correlations[77,78] and lack of any relationship between fractal dimensions and the fracture toughness and fatigue threshold have been reported [76,80].

### *Methodologies*

The specimens used in the fracture surface and profiles characterizations were open hole fatigue samples fatigued at  $\sigma_{\text{max}} = 170 \text{ MPa}$  for the old alloy and at  $\sigma_{\text{max}} 172$  and  $207 \text{ MPa}$  for new one with  $R = 0.1$ . Old alloy sample had secondary cracks at the unfailed hole, Figure 49. These cracks were used to identify microstructural features on both sides of the crack path at the same time. The path of both primary and secondary cracks, had been also examined in details in search for the microstructural evidences of fatigue damage.

### Vertical sections

Vertical sectioning was used to obtain fractal dimensions and surface roughness parameters. One of the method used was trisector technique [74] which allows for the assumption-free estimation of the surface roughness with the error not exceeding 6% [86]. To prevent any damage to the fracture surface during cutting, all fatigued specimens for vertical sectioning were electroplated with approximately 20  $\mu\text{m}$  layer of copper. The solution used consisted of 250 g  $\text{CuSO}_4 \cdot 5\text{H}_2\text{O}$  + 50 ml  $\text{H}_2\text{SO}_4$  + 1 liter  $\text{H}_2\text{O}$ , which is a modification of the one recommended by Cheng *et al.* [99]. The coating was applied at room temperature for 30 minutes at voltage of 5 V. Before cutting the specimens were cold-mounted in plastic resin. The samples were then cut into four parts, as shown in Figure 50. The first two parts covered the fatigue crack propagation region. Part I included crack origin and was approximately 800  $\mu\text{m}$  long, which was about twice the initial plastic zone size (estimations of the plastic zone plastic is discussed later in this section). The last two parts include the final fast failure region. As recommended in the trisector method [74, 86] each part was cut by three vertical cross sections 120° apart, Figure 50, with a low-speed diamond saw. The specimens were then ground with 600 grit sandpaper and polished with first 1.0 and than 0.25  $\mu\text{m}$  diamond paste. The obtained crack profiles were photographed using an optical microscope and magnification of 500X. Each photograph was labeled to indicate the relative profile position with respect to the crack origin.

As the first step in the trisector procedure, the fracture surface profile parameters,  $R_L$ , were measured along three cross sections cut at different angles  $\Phi_p$  with respect to the crack propagation direction. The surface roughness parameter was then estimated using the formula [74]:

$$\text{eq. 45} \quad R_s = \overline{R_L \cdot \psi}$$

where  $\psi$  is profile structure factor equal:

$$\text{eq. 46} \quad \psi = \int_0^\pi \sin \theta \int_0^\pi \left| \cos\left(\theta + \frac{\pi}{2} - \alpha\right) \right| f(\alpha) d\alpha d\theta$$

and where  $f(\alpha, \Phi_p)$  is the profile orientation distribution function, obtained by measuring the angles between the profile segments and the crack propagation plane. One  $R_s$  value was calculated for each of the parts shown in Figure 50 allowing for the analysis of the changes in the fracture surface morphologies along the crack path.

The differences between fatigue fracture surface characteristics in the old and new alloys were estimated using the data from confocal laser scanning microscopy (CLSM) obtained on the 2LM31 Lasertec microscope. In this case the fracture surface specimens required only ultrasonically cleaning before scanning. The determinations of the crack profiles were made at magnification 750X and covered whole crack length. Example of the obtained profiles are in Figure 51.

All measurements of fracture surface profiles obtained from trisector method and confocal microscopy were automated by developing a customized fractographic analysis program. The program required as input images files with fracture surface profiles. It then calculated all fracture surface characteristics including angular distributions of the line segments, structure factors, roughness parameters and fractal dimensions.

### *Crack path*

For the old 7050 alloy the fractography also included characterizations of the microstructural features on the crack path. The open hole sample used for this purpose was fatigued at  $\sigma_{\max} = 170$  MPa and  $R=0.1$ . It contained secondary cracks which were used in this part of the study, Figure 49. The sample was sectioned along crack length at 1/3 and 2/3 thickness using a low speed diamond saw. The sections were mechanically ground on wet SiC 600 grit paper and then polished using 1 mm with diamond paste and ethanol. The specimens were examined using a scanning electron microscope (SEM) first in as-polished conditions and then after etching for 30 seconds with Keller's agent to reveal crack path features. These examinations were used to determine 1) the crack roughness parameter, 2) the relationship of the crack path to the grain structure, 3) the

number of second phase particles intercepts and 4) the severity of microcracking. The characterizations were performed for two different cracks.

To determine if a fatigue crack deflects toward constituent particles the average number of particles per unit length of a straight line have been compared with the actual number of particles per unit crack length. In both measurements the enlarged photographs of the entire crack length were used. The measurements of the expected number of particles for a straight crack have been made using a scan grid of parallel lines spaced 0.5 cm apart. Because of the anisotropy of constituent particle spatial distribution the grid was always aligned with the average direction of crack propagation. Alternatively, the number of the constituent particle intercepts per unit length along the actual crack path have been obtained by measuring the crack lengths and total number of particles intersected by the crack.

The SEM studies of the crack path were augmented with the TEM examination to determine if there was any change in the dislocation structure in the vicinity of the crack path. Specifically, the evidences of dislocation activities in or near the cyclic plastic zones were studied. The samples used were cut from various sections along the fatigue crack path with each sample contained either starting, middle or end regions of the crack. The samples were dimpled using a solution of 10 % nitric acid and 90 % water at room temperature and a voltage of 25 V. Final polish and perforation was done with a solution of 30 % nitric acid and 70 % methanol at a temperature of -30 °C and a voltage of 15 - 18 V.

## *Results and Discussion*

### *Surface roughness and fractal dimension*

Figure 52 shows a typical experimental profile orientation distribution function  $f(\alpha, \Phi_p)$  for the fracture surface profile of the new 7050-T7451 plate alloy fatigued at  $\sigma_{\max} = 206$  MPa. The maximum is at about 90°, which corresponds to the general crack

propagation direction. The distribution is relatively flat, which means that there is considerable amount of crack deflection in the profile. Figure 53 show an example of the plot used for estimating fractal dimensions. The ruler lengths used were from 1 to 100  $\mu\text{m}$  although, theoretically, they should cover the entire size range from 0 to  $\infty$ . In practice, however, the minimum ruler length can not be lower than by the resolution limit while the maximum is limited by the specimen size. The actual minimum ruler length used in the measurements corresponded to the sizes of the smallest pores and constituent particles while maximum size was in the range of the largest grains. This range covered then the size ranges of the microstructure features involved in the fatigue process. All obtained fractal plots showed excellent linearity with the standard error of the fractal dimension  $d$ , equivalent to the slope, of less than 0.4%. This means that the fatigue fracture surfaces in the 7050-T7451 alloys were fractal in nature.

Figure 54 shows change of the roughness parameter and the fractal dimensions, obtained using trisector method, along the fatigue crack length of the new alloy cycled with  $\sigma_{max} = 206 \text{ MPa}$ . It is evident that neither of the two parameters is constants. They are the smallest near the crack origin, increase gradually as the crack grow and then level off in the final ductile failure region. From the two only the roughness parameter has clear physical interpretation - it is the ratio of the fractured surface true and projected areas. Fractal dimension on the other hand can be considered proportional to the surface roughness. The advantage of using the later is in its independence on the ruler length which makes it a unique characteristic of the fracture surface. The obtained fractal dimensions are comparable with those measured in other aluminum alloys. In particular, our results are similar to those reported for fatigue precracks fracture toughness specimens for the Al-Cu-Li alloys [80]. The change of  $R_s$  along the crack path are moderate with overall increase of about 10%. For fractal dimension the increase is only 3%.

The validity of the  $R_L - R_s$  conversion formulas listed in Table XXV have been tested using the  $R_L$  data obtained from the vertical sectioning and  $R_s$  results from the

trisector method. Figure 55 shows the results together with the best fit least-squares line marked as RS\_Gokhale. The slope of this line is 1.168 which is comparable to the formula[98]:

eq. 47 
$$R_s = 1.16 R_L$$

which is the first equation in Table XXV. The difference between the experimental and theoretical slopes is less than 1%. Eq. 47 provides then a good approximation for surface roughness parameter for the studied material. The results in Figure 55 can be also compared with relation between  $R_s$  and  $R_L$  for a surface with random curvature[90]

eq. 48 
$$R_s = (4/\pi) R_L$$

which represents the upper bound for the  $R_s$ . This relation is shown as a dotted line in Figure 55. As expected, the experimental data from the trisector method are below this upper limit.

The differences in fracture surface morphologies of the old and new alloys were quantified using the surface roughness and fractal dimension were measured using CLSM method. The samples used were fatigued at  $\sigma_{\max}$  equal 170 and 172 MPa respectively. Figure 56 shows the variations of both roughness parameters and fractal dimensions along the crack paths. As for trisector method, both  $R_L$  and  $d$  increase with crack length. This means that as the fatigue crack grow its surfaces becomes rougher. In each alloy the changes of  $R_L$  and  $d$  are similar along entire crack paths. However, the new alloy has consistently rougher fracture surface, particularly in the initial region. The average roughness parameter was 1.342 for new and 1.204 for old alloy and fractal dimensions were 1.063 and 1.052 respectively. These differences can be attributed exclusively to the differences in the microstructures. From possible culprits the precipitate structures had to be eliminated because they were similar in both alloys. The volume fractions of micropores in both alloys were about 0.1% hence their effect on the fracture surface morphology is very unlikely - they mainly act as crack initiators. The constituent particles do deflect cracks path, but since they were in similar amounts and sizes in both alloys, they could not be responsible for the observed morphological differences. This leaves unrecrystallized grains, which were indeed quite different in both alloys. The average recrystallized grains

sizes were 87  $\mu\text{m}$  in the new and 138  $\mu\text{m}$  in the old alloy. The smaller grain size in the new alloys results in larger number of both transgranular and intergranular crack segments which increases surface roughness.

#### *Microstructural Fatigue Damage on Crack Path*

Microstructural fatigue damage in 7050-T7451 alloys can take number of forms. These alloys have complex, partially recrystallized structures with matrix and grain boundary precipitates, constituent particles, microporosities and precipitation free zones all prone to fatigue damage. As a result the crack is not straight but propagates tortuously through the matrix by linking-up with microcracks formed ahead of the crack tip at constituent particles, grain boundaries, slip planes, etc. Each of those mechanisms constitutes different type of microstructural damage and all of them were identified for the 7050-T7451 plate alloy.

#### *Grain Structure*

The extends of the interactions between crack and the grain structure have been quantified by measuring the fractions of the crack path through various types of grains and/or grain boundaries. Since the material was partially recrystallized, the crack could pass transgranularly either through the recrystallized grain or unrecrystallized grains with subgrains. Intergranular portions of the crack path could be separated into following types, depending on the boundaries present: (1) unrecrystallized/ recrystallized, (2) recrystallized/recrystallized and (3) unrecrystallized/unrecrystallized. Crack path percentages through such defined regions are in Table XXVII and Figure 57.

There was a definite preference toward a transgranular path through unrecrystallized grains. This is expected as the material was only 20 % recrystallized. The fractions of the recrystallized grains encountered by the crack varied, but they were on the average lower than the recrystallization levels. Intergranular crack path constituted between 6 to 40% of the total and it was mostly between unrecrystallized and recrystallized grains. This

implies that these boundaries are the most susceptible to the fatigue damage. Small percentage of the transgranular cracks in the unrecrystallized grains propagated along subgrain boundaries.

### *Second Phase Particles*

It was also observed that the main crack frequently branched and had secondary microcracks. In many instances the branches grew towards and into constituent particles and/or extended along adjacent grain and subgrain boundaries. The microcracks were both at the front and on both sides of the primary crack and usually in the vicinity of constituent particles, see Appendix F. The growth of fatigue crack was then preceded by microcracking, with constituent particles serving as the nucleation sites. The main crack most likely propagated towards the microcracks resulting in crack path deflections. To test the hypothesis that the crack deflects toward particles the number of constituent particles on the crack path have been compared with the expected number of particle intercepts by a straight line. Results, summarized in Table XXVIII and Figure 58, show that the number of particles intercepted by the crack is always greater than the expected average for the straight line. In all cases the null hypothesis that they were the same had to be rejected at the significance level less than 0.1% [100]. This means that there is less than 0.1% chance that the number of particles intercepted by the crack is the same as that for the straight line ( the actual calculated probability is even smaller and is in the  $1 \times 10^{-10}$  % range). It is thus justifiable to conclude that the constituent particles do affect the crack path by causing deflections.

### *Precipitates and Dislocations.*

We also looked for evidences of the fatigue damage to the precipitate and dislocation structures. For this purpose the microstructures at the vicinity of the fatigue crack have been compared to that of the bulk material. Since the samples were subjected to high cycle fatigue, the most probable region, if any, where the damage would occur was at the reversible plastic zone. The size of that zone, can be estimated from relation [101]:

eq. 49

$$r_c = \frac{1}{\pi} \left( \frac{\Delta K}{2 \sigma_y} \right)^2$$

where  $\Delta K$  is the stress intensity amplitude and  $\sigma_y$  is material yield strength (equal 450 MPa for 7050-T7451 alloy). The expressions for the  $\Delta K$  in eq. 49 are different for the short and long cracks, see Appendix F. The stress intensity in the former case can be approximated as [102,103]:

$$\Delta K = 3.36 \Delta \sigma \sqrt{\pi L} \sqrt{\frac{2R + 2L}{2R + L}} \quad \text{eq. 50}$$

where  $L$  is crack length,  $R$  the hole radius and  $\Delta \sigma$  is stress amplitude (equal in this case 153 MPa). For the long cracks both cracks and the hole can be treated as a through thickness center crack, Figure 49, of length  $2(R+L)$  with  $\Delta K$  is equal to [104]:

$$\Delta K = \Delta \sigma \sqrt{\pi(R+L)} \left( \sec \frac{\pi(R+L)}{W} \right)^{1/2} \quad \text{eq. 51}$$

where  $W$  is the specimen width. The change of the cyclic plastic zone size with crack length calculated using equations 49-51 is shown in Figure 59. For the initial crack of the size of a pore, the cyclic plastic zone is about 10  $\mu\text{m}$ . At the failure, when the cracks are 2.5 to 3.5 mm long, the zone size increases to about 250  $\mu\text{m}$  which is about twice the size of a typical unrecrystallized grain. To see any fatigue damage, the TEM sample had to be then perforated in a grain adjacent to the fatigue crack. Such accuracy is extremely difficult to achieve, however we were able to perforate one of the samples within 10-20  $\mu\text{m}$  from the plastic zone. The examination of that particular sample show no evidence of any fatigue damage to the precipitate structure or debonding at the grain boundaries. The dislocation structure was also no different than that of the bulk material and without any grouping and/or banding. These results are consistent with the literature on 7XXX alloys [105,106]. Additional details pertaining to the crack path can be found in Appendix F [107]

### *Correlation between fracture surface characteristics and fatigue lives*

The effects of crack deflections, hence also the fracture surface roughness, on the crack propagation rates have been studied by Suresh[108]. Using an idealized periodic deflected crack profile, he introduced a parameter describing the degree of crack tilting,  $D$ , defined as:

eq. 52 
$$D = \frac{T}{T + S}$$

where  $T$  is the distance over which the tilted crack advances along the kink and  $S$  is the distance over which the plane of the growing crack is normal to the far field tensile direction. The crack propagation rates for this periodically deflected crack along the projected mode I plane is:

eq. 53 
$$\frac{da}{dN} = \{D \cos \theta + (1 - D)\} \left( \frac{da}{dN} \right)_L$$

where  $(da/dN)_L$  is the growth rate of a straight crack and  $\theta$  is the tilting angle. To investigate the effects of the crack deflection on the crack growth rates in the 7050 alloys, we have used the surface roughness experimental data to calculate the values of  $T$ ,  $S$  and  $\theta$ . eq. 53 was then used to calculate the magnitudes of the effect of crack deflection on crack propagation rates. Results are plotted in Figure 60 showing that the crack propagation rate decreases as both  $D$  and  $\theta$  increase. For aluminum alloys, the typical values of  $D$  is 0.75 and  $\theta$  is about  $45^\circ$ [101]. This results in the reduction of the crack propagation rate by about 22%. In the investigated alloys the values of  $D$  and  $\theta$  were 0.93 and  $37^\circ$ , which gives crack propagation rate reduction of about 16%.

We also considered possibility of correlating fractal dimension with fatigue live. Our results show that an increase in the values of  $R_L$  and  $d$  for old and new alloys fatigued at constant maximum stress of 172 MPa correspond to an increase in the fatigue lives from 29,564 and 1,842,960 cycles. This suggests correlation, however it would be very dangerous to postulate a universal relation. This is because the fracture surfaces have

different morphology at different regions, hence it would be inappropriate to use an average value of fractal dimension. Moreover, the crack propagation rate is not constant, but increases exponentially with crack length. The crack can then spend majority of its fatigue life as a small crack extending only by the small portion of total specimen cross-section. In correlating fractal dimensions with fatigue lives one should use a weighted average that would take into account time spent at different locations. Since the weight function are impossible to know *a priori*, also the meaningful correlation would be difficult to make. Another possible reason for difficulty in utilizing fractal dimensions is that they can be obtained using different techniques, with each of them giving different index for the same surface. Although the fractal dimension measured in this investigation shows qualitative agreement with fatigue life, more works, both theoretical and experimental, is need to quantify those correlations.

### Summary

- The fatigue fracture surfaces and the microstructure in the adjacent areas have been characterized in old and new alloys using optical, SEM, TEM, and confocal laser microscopies as well as vertical sectioning and trisector methods.
- In both alloys the roughness parameters and fractal dimension increased with fatigue crack length and leveled off at the final fast fracture region. The surface roughness parameter was inversely proportional to the grain size. The smaller grain size in the new alloy resulted in the rougher surface and longer fatigue life.
- The fatigue cracks path is 60 to 95% transgranular with no preference towards unrecrystallized or recrystallized grains. The intergranular portion of the path is preferentially between unrecrystallized and recrystallized grains.
- Microstructural examinations showed that deflections of crack paths have been controlled by the second phase particles. No change in dislocation structure and no

alterations of the precipitate structure was observed in the vicinity of the fatigue cracks.

- Estimations of the effects of the crack deflections on the crack propagation rates suggest that they can result in up to 16% decrease in the crack propagation rate in the 7050-T7451 alloys.

## ***Modeling***

### **Size Distributions of Fatigue Crack Initiating Features**

All crack growth fatigue life predictions require as input either average initial crack size or crack size distribution. Since in the investigated alloys fatigue initiated predominantly from micropores and constituent particles, it would be tempting to assume that initial crack sizes and the size distributions of these features are equivalent. As evident from Figure 45 and 46 such assumption would be incorrect. The figures compare maximum pore dimensions obtained for the old and new alloys from metallography with the actual sizes of the crack initiating pores for smooth fatigue samples. For both alloys the crack initiating pores are at least order of magnitude larger than those found on the metallographic sections. The difference is due to the fact that the dominant fatigue crack does not initiate from a randomly chosen pore but from the one that generates the largest stress intensity. In smooth samples these are the largest surface pore, hence the size distribution of those pores, one from each sample, constitutes distribution of the actual initial cracks. The problem of finding the latter reduces then to finding the extreme distributions from the parent distribution obtained from metallographic measurements[67,109].

### ***Extreme value statistic***

The true size distributions of the pores or particles, or dispersions in general, can be obtained from the metallographic characterizations using the procedures described in the proceeding sections [23]. Let us assume that both the cumulative size distribution, cdf or  $F_D(d)$ , and the probability density function, pdf or  $f_D(d)$ , obtained from such measurements are known. Let us also assume that we know the number of pores or particles in the sample surface region,  $n$ , which we shall call "sample size". The extreme value distributions of the largest dispersions in the surface region can be then obtained from the following expressions[67]:

$$\begin{aligned}
\text{cdf: } F_{D_n}(d) &= [F_D(d)]^n \\
\text{pdf: } f_{D_n}(d) &= \frac{dF_{D_n}(d)}{dd} = n[F_D(d)]^{n-1} f_D(d)
\end{aligned}
\tag{eq. 54}$$

where  $F_{D_n}$  and  $f_{D_n}$  are extreme value cdf and pdf functions. Equations (54) are useful only for small sample sizes. For large  $n$ , expected in our case, they degenerate to either 0 or 1. The problem can be eliminated by using the following large sample asymptotic equivalents of equations (54) [110]:

$$\begin{aligned}
\text{cdf: } F_{D_n}(d) &= \exp\{-n[1 - F_D(d)]\} \\
\text{pdf: } f_{D_n}(d) &= n f_D(d) \exp\{-n[1 - F_D(d)]\}
\end{aligned}
\tag{eq. 55}$$

which give finite results for any  $n$ .

Another problem with equations (54) and (55) is that they are valid only for a constant sample size. When sample size vary, as is the case of the number of pores or particles at the sample surface region, equation (54) for cdf has to be replaced with[67]:

$$\text{cdf: } F_{D_n}(d) = \sum_{n=0}^{\infty} p_n [F_D(d)]^n \tag{eq. 56}$$

where  $p_n$  is the probability that sample has size  $n$ . For our purposes  $p_n$  can be adequately approximated by the Poisson distribution[111]:

$$p_k(k, n) = \frac{n^k}{k!} e^{-n} \tag{eq. 57}$$

where  $n$  is the expected average. Combining Eqs. (56) and (57) leads to:

$$\begin{aligned}
\text{cdf: } F_{D_n}(y) &= \sum_{k=0}^{\infty} \frac{n^k}{k!} e^{-n} [F_D(d)]^k \\
&= e^{-n} \sum_{k=0}^{\infty} \frac{1}{k!} [n F_D(d)]^k \\
&= e^{-n} e^{n F_D(d)} \\
&= \exp\{-n[1 - F_D(d)]\}
\end{aligned}
\tag{eq. 58}$$

where we took advantage of the relationship:

$$\sum_{n=0}^{\infty} \frac{x^n}{n!} = e^x \quad \text{eq. 59}$$

Note that equation (58) and equation (55a), are identical. This means that for Poisson distribution of sample sizes the extreme value distribution does not degenerate. Equations (55) can be then used for both constant and variable sample sizes.

Now, depending on the type of the parent distribution, the extreme value cdf's can have, theoretically, three possible asymptotic forms [67,109]. In particular, if the parent distribution is of the exponential type, its asymptotic form is Type I or Gumbel distribution:

$$F(x) = \exp[-\exp(A_n x)] \quad \text{eq. 60}$$

For the polynomial parent, the limiting distribution has Type II or Frechet form:

$$F(x) = \exp(-A_n x^{-k}). \quad \text{eq. 61}$$

and, when the parent has an upper bound, the Type III or Weibull asymptote follows:

$$F(x) = \exp[-A_n (B_n - x)^k] \quad \text{eq. 62}$$

In all cases  $k$  is a constant and  $A_n$  and  $B_n$  are functions of the sample size. The asymptotic forms, or domains of attractions, for other common continuous distributions are also known and they can be found for instance in reference [67]. If the type of the parent distribution can be identified, it is always possible to find the type of its extreme value asymptote. However, the problem of identifying parent distribution for the extreme value purposes is slightly different from the one of finding the best fit to the experimental data. This is because the estimates of the extreme largest values, which we are interested in, are based on the extrapolations of the right tail of the parent distribution to the large size region. The parameters of the parent distribution should be then obtained in this case by weighting tail data points the most. The weight function recommended for this purpose has the form [67]

$$w_i = \frac{1}{1 - p_i} \quad \text{eq. 63}$$

where  $p_i$  is an empirical cumulative probability of the ordered point number  $i$ . Another possibility is to use only the tail portion of the distribution in the extreme value

calculations, neglecting all small size data. It is evident that in both approaches the assumption about the shape of the parent distribution, and its tail in particular, has a detrimental effect on the precision of the extreme value calculations. In this work we assumed that the parents were either lognormal or of the Gumbel type. The lognormal distribution was chosen because it gave the best fit to the experimental data for both pores and constituents [23]. The Gumbel distribution is on the other hand a domain of attraction for the largest extremes for the lognormal cdf [67]. The Gumbel and lognormal distributions should be then tail equivalent which means that the former would be a good approximation for the tail of the later.

To identify the pore and the particle distribution types their experimental size distribution data were plotted on the appropriate probability papers. Examples of such plots for porosity in the old and new alloys are shown in Figure 61 (linear plots are included for comparison). Each plot has only data for maximum pore dimensions on LS planes in the plate center regions (parent distributions) and maximum dimensions of the actual fatigue crack initiating pores obtained from fractography(extreme values). The parent distributions on both lognormal and Gumbel probability plots are not straight. However, in all cases the right tails can be approximated with straight lines suggesting that the choice of both cdf's is justified. The extreme value distributions (fractographic data) in both cases are also reasonably linear except for few points corresponding to the largest pores. These largest pores have approximately the same size, about 450  $\mu\text{m}$  for old and 200  $\mu\text{m}$  for the new alloy, suggesting that each alloy may have a maximum pore size limit.

To find which continuous distribution was better suited for the extreme value calculations, they were both used for fitting the experimental parents. The equations used were:

$$\begin{aligned} \text{Lognormal cdf: } F(x) &= \frac{1}{\sqrt{2\pi}\sigma} \int_{-\infty}^x \frac{1}{t} \exp\left[-\frac{1}{2}\left(\frac{\ln t - \mu}{\sigma}\right)^2\right] dt \\ \text{Gumbel cdf: } F(x) &= \exp\left[-\exp\left(-\frac{\ln x - \mu_G}{\sigma_G}\right)\right] \end{aligned} \quad \text{eq. 64}$$

Both standard and weighted least-square fit, with weights calculated from Equation (63), were used. The standard fit was chosen to simulate indiscriminate use of the metallographic data and/or use of data obtained from measurements taken under low magnification. The weighted fit made better use of the right tails of the distribution and simulated use of results from metallographic examinations obtained under high magnification. The fitting results are in the "parent" column in Table XXIX and Table XXX. In all cases the correlation coefficients,  $R^2$ , for the standard least-square fits were greater than 0.95. There was also no significant difference in the goodness of fit between lognormal and Gumbel approximations.

As the next step the least-square method was used to estimate the best values of the sample sizes,  $N$ , which would result in the best fit of the extreme values predictions to the experimental fractographic data, Figure 62 to 65. In this case Eq. (55a) combined with Eq. (64) were used. Results are also in Table XXIX and Table XXX showing clear superiority of Gumbel distribution. The fit is also shown in Figure 62 to 65. The predictions of Gumbel distribution were particularly accurate for the large size ranges and notably for the new alloy (Table XXX). For that alloy the correlation coefficient for Gumbel distribution and standard fit is higher than that for the weighted fit. However, the probability plot shows that this is mostly due to large differences between predictions and experimental data in the small pore range, which is not critical for the worst case design, Figure 65. For the large pore sizes the predictions from the Gumbel distributions obtained from weighted fit are clearly superior.

The values of sample sizes,  $N$ , which gave the best approximations of the fracture surface data require close scrutiny. They represent the number of pores in the sample surface region which were interrogated, for the largest stress intensity, by the cyclic stress. To be physically plausible, these values should be between the total number of pores intersected by the specimen surface and the number of pores in the entire gage section volume, Table XXXI. For both alloys the sample sizes for lognormal distributions were either larger than the total number of pores in the sample or equal to the number of pores

in the surface layer from 1.4 to 2.7 mm thick. Both results are then unrealistic. For Gumbel distribution, the  $N$ -values were consistent with the number of pores either intersected by a sample surface about 0.6 to 5.5 mm wide or in a surface layer from 8 to 157  $\mu\text{m}$  thick. The last two values, obtained for Gumbel distribution using weighted fit, are the most physically appealing as they correspond to the surface layer of the order of the average pore size.

Results from the above preliminary considerations strongly suggested that fatigue crack initiating pore size distributions are indeed the extreme value cdf's of the pore size distribution obtained from metallographic sections with the sample size equal to the number of pores in the surface layer. However, they also showed that the predictions were very sensitive to the method used in estimating parameters of the parent distribution. In particular, when using weighted fit, the largest pore found on the metallographic section had detrimental influence on the value of those parameters. This is undesirable, because each metallographic characterization will lead to the detection of different largest pore resulting in different both parent and extreme distributions. To eliminate this problem it would be more appropriate not to use the weighted fit but rather utilize the whole right tail of the distribution with equal weight on each point. We recommend that for this purpose the right tail can be defined as the region with sizes greater than logarithmic average plus one logarithmic standard deviation, Figure 66. This assures that (1) only relevant data are included in the analysis and (2) that the extreme value estimations are obtained from the average properties of tail. This procedure has been used in all subsequent extreme value calculations.

### *Smooth Fatigue Samples*

The estimations of the initial crack sizes in the smooth fatigue samples were based on the metallographic data from the plate center regions using statistics of extreme. The calculations were carried out for the old, new and low porosity plates. Thin plate variant was excluded because for smooth samples from that alloy fatigue initiated as Stage I failures [13]. The size distributions used in the estimations consisted of particle or pore

largest diameters data obtained from TL, LS and ST sections. They were fitted with the lognormal distribution, eq. (64), to obtain the cut-off values of the tail section, Figure 66. The tails were then approximated with the Gumbel distributions, eq. (64), which were subsequently used as the parent distributions in all extreme value calculations. The fitting results are shown in Figure 67 to 70 and are summarized in Table XXXII.

Finding the extreme value distributions describing the initial crack sizes, eq. (55), requires knowledge of both the metallographic parent and the sample size,  $n$ . Our results from the proceeding section suggest that  $n$  is related to the number of pores in the sample gauge section. To find its value, the extreme value distributions were fitted to the fractographic data treating  $n$  as variable. The calculations were carried out only for the crack initiating features actually observed on the fracture surface and the obtained best  $n$ -values are listed in Table XXXII together with the number of particles or pores intersected by the sample surface. The ratios of the two quantities, also listed in the Table XXXII, have two interpretations. The first is that it represent the fraction of the sample total gauge section, in its center region, where the cracks are most likely to form. The second possibility is that it is the fraction of pores or particles which can serve as the crack nucleation sites. Accordingly, for old and new alloys, where cracks initiated exclusively from pores, it appears that they started from either the largest pore intersecting the central one-half portion of the total gauge section or that only half of the pores are capable of initiating a crack. Although both interpretations are physically plausible, we believe that the former is the correct one. This is because according to the later the  $n/n_{surf}$  ratios for both alloys should be different due to the differences in the pore sizes, volume fractions and shapes. Almost identical values suggest that they are controlled by the sample geometry, which was in both cases the same. For low porosity alloy, where fatigue cracks initiated both from pores and particle, the obtained results were quite different. For pores, the  $n/n_{surf}$  ratio was greater than one implying that cracks initiated from the largest pores in the surface layer about 260  $\mu\text{m}$  thick. This result is inconsistent with the one for old and new alloy. The difference can be attributed to the fact that in the low porosity alloy the crack initiating pores were always adjacent to the constituent particle. The reported

“pore” sizes were actually the sizes of the entire nucleation site which included both the pore and the particle. The pore sizes are then overestimated which results in the overestimated sample size. Using the true dimensions of the pores would on the other hand underestimate of the initial crack size leading to the underestimation of  $n$ . Since for the old and new alloys the  $n/n_{\text{surf}}$  ratio depended primarily on the sample geometry, the same should hold for the low porosity case. It was then assumed that for that low porosity alloy the  $n/n_{\text{surf}}$  ratio was also approximately 0.5. For particles in the same alloy the best-fit  $n$  was very small, corresponding to the interrogated area of about  $1.4 \text{ mm}^2$ . This means that the cracks did not initiate from the largest particle but from the largest particle with the potential for cracking or, perhaps, the largest already cracked particle. There were only 67 such particles intersected by the sample surface which was about 0.07% of the total. As a result the cracks nucleated preferentially from pores, despite the fact that the particles are larger and have larger area densities.

Our results indicate that sampling of the smooth samples for the particles and pores with the largest potential for initiating fatigue crack depends on the feature type. For pores, the one which initiates crack is the largest surface pore in the middle half of the sample gauge section. The sample size,  $n$ , for the extreme value distribution is then in this case equal to the half of the total number of surface pores. For particles, the crack do not initiate from the largest surface particle but from the largest particle which can break and form a crack. Based on the data for the low porosity alloy this would be the largest particle from the 0.07% of all surface particles which can form a crack. The sample size for particles is therefore equal to the 0.0007 times the total number of all particles in the sample surface region.

The above-defined sample sizes were used in predicting the expected size distributions of the fatigue crack initiating particles and pores using eq. (54). Parameters of the obtained extreme value distributions are in Table XXXII (Gumbel extreme) and the distributions are compared with experimental data in Figure 67 to 70. In all cases the predictions are quite accurate. The only exceptions are cracks initiating pores in the low

porosity alloy which have sizes slightly underestimated by the extreme calculations. Note that Table XXXII also contains predicted average sizes of the cracks initiating particles and pores. For new and old alloys the predicted sizes of cracks nucleating from pores are much larger than those for particles which explains why only pores served in these alloys as the crack nucleation sites. For low porosity alloy the predicted sizes of cracks from particles and pores were comparable, which resulted in the mixed nature of the nucleation sites.

### *Open Hole Fatigue Samples*

The sizes of initial cracks in the open hole samples were estimated using the same extreme value procedure as for the smooth samples. The metallographic pore and particle size data used in the calculations were from the TL, LS and ST planes from the center-plate locations. Since in the old and new alloys cracks initiated from particles and pores and in low porosity and thin plates from particles, only those cases were considered. The relevant cumulative distributions of bulk pore and particle sizes are in Figures 71 - 74. The figures also include parent distributions, fractographic data and predicted (extreme) distributions of the initial cracks. All input data used in the calculations and the parameters of the parent and predicted extreme distributions are summarized in Table XXXIII.

As in the smooth sample case, the sample sizes,  $n$ , for the extreme value calculations were obtained based on the experimental data using the best fit procedure. For the pores, the  $n$ -value was calculated as the average of the best-fit values for the old and new alloys. The obtained  $n$  was equal to the number of pores expected on about 90% of the total surface area of the two holes present in the sample (see  $n/n_{\text{surf}}$  ratios in Table XXXIII). However, as discussed in details by Yang at al.[112], because of the stress concentration around the hole, the highly stressed region includes in this case not only a portion of the hole inside but also an area on the front and back surfaces surrounding the hole, Figure 75. Yang at al. estimated how the size of that highly stressed area changes with its average stress. According to their results, Figure 75b, for pores in our case this

area will extend circumferentially by angle  $\theta = 19.5^\circ$  and radially by  $\delta \cong 3$  mm. This corresponds to the average stress in the highly stresses region equal to the 95% of the maximum in the circumferential and 60% of the maximum in the radial direction. Alternatively, the same sample sizes correspond to the number of pores in a search volume of 0.45 to 0.48 mm<sup>3</sup> which corresponds to the four through-thickness cylindrical search zones, about 220  $\mu$ m in diameter, at each hole maximum stress regions. The obtained sample sizes are then physically plausible, as they indeed correspond to the number of pores in the highly stressed region. The predicted distributions of the initial cracks starting from pores obtained using above results, Figure 71 and 72, are in very good agreement with the experimental data, particularly in the relevant, high size region.

For fatigue cracks initiating from particles the average extreme sample size was calculated as the average of the best fit values for all four alloy variants. The individual sample sizes, Table XXXIII, were in this case surprisingly small and varied from 1.1 to 59. Since sample size equal one corresponds to the case when any particle, independent on its size can serve as the crack nucleation size, obtained results suggest that cracks did not nucleated from the largest particles but from any particles susceptible to cracking. This is consistent with the our results for smooth specimens which also suggested that only some of the particles were capable of nucleating a crack. The predicted size distributions of the cracks initiating from particles are shown as dotted lines in Figures 71 to 74. The predictions are very good for the old and thin plate alloys and result in the overestimation of initial crack sizes in the new and underestimation in the low porosity plates. For the new and thin plate alloys, which had best fit sample sizes close to one, the initial crack size distributions could be adequately approximated with the parent distributions eliminating the need for the extreme value conversions.

The predictive capabilities of the proposed extreme value approach could be additionally tested by comparing the expected frequency of cracking from particles and pores with the experimental data. According to our fractographic results, Table XX to XXIV, for the open hole samples from the old and new alloys the fatigue cracks should

start predominantly from pores, while for the low porosity and new plates they should initiate from particles or as Stage I failures. Accordingly, it would be expected the predicted average sizes of the fatigue crack initiating pores in the old and new alloys should be greater than those of particles, while the reverse should hold for the low porosity and thin plates. Results from Table XXXIII ( $d(50\%)_{\text{extreme}}$ ) show however that for all alloys the predicted sizes of crack initiating pores are greater than those of particles. The discrepancy can be attributed to the difference in the driving forces for cracks initiating from particles and pores. These differences were analyzed by Trantina and Barishpolsky[113] who showed that for similar geometry a bonded cracked inclusion has crack driving force 15% greater than a void. Our results for the old and new alloy, where small fractions of fatigue cracks started from particles, are in accord with those predictions. They suggest that the cracked particles had the same crack driving force as the pores with from 2.7 to 3.8 times greater size. Considering the differences in the pore and particle geometry and that particles always have sharper initial cracks than pores, the obtained amplifications of the crack driving force by the particle is in the expected range. Using the particle size multiplication factor of 3.8 obtained for old alloy for the low porosity and thin plates gives particle equivalent crack initiating pore size of 105.3  $\mu\text{m}$  for the former and 70.3  $\mu\text{m}$  for the later alloy. These values are larger than the expected largest pores in the highly stressed regions, explaining why cracks did not start from pores in these two alloys. The predictions of the initial crack sizes in the open hole samples using the statistics of extreme are then self consistent demonstrating the utility of the proposed approach.

### *Summary*

- The initial true fatigue crack size distributions in the smooth and open hole fatigue samples have been estimated from the bulk pore and particle size data using the statistics of extreme.

- The initial crack sizes have been described using extreme Gumbel distribution obtained from the Gumbel parent fitted to the tail portion of the bulk pore and particle size metallographic data. The tail of the size distribution has been defined as region with feature sizes greater than logarithmic average plus one logarithmic standard deviation.
- For smooth fatigue specimens the extreme value sample size for pores was equal to the half of the total number of pores intersecting sample gauge section. For particles it was estimated as 0.0007 times the number of surface particles in the same region.
- For the open hole specimens the extreme value sample size for pores was equal to the number of pores in the highly stressed surface area extending  $19.5^\circ$  circumferentially up and down from the holes mid-sections and radially by about 3 mm on the hole front and back surfaces, Figure 75. For particles the sample size was on average equal to 0.00115 times the total number of surface particles in both holes.
- Small values of the sample sizes for particles indicate that not all particles are capable of generating a crack. It appears that the particles which nucleate fatigue cracks are not necessarily the largest particles at the surface or highly stressed regions, but the ones which are susceptible to cracking.
- Obtained results confirmed theoretical expectations that the initial crack driving force for cracked particles are larger than for pores. The driving force for a crack nucleating at a particle appears to be the same as for the cracks at pores with 2.7 to 3.8 times greater size.

## Life predictions

### *Introduction*

Information generated during material characterization phase of the program were used to develop relationships between the microstructural characteristics and fatigue lives. The goal of this part of the program was to formulate microstructure based fatigue life prediction models which would predict not only the average fatigue lives but also life distributions. Particular emphasis were put on testing the predictive capabilities of the existing models and on finding the methodologies of incorporating microstructural parameters into them.

All life prediction models can be divided into phenomenological and statistical. The first group consists of models based either on the Miner's type damage accumulation law or on the Paris/Erdogan crack growth equation[101]. These models usually have at least one parameter related to the material mechanical properties which, in turn, depends on microstructure. The phenomenological models have therefore potential for linking microstructural descriptors with fatigue life. In contrast, statistical models include parameters describing the statistical nature of the fatigue process. Such parameters rarely have physical meaning which make them unsuitable for linking fatigue life with the microstructural characteristics. However, since statistical models provide usually good fit to the fatigue data, they are useful for combining statistical descriptions of the nucleation and propagation stages of fatigue life. In this program we tested the predictive capabilities of the life predictions based on the crack growth phenomenological models. Changes in microstructural variables on the crack path were incorporated using the Monte-Carlo (MC) approach. The considered stochastic variables included (1) size distributions of the crack initiating features, (2) crack location, (3) changes of the crystallographic texture on the crack path and (4) microstructure related crack deflections. We also investigated capabilities of the Markov chain approach for potential use in integrating together various crack nucleation and growth models.

Our initial modeling work was focused on identifying the sources and magnitudes of scatter in fatigue lives of the 7050-T7451 plate alloys. From the preliminary fatigue testing results obtained by Alcoa team it appeared that for the smooth samples there was a definite correlation between fatigue lives and the sizes of both the actual crack initiating pores and the sizes of the intentionally introduced defects, Figure 76 [114]. However, since the scatter in the data was substantial, it was anticipated that both the initial crack size distribution and the changes in the microstructure along the crack path contribute to the scatter. The largest microstructural contributions to the variation in fatigue lives were expected to come from the crystallographic texture and crack deflections. This is because the texture at the crack tip controls local yield strength hence also the extend of the cyclic plastic zone. Since the texture changes along the crack path, one can expect fluctuations of the yield strength with crack length. Crack deviations from the straight path control on the other hand crack tip stress intensity. These deflections are result of the attractive interaction between constituent particles and the crack, preference to the crack propagation along weak inclined grain boundaries, etc. Both local texture and local crack deflections affect then local crack growth rate, contributing to the scatter in the fatigue lives.

The microstructural effects were expected to be the most significant at the initial stages of fatigue life in the smooth fatigue samples. For this samples the maximum stresses were smaller than for the open hole specimens which had stresses amplified by the concentration factor of 3. The cracks dispensed then more time in the former in the incipient stage where the local microstructural effects were strong. As a result, our efforts concentrated on modeling the distributions of fatigue lives for the smooth fatigue samples where microstructural effects were expected to be the strongest. Our objectives in this stage of the program were to:

- (1) Determine if the crack growth stage is proceeded by the substantial period of nucleation.

- (2) Estimate upper and lower bounds of the effects of the microstructural fluctuation on fatigue life.
- (3) Incorporate all findings into microstructure base Monte-Carlo life predictions model.

This approach complemented work by the Alcoa team which concentrated on the developed models for predicting fatigue lives of the open hole samples. Their results are described in references [13].

### *Crack Nucleation*

The number of nucleation cycles in the smooth samples were estimated by comparing the experimental cycles-to-failure data with the expected values obtained from the deterministic crack growth model. The experimental data used were for the old and new alloys tested at constant amplitude with maximum stress 240 MPa, R-value 0.1 and frequency 10 Hz [13]. The correlation between fatigue results and the actual sizes of the crack initiating pore is shown in Figure 77a. These results were compared with the expected fatigue lives were calculated using the experimental crack growth rate equation for the 7050-T7451 obtained from the data in Figure 78 [115]. The  $da/dN$  data are best described by the relation[115]:

$$\frac{da}{dN} = 7.5 \cdot 10^{-12} \Delta K^{4.175} \quad \text{eq. 65}$$

which gives result in m/cycle for  $\Delta K$  in MPa  $m^{1/2}$  and which is valid for stress intensities grater than the threshold,  $\Delta K_{th}$ , which is about 3.3 MPa. For intensities smaller than  $\Delta K_{th}$  it was assumed that the growth rate followed the dotted line shown in Figure 78. Such approximation of the  $da/dN$  curves is consistent with the expected small crack behavior [116,117]. Equation 65 was integrated numerically assuming that the initial crack sizes were equal to the actual measured sizes of the crack initiating pores and that cracks grew from the very first fatigue cycle. The expression for  $\Delta K$  used in the calculations was the one proposed by Newman and Raju[118] and the nucleation cycles were calculated as:

$$N_{nuc} = N_{exper.} - N_{predicted} \quad \text{eq. 66}$$

Obtained nucleation cycles are shown in Figure 78 b. For the majority of samples they were in the  $\pm 50,000$  cycles range (one sample from the new alloy had nucleation period equal 90,000 cycles and for one specimen from the old alloy it was -60,000 cycles). The averages were 15,000 cycles for the old alloy and -2,600 for the new one. Comparing those numbers with the average fatigue lives, which were 93,000 for the old and 135,000 for the new alloy, the nucleation periods were relatively short. What was surprising was a large number of samples with negative nucleation periods suggesting crack acceleration. Figure 77 b also suggested that there might be an inverse proportionality between the number of nucleation cycles and fatigue life. Since fatigue lives are also inversely proportional to the initial pore sizes, this means that 7050 alloys the crack initiating pore sizes and the number of nucleation cycles should be proportional. This relationship is explored in Figure 79. The scatter is substantial, but there seems to be a weak positive correlation. For small crack sizes the observed trend can be attributed to the well known phenomena of the accelerated growth of the small cracks [116]. Negative nucleation cycles were indeed observed for the smallest crack initiating pores. However, for large initial cracks the relationship is contrary to expectations, as one would expect no nucleation period for the large pores. A plausible source of the discrepancy is crack tip blunting at large pores which can lead to lower nucleation times.

Despite weak correlation between estimated nucleation periods and fatigue lives, for all practical purposes the fatigue crack nucleation times for the old and new 7050-T7451 plate alloys could be considered as random. Since there was no significant difference between the nucleation periods for both alloys, their nucleation data were plotted together on the normal probability plot in Figure 80. The plot shows excellent linearity suggesting random scatter in the nucleation times. The average number of nucleation cycles obtained from the plot was 6,100 with the standard deviation of 22,800. Small values of both statistics compared with the average fatigue lives suggests that nucleation periods are due to the random error with equal probability of the positive and negative deviations. As reported by Grandt et al. [119], similar trends would be expected

for the cracks nucleating from particles for the low porosity and thin plates and for crack nucleating from both feature types in open hole samples. As a result, in all subsequent simulations utilizing crack growth model it was assumed that the crack nucleation periods were random and negligible compared to the error introduced by the microstructural variables.

### *Magnitudes of Microstructural Effects*

The expected upper and lower limits for the fatigue lives resulting from the microstructural fluctuations were estimated using eq. 65. To introduce microstructural parameters the crack growth rate equation had to be re-written in the following form:

$$\frac{da}{dN} = C \Delta K^m = \mathcal{D}_{avg} \frac{C'}{\sigma_{ys}^n} \Delta K^m \quad \text{eq. 67}$$

where  $C = 7.5 \cdot 10^{-12}$ ,  $m = 4.175$ ,  $\mathcal{D}_{avg}$  is the correction for crack deflection,  $\sigma_{ys}$  is the yield strength and  $n$  is material constant assumed equal 1. The new  $da/dN$  equation has then constant  $C$  deconvoluted into the microstructure related components. In addition, since the yield strength can be expressed as a product of the Taylor factor,  $M_{avg}$ , and the critical resolved shear stress  $\tau_{crss}$

$$\sigma_{ys} = M_{avg} \cdot \tau_{crss} \quad \text{eq. 68}$$

eq. 67 can be replaced by:

$$\frac{da}{dN} = \mathcal{D}_{avg} \frac{C''}{M_{avg}^n} \Delta K^m \quad \text{eq. 69}$$

where

$$C'' = \frac{C'}{\tau_{crss}^n} \quad \text{eq. 70}$$

Comparing eqs. 67 and 69, with  $n=1$ , gives following expression for constant  $C''$ :

$$C'' = \frac{C \cdot M_{avg}}{D_{avg}} \quad \text{eq. 71}$$

Knowing the average Taylor factor and the crack deflection correction factor allows then for the calculation of constant  $C''$ . Eq. 69 can be subsequently numerically integrated with maximum and minimum values of  $D$  and  $M$  substituted for  $D_{avg}$  and  $M_{avg}$  to obtain the upper and lower estimates of the fatigue life fluctuations due to, respectively, crack deflections and texture. Additional variability of fatigue lives comes from the variations in the initial crack sizes. As discussed earlier, the size distributions of those cracks can be obtained from the metallographic pore and particle size distribution data using the statistics of extremes. Obtained results can be then used as initial crack sizes while integrating eq. 69 to obtain the spread in fatigue lives attributable to the distributions of pore and particle sizes. The bounds on fatigue lives from all above variables have been estimated for the case of the new alloy and smooth specimens. The results are described below. They represent typical effects expected in all alloy variants.

The magnitude of variations in fatigue life due to size distributions of crack initiating feature were estimated assuming that cracks start from pores. This assumption was consistent with our fractographic results for smooth fatigue samples for all alloy variants. The pore size data used were for the new alloy, which represented average expected behavior. In the calculations it was assumed that the upper and the lower size bounds correspond to, respectively, the one and the ninety nine percent fractiles of the predicted pore size extreme Gumbel distributions. The pore sizes were calculated from eq. 64 by solving it for  $d$ :

$$d = \exp\{\mu_{G-ext} - \sigma_{G-ext} \ln[-\ln F(d)]\} \quad \text{eq. 72}$$

where parameters  $\mu_{G-ext}$  and  $\sigma_{G-ext}$  were taken from table XXXIV and  $F(d)$  was the probability. Obtained initial crack size limits were 84 and 485  $\mu\text{m}$  and the predicted average initial size was 154  $\mu\text{m}$ . The corresponding crack growth curves are in Figure 81. They were obtained for  $\sigma_{max} = 240 \text{ MPa}$  using stress intensity from Raju and Newman

[118]. The initial crack was assumed to be of the thumbnail type with depth equal to the pore size and with average aspect ratio of the bulk pores. The predicted dispersion of fatigue lives was 150,000 cycles which is comparable to that of the experimental data.

The effects of fluctuations in crystallographic texture along the crack path enter our crack growth equation, eq. 69, through Taylor factor,  $M$ . To calculate this factors it is necessary to determine the average crystallographic texture (or more precisely the CODF function) and the stress state at the crack tip. Unfortunately, both are not only extremely difficult to measure but they also change with the crack size. It is nevertheless possible to evaluate the bounds of the Taylor factor for various textures and stress states. For aluminum and its alloys such estimates have been carried out by Bunge[120]. The Taylor factors obtained by him for metals with fcc structure were between 4.5 and 2.5 which with an average of 3.5. The crack growth curves obtained using those values are shown in Figure 82. They were calculated by again numerically integrating eq. 69 with the same  $\sigma_{max}$  and  $R$  as for initial crack sizes. The initial crack size was assumed 154  $\mu\text{m}$ , which corresponds to the average predicted size of the fatigue crack initiating pore in the new alloy. The obtained range of fatigue lives was 165,000 cycles. It should be however kept in mind that this represents the maximum one-sided effects. In reality the scatter will be smaller because the extreme conditions are not going to persist throughout the entire fatigue life. A more realistic estimate of texture effect was obtained by randomly varying  $M$  between 2.5 and 4.5 along the crack length using our MC model described later in the report. Such changes of  $M$  used in 1,000 MC simulations resulted in the predicted fatigue life range of only 5,200 cycles, Figure 82.

To evaluate the range of scatter resulting from microstructural crack deflections we used our experimental fracture surface roughness data. Although the data were obtained for the open hole samples we expected no significant change in roughness values for the smooth specimens. Following description proposed in reference [117], it was assumed that the crack had idealized periodic profile shown in Figure 83. For that profile the deflection correction factor is equal to:

$$\mathcal{D} = \mathcal{D}' \cos \Theta + (1 - \mathcal{D}') \quad \text{eq. 73}$$

where

$$\mathcal{D}' = \frac{D}{D - S} = \frac{R_L - 1}{R_L (1 - \cos \Theta)} \quad \text{eq. 74}$$

$D$  and  $S$  are define in Figure 83 and  $R_L$  is the profile roughness parameter. Combining last two equations gives:

$$\mathcal{D} = \frac{1}{R_L} \quad \text{eq. 75}$$

which facilitates calculation of the crack deflection parameter from the surface roughness data. The maximum profile roughness obtained from our fractographic measurements was 1.54 which substituted to equation 75, gives the smallest crack deflection correction factor. The upper limit for  $\mathcal{D}$  is one, corresponding to the straight crack without deflections. Crack growth curves obtained for those maximum and minimum  $\mathcal{D}$  values, and for their average, are in Figure 84. The calculations were performed for the same initial crack length and the loading conditions as for texture. The obtained fatigue life variability was 61,000 cycles which was less then that for texture. This is again a one-sided overestimation. To obtain a realistic estimate of the range, the  $\mathcal{D}$ -values were varied along the crack path uniformly between the upper and lower bounds. The resulting spread of fatigue lives was in this case only 2,200 cycles, Figure 84.

The scatter in fatigue lives for the 7050-T7451 plate alloys would be then expected to be controlled primarily by the size distribution of crack initiating pores, with other microstructural factors playing secondary role. Since the contribution of the variation of the initial crack sizes to the distribution of fatigue lives is so enormous, it would be interesting to evaluate the effect of an error in the estimation of the crack initiating pore sizes on the error in the predicted fatigue lives. The necessary relationship is given by eq. 69. This relation is plotted in Figure 85 for the average crack initiating pore size in the new alloy. Assuming that the error in estimating pore size does not exceed 20%, gives the

error of the fatigue life of about 10,000 cycles. The plot also shows that in order to have the scatter from pore size distribution comparable to that from texture, the pore sizes should vary by no more than  $\pm 4 \mu\text{m}$  from the average. For crack deflection this requirement is even more stringent, as the pore sizes should not fluctuate by more than  $\pm 2 \mu\text{m}$ . For the new alloy the effect of texture and crack deflections on fatigue life would be then comparable to that from pores if the spread of the pore size distribution is narrowed significantly below its current standard deviation of  $60 \mu\text{m}$ . Similar trends would be expected in the remaining 7050-T7451 alloy variants.

## Monte-Carlo Simulations

### Introduction

The propagation of the fatigue cracks through the real microstructure was simulated using the Monte-Carlo (MC) approach[121] . The reason for selecting the MC model was its ability to dynamically change the crack tip related microstructural parameters during crack growth[122,123]. This capability is extremely important in fatigue life predictions. As the crack length increases, its growth rate increases exponentially. Any changes in the crack tip environment when the crack is small are then much more detrimental to the fatigue life than those just before the final failure. For small crack the crack tip and the plastic zone are also small and they “sample” only few neighboring grains. Consequently, at this stage of fatigue the growth rate is controlled by the local microstructure. For a long crack the plastic zone extends over several grains hence crack propagation is controlled by the average material properties. Our Monte-Carlo model incorporated all these microstructural effects through eq. 69. When rewritten in the integral form, that equation has the form:

$$N = N_o + \int_{a_o}^{a_{crit}} \frac{M^n}{DC'' \Delta K^m} \cdot da \quad \text{eq. 76}$$

where  $N_o$  is number of nucleation cycles,  $a_o$  is an initial and  $a_{crit}$  final crack length with all other quantities defined earlier in the report. During MC simulations, equation 76 was integrated numerically with random values of  $a_o$  as input and with randomly selected values of Taylor factor,  $M$ , and crack deflection,  $D$ , for each integration steps. The number of nucleation cycles,  $N_o$ , was assumed zero in accord with our finding described earlier in this section. Final crack sizes,  $a_{crit}$ , were estimated from the fracture toughness values for a given material. Expressions for stress intensity factors for smooth fatigue samples were taken from refs. 118 and 124 and for open hole specimens from ref. 124 and 125. The calculations were repeated for various combinations of the random variables, giving the distribution of fatigue lives. The model and the MC program developed by us is

extremely flexible and it allows for the simulation of the effects from each individual variables and from their combinations.

The distribution of Taylor factors used in the simulations was obtained from the aforementioned Bunge's results [120] for various fcc crystal orientations and for deformation ranging from simple tension to plane strain. Since similar multitude of grain orientations and stress states is expected to be encountered by the crack tip along the crack path, these results can be directly used by the MC the fatigue crack growth models. The M-values compiled by Bunge suggest that for Al-alloys the distribution of Taylor factors is uniform between 2.5 and 4.5, with the average of 3.5, Figure 86a. However, such broad range is only valid for small cracks with plastic zone of the order of one grain. As crack grows, its plastic zone penetrates increasing number of grains, which means that due to averaging effect the range for the average Taylor factors decreases, as shown in Figure 86b. Eventually, when the number of grains at the crack tip region is large, their orientations can be considered as random. The Taylor factor becomes then constant and equal to the average value for a given material. The change of the Taylor factor shown in Figure 86b has been incorporated into our Monte-Carlo model. The critical number of grains,  $N_{crit}$ , for the transition to the constant value has been assumed equal twenty, following recommendations from the literature [126].

The effect of crack deviations from the straight path entered our MC model through the distribution of the crack deflection parameters,  $\mathcal{D}$ . The value of this parameter is defined by eq. 73 with all variables defined in Figure 83. The distribution of the  $\mathcal{D}$ -values can be obtained from the fracture surface roughness data, via eq. 75. The maximum value of  $\mathcal{D}$  is for the straight crack and it is equal one. The minimum value for the 7050 alloy was calculated from the described earlier fracture surface roughness data and it was 0.65. In all simulations it was assumed that the values of the deflection parameter were distributed uniformly between those two bounds. However, since fatigue cracks tend to deflect toward second phase particles [Appendix F], it should be possible to estimate deflection parameters from the nearest particle spacing and their relative

positions. Such data, shown in Figure 87, could be obtained from the tessellation analysis of the particle spatial distribution. If necessary, this method of estimating distributions of crack deflection could be easily incorporated into our program.

### *Smooth Fatigue Samples*

All MC fatigue life predictions for the smooth fatigue samples were carried out with initial crack sizes, texture and crack deflections as stochastic variables. Additional microstructure related parameters used in the calculations included average grain size, pore aspect ratios, fracture toughness and tensile strength. The input parameters employed are listed in Table XXXIV. The fatigue life distributions were estimated for the old, new and low porosity alloy variants. The thin plate was excluded because fatigue cracks in that alloy started not from particles or pores but as stage I failures [13]. For all remaining variants it was assumed that cracks initiated from pores. This assumption was supported by the fractographic observations and by the extreme value results which showed that largest surface pores were always significantly greater than particles, Table XXXVI. All initial cracks were assumed to be of the thumbnail type with lengths equal to the sizes of the extreme surface pores and with the average aspect ratio of the bulk pores. The crack lengths were generated using Gumbel extreme pore size distribution via equation 72. The distribution parameters used are also listed in Table XXXIV. As described in the earlier sections on modeling size distribution of initial crack sizes, the parameters of the extreme Gumbel distributions were obtained from Gumbel parents fitted to the tail portion of the bulk pore size metallographic data. During simulations the crack growth increment per iteration was set to be no more than 1/1000 of the smaller of the two main crack dimensions. The MC program had provisions to terminate when either stress intensity anywhere along the crack circumference reached  $K_{Ic}$  or if the stress at the unbroken ligament exceeded tensile strength. Reported results are for a minimum of one thousands runs for each maximum stress level.

Results of the MC simulations for the smooth fatigue samples are in Figures 88 to 93. Figures 88, 89 and 91 show comparison of the actual and predicted fatigue life distributions for the specific maximum stress levels while Figures 89, 91 and 93 show comparisons of the predicted S-N curves with the experimental data. It is self evident that the predictions for the old and new alloys are in very good agreement with the actual fatigue lives. Small differences between predictions and the data can be traced back to the differences between in the predicted and real crack initiating pore sizes, Figure 70. Judging from that figure the early failures should be slightly underestimated by the MC model for the old alloy. On the other hand the overestimation of the small crack initiating pores in both alloys by the extreme value model should translate to the underestimation of the long fatigue lives. These trends are indeed observed in the simulation results conforming the dominant effect of the crack initiating pore sizes on fatigue life. Since in all cases the error results in the underestimation of the true lives, the predictions are conservative. Although this is desirable from the point of view of the safe design it may result in the unnecessary overdesign of the components if the underprediction is substantial.

For the low porosity plate the MC predictions were in excellent agreement with the experimental data for early failures but underestimated both intermediate and long fatigue lives. In interpreting these results it should be kept in mind that the predictions were obtained assuming that all cracks initiated from pores. This assumption was based on the results from the extreme value analysis which implied that the largest surface pores were always larger than particles. However, fractographic examinations showed that in some of the low porosity samples failure initiated from particles, see figure 40 and 69. These crack initiating particles appeared as stringers which could be considered as unbonded inclusions. The driving force for cracks emanating from such inclusions is about 10 % smaller than the one from the pores of the same size [113]. The MC predictions assuming that cracks start from these particles would lead then to longer fatigue lives, hence non-conservative estimates. To make predictions conservative, it was then more appropriate to assume that porosity were the predominant nucleation sites. It was then

expected that the MC simulations would overpredict the real fatigue lives for the low porosity alloy. This turned out to be indeed the case, as seen in Figures 92 and 93.

The fatigue life predictions for smooth fatigue samples using the MC model combined with the statistics of extreme estimations of the initial crack sizes give excellent estimates of fatigue lives. The predictions can be obtained based only on the knowledge of the crack growth rate equation and metallographic pore and/or particle size data. Such minimal requirements make the method very useful and economical for rapid differentiation between fatigue qualities of different lots of the same or various material. The model could be also used in the parametric studies of the effects of the shapes and spatial distributions of crack initiating features on the fatigue lives. As such it can serve as a aid for the alloy designers and process engineers in optimizing the microstructures for fatigue life.

### *Open Hole Fatigue Samples*

For the open hole fatigue samples the MC simulations were carried out for all alloy variants with initial crack size, crack position along the hole bore, texture and crack deflections as random variables. All input parameters used are summarized in Table XXXV. The calculation procedure used in this case was the one developed by the Alcoa team [13, 119]. It assumed that the crack initiating particles and pores had at the onset additional circumferential cracks of the size equal to the sizes of their cyclic plastic zones. The stress intensity for such circumferential cracks are given by equation [113]:

$$K_{T-B} = \left[ \frac{2}{\pi} + B \left( 1.12 \cdot k_t - \frac{2}{\pi} - 1 \right) \left( \frac{R}{x+R} \right)^{10} + \left( \frac{R}{x+R} \right)^{18} \right] \cdot \sigma \sqrt{\pi x} \quad \text{eq. 77}$$

where  $B$  is a constant equal 1 for a void, 2 for a bonded and 0.3 for unbonded particle,  $k_t$  is particle or pore stress concentration factor,  $R$  is particle or pore size and  $x$  is the width of the circumferential crack. The effective stress intensity is then calculated from relation[119]:

$$K = \frac{K_{T-B}}{K_{penny}} K_{N-R} \quad \text{eq. 78}$$

where  $K_{penny}$  is stress intensity factor for the equivalent penny shape crack in the infinite body which is equal to

$$K_{penny} = \frac{2}{\pi} \sqrt{\pi(R+x)} \quad \text{eq. 79}$$

and  $K_{N-R}$  is a standard stress intensity for the thumbnail surface crack located at the surface of the bore of a hole [124, 125].

The two yet undetermined parameters of the procedure are initial circumferential crack width,  $x_o$ , and the stress concentration factor,  $k_t$ . The crack width was obtained from the condition proposed by Brockenbrough et al. [127]. This condition assumes that the width  $x_o$  is equal to the cyclic plastic zone size associated with the stress intensity  $\Delta K_{T-B}$ . Combining expression for the cyclic plastic zone size with eq. 77 gives the following expression for  $x_o$ :

$$\frac{2\sigma_{ys}}{\Delta\sigma} = \frac{2}{\pi} + B \left( 1.12 \cdot k_t - \frac{2}{\pi} - 1 \right) \left( \frac{R}{x_o + R} \right)^{10} + \left( \frac{R}{x_o + R} \right)^{18} \quad \text{eq. 80}$$

which needs to be solved using a numerical method with  $\sigma_{ys}$  equal to the material yield strength and  $\Delta\sigma$  to the stress range of the loading cycle. In all simulations the initial circumferential crack sizes were estimated from above equation. The initial crack size,  $R$ , was assumed equal to the crack initiating feature size and  $B$  was assumed equal 2 for particles and 1 for pores. As to the values of the elastic stress concentration factor,  $k_t$ , they are in general known only for the well defined shapes. For instance,  $k_t$  is equal 2.05 for a spherical void, 3.45 for an oblate ellipsoid and on the order of one for bonded uncracked particle with large aspect ratio [113]. For real particles and pores with unconventional shapes and for the cases when particles cannot be treated as rigid inclusions the stress concentration factors are difficult to estimate. Following procedure developed by the Alcoa team the  $k_t$  values were then assumed as adjustable parameters [13]. Their values were estimated by noting that for infinite fatigue life the circumferential cracks should be null, hence

$$\frac{R}{R + x_o} \Rightarrow 1 \quad \text{eq. 81}$$

Substituting above condition to eq. 80 and solving for  $k_t$  gives:

$$k_t = \frac{1}{1.12} \left[ \frac{1}{B} \left( \frac{2\sigma_{ys}}{\Delta\sigma_{\infty}} - \frac{2}{\pi} - 1 \right) + \frac{2}{\pi} + 1 \right] \quad \text{eq. 82}$$

where  $\Delta\sigma_{\infty}$  is stress range corresponding to an infinite fatigue life. To estimate  $k_t$  it is then necessary to find the fatigue limit  $\Delta\sigma_{\infty}$ . Following Alcoa's Team procedure, the values of  $\Delta\sigma_{\infty}$  have been found from the best fit of the fatigue life distributions obtained from MC model for the lowest experimental  $\Delta\sigma$  level to the experimental data. The obtained values of the  $\Delta\sigma_{\infty}$  are listed in Table XXXV, together with the resulting stress concentration factors  $k_t$ . The estimated fatigue limits varied from about 75 MPa for an old alloy to 115 MPa for the thin plate alloy variant. The new and low porosity plates had fatigue limits in the order of 100 MPa. As to the obtained stress concentration factors,  $k_t$ , they varied from 10.67 for the old alloy to 7.25 for the thin plate. For new and low porosity variants the stress concentration factors had intermediate values of about 8.

In interpreting estimated values of the stress concentration factors,  $k_t$ , it should be kept in mind that during MC fatigue life simulations for the open hole samples it was assumed that in old and new alloys the cracks initiated from pores and in low and thin plates from particles. This assumptions were based on the results from the fractographic studies. However, our extreme value analysis of the sizes of the fatigue crack initiating features in the open hole samples suggested that at the hole region the surface pores were always greater than particles. Our suggestion was that to initiate crack from a particle would require an initial crack driving force for that particles to be larger than that for the larger pores. The driving force for a crack can be assumed proportional to the strain energy released rate which, in turn, is proportional to the square of the initial stress intensity factor  $K_{T-B}$ . Since the values of  $K_{T-B}$ , eq. 77, are larger for the crack emanating from the bonded particle than for the same size and shape pore, our results are consistent with the expectations. The larger values of the obtained stress concentration factor for the pores are also consistent with the published data on the stress concentrations factors for

particles and voids[128]. An additional detailed analysis of the effect of the shapes of particles and pores on the stress concentrations and on the expected fatigue lives can be found in the final report by Alcoa team [13].

Based on the above, our procedure for estimating distributions of fatigue lives for the open hole samples involved two-step approach. The first step was estimation of the stress concentration factors,  $k_t$ , and fatigue limits,  $\Delta\sigma_\infty$ , from the experimental data for the lowest stress levels for a given material via least square procedure. The second step consisted of actual predictions of full  $S-N$  curves for the stresses greater than  $\Delta\sigma_\infty$ . The random variables used during simulations included crack size, crack position within the hole, texture and crack deflections. Results of the MC prediction using above procedure have been compiled in Figures 94 to 97. Each figure includes results from the simulations for four to five stress levels with minimum of on thousand simulations for each level. The results are compared with the experimental data obtained for the similar stress levels. The agreement is in general very good. For the old and new alloys there is a tendency for underestimation of both short and long fatigue lives by the MC results. This trend is similar to that for the smooth fatigue samples, and is a carry over from the slight overestimation of the sizes of the fatigue crack initiating pores by the extreme value procedure, Figures 71 and 72. For the low porosity and thin plate alloys the MC model predicts correctly both short and intermediate fatigue lives but underestimates long times to failure. This is again a result of the overestimation of the sizes of the smallest fatigue crack initiating particle sizes by the extreme value procedure. Additional underestimation of the fatigue lives could have come from the crack transition procedure employed in all simulations. Following literature recommendation [129,130,131] it was assumed that as soon as the thumbnail crack reaches the sample surface, it becomes a quarter-elliptical corner crack. Such assumption results in a sudden increase of the crack size which could lead to an underestimation of the fatigue lives. The error due to the "transition" effect would be particularly significant if the starting crack was positioned along the crack bore not far from the surface.

Obtained results suggests that the use of the MC fatigue crack growth model combined with the statistics of extreme estimates of initial crack size distribution is a viable approach to predicting fatigue life distributions for the 7050-T7451 plate alloys. The minimum set of data necessary for the predictions includes crack growth rate equation, metallographic size distributions data for particles and pores and either fatigue limit or a stress concentration factors for the largest particles and pores. In our investigation the stress concentrations were obtained experimentally, but they could be in principle estimated using a finite element method. The accuracy of the predictions is sufficient for the use in comparing fatigue quality of various lots of the same material and for the quality control purposes.

### Markov Chain Model

A complete description of fatigue process requires sequential use of several specialized models for different stages of fatigue life. One of the possible ways of combining those models is by using a Markov chain approach [132]. In the core of that approach is the construction of a matrix containing probabilities of transitions between different stages of fatigue life. In our case such a matrix would be filled with the probabilities of crack nucleation and crack extensions from one position to another. It will have the following general form:

$$\mathbf{P} = \begin{bmatrix} p_{11} & p_{12} & p_{13} & \dots & \dots & p_{1n} \\ 0 & p_{22} & p_{23} & \dots & \dots & p_{2n} \\ 0 & 0 & p_{33} & \dots & \dots & p_{3n} \\ \vdots & \vdots & \vdots & \ddots & \ddots & \vdots \\ \vdots & \vdots & \vdots & \ddots & \ddots & \vdots \\ 0 & 0 & 0 & \dots & \dots & 1 \end{bmatrix} \quad \text{eq. 83}$$

where  $p_{11}$  could be for instance a probability that the initial crack does not grow during some predetermined number of cycles(duty cycle);  $p_{12}$  that it grows one step forward and so on. The last column contains probabilities of catastrophic failures for different crack lengths. All terms below diagonal are zero, because crack healing is excluded.

The distribution of initial crack lengths can be incorporated into the model by assigning different probabilities to the initial crack positions through the probability vector:

$$\mathbf{v} = (v_1, v_2, v_3, \dots, v_n) \quad \text{eq. 84}$$

where  $\sum_{i=1}^n v_i = 1$ , and  $v_1$  is the fraction of cracks with the smallest possible initial lengths,  $v_2$

fraction of cracks with the size corresponding to the second position in the transition matrix etc. Finding distribution of crack sizes after one duty cycle can be then calculated from relation [111, 132]:

$$\mathbf{v}_1 = \mathbf{v} \cdot \mathbf{P} \quad \text{eq. 85}$$

and after  $n$  duty cycles it is described by the vector:

$$\mathbf{v}_n = \mathbf{v} \cdot \mathbf{P}^n \quad \text{eq. 86}$$

The last component of the probability vector is of particular interest because it describes the cumulative probability of failure. Plotting the value of that component versus number of duty cycles gives then the plot of cumulative failure probabilities.

We have tested the most basic version of the above Markov chain model to check its ability to reproduce the expected fatigue behaviors. The model used by us was the B-model [132] with the probability matrix in the form:

$$\mathbf{P} = \begin{bmatrix} p & q & 0 & \dots & 0 & 0 \\ 0 & p & q & \dots & 0 & 0 \\ 0 & 0 & p & \dots & 0 & 0 \\ \dots & \dots & \dots & \dots & \dots & \dots \\ 0 & 0 & 0 & \dots & p & q \\ 0 & 0 & 0 & \dots & \dots & 1 \end{bmatrix} \quad \text{eq. 87}$$

This model assumes then that after one duty cycle probability that crack does not grow is  $p$  and that it grows one unit forward is  $q$ . The optimum size of the matrix,  $n$ , and the probabilities  $p$  and  $q$  which best fit fatigue data can be calculated from conditions[132]:

$$p + q = 1 \quad \text{eq. 88}$$

$$\bar{N} = (n-1) \left( 1 + \frac{p}{q} \right) \quad \text{eq. 89}$$

$$\sigma^2 = (n-1) \left( 1 + \frac{p}{q} \right) \frac{p}{q} \quad \text{eq. 90}$$

where  $\bar{N}$  and  $\sigma$  are the average and standard deviation of the number of cycles to failure. The cumulative failure probability after  $x$  duty cycles,  $F(x; 1, n)$ , is in this case given by relation [132]:

$$F(x; 1, n) = \sum_{i=n-1}^x \binom{i-1}{i-n+1} p^{i-n+1} q^{n-1} \quad \text{eq. 91}$$

The model was tested on the fatigue data for smooth samples from old and new alloys. Figure 98 shows the results of the best fit, solid lines, compared with the experimental data. The probability vector used in the calculations for both alloys was  $(1, 0, 0, \dots)$ . The results show that the optimum matrix size is 12 for the old and 27 for the new alloy. This means that, contrary to the expectation, the probability  $p$  that the crack moves forward

during each duty cycle is larger for the new than for the old alloy. To eliminate this anomaly it was necessary to sacrifice best fit for the new alloy to obtain the same size of the transition matrix as for the old alloys. The result is shown as dotted line in Figure 98. The values of  $p$  and  $q$  for both alloys can be now directly compared. They indicate that the probability of crack moves forward during each duty cycle in an old alloy is twice that of the new one.

The model has been also interrogated for the responses to the increased initial crack size and changes in the crack growth rates. The large initial crack size was simulated by changing the starting probability vector. Results from one of such simulation for twelve-step model are in Figure 99. It turned out that by increasing the initial crack size in the probability vector of the new alloy from position one to six, its distribution of fatigue life become similar to that of the old alloy. The changes in the crack growth rates were simulated by changing some of the values in the transition matrix. Figure 100 shows change in the failure distribution function when the value of  $p$  in the first row of the transition matrix was changed from 0.922 to 0.95. This simulates initial retardation of the crack growth. As expected, the distribution curve shifted to the right. When all  $p$  values were changed to 0.95 the change in the fatigue life distribution, as shown in Figure 101, was more significant.

The results of testing showed that the Markov chain model is capable of reproducing all expected fatigue behaviors. The components of the probability matrix have been obtained by the best fit method, but they could be alternatively coupled to the probabilities of the microscopic crack propagation events through the crack nucleation and propagation models. However, based on the results of the fatigue life predictions obtained by us and by Alcoa group, the crack propagation models alone are sufficient to describe fatigue life distribution in the studied alloys. Hence it appears that there may be no need for employing Markov chain model to the predictions of fatigue life in 7050 alloys.

### *Summary*

- A versatile Monte-Carlo fatigue life prediction model based on the crack growth approach utilizing Paris-Erdogan type crack growth law has been developed. The model utilizes (1) initial crack size, (2) crack location, (3) texture fluctuations on the crack path and (4) crack deflections from the crack path as stochastic variables. It is capable of handling various types of crack geometry for the smooth and open hole sample types.
- The predictive capabilities and utility of the Markov chain approach to the fatigue life estimation of the 7050-T7451 have been also studied. Interrogation of the model showed that it is capable of correctly predicting changes in fatigue lives due to the variability in initial crack sizes, nucleation periods and crack growth rates and that it is capable of combining together crack nucleation and propagation models. However, our subsequent studies have shown that there is no need for such capabilities in case of predicting fatigue lives of the 7050-T7451 alloys.
- Predicted fatigue lives using Monte-Carlo model and fractographically measured actual initial crack sizes as input were in excellent agreement with the experimental results. The deviations between predicted and experimental fatigue lives have been assumed as representations of the expected crack nucleation times. These nucleation times were random in nature with the average of 6,100 cycles and standard deviation of 22,800 cycles.
- The Monte-Carlo model was used to estimate the expected maximum magnitudes of the scatter in fatigue lives of the 7050 alloys due to the size distribution of the crack initiating features and fluctuations of the crystallographic texture and crack deflections along the crack path. For the maximum cyclic stress amplitude of 240 MPa and r-value of 0.1, the maximum estimated fatigue life variations were 150,000 cycles due to size

variations of the crack initiating pores and 5,200 and 2,200 cycles due to, respectively, texture and crack deflections.

- In the new alloy variant the effects of the initial crack size distribution on the spread of fatigue lives can be made comparable to that from texture and/or crack deflections, if the standard deviation of the sizes of the crack initiating pores were narrowed down from the current value of 60  $\mu\text{m}$  to about 2 to 4  $\mu\text{m}$ . Similar magnitude of change would be required in all remaining alloy variants.
- The Monte-Carlo model combined with the statistics of extreme estimation of the sizes of initial cracks showed excellent predictive capabilities of both average fatigue lives and life distributions for various stress levels for all alloy variants and sample geometry. The predictions were obtained based on the minimal requirement of input data which included crack growth rate equation and results from the standard metallographic characterizations of the particle and pore size distributions.
- The proposed fatigue life prediction methodology represents very useful and economical alternative to the lengthy fatigue testing programs. It allows for rapid differentiation between fatigue qualities of different material variants and on the parametric studies of the effects of the microstructural variables on fatigue lives. It also should serve as a design aid for the alloy designers and process engineers in optimizing microstructures for fatigue life.

## ***Part II: Fatigue of HSLA-80 weldments***

### **Introduction**

All life prediction and microstructure characterization methodologies developed for the aluminum 7050 plates should be also applicable to other metallic alloys. The obvious limitation is that both the microstructure of the alloy of interest and the mechanisms controlling its fatigue behavior should be similar to that of the 7XXX alloys. The purpose of the part of the program described in this section was then to test the possibility of applying the methodologies developed for aluminum to HSLA-80 steels. The HSLA-80 steels are extensively used in the naval ship hull structures. Like aluminum alloys they are heat treatable with grain sizes ranging from 0.3 to 9  $\mu\text{m}$ , inclusions from 2 to 12  $\mu\text{m}$  in size and copper precipitates 5 to 25 nm in diameter [133]. In the as received conditions the fatigue cracks in the HSLA-80 plates tend to initiate from inclusions. After heat-treatment the preferred nucleation sites are lath-like features[133]. The HSLA steels have tensile and yield strengths of the order of 99.0 to 108 ksi (683 to 745 MPa) and 92.5 to 97.2 ksi (638 to 671 MPa) respectively[134,135]. In naval applications they are used in welded structures, which necessitates assessment of the fatigue lives of their weld joints. Accordingly, our goal was to adopt the life prediction methodology developed for the 7050 alloys to the HSLA-80 weldments. Of particular interest was the capability of being able to predict fatigue lives of the welds subjected to the variable loading based on the constant amplitude fatigue data.

In developing the strategy for formulating life predictions methodology for the HSLA-80 weldments, it was necessary take under consideration additional stochastic variables not present in 7050 alloys. The most important of them were (1) location and size of the welding microcracks, (2) weld geometry, (3) presence of welding defects, (4) residual stresses and (5) variations in the loading spectrum. In principle the sizes and locations of the welding microcracks and statistics relating to welding defects could be obtained from the fractographic examinations of the broken fatigue samples. Weld geometry could be also measured without difficulty and its effects on the crack growth

rates a well known[136,137]. The magnitudes of the residual stresses are however extremely difficult to estimate. They could be equal to the yield strength and change both with crack position and size.[138,139,140]. The effects of those stresses on fatigue life are then usually unknown as they defy quantitative description. The uncertainties associated with the loading spectrum could be on the other hand eliminated by subjecting all samples to the same block loading conditions. To make the problem manageable requires then formulation of the model which would combine stochastic variables. Consequently, our goal was to formulate variable amplitude life predictions model with minimal number of variables which could be obtained from the constant amplitude fatigue tests.

## Fatigue Results

### *S-N Testing*

All fatigue testing of the HSLA-80 weld samples were conducted at the Naval Surface Warfare Center, Carderock Division, MD by dr. David Khil. The specimens used were of the dog-bone type with center butt weld. The minimum center section at the weld area had nominal dimensions of 25.4 by 12.7 mm (1" by 0.5"). The tests were conducted both under constant amplitude and random loading conditions and for both positive and negative average stresses. The basic loading spectrum used in all random loadings is shown in Figure 102. It was generated using first-order autoregressive method developed by Sarkani [141]. This method allows for generation of the sets of random peaks using Rayleigh distribution in the form[121]:

$$f(x) = \frac{x}{\alpha^2} \exp\left\{-\frac{1}{2}\left(\frac{x}{\alpha}\right)^2\right\} \text{ eq. 92}$$

with  $\alpha$  equal 1 and with the correlation between proceeding or following peaks of 0.95. The particular spectrum shown in Figure 102 was obtained by generating 10,000 peaks; the odd-numbered peaks served as maxima and the even-numbered, after multiplying by -1, as minima. As a result the spectrum contained 5,000  $\Delta\sigma$  values which due to the high value of the autocorrelation coefficient had average close to zero. This set of  $\Delta\sigma$  values

constituted a unit *RMS* loading used in all variable amplitude tests [142]. Some basic characteristics of the spectrum and  $\Delta\sigma$  values are listed in the Figure 102.

During testing the waveform load generator connected the picks with a smooth heversine curve to form a control signal for the fatigue machine. For a specific test each peak was also multiplied by the test's *RMS* value and the entire spectrum was shifted to the required average stress,  $\sigma_m$ , level. The obtained 5,000 loading cycles were then applied to the specimen repeatedly until failure [142]. It is important to point out that the maximum stress for a given test was  $4.34 \cdot RMS + \sigma_m$  and the largest  $\Delta\sigma$  during each test was about eight times the *RMS*.

#### *Constant amplitude*

The results of the fatigue testing under constant amplitude loading conditions are summarized in Table XXXVI. The set included seven samples which had been fatigued at the stress ranges from 25 to 160 ksi with superimposed average stresses of 0 to 37.5 ksi. The tests covered then the span of R-ratios from -1 to 0.5. The results are also shown in a form of three-dimensional S-N plot in Figure 103. As expected the fatigue lives increased with decreasing stress range (vertical axis) and decreasing average stress.

#### *Variable amplitude*

Table XXXVII summarizes the results of the tests conducted under variable amplitude loading conditions. The 33 samples tested in this case were fatigued to failure under spectrum loading with *RMS* values ranging from 7.5 to 20 ksi and with the average stresses from -20 to 20 ksi. The results are shown in Figure 104 in a form of the *RMS* vs. average stress vs. cycles to failure graph. The general trends are again towards decrease in fatigue life with increasing *RMS* and/or average stress. These trends are explored further in Figure 105 and Figure 106. The former shows the fatigue life curves for the constant average stresses. The *RMS* values represent in this case multiplication factors which were applied, for a given test, to the peak values of the loading spectrum shown in Figure 102. To obtain the average stress range,  $\langle\Delta\sigma\rangle$ , the *RMS* need to be multiplied by the average stress range for the unit spectrum,  $\langle\Delta\sigma_o\rangle$ , which was 2.5058. Accordingly

$$\langle \Delta \sigma \rangle = 2.5058 \cdot RMS \quad \text{eq. 93}$$

Despite appreciable scatter, the constant average stress curves shown in Figure 105 indicate clear trend of increasing fatigue life with decreasing *RMS*. None of the curves suggest the presence of fatigue limit. It is also apparent that an increase in the average stress,  $\sigma_m$ , leads to shorter fatigue life. There is also no indication of the change in trends for the negative average stresses, Figure 106. Since under ordinary circumstances the negative cycles are expected to contribute substantially less to fatigue damage than the positive ones [143], one would expect change in slope on the  $\sigma_m$  vs. *N* curves for the negative  $\sigma_m$  values. The absence of that effect can be attributed to the presence of the positive internal stresses from the weld [137]. Figure 106 suggests that for the considered loading conditions the trends for the positive average stresses extent, without change, to the negative  $\sigma_m$  values.

### *Fractography*

All HSLA-80 fatigued weld samples were analyzed using optical stereo-microscope to identify crack nucleation site, fracture surface features and weld geometry. In addition, several of the samples were also examined under the SEM. Results of all examinations are summarized in Table XXXVI and Table XXXVII for, respectively, samples fatigued under constant and variable amplitude loading. Optical light fractographs of the fracture surfaces of all samples have been catalogued in Appendix A. The geometrical characteristics of the welds such as reinforcement width, heights and flank angles have been defined in Figure 107a and their values are listed in the tables. Note that it was possible to measure flank angles only on the intact side of the weld.

The fracture surfaces of all weld samples have been categorized as consisting of edge, side or shear macrocracks, Figure 107b. The majority of the samples had edge macrocracks. These cracks typically started at the weld toe stress concentration region from welding microcracks. The microcrack sizes could not be assessed due to the absence of distinguishing marks at the onset of the fatigue propagation region. However, since they originate on different levels, their presence could be inferred from the presence of

micro-ratchet separation lines. During fatigue the microcracks linked-up to form macrocrack which then spread outward along the edge by absorbing additional microcracks. In most of the samples there were more than one edge macrocracks, separated by macro-ratchet lines, e.g. Figures A20, 34 and 39. In few instances the same crack nucleation and propagation mechanism have been observed for the macrocracks originating on the sample side, e.g. Figures A36 and 40.

In nine of the samples the cracks originated from the lack of penetration and/or fusion welding defects. Typical examples of such failures from the former type of defect can be found in Figures A3, 23 and 24. The cracks started there in the weld root region and propagated perpendicular to the loading direction. The presence of the fusion defect resulted on the other hand in the shear type failures, see for example Figures A7, 10 and 24. In those cases the failures typically originated also from the lack of penetration defect but propagated along weld/base-metal boundary on a plane inclined to the acting load.

The presence of the lack of the penetration and/or fusion defects did not lead to the automatic degradation of fatigue life. The lives were lower than expected only in three out of nine samples with those defects, see Figures A14, 24 and 29. A possible explanation of this behavior could be the relaxation of the internal stresses in the vicinity of incomplete penetration and fusion defects. Additional six cases of unusually low fatigue, see Figures A9, 16, 19, 20, 31 and 33, were associated with presence of the multiple macro and/or microcracks. This is as expected. Since the multiple small cracks rapidly link-up during initial stage of fatigue life, they will immediately form large macrocrack with concomitant deterioration of fatigue live. The coalescence of the smaller cracks is evident from the macrocrack shape. For a single edge crack propagating without interference of internal stresses the equilibrium aspect ratio is about 0.85 [144]. Large aspect ratios of the edge macrocracks observed in our weld samples were result of the link-up process.

Additional question that was addressed during fractographic examinations was the presence of fracture surface striations corresponding to the peak loads. Their presence and

appearance is important from the practical point of view because they could provide information about both load and environmental history of a given sample. For the samples fatigued with constant amplitude loading the striations correspond to the individual loading cycles. Their spacing is proportional to the stress amplitude and it may be too small to resolve for low amplitude cycles, particularly when crack is small. This was indeed the case for the stress range values less than 100 ksi. The only constant amplitude samples with resolvable striations were the ones with  $\Delta\sigma$  equal 100 and 160 ksi, Figure A1 and 2. For the variable amplitude loading the detectable striations correspond not to the individual cycles but to the cycles with the largest amplitudes. As already discussed, the variable amplitude loading spectrum used during all fatigue tests, Figure 102, consisted of 5,000  $\Delta\sigma$  values. The maximum  $\Delta\sigma$  of the basic spectrum was 8.397 ksi, but the spectrum also contained two additional  $\Delta\sigma$  values above 8 ksi, nine between 7 and 8 ksi and thirty eight between 6 and 7 ksi. However, these largest  $\Delta\sigma$  cycles appeared in clusters and there was only one cluster with  $\Delta\sigma$  greater than 8 ksi, three with maximum stress range between 7 and 8 ksi and about ten with  $\Delta\sigma$  between 6 and 7 ksi. These numbers correspond then to the number of bands that should form on the fracture surface during one loading block. Comparing these numbers with the observed number of marks, see for instance Figures A9, 12, 17 and 26, it appears that clusters with  $\Delta\sigma$ 's larger than about 7 ksi could be resolved from the optical fractographs. Resolutions of bands from clusters with smaller stress amplitudes necessitates use of the SEM.

## Modeling

Our objectives for modeling fatigue behavior of the HSLA-80 weldments were to (1) extend our methodology developed for the Al-alloys to steels and (2) to assess the possibility of predicting fatigue lives of weldments under random loading from the constant amplitude test data. The problems of predicting fatigue lives of HSLA-80 weldments and the 7050 aluminum alloys are only similar in their crack growth aspects. In both cases the cracks can be assumed to be present at the virgin material and that they grow from the very first loading cycle. However, in 7050 aluminum alloys the cracks can

be estimated from the sizes of the porosity and constituent particles, while for steel weldments they are both random in sizes and location. Moreover, in 7050 alloys fatigue process involves growth of one dominant crack while in steel weldments it comprises from growth and link-up of several smaller cracks under additional influence of the unknown internal stresses. Our strategy for developing fatigue live description for weldments was then to based our model on a specialized crack growth equation which would (1) include parameters attainable from the constant amplitude tests and (2) had provisions for the effects of the variable amplitude loading spectra. After reviewing predictive capabilities of the numerous existing crack growth equations [143,145,146] we propose to use the following crack growth Paris-Erdogan type law for the steel weldments:

$$\frac{da}{dN} = C \frac{\Delta K^n}{\left[1 - \left(\frac{K_m}{K_c}\right)^m\right]^n} \quad \text{eq. 94}$$

where  $K_m$  is the average stress intensity and  $C$ ,  $m$ ,  $n$  and  $K_c$  are material/weldment constants. Note that the proposed equation leads to the infinite crack growth rate when the average stress intensity,  $K_m$ , reaches a critical value  $K_c$ . However, it does not include the term associated with the internal stresses. The omission of the latter is in accord with the reported literature results which suggests no significant improvement in the predictive capabilities of the models by the incorporation of the internal stress terms[135,137,147]. Equation 94 also does not account for the interactions between cycles. As will be shown later in this section these interactions could be described by an additional parameter which, however, would not lead to any significant improvement of the model.

To obtain the standard fatigue S-N curves from eq.94 it is necessary to convert all stress intensity terms to stresses and then solve the equation for the number of cycles to failure,  $N$ . The  $K$ - $\sigma$  conversions can be carried out using the standard relations:

$$K = Y\sigma\sqrt{a} \quad \text{eq. 95}$$

and

$$\Delta K = Y\Delta\sigma\sqrt{a} \quad \text{eq. 96}$$

where  $Y$  is a geometrical factor. The relations assume that the geometrical factor does not change significantly during the entire fatigue life which may be an oversimplification in some cases. After substituting eq. 95 and eq. 96 to eq. 94 one obtains:

$$\frac{da}{dN} = C \frac{(Y\Delta\sigma\sqrt{a})^n}{\left[1 - \left(\frac{\sigma_m}{\sigma_c}\right)^m\right]^n} \quad \text{eq. 97}$$

which, after integrating, gives:

$$\frac{a_{cr}^{1-n/2} - a_o^{1-n/2}}{1 - \frac{n}{2}} = C \int \frac{(Y\Delta\sigma)^n}{\left[1 - (\sigma_m/\sigma_c)^m\right]^n} dN \quad \text{eq. 98}$$

and where  $a_o$  and  $a_{cr}$  are initial and the final crack sizes, respectively. Making standard assumption that  $n > 2$ ,  $a_o \ll a_{cr}$  and replacing integral with the sum reduces last equation to:

$$1 = \sum_{i=1}^{N_f} \left[ \Delta\sigma_i \frac{Y[C(n/2 - 1)a_o^{n/2-1}]^{1/n}}{1 - (\sigma_{mi}/\sigma_c)^m} \right]^n \quad \text{eq. 99}$$

where  $N_f$  is the number of cycles to failure and  $\Delta\sigma_i$  and  $\sigma_{mi}$  are stress range and the average stress for cycle  $i$ . From the boundary conditions that when an average stress  $\sigma_m$  equal zero the fracture after one cycle takes place when the stress range  $\Delta\sigma$  is twice some critical value  $\sigma_{cl}$ , one would have:

$$2\sigma_{cl} = \frac{1}{Y[C(n/2 - 1)a_o^{n/2-1}]^{1/n}} \quad \text{eq. 100}$$

Note that critical stresses  $\sigma_{cl}$  and  $\sigma_c$  should be the same as both represent the stress amplitude corresponding to the failure after one cycle. As such they should represent the critical stress for fracture resulting from an average weld crack of size  $a_o$ . However, to keep the model general  $\sigma_{cl}$  and  $\sigma_c$  will be treated as separate materials constants. By combining the last two equations, eq. 99 can be rewritten in a simplified form as:

$$1 = \sum_{i=1}^{N_f} \left[ \frac{\Delta\sigma_i}{2\sigma_{cl} \left[ 1 - (\sigma_{mi}/\sigma_c)^m \right]} \right]^n \quad \text{eq. 101}$$

which represents a damage accumulation law. This law states that the fatigue process terminates by fracture when the sum of the terms in square brackets, raised to the  $n$ -th power, accumulates to one. Each term of the sum represents then a fraction of damage inflicted by one cycle with average stress  $\sigma_m$  and stress range  $\Delta\sigma$ . This fraction is precisely equal to the reciprocal of the total number of cycles to failure at the same conditions,  $N_f(\sigma_m, \Delta\sigma)$ , which means that

$$N_f(\sigma_{mi}, \Delta\sigma_i) = \left[ \frac{\Delta\sigma_i}{2\sigma_{cl} \left[ 1 - (\sigma_{mi}/\sigma_c)^m \right]} \right]^{-n} \quad \text{eq. 102}$$

The damage accumulation law represented by eq. 101 reduces then to the Palmgren-Miner equation in the form:

$$1 = \sum_{i=1}^{N_f} \frac{1}{N_f(\sigma_{mi}, \Delta\sigma_i)} \quad \text{eq. 103}$$

In addition, by solving eq. 102 for  $\Delta\sigma_i$  and dropping cycle numbers,  $i$ 's, one obtains:

$$\Delta\sigma = \frac{2\sigma_{cl}}{N_f^{1/n}} \left[ 1 - (\sigma_m/\sigma_c)^m \right] \quad \text{eq. 104}$$

which is a Goodman type relation representing maximum stress range  $\Delta\sigma$  for the failure after  $N_f$  constant amplitude cycles with an average stress  $\sigma_m$ . Note that for  $\sigma_m$  equal zero the expression in brackets is equal one. The ratio in front of the bracket represents then stress range which cause failure after  $N_f$  constant amplitude cycles with average stress equal zero:

$$\Delta\sigma(\sigma_m = 0) = \frac{2\sigma_{cl}}{N_f^{1/n}} \quad \text{eq. 105}$$

The proposed model is then consistent with both the Palmgren-Miner damage accumulation law and with the Goodman type relations for the maximum stress ranges.

In order to make life prediction using the proposed model, it is necessary to estimate parameters  $n$ ,  $m$ ,  $\sigma_c$  and  $\sigma_{cl}$  and use equation 101 to find the number of cycles to failure  $N_f$ . The procedure of finding all parameters and the fatigue lives could be substantially simplified if the summation term could be eliminated and replaced with the average characteristics of the loading spectrum. In the general case of a random loading with varying both stress amplitude and the mean, equation 101 can be approximated by:

$$1 = \frac{N_f}{(2\sigma_{cl})^n} \cdot \left\langle \left[ \frac{\Delta\sigma_i}{1 - (\sigma_{mi}/\sigma_c)^m} \right]^n \right\rangle \quad \text{eq. 106}$$

where angular brackets represent the average value. Not much is gained here as the estimation of the bracketed term requires the same summation as the one needed when using eq. 101. However, as will be shown below, additional simplifications are possible for the cases when the loading spectrum has constant average stress and variable amplitude or when both the amplitude and the average stress are constant.

### *Constant Average Stress*

This is the case relevant for the random loading spectrum used in our fatigue tests, Figure 102. Due to the high correlation between successive peaks, the average value was in this case constant while the stress ranges varied randomly from zero to the maximum value of 8.397. For such constant average stress loading conditions eq. 106 can be simplified to:

$$1 = \frac{N_f \langle \Delta\sigma^n \rangle}{\left\{ 2\sigma_{cl} \left[ 1 - (\sigma_m/\sigma_c)^m \right] \right\}^n} \quad \text{eq. 107}$$

which, assuming that all parameters are known, requires only estimate of the  $n$ -th moment of the  $\Delta\sigma$ 's to find the fatigue life. This result suggests that the proper statistic of the loading spectrum which need to be used for correlations with fatigue life is not spectrum average or *RMS* value, as it is often tacitly assumed, but its moment corresponding to the power in the crack growth equation.

Additional question that could be addressed at this point is the interaction between the effects of the successive cycles. For instance, it is well documented that the overloads can lead to the retardation of the crack growth rate during subsequent lower amplitude loading cycles [143]. Such effects can be incorporate into the model by introducing a multiplicative interaction parameter,  $\gamma$ , which modify the values of  $\Delta\sigma$  through relation:

$$1 = \frac{N_f \langle (\gamma \cdot \Delta\sigma)^n \rangle}{\left\{ 2\sigma_{cl} \left[ 1 - (\sigma_m/\sigma_c)^m \right] \right\}^n} \quad \text{eq. 108}$$

The values of  $\gamma$  should be in most instances smaller than one. However, for the loading spectrum where the differences between the successive  $\Delta\sigma$  values are small, as it is the case for the loading spectrum in Figure 102, the value of  $\gamma$  should be on the order of one.

### *Constant Amplitude*

For the constant amplitude loading conditions all values of  $\Delta\sigma$  are the same and eq. 106 reduces to:

$$1 = \frac{N_f \Delta\sigma^n}{\left\{ 2\sigma_{cl} \left[ 1 - (\sigma_m/\sigma_c)^m \right] \right\}^n} \quad \text{eq. 109}$$

This relation is a familiar Basquin relation which can be written in the standard form as:

$$N_f = A \cdot \Delta\sigma^{-n} \quad \text{eq. 110}$$

where

$$A = \left\{ 2\sigma_{cl} \left[ 1 - (\sigma_m/\sigma_c)^m \right] \right\}^n \quad \text{eq. 111}$$

The exponent  $n$  is then, as expected, the slope on the standard S-N fatigue curve and constant  $A^{1/n}$  represents the intercept of the curve with the  $\Delta\sigma$  axis.

Equation 109 can be also used as a base for finding the parameters of the model from the constant amplitude  $N_f\text{-}\Delta\sigma$  data. The most straight-forward way to proceed would be to use a nonlinear best fit to find all parameters simultaneously. The procedure could be

made slightly less cumbersome if the value of  $m$  was known *a priori*. As discussed in the context of eq. 104 this parameter represents the exponent in the Goodman-type average stress vs. maximum stress amplitude relation. The upper and lower bound for  $m$  are 1, according to Goodman, and 2, according to Soderberg [143]. Since Goodman approximation leads to the conservative estimates of fatigue lives, it would be recommended to use  $m = 1$  to reduce the number of adjustable parameters of the model.

### Verifications and Predictions

As indicated earlier in this section, the goal of modeling fatigue behavior of the HSLA-80 weldments was to be able to predict fatigue lives of weldments subjected to random loading from the constant amplitude fatigue data. The adopted model verification strategy was then to (1) estimate the parameters of the model using constant amplitude data from Table XXXVI in conjunction with constant amplitude eqs. 109 - 111 and then (2) use the obtained parameters to predict fatigue lives under random loading conditions *via* eq. 108. The predictions were then compared with the experimental random fatigue results compiled in Table XXXVII.

All parameters of the model were estimated using nonlinear fit of the constant amplitude data to eq. 109. To limit the number of degrees of freedom and to make predictions conservative the value of exponent  $m$  was set to one. The three remaining parameters were then exponent  $n$  and the critical stresses  $\sigma_c$  and  $\sigma_{cl}$ . Their best values have been estimated to be:

$$\begin{aligned} n &= 6.61 \\ \sigma_c &= 195 \text{ ksi} \\ \sigma_{cl} &= 177.6 \text{ ksi} \end{aligned} \quad \text{eq. 112}$$

The correctness of the model and the goodness of fit of the model to the data can be assessed visually by plotting normalized stress amplitude  $\Delta\sigma/(1 - \sigma_m/\sigma_c)$  vs.  $N_f$  on the log-log scale. If the model is correct, the data should follow a straight line with slope  $n$ . Figure 108 shows that it was indeed the case. The estimated correlation coefficient of the model

was 0.9884. Consequently, the fatigue behavior of the HSLA-80 butt-welded joint subjected to the constant amplitude loading conditions can be described by relation:

$$N_f = \left\{ \frac{355.2}{\Delta\sigma} \left[ 1 - \frac{\sigma_m}{195} \right] \right\}^{6.61} \quad \text{eq. 113}$$

where  $\Delta\sigma$  and  $\sigma_m$  should be substituted in ksi. Predictions of the model for variable amplitude loading can be obtained by substituting all parameters, eqs. 112, to eq. 108 which gives:

$$N_f = \frac{1}{\langle (\gamma\Delta\sigma)^{6.61} \rangle} \left\{ 355.2 \left[ 1 - \frac{\sigma_m}{195} \right] \right\}^{6.61} \quad \text{eq. 114}$$

Predictions from eq. 114, with  $\gamma=1$ , have been compared with the experimental data in Figure 109. The correlation was in this case 0.9153 which suggests that the model has excellent predictive capabilities for the variable amplitude loading. An attempt to improve the predictions by changing the value of the cycle interaction parameter  $\gamma$  did not result in a significant improvement of the fit. The best estimate of  $\gamma$  turned out to be 0.98 which resulted in an increase of the correlation to 0.9283. This small improvement does not justify inclusion of the parameter  $\gamma$  in the current version of the model. As suggested earlier, the value of  $\gamma$  close to one could be a result of the strong correlation between cycles in the loading spectrum used in our variable amplitude tests. The predictions and the experimental data for both constant and variable amplitude loading are shown together in Figure 110.

Details on the conversions of the *RMS* values, Table XXXVII, to the  $\Delta\sigma$ 's and on the estimations of *n*-th moments warrant additional explanations. Since the values of the peak loads for variable loading were obtained by multiplying the peaks of the basic spectrum, Figure 102, by *RMS* [142], hence:

$$\Delta\sigma = RMS \cdot (\sigma_{\max 0} - \sigma_{\min 0}) = RMS \cdot \Delta\sigma_0 \quad \text{eq. 115}$$

where  $\Delta\sigma_0$  is the stress range of the basic spectrum. Consequently, the *n*-th moment of the  $\Delta\sigma$  values is equal to:

$$\langle \Delta \sigma^n \rangle = \left\langle \left[ RMS \cdot (\sigma_{\max 0} - \sigma_{\min 0}) \right]^n \right\rangle = RMS^n \cdot \langle \Delta \sigma_0^n \rangle \quad \text{eq. 116}$$

To find  $n$ -th moment for a given RMS it is then necessary to know the corresponding moment of the basic spectrum  $\langle \Delta \sigma_0^n \rangle$ . The values of those moments for the loading spectrum used for our weldment samples, are plotted as a function of  $n$  in Figure 111. Combining now equations 114 and 116 leads to

$$N_f = \frac{1}{\langle \Delta \sigma_0^{6.61} \rangle} \left\{ \frac{355.2}{\gamma \cdot RMS} \left[ 1 - \frac{\sigma_m}{195} \right] \right\}^{6.61} \quad \text{eq. 117}$$

which gives number of cycles to failure as a function of  $RMS$ . Since in our case  $\gamma = 1$  and  $\langle \Delta \sigma_0^{6.61} \rangle = 8349.7$ , hence the last relation reduces to:

$$N_f = \frac{1}{8349.7} \left\{ \frac{355.2}{RMS} \left[ 1 - \frac{\sigma_m}{195} \right] \right\}^{6.61} \quad \text{eq. 118}$$

where, for correct result, both  $RMS$  and  $\sigma_m$  should be substituted in ksi.

Additional verification of the proposed model can be obtained by comparing the predicted fatigue curves with the variable amplitude fatigue experimental results compiled in Table XXXVII. To facilitate such comparison the predicted  $RMS$  vs.  $N$  and  $\sigma_m$  vs.  $N$  curves have been shown together with experimental data in Figure 112 and Figure 113. Despite appreciable scatter in the data, the predictions compare favorably with the experimental results. The largest differences are on the  $\sigma_m$  vs.  $N$  plots for the small  $RMS$  values. In general, however, the predictive capabilities of the model are remarkably good. Figure 114 to Figure 117 show additionally compilation of the predicted sets of the various type of the fatigue S-N curves for either constant average stress or stress amplitude. The curves were generated using eq. 114 for  $\Delta \sigma$  and  $\sigma_m$  as input and eq. 118 when  $RMS$  and  $\sigma_m$  were used instead. Note that in all variable loading cases the average stress range is represented by  $\langle \Delta \sigma^n \rangle^{1/n}$ . For the constant amplitude fatigue this quantity reduces, as it should, to the  $\Delta \sigma$ .

The proposed methodology also allows for the constructions of the Goodman type diagrams. As for the S-N curves these diagrams can have the average stress range represented by either  $\langle \Delta \sigma^n \rangle^{1/n}$  or *RMS*. In the first case the set of the  $\langle \Delta \sigma^n \rangle^{1/n}$  vs.  $\sigma_m$  lines for the specific values of the cycles to failure,  $N_f$ , can be obtained from eq. 114 after rearranging it to the following form:

$$\langle \Delta \sigma^{6.61} \rangle^{1/6.61} = \frac{355.2}{N_f^{1/6.61}} \left[ 1 - \frac{\sigma_m}{195} \right] \quad \text{eq. 119}$$

A set of such lines is shown in Figure 118. For the diagram with the *RMS* values on the vertical axis, the *RMS* vs.  $\sigma_m$  lines could be obtained from eq. 118. When solved for *RMS* this equation yields:

$$RMS = \frac{355.2}{(8349.7 \cdot N_f)^{1/6.61}} \left[ 1 - \frac{\sigma_m}{195} \right] \quad \text{eq. 120}$$

which gives maximum values of *RMS* for a specific combination of  $N_f$  and  $\sigma_m$ . The *RMS* vs.  $\sigma_m$  lines for constant number of cycles to failure,  $N_f$ , from  $10^3$  to  $10^6$  have been compiled in Figure 119. They were calculated using last equation. Note that the lines have been extended to the negative  $\sigma_m$  values. Such extensions are justified by the presence of the large positive internal stresses commonly observed in the welded structures [137].

## Summary

- Fatigue behavior of the HSLA-80 butt welds have been studied. The samples used in the investigations had dog-bone center butt weld configuration and were tested both under constant amplitude and random loading conditions.
- The composite fractographs of the fracture surfaces of all tested samples are in Appendix A. Their analysis showed that the fatigue cracks initiated predominantly from welding microcracks located randomly along the weld toe. During fatigue these cracks grow and linked-up to form a macrocrack which eventually caused failure.
- Fracture surfaces had distinguishable bands corresponding to the high variable amplitude loading clusters. The bands with basic spectrum  $\Delta \sigma$  values in excess of 7 ksi can be resolved under optical microscope.

- A self consistent model describing crack growth, S-N curves and Goodman diagrams for the studied weldments has been proposed. The model has three parameters which can be obtained from the standard constant amplitude fatigue tests.
- The verification of the model showed that the parameters obtained based on the constant amplitude fatigue data gave excellent predictions of the results of the variable amplitude tests.
- The model has been used to generate S-N fatigue curves and Goodman diagrams. These curves can be used for assessing the live expectancy of the butt-welded joints of the HSLA-80 steels exposed to both constant amplitude and random loading conditions.

## ***Overall Summary***

- Two versions of the microstructure based fatigue life predictions models, one for aluminum airframe 7050-T7451 plate alloys and one for the ship hull HSLA-80 weldments, have been developed. Both versions of the model are based on the Paris-Erdogan type crack growth laws.
- The 7050 alloy version of the model utilizes Monte-Carlo approach with initial crack size distribution, crack location, texture fluctuation on the crack path and crack deflections as stochastic variables. The model requires as input crack growth equation and standard microstructural data from routine metallographic measurements. The model has excellent predictive capabilities for constant amplitude loading conditions for samples both with and without stress concentrators.
- The proposed version of the model for the HSLA-80 steel weldments has a close form solution with three materials parameters. All parameters can be obtained from the constant amplitude fatigue tests. The model has exceptional predictive capabilities both for the constant amplitude and variable loading conditions.
- A new protocol for estimating incipient fatigue crack size distributions from the bulk microstructural data has been developed. This protocol is based on the statistics of extremes and has been very effective in predicting size distributions of the initial fatigue crack distributions in the 7050-T7451 plate alloys.
- A first ever complete database on the fatigue relevant microstructure and fracture surface characteristics of the 7050-T7451 plate alloys has been assembled. This database includes results of the quantification of the alloy grain, subgrain, pore, constituent particle and precipitate structures. It also contains detailed information on

the types and size distributions of the actual fatigue crack initiating features and changes of the crack path and fracture surface characteristics with crack length.

- A set of forty composite fractographs of complete fracture surfaces of the HSLA-80 steel butt weldments has been assembled. These fractographs document types of fatigue failures expected in the weldments under both constant and variable amplitude loading conditions.
- A number of microstructural characterizations and life prediction programs have been developed. All programs have been extensively tested and verified and they can be run on any PC based system.

### ***Acknowledgments***

The funding for this program was provided by the office of Naval Research under Grant N00014-91-J-1299. The author is indebted to Dr. A. K. Vasudevan, the program manager for valuable discussions, Drs. P. E. Magnusen, R. J. Bucci and A. J. Hinkle from Alcoa Technical Center for technical assistance and collaboration on the 7050 part of the program and Dr. D. Khil from Naval Surface Warfare Center, Cerderock Division, for providing fatigue data and HSLA-80 weld samples. Special thanks are due to Dr. J. Zhang and Ms. A. J. Luevano, formerly from UCLA, for performing metallographic and fractographic studies of the 7050-T7451 samples and valuable help throughout the program.

## **List of Publications and Presentations**

### *Publications:*

1. J. Zhang, A. J. Luevano and M. A. Przystupa, "Quantitative Analysis of Heterogeneous Grain Structures on Plane Sections", *Scripta Metallurgica et Materialia*, 26 (1992) pp. 1061-1066.
2. J. Zhang, A. J. Luevano and M. A. Przystupa, "Microstructural Models for Quantitative Analysis of Grains and Second-Phase Particles", *Materials Characterization*, 33 (1994) pp. 175-185.
3. A. J. Luevano J. Zhang, and M. A. Przystupa, "Accumulation of Microstructural Damage Due to Fatigue of High-Strength Aluminum Alloys", *J. of Materials and Performance*, 3 (1994) pp. 47-54.
4. M. A. Przystupa, "Estimation of True Size Distribution of Partially Aligned Same-Shape Ellipsoidal Particles", Accepted for publication in *Scripta Materialia*.
5. M. A. Przystupa, R. J. Bucci, P. E. Magnusen and A. J. Hinkle, "Microstructure Based Fatigue Life Predictions for Thick Plate 7050-T7451 Airframe Alloys", Accepted for publication in *International J. of Fatigue*.
6. J. Zhang, M. A. Przystupa and A. J. Luevano, "Characterizations of Pore and Constituent Particle Populations in 7050-T7451 Aluminum Plate Alloys", Submitted to *Mat. and Metll. Transactions A*.

*Presentations:*

1. J. Zhang, A. J. Luevano, M. A. Przystupa, "Quantitative Evaluation of Grain Sizes and Shapes of Aluminum 7050 Alloys", TMS Annual Meeting, San Diego, California, March 1992.
2. A. J. Luevano, J. Zhang, M. A. Przystupa, "Phase Identification and Grain Boundary Precipitates Characterization of the Aluminum Alloy 7050 in the T7 Temper", TMS Annual Meeting, San Diego, California, March 1992.
3. M. A. Przystupa, J. Zhang, A. J. Luevano, "The Effect of Microstructural Fluctuations on Fatigue Life Distributions in Aluminum Alloys", TMS Annual Meeting, San Diego, California, March 1992.
4. J. Zhang, A. J. Luévano and M. A. Przystupa, "Quantative Characterization of Pores and Constituent Particles in the Aluminum 7050 Alloy" TMS Fall Meeting in Chicago, November 1-5, 1992.
5. M. A. Przystupa, J. Zhang, A. J. Luévano, "Distributions of Microstructural Features on the Fatigue Crack Path in the Aluminum 7050 Alloy: TMS Fall Meeting in Chicago, November 1-5, 1992.
6. A. J. Luévano, J. Zhang and M. A. Przystupa, "Characterization of Grain Boundary Precipitates in the aluminum 7050-7451 Alloy: TMS Fall Meeting in Chicago, November 1-5, 1992.
7. J. Zhang, A. J. Luévano and M. A. Przystupa "Quantative analysis of Fatigued Fracture Surfaces of the Aluminum 7050 Alloy", TMS Annual Meeting, Denver, February 21-25, 1993.

8. M. A. Przystupa, J. Zhang, A. J. Luévano and P. E. Magnusen, "Predictions of the Size Distributions of the Fatigue Crack Initiating Flaws", TMS Annual Meeting, Denver, February 21-25, 1993.
9. A. J. Luévano, M. A. Przystupa and J. Zhang, "Accumulation of Microstructural Damage During Fatigue of High Strength Al Alloys" Aeromat '93, Anaheim, June 8-10, 1993.
10. M. A. Przystupa, "Estimation of the Size Distributions of the Fatigue Crack Initiating Pores in Aluminum Alloys", Conference on Extreme Value Theory and its Application, Gaithersburgh, May 2 - 7, 1993 - Invited Presentation.
11. M. A. Przystupa, J. Zhang and A. J. Luévano, "Size Distributions of the Fatigue Crack Initiating Flaws", TMS Fall Meeting in Pittsburgh, October 17-21, 1993 - Invited Presentation.
12. M. A. Przystupa, "Incorporation of Materials Microstructural Fluctuations into Mechanical Behavior Models", Materials Science Seminar Series, Univ. of California, Irvine, April 1994 - Invited Presentation.
13. M. A. Przystupa, A. J. Luevano and J. Zhang, "Effect of Microstructural Fluctuations on Fracture and Fatigue Behavior of Advanced Aluminum Alloys", AeroMat'94, Anaheim, California, June 1994 - Invited Presentation.
14. M. A. Przystupa, J. Zhang, A. J. Luevano, R. J. Bucci, P. E. Magnusen and A. J. Hinkle, "Microstructural Characterization of High Strength Aluminum Alloys for Fatigue Durability Assessments", 27th Annual Intern. Metallographic Society (IMS) Convention, Montreal, July 1994 - Invited Presentation.

15. M. A. Przystupa, "Modeling Materials Fatigue Reliability", Department of Materials Science and Engineering Seminar Series, Univ. of California, Los Angeles, September 1994.
16. M. A. Przystupa, et al., "Through Thickness Microstructural Gradients in the Thick Plate Aluminum 7050-T7451 Alloys", 1996 TMS Annual Meeting, Anaheim, California, February 4-8, 1996.
17. M. A. Przystupa, et al. "Microstructure Based Fatigue Life Predictions for Thick Plate 7050-T7451", First International Conference on Fatigue Damage in Structural Materials, Hyannis, MA, September 22-27, 1996.

## References

---

1. T. Swift, "Damage Tolerance in Pressurized Fuselages", 11<sup>th</sup> Plantema Memorial Lecture, 14<sup>th</sup> Symposium of the International Committee on Aeronautical Fatigue (ICAF), Ottawa, Canada, June 1987.
2. U. G. Goranson, "Fatigue Issues in Aircraft Maintenance and Repairs", 1<sup>st</sup> International Conference on Fatigue in Structural Materials, Hyannis, September 1996, to be published in *Int. J of Fatigue*.
3. T. Swift, "Widespread Fatigue Damage Monitoring - Issues and Concerns", 5<sup>th</sup> International Conference on Structural Airworthiness on New and Aging Aircraft, Hamburg, June 1993.
4. D. L. Davidson and J. Lankford, *Int. Materials Reviews*, v. 37, 1992, pp. 45-76.
5. A. K. Vasudevan, K. Sadananda and N. Louat, *Mater. Sci. Eng.*, v. A188, 1994, pp. 1-22.
6. "Advances in Fatigue Lifetime Predictive Techniques", ASTM STP 1122, M. R. Mitchell and R. W. Landgraf, eds., American Society for Testing and Materials, Philadelphia, 1992.
7. "Advances in Fatigue Lifetime Predictive Techniques", ASTM STP 1211, M. R. Mitchell and R. W. Landgraf, eds., American Society for Testing and Materials, Philadelphia, 1993.
8. P. E. Magnusen, A. J. Hinkle, R. J. Bucci, R. L. Rolf and D. A. Lukasak, "Methodology for the Assessment of Material Quality Effects on Airframe Fatigue Durability," *Fatigue 90*, Honolulu, HA July 15-20.
9. P. E. Magnusen, A. J. Hinkle, W. Kaiser, R. J. Bucci and R. L. Rolf, *J. of Testing and Evaluation*, November 1990, pp. 439-445.
10. P. E. Magnusen, R. J. Bucci, A. J. Hinkle, M. E. Artley and R. L. Rolf, "The influence of Material Quality on Airframe Structural Durability," *Advances in Fracture Research*, 2, edited by Salama et al. pp. 999-1006, (1989).

- 
11. M. A. Przystupa, J. Zhang and A. J. Luévano, "Development of the microstructure based stochastic life prediction models," Program Report, ONR Grant No. N00014-91-J-1299, UCLA, August 1993.
  12. J. R. Brockenbrough, R. J. Bucci, A. J. Hinkle, J. Liu, P. E. Magnusen, and S. M. Miyasato, "Role of microstructure on fatigue durability of aluminum aircraft alloys," *Alcoa Report*, Alcoa Laboratories, Alcoa Center, PA 15069, April 1993.
  13. P. E. Magnusen, R. J. Bucci, A. J. Hinkle, J. R. Brockenbrough, H. J. Konish and S. M. Miyasato, "Final Report: Role of microstructure on fatigue durability of aluminum aircraft alloys," Final Report fo ONR Contract N00014-91-C-0128, Alcoa Laboratories, Alcoa Center, PA 15069, April 1993.
  14. M. A. Przystupa, Progress Report, ONR Grant No: N00014-91-J-1299, UCLA, June 1991.
  15. M. A. Przystupa, J. Zhang and A. J. Luevano, Progress Report, ONR Grant No: N00014-91-J-1299, UCLA, March 1994.
  16. J. Zhang, A. J. Luévano and M. A. Przystupa, "Microstructural Models for Quantitative Analysis of Grain and Particle Shapes", *Materials Characterization*, 33 (1994) 175-185.
  17. J. Zhang, A. J. Luevano and M. A. Przystupa, *Scripta Mat.*, v. 26, 1992, pp. 1061-1066.
  18. M. A. Przystupa, J. Zhang and A. J. Luevano, Progress Report, ONR Grant No: N00014-91-J-1299, UCLA, February 1992.
  19. J. A. Szpunar and B. K. Tanner, *J. of Mater. Sc.*, 19 (1984) 3254.
  20. H.-J. Bunge, "Texture Analysis in Materials Science", Butterworth & Co 1982.
  21. S. A. Saltykov, *Stereometric Metallography*, Second Edition, Moscow, Metallurgizdat, (1958).
  22. H. C. Hamaker, "Approximating the cumulative normal distribution and its inverse", *Applied Statistics*, 27, pp. 76-79, (1978).
  23. E. E. Underwood, *Quantitative Stereology*, Addison-Wesley Publishing Company, Reading, Massachusetts, (1970).

- 
24. R. T. DeHoff and F. N. Rhines, editors, *Quantitative Microscopy*, McGraw-Hill Book Company, New York, NY 10036, USA (1968).
  25. G. F. Vander Voort, *Metallography Principles and Practice*, McGraw-Hill Book Company, New York, NY 10036, USA (1984).
  26. S. I. Tomkeieff, "Linear Intercepts, Areas and Volumes", *Nature*, 155, pp. 24, January, (1945).
  27. S. D. Wicksell, "The corpuscle problem. A mathematical study of a diametric problem," *Biometrika*, vol. 17, pp. 84-99, 1925.
  28. R. T. DeHoff, "The determination of the size distribution of ellipsoidal particles from measurements made on random plane sections," *Transactions of The Metallurgical Society of AIME*, vol. 224, pp. 474-477, June 1962.
  29. R. T. DeHoff and P. Bousquet, "Estimation of the size distribution of triaxial ellipsoidal particles from the distribution of linear intercepts," *J. of Microscopy*, vol. 92, pt. 2, October 1970, pp. 119-135.
  30. H. J. G. Gundersen and E. B. Jensen, "Particle sizes and their distributions estimated from line- and point sampled intercepts. Including graphical unfolding," *J. of Microscopy*, vol. 131, pt. 3, September 1983, pp. 291-310.
  31. D. C. Sterio, "The unbiased estimation of number and sizes of arbitrary particles using the disector," *J. of Microscopy*, vol. 134, pt. 2, May 1984, pp. 127-136.
  32. E. B. Jensen and H. J. G. Gundersen, "The stereological estimation of moments of particle volume," *J. Appl. Prob.* vol. 22, pp. 82-98, 1985.
  33. H. J. G. Gundersen, "Stereology of arbitrary particles," *J. of Microscopy*, vol. 143, pt. 1, July 1986, pp. 3-45.
  34. L. M. Cruz-Orive, "Particle number can be estimated using a disector of unknown thickness: the selector," *J. of Microscopy*, vol. 145, pt. 2, February 1987, pp. 121-142.
  35. 18. H. J. G. Gundersen and E. B. Jensen, "Stereological estimation of the volume-weighted mean volume of arbitrary particles observed on random sections," *J. of Microscopy*, vol. 138, pt. 2, May 1985, pp. 127-142.

- 
36. S. Srinivasan, J. C. Russ and R. O. Scattergood, "Grain size measurements using the point-sampled intercept technique," *Scripta METALLURGICA et MATERIALIA*, vol. 25, pp. 931-934, 1991.
  37. G. F. Vander Voort and A. M. Gokhale, "Comments on 'Grain size measurements using the point-sampled intercept technique'," *Scripta METALLURGICA et MATERIALIA*, vol. 26, pp. 1655-1660, 1992.
  38. S. Srinivasan, J. C. Russ and R. O. Scattergood, "Reply to *Comments on Grain size measurements using the point-sampled intercept technique* by G.F. Vander Voort and A. M. Gokhale," *Scripta METALLURGICA et MATERIALIA*, vol. 25, pp. 1661-1662, 1992.
  39. T. -S. Liu, D. G. Harlow, and T. J. Delph, "Stereological analysis of creep cavities on polished sections", *Metallography*, 21. pp. 55-76 (1988).
  40. L. Karlsson and R. Sandstrom, "Evaluation of three-dimensional size distributions of inclusions," *Metallography*, vol. 19, pp. 143-176, 1986.
  41. Goodness-of-Fit Techniques, R. B. D'Agostina and M. A. Stephens, Marcel Dekker, Inc, pp. 7-62, 1986.
  42. R. T. DeHoff, "The estimation of particle-size distributions from simple counting measurement made on random plane sections," *Transactions of The Metallurgical Society of AIME*, 233, pp. 25-29, Jan. 1965.
  43. K. Sobczyk and B. F. Spencer, Jr., *Random Fatigue: From Data to Theory*, Academic Press, Inc., San Diego, CA, 1992.
  44. R. T. DeHoff: *Trans. Metall. Soc. AIME*, 1965, vol. 233, pp. 25-29.
  45. D. Greeley, J. D. Crapo and R. T. Vollmer: *J. Microscopy*, 1978, vol. 114, pp. 31-39.
  46. J. D. Crapo and D. Greeley: *J. Microscopy*, 1978, vol. 114, pp. 41-48.
  47. G. M. Tallis: *Biometrics*, 1970, vol. 26, pp. 87-103.
  48. M. G. Kendall and P. A. P. Moran: *Geometrical Probability*, Hafner Publishing Company, NY, 1963, pp. 86-89.
  49. G. F. Vander Voort, "Computer-aided microstructural analysis of specialty steels", *Materials Characterization*, 27, pp. 241-260, (1991).

- 
50. M. T. Shehata and J. D. Boyd, "Measurement of spatial distribution of inclusions", *Inclusions and Their Influence on Material Behavior*, R. Rungta ed. ASM International, Metals Park, OH, pp. 123-131, (1988).
  51. H. Schwarz and H. E. Exner, "The Characterization of the Arrangement of Feature Centriods in Planes and Volumes", *J. Microscopy*, pp.129-55, (1983).
  52. P. J. Wray, O. Richmond, H. L. Morrison, "Use of the Dirichlet Tessellation for Characterizing and Modeling Nonregular Dispersions of Second-Phase Particles", *Metallography*, 16, pp. 39-58, (1983).
  53. W. A. Spitzig, J. F. Kelly and O. Richmond, "Quantitative Characterization of Second-Phase Population", *Metallography*, 18, pp. 235-261, (1985).
  54. H. Hermann, H. Wendrock and D. Stoyan, "Cell-Area Distributions of Planar Voronoi Mosaics", *Metallography*, 23, pp.189-200, (1989).
  55. T. N. Ronus, J. M. Fridy, K. B. Lippert and O. Richmond, "Quantitative characterization and modeling of second phase populations through the use of tessellations", *Simulation and Theory of Evolving Microstructures*, M. P. Anderson and A. D. Rollett eds. The Mineral, Metals & Materials Society, pp. 269-275, (1990).
  56. J. R. Brockenbrough, W. H. Hunt Jr. and O. Richmond, "A reinforced material model using actual microstructural geometry", *Scripta Metallurgia et Materialia*, 27, pp. 385-390, (1992).
  57. R. K. Everett, "Analysis and modeling of fiber clustering in composites using N-tuples", *Scripta Metallurgia et Materialia*, 28, pp. 663-668, (1993).
  58. W. B. James, "Use of image analysis for assessing the inclusion content of low-alloy steel powders for forging applications", *Practical Applications of Quantitative Metallography*, ASTM STP 839, J. L. McCall and J. H. Steele, Jr., eds., American Society for Testing and Materials, Philadelphia, pp. 132-145, (1984).
  59. A. Bowyer, "", *The Computer J.*, 24, 2, pp. 162, (1981).
  60. D. F. Watson, *The Computer J.*, 24, 2, pp. 167, (1981).
  61. C. L. Lawson, *Computer Aided Geometric Design* 3, pp. 231, (1986).

- 
62. I. Saxl, "Contact distances and random free paths," *J. Microscopy*, 170, Pt. 1, pp.53-64, (1993).
63. D. Stoyan, W. S. Kendall and J. Mecke, *Stochastic Geometry and its Applications*. Akademie Verlag, Berlin. (1987)
64. J. Serra, *Image Analysis and Mathematical Morphology*. Academic Press. London. (1982).
65. L. A. Santalo, *Integral Geometry and Geometrical Probability*. Addison-Wesley, Reading, Mass. (1976).
66. H. C. Hamaker, "Approximating the Cumulative Normal Distribution and its Inverse", *Applied Statistics*, 27, (1978) pp.76-79.
67. E. Castillo, "Extreme Value Theory in Engineering", Academic Press, Inc., San Diego, 1988.
68. P.M. Kelly, A. Josten, R. G. Blake and J. G. Napier, *Phys. Stat. Sol.*, 31A (1975) 771.
69. A. Uguz and J. W. Martin, *Materials Characterization*, 27, (1991) 147.
70. J. K. Park and A. J. Ardell, *Metallurgical Transactions A*, 14A, (1983) 1957.
71. Unwin and Nicolson, *Acta Metall*, 17, (1969) 1379.
72. J. K. Park and A. J. Ardell, *Acta Metall*, 34, (1986) 2399.
73. A. J. Ardell, *Acta Metall*, 20, (1972) 601,.
74. A. M. Gokhale and E. E. Underwood, "A general method for estimation of fracture surface roughness: Part I. Theoretical Aspects", *Met. Trans. A*, vol. 21A, pp 1193-1199, May 1990.
75. E. E. Underwood and K. Banerji, "Fractals in fractography", *Materials Science and Engineering*, vol. 80, pp 1-14, 1986.
76. C. S. Pande, L. E. Richards, N. Louat, B. D. Dempsey and A. J. Schwoeble, "Fractal characterization of fractured surfaces," *Acta Metallurgica*, vol. 35, No. 7, pp1633-37, 1987.

- 
77. Z. G. Wang, D. L. Chen, X. X. Jiang, S. H. Ai and C. H. Shih, "Relationship between fractal dimension and fatigue threshold value in dual-phase steels," *Scripta Metallurgica*, vol. 22, pp 827-32, 1988.
78. Z. Q. Mu and C. W. Lung, *Journal of Physics D: Applied Physics*, vol. 21. No. 5, pp. 848, May 1988.
79. E. Hornbogen, "Fractals in microstructure of metals," *International Materials Reviews*, vol 34 No. 6, pp277-96, 1989.
80. D. J. Alexander, "Quantitative analysis of fracture surfaces using fractals", *Quantitative Methods in Fractography*, ASTM STP 1085, B. M. Strauss and S. K. Putatunda, Eds., American Society for Testing and Materials, Philadelphia, pp 39-51, 1990.
81. Yang Jingjun, Zhou Xingyang and Ke Wei, "Fractal in fatigue fractography", *Chin. J. Met. Sci. Technol.*, vol. 6, pp112-116, 1990.
82. Y. L. Tsai and J. J. Mecholsky, Jr., "Fractal fracture of single crystal silicon", *J. Mater. Res.*, Vol. 6, No. 6, pp 1248-63, June 1991.
83. Y. Fahmy, J. C. Russ and C. C. Koch, "Application of fractal geometry measurements to the evaluation of fracture toughness of brittle intermetallics" *J. Mater. Res.*, Vol. 6, No. 9, pp1856-61, Sep. 1991.
84. P. R. Stupak, J. H. Kang and J. A. Donovan, "Computer-aided fractal analysis of rubber wear surfaces", *Materials Characterization*, vol. 27, pp 231-240, 1991.
85. D. A. Lange, H. M. Jennings and S. P. Shah, "Relationship between fracture surface roughness and fracture behavior of cement paste and mortar," *J. Am. Ceram. Soc.*, 76, pp. 589-597, (1993).
86. A. M. Gokhale and W. J. Drury, "A general method for estimation of fracture surface roughness: Part II. Practical Considerations", *Met. Trans. A*, vol. 21A, pp 1201-1207, May 1990.
87. A. M. Gokhale and K. Banerji, "Criteria for selecting the optimum resolution for quantitative analysis of fracture surfaces", *Image Analysis and Metallography*, Editors: P.J. Kenny, G. S. Cole, D. O. Northwood, J. Wylie, G. F. Vander Voort, pp 67-79, 1990.

- 
88. S. J. Jones, A. Boyde and K. Piper, "Confocal microscopic mapping of osteoclastic resorption," *Microscopy and Analysis*, July 1992.
  89. B. B. Mandelbrot: *Fractal Geometry of Nature*, Pub. W. H. Freeman and Company, New York, NY, 1982.
  90. E. E. Underwood, "The new quantitative fractography for analyzing metallic surfaces," *J. of Metals*, 42, pp. 10-15, October 1990.
  91. J. C. Russ, "Computer-assisted image analysis in quantitative fractography," *J. of Metals*, 42, pp. 16-19, October 1990.
  92. S. M. El-Soudani, "Quantitative fractography and fracture mechanics characterization," *J. of Metals*, 42, pp. 20-27, October 1990.
  93. J. J. Friel and C. S. Pande, "A direct determination of fractal dimension of fracture surfaces using scanning electron microscopy and stereoscopy," *J. Mater. Res.*, 8, No. 1, pp. 100-104, 1993.
  94. R. A. Scriven and H. D. Willians, *Trans. AIME*, 223, p. 1593, (1965).
  95. S. M. El-Soudani, "Profilometric analysis of fractures," *Metallography*, 11, pp. 247-336, (1978).
  96. M. Coster and J. L. Chermant, *Int. Metals Rev.*, 28, (4), pp. 228-, (1983).
  97. E. E. Underwood, Proc. 7th Int. Cong. for Stereology, Caen, France, *Acta Ster.*, 6, Suppl. III, pp. 885, (1987).
  98. A. M. Gokhale and E. E. Underwood, "", *Acta Ster.*, 8, (1), pp. 43-, (1989).
  99. J. Cheng, M. Yuan, C. N. J. Wagner and A. J. Ardell, "Fractographic fingerprinting of proton-irradiation-induced disordering and amorphization of intermetallic compounds", *J. Mater. Res.*, Vol. 4, No. 3, pp 565-78, May/June 1989.
  100. E. L. Crow, F. A. Davis and M. W. Maxfield, pp 37 in *Statistical Manual*, Pub. Dover Publications, Inc., New York, 1960.
  101. S. Suresh, *Fatigue of Materials*, Cambridge University Press, pp. 260, 1992.
  102. R.C. Shah, *Stress Intensity Factors for Through and Part-Through Cracks Originating at Fastener Holes*, pp. 429-459 in *Mechanics of Crack Growth*, ASTM STP 590, American Society for Testing and Materials, 1976.

- 
103. O. L. Bowie, *Journal of Mathematics and Physics*, 35, (1956) 60-71.
  104. D. Broek, pg 85 in *Elementary Engineering Fracture Mechanics*, 4th edition, Pub. Kluwer Academic Publishers, Dordrecht, The Netherlands, 1991.
  105. C. Laird, Mechanisms and Theories of Fatigue, pp 149 - 204 in *Fatigue and Microstructure*, Pub. American Society for Metals, Metals Park, Ohio, 1978.
  106. E. J. Coyne, Jr. and E. A. Starke, Jr., The effect of microstructure on the fatigue crack growth behaviour of an Al-Zn-Mg-(Zr) alloy, *International Journal of Fracture*, 15[5],(1979) 405 - 417.
  107. A. J. Luevano, J. Zhang and M. A. Przystupa, *J. of Mater. And Performance*, v. 31, 1994, pp. 47-54.
  108. S. Suresh, "Crack Deflection: implications for the growth of long and short fatigue cracks," *Met. Trans.* 14A, pp. 2375-85, (1983).
  109. E. J. Gumbel, "Statistics of Extremes", Columbia University Press, New York, 1958.
  110. H. Cramer, "Mathematical Methods of Statistics", Princeton University Press, Princeton, 1946.
  111. W. Feller, "An Introduction to Probability Theory and Its Applications", vol. I, 3rd edition, John Wiley & Sons, Inc., New York, 1968.
  112. J. N. Yang, S. D. Manning, J. L. Rudd and R. M. Bader, "Investigation of Mechanics-Based Equivalent Initial Flaw Size Approach", ICAF'95, International Committee on Aeronautical Fatigue, Melbourne, Australia, May 1995.
  113. G. G. Trantina and M. Barishpolsky, "Elasto-Plastic Analysis of Small Defects - Void and Inclusion", *Eng Fract. Mech.*, vol. 20, pp. 1-10, 1984
  114. C. R. Owen, R. J. Bucci and R. J. Kegarise, *J. of Aircraft*, vol. 26, pp. 178-184, 1989.
  115. P. E. Magnusen, A. J. Hinkle, W. T. Kaiser, R. J. Bucci and R. L. Rolf, "Durability Assessment Based on Initial Material Quality", Alcoa Laboratories Report No. 57-89-07.
  116. "Small Fatigue Cracks", ed. by R. O. Ritchie and J. Lankford, TMS, Warrendale, PA 1986.

- 
117. S. Suresh, "Fatigue of Metals", Cambridge University Press, Cambridge, 1992.
118. I. S. Raju and J. C. Newman, in Fracture Mechanics: Seventeenth Volume, ASTM, STP 905, ed. by J. H. Underwood et al., pp. 789-805, ASTM, Philadelphia, 1986.
119. Grandt, A. F. et al, Fatigue Frac. Engng Mater. Struct., v. 16, pp. 199-213, 1993.
120. H. J. Bunge, "Some Applications of the Taylor Theory of Polycrystal Plasticity", *Kristall und Technik*, v. 5, pp. 145-175, 1970.
121. H-S. Ang and W. H. Tang, "Probability Concepts in Engineering Planning and Design", vol. II, Copyright 1990 by the authors.
122. B. N. Cox, "Induction from Monte Carlo Simulations of Small Fatigue Cracks", *Engineering Fracture Mechanics*, vol. 33, pp. 655-670, 1989.
123. A. J. Hinkle and A. F. Grandt, Jr., "Predicting the Influence of Initial Material Quality on Fatigue Life", Proc. of the 17th ICAF Symposium on "Durability and Structural Reliability of Airframes", ICAF93, Stockholm, Sweden, June 9-11, 1993.
124. A. Liu, "Summary of Stress-Intensity Factors", ASM Handbook Vol. 19, Fatigue and Fracture, ASM International, Materials Park, OH, 1996, pp. 980-1000.
125. J. C. Newman, Jr. and I. S. Raju, in Fracture Mechanics: Fourteenth Symposium - Volume I: Theory and Analysis, ASTM STP 791, ed. by J. C. Lewis and G. Sines, pp. I-238-I-265, ASTM, 1983.
126. K. S. Chan and J. Lankford, "The Role of Microstructural Dissimilitude in Fatigue and Fracture of Small Cracks", *Acta Met.*, v. 36, pp. 193-206, 1988.
127. J. R. Brockenbrough, A. J. Hinkle, P. E. Magnusen and R. J. Bucci, "Microstructurally Base Model of Fatigue Initiation and Growth", Alcoa Laboratories Progress Report, ONR Contract N00014-01-C-0128, April 1994.
128. R. E. Peterson, "Stress Concentration Factors", John Wiley & Sons, Inc., New York, 1974
129. B. J. Heath and A. F. Grant, Jr., *Eng. Fract. Mech.*, vol. 19, pp. 665-673. 1984.

- 
130. A. F. Grant, Jr., R. Perez and D. E. Tritsch, "Cyclic Growth and Coalescence of Multiple Fatigue Cracks", *Fracture 84*, ed. By S. R. Valluri et al., Pergamon Press, 1984, pp.1571-1578,
  131. A. F. Grant, Jr., A. B. Thakker and D. E. Tritsch, in *Fracture Mechanics: Seventeenth Volume*, ASTM, STP 905, ed. by J. H. Underwood et al., pp. 239-252, ASTM, Philadelphia, 1986.
  132. J. L. Bogdanov and F. Kozin, "Probabilistic Models of Cumulative Damage", John Wiley & Sons, Inc., New York, 1985.
  133. R. C. McClung, K. S. Chan, D. L. Davidson and T. Y. Torng, "Microstructure-Based Fatigue Life Prediction Methods for Naval Steel Structures", Final Report, ONR Contract No. N00014-91-C-0214, Southwest Research Institute, San Antonio, September 1994.
  134. L. R. Link, "Fatigue Crack Growth of Weldments", ASTM STP 1058, H.I. McHenry and J. M. Potter, Eds., ASTM, Philadelphia, 1990, pp. 16-33.
  135. S. Sarkani, D. P. Kihl and J. E. Beach, *J. Struct. Engrg.*, ASCE, v. 118, 1992, pp. 296-311.
  136. F. V. Lawrence, *Welding Research Supplement*, pp. 212s-220s, May 1973.
  137. T. R. Gurney, "Fatigue of Welded Structures", 2<sup>nd</sup> ed., Cambridge University Press, Cambridge, 1979.
  138. "Residual Stresses and Their Effect", The Welding Institute, Abington Hall, Abington, Cambridge, CB1 6AL, 1981.
  139. J. E. M. Braid and J. F. Knott, in *Advances in Fracture Research, Fracture 81*, ed. By D. Francois, Pergamon Press, 1981, pp. 2061-2069.
  140. J. Carlsson, in *Advances in Fracture Research, Fracture 84*, ed. by S. R. Valluri et al., Pergamon Press, 1984, pp. 751-762.
  141. S. Sarkani, "Feasibility of auto-regressive simulation model for fatigue studies" *J. Struct. Engrg.*, ASCE, v. 116, 1990, pp. 2481-2495.
  142. D. Khil, Private Communication, Naval Surface Warfare Center, Carderock Division, MD, October 1995.

- 
143. S. Suresh, "Fatigue of Materials", Cambridge University Press, Cambridge, 1992.
144. K. S. Ravichandran, "Effect of Crack Shape on Crack Growth", ASM Handbook, v. 19, *Fatigue and Fracture*, ASM International, Material Park, OH, 1966, pp. 159-167.
145. D. W. Hoepfner and W. E. Krupp, *Eng. Fract. Mech.*, v. 6, 1974, pp. 47-70.
146. L. D. Lutes, M. Corazao, S. J. Hu and J. Zimmerman, *J. Struct. Engrg.*, ASCE, v. 110, 1984, pp. 2585-2601.
147. S. Sarkani, L. D. Lutes, P. E. Hughes and D. P. Kihl, *J. Struct. Engrg.*, ASCE, v. 117, 1991, pp. 1852-1867.

## ***List of Tables***

Table I. Mechanical Properties of the Investigated 7050-T7451 Plate Alloys.

Table II. Fatigue Testing Conditions for the Investigated 7050-T7451 Plate Alloys.

Table III. Summary of Quantitative Characterizations Performed on the Investigated Variants of Aluminum 7050-T7451 Plate Alloys.

Table IV. Characteristics of the Recrystallized Grains in the 7050-T7451 Plate Alloys.

Table V. Characteristics of the Unrecrystallized Grains in the 7050-T7451 Plate Alloy.

Table VI. Results of Fitting Recrystallized Grain Sizes with Normal Distributions; 7050-T7451 Plate Alloys.

Table VII. Results of Fitting Unrecrystallized Grain Sizes with Normal Distributions; 7050-T7451 Plate Alloys.

Table VIII. Size, Shape and Orientation of Porosities in the Bulk 7050-T7451 Plate Alloys

Table IX. Results of Approximating Pore Sizes with Lognormal Distributions, Bulk 7050-T7451 Plate Alloys

Table X. True 3-D Pore and Constituent Particle Sizes Obtained from Numerical Method, Bulk 7050-T7451 Plate Alloy

Table XI. True 3-D aspect ratios for pores in 7050-T7451 plate alloy obtained from the computer model.

Table XII. Characteristics of the true 3-D pore and constituent particle size distributions for the 7050-T7451 old and new plate alloys

Table XIII. Comparison of average 2-D and 3-D intercept lengths for the pores and constituent particles in the 7050-T7451 old and new plate alloy

Table XIV. Size, Shape and Orientation of Constituent Particles in the Bulk 7050-T7451 Plate Alloys

Table XV. Results of Approximating Particle Sizes with Lognormal Distribution, Bulk 7050-T7451 Plate Alloys

Table XVI. Results of the Tessellation Analysis for the Pores and Constituent Particles in the Old 7050-T7451 Plate Alloy

Table XVII. Spatial Distribution Parameters Q and R for the Pore and Particles in the Old and New 7050-T7451 Plate Alloys, Center Section.

Table XVIII. Comparison of Particle and Pore Size Data Corrected for Magnification Effect: 7050-T7451 Alloys, Plate Center Location.

Table XIX. Average Sizes, Area Fractions and Spacings of the Grain Boundary Precipitates in the Old and New 7050-T7451 Plate Alloys.

Table XX. Characteristics of the fatigue crack initiation sites in the aluminum 7050-T7451 plate alloys, smooth bar samples examined at UCLA. (10 Hz,  $R = 0.1$ , L orientation)

Table XXI. Characteristics of the fatigue crack initiation sites in the aluminum 7050-T7451 old plate alloy, open hole samples. (30 Hz,  $R = 0.1$ , LT orientation).

Table XXII. Characteristics of the fatigue crack initiation sites in the aluminum 7050-T7451 new plate alloy, open hole samples. (30 Hz,  $R = 0.1$ , LT orientation)

Table XXIII. Characteristics of the fatigue crack initiation sites in the aluminum 7050-T7451 low porosity plate alloy, open hole samples. (30 Hz,  $R = 0.1$ , LT orientation)

Table XXIV. Characteristics of the fatigue crack initiation sites in the aluminum 7050-T7451 1 in. thin plate alloy, open hole samples. (30 Hz,  $R = 0.1$ , LT orientation)

Table XXV. Some formulas converting profile roughness to surface roughness

Table XXVI. Crack lengths and roughness parameters for open hole fatigue sample, old 7050-T7451 plate alloy.

Table XXVII. Percentage of crack length in various regions of grain structure. Old 7050-T7451 plate alloy, open hole fatigue sample.

Table XXVIII. Constituent particle line densities along crack path and along straight line. Old 7050-T7451 alloy, open hole fatigue sample.

Table XXIX. Parameters of the Lognormal Approximations of the Pore Size Parent Distributions and of the Calculated from them Extreme Value Distributions.

Table XXX. Parameters of the Gumbel Approximations of the Pore Size Parent Distributions and of the Calculated from them Extreme Value Distributions.

Table XXXI. Interrogated Areas and/or Volumes Calculated from the Best Estimates of the Extreme Value Distribution Sample Size, N.

Table XXXII. Information Pertaining to the Parent and Extreme Value Distributions Used in Fatigue Life Predictions for the Smooth Fatigue Samples for the 7050-T7451 Plate Alloys.

Table XXXIII. Information Pertaining to the Parent and Extreme Value Distributions Used in Fatigue Life Predictions for the Open Hole Fatigue Samples for the 7050-T7451 Plate Alloys.

Table XXXIV. Input Data for Monte-Carlo Life Predictions for Smooth Fatigue Samples, 7050-T7451 Plate Alloys.

Table XXXV. Input Data for Monte-Carlo Life Predictions for Open Hole Fatigue Samples, 7050-T7451 Plate Alloys.

Table XXXVI. Results of the Fatigue Testing of the HSLA-80 Steel Butt Weld Samples  
Subjected to the Constant Amplitude Loading.

Table XXXVII. Results of the Fatigue Testing of the HSLA-80 Steel Butt Weld Samples  
Subjected to the Variable Amplitude Loading.

## Tables

Table I. Mechanical Properties of the Investigated 7050-T7451 Plate Alloys.

Alloy		Old	New	Low Poros.	Thin Plate
Plate thickness (in)		5.7	5.7	6	1
Longitud.	UTS (ksi)	74.5	74.6		76.1
	$\sigma_{ys}$ (ksi)	66.5	65.9		66.7
	$K_{IcL-T}$ (ksi·in <sup>1/2</sup> )	31.0	29.4		42.6
Long Transverse	UTS (ksi)	74.9	76.0		76.4
	$\sigma_{ys}$ (ksi)	64.7	65.1		66.8
Short Transverse	UTS (ksi)	70.5	72.4	71.0	
	$\sigma_{ys}$ (ksi)	60.7	60.8	60.6	

Table II. Fatigue Testing Conditions for the Investigated 7050-T7451 Plate Alloys.

Fatigue Sample Type	Max. Net Stress MPa (ksi)	Old Alloy	New Alloy	Low Porosity	Thin Plate
		No. of Samples	No. of Samples	No. of Samples	No. of Samples
Smooth (10 Hz)	241 (35)	40	20	19	10
	276 (40)				
	310 (45)				
Open Hole (30 Hz)	224 (32.5)	10	5	5	5
	212 (30.8)				5
	207 (30)				
	190 (27.5)				
	172 (25)				5
	170 (24.6)	10	5	4	2
	155 (22.5)				
	138 (20)				
	128 (18.5)	9	5	5	
	102 (14.8)	10			

All fatigue samples had LT orientation, R = 0.1

Table III. Summary of Quantitative Characterizations Performed on the Investigated Variants  
of the Aluminum 7050-T7451 Plate Alloys

Alloy	Fractography			Metallography/TEM					
	Crack Nucleation Sites	Fracture Surface Character.	Crack Path Features	Location	Planes	Grains	Pores	Const. Particles	Precipit.
Old	✓	✓	✓	Surface Quarter Center	TL LS ST	✓	✓	✓	✓
New	✓	✓		Surface Quarter Center	TL LS ST	✓ Subgrains on TL, ctr.	✓	✓	
Low Porosity	✓			Center	TL LS ST		✓	✓	
Thin Plate	✓			Center	TL LS ST		✓	✓	

Table IV. Characteristics of the Recrystallized Grains in the 7050-T7451 Plate  
Alloys.

Alloy	Location	Test Plane	Size, D $\mu\text{m}$	Area Frac. %	Aspect Ratio	Shape Index, SI
NEW	Center	TL	54.2	22.0	1.8	0.71
		LS	40.7	17.5	2.3	0.65
		ST	36.1	17.2	2.0	0.67
	Quarter	TL	39.5	21.0	1.8	0.68
		LS	33.3	24.2	2.6	0.58
		ST	29.5	20.7	2.1	0.66
	Surface	TL	36.5	3.1	1.7	0.60
		LS	32.3	3.7	2.1	0.68
		ST	40.5	3.6	2.1	0.69
	Average		38.1	14.8	2.1	0.66
OLD	Center	TL	44.5	17.6	1.9	0.68
		LS	36.0	19.0	2.1	0.65
		ST	36.2	14.0	2.0	0.66
	Quarter	TL	39.3	2.3	1.9	0.70
		LS	31.3	1.8	2.9	0.59
		ST	33.3	2.3	2.1	0.68
	Surface	TL	30.8	1.1	1.9	0.69
		LS	21.8	0.1	2.0	0.70
		ST	31.1	0.8	3.9	0.48
	Average		33.8	6.5	2.3	0.65

Table V. Characteristics of the Unrecrystallized Grains in the 7050-T7451 Plate Alloy.

Alloy	Location	Test Plane	Size, D μm	Area Frac. %	Aspect Ratio	Shape Index, SI
NEW	Center	TL	161.5	78.0	1.9	0.69
		LS	103.5	82.5	3.3	0.53
		ST	93.6	82.8	2.5	0.61
	Quarter	TL	111.5	79.0	1.9	0.70
		LS	74.8	75.8	2.8	0.58
		ST	76.7	79.3	2.6	0.61
	Surface	TL	71.6	96.9	1.9	0.68
		LS	43.8	96.3	3.0	0.55
		ST	49.6	96.4	2.6	0.60
	Average		87.4	85.2	2.5	0.62
OLD	Center	TL	116.1	82.4	1.8	0.73
		LS	79.0	81.0	2.6	0.59
		ST	76.0	86.0	2.4	0.60
	Quarter	TL	217.4	97.7	2.3	0.70
		LS	188.6	98.2	3.8	0.51
		ST	141.6	97.7	2.9	0.58
	Surface	TL	168.9	98.9	1.9	0.70
		LS	139.3	99.9	4.3	0.47
		ST	112.5	99.2	2.9	0.57
	Average		137.7	93.5	2.7	0.61

Table VI. Results of Fitting Recrystallized Grain Sizes with Normal Distributions;  
7050-T7451 Plate Alloys.

Alloy	Location	Test Plane	Avg. Size D $\mu\text{m}$	$\Delta_{95\%}$ $\mu\text{m}$	Std. Dev. $\mu\text{m}$	$R^2$
NEW	Center	TL	59.3	4.5	30.0	0.942
		LS	46.0	2.8	20.4	0.942
		ST	35.3	0.9	7.4	0.935
	Quarter	TL	40.4	3.5	22.1	0.920
		LS	33.4	2.8	18.7	0.911
		ST	33.0	2.0	15.1	0.953
	Surface	TL	39.4	12.8	25.3	0.807
		LS	37.5	6.2	16.2	0.627
		ST	32.9	9.4	21.4	0.712
OLD	Center	TL	49.1	3.6	24.1	0.957
		LS	38.4	2.0	17.5	0.959
		ST	36.5	2.7	19.5	0.913
	Quarter	TL	42.4	6.2	19.8	0.825
		LS	33.6	4.7	16.7	0.890
		ST	35.0	4.3	16.9	0.854
	Surface	TL	33.9	5.1	14.7	0.882
		LS	21.5	4.6	5.7	0.382
		ST	33.6	7.6	16.5	0.766

$\Delta_{95\%}$  - 95% confidence limit for the mean

R - correlation coefficient

Table VII. Results of Fitting Unrecrystallized Grain Sizes with Normal Distributions; 7050-T7451 Plate Alloys.

Alloy	Location	Test Plane	Avg. Size D $\mu\text{m}$	$\Delta_{95\%}$ $\mu\text{m}$	Std. Dev. $\mu\text{m}$	$R^2$
NEW	Center	TL	144.7	22.7	106.7	0.90
		LS	106.0	10.4	66.5	0.93
		ST	91.6	8.3	60.1	0.94
	Quarter	TL	111.3	15.2	70.0	0.92
		LS	78.8	8.6	45.4	0.95
		ST	82.5	8.1	47.4	0.95
	Surface	TL	68.6	6.1	43.6	0.94
		LS	46.3	2.6	25.2	0.97
		ST	51.7	3.8	29.9	0.95
OLD	Center	TL	120.3	10.6	69.8	0.93
		LS	73.6	6.2	49.6	0.92
		ST	66.5	5.1	45.7	0.90
	Quarter	TL	155.5	21.2	110.5	0.90
		LS	138.8	13.1	95.7	0.90
		ST	115.7	9.6	68.8	0.91
	Surface	TL	190.1	33.7	145.8	0.82
		LS	177.7	32.9	135.3	0.87
		ST	143.1	14.8	85.1	0.94

$\Delta_{95\%}$  - 95% confidence limit for the mean

R - correlation coefficient

Table VIII. Size, Shape and Orientation of Porosities in the Bulk 7050-T7451

## Plate Alloys

Alloy	Location	Test Plane	Size, D $\mu\text{m}$	Area Fract. %	Aspect Ratio	Shape Index SI	Orient. Factor $\Omega$	Area Density $\text{mm}^{-2}$	Scan Area $\text{mm}^2$	No. of Pores N
NEW	Center	TL	3.5	0.11	1.55	0.809	0.11	69.4	2.812	195
		LS	3.7	0.20	1.49	0.800	0.48	89.4	2.583	231
		ST	3.9	0.14	1.56	0.805	0.39	69.4	2.884	200
	Quarter	TL	3.9	0.08	1.52	0.815	0.16	41.6	2.403	100
		LS	3.5	0.08	1.52	0.823	0.46	54.1	2.403	130
		ST	4.0	0.09	1.46	0.829	0.27	54.9	2.403	132
	Surface	TL	2.9	0.07	1.47	0.831	0.35	64.3	3.124	201
		LS	2.7	0.08	1.52	0.815	0.65	77.2	2.643	204
		ST	3.1	0.07	1.53	0.815	0.55	63.1	3.124	197
	Weighted Aver.		3.4	0.11	1.51	0.815	0.40	67.7	2.751	187
OLD	Center	TL	3.3	0.12	1.50	0.811	0.35	95.7	2.163	207
		LS	4.7	0.37	1.45	0.834	0.30	158.7	1.802	286
		ST	5.5	0.29	1.51	0.820	0.46	92.9	2.163	201
	Quarter	TL	3.1	0.14	1.45	0.834	0.41	130.6	1.562	204
		LS	2.6	0.04	1.42	0.839	0.35	50.8	2.403	122
		ST	3.1	0.08	1.41	0.843	0.30	68.7	2.403	165
	Surface	TL	3.1	0.07	1.50	0.813	0.15	65.3	2.403	157
		LS	2.5	0.06	1.40	0.845	0.36	76.0	2.643	201
		ST	2.7	0.04	1.41	0.842	0.24	50.7	2.523	128
	Weighted Aver.		3.5	0.16	1.45	0.831	0.33	95.8	2.177	198
LOW POROS.	Center	TL	13.4	0.044	1.485	0.75		2.3	21.9	51
		LS	10.2	0.037	1.238	0.53		4.5	20.6	93
		ST	10.5	0.011	1.331	0.54		1.2	22.9	27
	Weighted Aver.		11.2	0.035	1.327	0.60		3.3	21.4	70
THIN PLATE	Center	TL	11.4	0.012	1.524	0.68		1.0	17.2	17
		LS	18.7	0.034	1.427	0.76		1.2	24.3	30
		ST	8.3	0.012	1.082	0.28		2.6	22.3	59
	Weighted Aver.		11.7	0.018	1.251	0.48		2.0	22.0	44

Note: Old and new alloys characterize at 900X, low porosity and thin plates at 100X

Table IX. Results of Approximating Pore Sizes with Lognormal Distributions,  
Bulk 7050-T7451 Plate Alloys

Alloy	Location	Test Plane	Size, D $\mu\text{m}$	Fitting Avg., $\mu\text{m}$	Std. Dev $\mu\text{m}$	R <sup>2</sup>
NEW	Center	TL	3.55	3.26	1.55	0.943
		LS	3.67	3.04	1.74	0.970
		ST	3.90	3.65	1.56	0.945
	Quarter	TL	3.91	3.62	1.53	0.929
		LS	3.50	3.53	1.45	0.949
		ST	4.03	3.18	1.55	0.898
	Surface	TL	2.91	3.04	1.39	0.937
		LS	2.73	2.90	1.38	0.903
		ST	3.07	2.23	1.43	0.860
OLD	Center	TL	3.27	3.02	1.45	0.957
		LS	4.69	3.67	1.74	0.977
		ST	5.48	3.87	1.63	0.890
	Quarter	TL	3.07	2.69	1.49	0.890
		LS	2.64	2.54	1.40	0.837
		ST	3.11	3.02	1.43	0.880
	Surface	TL	3.07	2.87	1.37	0.874
		LS	2.48	2.61	1.36	0.906
		ST	2.73	2.38	1.42	0.816
LOW POROSITY	Center	TL	13.05	12.84	1.21	0.983
		LS	10.50	10.41	1.14	0.929
		ST	10.31	10.17	1.20	0.950
THIN PLATE	Center	TL	11.24	11.03	1.25	0.927
		LS	18.12	17.26	0.15	0.962
		ST	9.12	9.08	1.10	0.857

Table X. True 3-D Pore and Constituent Particle Sizes Obtained from Numerical Method, Bulk 7050-T7451 Plate Alloy

Alloy	Feature	Location	A $\mu\text{m}$	A/B	A/C	$L_{ij}$ ( $\mu\text{m}$ )					
						ST - plane		LS - plane		TL - plane	
						Exp.	Sim.	Exp.	Sim.	Exp.	Sim.
NEW	Pores	Surface	2.27 $\pm 1.36$	1.5	1.8	2.23 $\pm 1.4$	2.45 $\pm 1.4$	2.90 $\pm 1.4$	2.69 $\pm 1.4$	3.04 $\pm 1.4$	2.73 $\pm 1.4$
		Quarter	2.91 $\pm 1.43$	1.1	1.8	3.18 $\pm 1.6$	3.30 $\pm 1.5$	3.53 $\pm 1.5$	3.63 $\pm 1.5$	3.62 $\pm 1.5$	3.63 $\pm 1.5$
		Center	3.38 $\pm 1.41$	1.3	1.8	3.65 $\pm 1.6$	3.59 $\pm 1.5$	3.04 $\pm 1.7$	3.50 $\pm 1.6$	3.26 $\pm 1.5$	3.86 $\pm 1.5$
	Particles	Surface	4.85 $\pm 1.15$	1.5	3.0	3.41 $\pm 1.3$	3.28 $\pm 1.4$	3.78 $\pm 1.4$	3.38 $\pm 1.4$	3.76 $\pm 1.4$	3.47 $\pm 1.4$
		Quarter	4.88 $\pm 1.37$	1.5	2.8	4.07 $\pm 1.4$	3.91 $\pm 1.5$	4.29 $\pm 1.5$	3.73 $\pm 1.4$	4.13 $\pm 1.4$	4.17 $\pm 1.5$
		Center	6.82 $\pm 1.27$	1.5	3.0	3.45 $\pm 1.6$	4.32 $\pm 1.6$	5.10 $\pm 1.5$	4.46 $\pm 1.6$	5.30 $\pm 1.7$	5.06 $\pm 1.5$
OLD	Pores	Surface	2.36 $\pm 1.33$	1.3	1.8	2.38 $\pm 1.4$	2.45 $\pm 1.4$	2.61 $\pm 1.4$	2.68 $\pm 1.4$	2.87 $\pm 1.3$	2.77 $\pm 1.4$
		Quarter	2.43 $\pm 1.34$	1.2	1.8	3.02 $\pm 1.4$	2.78 $\pm 1.4$	2.54 $\pm 1.4$	2.73 $\pm 1.4$	2.69 $\pm 1.5$	2.89 $\pm 1.4$
		Center	3.034 $\pm 1.44$	1.1	1.8	3.87 $\pm 1.6$	3.59 $\pm 1.6$	3.67 $\pm 1.7$	3.44 $\pm 1.6$	3.02 $\pm 1.5$	3.80 $\pm 1.5$
	Particles	Surface	4.484 $\pm 1.34$	1.5	3.0	3.34 $\pm 1.4$	3.50 $\pm 1.4$	4.01 $\pm 1.4$	3.34 $\pm 1.4$	4.07 $\pm 1.4$	3.76 $\pm 1.5$
		Quarter	5.52 $\pm 1.40$	1.5	2.8	4.62 $\pm 1.6$	4.04 $\pm 1.6$	4.18 $\pm 1.5$	4.35 $\pm 1.6$	4.74 $\pm 1.7$	4.79 $\pm 1.7$
		Center	7.29 $\pm 1.28$	2.5	2.5	3.81 $\pm 1.6$	4.03 $\pm 1.6$	5.80 $\pm 1.7$	5.02 $\pm 1.7$	5.27 $\pm 1.6$	4.59 $\pm 1.6$

A, B, C - 3-D true lengths of the pore major diameters

Exp. - experimental data

Sim. - results for the model microstructure

Table XI. True 3-D aspect ratios for pores in 7050-T7451 plate alloy obtained from the computer model.

Alloy	Location	A/B	A/C
Old	Center	1.562	1.792
	Quarter	1.468	1.654
	Surface	1.453	1.848
New	Center	1.504	1.614
	Quarter	1.508	1.904
	Surface	1.340	1.682

Table XII. Characteristics of the true 3-D pore and constituent particle size distributions for the 7050-T7451 old and new plate alloys

Feature	Alloy	Location	$\mu_a$ $\mu\text{m}$	$\sigma_a$ $\mu\text{m}$	A/B	A/B
Pores	New	Surface	2.72	1.25	1.34	1.68
		Quarter	3.25	1.42	1.51	1.90
		Center	3.10	1.47	1.50	1.61
	Old	Surface	2.37	1.60	1.45	1.85
		Quarter	2.64	1.31	1.47	1.65
		Center	3.30	1.54	1.56	1.79
Const. Particles	New	Surface	3.76	1.60	2.34	2.41
		Quarter	4.78	1.48	2.33	2.48
		Center	6.63	1.34	1.79	2.30
	Old	Surface	3.79	1.42	1.71	1.90
		Quarter	5.60	1.35	1.78	1.77
		Center	7.68	1.17	2.06	2.36

Table XIII. Comparison of average 2-D and 3-D intercept lengths for the pores and constituent particles in the 7050-T7451 old and new plate alloy

Feature	Alloy	Location	$L_3$ $\mu\text{m}$	$L_{\parallel,TL}$ $\mu\text{m}$	$L_{\parallel,LS}$ $\mu\text{m}$	$L_{\parallel,ST}$ $\mu\text{m}$
Pores	New	Surface	2.65	2.30	2.21	2.34
		Quarter	2.83	2.76	2.68	2.42
		Center	2.93	2.51	2.20	2.76
	Old	Surface	2.13	2.17	2.00	1.84
		Quarter	2.50	2.05	1.94	2.31
		Center	2.93	2.31	2.88	2.93
Const. Particles	New	Surface	2.30	2.71	2.70	2.48
		Quarter	3.14	2.96	3.05	2.86
		Center	4.40	3.94	3.59	2.60
	Old	Surface	3.00	3.08	2.91	2.50
		Quarter	4.27	3.52	3.09	3.40
		Center	5.30	3.79	4.03	2.79

Table XIV. Size, Shape and Orientation of Constituent Particles in the Bulk  
7050-T7451 Plate Alloys

Alloy	Location	Test Plane	Size, D $\mu\text{m}$	Area Fract. %	Aspect Ratio	Shape Index SI	Orient. Factor $\Omega$	Area Density $\text{mm}^{-2}$	Scan Area $\text{mm}^2$	No. of Partic. N
NEW	Center	TL	6.2	0.54	1.78	0.748	0.22	94.3	2.163	204
		LS	4.8	0.48	2.35	0.663	0.75	69.3	2.583	179
		ST	3.7	0.85	2.27	0.663	0.59	297.8	1.081	322
	Quarter	TL	3.7	0.35	2.33	0.671	0.17	140.8	1.442	203
		LS	4.1	0.64	2.48	0.659	0.71	216.4	0.961	208
		ST	3.8	0.35	2.53	0.646	0.55	135.7	1.562	212
	Surface	TL	3.4	1.12	2.34	0.674	0.43	509.8	0.481	245
		LS	3.3	0.74	2.41	0.652	0.74	371.2	0.601	223
		ST	3.0	0.46	2.05	0.712	0.53	295.5	0.721	213
	Weighted Aver.		4.0	0.64	2.28	0.675	0.52	249.1	1.235	230
OLD	Center	TL	6.1	0.63	2.06	0.704	0.41	94.3	2.163	204
		LS	6.4	0.52	2.36	0.655	0.70	66.9	3.004	201
		ST	4.6	0.91	1.62	0.790	0.56	327.4	0.721	236
	Quarter	TL	5.7	0.84	1.78	0.761	0.15	186.8	1.081	202
		LS	4.4	0.71	1.77	0.761	0.29	249.7	0.841	210
		ST	5.0	0.93	1.87	0.747	0.45	252.1	0.841	212
	Surface	TL	4.0	0.75	1.71	0.769	0.32	328.0	0.613	201
		LS	3.6	0.55	1.90	0.736	0.63	254.4	0.841	214
		ST	3.1	0.45	1.76	0.760	0.35	303.8	0.721	219
	Weighted Aver.		4.7	0.70	1.86	0.744	0.43	231.9	1.185	212
LOW POROS.	Center	TL	12.2	1.031	1.353	0.62		50.9	21.9	1113
		LS	10.2	0.707	1.122	0.47		59.2	20.6	1223
		ST	10.9	0.389	1.100	0.55		30.4	22.9	697
	Weighted Aver.		11.1	0.753	1.202	0.54		49.6	21.6	1062
THIN PLATE	Center	TL	11.9	0.230	1.352	0.58		13.3	17.2	230
		LS	12.0	0.306	1.163	0.69		24.8	24.3	601
		ST	9.3	0.178	0.837	0.42		24.4	22.3	543
	Weighted Aver.		11.0	0.243	1.066	0.57		22.7	22.3	516

Note: Old and new alloys characterize at 900X, low porosity and thin plates at 100X

Table XV. Results of Approximating Particle Sizes with Lognormal Distribution,  
Bulk 7050-T7451 Plate Alloys

Alloy	Location	Test Plane	Size, D $\mu\text{m}$	Fitting Avg., $\mu\text{m}$	Std. Dev $\mu\text{m}$	R <sup>2</sup>
NEW	Center	TL	6.20	5.30	1.73	0.989
		LS	4.84	5.10	1.50	0.663
		ST	3.71	3.45	1.65	0.663
	Quarter	TL	3.72	4.13	1.42	0.922
		LS	4.13	4.29	1.47	0.941
		ST	3.77	4.07	1.44	0.941
	Surface	TL	3.44	3.76	1.41	0.915
		LS	3.35	3.78	1.36	0.896
		ST	2.97	3.41	1.32	0.908
OLD	Center	TL	6.14	5.27	1.63	0.961
		LS	6.38	5.80	1.69	0.993
		ST	4.57	3.81	1.55	0.959
	Quarter	TL	5.67	4.74	1.68	0.943
		LS	4.38	4.18	1.52	0.928
		ST	4.99	4.62	1.58	0.930
	Surface	TL	4.04	4.07	1.44	0.956
		LS	3.64	4.01	1.39	0.964
		ST	3.12	3.34	1.41	0.931
LOW POROSITY	Center	TL	12.45	12.15	1.24	0.969
		LS	11.37	11.16	1.20	0.942
		ST	11.30	11.12	1.19	0.980
THIN PLATE	Center	TL	12.30	12.11	1.20	0.991
		LS	12.13	11.95	1.17	0.860
		ST	10.20	10.11	1.14	0.963

Table XVI. Results of the Tessellation Analysis for the Pores and Constituent  
 Particles in the Old 7050-T7451 Plate Alloy  
 (ST Plane, Center Section)

(a) PORES

	Average	Minimum	Max.	St. Dev.	Geo.Av	Median
Near-Neigbr. ( $\mu\text{m}$ )	114	2.83	324	65.3	91.5	116
Nearest-Nbr. ( $\mu\text{m}$ )	48.2	2.83	156	33.2	35	42.5
Local V.F. %	.00502	.000129	0.156	.0141	.00168	.00146
Pore Area ( $\mu\text{m}^2$ )	30.8	2.3	520	61.9	14.1	11.7
Cell Area ( $\text{mm}^2$ )	.0108	.000439	.033	.00714	.00842	.00952
Cell Sides No.	5.74	3	15			

(b) PARTICLES

	Average	Minimum	Max.	St. Dev.	Geo.Av	Median
Near-Neigbr. ( $\mu\text{m}$ )	58.0	1.0	194	38.2	44.0	66.6
Nearest-Nbr. ( $\mu\text{m}$ )	25.2	1.0	119	19.2	17.9	21.3
Local V.F. %	.0413	.000262	4.38	.292	.007	.00628
Part. Area ( $\mu\text{m}^2$ )	27.8	3.00	266	44.5	14.8	12.2
Cell Area ( $\text{mm}^2$ )	.0033	.000029	.0216	.0034	.0021	.0022
Cell Sides No.	5.76	3	15			

Table XVII. Spatial Distribution Parameters Q and R for the Pore and Particles in the Old and New 7050-T7451 Plate Alloys, Center Section.

Alloy	Feature	Plane	Q	R	Observed		Random		Spatial Distribution type
					NND	STD	NND	STD	
NEW	Pore	TL	0.923	1.264	55.2	39.50	59.80	31.26	Rand. with clust.
		LS	0.857	1.461	45.8	40.80	53.44	27.94	Rand. with clust.
		ST	0.933	1.210	57.5	39.00	61.64	32.22	Rand. with clust.
	Partic.	TL	0.679	1.273	35.3	34.60	51.98	27.17	Rand. with clust.
		LS	0.663	1.160	39.9	36.50	60.22	31.48	Rand. with clust.
		ST	0.814	1.138	23.0	16.80	28.25	14.76	Rand. with clust.
OLD	Pore	TL	0.867	1.303	44.3	34.80	51.10	26.71	Rand. with clust.
		LS	0.892	1.016	33.1	19.70	37.11	19.40	Rand. with clust.
		ST	0.929	1.225	48.2	33.20	51.86	27.11	Rand. with clust.
	Partic.	TL	0.572	1.079	29.3	28.90	51.22	26.77	Rand. with clust.
		LS	0.739	1.333	45.5	42.90	61.58	32.19	Rand. with clust.
		ST	0.912	1.329	25.2	19.20	27.64	14.45	Rand. with clust.

NND - Nearest Neighbor Distance. ( $\mu\text{m}$ )

STD - Standard Deviation. ( $\mu\text{m}$ )

Table XVIII. Comparison of Particle and Pore Size Data Corrected for Magnification Effect: 7050-T7451 Alloys, Plate Center Location.

Alloy	Test Plane	Pores		Particles	
		Censoring %	$L_{II}$ at 100X $\mu\text{m}$	Censoring %	$L_{II}$ at 100X $\mu\text{m}$
NEW	TL	85	6.13	45	7.35
	LS	85	6.75	45	6.50
	ST	75	6.09	75	6.14
OLD	TL	90	5.56	55	7.62
	LS	85	8.15	45	7.94
	ST	80	7.24	75	6.31
LOW POROSITY	TL	0	12.84	0	12.84
	LS	0	10.41	0	10.41
	ST	0	10.17	0	10.17
THIN PLATE	TL	0	11.03	0	12.11
	LS	0	17.26	0	11.95
	ST	0	9.08	0	10.11

Table XIX. Average Sizes, Area Fractions and Spacings of the Grain Boundary Precipitates in the Old and New 7050-T7451 Plate Alloys.

Alloy	Location		Diameter nm	Area frac. $A_f$ %	$N_a$ $\mu\text{m}^{-2}$	ctr-to-ctr spacing nm	surf-to- surf spacing nm
New	Surface	Average	43	21.1	174.8	105	63
		S.dev.	11	8.0	78.0	37	29
	Center	Average	138	29.3	29.5	264	126
		S.dev.	67	11.7	23.1	91	28
Old	Surface	Average	35	9.8	328.7	119	85
		S.dev.	7	2.6	280.9	28	23
	Center	Average	124	25.1	297.2	267	143
		S.dev.	68	16.7	269.1	139	87

Table XX. Characteristics of the fatigue crack initiation sites in the aluminum 7050-T7451 plate alloys, smooth bar samples examined at UCLA. (10 Hz, R = 0.1, L orientation)

Old Quality Plate								
Sample #	Max Stress	Cycles to Failure	Initiation site	Site Dimensions		Max. Length	Dist. from edge	Comments
	ksi			a (μm)	c (μm)			
C3	35.0	79290	pore	121.7	326.1	326.1	0.0	
B3	35.0	72521	pore	217.6	336.0	336.0	0.0	
B5	35.0	70511	pore	240.0	392.0	392.0	25.4	
A4	35.0	73549	pore	96.7	223.3	223.3	0.0	
New Quality Plate								
Sample #	Max Stress	Cycles to Failure	Initiation site	Site Dimensions		Max. Length	Dist. from edge	Comments
	ksi			a (μm)	c (μm)			
A4	35.0	128412	pore	198.3	114.8	198.3	25.4	
B1	35.0	167284	pore	58.5	86.2	86.2	0.0	
C3	35.0	135330	pore	90.8	64.6	90.8	0.0	
C1	35.0	150733	pore	82.1	65.3	82.1	0.0	
1 in. Thin Plate								
Sample #	Max Stress	Cycles to Failure	Initiation site	Site Dimensions		Max. Length	Dist. from edge	Comments
	ksi			a (μm)	c (μm)			
705739-1	45	8510912	Stage I					
705739-4	45	12487199	Stage I					
705739-5	45	8251978	Stage I					
705739-7	45	6803800	Stage I					
705739-8	45	8357960	Stage I					
705739-10	45	1707417	Mg <sub>2</sub> Si particle	12.4	10.9	12.4	6.9	

CRKSITES.XLW:Smooth Samples - New

Table XXI. Characteristics of the fatigue crack initiation sites in the aluminum  
7050-T7451 old plate alloy, open hole samples. (30 Hz, R = 0.1, LT orientation).

Sample #	Fractogr. at	Max. Stress	Cycles to Failure	Initiation site	Site Dimensions		Max. Length	Distance from		Comments
		ksi			a	c		hole	corner	
					( $\mu\text{m}$ )	( $\mu\text{m}$ )	( $\mu\text{m}$ )	( $\mu\text{m}$ )	( $\mu\text{m}$ )	
416-961: B-2-7	UCLA	30.8	27500	pores + Fe constituents	58.8	27.1	58.8	0.0	1188	primary site
"				constituent	17.6	17.6	17.6	0.0	1250	
416-961: C-2-1	UCLA	30.8	28323	pore	35.8	33.0	35.8	0.0	1529	
416-961: C-2-6	UCLA	30.8	20590	Fe constituent + pores	37.1	44.4	44.4	0.0	1768	primary site
"				pore	15.8	29.1	29.1	18.2	1118	
416-961: A-2-2	UCLA	30.8	17806	pore	61.0	139.1	139.1	0.0	1226	primary site
"				pore	38.6	63.8	63.8	5.7	1742	
416-961: B-2-1	UCLA	30.8	19967	Fe constituent + pores	26.7	51.3	51.3	0.0	1303	primary site
"				pore	22.9	38.9	38.9	0.0	1356	
416-971: A-2-4	UCLA	30.8	17888	pore	83.8	105.0	105.0	0.0	1150	
416-971: B-2-5	UCLA	30.8	22011	pore	51.7	113.3	113.3	25.0	448.5	primary site
"				Fe constituent	48.3	38.3	48.3	0.0	?	
416-971: A-2-3	UCLA	30.8	23754	pore	15.6	28.9	28.9	10.0	813.3	
416-971: C-2-7	UCLA	30.8	25557	pore	56.3	101.3	101.3	10.0	637.5	
416-971: C-2-4	UCLA	30.8	15949	pore	193.0	308.8	308.8	7.0	238.9	primary site
"				pore + Fe constituents	11.3	20.0	20.0	16.9	?	
416-961: C-2-2	Alcoa	24.6	35785	pore	118.9	301.8	301.8	0.0	?	
416-961: A-2-6	Alcoa	24.6	33910	pore	85.1	198.1	213.4	0.0	101.6	
"				pore	82.8	199.6	199.6	0.0		secondary crack
416-961: B-2-6	Alcoa	24.6	47812	pore	144.3	145.3	184.9	0.0		
416-961: A-2-4	Alcoa	24.6	45406	pore	141.5	201.4	230.4	0.0	292.1	
416-961: C-2-5	Alcoa	24.6	46641	pore	163.6	447.0	451.1	0.0		
"	Alcoa	24.6		pore	78.2	256.0	256.0	0.0		secondary crack
416-971: A-2-7	Alcoa	24.6	49285	pore	116.8	135.1	159.5	0.0		
"	Alcoa	24.6		pore	39.1	93.5	93.5	0.0		secondary crack
416-971: C-2-3	Alcoa	24.6	42889	pore	122.9	241.8	241.8	0.0		
416-971: B-2-6	Alcoa	24.6	45836	pore	135.4	274.3	280.2	0.0		
416-971: B-2-7	Alcoa	24.6	49292	pore	95.5	184.9	184.9	0.0		
"	Alcoa	24.6		pore	34.3	34.3	34.3	0.0		secondary crack
590156-B-2-1	Alcoa	24.6	55290	Corner burr						
416-961: C-2-7	UCLA	18.5	119328	pore	72.0	123.2	123.2	14.0	1333	
416-961: B-2-5	UCLA	18.5	164739	pore	20.8	59.6	59.6	1.6	880.0	
416-961: C-2-3	UCLA	18.5	109775	pore	55.3	107.1	107.1	0.0	133.3	primary site
"				pore + Fe constituents	48.8	69.4	69.4	0.0	1173	
416-961: B-2-3	UCLA	18.5	119278	pore + Fe constituents	105.9	216.5	216.5	0.0	725.0	primary site
"				pore + Fe constituents	104.0	65.6	104.0	0.0	557.6	
416-971: C-2-1	UCLA	18.5	180611	pore + Fe constituents	99.4	227.9	227.9	0.0	1649	
416-971: B-2-3	UCLA	18.5	181971	pore	149.3	168.0	168.0	8.0	800.0	
416-971: A-2-1	UCLA	18.5	171245	pore + Fe constituents	27.3	92.7	92.7	0.0	1100	primary site
"				pore + Fe constituents	28.6	41.0	41.0	0.0	991.3	
416-971: B-2-4	UCLA	18.5	969579	pore + Fe constituents	175.0	327.5	327.5	3000	0.0	internal
416-971: A-2-2	UCLA	18.5	172288	pore + Fe constituents	97.0	57.0	97.0	0.0	558.2	primary site
"				pore	32.5	62.5	62.5	4.4	156.3	
416-961: A-2-1	UCLA	14.8	222798	pore	90.0	76.3	90.0	11.3	1236	
416-961: C-2-4	UCLA	14.8	323600	pore + Fe constituents	100.4	119.2	119.2	8.2	1200	
416-961: B-2-2	UCLA	14.8	3E+06	Stage I						
416-961: A-2-7	UCLA	14.8	356549	pore	46.3	145.3	145.3	14.7	1032	
416-961: A-2-5	UCLA	14.8	313328	pore + Fe constituents	81.3	87.5	87.5	0.0	1061	
416-971: C-2-2	UCLA	14.8	309256	pore + Fe constituents	90.5	181.0	181.0	3.8	893.3	
416-971: C-2-6	UCLA	14.8	738525	pore	40.9	73.5	73.5	0.9	530.4	
416-971: A-2-6	UCLA	14.8	384130	pore	63.1	76.9	76.9	13.8	1148	
416-971: A-2-5	UCLA	14.8	5E+06	Stage I					15.8	
416-971: B-2-2	UCLA	14.8	214355	pore	56.0	115.2	115.2	0.0	1325	primary site
"				pore	27.9	92.1	92.1	0.0	800.0	

CRKSITES.XLW: Open Hole Samples - New

Table XXII. Characteristics of the fatigue crack initiation sites in the aluminum  
7050-T7451 new plate alloy, open hole samples. (30 Hz, R = 0.1, LT orientation)

Sample #	Fractogr. at	Max.	Cycles to Failure	Initiation site	Site Dimensions		Max Length	Dist. from		Comments
		Stress ksi			a ( $\mu\text{m}$ )	c ( $\mu\text{m}$ )		hole ( $\mu\text{m}$ )	corner ( $\mu\text{m}$ )	
A4-2	UCLA	20.0	1E+06	pore	6.1	9.1	9.1	45.0	70.0	Did not fail Did not fail
A5-1	UCLA	20.0	5E+06	pore	44.0	78.0	78.0	229.6	185.2	
B1-1	UCLA	20.0	1E+07	pore	25.9	21.1	25.9	78.9	1100	
A-5-2		20.0	1E+06							
B-1-2		20.0	1E+06							
C3-2	UCLA	22.5	84802	pore	40.7	53.1	53.1	0.0	1029	
C3-1	UCLA	22.5	266450	pore	18.3	21.7	21.7	13.3	3.3	
C1-2	UCLA	22.5	3E+06	pore + Fe constituents	16.0	21.0	21.0	88.2	126.5	
B5-2	UCLA	22.5	4E+06	pore	107.3	161.0	161.0	190.5	428.6	
C1-1	UCLA	22.5	4E+06	constituent	15.4	19.5	19.5	0.0	938.8	
A3-1	Alcoa	25.0	55848	pore	68.6	99.1	109.2	1549	0.0	spec. surface
A2-2	Alcoa	25.0	141250	pore	63.5	121.9	127.0	1461	0.0	
A4-1	Alcoa	25.0	180413	pore	83.8	142.2	154.9	533.4	0.0	
A3-2	Alcoa	25.0	195180	pore	33.0	111.8	114.3	0.0	706.1	
A2-1	Alcoa	25.0	198871	pore	27.9	99.1	99.1	88.9	0.0	
B4-1	UCLA	30.0	32871	pore + Fe constituents	13.1	34.3	34.3	5.1	470.1	primary site
				pore + Mg <sub>2</sub> Si particles	48.0	80.7	80.7	9.5	500.0	
B5-1	UCLA	30.0	39402	?	<50	<61	0.0	0.0	0.0	site damaged
B4-2	UCLA	30.0	39978	pore	27.9	59.1	59.1	15.7	1270	primary site
B3-1	UCLA	30.0	46207	constituent	5.6	8.1	8.1	0.0	969.7	
				pore	10.8	14.1	14.1	1.6	545.5	
B3-0	UCLA	30.0	49267	pore	41.6	47.3	47.3	7.3	173.0	

CRKSITES.XLW:Open Hole Samples - New

Table XXIII. Characteristics of the fatigue crack initiation sites in the aluminum 7050-T7451 low porosity plate alloy, open hole samples. (30 Hz, R = 0.1, LT orientation)

Sample #	Fractogr. at	Max	Cycles to Failure	Initiation site	Site Dimensions		Max.	Dist. from		Comments
		Stress ksi			a ( $\mu\text{m}$ )	c ( $\mu\text{m}$ )	Length ( $\mu\text{m}$ )	hole ( $\mu\text{m}$ )	corner ( $\mu\text{m}$ )	
590553-LT11	UCLA	20	428453	Fe constituent	32.0	11.9	32.0	0.0	973.6	internal
590553-LT12	UCLA	20	6E+06	Stage I	194.6	256.8	256.8	78.5	229.6	
590553-LT13	UCLA	20	7E+06	Stage I						
590553-LT14		20	1E+07							
590553-LT15		20	1E+07							
590553-LT16	UCLA	22.5	230350	Fe constituent	94.0	67.1	94.0	0.0	12.2	particle cluster
590553-LT17	UCLA	22.5	782052	Fe constituent	23.1	36.8	36.8	0.0	1501	
590553-LT18	UCLA	22.5	1E+06	Mg <sub>2</sub> Si particle	7.6	8.4	8.4	0.0	415.0	
590553-LT19	UCLA	22.5	94081	Fe constituent	41.7	50.0	50.0	0.0	0.0	
590553-LT1	Alcoa	25	58740	Fe constituent	27.9	45.5	45.5	0.0	7.1	
590553-LT2	Alcoa	25	106857	Fe constituent	36.6	47.0	47.0	0.0	18.5	internal
590553-LT3	Alcoa	25	136467	Fe constituent	19.3	56.6	56.6	0.0	0.0	
590553-LT4	Alcoa	25	111781	Fe const + pores	33.5	128.0	128.0	37.1	315.0	
590553-LT5	Alcoa	25	852700	Fe constituent	45.0	33.3	45.0	10.9	546.1	
590553-LT6	UCLA	30	43998	Fe constituent	128.3	100.1	128.3	0.0	718.8	
590553-LT7	UCLA	30	52939	Fe constituent	14.2	23.4	23.4	0.0	36.6	same side
"				Fe constituent	30.7	26.7	30.7	0.0	####	
590553-LT8	UCLA	30	51641	Fe constituent	9.7	12.7	12.7	0.0	0.0	
590553-LT9	UCLA	30	49750	Fe constituent	62.0	68.6	68.6	0.0	16.8	
590553-LT10	UCLA	30	58535	Fe constituent	9.7	14.2	14.2	0.0	####	

CRKSITES.XLW:Open Hole Samples - New

Table XXIV. Characteristics of the fatigue crack initiation sites in the aluminum  
7050-T7451 1 in. thin plate alloy, open hole samples. (30 Hz, R = 0.1, LT  
orientation

Sample #	Fractogr. at	Max	Cycles to Failure	Initiation site	Site Dimensions		Max.	Dist. from		Comments
		Stress			a	c	Length	hole	corner	
		ksi			( $\mu\text{m}$ )	( $\mu\text{m}$ )	( $\mu\text{m}$ )	( $\mu\text{m}$ )	( $\mu\text{m}$ )	
705739-19	UCLA	22.5	9E+06	Stage I				0.0	1532	Did not fail
705739-4		22.5	1E+07							
705739-2	UCLA	25	703238	Fe constituents	16.3	20.3	20.3	0.0	640.1	
705739-16	UCLA	25	4E+06	Stage I					1483	
705739-11	UCLA	25	5E+06	Stage I					40.6	secondary crack
705739-6	UCLA	25	5E+06	Stage I					81.3	
705739-21	UCLA	25	6E+06	Stage I				41.7	1214	
705739-12	UCLA	27.5	66611	Mg <sub>2</sub> Si particles	8.4	4.6	8.4	3.0	365.8	
705739-23	Alcoa	27.5	91406	Fe & Mg <sub>2</sub> Si particles	10.7	24.4	24.4	0.0	0.0	
705739-7	UCLA	27.5	91822	Fe constituents	8.9	8.1	8.9	0.0	596.9	
705739-3	UCLA	27.5	103182	Fe constituents	6.6	20.8	20.8	1.5	15.2	
705739-17	UCLA	27.5	266336	Mg <sub>2</sub> Si particles	7.6	4.6	7.6	7.6	0.0	
705739-5	UCLA	30	34907	Fe constituents	13.5	26.7	26.7	0.0	50.8	
705739-20	UCLA	30	55981	Mg <sub>2</sub> Si particles	13.7	12.4	13.7	0.0	619.8	
"				Fe constituents	7.6	12.7	12.7	0.0	1864	
705739-15	UCLA	30	61560	Fe constituents	22.4	20.6	22.4	0.0	612.1	
"				Fe constituents	11.9	15.0	15.0	0.0	774.7	
"				Fe constituents	9.9	10.7	10.7	0.0	0.0	
705739-10	UCLA	30	63478	Fe constituents	13.7	6.6	13.7	0.0	807.7	
705739-1	UCLA	30	67134	Fe constituents	17.0	18.8	18.8	0.0	838.2	
705739-8	UCLA	32.5	36256	Fe constituents	18.8	17.8	18.8	0.0	1290	
"				Fe constituents	19.3	8.6	19.3	0.0	914.4	
705739-9	UCLA	32.5	42226	Fe constituents	26.9	10.9	26.9	0.0	1468	
"				Fe constituents	12.7	8.1	12.7	0.0	937.3	
"				Fe constituents	9.7	6.6	9.7	0.0	2733	
705739-13	UCLA	32.5	44094	Fe constituents	13.5	23.9	23.9	0.0	983.0	
"				Mg <sub>2</sub> Si particles	5.8	7.9	7.9	0.0	22.9	
705739-14	UCLA	32.5	44280	Mg <sub>2</sub> Si particles	11.9	7.6	11.9	0.0	485.1	
"				Mg <sub>2</sub> Si particles	14.7	13.2	14.7	0.0	1209	
"				?				0.0		
705739-18	UCLA	32.5	52918	Fe constituents	11.9	5.8	11.9	0.0	751.8	
"				Fe constituents	15.7	16.3	16.3	0.0	1384	

CRKSITES.XLW:Open Hole Samples - New

Table XXV. Some formulas converting profile roughness to surface roughness

Formula	Application	Authors
$R_s = 1.16R_L$	For all surfaces	Scriven and William (1965)
$R_s = \frac{4}{\pi} R_L$	For random curvature fracture surface	El-Sadani (1978)
$R_s = \frac{R_L + \frac{\pi}{2} - 2}{\frac{\pi}{2} - 1}$	$R_L < \frac{\pi}{2}$	Coster (1983)
$R_s = \frac{4}{\pi} (R_L - 1) + 1$	For all surfaces	Underwood (1985)
$R_s = \overline{R_L} \cdot \psi$	For trisector method	Gokhale and Underwood (1990)

Table XXVI. Crack lengths and roughness parameters for open hole fatigue sample, old 7050-T7451 plate alloy.

Crack Identification	Section	Projected Length ( $\mu\text{m}$ )	Actual Length ( $\mu\text{m}$ )	Profile Roughness Parameter
#1	Surface	1937	2400	1.24
	1/3 thickness	2771	3277	1.18
	2/3 thickness	2773	3307	1.19
#2	Surface	3292	3635	1.10
	1/3 thickness	3600	4037	1.12
	2/3 thickness	3433	4171	1.22

Table XXVII. Percentage of crack length in various regions of grain structure.

Old 7050-T7451 plate alloy, open hole fatigue sample.

Sample		Transgranular Crack Path			Intergranular Crack Path				
Crack No.	Section	Unrecr. (%)	Recrys (%)	Total (%)	u/r (%)	r/r (%)	u/u (%)	Subgr. (%)	Total (%)
#1	front surface	76.1	12.3	88.4	2.2	1.5	-	7.9	11.6
	1/3 thickness	5.4	5.9	60.2	25.8	7.2	5.1	1.7	39.8
	2/3 thickness	63.4	22.4	85.8	12.6	-	1.5	-	14.2
	back surface	65.6	12.8	78.4	12.8	8.8	-	-	21.6
#2	surface	65.8	26.2	92.0	8.0	-	-	-	8.0
	1/3 thickness	75.7	18.5	94.2	5.8	-	-	-	5.8

u/u = unrecrystallized/recrystallized

r/r = recrystallized/recrystallized

u/u = unrecrystallized/unrecrystallized

Table XXVIII. Constituent particle line densities along crack path and along straight line. Old 7050-T7451 alloy, open hole fatigue sample.

Crack Number	Section	Straight Line (No./ $\mu\text{m}$ )	Crack Path (No./ $\mu\text{m}$ )	Significance Level (%)
#1	surface	$9.9 \times 10^{-4} \pm 6.5 \times 10^{-4}$	$2.0 \times 10^{-3}$	< 0.1
	1/3 thickness	$8.7 \times 10^{-4} \pm 4.5 \times 10^{-4}$	$2.1 \times 10^{-3}$	< 0.1
	2/3 thickness	$9.4 \times 10^{-4} \pm 5.8 \times 10^{-4}$	$1.6 \times 10^{-3}$	< 0.1
#2	surface	$8.0 \times 10^{-4} \pm 5.8 \times 10^{-4}$	$1.3 \times 10^{-3}$	< 0.1
	1/3 thickness	$1.2 \times 10^{-4} \pm 5.8 \times 10^{-4}$	$1.9 \times 10^{-3}$	< 0.1
	2/3 thickness	$1.0 \times 10^{-3} \pm 4.1 \times 10^{-4}$	$2.2 \times 10^{-3}$	< 0.1

Table XXIX. Parameters of the Lognormal Approximations of the Pore Size Parent Distributions and of the Calculated from them Extreme Value Distributions.

Alloy	Standard Fit					Weighted Fit			
	Parent			Extreme		Parent		Extreme	
	$\mu(\mu\text{m})$	$\sigma(\mu\text{m})$	$R^2$	N	$R^2$	$\mu(\mu\text{m})$	$\sigma(\mu\text{m})$	N	$R^2$
Old	1.572	0.536	0.954	$2.36 \cdot 10^{14}$	0.420	1.151	0.795	$6.41 \cdot 10^7$	0.710
New	1.332	0.623	0.980	$8.93 \cdot 10^7$	0.554	1.626	0.453	$4.78 \cdot 10^{11}$	0.385

Table XXX. Parameters of the Gumbel Approximations of the Pore Size Parent Distributions and of the Calculated from them Extreme Value Distributions.

Alloy	Standard Fit					Weighted Fit			
	Parent			Extreme		Parent		Extreme	
	$\mu(\mu\text{m})$	$\sigma(\mu\text{m})$	$R^2$	N	$R^2$	$\mu(\mu\text{m})$	$\sigma(\mu\text{m})$	N	$R^2$
Old	1.334	0.413	0.983	25,633	0.936	1.544	0.306	424,197	0.953
New	1.048	0.495	0.963	1,868	0.914	1.729	0.197	$6.46 \cdot 10^6$	0.855

$\mu$  - average

$\sigma$  - standard deviation

$R^2$  - correlation coefficient

N - extreme value distribution sample size

Table XXXI. Interrogated Areas and/or Volumes Calculated from the Best Estimates of the Extreme Value Distribution Sample Size, N.

Alloy	$N_v$ $\text{mm}^{-3}$	$N_a$ $\text{mm}^{-2}$	No. of Pores in a sample	No. of Surface Pores	Distribution Type	Fit Type	Sample size for best fit	Size of interrogated area or volume
Old	25,843	116	$1.66 \cdot 10^8$	234,707	Lognormal	Standard	$2.36 \cdot 10^{14}$	NA
						Weighted	$6.41 \cdot 10^7$	1.37 mm thick surface layer
					Gumbel	Standard	25,633	5.55 mm wide surface band
						Weighted	424,197	8.1 $\mu\text{m}$ thick surface layer
New	20,513	76	$1.32 \cdot 10^8$	154,039	Lognormal	Standard	$8.93 \cdot 10^7$	2.74 mm thick surface layer
						Weighted	$4.78 \cdot 10^{11}$	NA
					Gumbel	Standard	1,868	0.62 mm wide surface band
						Weighted	$6.46 \cdot 10^8$	157 $\mu\text{m}$ thick surface layer

Note: All calculations assume smooth fatigue sample with 12.7 mm diameter and 50.8 mm gage length

$N_v$  - Number of pores per unit volume

$N_a$  - Number of pores per unit cross-section area

NA - sample size greater than the number of pores in a smooth fatigue sample

Table XXXII. Information Pertaining to the Parent and Extreme Value Distributions Used in Fatigue Life Predictions for the Smooth Fatigue Samples for the 7050-T7451 Plate Alloys.

Descriptions		Old Alloy		New Alloy		Low Porosity	
		Pores	Part	Pores	Part	Pores	Part
Metallo- graphy	$d_{avg}$	5.6	11.2	5.3	10.9	13.6	16.1
	S.Dev.	4.2	11.2	3.7	7.8	5.5	10.5
	$(\log d)_{avg}$	1.553	2.054	1.488	2.154	2.527	2.598
	$\log S.Dev$	0.549	0.841	0.591	0.717	0.411	0.590
	Area Dens.mm <sup>-2</sup>	115.8	164.3	76.1	153.8	3.3	49.6
	$n_{surf}$	234,639	333,008	154,242	311,726	6,628	100,531
	$d_{tail}$	8.2	18.1	8.0	17.7	18.9	24.3
Gumbel Parent	$\mu_G$	1.551	2.447	1.647	2.375	2.652	2.805
	$\sigma_G$	0.350	0.346	0.286	0.288	0.168	0.255
Best fit	Best n	112,827		81,030		63,258	67
	$n/n_{surf}$	0.481		0.525		9.544	0.0007
Gumbel Extreme	$n/n_{surf-used}$	0.500	0.0007	0.500	0.0007	0.500	0.0007
	$\mu_{G-extreme}$	5.644	4.317	4.871	3.912	4.011	3.878
	$\sigma_{G-extreme}$	0.350	0.346	0.286	0.288	0.168	0.255
	$d(50\%)_{extreme}$	321.2	85.1	144.9	55.6	58.7	53.0
Frac. Surf.	$d_{measured}$	316.1		146.7		96.1	53.0

(All dimensions in  $\mu m$ )

Table XXXIII. Information Pertaining to the Parent and Extreme Value Distributions Used in Fatigue Life Predictions for the Open Hole Fatigue Samples for the 7050-T7451 Plate Alloys.

Descriptions		Old Alloy		New Alloy		Low Porosity		Thin Plate	
		Pores	Part	Pores	Part	Pores	Part	Pores	Part
Metallo- graphy	$d_{avg}$	5.6	11.2	5.3	10.9	13.6	16.1	13.1	13.6
	S.Dev.	4.2	11.2	3.7	7.8	5.5	10.5	8.8	6.9
	$(\log d)_{avg}$	1.553	2.054	1.488	2.154	2.527	2.598	2.379	2.486
	$\log S.Dev$	0.549	0.841	0.591	0.717	0.411	0.590	0.600	0.508
	Area Dens.mm <sup>2</sup>	115.8	164.3	76.1	153.8	3.3	49.6	2.0	22.7
	$n_{surf}$	5,485	7,784	3,605	7,287	155	2,350	95	1,075
	$d_{tail}$	8.2	18.1	8.0	17.7	18.9	24.3	19.7	20.0
Gumbel Parent	$\mu_G$	1.551	2.447	1.647	2.375	2.652	2.805	2.518	2.681
	$\sigma_G$	0.350	0.346	0.286	0.288	0.168	0.255	0.309	0.191
Best fit	Best n	9,784	26	6,491	1.7	59		1.1	
	$n/n_{surf}$	0.892	0.0017	0.900	0.0001	0.0126		0.0005	
	Search Vol. mm <sup>3</sup>	0.476	0.002	0.454	0.0001	0.019		0.0007	
Gumbel Extreme	$n/n_{surf-used}$	0.896	0.0012	0.896	0.0012	0.896	0.0012	0.896	0.0012
	$\mu_{G-extreme}$	4.773	3.438	4.159	3.180	3.595	3.229	4.104	2.850
	$\sigma_{G-extreme}$	0.350	0.346	0.286	0.288	0.168	0.255	0.309	0.191
	$d(50\%)_{extreme}$	134.4	35.3	71.1	26.7	38.7	27.7	67.8	18.5
Frac. Surf.	$d_{measured}$	134.2	40.4	71.2	13.8	51.3		15.9	

(All dimensions in  $\mu m$ )

Table XXXIV. Input Data for Monte-Carlo Life Predictions for Smooth Fatigue  
Samples, 7050-T7451 Plate Alloys.

Description	Old	New	Low Porosity
$K_{Ic}$ - MPa m <sup>1/2</sup>	34.1	32.3	39.6*
$\sigma_{UTS}$ - MPa	516.8	524.4	525*
$D_{grain}$ - $\mu$ m	99	105	100*
Crack Initiator	Pore	Pore	Pore
Avg. Pore Aspect Ratio	1.45	1.51	1.02
Pore Gumbel $\mu_{G-extr}$	5.64	4.87	4.01
Extr. Distribution $\sigma_{G-extr}$	0.350	0.286	0.168

\* estimates

Table XXXV. Input Data for Monte-Carlo Life Predictions for Open Hole Fatigue  
Samples, 7050-T7451 Plate Alloys.

Description	Old	New	Low Porosity	Thin Plate
$K_{Ic}$ - MPa m <sup>1/2</sup>	34.1	32.3	39.6*	46.9
$\sigma_{UTS}$ - MPa	516.8	524.4	525*	527.2
$\sigma_{YS}$ - MPa	446.4	449.2	455*	460.9
$D_{grain}$ - $\mu$ m	99	105	100*	100*
Crack Initiator	Pore	Pore	Particle	Particle
Avg. Pore Aspect Ratio	1.45	1.51	1.20	1.06
Pore Gumbel $\mu_{G-extr}$	4.77	4.16	3.23	2.85
Extr. Distribution $\sigma_{G-extr}$	0.350	0.286	0.255	0.191
$\Delta\sigma_{\infty}$ - MPa	74.70	100.96	100.95	113.57
$k_t$	10.672	7.945	8.048	7.247

\* estimates

Table XXXVI. Results of the Fatigue Testing of the HSLA-80 Steel Butt Weld Samples Subjected to the Constant Amplitude Loading.

No	Spec. ID	$\Delta\sigma$ (ksi)	Mean Stress (ksi)	R ratio	Cycles to failure	Weld Reinforcement				No of macro cracks	Crack type
						width (mm)	height #1 (mm)	height #2 (mm)	angle #1 (mm)	angle #2 (mm)	
1	28-08	160	0	-1	194	13.68	3.1	2.5	31	26	2
2	22-09	100	0	-1	10,360	15	1.4	2.46	14	17	1
3	28-19	52.5	43.75	0.25	56,960	15.12	1.8	1.26	10	30	1
4	22-12	50	25	0	188,096	16.14	1.3	0.78	9	17	2
5	08-03	45	37.5	0.25	544,797	14.66	1.52	1	17	16	1
6	14-14	37.5	31.25	0.25	480,464	15.62	1.54	1.5	19	24	1
7	10-06	25	37.5	0.5	1,049,860	16.2	2.94	1.48	18	29	2

Table XXXVII. Results of the Fatigue Testing of the HSLA-80 Steel Butt Weld Samples Subjected to the Variable Amplitude Loading.

No	Spec. ID	RMS Stress (ksi)	Mean Stress (ksi)	Cycles to failure	Weld Reinforcement				No of macro cracks	Crack type
					width (mm)	height #1 (mm)	height #2 (mm)	angle #1 (mm)	angle #2 (mm)	
1	26-05	20	5	30,574	15	2.9	2.66	25	33	edge
2	02-10	20	0	28,054	12.82	2.36	1.86	22	15	edge + side
3	32-07	20	-5	31,709	13.6	1.9	1.9	19	34	edge + V-shear from weld defect
4	24-10	17.5	15	28,149	15.5	1.73	1.73	26	14	edge + V-shear from weld defect
5	16-01	17.5	10	43,100	15.6	2.55	2.55	25	32	edge
6	32-04	17.5	5	64,298	15.56	1.18	2.04	12	24	edge + shear from weld defect
7	30-19	17.5	0	53,955	17.6	1.55	1.55	21	8	edge + corner
8	18-08	17.5	-5	93,147	15.2	2.06	1.22	19	31	edge + weld defect
9	22-14	17.5	-10	41,708	15	1.24	1.08	17	20	edge
10	26-21	15	20	73,144	21.5	1.84	1.3	15	18	edge
11	30-20	15	15	114,309	16.86	1.48	1.62	25	17	edge + shear
12	14-17	15	10	93,146	18.8	1.58	1.56	18	16	edge + corner
13	22-13	15	5	72,477	15.14	1.08	0.68	8	14	edge
14	32-18	15	0	162,416	15	0.76	1.04	9	20	edge + corner
15	20-16	15	-5	222,468	14.5	1.24	1.42	17	18	edge
16	16-19	15	-10	278,198	15.48	1.82	1.82	13	25	edge + weld defect
17	24-19	15	-15	260,217	15.44	3.06	1.24	26	35	edge + weld defect
18	32-20	15	-20	696,720	14.8	1.4	1.1	23	13	edge
19	20-01	12.5	20	245,634	16.52	1.3	2.04	21	25	edge
20	22-19	12.5	15	271,993	15.04	1.78	1.66	15	18	edge
21	26-19	12.5	10	472,993	17.04	1.54	1.28	21	11	edge
22	18-19	12.5	5	169,211	16.18	1.8	2.1	14	18	side + shear from weld defect
23	10-12	12.5	0	725,230	15.24	1.4	1	20	14	edge
24	14-16	12.5	-5	517,733	15.5	1.64	1.34	16	17	edge
25	08-17	12.5	-10	3,490,091	14.1	1.6	1.14	19	18	edge
26	06-09	12.5	-15	1,121,328	15.12	1.78	1.52	19	20	edge
27	12-05	12.5	-20	6,305,613	15.12	0.94	1.4	34	14	edge
28	18-07	10	20	480,622	18.04	2.46	2.68	14	28	edge
29	26-20	10	15	769,207	16.94	1.42	1.74	14	26	side
30	22-03	10	10	932,569	15.5	1.42	1.16	18	16	edge
31	20-09	10	5	1,515,599	14.8	0.86	0.74	16	21	edge
32	14-10	10	0	2,253,059	14.42	2.74	1.14	13	18	edge
33	10-10	7.5	20	3,692,270	15.8	1.58	1.74	19	25	side

## **List of Figures**

Figure 1. Fatigue smooth and open hole samples used in the investigation.

Figure 2. Schematic showing designation of planes used in the report.

Figure 3. Composite 3-D micrographs showing typical microstructures of the 7050-T7451 alloys.

Figure 4. Through-thickness recrystallization gradients in the new and old 7050-T7451 plate alloys.

Figure 5. Cumulative size distributions of the recrystallized grain size in the 7050-T7451 old and new plate alloys. Size represented by the grains average intercept length.

Figure 6. Cumulative size distributions of the unrecrystallized grain sizes in the 7050-T7452 old and new plate alloys. Size represented by the grains average intercept length.

Figure 7. Change of the average intercept lengths,  $L_{II}/2$ , of the recrystallized grains with direction for 7050-T7451 alloy: (a) old and (b) new plate alloys.

Figure 8. Change of the average intercept lengths,  $L_{II}/2$ , of the unrecrystallized grains with direction for 7050-T7451 alloy: (a) old and (b) new plate alloys.

Figure 9. Pore and particle volume fractions in the 7050-T7451 plates.

Figure 10. Crossections of pores found on the ST-plane, plate center region, old 7050-T7451 alloy.

Figure 11. Average shapes of porosities in the old and new 7050-T7451 alloys. Size represented by  $L_2(\alpha)/2$ .

Figure 12. Average shapes of porosities in the low porosity and thin plate 7050-T7451 alloys, center section. Size represented by  $L_2(\alpha)/2$ .

Figure 13. Through-thickness average pore and particle size gradients in the 7050-T7451 plate alloys.

Figure 14. Cumulative pore size distributions on 2-D sections for old and new 7050-T7451 plate alloys

Figure 15. Example of the pore (a) size distribution and (b) lognormal fit for the old 7050-T7451 alloy, LS-plane, plate center.

Figure 16. Cumulative pore size distributions on 2-D sections for the low porosity and thin plate 7050-T7451 alloys.

Figure 17. Example of the corrections of the intercept length distributions for the resolution limit effect. Numbers indicate assumed percentages of undetected small pores. Data for pores in 7050-T7451 low porosity plate, LS-plane, center.

Figure 18. Angular variation of the normalized average intercept lengths of the pore and constituent particle sections on the LS-planes for the old 7050-T7451 alloy variant, plate center. (See text for definitions of  $d_g$  and  $d_{avg}$ )

Figure 19. Through-thickness shape index gradients for the 7050-T7451 plate alloys

Figure 20. Through-thickness orientation factor,  $\Omega$ , gradients in the 7050-T7451 plate alloys

Figure 21. Orientation distribution of pore and particle major axes: new alloy.

Figure 22. Comparison of the 3-D size distributions obtained using numerical method with the 2-D experimental data for new 7050-T7451 plate alloy

Figure 23. Comparison of the measured, 2-D, and simulated true 3-D size distributions of the pore average intercept lengths obtained from the DeHoff's distribution method (see text for details). New 7050-T7451 plate alloy, plate center.

Figure 24. Crossections of constituent particles found on the ST-plane, plate center region, old 7050-T7451

Figure 25. Average shapes of constituent particles in the old and new 7050-T7451 alloys. Size represented by average intercept length  $L_{II}$ .

Figure 26. Average shapes of constituent particles in the low porosity and thin plate 7050-T7451 alloys, center section. Size represented by average intercept length  $L_{II}$ .

Figure 27. Size distributions of constituent particle sections on indicated planes and locations for 7050-T7451 old and new plate alloys.

Figure 28. Size distributions of constituent particle sections on indicated planes at the centers of the 7050-T7451 low porosity and thin plates.

Figure 29. The Dirichlet tessellation cells constructed on the pore centers indicated by points: old 7050-T7451 plate alloy, ST plane, center.

Figure 30. Results of the characterizations of the pore and constituent particle spatial distribution using Q and R method: 7050-T7451 new and old alloys.

Figure 31. Change of the normalized intercept lengths with direction for tessellation cells from Figure 29. The  $d-\alpha$  curve for the rectangular random point pattern is shown for comparison.

Figure 32. Example showing right tail equivalence of the 2-D and 3-D pore size distributions. 3-D distribution obtained using Saltykov method assuming that the pores are prolate spheroids with aspect ratios of 1.82. Old 7050-T7451 plate alloy, center.

Figure 33. Dark field image of hexagonal precipitates on a typical boundary in the 7050-T7451 plate alloy.

Figure 34. Grain boundary from the center of the 7050-T7451 plate containing a multiple precipitate variants.

Figure 35. Micrographs showing large precipitates on low angle boundaries in the 7050-T7451 plate alloy.

Figure 36. Size distributions of the grain boundary precipitates for surface and center sections of the old and new 7050-T7451 plate alloys.

Figure 37. Percentages of different types of the fatigue crack nucleation sites in smooth-bar fatigue samples for the studied four variants of the 7050-T7451 plate alloys. LT orientation, constant amplitude loading, 30 Hz,  $R = 0.1$ , maximum stresses from 100 to 225 MPa.

Figure 38. Percentages of different types of the fatigue crack nucleation sites in open hole fatigue samples for the studied four variants of the 7050-T7451 plate alloys. LT orientation, constant amplitude loading, 30 Hz,  $R = 0.1$ , maximum stress from 100 to 225 MPa.

Figure 39. Results of fatigue testing of the smooth bar samples for the four investigated variants of the 7050-T7451 plate alloys

Figure 40. Effect of the changes of the fatigue crack initiating features size and type on fatigue performance of different variants of the 7050-T7451 plate alloys. Note that the data for Stage I initiation sites are not plotted because they do not have associated size characteristics.

Figure 41. S-N fatigue results for old 7050-T7451 plate alloy, open hole samples.

Figure 42. S-N fatigue results for new 7050-T7451 plate alloy, open hole samples.

Figure 43. S-N fatigue results for thin plate 7050-T7451 alloy, open hole samples.

Figure 44. S-N fatigue results for low porosity 7050-T7451 plate alloy, open hole samples.

Figure 45. Effect of the maximum stress level on the size distributions of the fatigue crack initiating pores in the old 7050-T7451 plate alloy. Open hole and smooth fatigue samples, LT orientation.

Figure 46. Effect of the maximum stress level on the size distributions of the fatigue crack initiating pores in the new 7050-T7451 plate alloy. Open hole and smooth fatigue samples, LT orientation.

Figure 47. Effect of the maximum stress on the average size of the fatigue crack initiating pores in the old and new 7050-T7451 plate alloy. Open hole fatigue samples, LT orientation.

Figure 48. Comparison of the effects of the maximum stress level on the average size of the fatigue crack initiating pores in the open hole and smooth fatigue samples. Old and new 7050-T7451 plate alloy, LT orientation.

Figure 49. Designations of cracks used in the studies of crack profiles and distributions of microstructural features along the crack path.

Figure 50. Schematic showing sectioning of the open hole specimens for fractographic studies. Part I is next to the open hole crack initiation region.

Figure 51. Example of the crack profiles obtained using confocal laser scanning microscopy (CLSM) for 7050-T7451 open hole sample failure.

Figure 52. Distribution of angular orientations of crack segments for fatigue crack in the open hole 7050-T7451 new alloy sample,  $\sigma_{\max} = 206$  MPa,  $R = 0.1$ . Crack average plane corresponds to  $90^\circ$ , cutting plane at  $60^\circ$  to the crack growth direction.

Figure 53. Typical fractal plot for the fracture surface profile parallel to the crack front for the new 7050-T7451 plate alloy fatigued at  $\sigma_{\max} = 206$  MPa,  $R = 0.1$ . The plot shows excellent linearity with the slope, corresponding to fractal dimension  $d$ , equal 1.1142.

Figure 54. Change of the roughness parameter,  $R_s$ , and fractal dimension,  $d$ , with crack length for the fracture surface of the new 7050-T7451 plate alloy fatigued at  $\sigma_{\max} = 206$  MPa,  $R = 0.1$ . The values of  $R_s$  were obtained from the trisector method.

Figure 55. Correlation between  $R_s$  and  $R_L$  for experimental results (solid line) and for the random surface (dotted line). The points represent results obtained from the trisector method.

Figure 56. Change of the roughness parameter,  $R_L$ , and fractal dimension,  $d$ , with crack length for the fracture surface of 7050-T7451 plate alloy. The values of  $R_L$  were obtained from the confocal laser scanning microscopy (CLSM) method.

Figure 57. Percentages of different microstructural features along (a) transgranular and (b) intergranular crack path for old 7050-T7451 alloy, open hole fatigue sample.

Figure 58. Comparison of the line densities of constituent particles along crack path with those for a straight line through the microstructure. 7050-T7451 plate alloy, open hole fatigue sample.

Figure 59. Changes in plastic zone size with crack length in 7050-T7451 plate alloy.

Figure 60. Effects of crack deflection angle,  $\theta$ , and extent of crack tilt,  $D$ , on the relative crack propagation rate. Typical values for aluminum alloys are  $\theta = 45^\circ$  and  $D = 0.75$ .

Figure 61. Comparison of the bulk (metallography) and the actual crack initiating pore sizes (fractography) for the old and new 7050-T7451 plate alloys on (a) linear, (b) lognormal and (c) Gumbel probability plots.

Figure 62. Comparison of the extreme value predictions of the sizes of the crack initiating pores with fractographic data. Predictions obtained using standard and weighted lognormal fits to the metallographic data: old 7050 alloy, LS-plane, center.

Figure 63. Comparison of the extreme value predictions of the sizes of the crack initiating pores with fractographic data. Predictions obtained using standard and weighted lognormal fits to the metallographic data: new 7050 alloy, LS-plane, center.

Figure 64. Comparison of the extreme value predictions of the sizes of the crack initiating pores with fractographic data. Predictions obtained using standard and weighted Gumbel fits to the metallographic data: old 7050 alloy, LS-plane , center.

Figure 65. Comparison of the extreme value predictions of the sizes of the crack initiating pores with fractographic data. Predictions obtained using standard and weighted Gumbel fits to the metallographic data: old 7050 alloy, LS-plane , center.

Figure 66. Schematic showing part of the parent distribution relevant for the extreme value predictions of the size distributions of the crack initiating features.

Figure 67. Old 7050 alloy, smooth fatigue samples,  $\sigma_{max} = 240$  MPa,  $R = 0.1$ . Comparison of the predicted (extreme) and actual (fractography) crack initiating pore size distributions. Predictions obtained from the parent fitted to the tail section of the bulk pore size data.

Figure 68. New 7050 alloy, smooth fatigue samples,  $\sigma_{max} = 240$  MPa,  $R = 0.1$ . Comparison of the predicted (extreme) and actual (fractography) crack initiating pore size distributions. Predictions obtained from the parent fitted to the tail section of the bulk pore size data.

Figure 69. Low porosity 7050 alloy, smooth fatigue samples,  $\sigma_{max} = 276$  MPa,  $R = 0.1$ . Comparison of predicted (extreme) and actual (fractography) crack initiating (a) pore and (b) particle size distributions. Predictions obtained from the parent fitted to the tail section of the bulk size data.

Figure 70. Comparison of the predicted and actual size distributions of the fatigue crack initiating pores in smooth fatigue samples of indicated alloys. Old and new alloys tested at  $\sigma_{max} = 240$  MPa and low porosity at  $\sigma_{max} = 276$  MPa,  $R = 0.1$ .

Figure 71. Old 7050 alloy, open hole fatigue samples. Comparison of the predicted (extreme) and actual (fractography) crack initiating (a) pore and (b) particle size distributions. Predictions obtained from the parent fitted to the tail section of the bulk pore size data.

Figure 72. New 7050 alloy, open hole fatigue samples. Comparison of the predicted (extreme) and actual (fractography) crack initiating (a) pore and (b) particle size distributions. Predictions obtained from the parent fitted to the tail section of the bulk pore size data.

Figure 73. Low porosity 7050 alloy, open hole fatigue samples. Comparison of predicted (extreme) and actual (fractography) crack initiating particle size distributions. Predictions obtained from the parent fitted to the tail section of the bulk size data.

Figure 74. Thin plate 7050 alloy, open hole fatigue samples. Comparison of predicted (extreme) and actual (fractography) crack initiating particle size distributions. Predictions obtained from the parent fitted to the tail section of the bulk size data.

Figure 75. (a) Schematic showing highly stressed surface area extending by angle  $\theta$  circumferentially inside the hole and by  $\delta$  in the radial direction on the hole front and back surfaces. (b) Change of the average radial stress in the highly stressed area as a function of the area size - after Yang et al.[112]

Figure 76. Correlation between fatigue lives and sizes of the fatigue crack initiating pores for 7050-T7451 alloys. Data compiled by Alcoa team.

Figure 77. Correlation between fatigue life and (a) crack initiating pore sizes and (b) estimated numbers of crack nucleation cycles for the investigated new and old 7050-T7451 alloy. Smooth fatigue samples, LT orientation, center.

Figure 78. Fatigue crack growth rate data for the 7050-T7451 plate alloys. Data compiled by Alcoa team[13].

Figure 79. Correlation between estimated number of nucleation cycles and crack initiating pore size for the old and new 7050-T7451 plate alloys. Smooth fatigue samples, LT orientation, center.

Figure 80. Normal cumulative probability plot of the estimated crack nucleation cycles for the old and new 7050-T7451 plate alloys. Smooth fatigue samples, LT orientation, center.

Figure 81. Effect of the scatter in the fatigue crack initiating flaw sizes on the distribution of fatigue lives. Crack growth curves are for the predicted sizes of the crack initiating pores corresponding to the 1 and 99 percentiles of Gumbel extreme distribution. Smooth fatigue samples, new 7050-T7451 new alloy fatigued at  $\sigma_{\max} = 240$  MPa and  $R = 0.1$ .

Figure 82. Effects of crystallographic texture on fatigue life. Crack growth curves for the maximum and minimum values of Taylor factor,  $M$ , expected in for the 7050 alloys. Random curve corresponds to random variations of texture on the crack path. Smooth fatigue samples fatigued at  $\sigma_{\max} = 240$  MPa and  $R = 0.1$ .

Figure 83. Idealized crack profile assumed for modeling microstructural crack deflections.

Figure 84. Effects of microstructural crack deflections on fatigue life. Crack growth curves for the maximum and minimum values of crack deflection coefficient,  $R$ , expected for the 7050 alloys. Random curve corresponds to random variations of texture on the crack path. Smooth fatigue samples fatigued at  $\sigma_{\max} = 240$  MPa and  $R = 0.1$ .

Figure 85. Relation between the error of the estimated initial crack sizes and the error in predicted fatigue lives for the new 7050-T7451 plate alloy.

Figure 86. Schematic showing (a) shape of the uniform Taylor factor distribution and (b) change of the distribution range with the number of grains at the crack tip assumed during Monte-Carlo simulations.

Figure 87. Examples of data on (a) distribution of near neighbor spacings and (b) distributions of near neighbor positions obtained from tessellation analysis. 7050-T7451 plate alloys, constituent particles, LS plane, center region.

Figure 88. Comparison of the distributions of fatigue lives predicted using Monte-Carlo model with experimental data for smooth fatigue samples, old 7050-T7451 plate alloy.

Figure 89. Comparison of the S-N fatigue curves obtained from the Monte-Carlo fatigue life predictions with experimental data for the smooth fatigue samples, old 7050-T7451 plate alloy.

Figure 90. Comparison of the distributions of fatigue lives predicted using Monte-Carlo model with experimental data for smooth fatigue samples, new 7050-T7451 plate alloy.

Figure 91. Comparison of the S-N fatigue curves obtained from the Monte-Carlo fatigue life predictions with experimental data for the smooth fatigue samples, new 7050-T7451 plate alloy.

Figure 92. Comparison of the distributions of fatigue lives predicted using Monte-Carlo model with experimental data for smooth fatigue samples, low porosity 7050-T7451 plate alloy.

Figure 93. Comparison of the S-N fatigue curves obtained from the Monte-Carlo fatigue life predictions with experimental data for the smooth fatigue samples, low porosity 7050-T7451 plate alloy.

Figure 94. Comparison of the S-N fatigue curves obtained from the Monte-Carlo fatigue life predictions with experimental data for the open hole fatigue samples, old 7050-T7451 plate alloy.

Figure 95. Comparison of the S-N fatigue curves obtained from the Monte-Carlo fatigue life predictions with experimental data for the open hole fatigue samples, new 7050-T7451 plate alloy.

Figure 96. Comparison of the S-N fatigue curves obtained from the Monte-Carlo fatigue life predictions with experimental data for the open hole fatigue samples, low porosity 7050-T7451 plate alloy.

Figure 97. Comparison of the S-N fatigue curves obtained from the Monte-Carlo fatigue life predictions with experimental data for the open hole fatigue samples, thin plate 7050-T7451 alloy.

Figure 98. Comparison of the fatigue data for old and new 7050 alloys with the predictions from the Markov B-model.  $\sigma_{\max}=240$  MPa,  $R = 0.1$ ,  $n$  is the size of the transition matrix,  $p$  is probability that crack does not grow during one duty cycle.

Figure 99. Results of the simulation of the effect of the increase of the initial crack length on the Markov chain model prediction. Notation and loading the same as on the previous figure.

Figure 100. Effect of the change of the probability  $p$  in the first row of the transition matrix on the distribution of the fatigue life predicted by the Markov B-model.

Figure 101. Effect of the change of all p-values in the entire transition matrix on the distribution of the fatigue life predicted by the Markov B-model.

Figure 102. Unit *RMS* loading spectrum used in all variable amplitude fatigue testing of the HSLA-80 steel weldments.

Figure 103. Results of the constant amplitude fatigue testing of the dog-bone type specimens from HSLA-80 steel with center butt weld.

Figure 104. Results of the variable amplitude fatigue testing of the dog-bone type specimens from HSLA-80 steel with center butt weld.

Figure 105. Fatigue curves for constant average stresses for the dog-bone specimens from HSLA-80 steel with center butt weld tested under variable loading conditions. The *RMS* values represent the multiplication factors applied to the unit spectrum loading shown in Figure 98 and  $\langle \Delta \sigma \rangle = 2.5058 \cdot RMS$ .

Figure 106. Fatigue curves for constant *RMS* stresses for the dog-bone specimens from HSLA-80 steel with center butt weld tested under variable loading conditions. The *RMS* values represent the multiplication factors applied to the unit spectrum loading shown in Figure 98 and  $\langle \Delta \sigma \rangle = 2.5058 \cdot RMS$ .

Figure 107. Schematics showing (a) geometrical parameters used for characterizing reinforcement and (b) crack types observed in the HSLA-80 weldments.

Figure 108. Normalized S-N curve illustrating goodness of fit of the model to the constant amplitude fatigue data for HSLA-80 weldments.

Figure 109. Normalized S-N curve showing comparison of the predictions with the experimental random fatigue data for HSLA-80 weldments. The model parameters estimated from the constant amplitude data.

Figure 110. Normalized S-N curve showing comparison of the predictions with the constant and variable amplitude fatigue data for HSLA-80 weldments. The parameters of the model estimated using constant amplitude data.

Figure 111. Values of the first eight moments of the stress ranges,  $\Delta\sigma_0$ , of the basic variable amplitude spectrum loading shown from Figure 98.

Figure 112. Comparison of the predicted  $RMS$  vs.  $N$  fatigue curves with experimental data for constant average stress for the HSLA-80 steel butt welds.

Figure 113. Comparison of the predicted  $\sigma_m$  vs.  $N$  fatigue curves with experimental data for constant  $RMS$  values for the HSLA-80 steel butt welds.

Figure 114. Predicted  $\Delta\sigma$  vs.  $N$  fatigue curves for constant average stresses for the HSLA-80 steel butt welds subjected to either constant or variable amplitude loading. Note that  $n=6.61$  and  $\langle\Delta\sigma^n\rangle^{1/n}$  reduces to  $\Delta\sigma$  for constant amplitude loading.

Figure 115. Predicted  $RMS$  vs.  $N$  fatigue curves for constant average stresses for the HSLA-80 steel butt welds subjected to either constant or variable amplitude loading.

Figure 116. Predicted  $\sigma_m$  vs.  $N$  fatigue curves for constant average stress ranges for the HSLA-80 steel butt welds subjected to either constant or variable amplitude loading. Note that  $n=6.61$  and  $\langle\Delta\sigma^n\rangle^{1/n}$  reduces to  $\Delta\sigma$  for constant amplitude loading.

Figure 117. Predicted  $\sigma_m$  vs.  $N$  fatigue curves for constant  $RMS$  values for the HSLA-80 steel butt welds subjected to either constant or variable amplitude loading.

Figure 118. Predicted Goodman diagram in terms of the average stress range represented by  $\langle \Delta \sigma^n \rangle^{1/n}$  vs. average stress  $\sigma_m$  for the HSLA-80 steel butt welds subjected to either constant or variable amplitude loading.

Figure 119. Predicted Goodman diagram in terms of the average stress range represented by  $RMS$  vs. average stress  $\sigma_m$  for the HSLA-80 steel butt welds subjected to either constant or variable amplitude loading.

## Figures

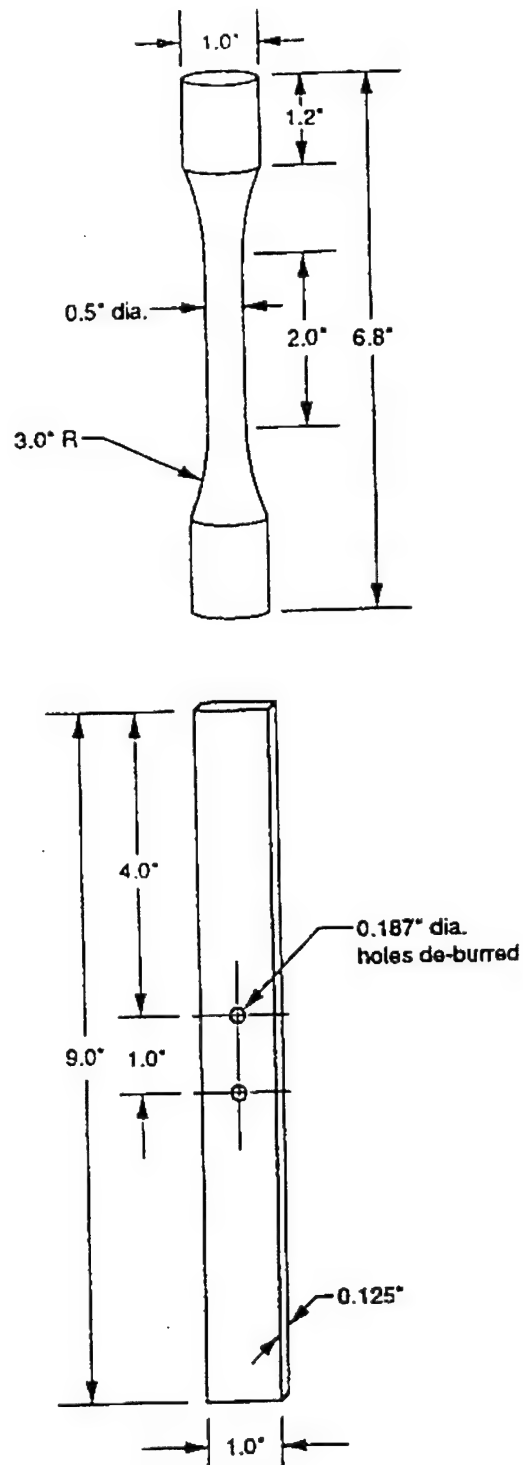


Figure 1. Fatigue smooth and open hole samples used in the investigation.

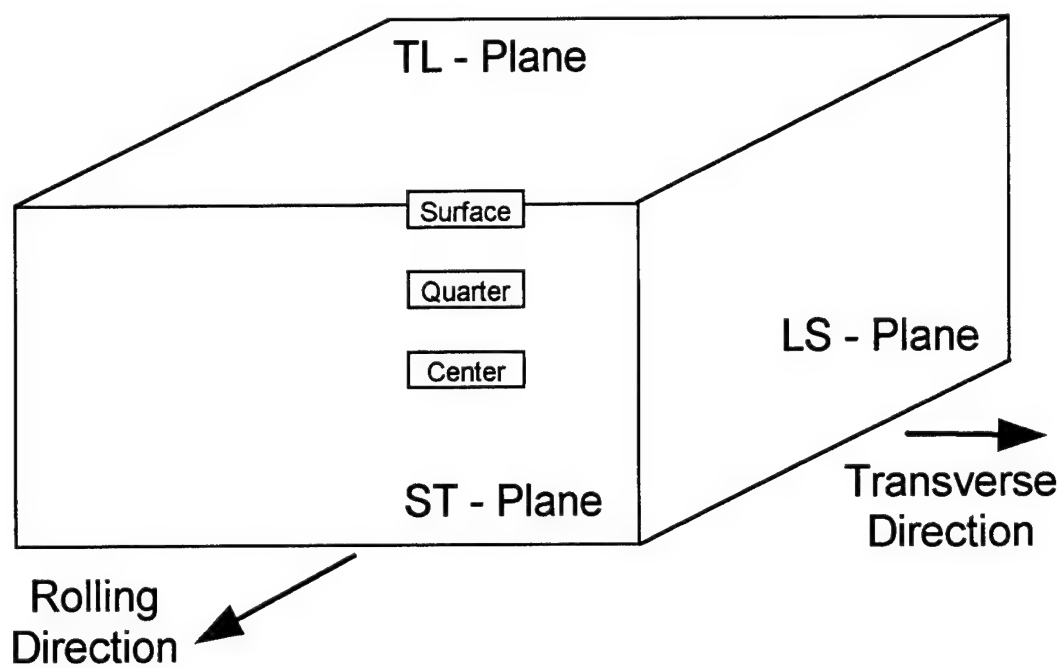


Figure 2. Schematic showing designation of planes used in the report

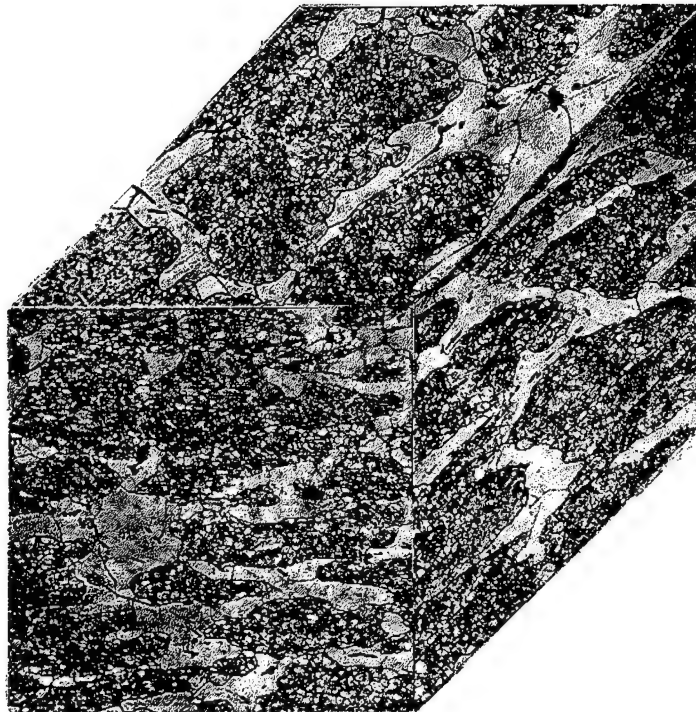


Figure 3. Composite micrograph showing typical microstructures of the 7050-T7451 alloys.

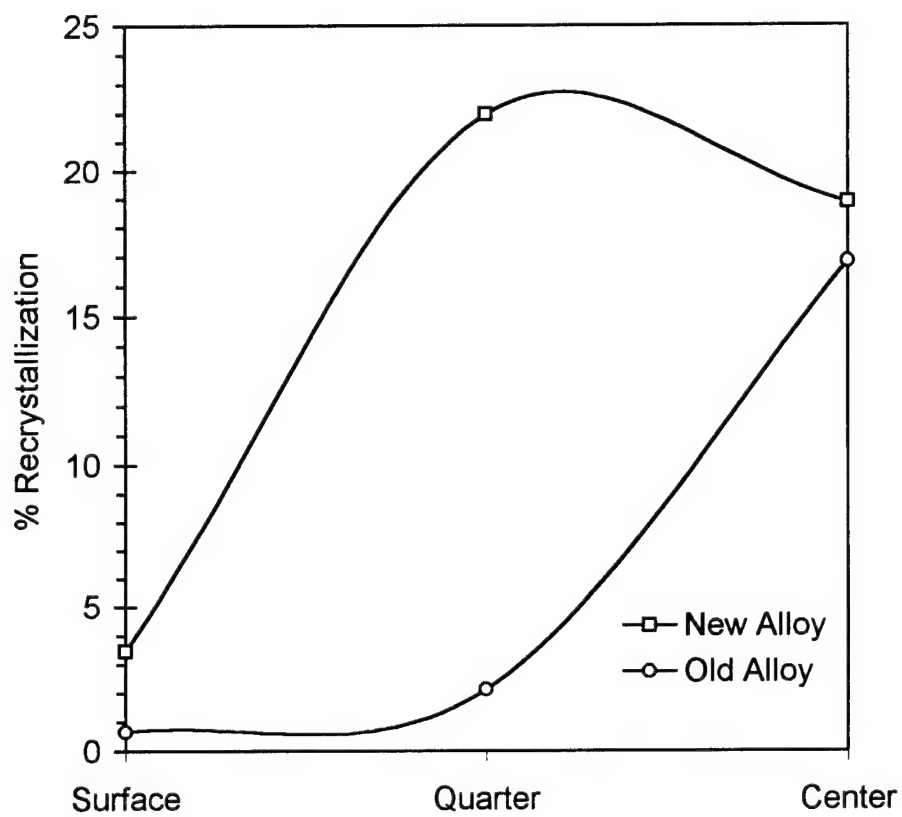


Figure 4. Through-thickness recrystallization gradients in the new and old 7050-T7451 plate alloys.

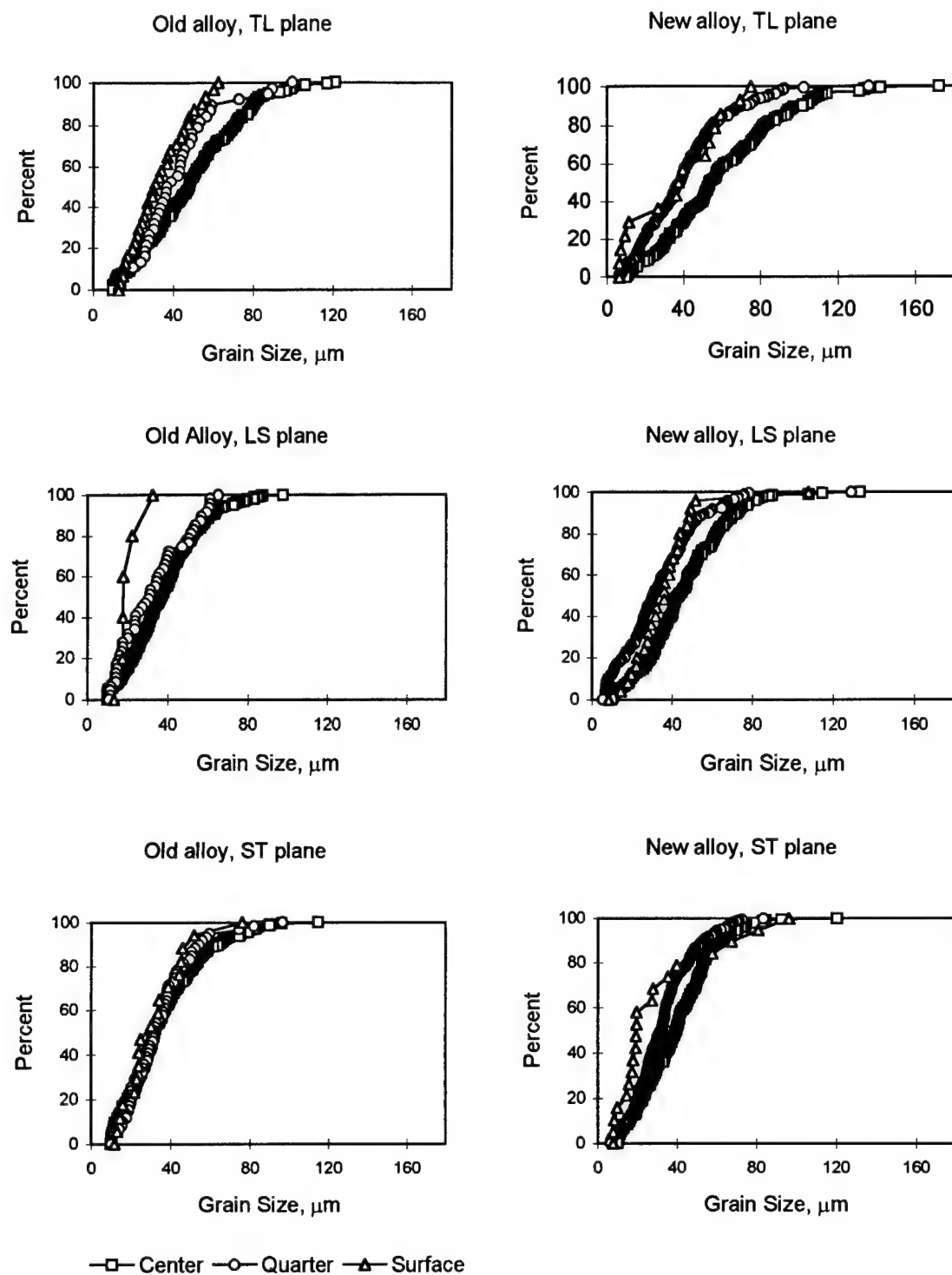


Figure 5. Cumulative size distributions of the recrystallized grain size in the 7050-T7451 old and new plate alloys. Size represented by the grains average intercept length.

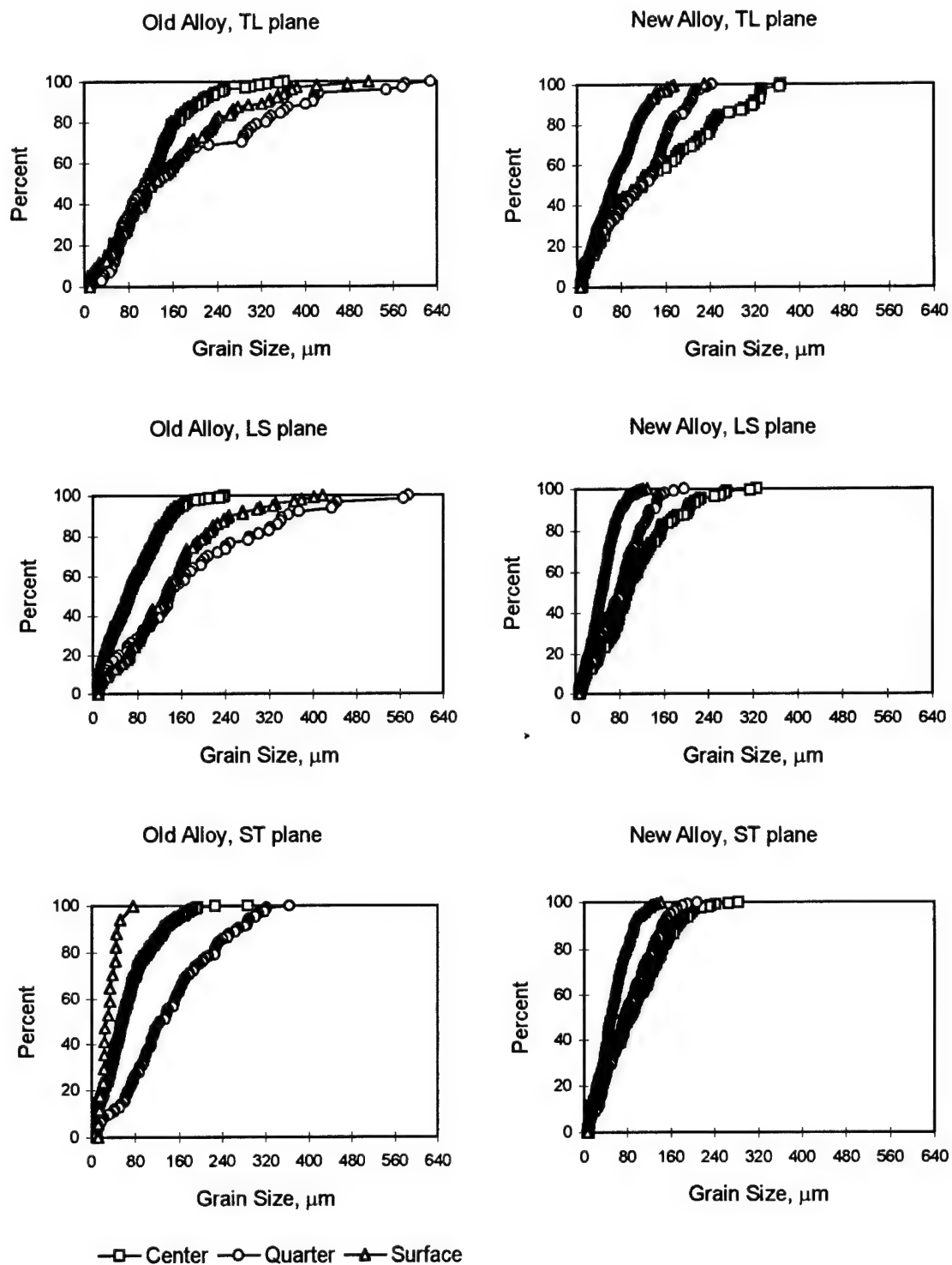
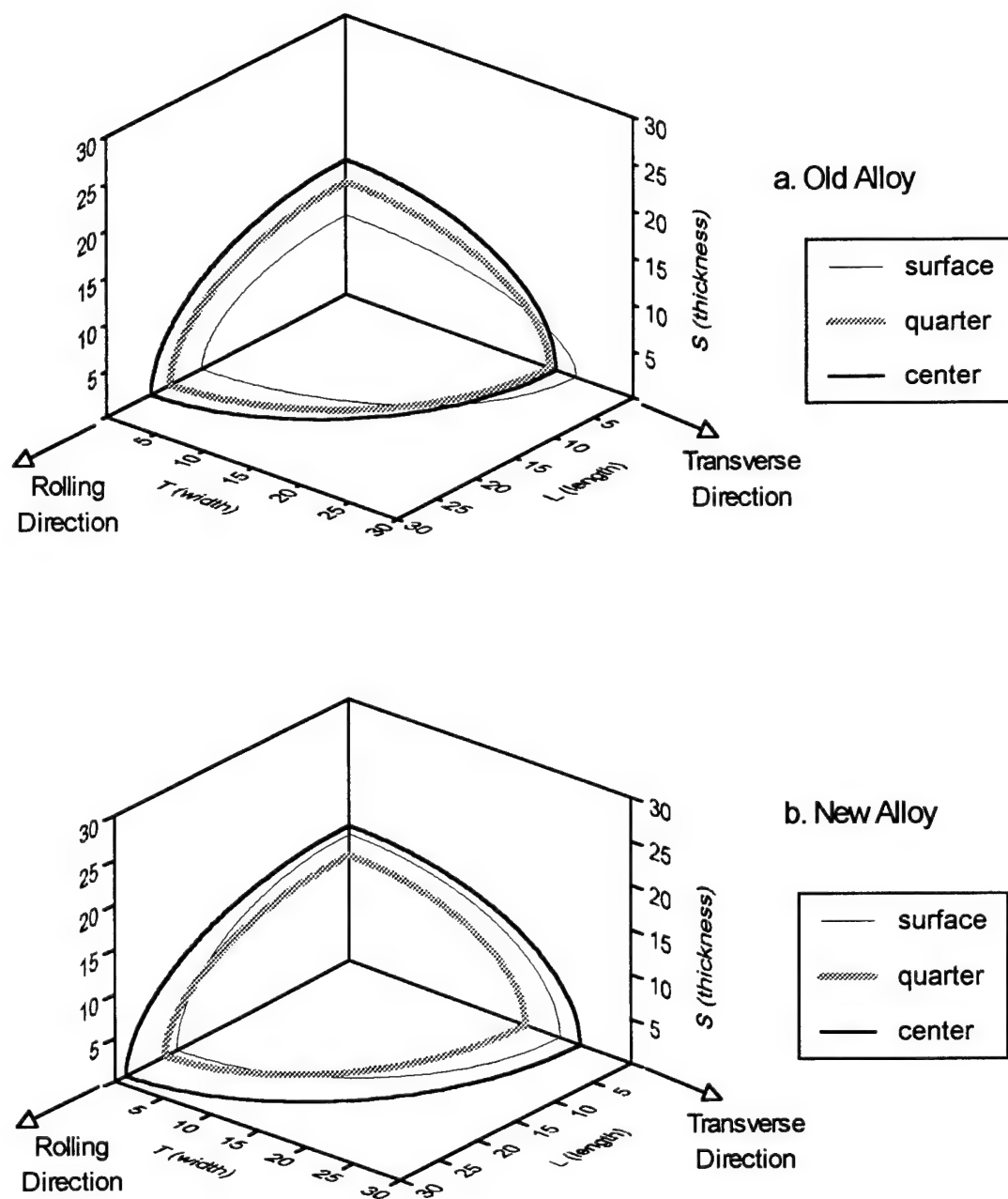


Figure 6. Cumulative size distributions of the unrecrystallized grain sizes in the 7050-T7452 old and new plate alloys. Size represented by the grains average intercept length.

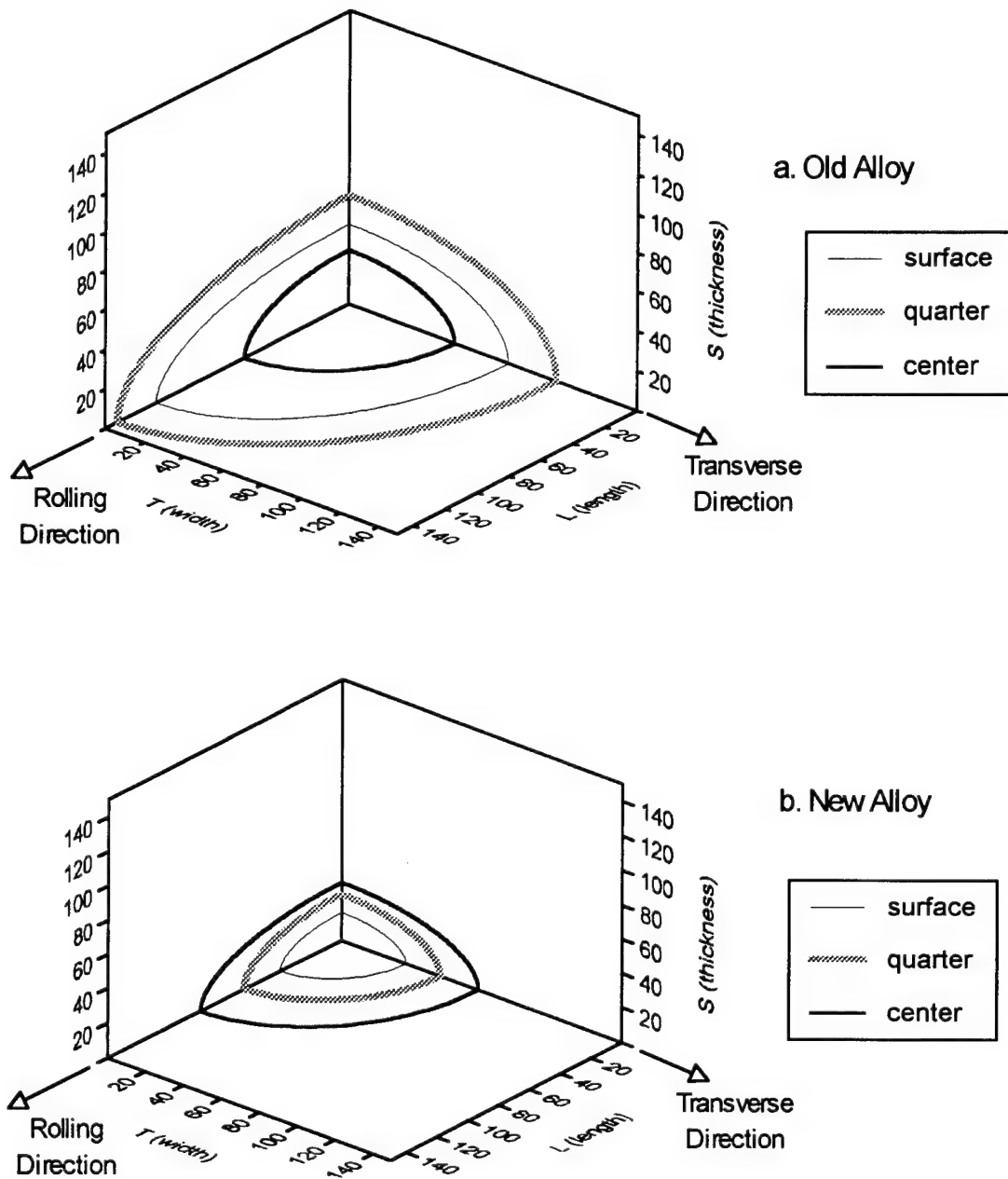
## Characteristics of Recrystallized Grain Structure in the 7050-T7451 Plate Alloy



3D-RX.DGR

Figure 7. Change of the average intercept lengths,  $L_{II}/2$ , of the recrystallized grains with direction for 7050-T7451 alloy: (a) old and (b) new plate alloys.

## Characteristics of Unrecrystallized Grain Structures in the 7050-T7451 Plate Alloys



3D-UNRX.DGR

Figure 8. Change of the average intercept lengths,  $L_{II}/2$ , of the unrecrystallized grains with direction for 7050-T7451 alloy: (a) old and (b) new plate alloys.

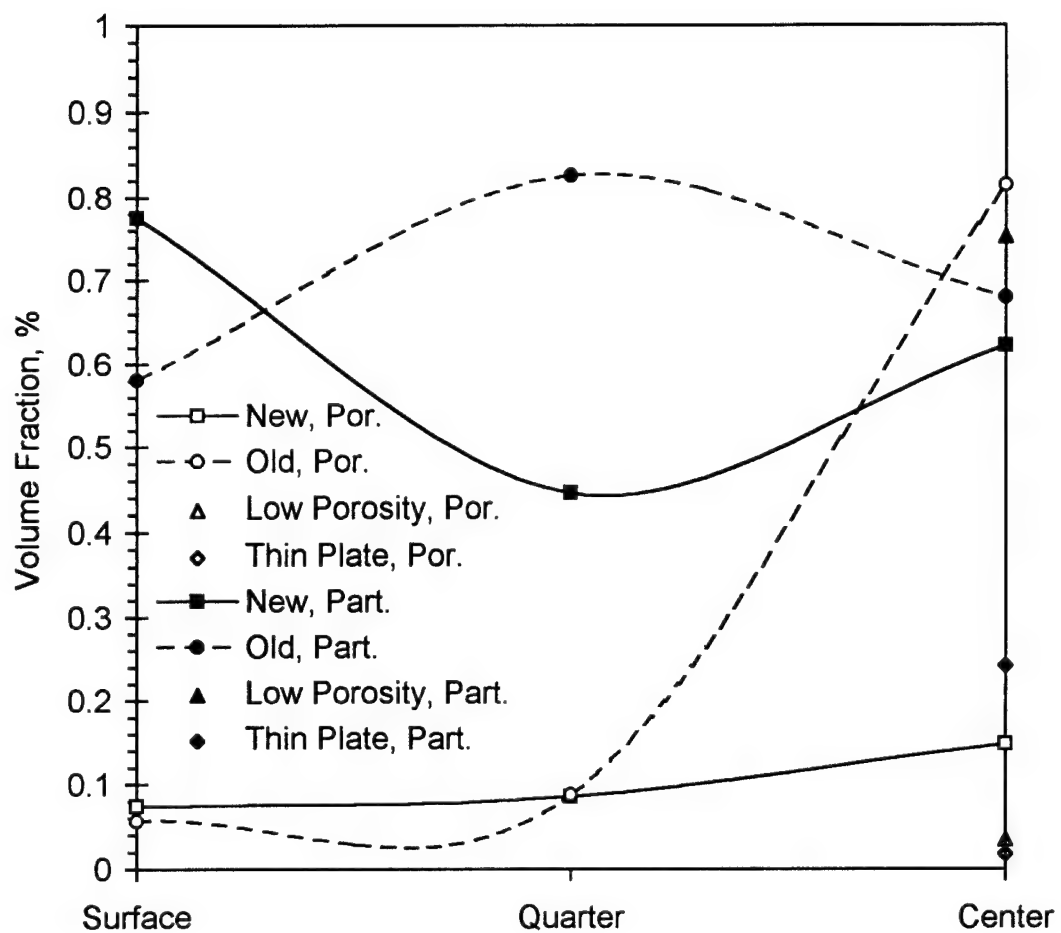


Figure 9. Pore and particle volume fractions in the 7050-T7451 plates.

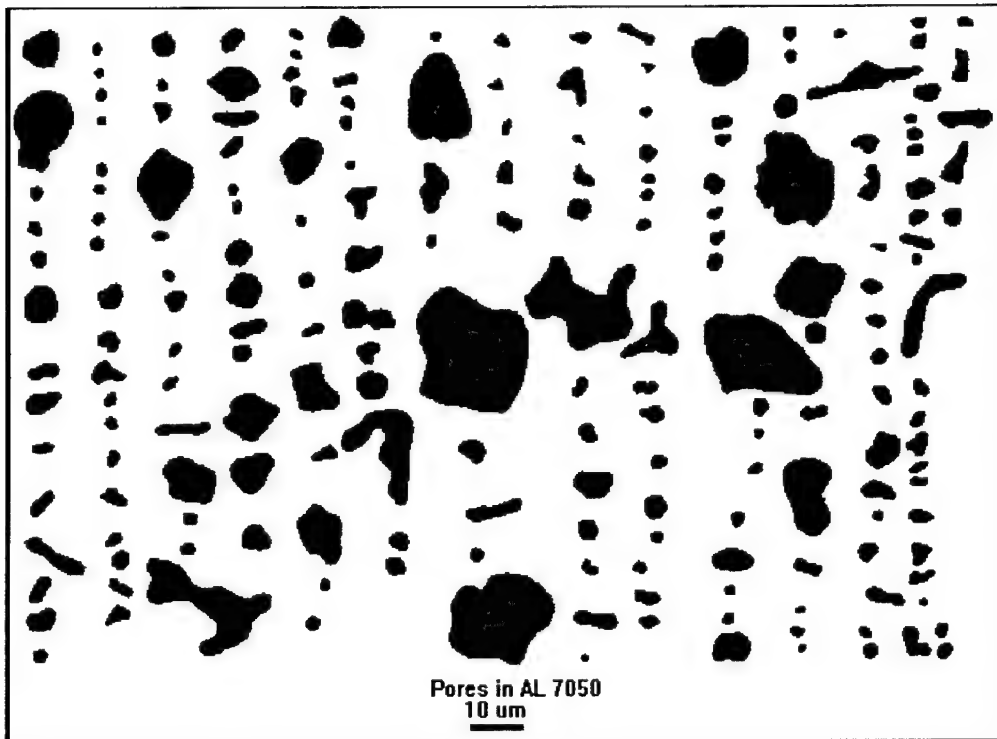


Figure 10. Crosssections of pores found on the ST-plane, plate center region, old 7050-T7451 alloy.

# Characteristics of Micropores in the 7050-T7451 Plate Alloys

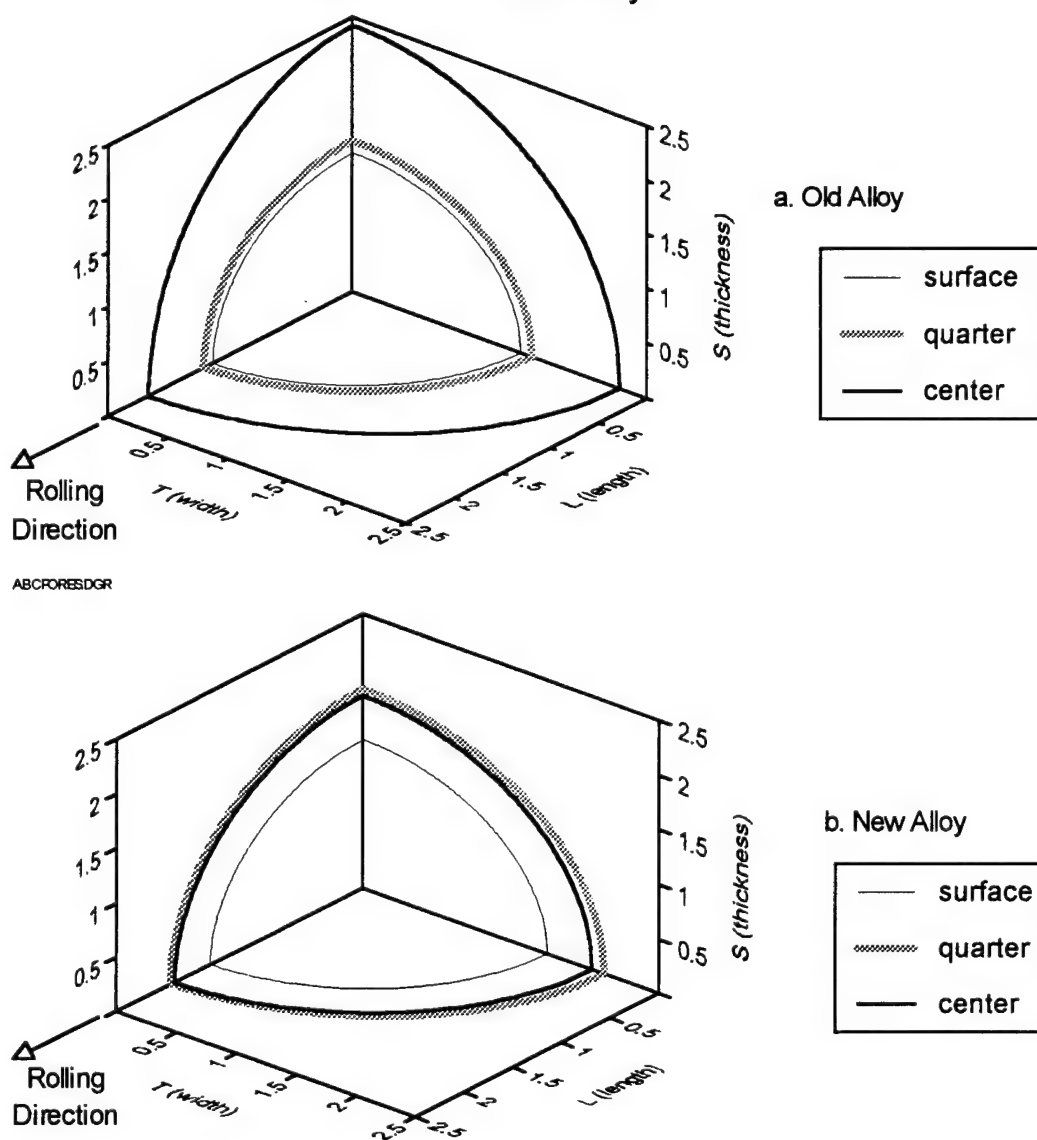


Figure 11. Average shapes of porosities in the old and new 7050-T7451 alloys. Size represented by  $L_2(\alpha)/2$ .

## Characteristics of Porosities in the 7050-T7451 Alloys

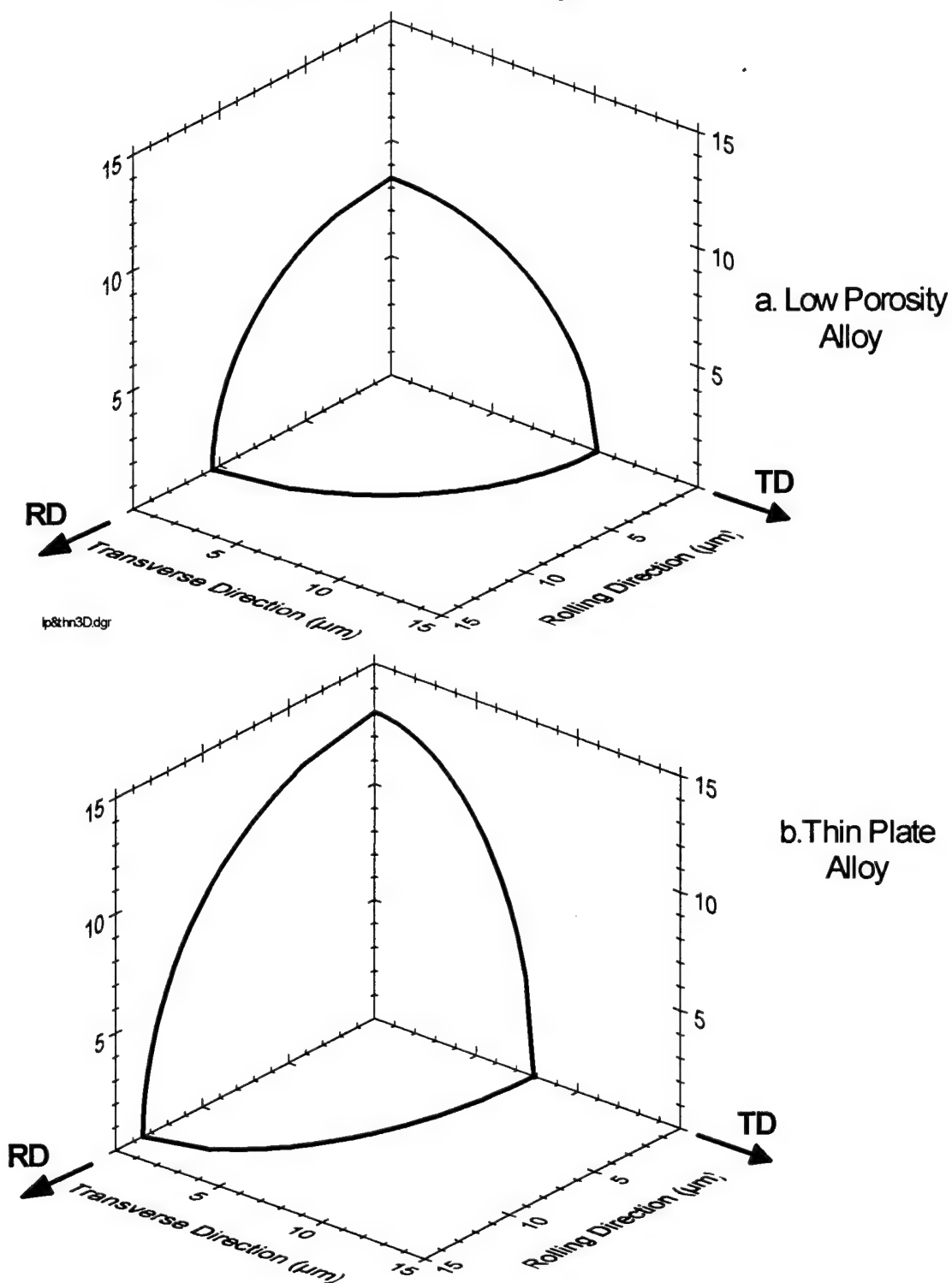


Figure 12. Average shapes of porosities in the low porosity and thin plate 7050-T7451 alloys, center section. Size represented by  $L_2(\alpha)/2$ .

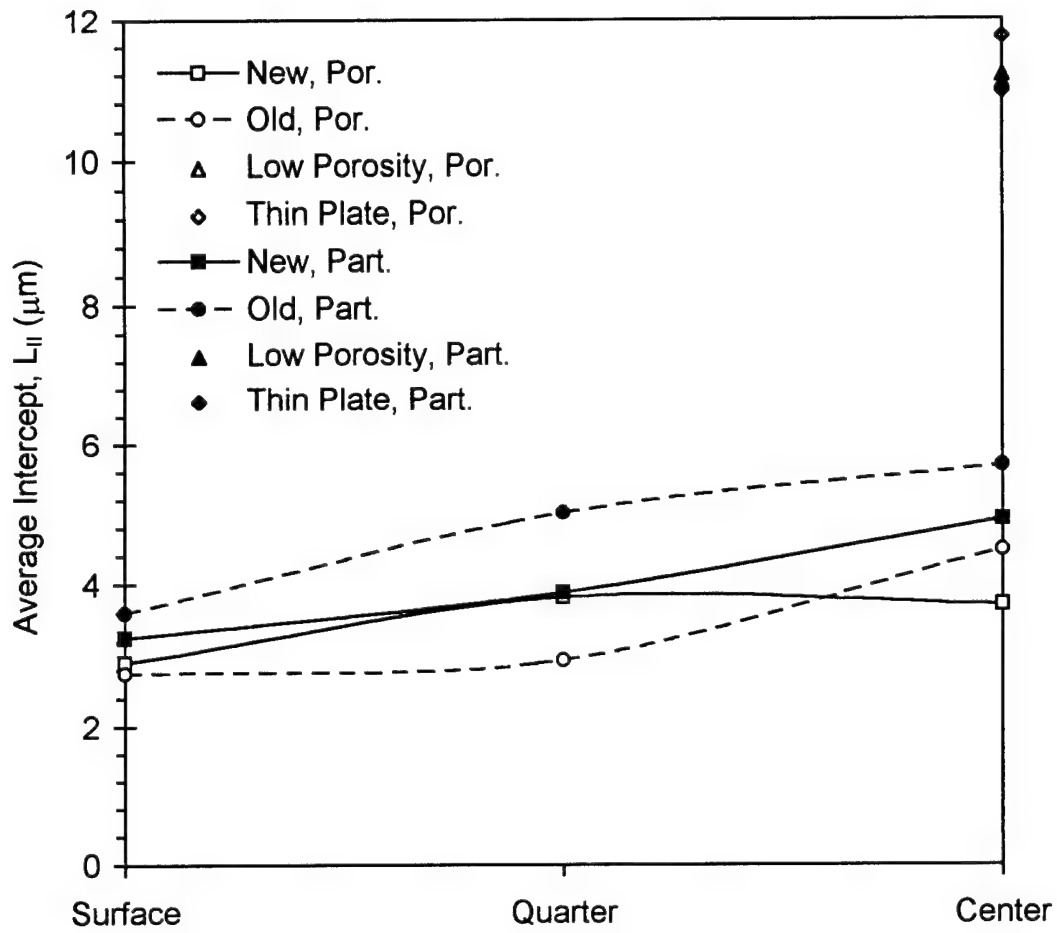


Figure 13. Through-thickness average pore and particle size gradients in the 7050-T7451 plate alloys.

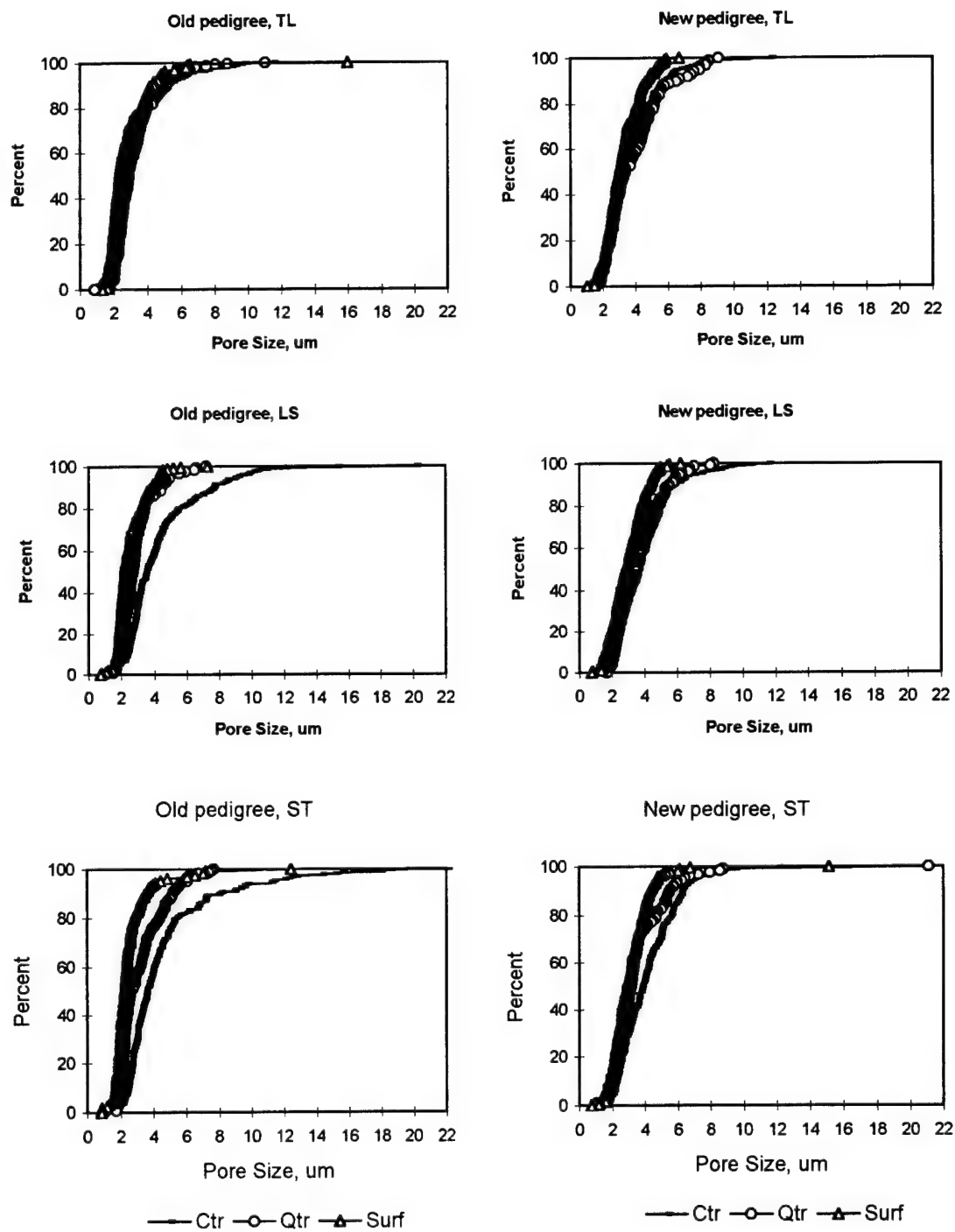
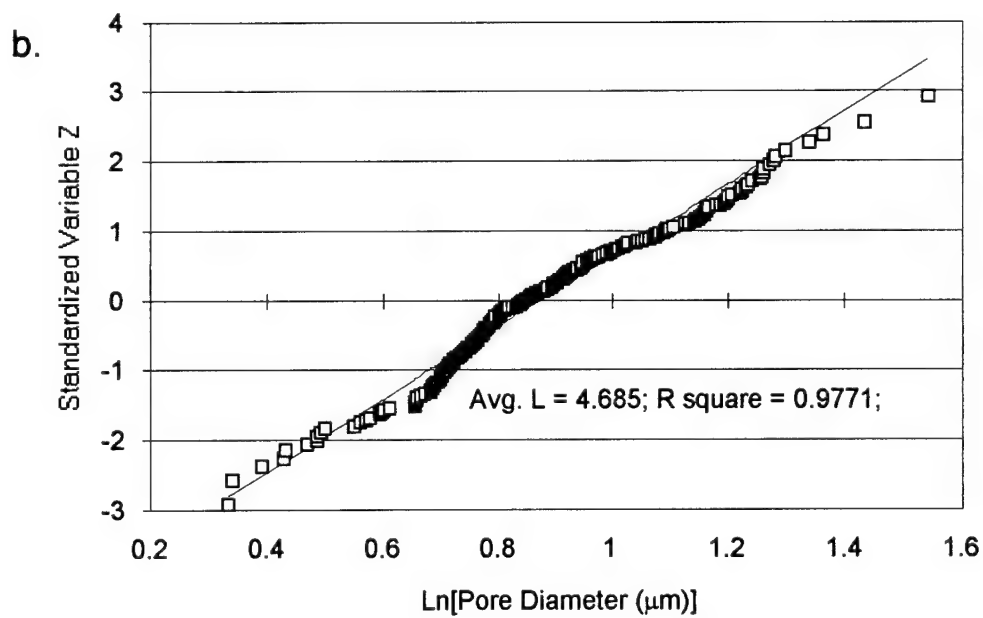
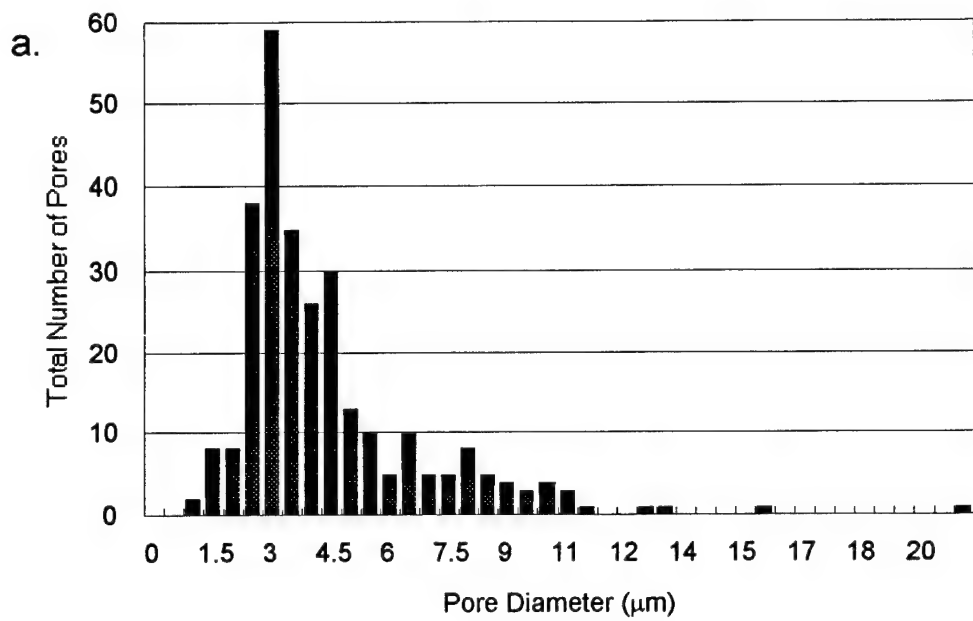


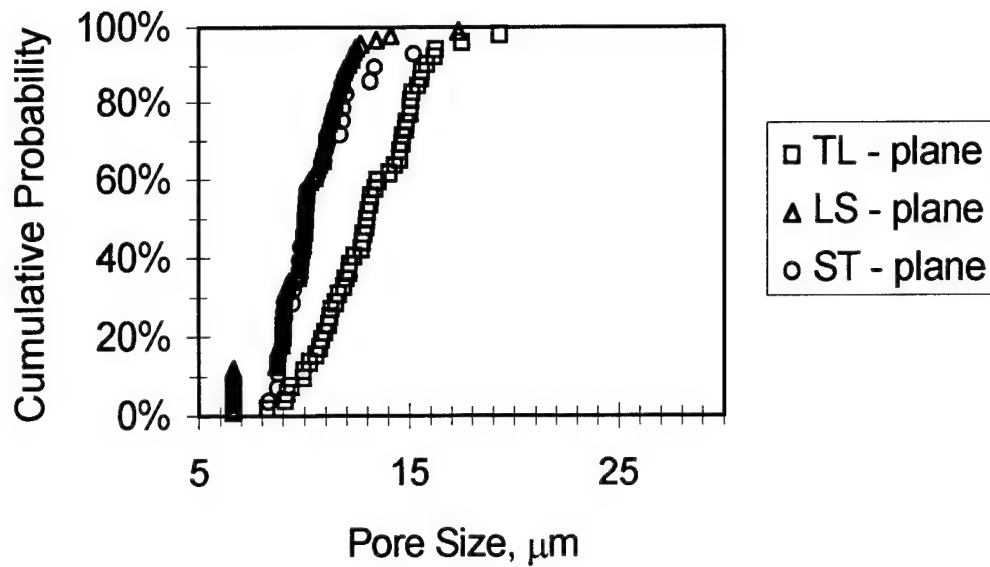
Figure 14. Cumulative pore size distributions on 2-D sections for old and new 7050-T7451 plate alloys



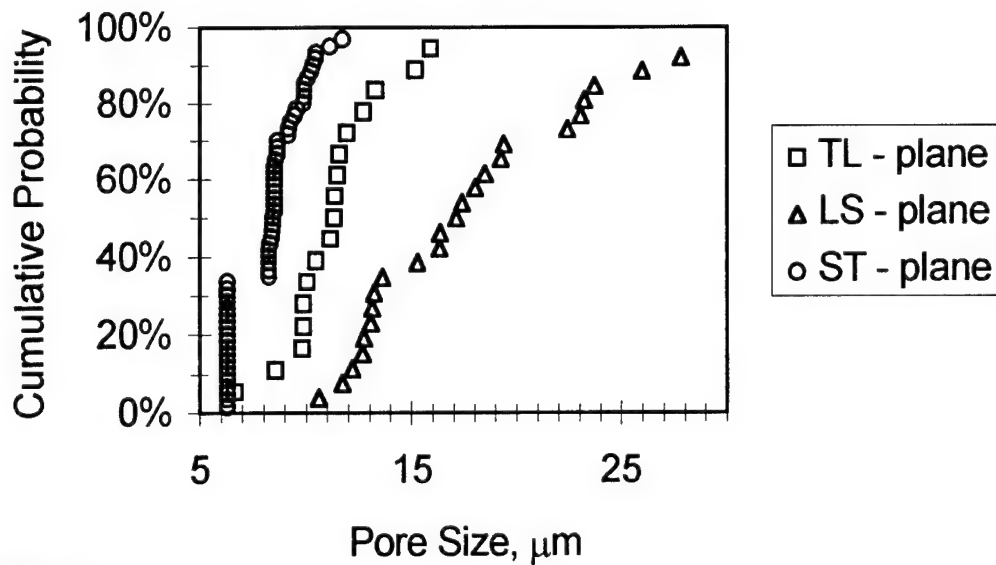
oldvsc.xls

Figure 15. Example of the pore (a) size distribution and (b) lognormal fit for the old 7050-T7451 alloy, LS-plane, plate center.

# Low Porosity 7050-T7451 Plate Alloy Porosities



# Thin Plate 7050-T7451 Alloy Porosities



THNV&P.XL

Figure 16. Cumulative pore size distributions on 2-D sections for the low porosity and thin plate 7050-T7451 alloys.

Correction for Left-Censoring  
7050-T7451, Low Porosity Plate, Pores, LS-Plane

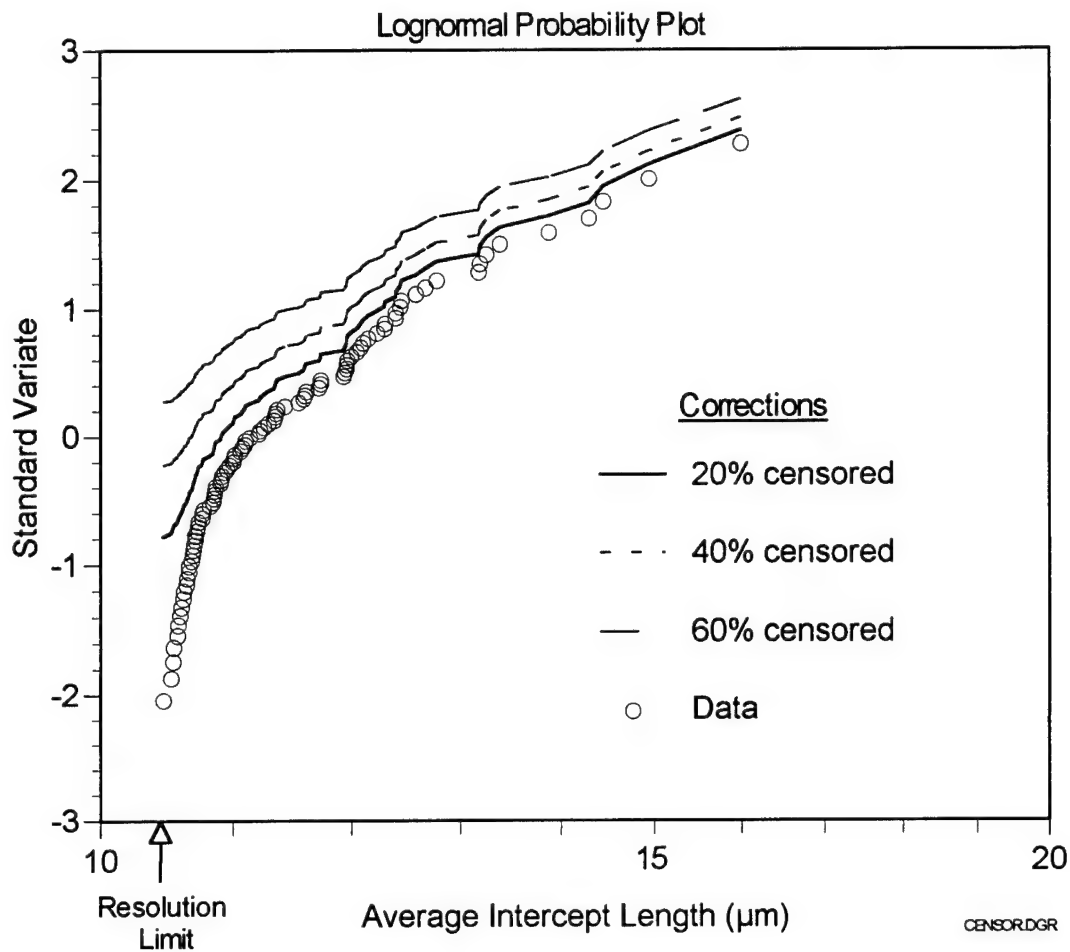


Figure 17. Example of the corrections of the intercept length distributions for the resolution limit effect. Numbers indicate assumed percentages of undetected small pores. Data for pores in 7050-T7451 low porosity plate, LS-plane, center.

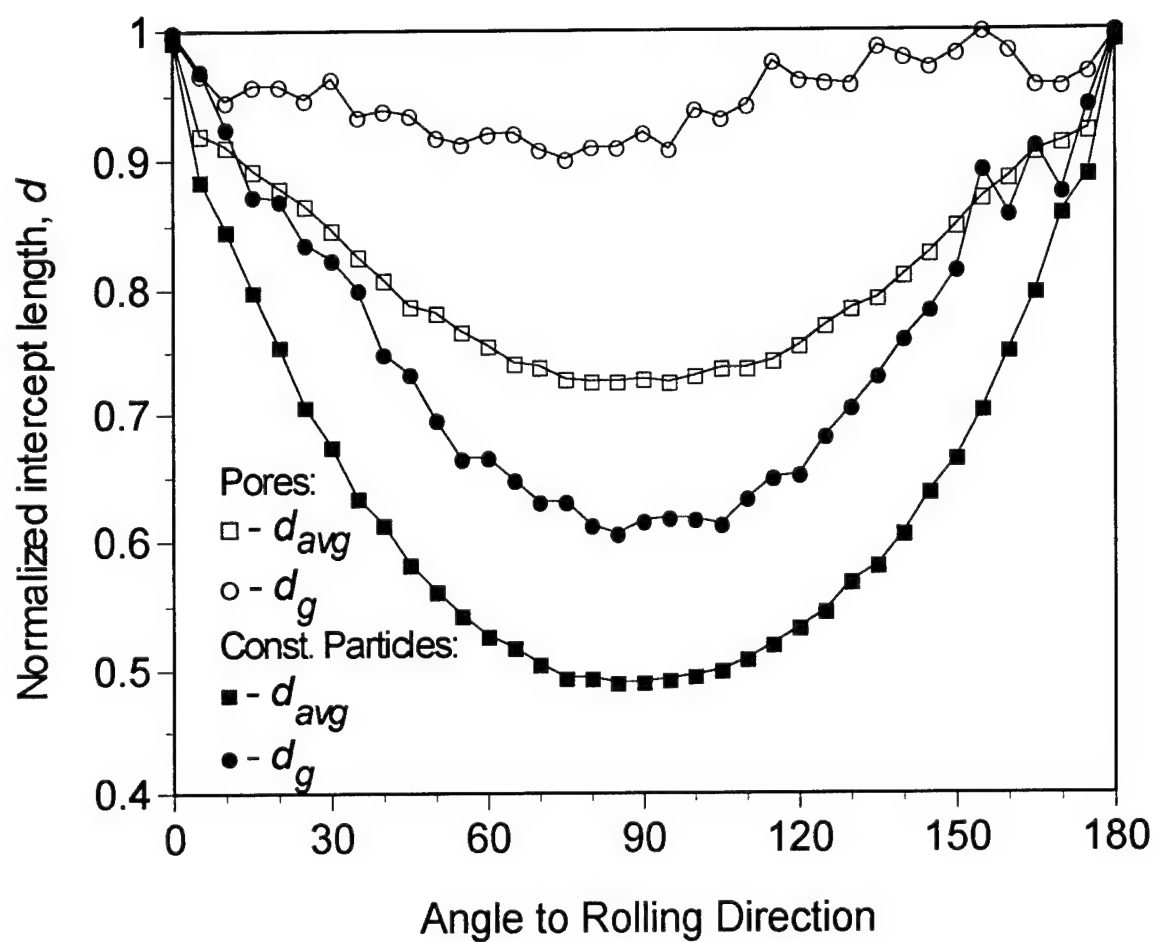


Figure 18. Angular variation of the normalized average intercept lengths of the pore and constituent particle sections on the LS-planes for the old 7050-T7451 alloy variant, plate center. (See text for definitions of  $d_g$  and  $d_{avg}$ )

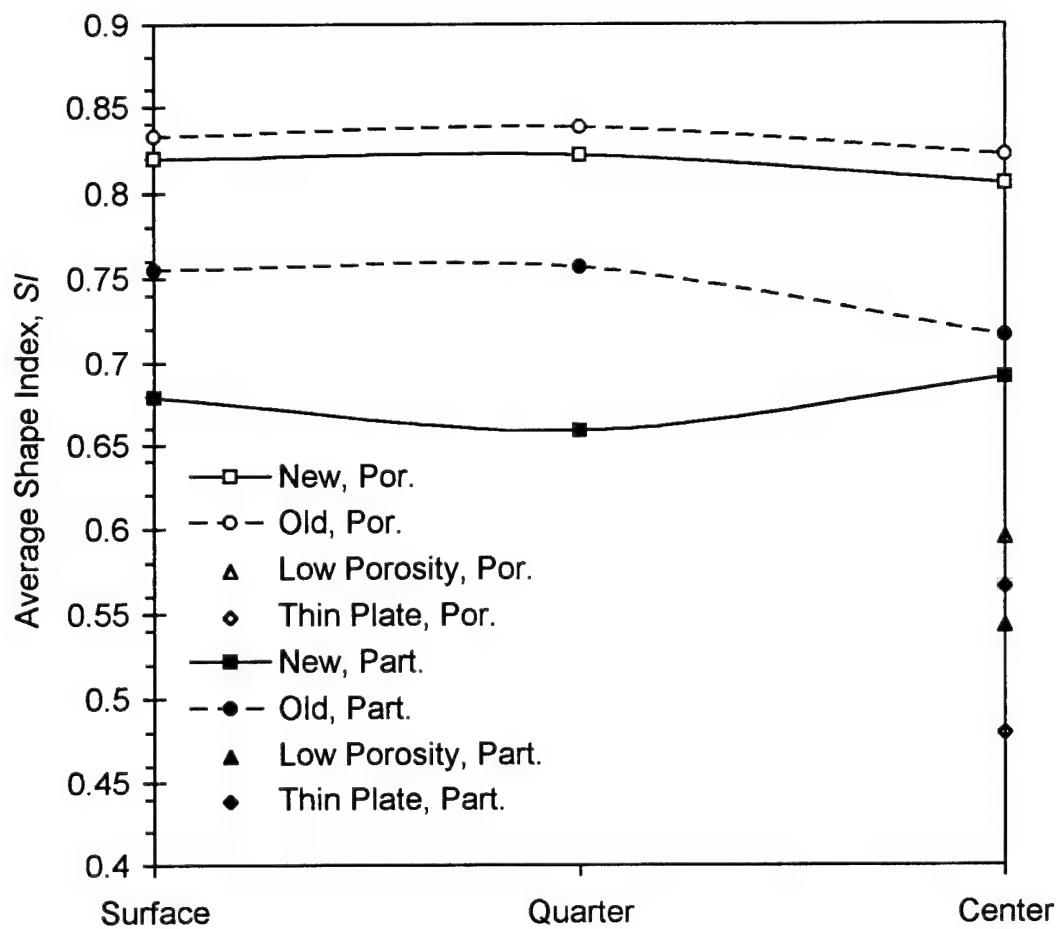


Figure 19. Through-thickness shape index gradients for the 7050-T7451 plate alloys.

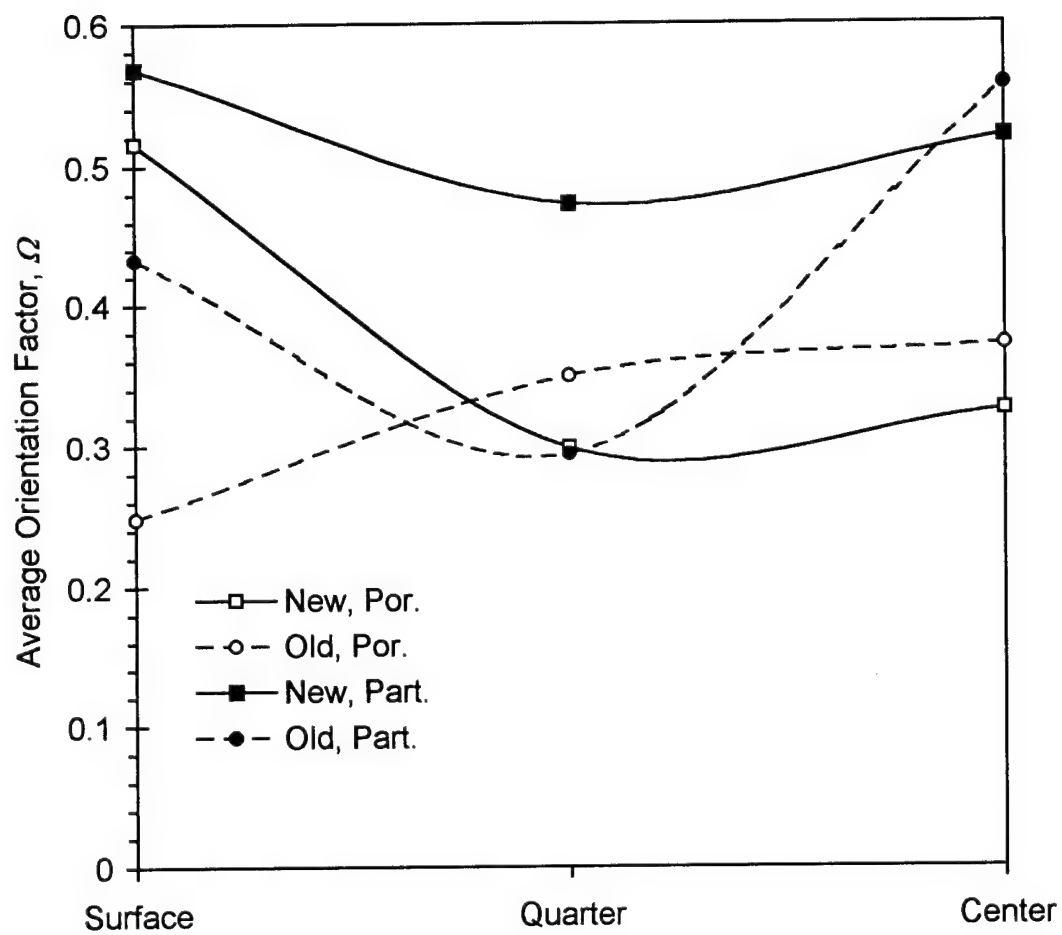
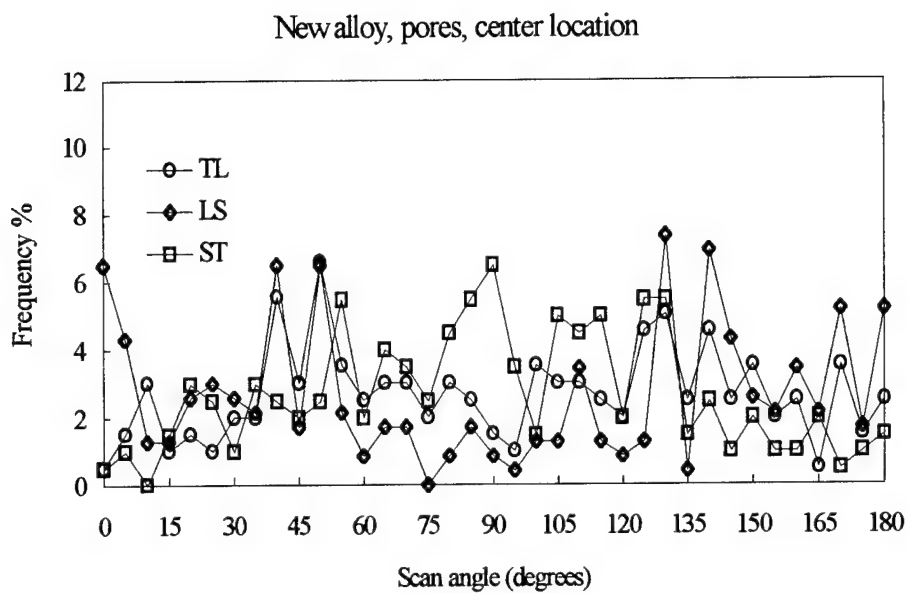
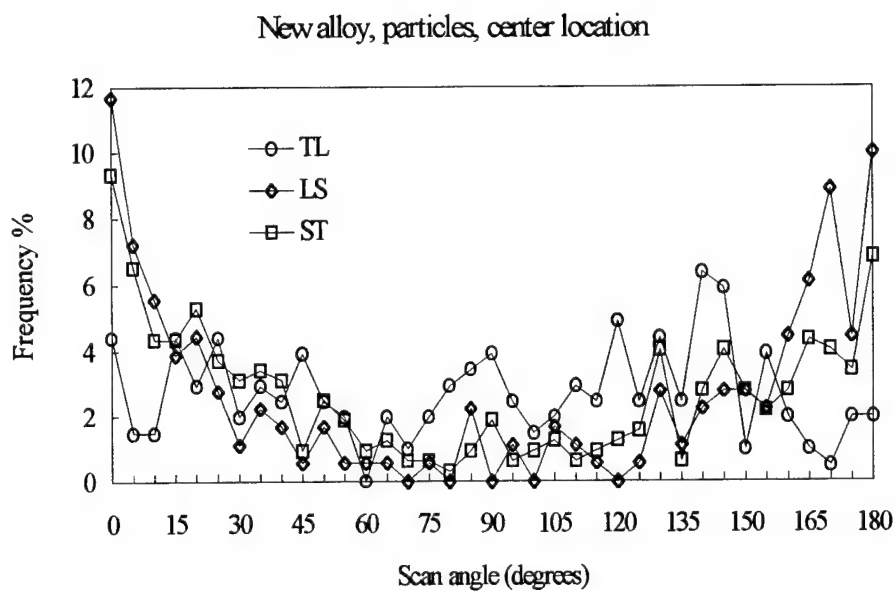


Figure 20. Through-thickness orientation factor,  $\Omega$ , gradients in the 7050-T7451 plate alloys



PORECTR.XLS

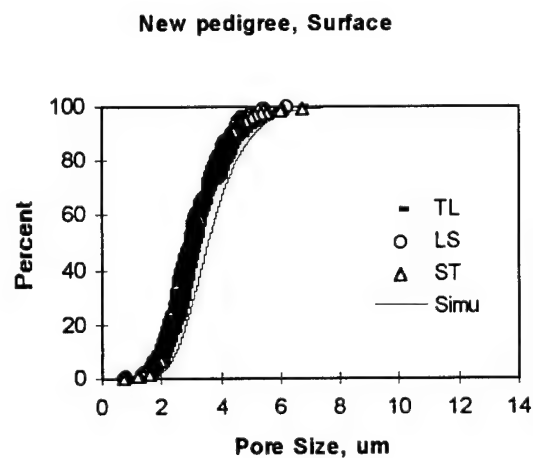
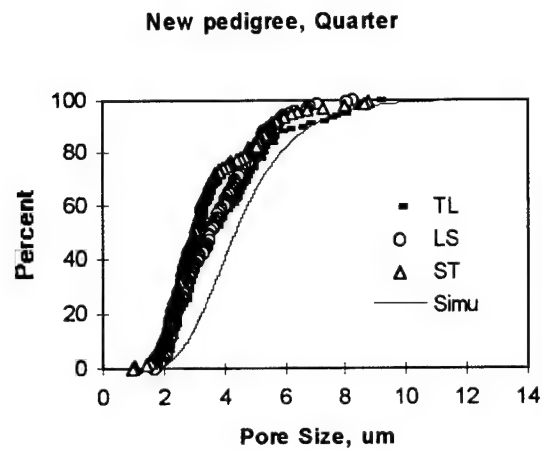
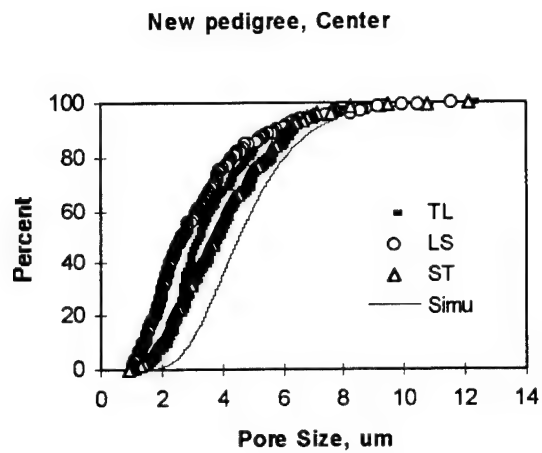
(a)



ANGLEPTC.XLS

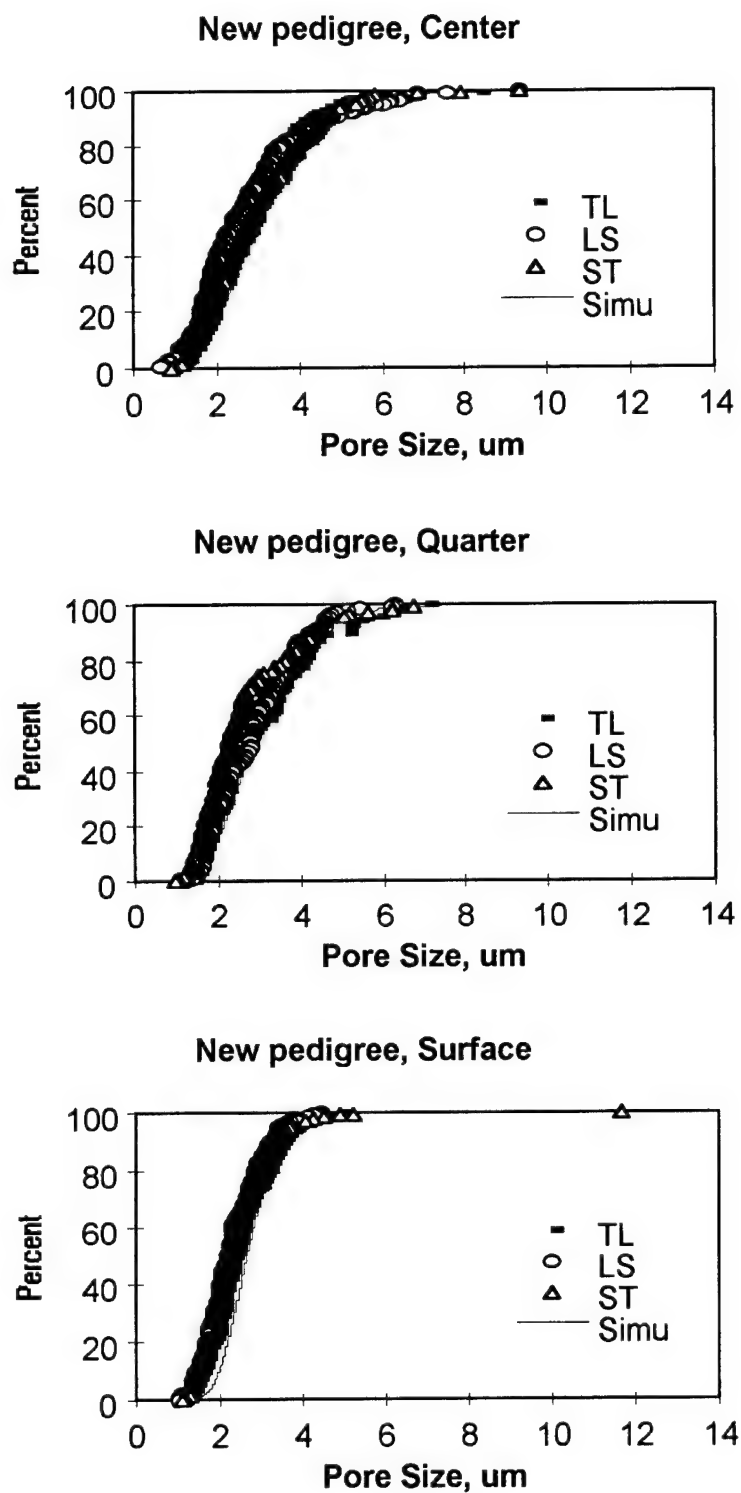
(b)

Figure 21. Orientation distribution of pore and particle major axes: new alloy.



3DMATCH.XLS

Figure 22. Comparison of the 3-D size distributions obtained using numerical method with the 2-D experimental data for new 7050-T7451 plate alloy



3DFIG4.XLS

Figure 23. Comparison of the measured, 2-D, and simulated true 3-D sizedistributions of the pore average intercept lengths obtained from the DeHoff's distribution method (see text for details).

New 7050-T7451 plate alloy, plate center.

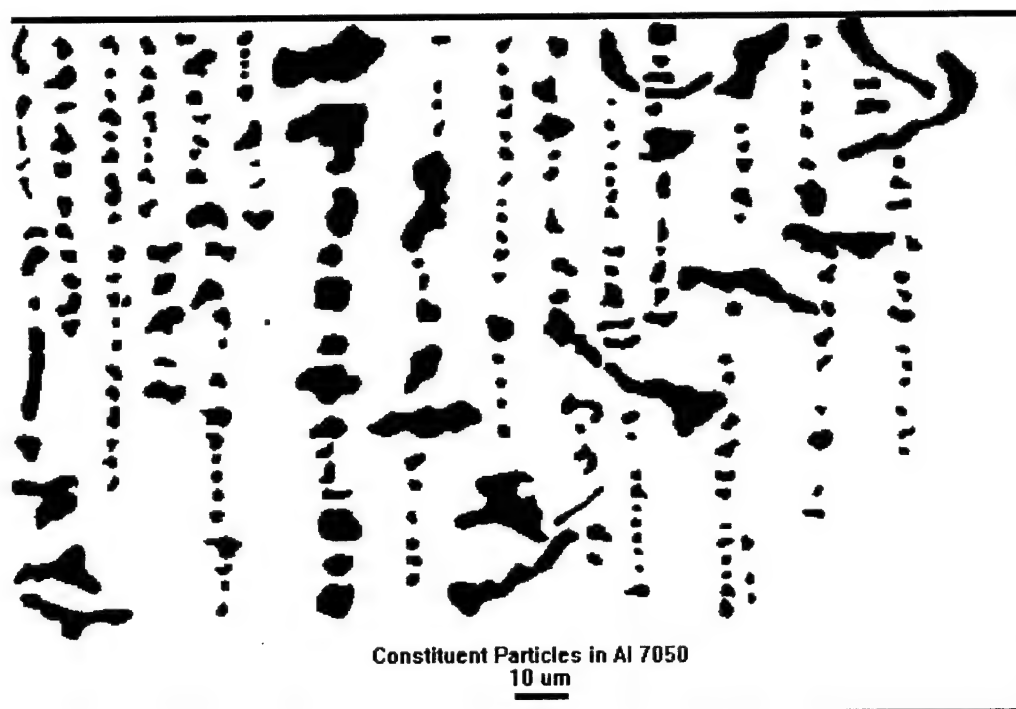
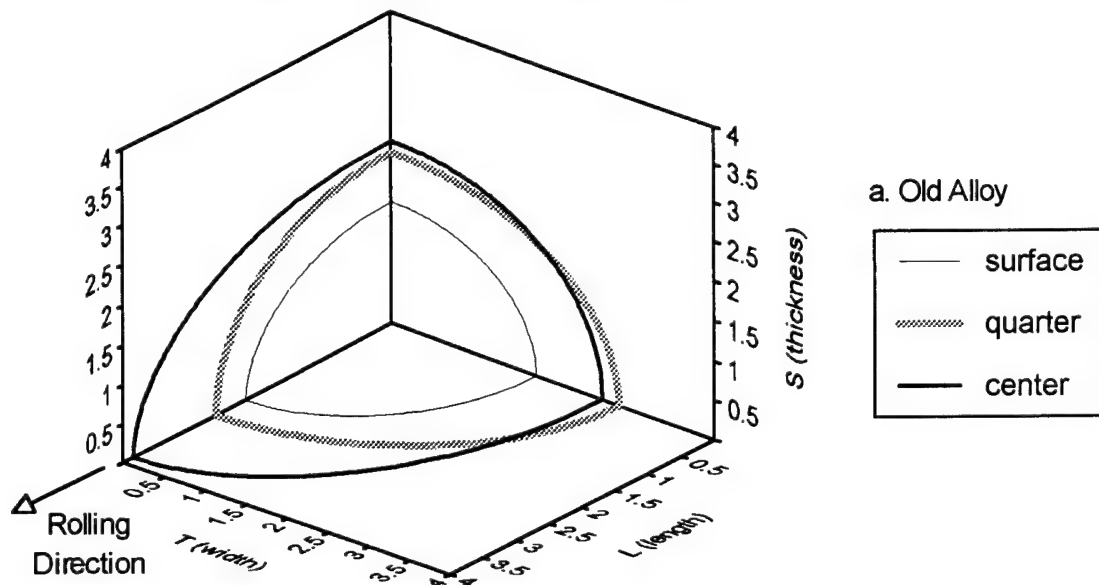


Figure 24. Crossections of constituent particles found on the ST-plane, plate center region, old 7050-T7451

# Characteristics of Constituent Particles in the 7050-T7451 Plate Alloy



ABCPTCSDGR

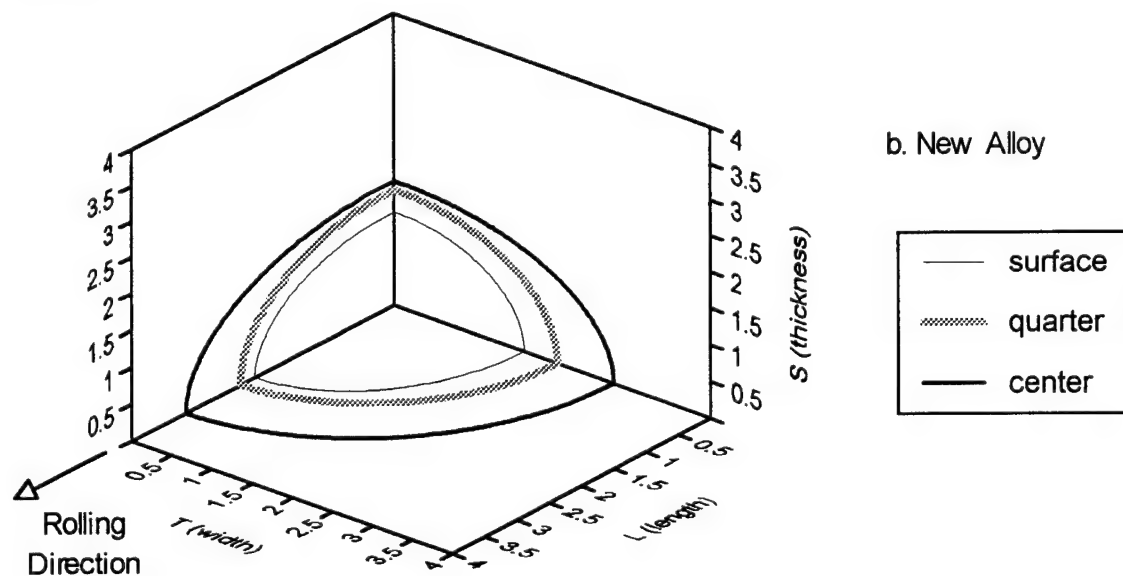


Figure 25. Average shapes of constituent particles in the old and new 7050-T7451 alloys

## Characteristics of Constituent Particles in the 7050-T7451 Alloys

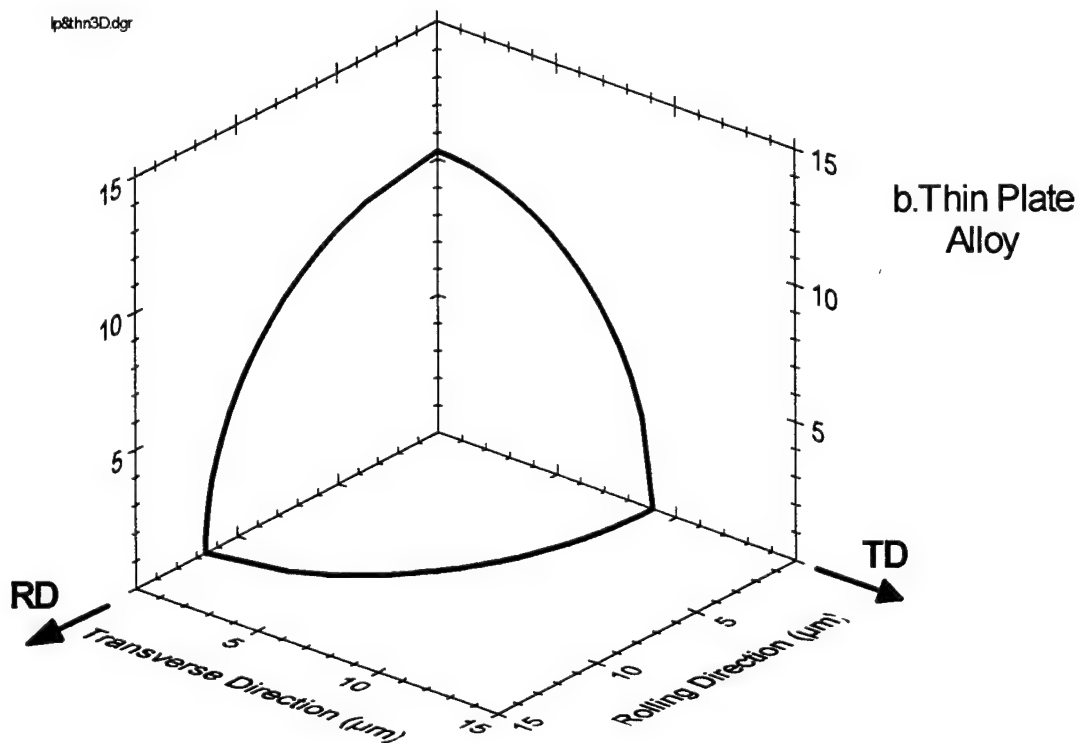
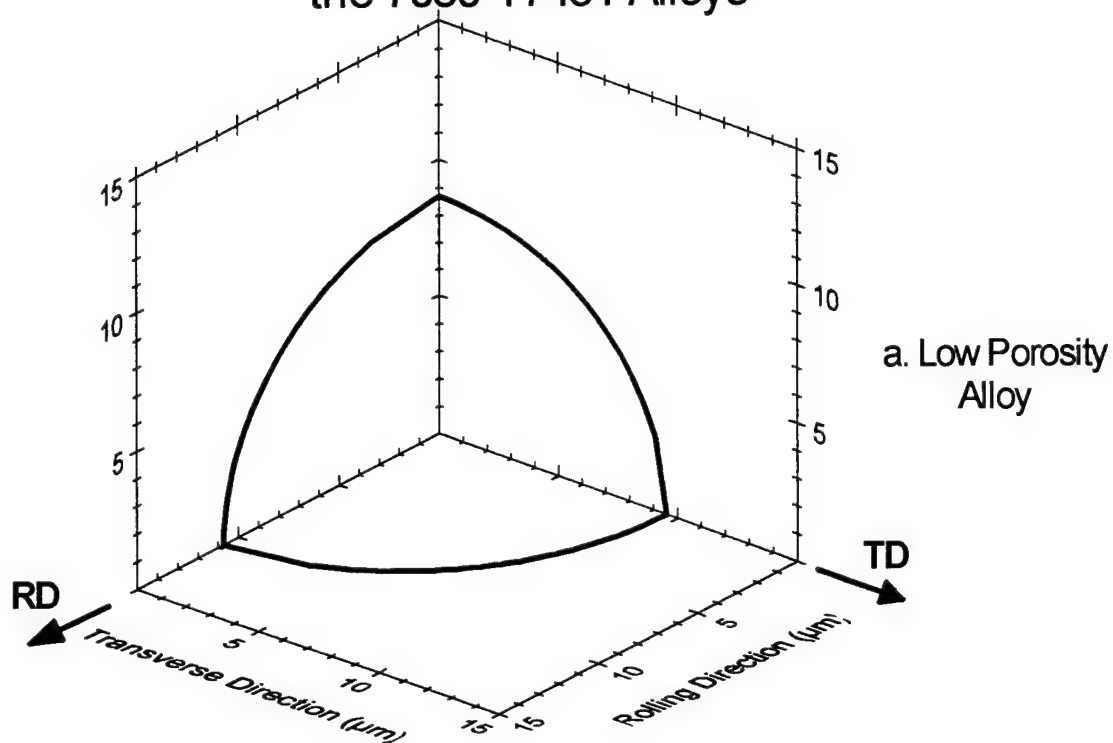


Figure 26. Average shapes of constituent particles in the low porosity and thin plate 7050-T7451 alloys, center section.

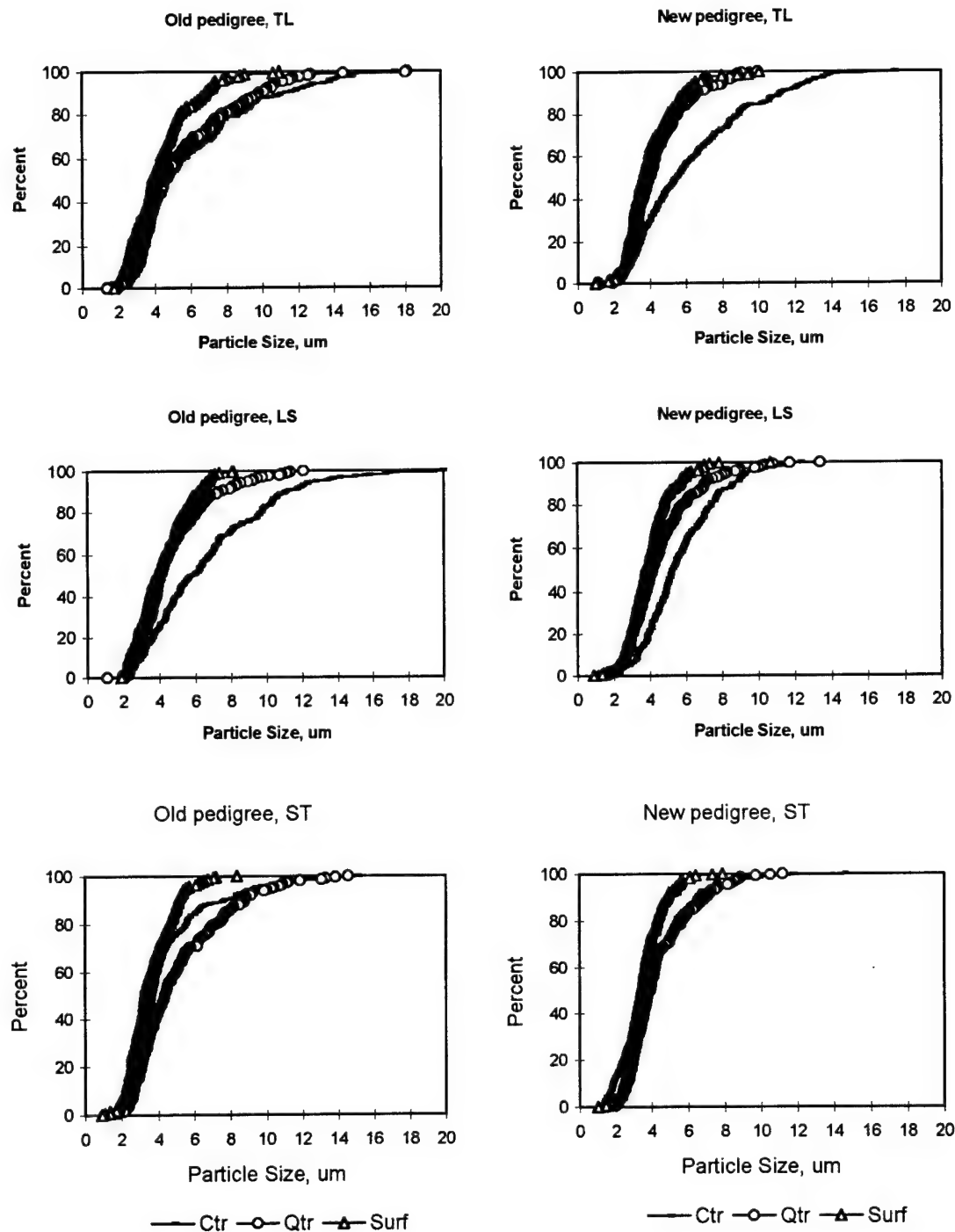
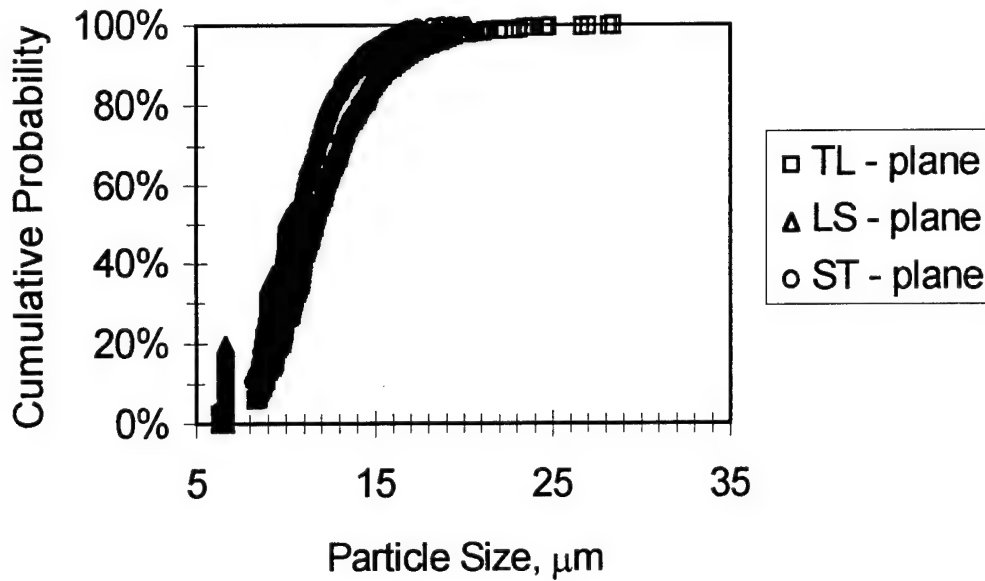


Figure 27. Size distributions of constituent particle sections on indicated planes and locations for 7050-T7451 old and new plate alloys.

Low Porosity 7050-T7451 Plate Alloy  
Constituent Particles



Thin Plate 7050-T7451 Alloy  
Constituent Particles

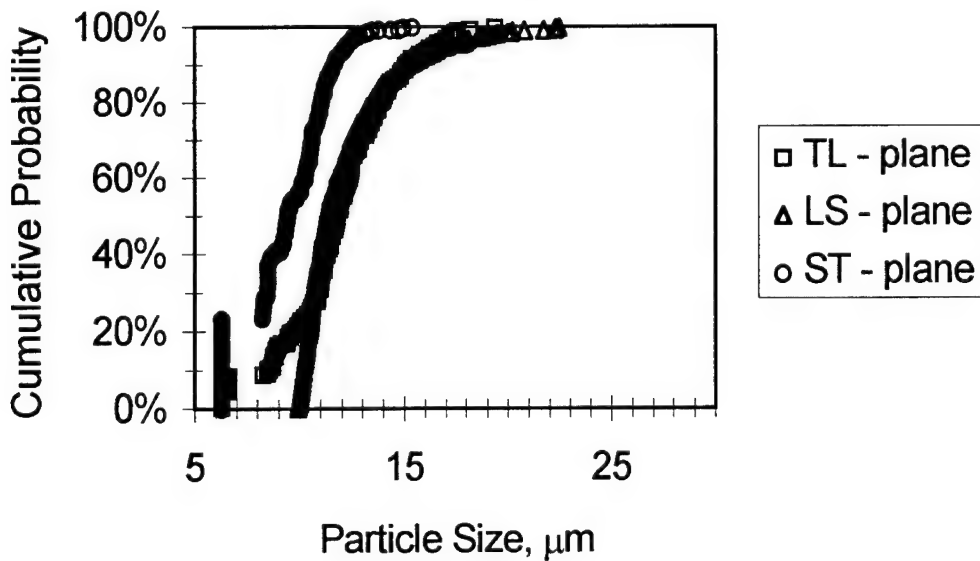


Figure 28. Size distributions of constituent particle sections on indicated planes at the centers of the 7050-T7451 low porosity and thin plates.

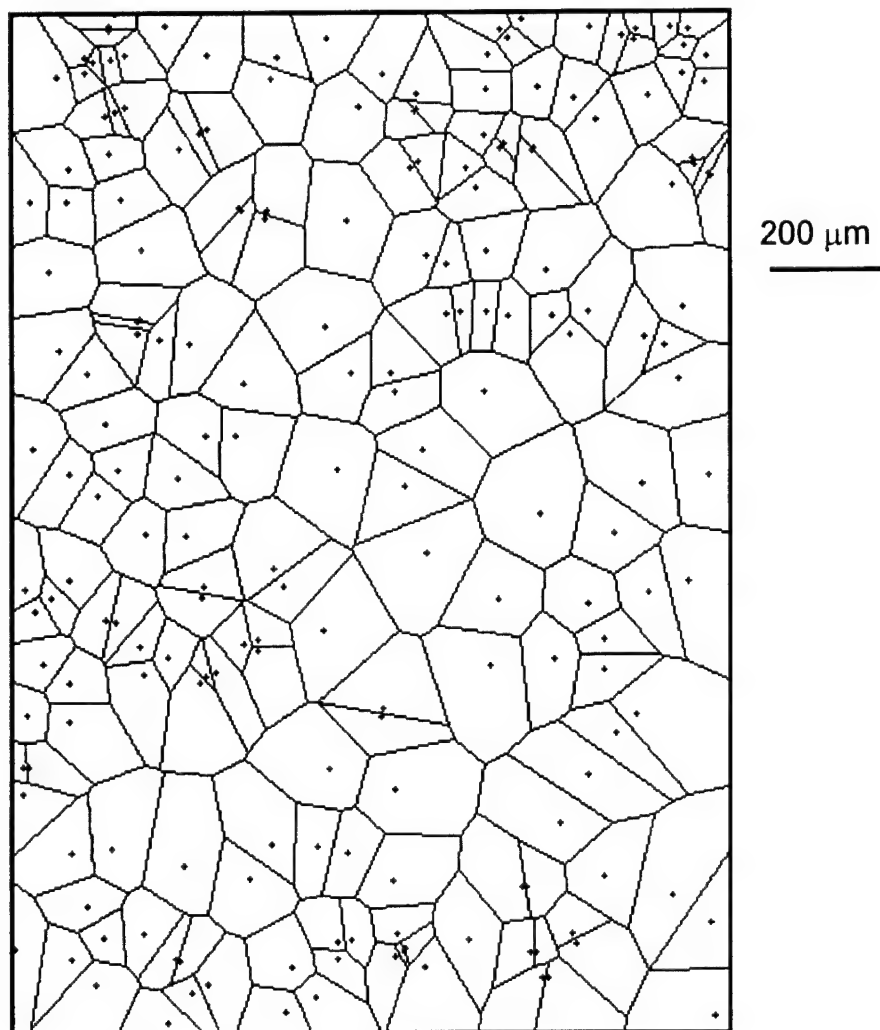


Figure 29. The Dirichlet tessellation cells constructed on the pore centers indicated by points: old 7050-T7451 plate alloy, ST plane, center.

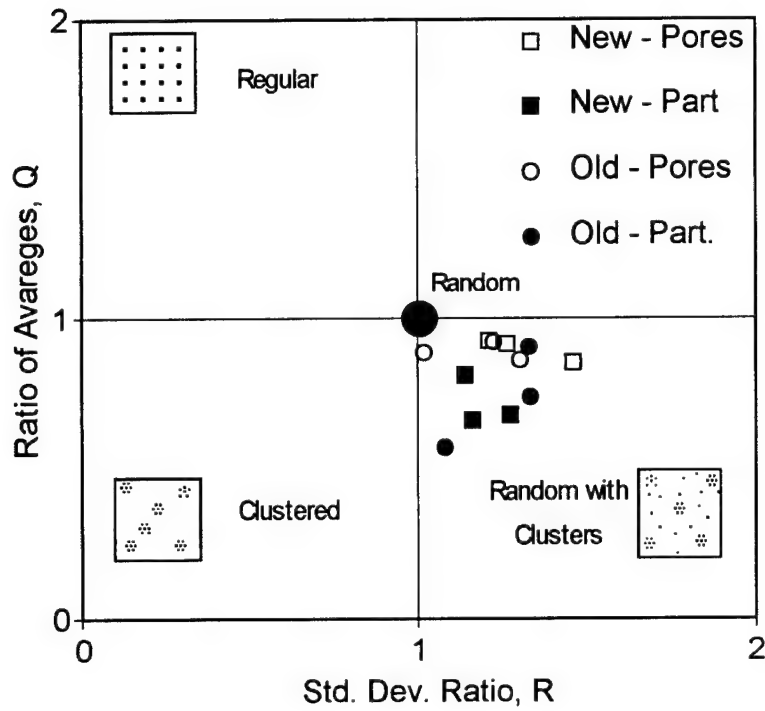


Figure 30. Results of the characterizations of the pore and constituent particle spatial distribution using Q and R method: 7050-T7451 new and old alloys.

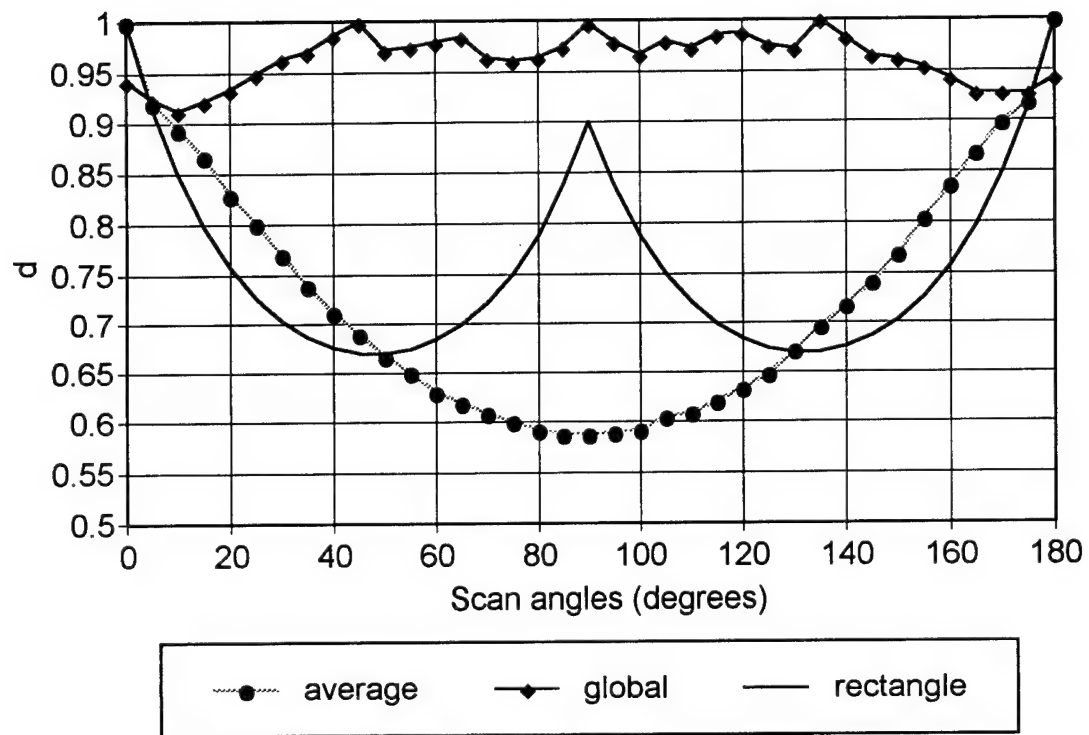
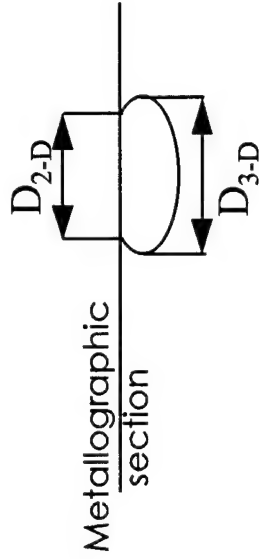
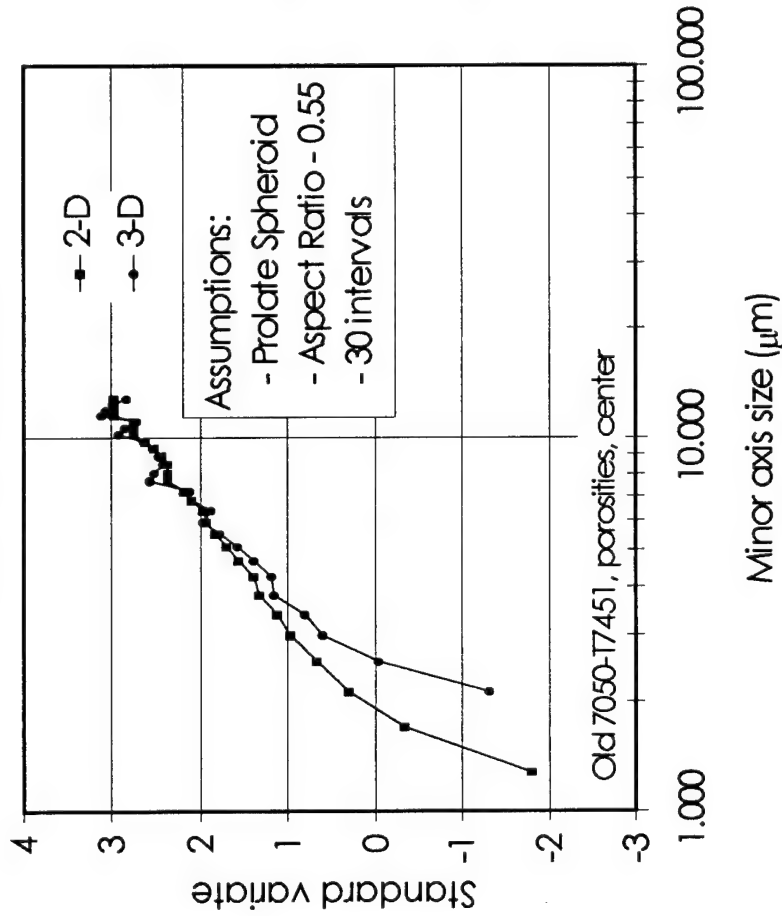


Figure 31. Change of the normalized intercept lengths with direction for tessellation cells from Figure 29. The d-a curve for the rectangular random point pattern is shown for comparison.

# 2-D to 3-D Size Transformation Lognormal Probability Plo



- ◆ 3-D and 2-D distributions converge for large pore sizes
- ◆ 3-D distribution can be safely approximated with 2-D distribution at right tail region

REV1-95 PPT

Figure 32. Example showing right tail equivalence of the 2-D and 3-D pore size distributions. 3-D distribution obtained using Saltykov method assuming that the pores are prolate spheroids with aspect ratios of 1.82. Old 7050-T7451 plate alloy, center.

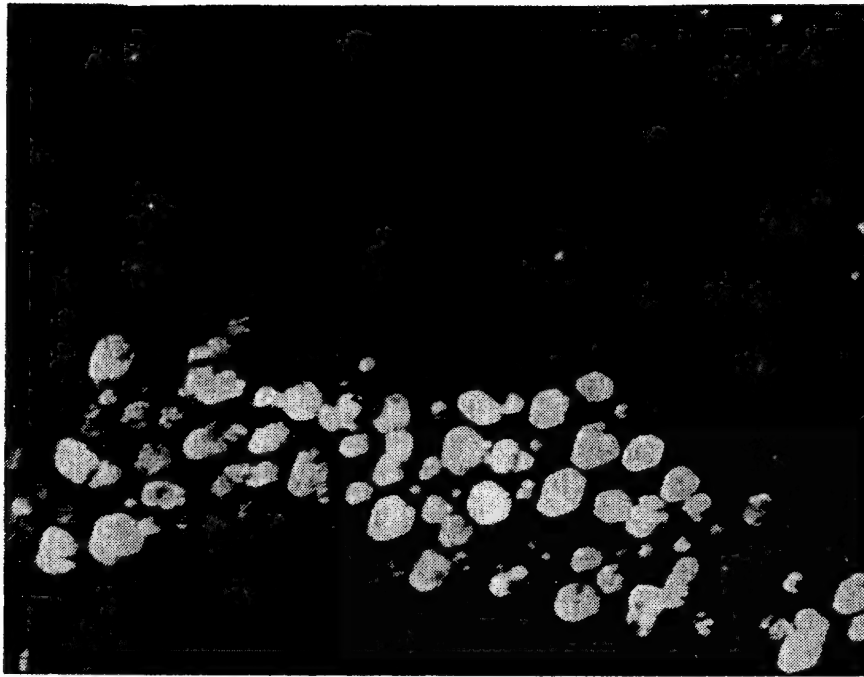


Figure 33. Dark field image of hexagonal precipitates on a typical boundary in the 7050-T7451 plate alloy.

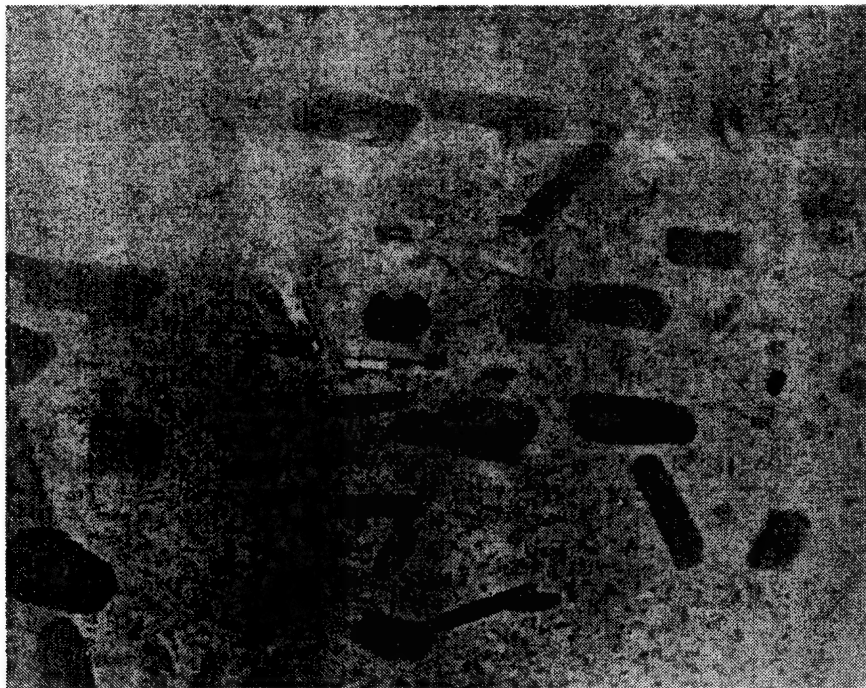
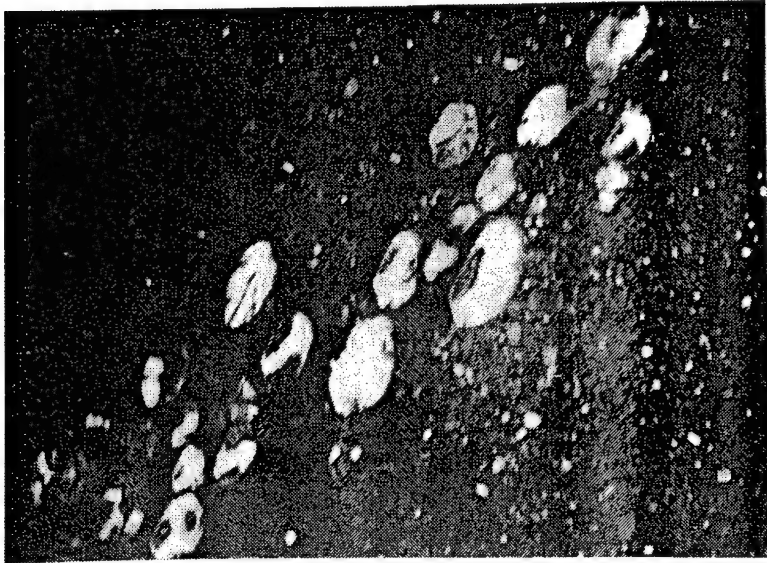
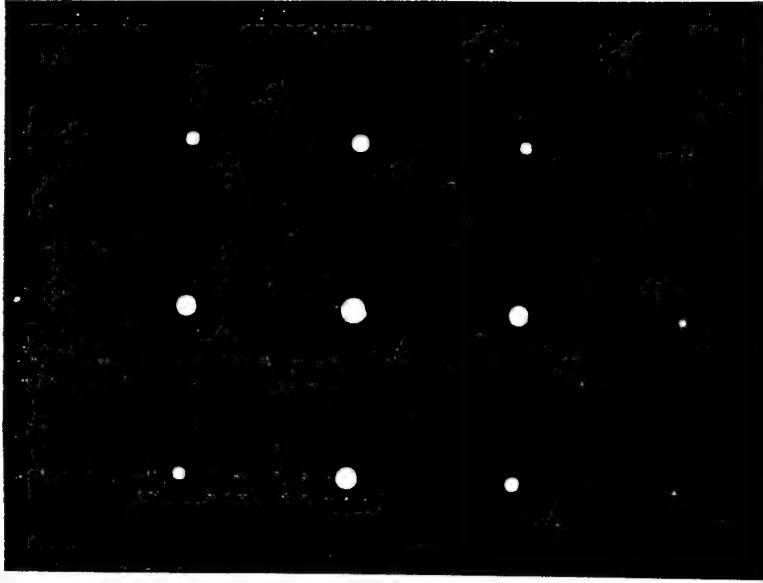


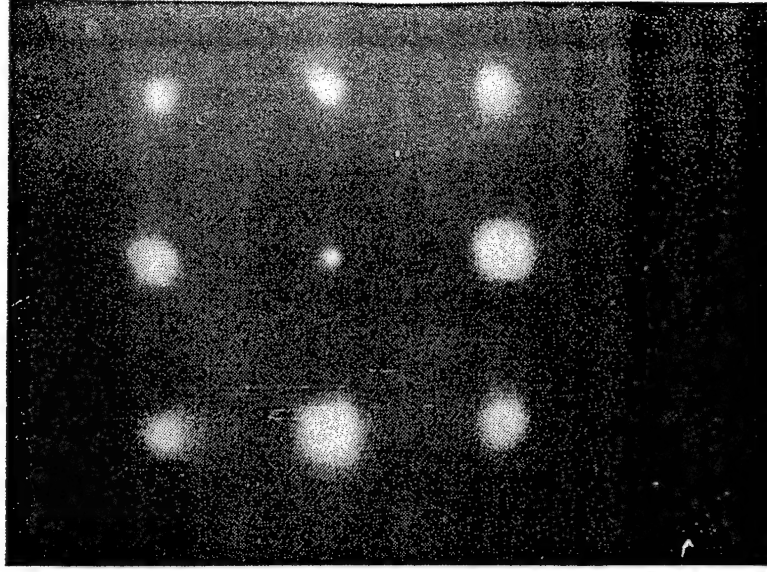
Figure 34. Grain boundary from the center of the 7050-T7451 plate containing a multiple precipitate variants.



**GRAIN BOUNDARY  
PRECIPITATES**



**DIFFRACTION PATTERN FOR  
ONE GRAIN (KICKUCHI  
PATTERN CENTERED)**



**DIFFRACTION PATTERN FOR  
OTHER GRAIN (KICKUCHI  
PATTERN SHIFTED)**

Figure 35. Micrographs showing large precipitates on low angle boundaries in the 7050-T7451 plate alloy.

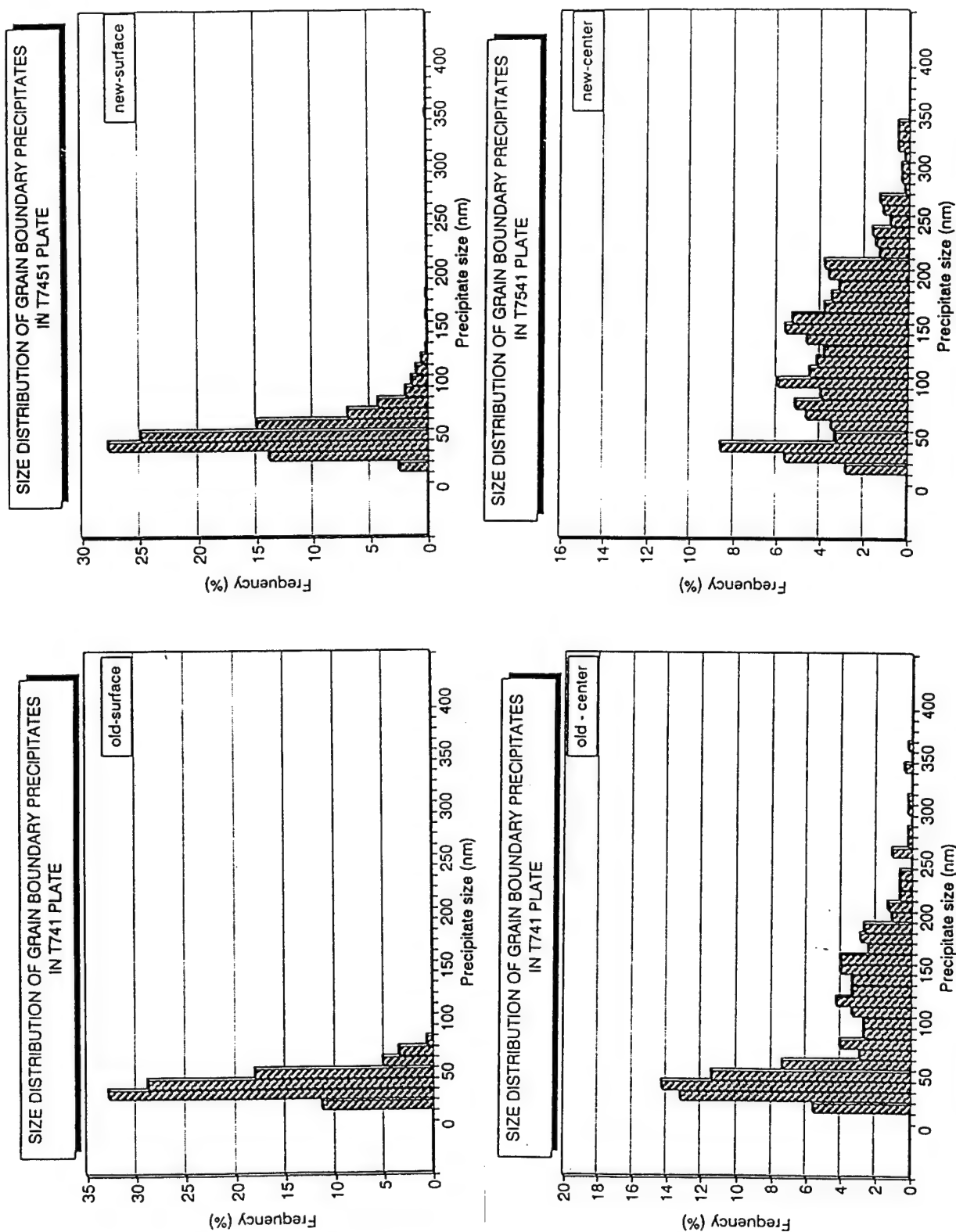


Figure 36. Size distributions of the grain boundary precipitates for Surface and center sections of the old and new 2050-T7451 plate alloys.

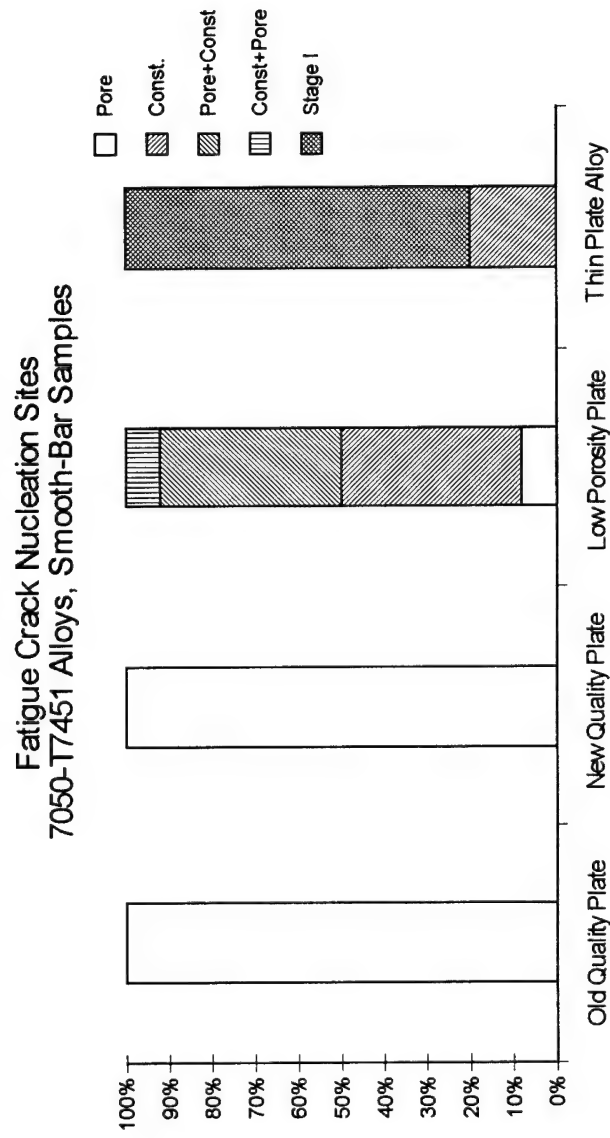


Figure 37. Percentages of different types of the fatigue crack nucleation sites in smooth-bar fatigue samples for the studied four variants of the 7050-T7451 plate alloys. LT orientation, constant amplitude loading, 30 Hz,  $R = 0.1$ , maximum stresses from 100 to 225 MPa.

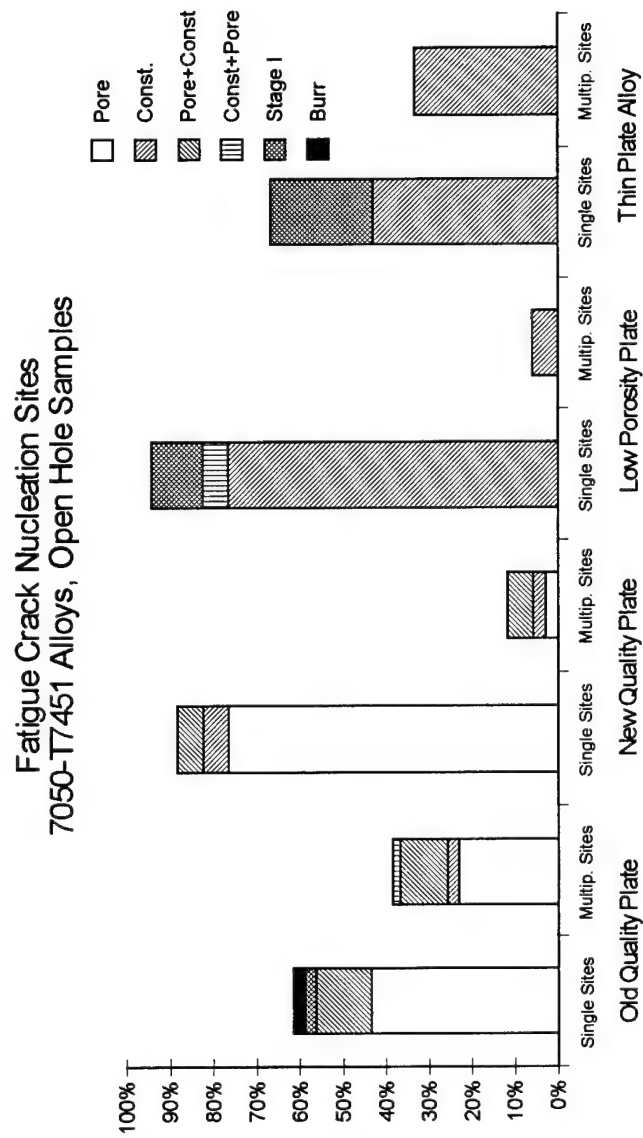


Figure 38. Percentages of different types of the fatigue crack nucleation sites in open hole fatigue samples for the studied four variants of the 7050-T7451 plate alloys. LT orientation, constant amplitude loading, 30 Hz,  $R = 0.1$ , maximum stress from 100 to 225 MPa.

7050-T7451 Plate Alloys  
Smooth Bar Samples, 10 Hz, R = 0.1, LT Orientation

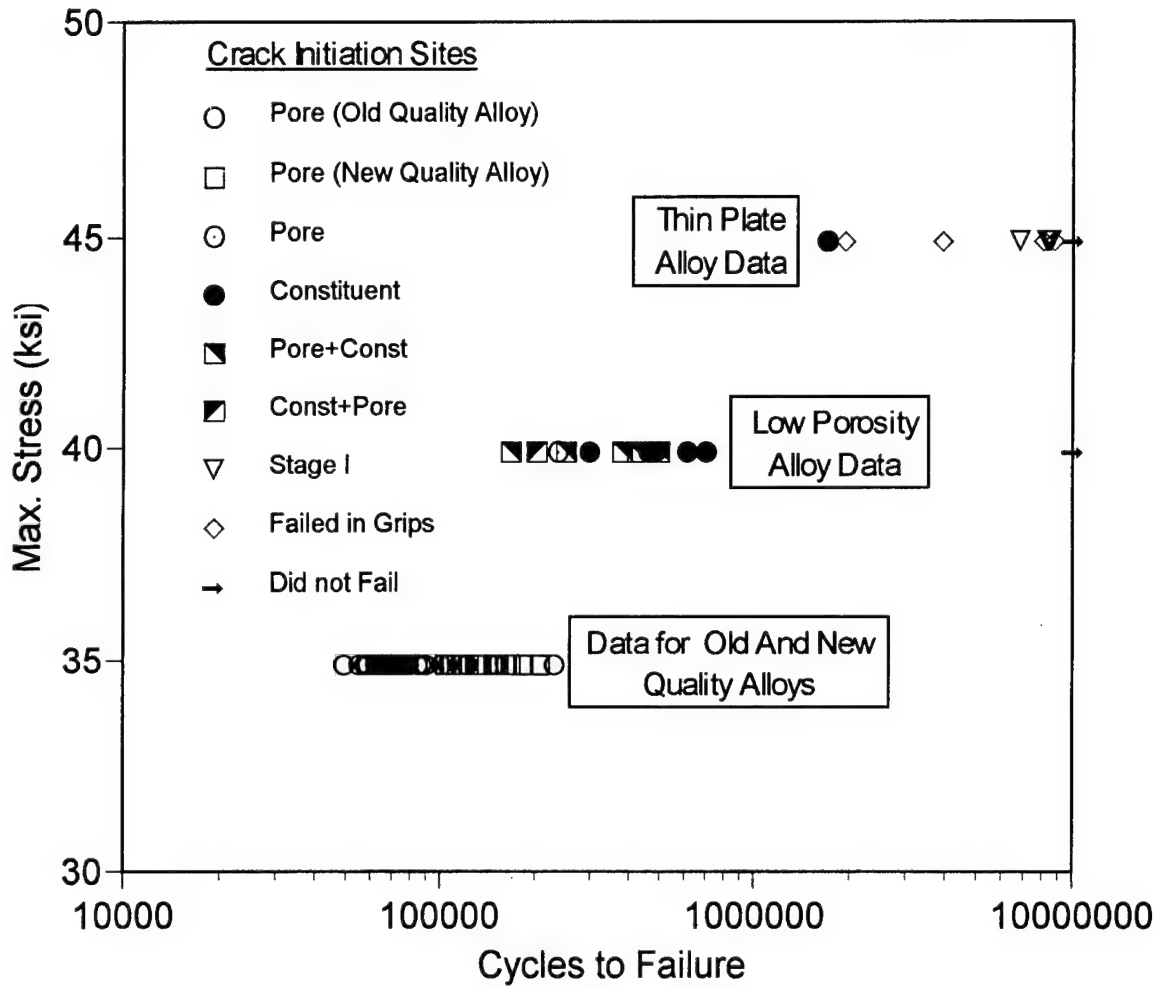


Figure 39. Results of fatigue testing of the smooth bar samples for the four investigated variants of the 7050-T7451 plate alloys

# Effect of Processing on Fatigue Performance of 7050-T7451 Aluminum Plate Alloys

Smooth Fatigue Samples, LT Orientation, R = 0.1

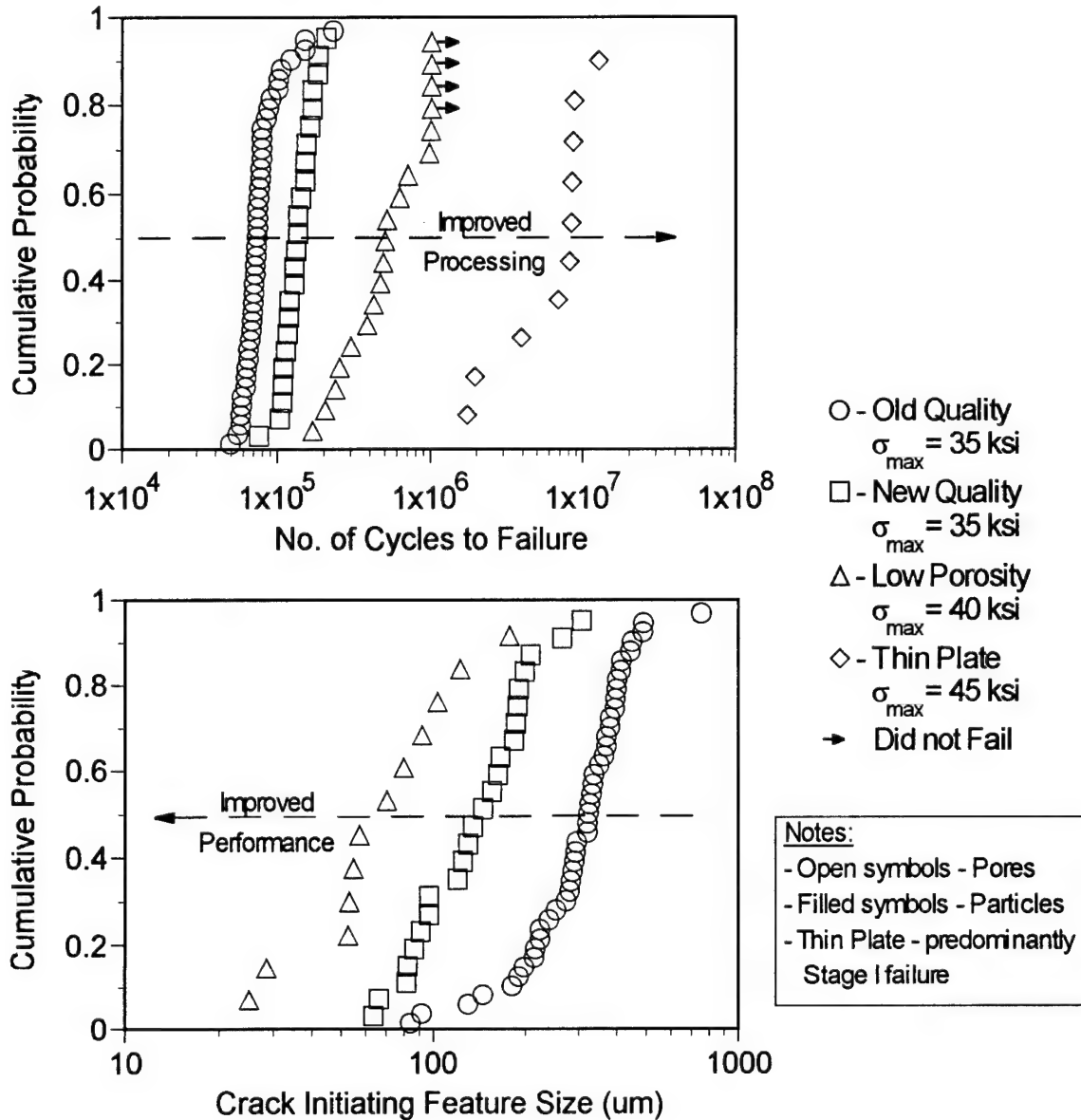


Figure 40. Effect of the changes of the fatigue crack initiating features size and type on fatigue performance of different variants of the 7050-T7451 plate alloys. Note that the data for Stage I initiation sites are not plotted because they do not have associated size characteristics.

7050-T7451 Old Quality Alloy  
Open Hole Samples, 30 Hz, R = 0.1, LT Orientation

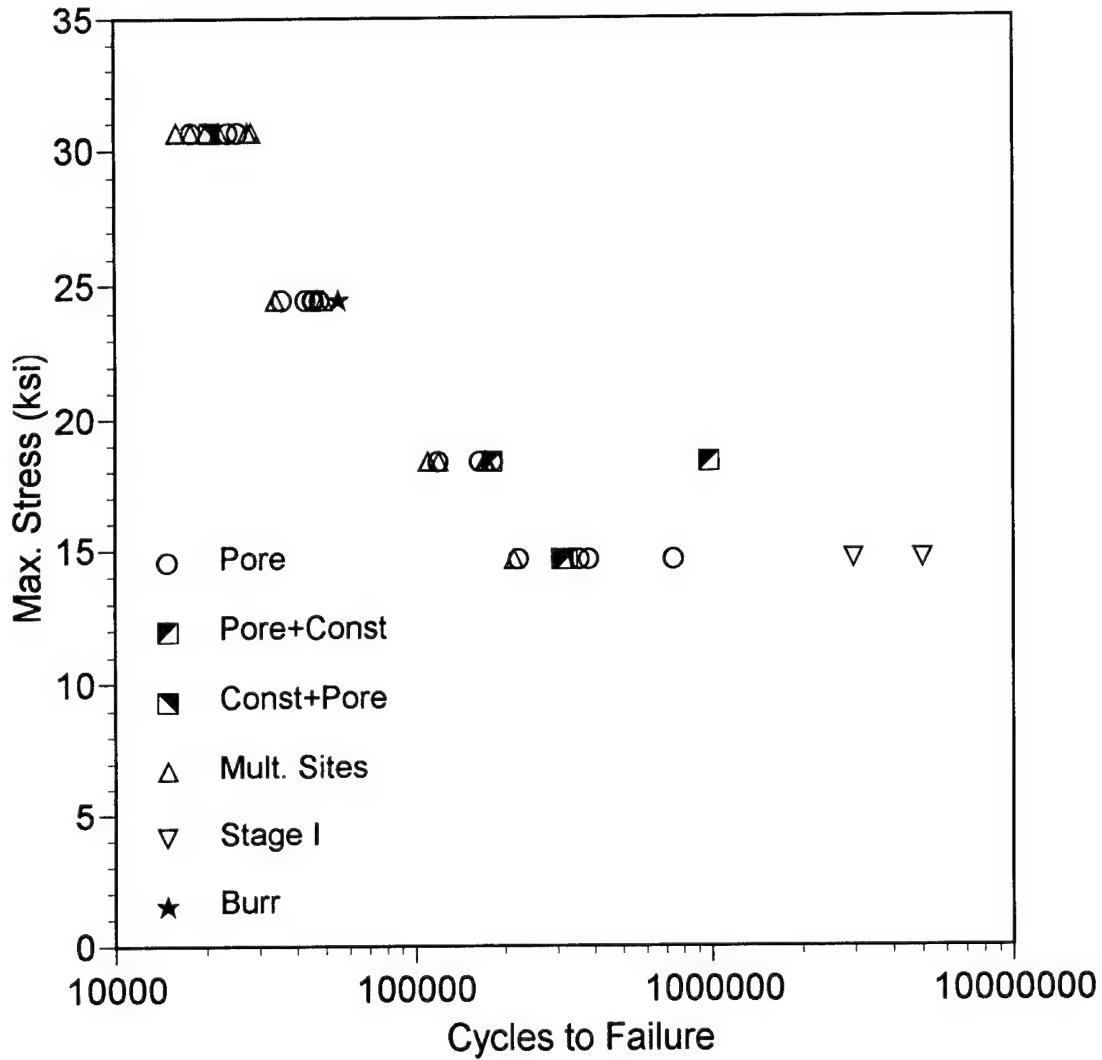


Figure 41. S-N fatigue results for old 7050-T7451 plate alloy, open hole samples.

7050-T7451 New Quality Alloy  
Open Hole Samples, 30 Hz, R = 0.1, LT Orientation

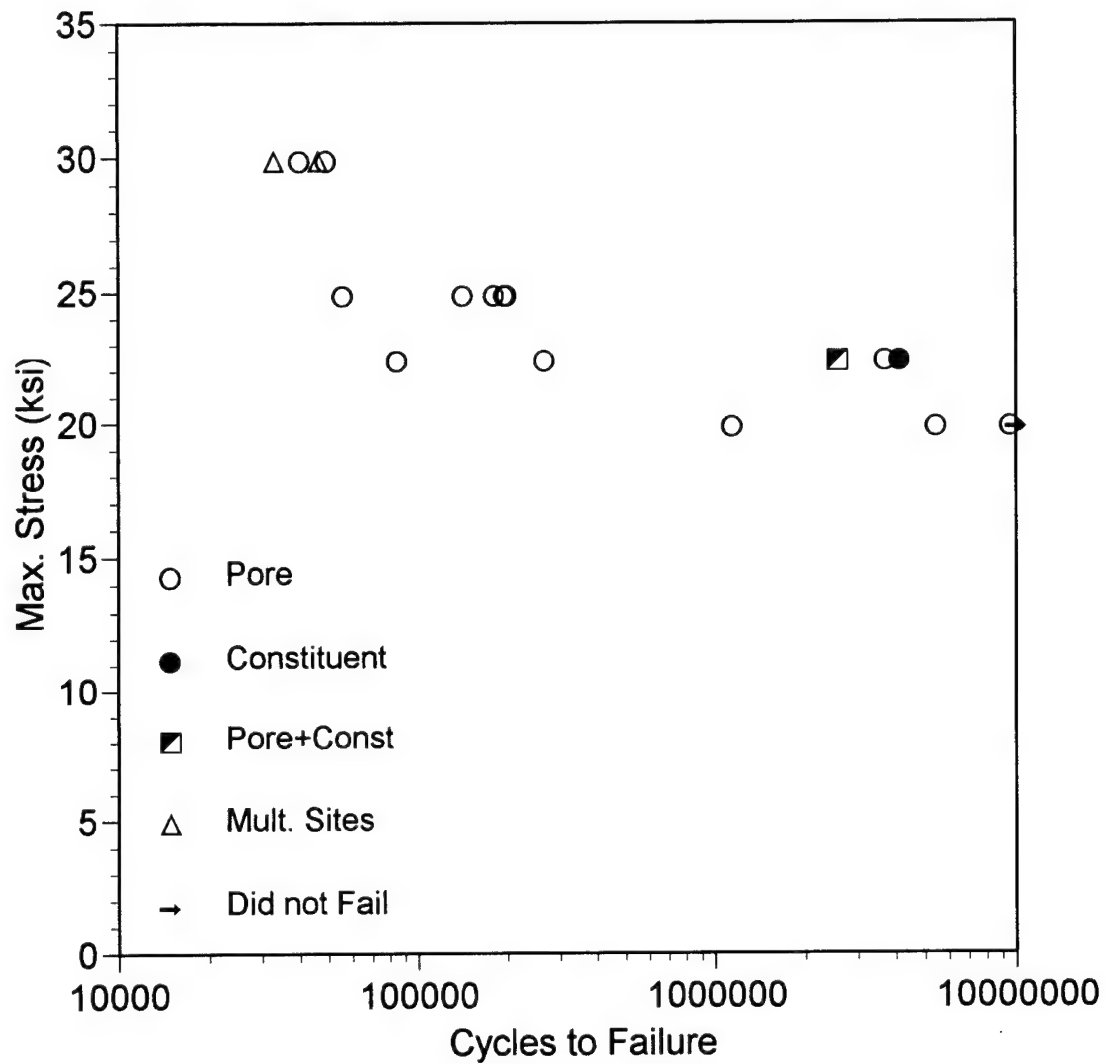


Figure 42. S-N fatigue results for new 7050-T7451 plate alloy, open hole samples.

7050-T7451 Low Porosity Plate Alloy  
Open Hole Samples, 30 Hz, R = 0.1, LT Orientation

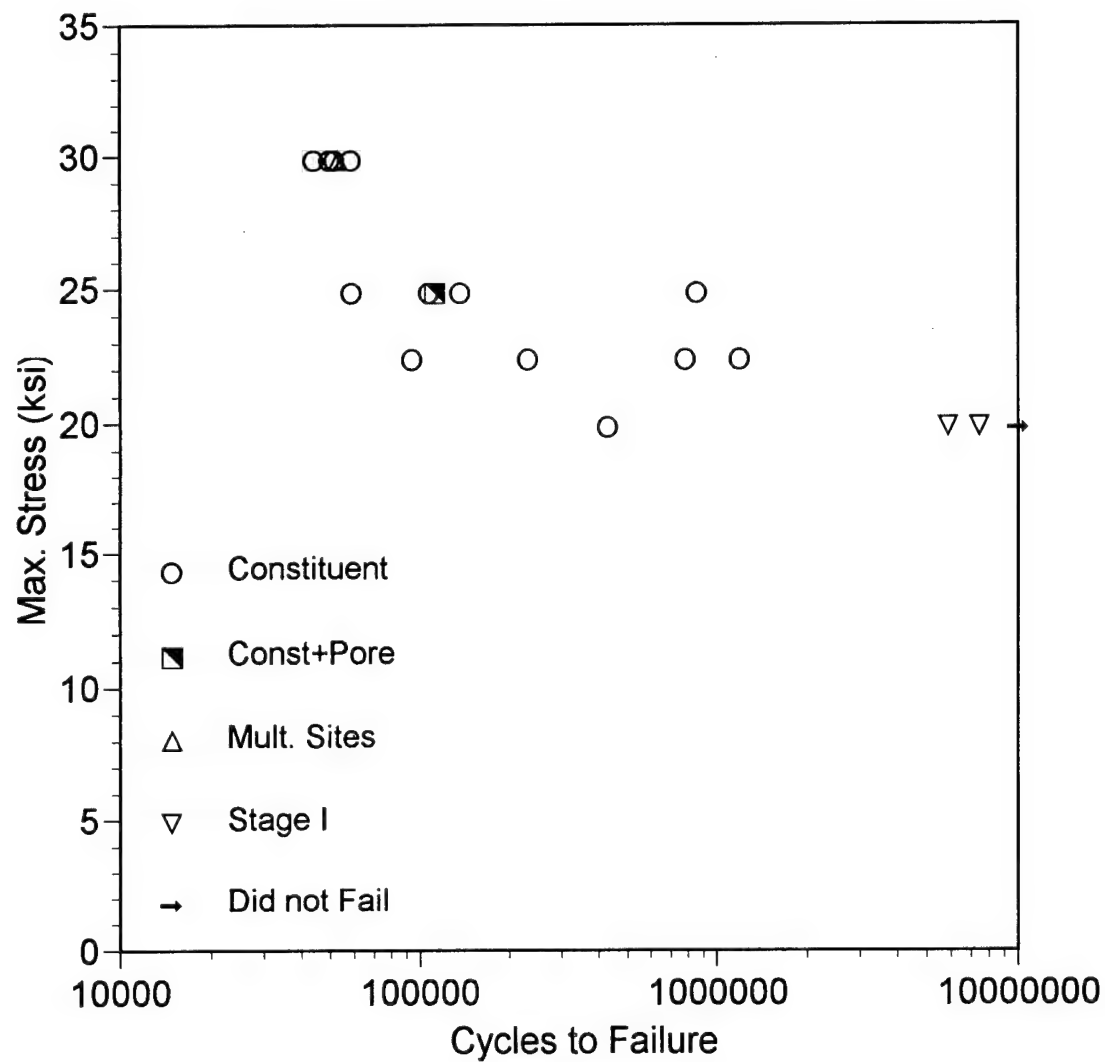


Figure 43. S-N fatigue results for thin plate 7050-T7451 alloy, open hole samples.

7050-T7451 Thin Plate Alloy  
Open Hole Samples, 30 Hz, R = 0.1, LT Orientation

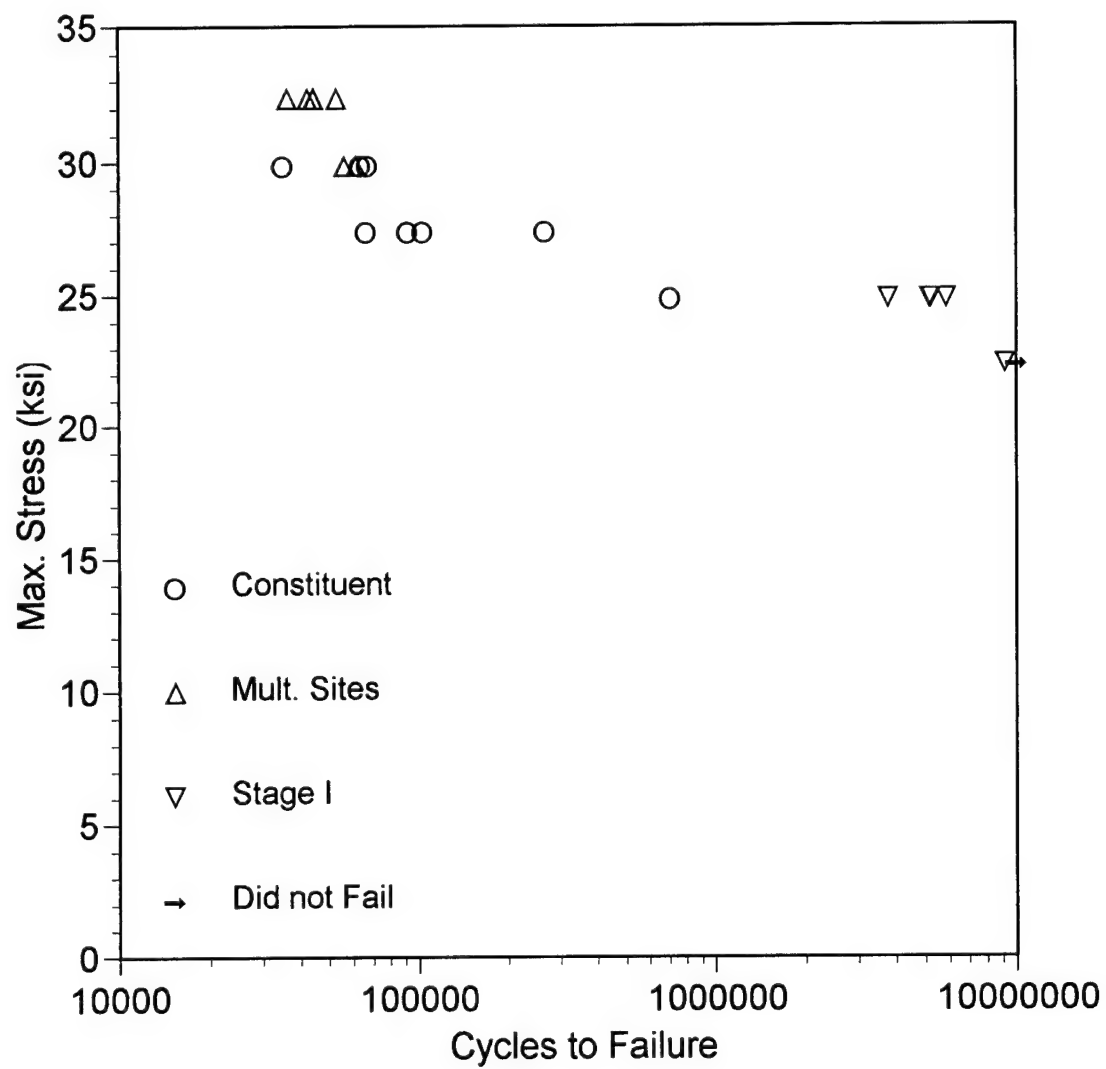


Figure 44. S-N fatigue results for low porosity 7050-T7451 plate alloy, open hole samples.

## Effect of Maximum Stress Level on Fatigue Crack Initiating Pore Sizes Distributions

Old Quality 7050-T7451 Plate Alloy,  $R = 0.1$

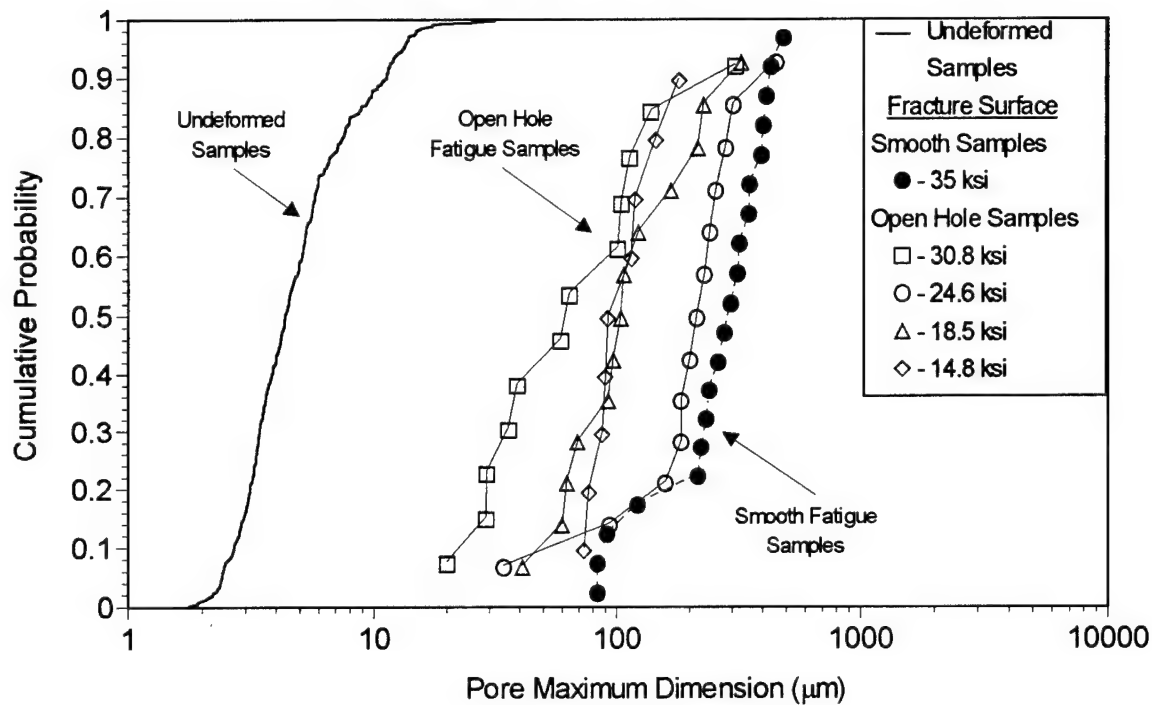


Figure 45. Effect of the maximum stress level on the size distributions of the fatigue crack initiating pores in the old 7050-T7451 plate alloy. Open hole and smooth fatigue samples, LT orientation.

## Change of the Fatigue Crack Initiating Pore Sizes with Maximum Stress Level

New 7050-T7451 Plate Alloy,  $R = 0.1$

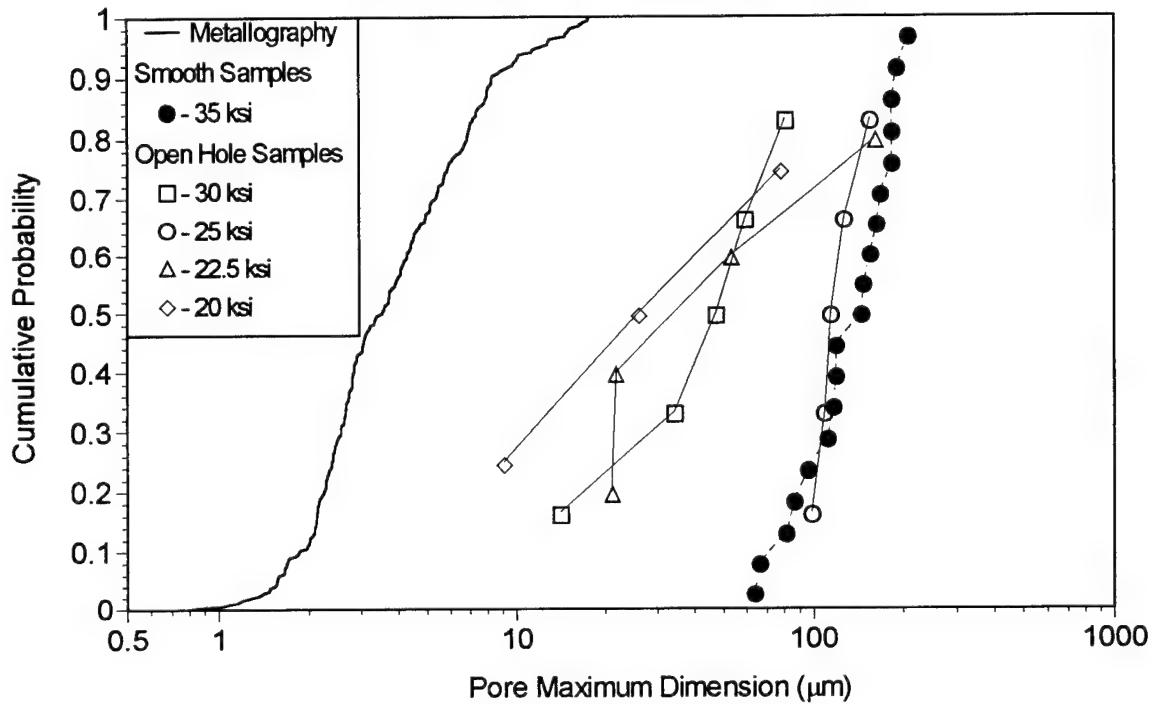


Figure 46. Effect of the maximum stress level on the size distributions of the fatigue crack initiating pores in the new 7050-T7451 plate alloy. Open hole and smooth fatigue samples, LT orientation.

## Change of the Average Size of the Fatigue Crack Initiating Pores with Maximum Stress Level

7050-T7451 Plate Alloys, Open Hole Samples,  $R = 0.1$

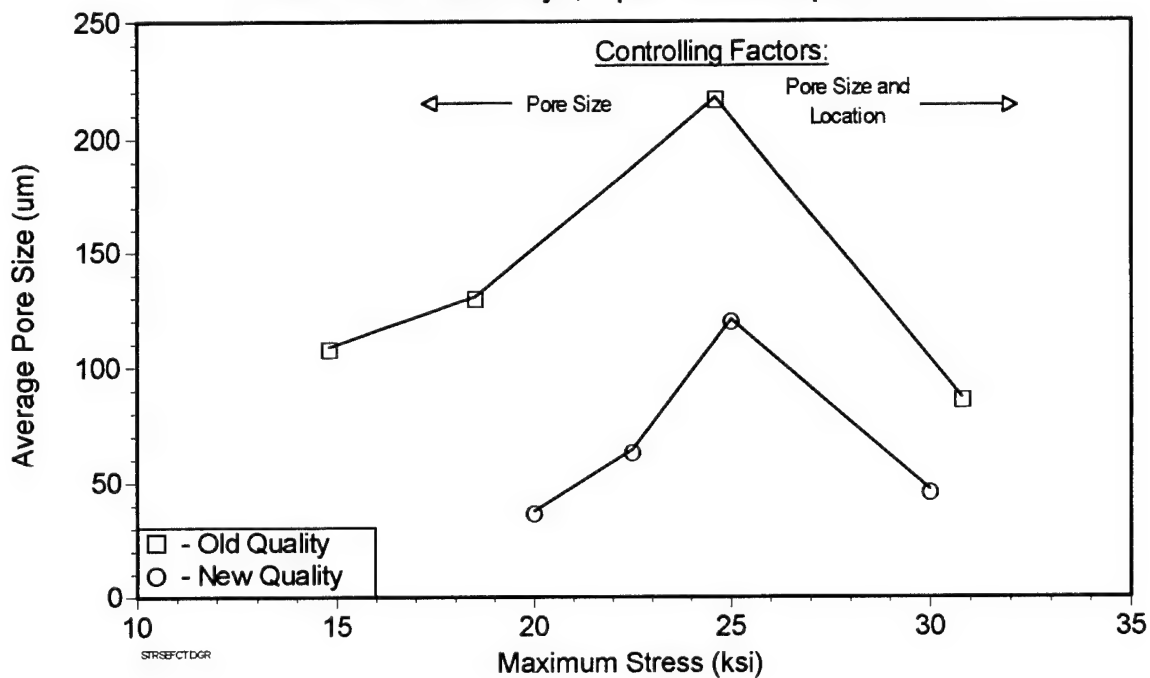


Figure 47. Effect of the maximum stress on the average size of the fatigue crack initiating pores in the old and new 7050-T7451 plate alloy. Open hole fatigue samples, LT orientation.

## Effect of Maximum Stress Level on the Average Size of the Fatigue Crack Initiating Pores

7050-T7451 Plate Alloys, R = 0.1

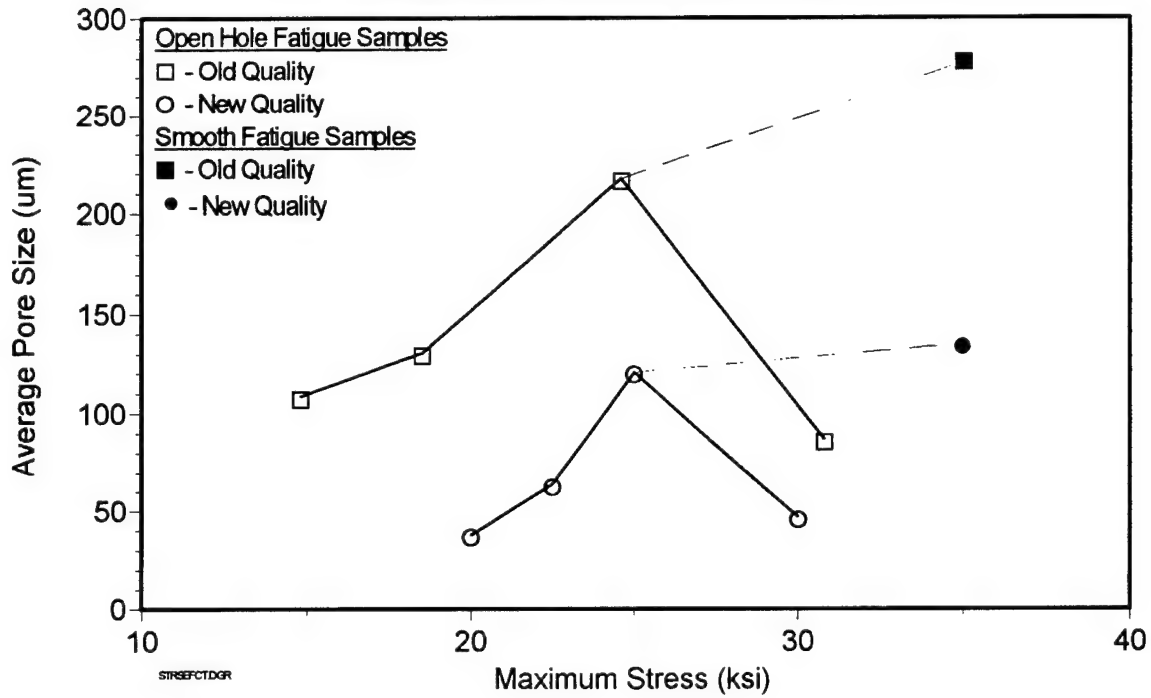


Figure 48. Comparison of the effects of the maximum stress level on the average size of the fatigue crack initiating pores in the open hole and smooth fatigue samples. Old and new 7050-T7451 plate alloy, LT orientation.

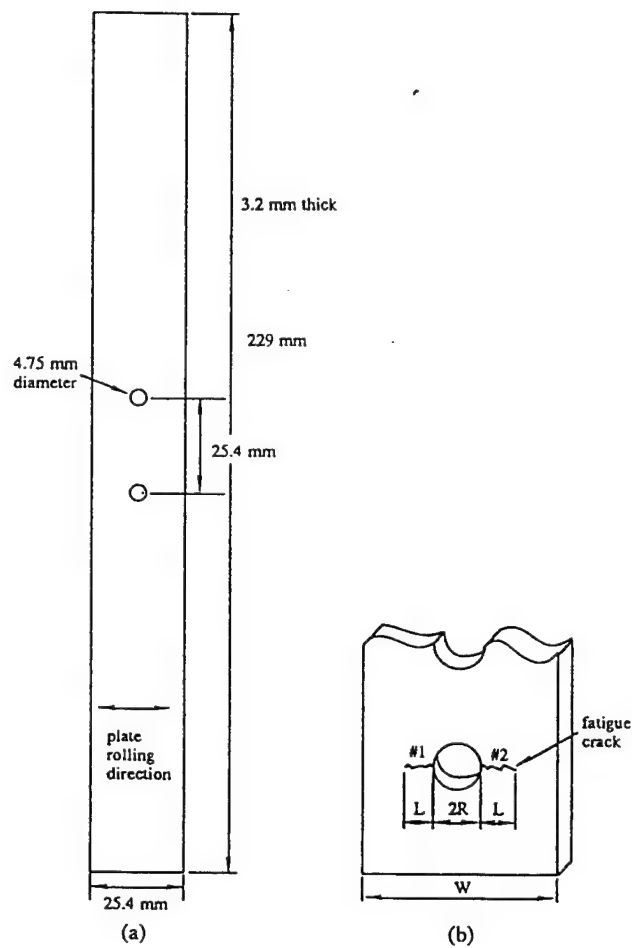


Figure 49. Designations of cracks used in the studies of crack profiles and distributions of microstructural features along the crack path.

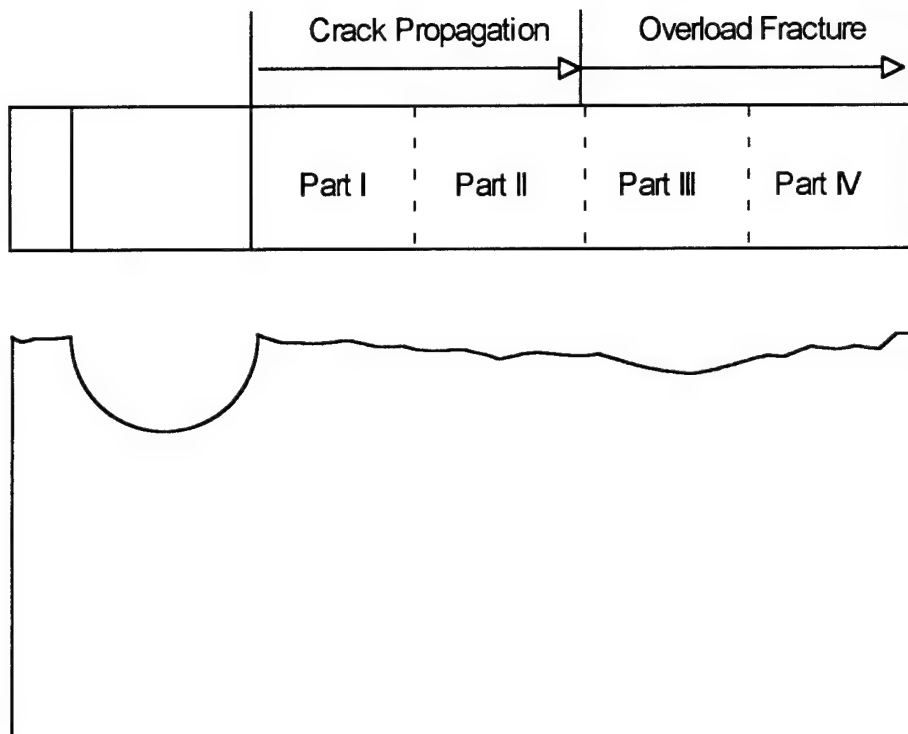


Figure 50. Schematic showing sectioning of the open hole specimens for fractographic studies. Part I is next to the open hole crack initiation region.

## 3-D profile

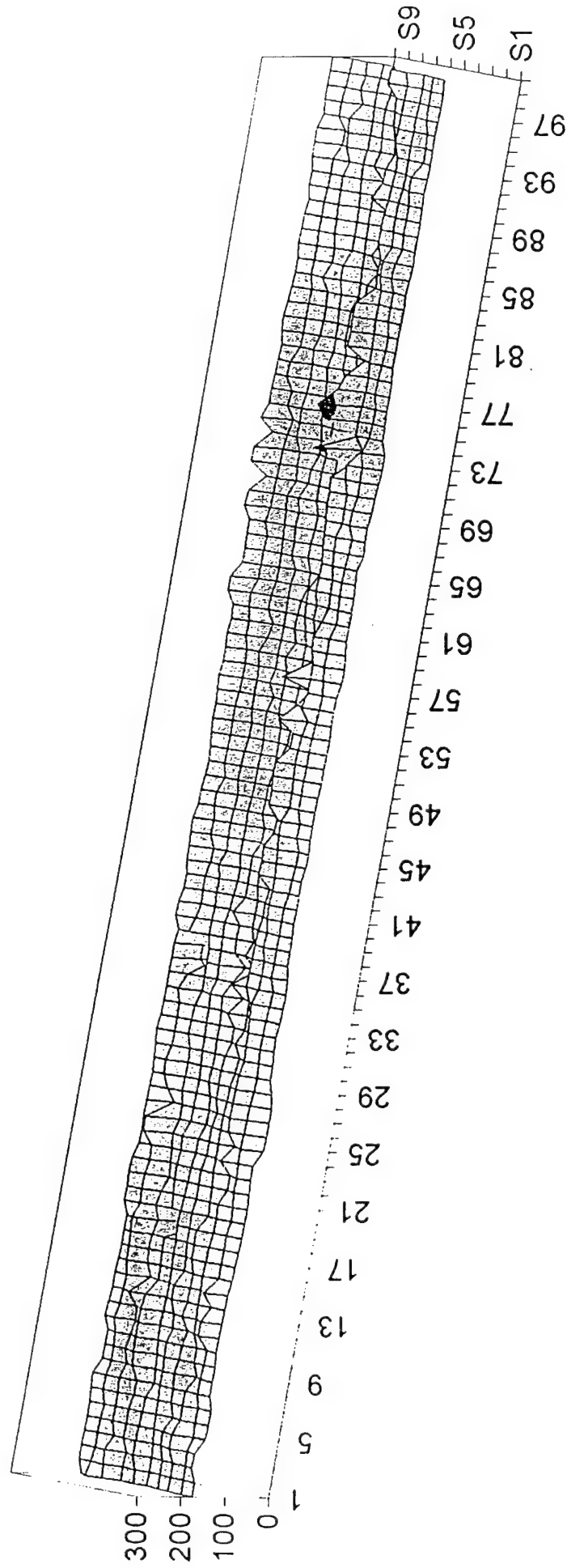


Figure 51. Example of the crack profiles obtained using confocal laser scanning microscopy (CLSM) for 7050-T7451 open hole sample failure.

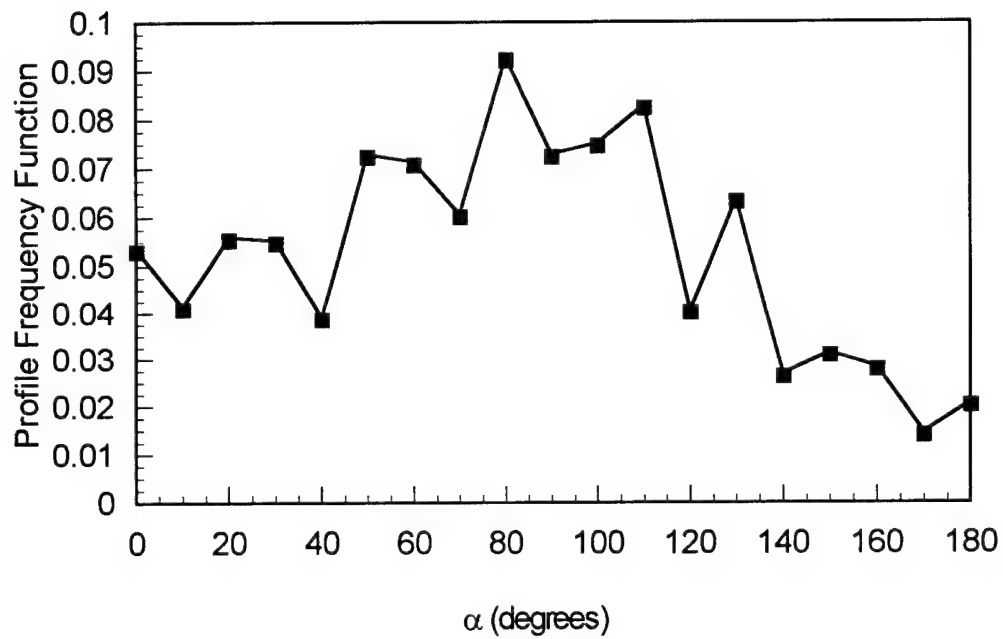


Figure 52. Distribution of angular orientations of crack segments for fatigue crack in the open hole 7050-T7451 new alloy sample,  $\sigma_{\max} = 206$  MPa,  $R = 0.1$ . Crack average plane corresponds to  $90^\circ$ , cutting plane at  $60^\circ$  to the crack growth direction.

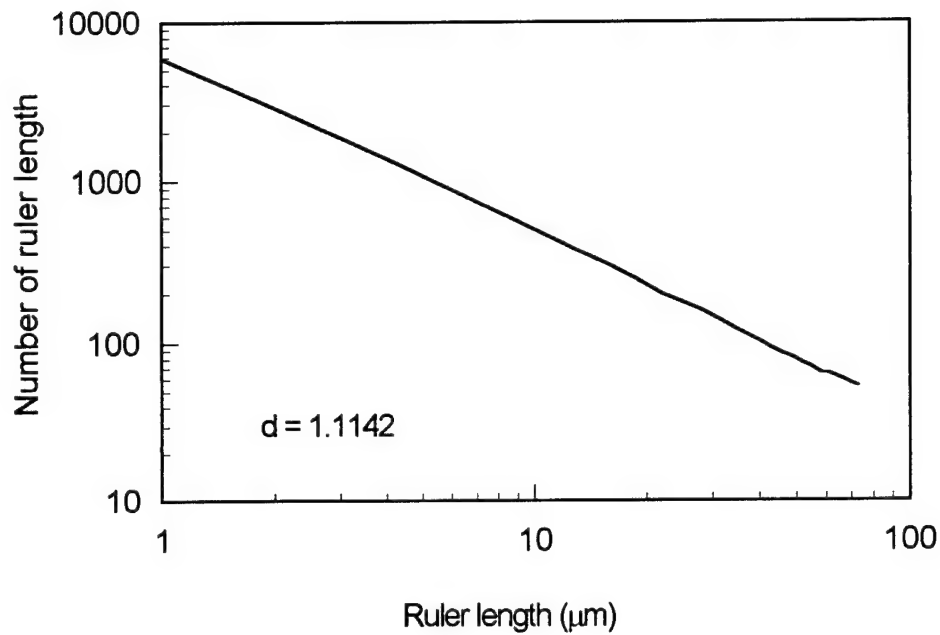


Figure 53. Typical fractal plot for the fracture surface profile parallel to the crack front for the new 7050-T7451 plate alloy fatigued at  $\sigma_{\text{max}} = 206 \text{ MPa}$ ,  $R = 0.1$ . The plot shows excellent linearity with the slope, corresponding to fractal dimension  $d$ , equal 1.1142.

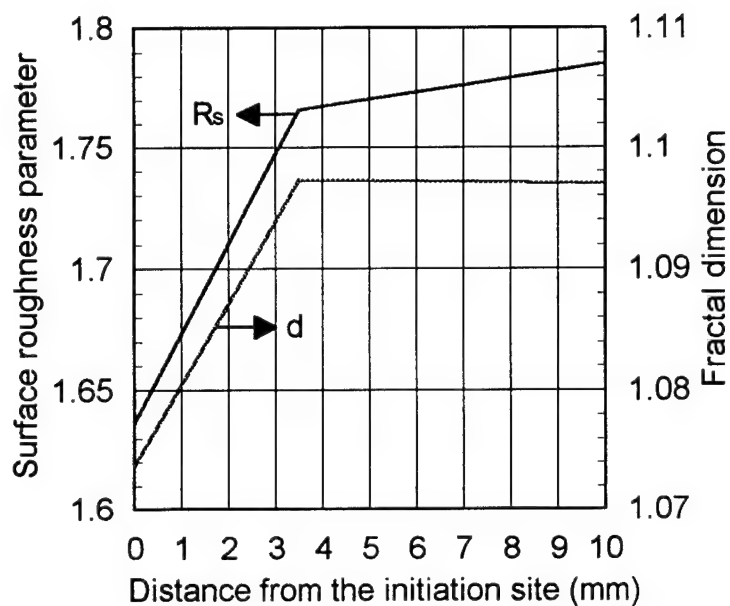


Figure 54. Change of the roughness parameter,  $R_s$ , and fractal dimension,  $d$ , with crack length for the fracture surface of the new 7050-T7451 plate alloy fatigued at  $\sigma_{\max} = 206$  MPa,  $R = 0.1$ . The values of  $R_s$  were obtained from the trisector method.

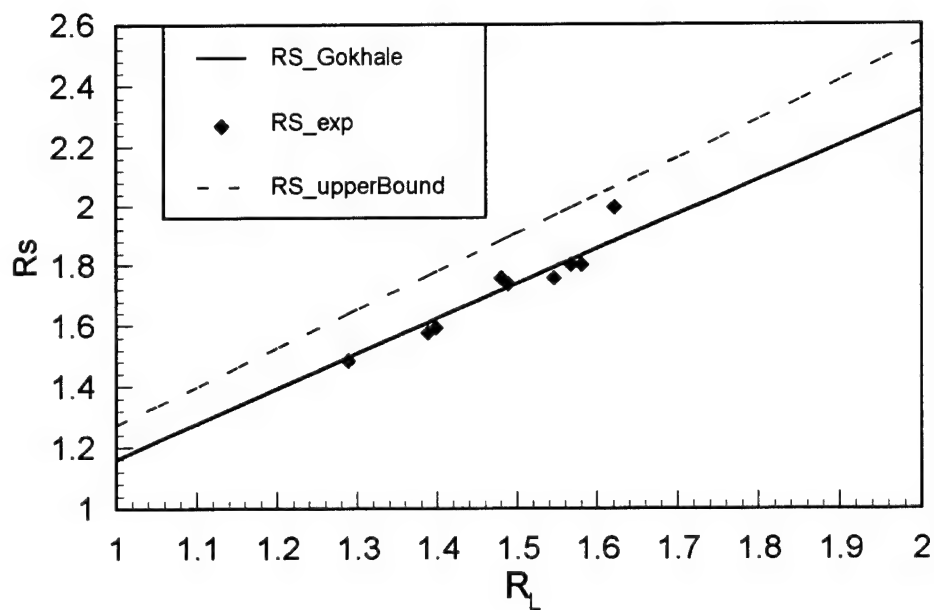


Figure 55. Correlation between  $R_s$  and  $R_L$  for experimental results (solid line) and for the random surface (dotted line). The points represent results obtained from the trisector method.

## Fracture Surface Characteristics of 7050-T7451 Plate Alloys

Open hole samples,  $s_{max}=170$  MPa,  $R = 0.1$ , 10 Hz

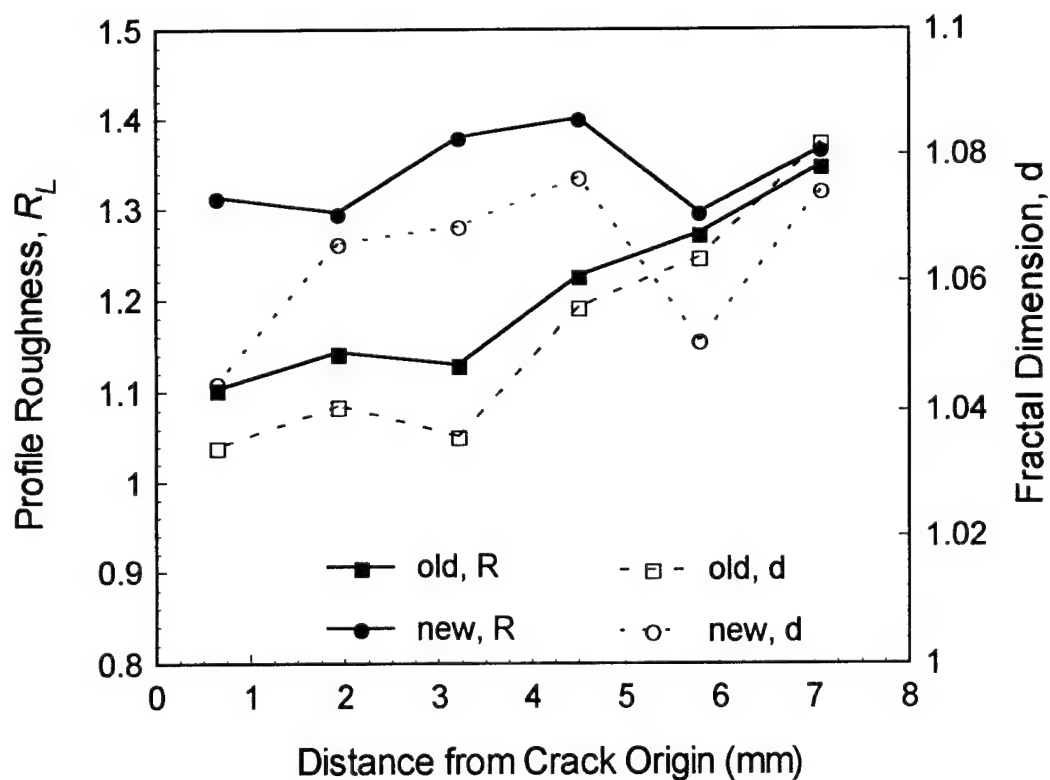


Figure 56. Change of the roughness parameter,  $R_L$ , and fractal dimension,  $d$ , with crack length for the fracture surface of 7050-T7451 plate alloy. The values of  $R_L$  were obtained from the confocal laser scanning microscopy (CLSM) method.

# Fatigue Crack Path Characteristics 7050-T7451 Plate Alloy, Open-Hole Sample

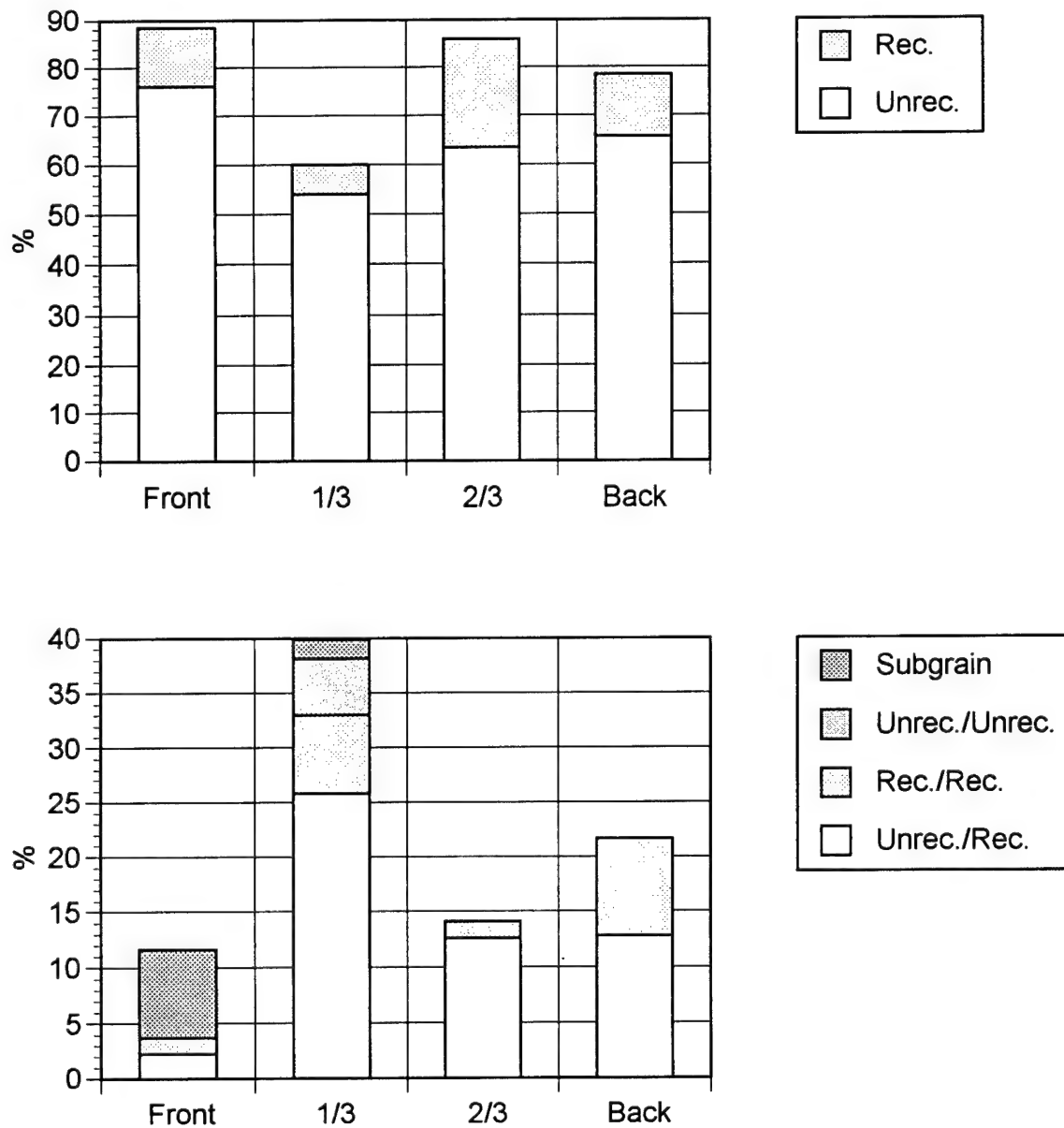


Figure 57. Percentages of different microstructural features along (a) transgranular and (b) intergranular crack path for old 7050-T7451 alloy, open hole fatigue sample.

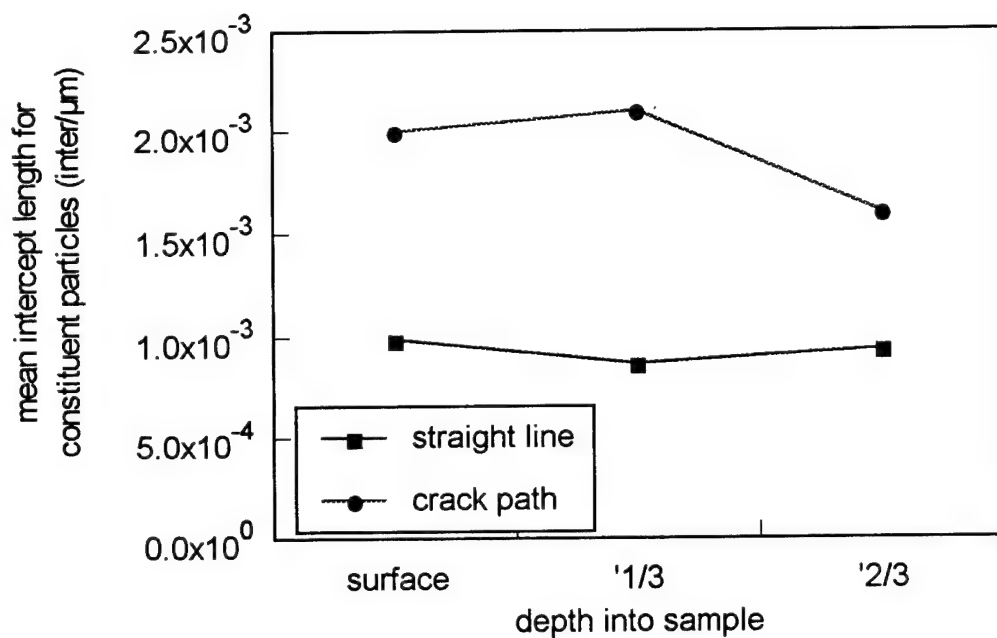


Figure 58. Comparison of the line densities of constituent particles along crack path with those for a straight line through the microstructure. 7050-T7451 plate alloy, open hole fatigue sample.

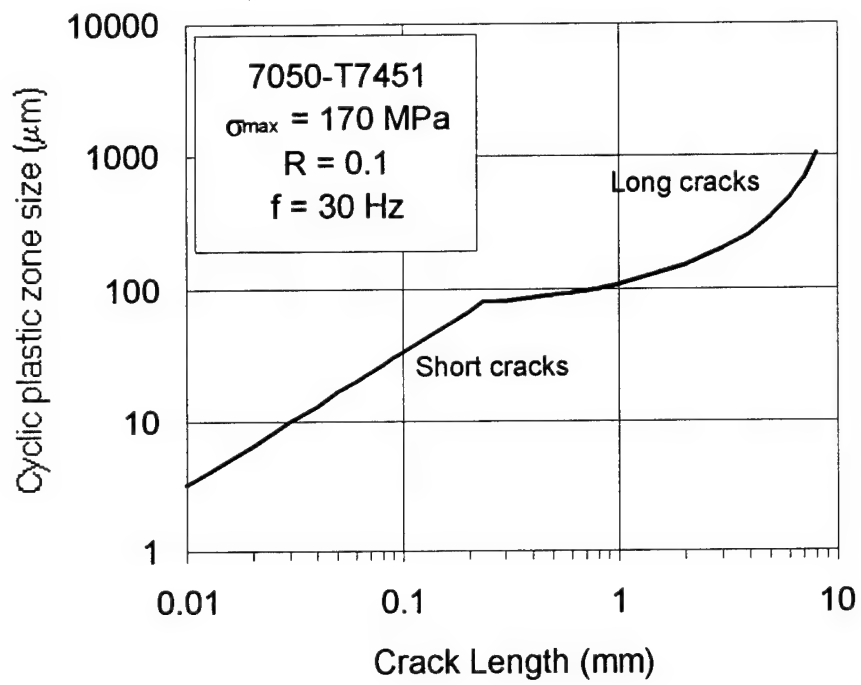


Figure 59. Changes in plastic zone size with crack length in 7050-T7451 plate alloy.

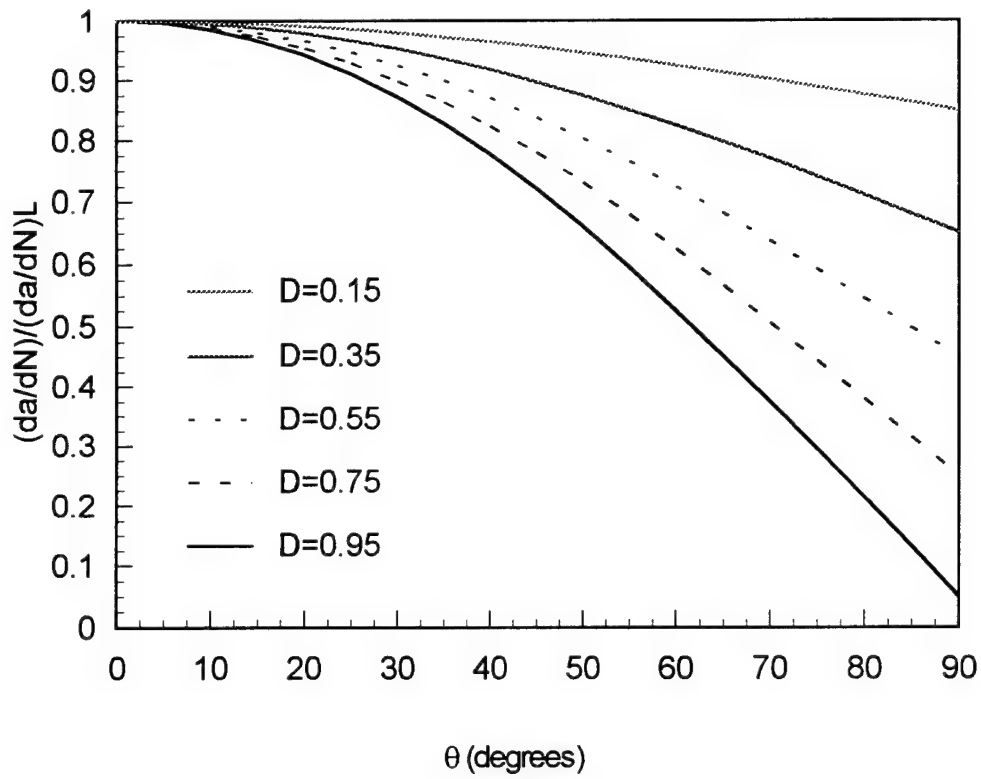


Figure 60. Effects of crack deflection angle,  $\theta$ , and extent of crack tilt,  $D$ , on the relative crack propagation rate. Typical values for aluminum alloys are  $\theta = 45^\circ$  and  $D = 0.75$ .

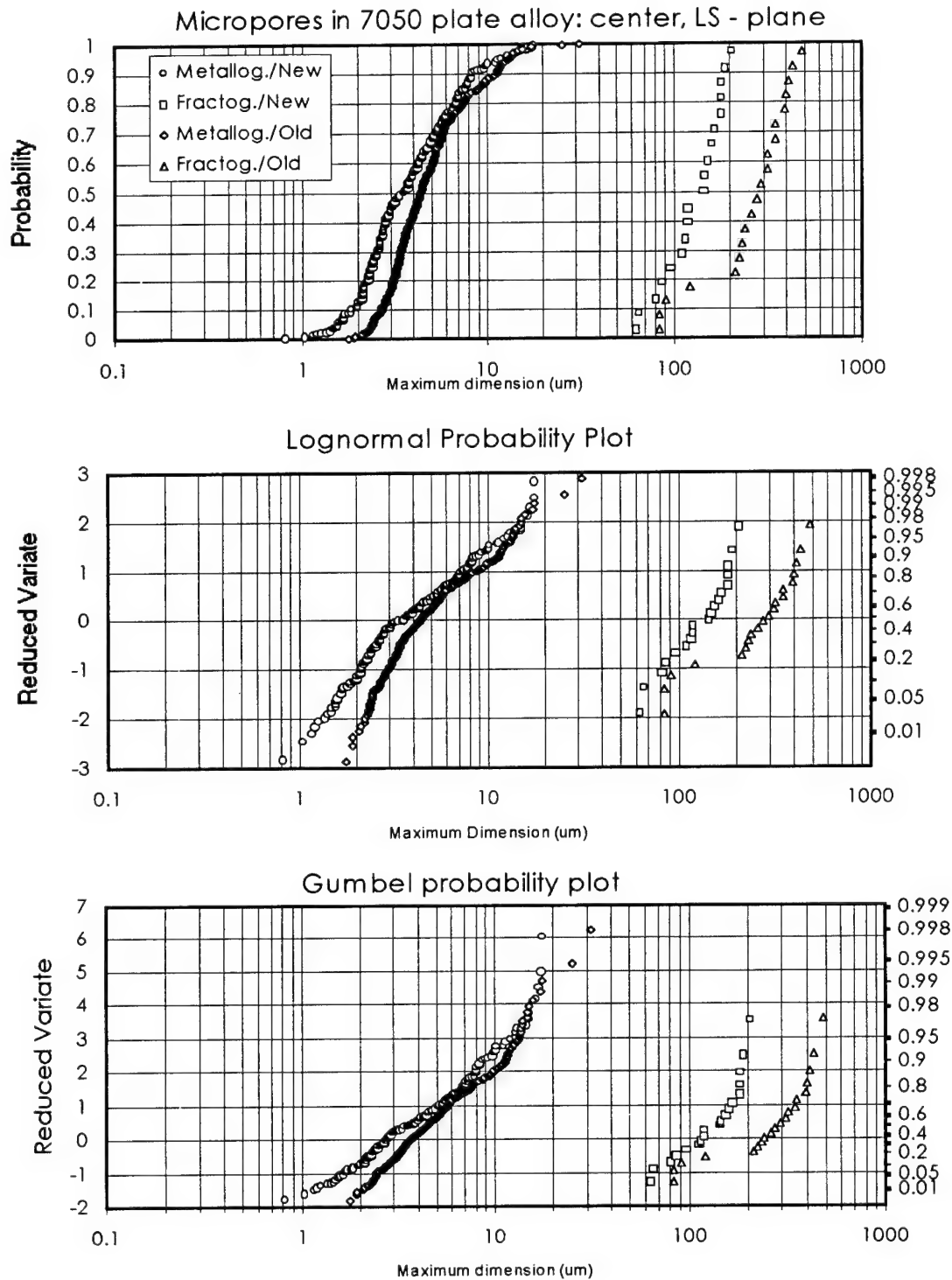


Figure 61. Comparison of the bulk (metallography) and the actual crack initiating pore sizes (fractography) for the old and new 7050-T7451 plate alloys on (a) linear, (b) lognormal and (c) Gumbel probability plots.

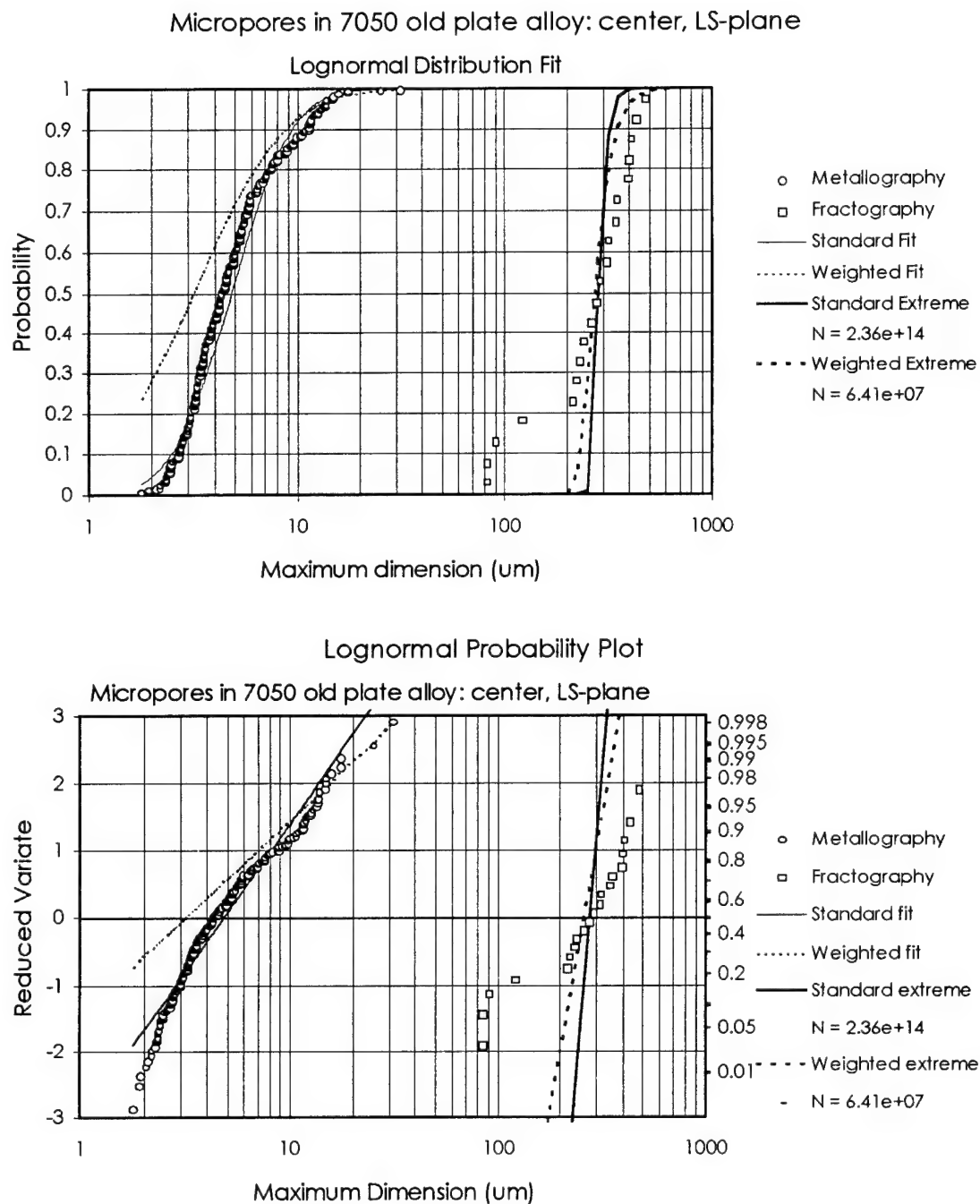


Figure 62. Comparison of the extreme value predictions of the sizes of the crack initiating pores with fractographic data. Predictions obtained using standard and weighted lognormal fits to the metallographic data: old 7050 alloy, LS-plane, center.

# Micropores in 7050 new plate alloy: center, LS-plane

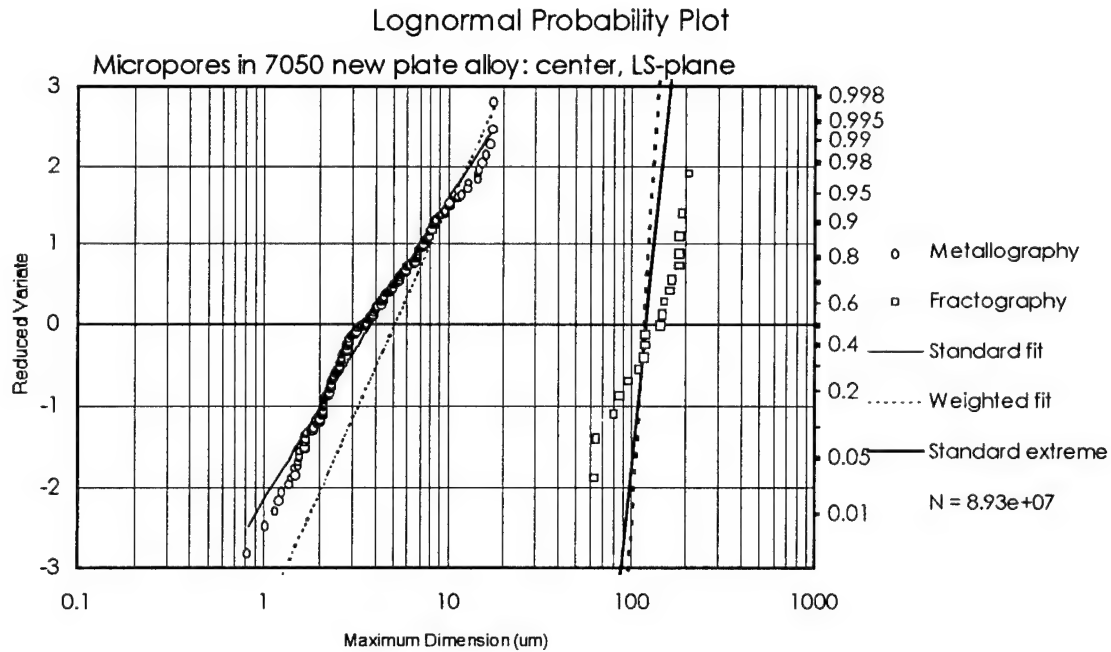
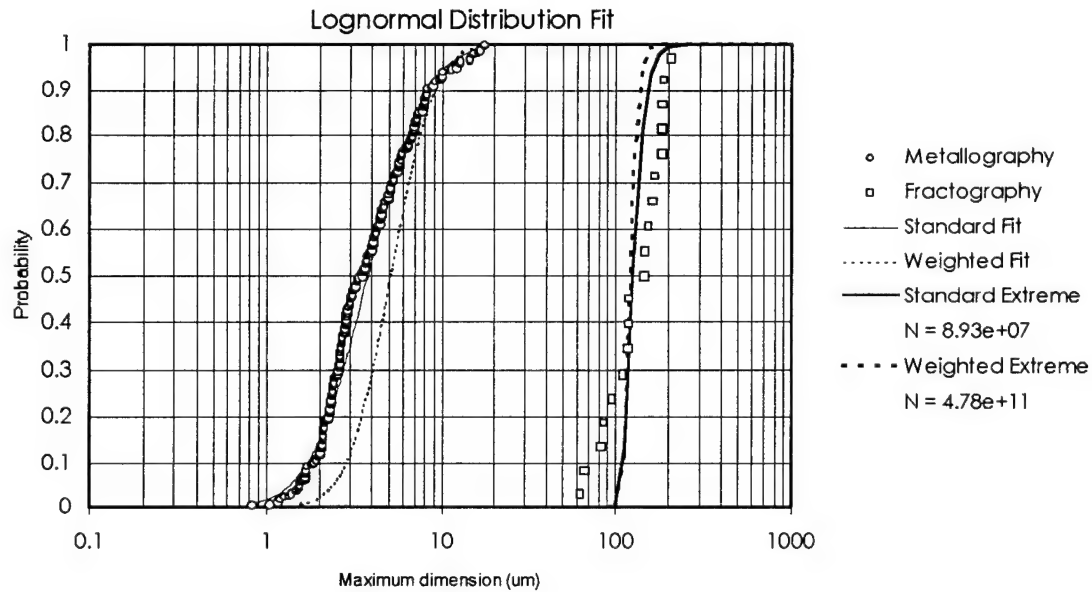


Figure 63. Comparison of the extreme value predictions of the sizes of the crack initiating pores with fractographic data. Predictions obtained using standard and weighted lognormal fits to the metallographic data: new 7050 alloy, LS-plane , center.

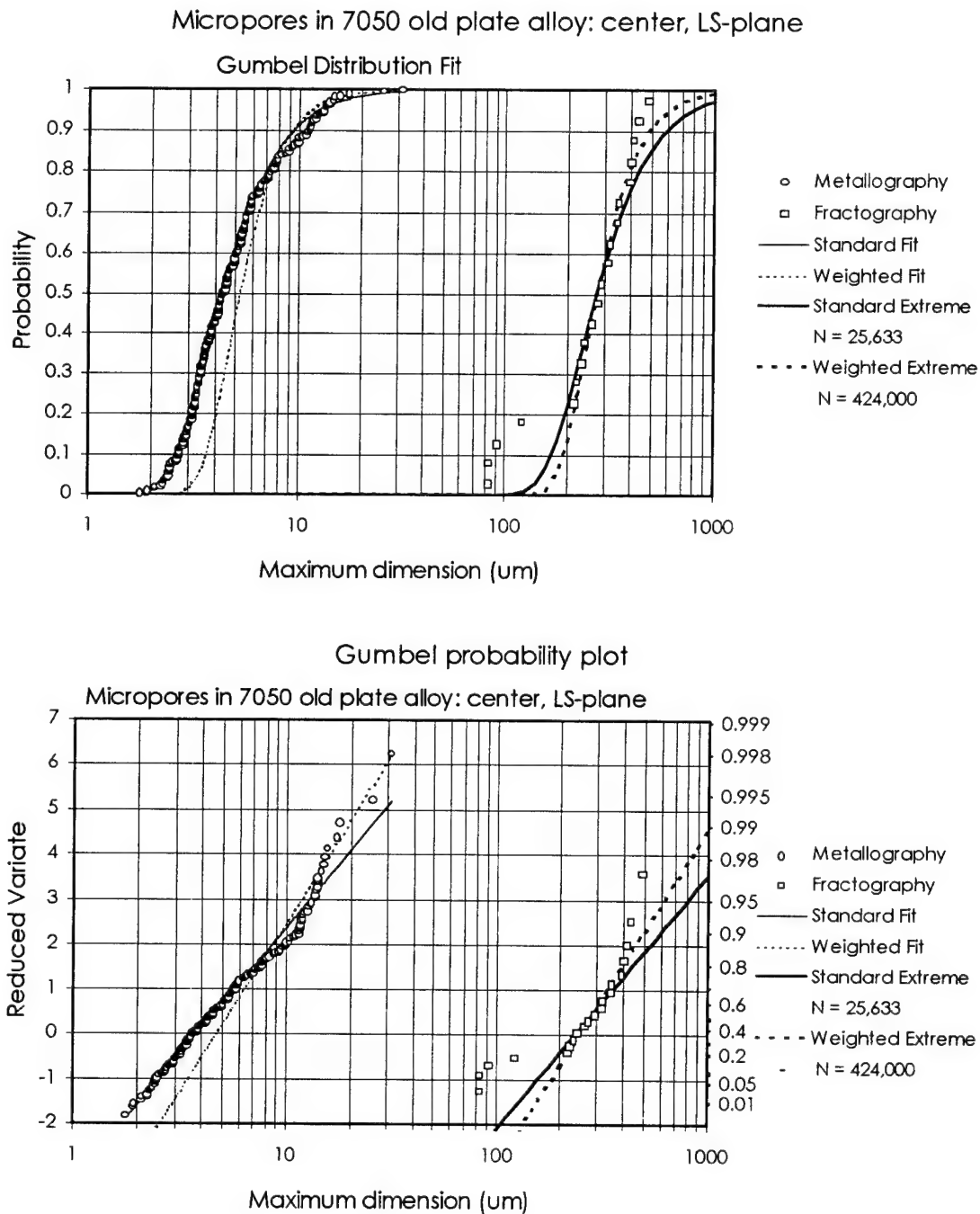


Figure 64. Comparison of the extreme value predictions of the sizes of the crack initiating pores with fractographic data. Predictions obtained using standard and weighted Gumbel fits to the metallographic data: old 7050 alloy, LS-plane , center.

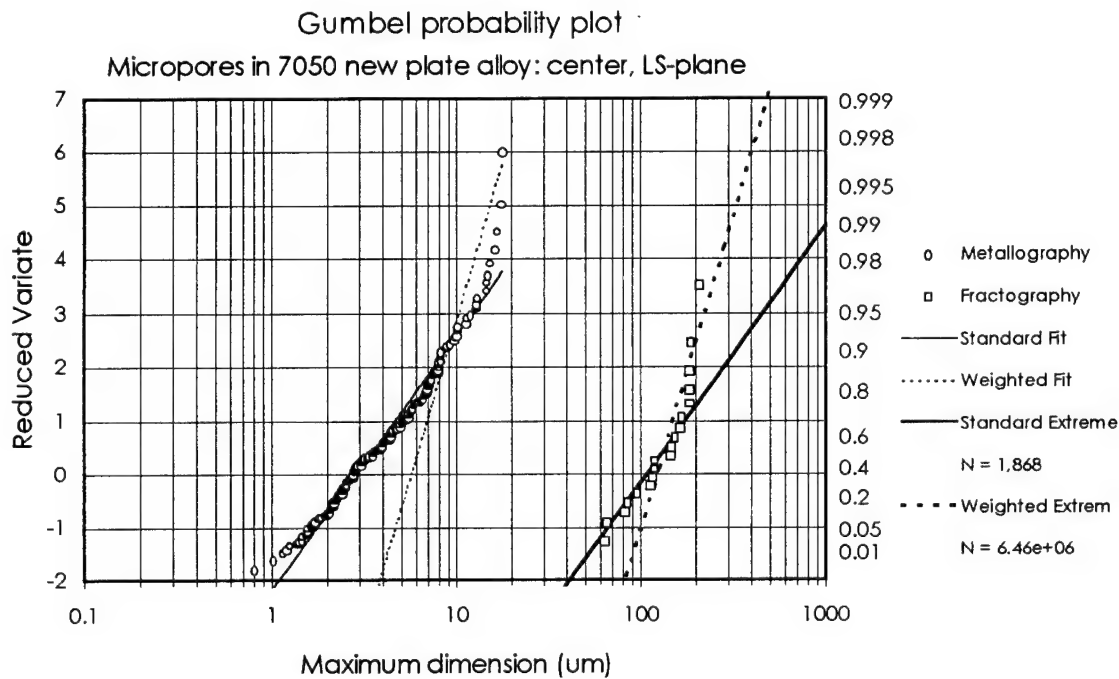
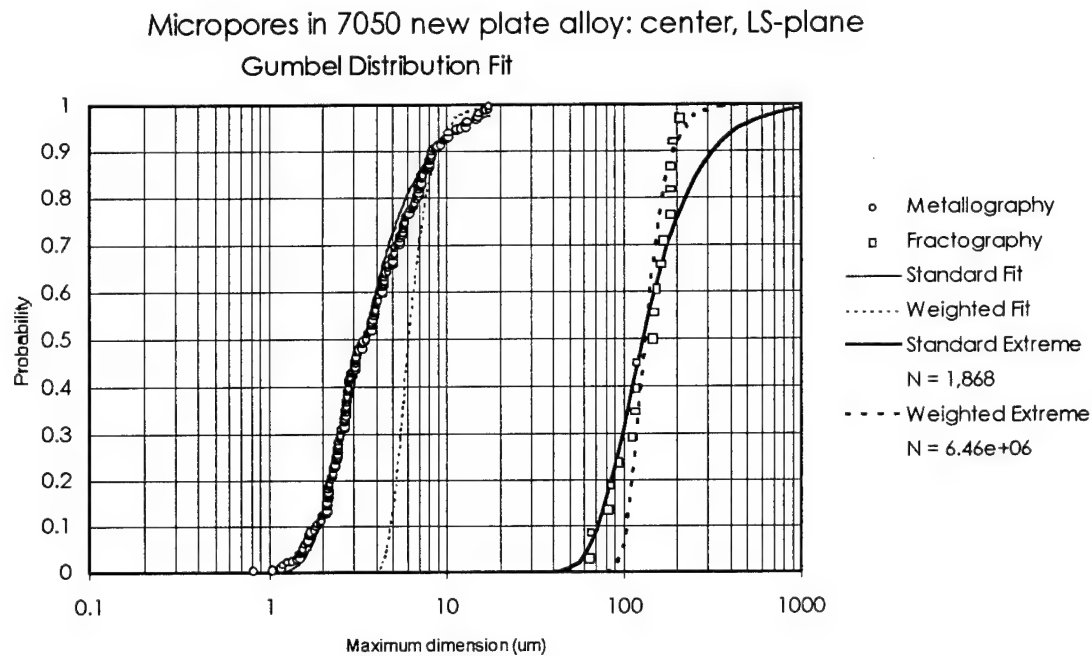


Figure 65. Comparison of the extreme value predictions of the sizes of the crack initiating pores with fractographic data. Predictions obtained using standard and weighted Gumbel fits to the metallographic data: old 7050 alloy, LS-plane , center.

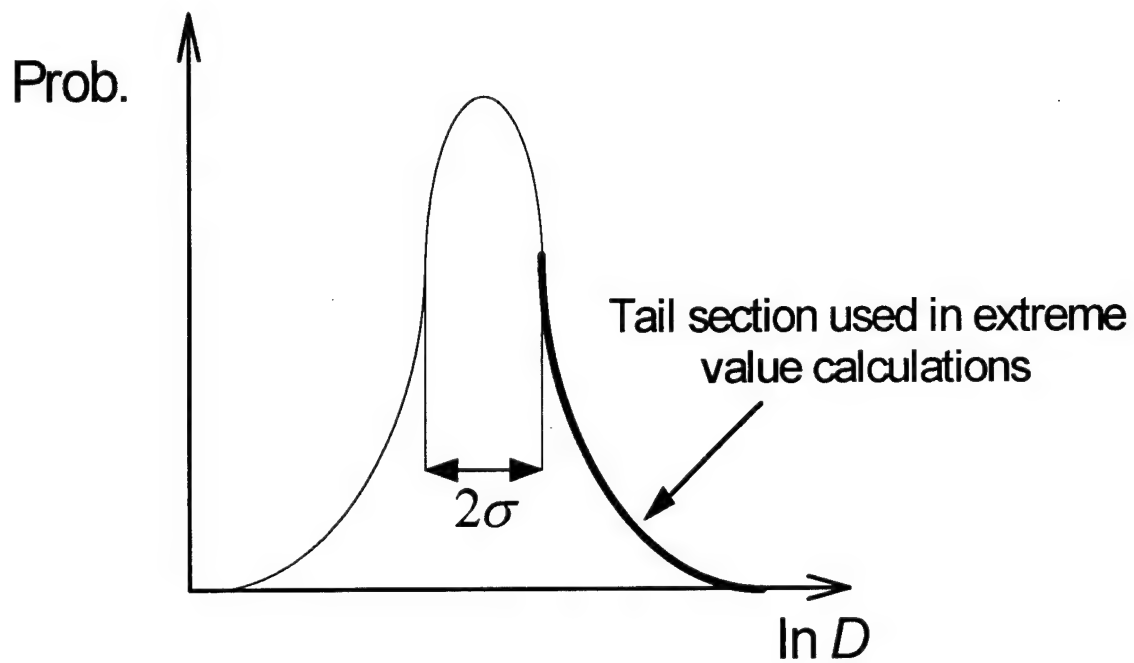


Figure 66. Schematic showing part of the parent distribution relevant for the extreme value predictions of the size distributions of the crack initiating features.

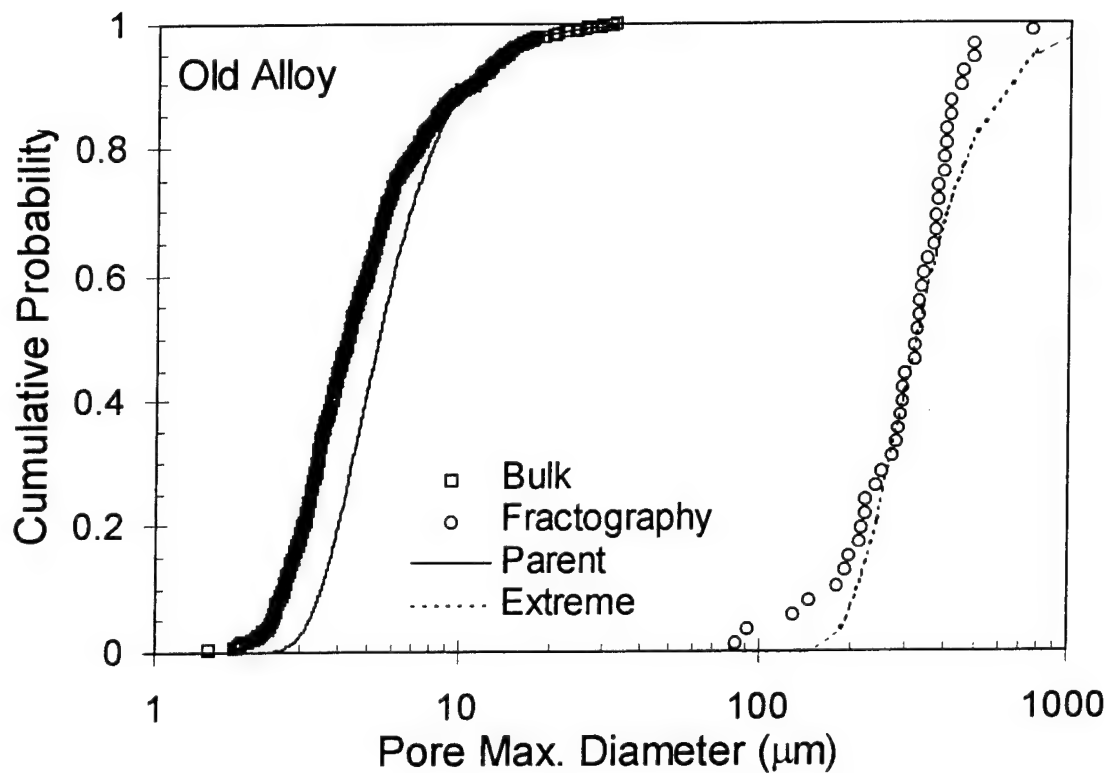


Figure 67. Old 7050 alloy, smooth fatigue samples,  $\sigma_{max} = 240$  MPa,  $R = 0.1$ . Comparison of the predicted (extreme) and actual (fractography) crack initiating pore size distributions. Predictions obtained from the parent fitted to the tail section of the bulk pore size data.

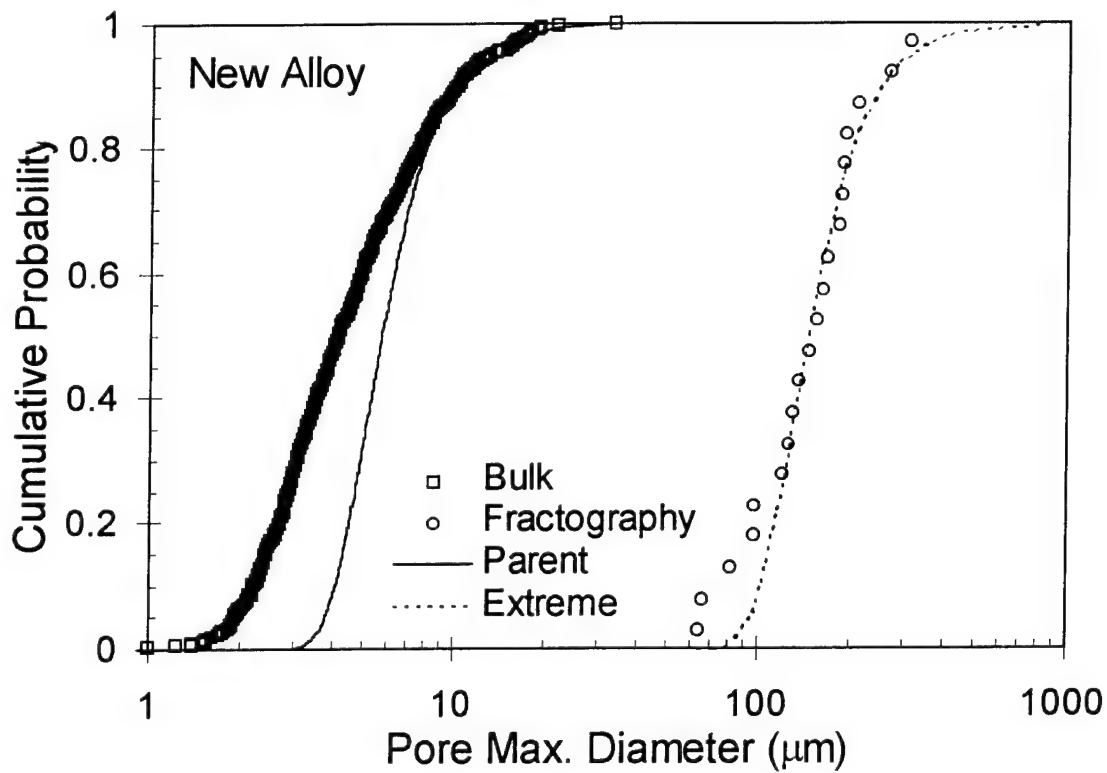


Figure 68. New 7050 alloy, smooth fatigue samples,  $\sigma_{max} = 240$  MPa,  $R = 0.1$ .

Comparison of the predicted (extreme) and actual (fractography) crack initiating pore size distributions. Predictions obtained from the parent fitted to the tail section of the bulk pore size data.

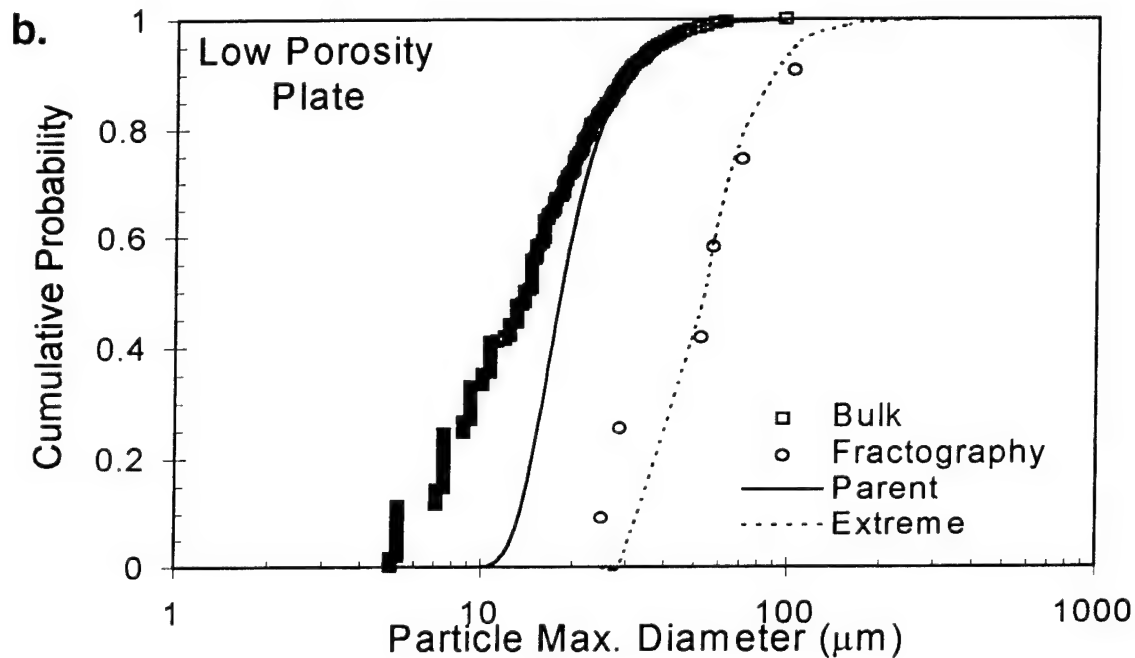
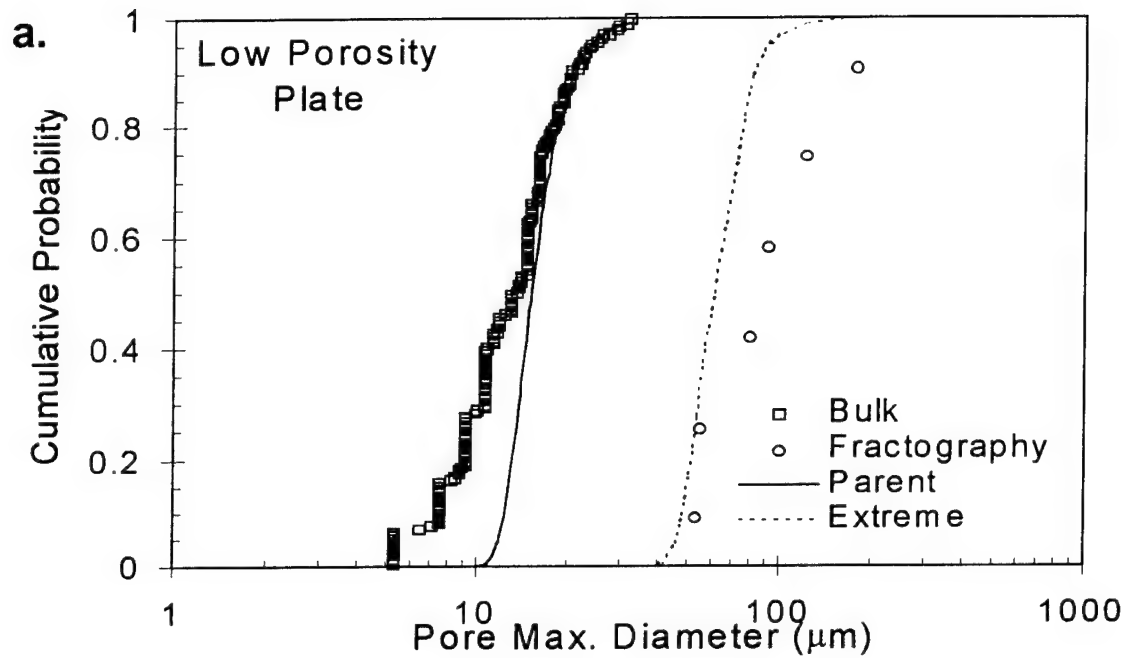


Figure 69. Low porosity 7050 alloy, smooth fatigue samples,  $\sigma_{max} = 276$  MPa,  $R = 0.1$ .

Comparison of predicted (extreme) and actual (fractography) crack initiating (a) pore and (b) particle size distributions. Predictions obtained from the parent fitted to the tail section of the bulk size data.

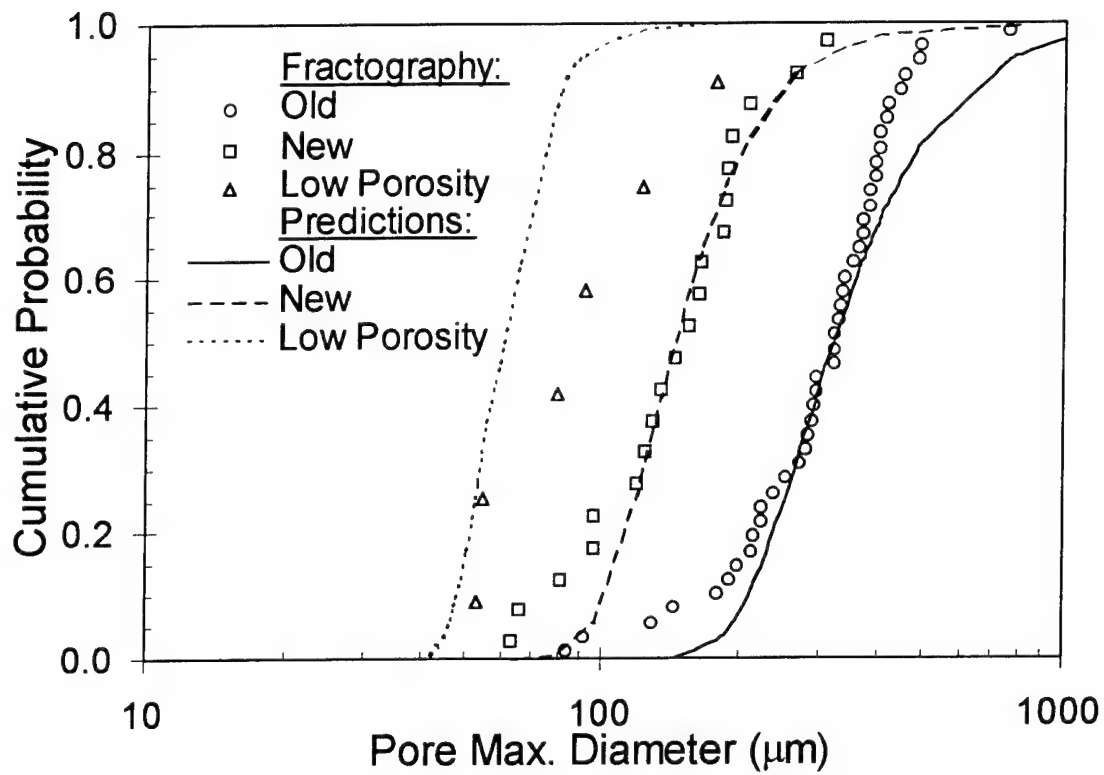


Figure 70. Comparison of the predicted and actual size distributions of the fatigue crack initiating pores in smooth fatigue samples of indicated alloys. Old and new alloys tested at  $\sigma_{max} = 240$  MPa and low porosity at  $\sigma_{max} = 276$  MPa,  $R = 0.1$ .

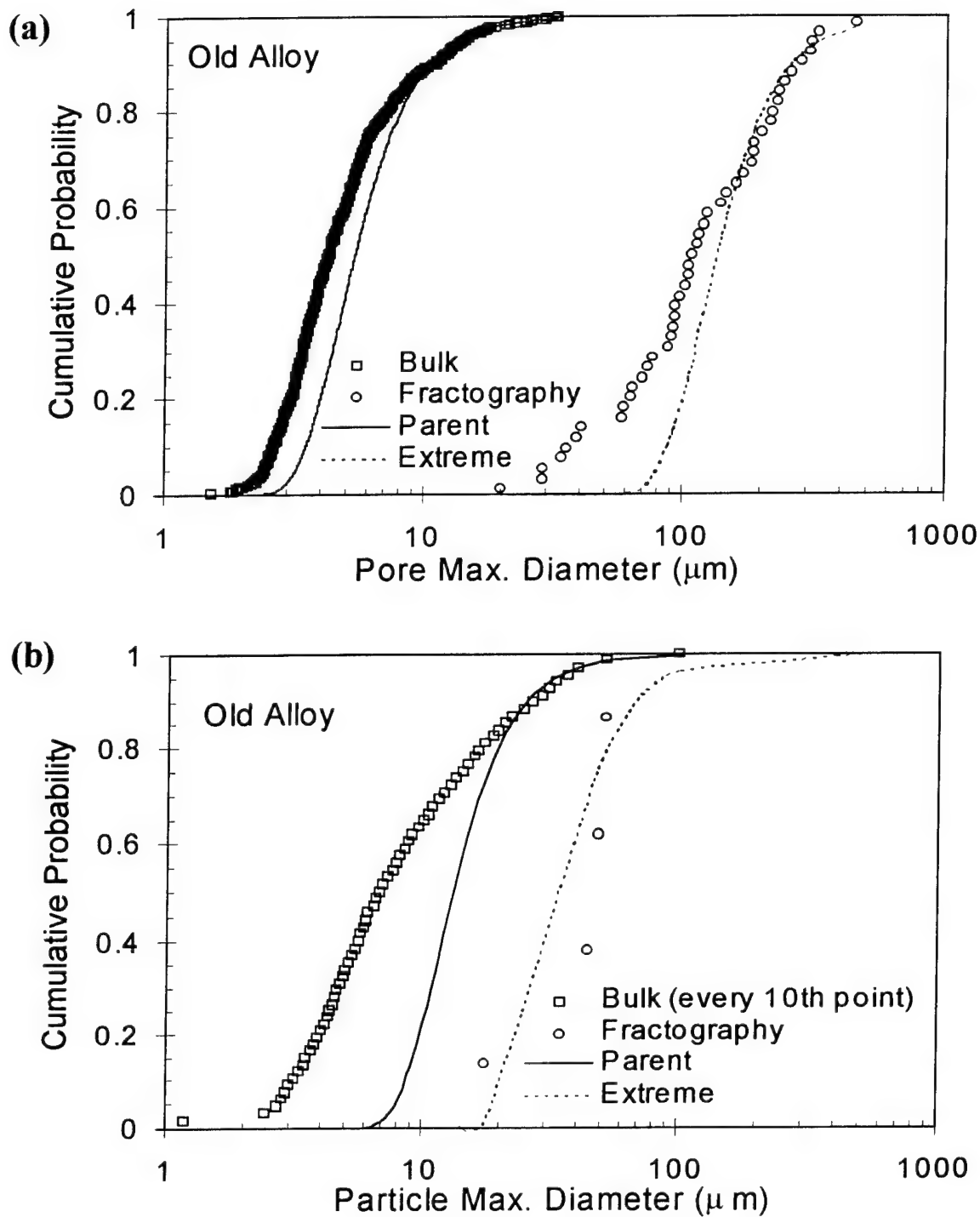


Figure 71. Old 7050 alloy, open hole fatigue samples. Comparison of the predicted (extreme) and actual (fractography) crack initiating (a) pore and (b) particle size distributions. Predictions obtained from the parent fitted to the tail section of the bulk pore size data.

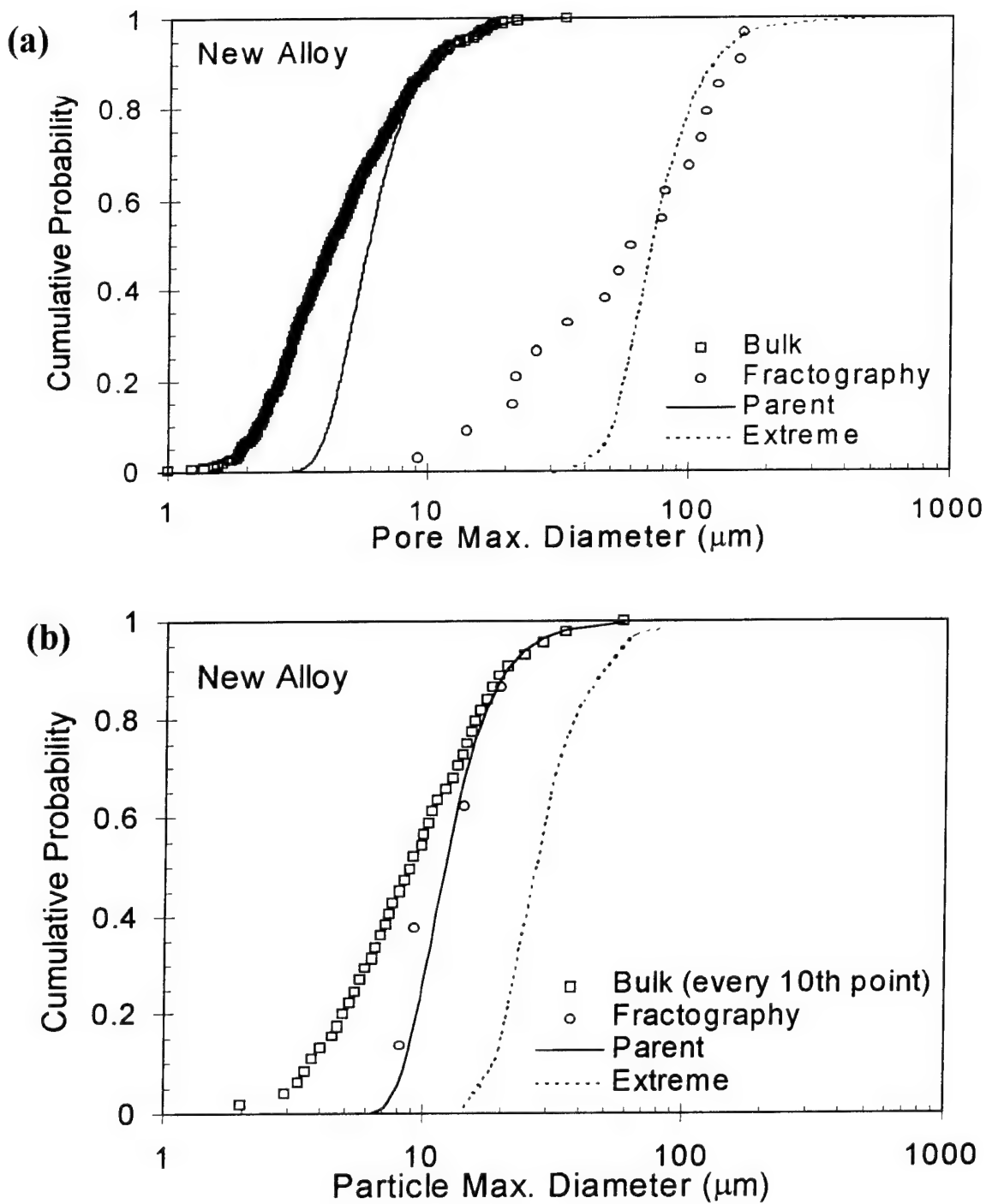


Figure 72. New 7050 alloy, open hole fatigue samples. Comparison of the predicted (extreme) and actual (fractography) crack initiating (a) pore and (b) particle size distributions. Predictions obtained from the parent fitted to the tail section of the bulk pore size data.

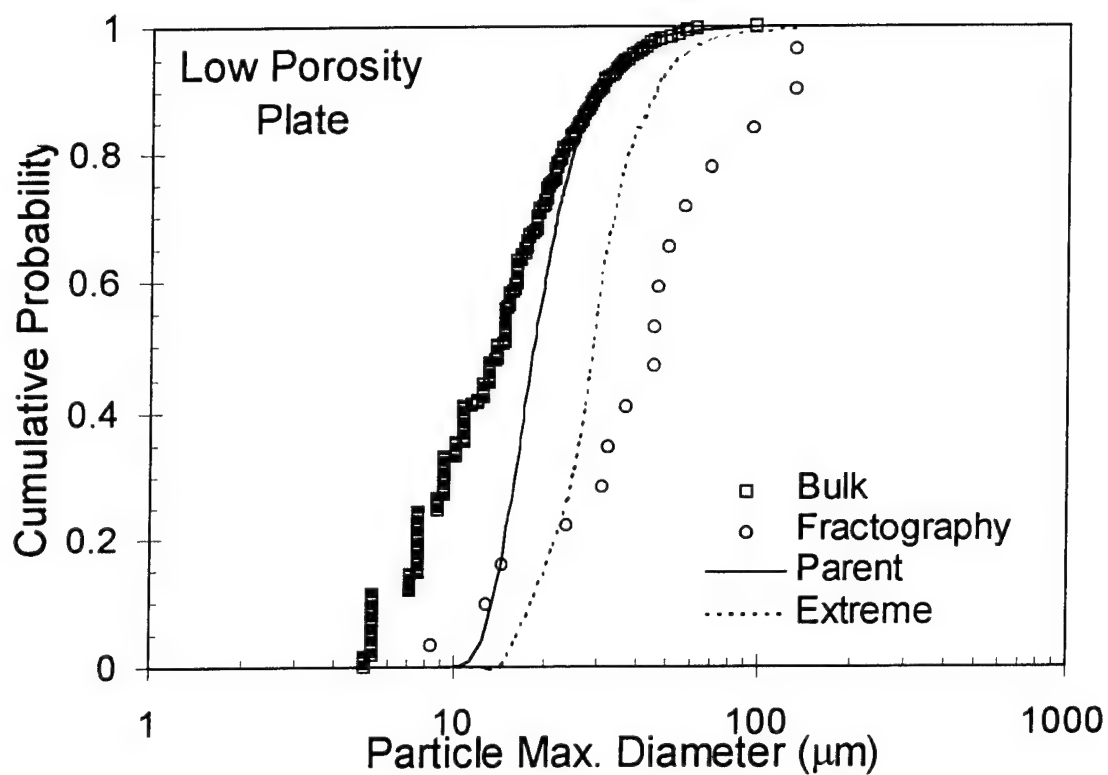


Figure 73. Low porosity 7050 alloy, open hole fatigue samples. Comparison of predicted (extreme) and actual (fractography) crack initiating particle size distributions. Predictions obtained from the parent fitted to the tail section of the bulk size data.

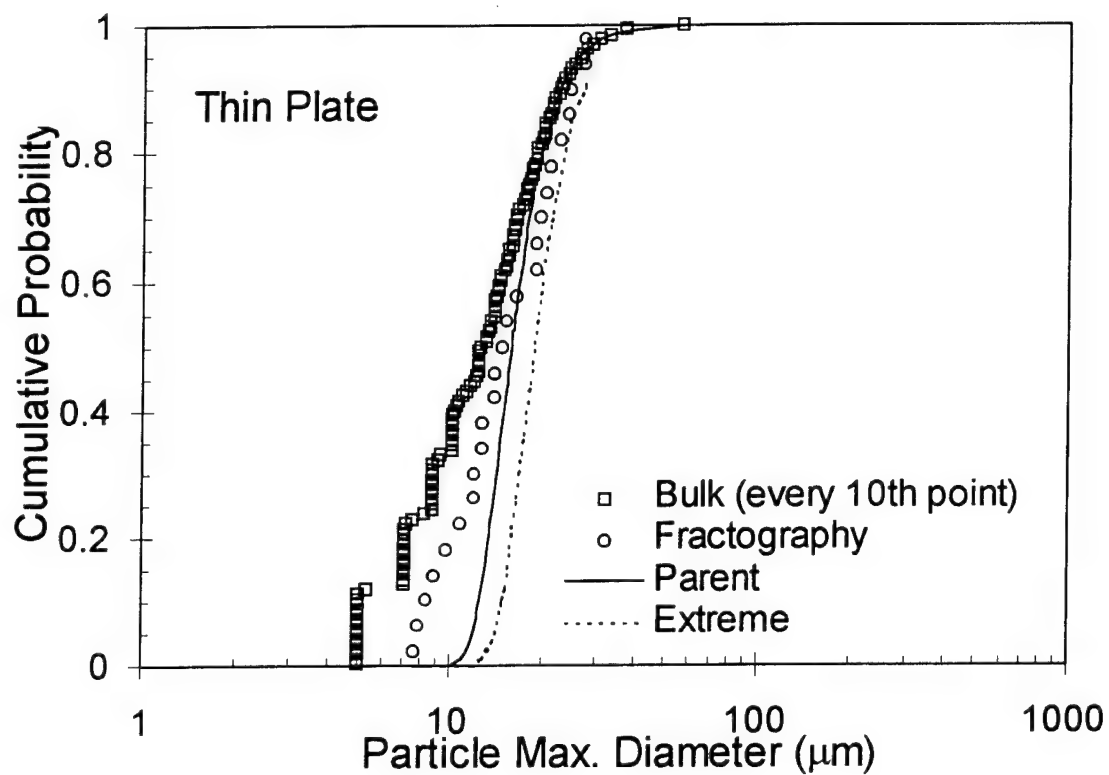
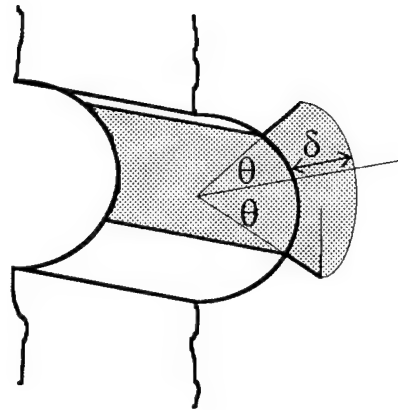


Figure 74. Thin plate 7050 alloy, open hole fatigue samples. Comparison of predicted (extreme) and actual (fractography) crack initiating particle size distributions. Predictions obtained from the parent fitted to the tail section of the bulk size data.

(a)



(b)

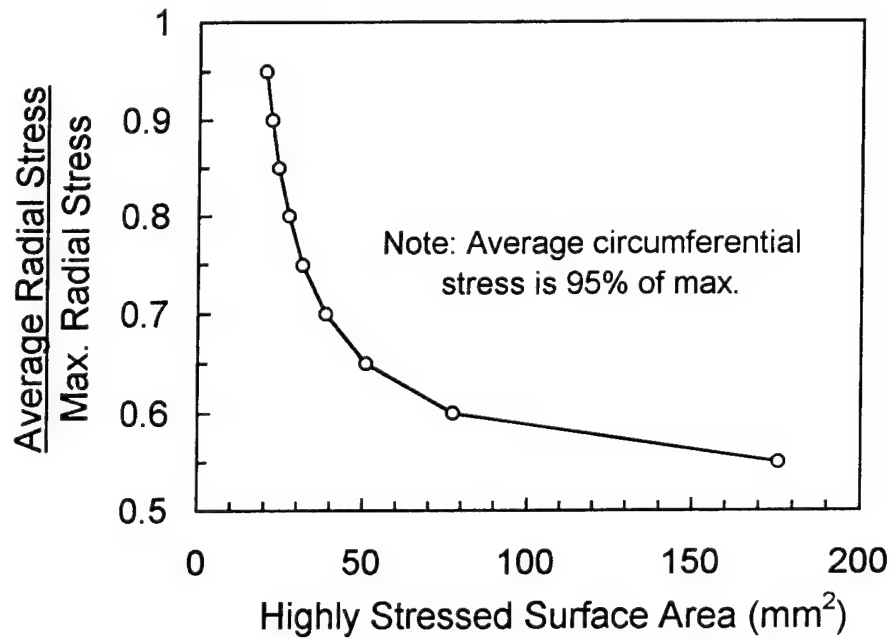


Figure 75. (a) Schematic showing highly stressed surface area extending by angle  $\theta$  circumferentially inside the hole and by  $\delta$  in the radial direction on the hole front and back surfaces. (b) Change of the average radial stress in the highly stressed area as a function of the area size - after Yang et al.[112]

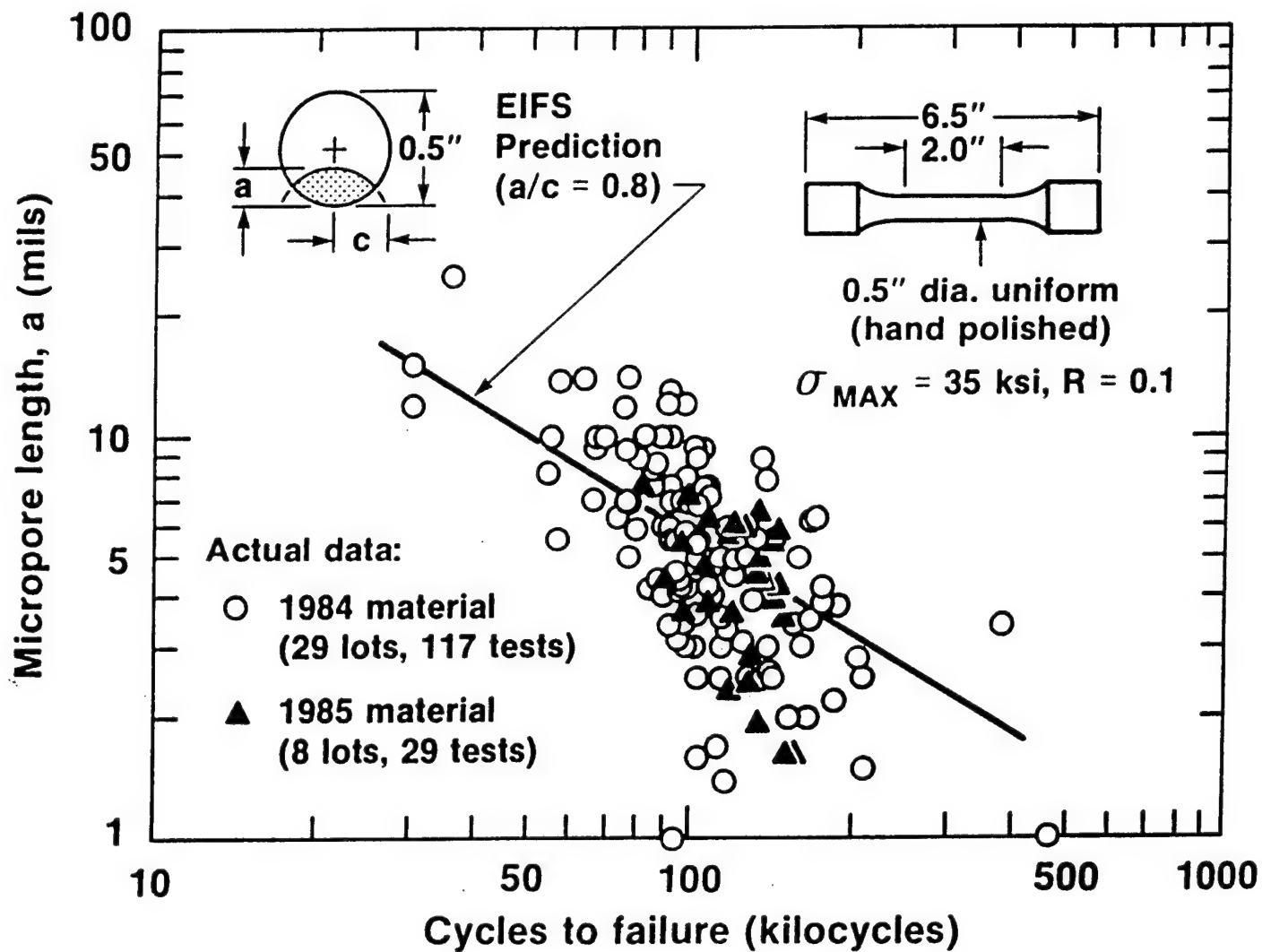


Figure 76. Correlation between fatigue lives and sizes of the fatigue crack initiating pores for 7050-T7451 alloys. Data compiled by Alcoa team.

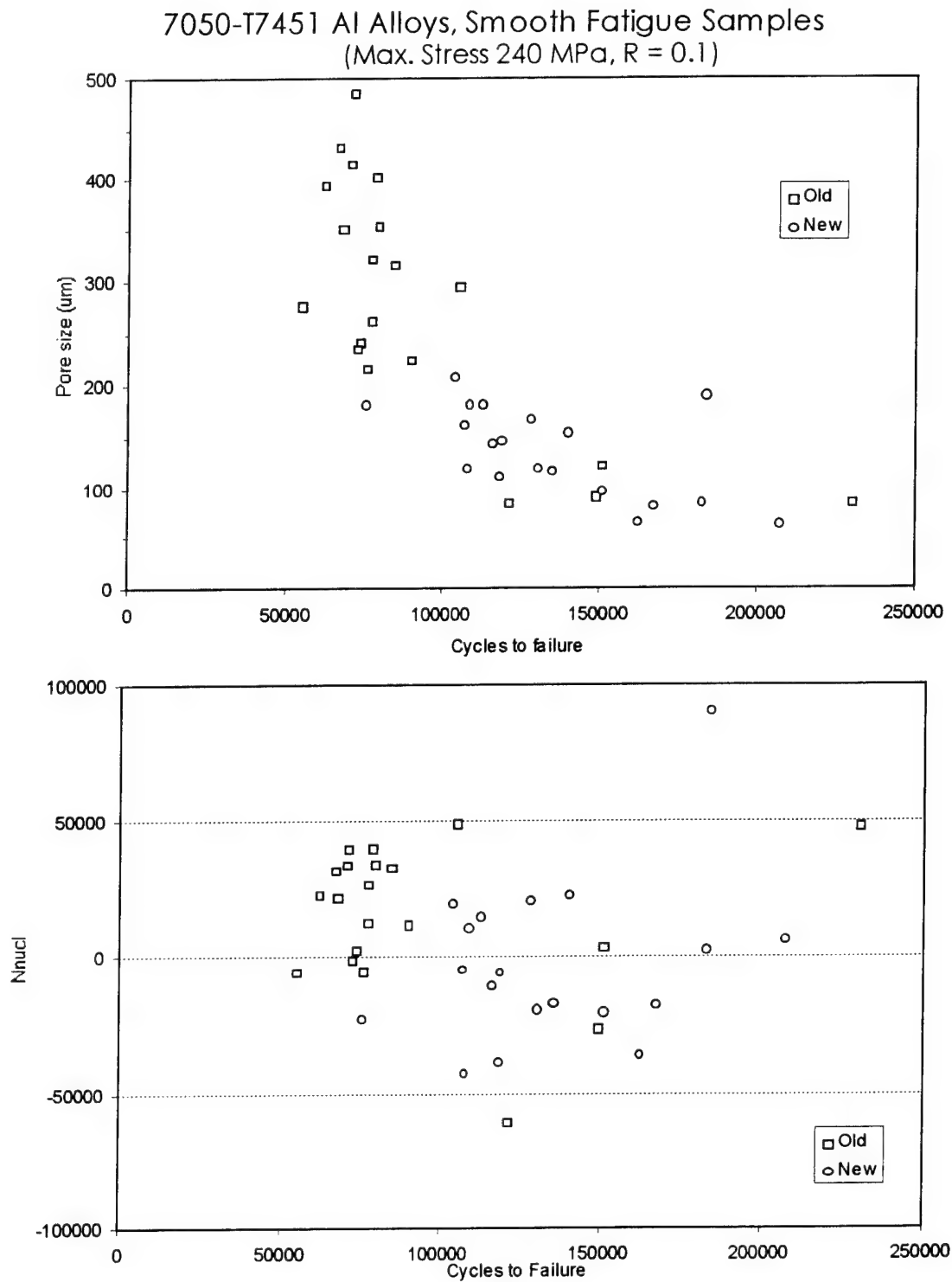
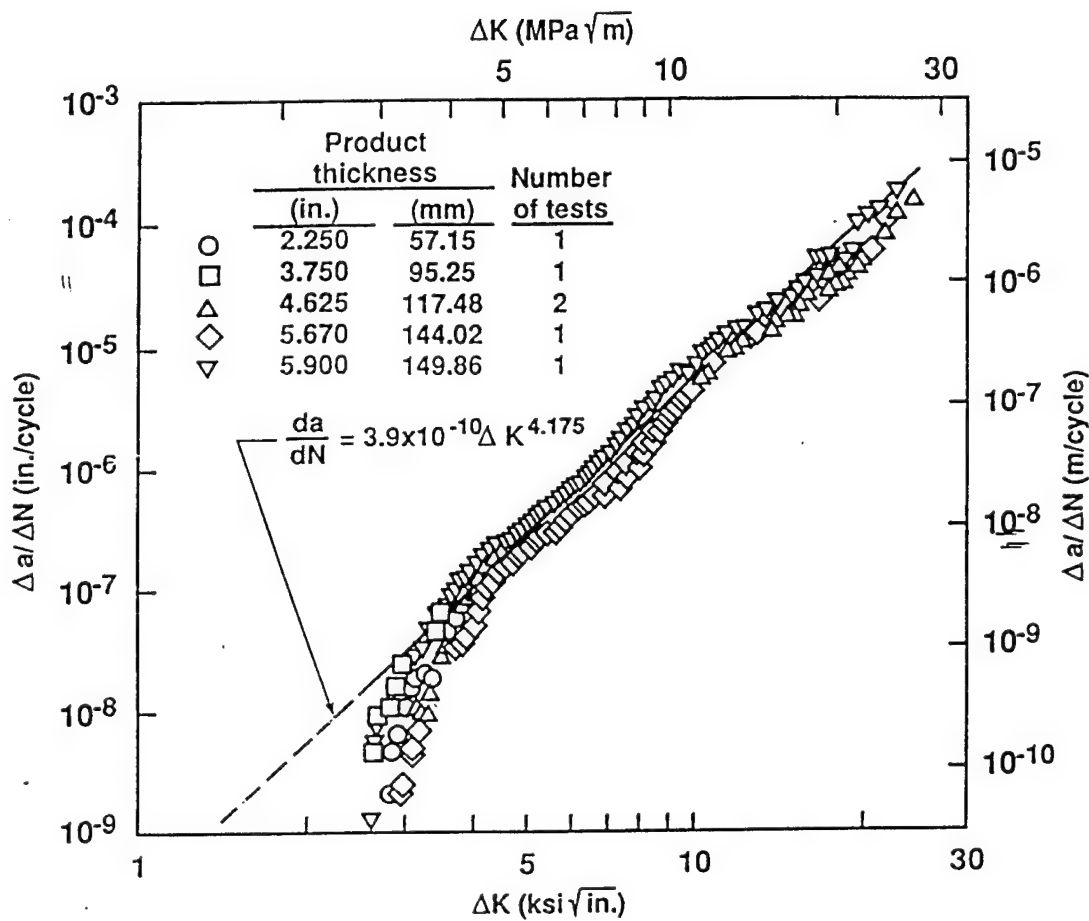


Figure 77. Correlation between fatigue life and (a) crack initiating pore sizes and (b) estimated numbers of crack nucleation cycles for new and old 7050-T7451 alloy. Smooth fatigue samples, LT orientation, center.



Fatigue Crack Growth Rates  
(T-L Orientation, R = 0.1, High Humidity Air)

Figure 78. Fatigue crack growth rate data for 7050-T7451 plate alloys. Data compiled by Alcoa team.

Nucleation Cycles  
7050 Al Alloys, Smooth Fatigue Samples  
(Max. Stress 240 MPa, R = 0.1)

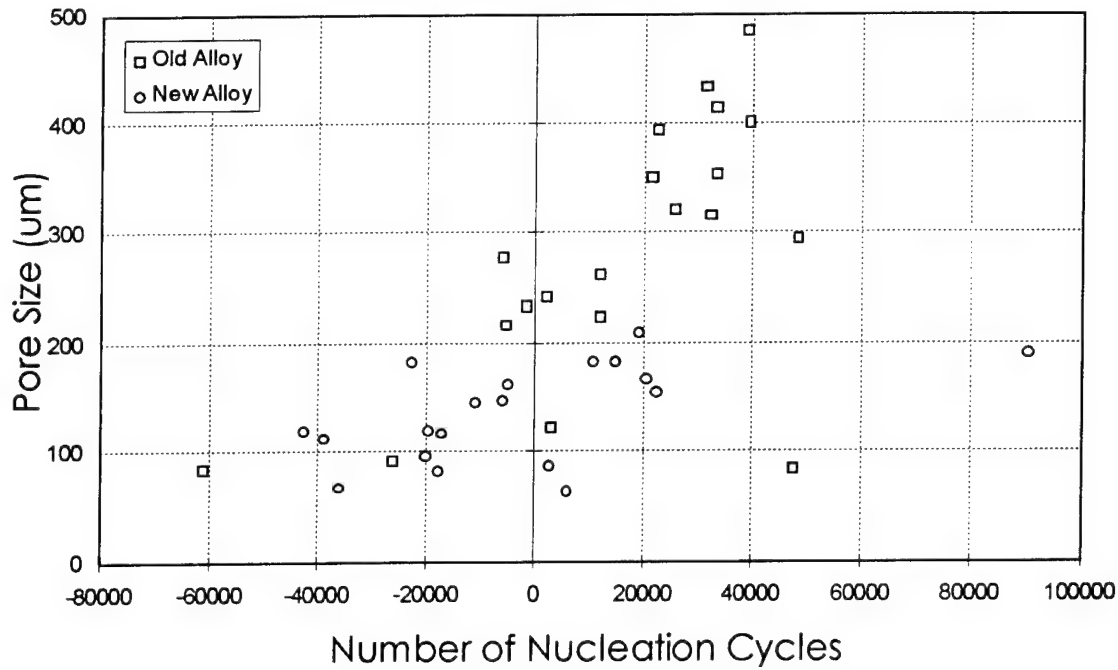


Figure 79. Correlation between estimated number of nucleation cycles and crack initiating pore sizes for the old and new 7050-T7451 plate alloys. Smooth fatigue samples, LT orientation, center.

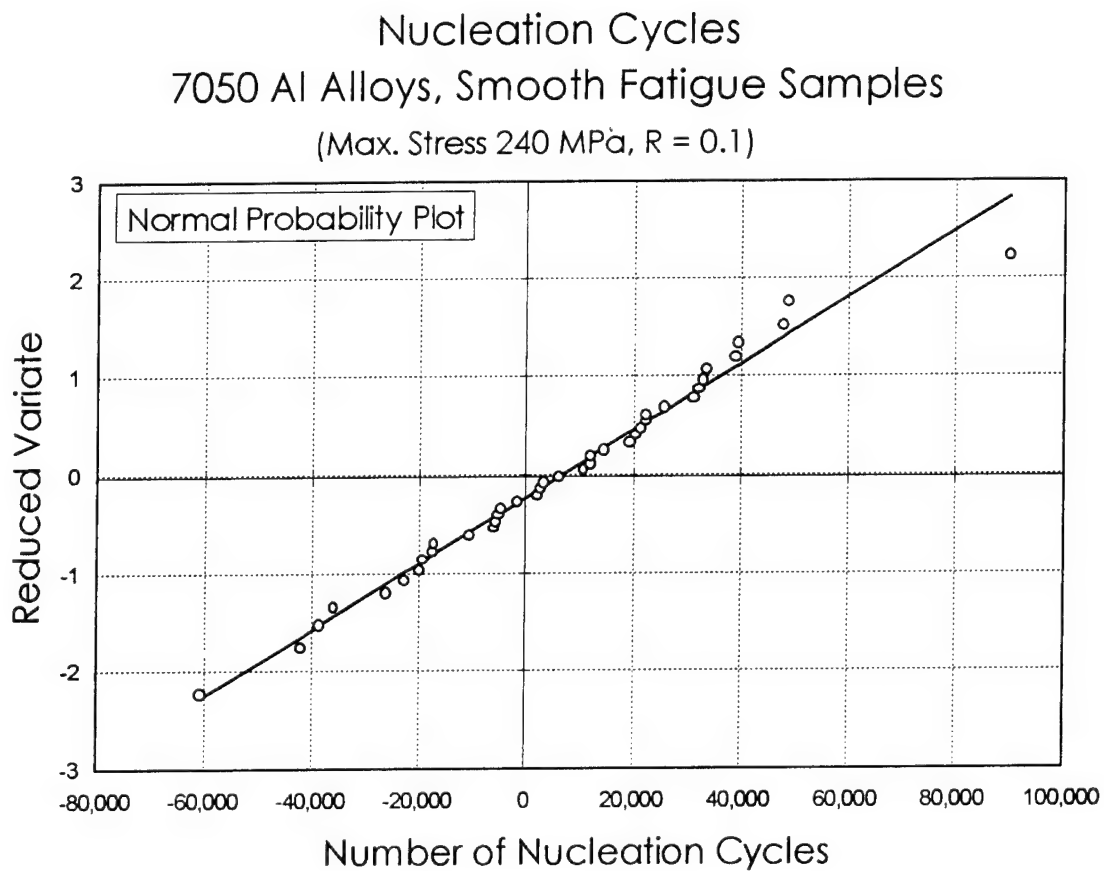
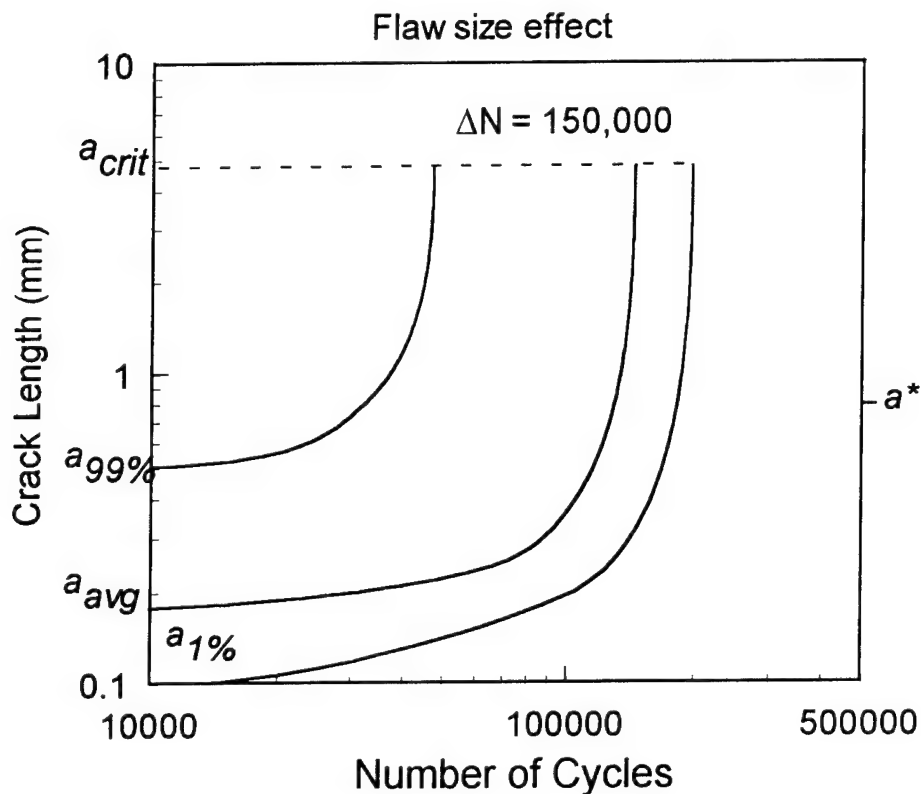


Figure 80. Normal cumulative probability plot for the estimated crack nucleation cycles for the old and new 7050-T7451 plate alloys. Smooth fatigue samples, LT orientation, center.

## Microstructural Effects on Fatigue Life

7050-T7451 New Plate Alloy, Smooth Samples,  $\sigma_{\max} = 241 \text{ MPa}$ ,  $R = 1$

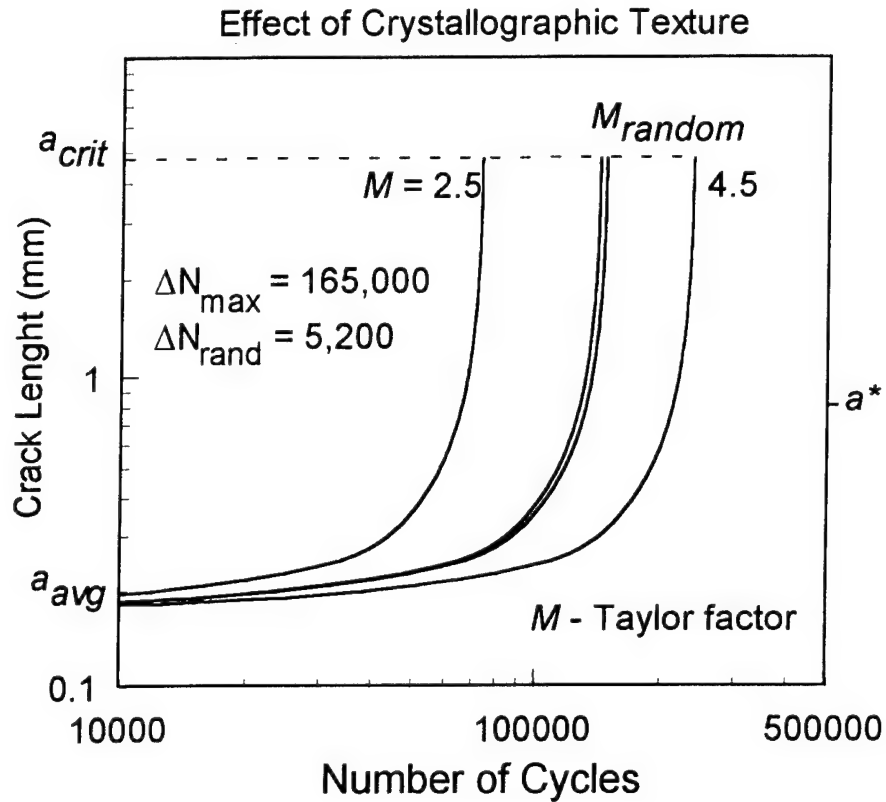


$a^*$  - crack size corresponding to the crack front length of the order of twenty five grains

Figure 81. Effect of the scatter in the fatigue crack initiating flaw sizes on the distribution of fatigue lives. Crack growth curves are for the predicted sizes of the crack initiating pores corresponding to the 1 and 99 percentiles of Gumbel extreme distribution. Smooth fatigue samples, new 7050-T7451 new alloy fatigued at  $\sigma_{\max} = 240 \text{ MPa}$  and  $R = 0.1$ .

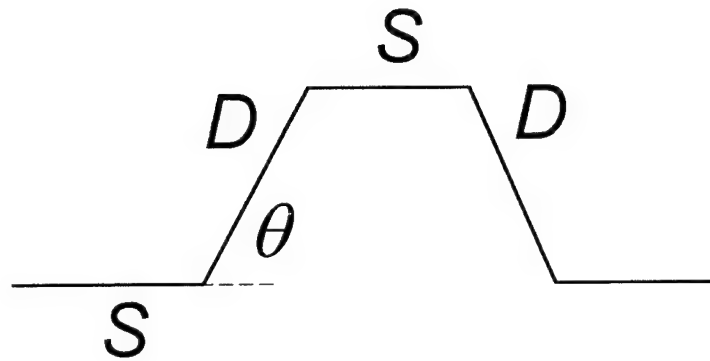
## Microstructural Effects on Fatigue Life

7050-T7451 New Plate Alloy, Smooth Samples,  $\sigma_{\max} = 241 \text{ MPa}$ ,  $R = 1$



$a^*$  - crack size corresponding to the crack front length of the order of twenty five grains

Figure 82. Effects of crystallographic texture on fatigue life. Crack growth curves for the maximum and minimum values of Taylor factor,  $M$ , expected in for the 7050 alloys. Random curve corresponds to random variations of texture on the crack path. Smooth fatigue samples fatigued at  $\sigma_{\max} = 240 \text{ MPa}$  and  $R = 0.1$ .



$$\mathcal{D}' = \frac{D}{D + S}$$

$\mathcal{D}'$  - from roughness data, grain sizes, particle spatial distribution

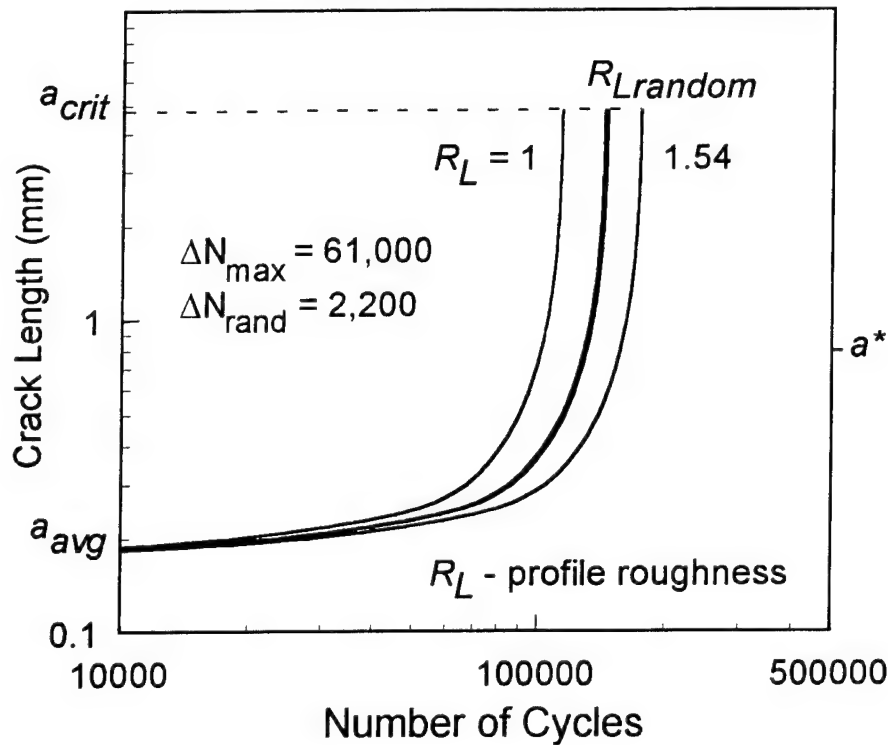
$\theta$  - from crack profiles, particle and boundary arrangements

Figure 83. Idealized crack profile assumed for modeling microstructural crack deflections.

## Microstructural Effects on Fatigue Life

7050-T7451 New Plate Alloy, Smooth Samples,  $\sigma_{\max} = 241 \text{ MPa}$ ,  $R = 1$

### Effect of Crack Deflections



$a^*$  - crack size corresponding to the crack front length of the order of twenty five grains

Figure 84. Effects of microstructural crack deflections on fatigue life. Crack growth curves for the maximum and minimum values of crack deflection coefficient,  $R$ , expected for the 7050 alloys. Random curve corresponds to random variations of texture on the crack path. Smooth fatigue samples fatigued at  $\sigma_{\max} = 240 \text{ MPa}$  and  $R = 0.1$ .

## New 7050-T7451 Plate Alloys Smooth Fatigue Samples

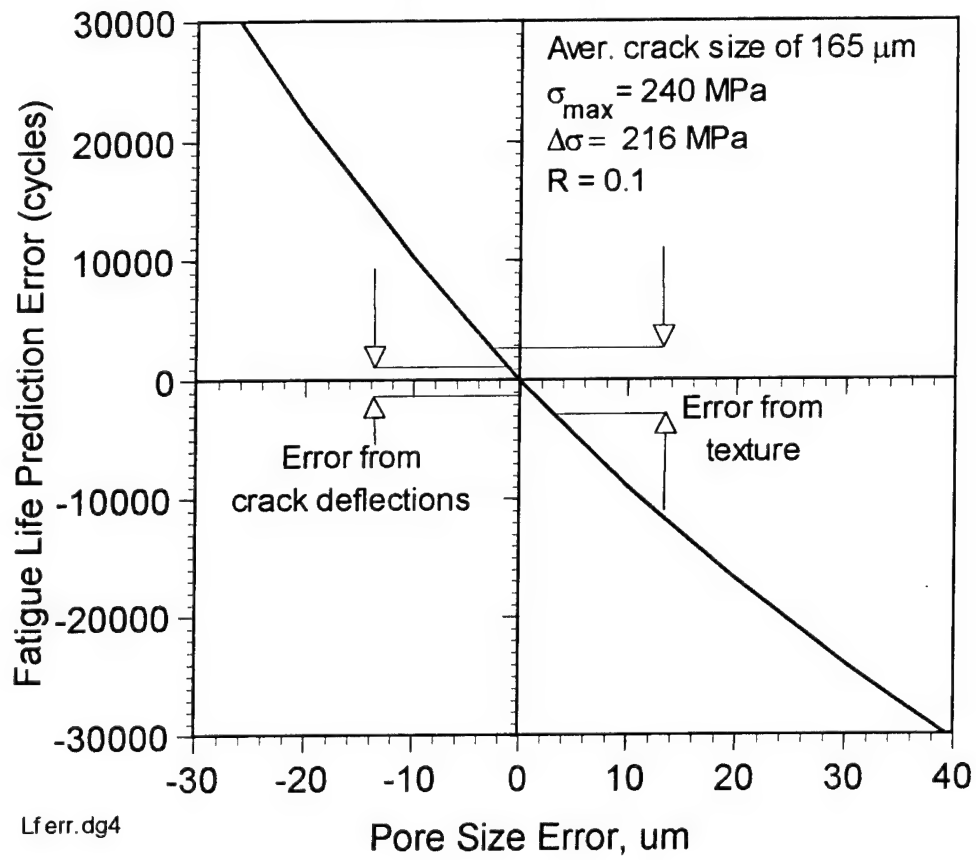
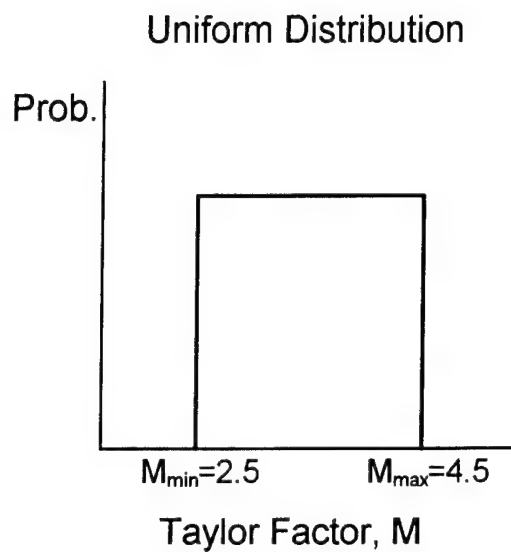
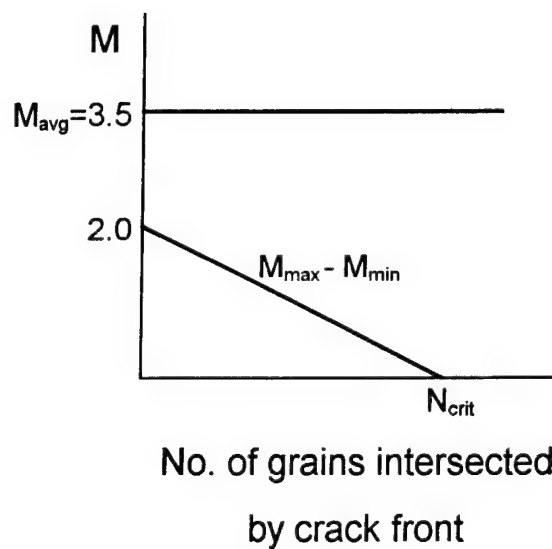


Figure 85. Relation between the error of the estimated initial crack sizes and the error in predicted fatigue lives for the new 7050-T7451 plate alloy.



(a)



(b)

Figure 86. Schematic showing (a) shape of the uniform Taylor factor distribution and (b) change of the distribution range with the number of grains at the crack tip assumed during Monte-Carlo simulations.

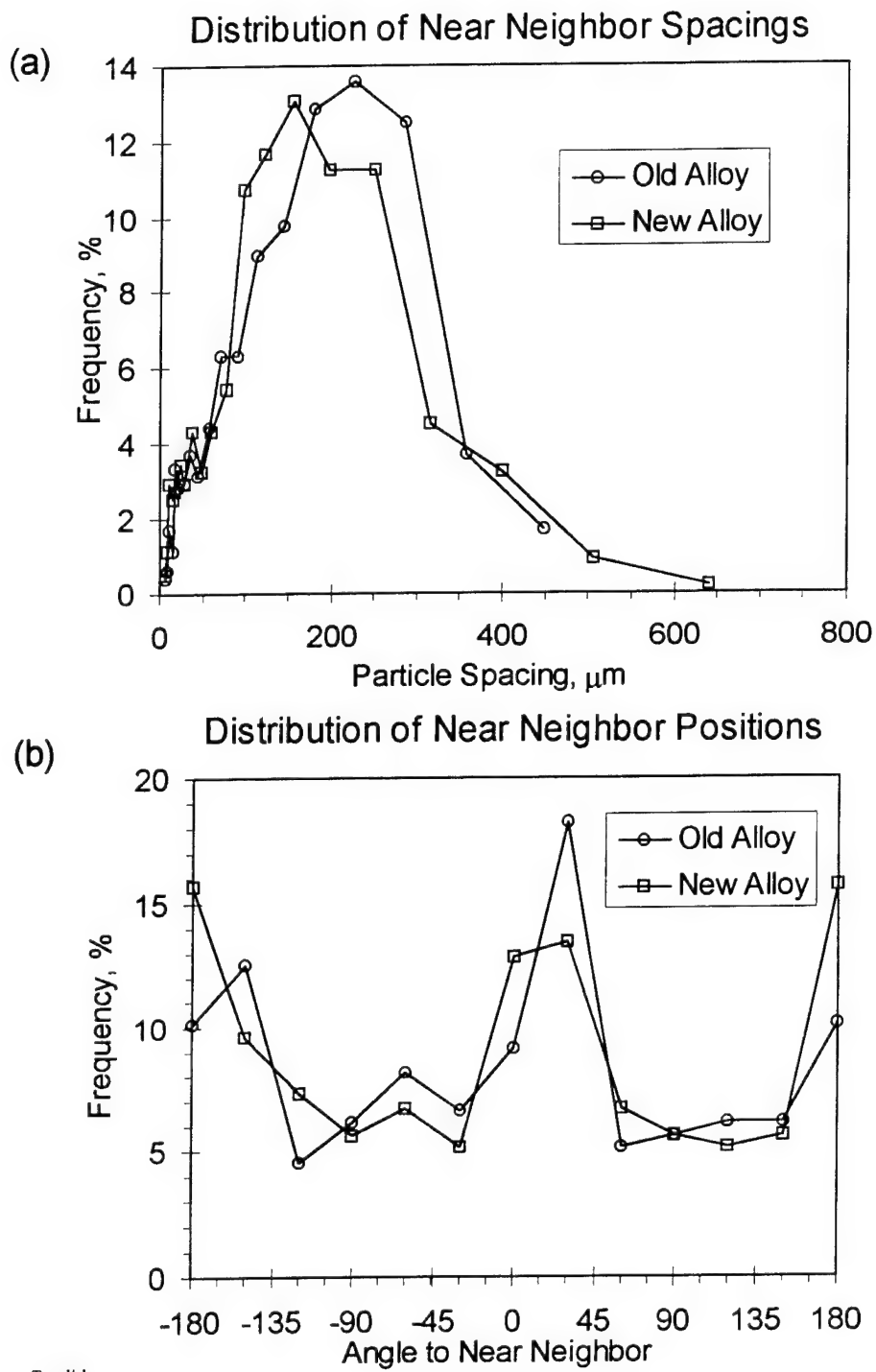


Figure 87. Examples of data on (a) distribution of near neighbor spacings and (b) distribution of near neighbor positions obtained from the tessellation analysis. 7050-T7451 plate alloys, constituent particles, LS plane, plate center.

Old 7050-T7451 Plate Alloy  
Smooth fatigue samples,  $R = 0.1$ , 10 Hz

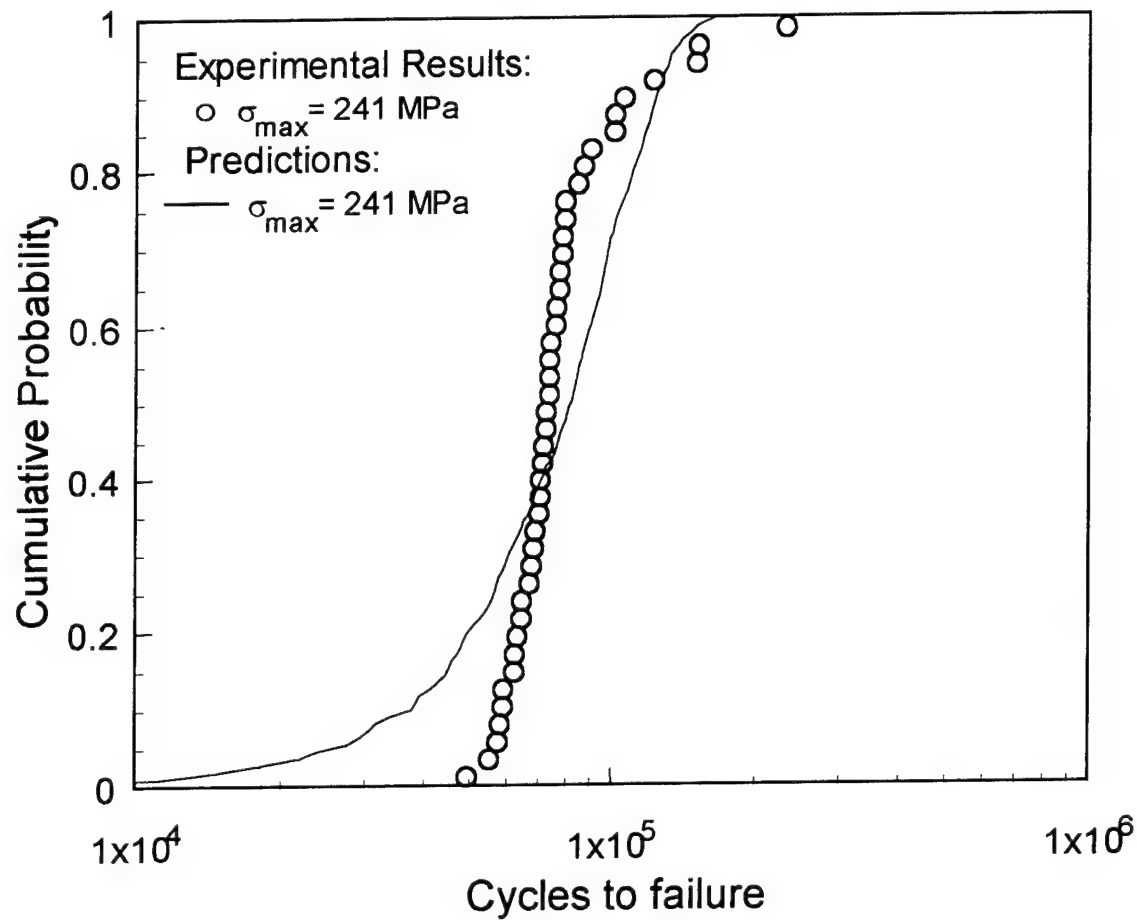


Figure 88. Comparison of the distributions of fatigue lives predicted using Monte-Carlo model with experimental data for smooth fatigue samples, old 7050-T7451 plate alloy.

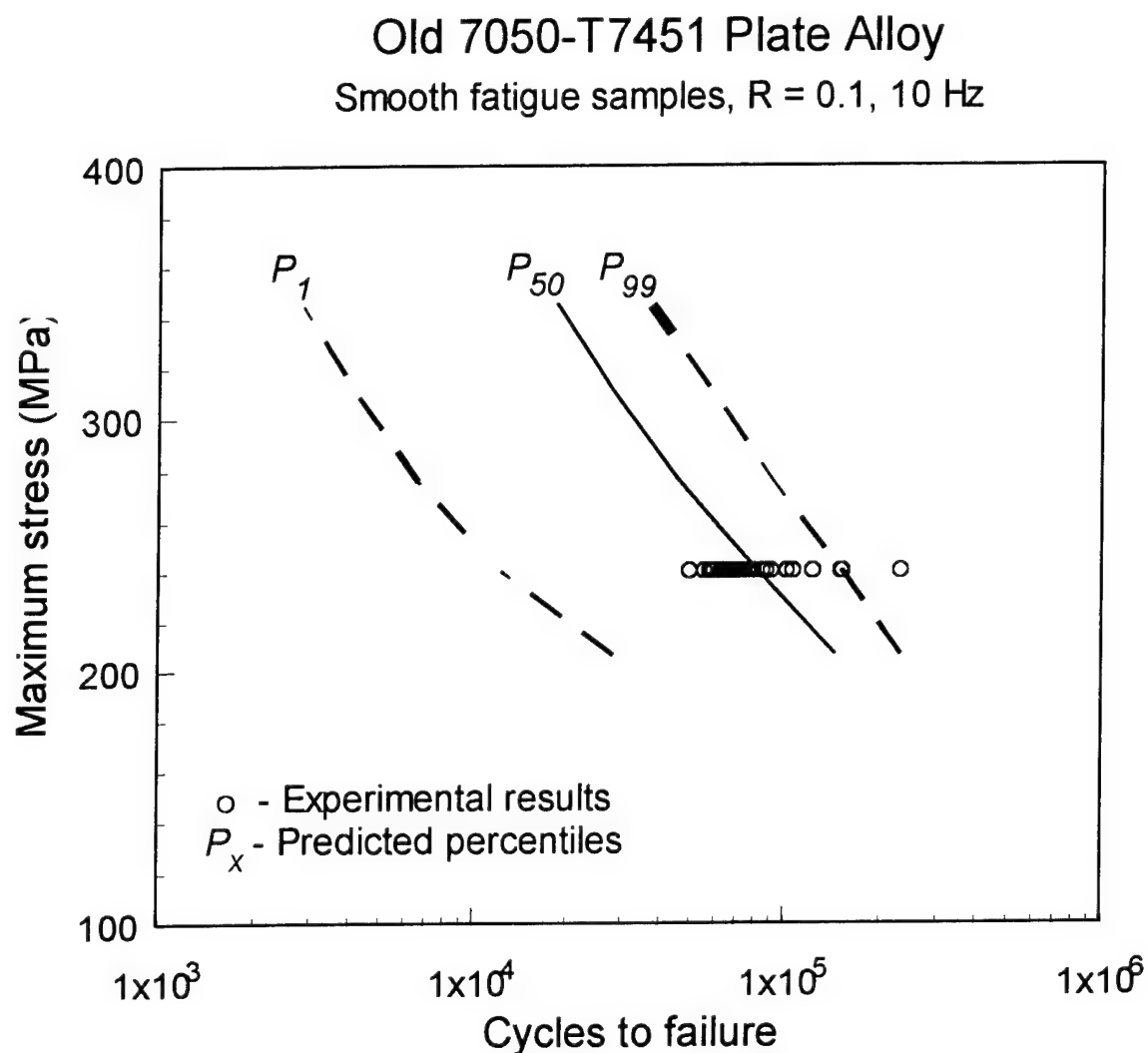


Figure 89. Comparison of the S-N fatigue curves obtained from the Monte-Carlo fatigue life predictions with experimental data for the open hole fatigue samples, old 7050-745 plate alloy

# New 7050-T7451 Plate Alloy

Smooth fatigue samples,  $R = 0.1$ , 10 Hz

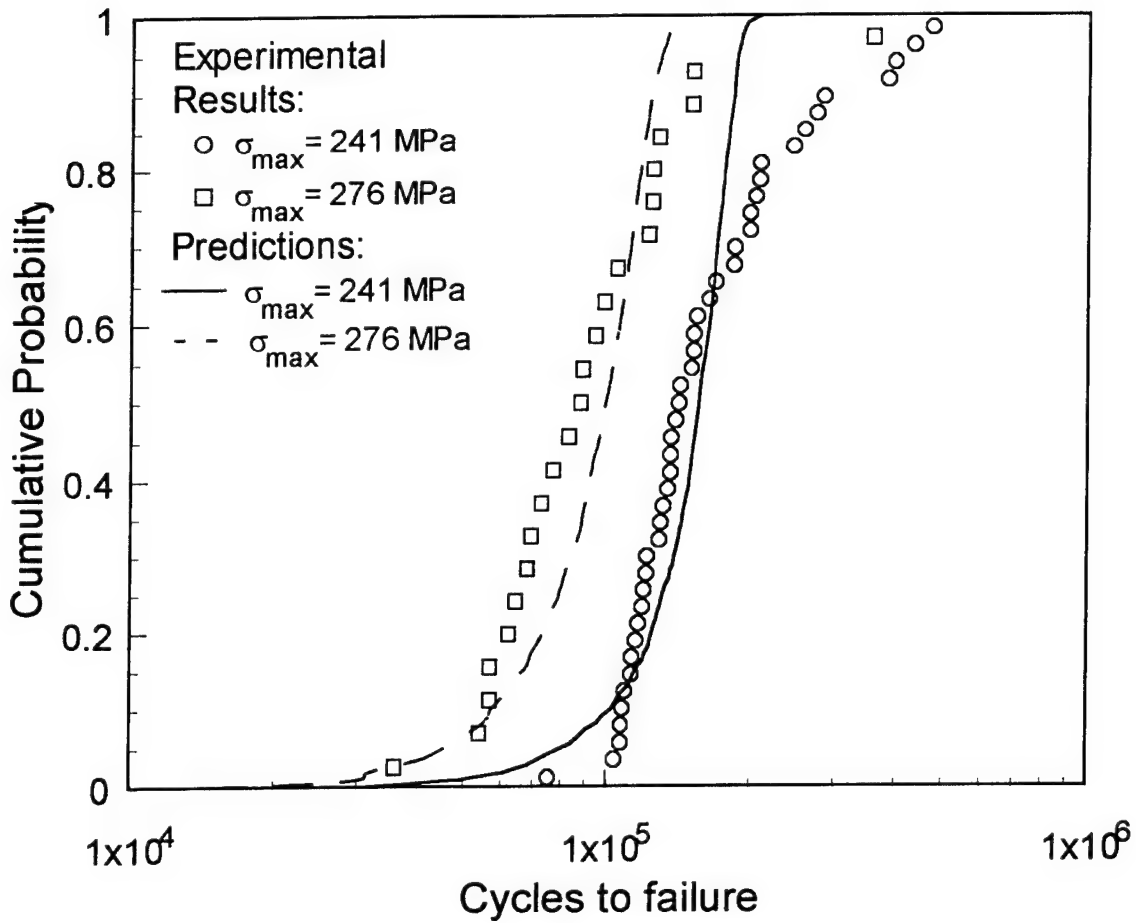


Figure 90. Comparison of the distributions of fatigue lives predicted using Monte-Carlo model with experimental data for smooth fatigue samples, new 7050-T7451 plate alloy.

# New 7050-T7451 Plate Alloy Smooth fatigue samples, $R = 0.1$ , 10 Hz

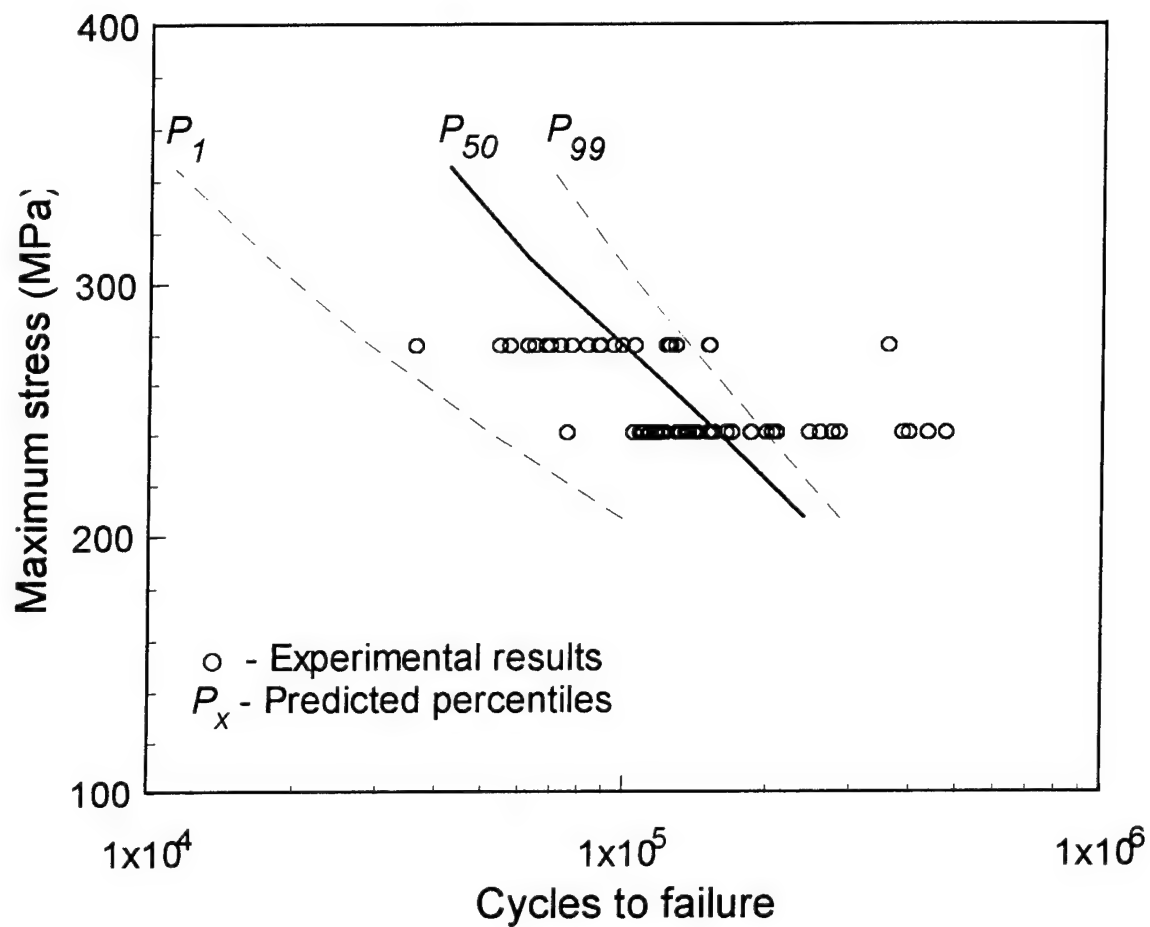


Figure 91. Comparison of the S-N fatigue curves obtained from the Monte-Carlo fatigue life predictions with experimental data for the open hole fatigue samples, new 7050-T7451 plate alloy.

## Low Porosity 7050-T7451 Plate Alloy

Smooth fatigue samples,  $R = 0.1$ , 10 Hz

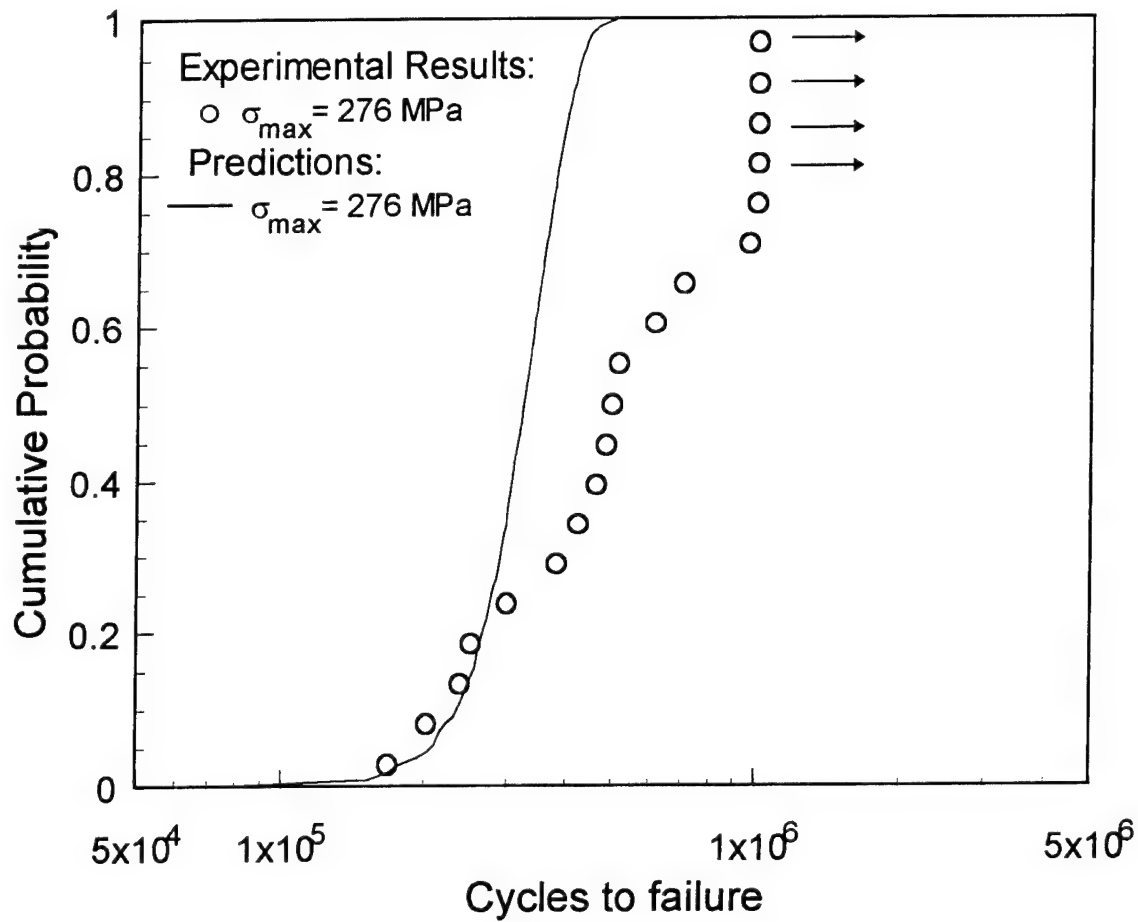


Figure 92. Comparison of the distributions of fatigue lives predicted using Monte-Carlo model with experimental data for smooth fatigue samples, low porosity 7050-T7451 plate alloy.

## Low Porosity 7050-T7451 Plate Alloy

Smooth fatigue samples,  $R = 0.1$ , 10 Hz

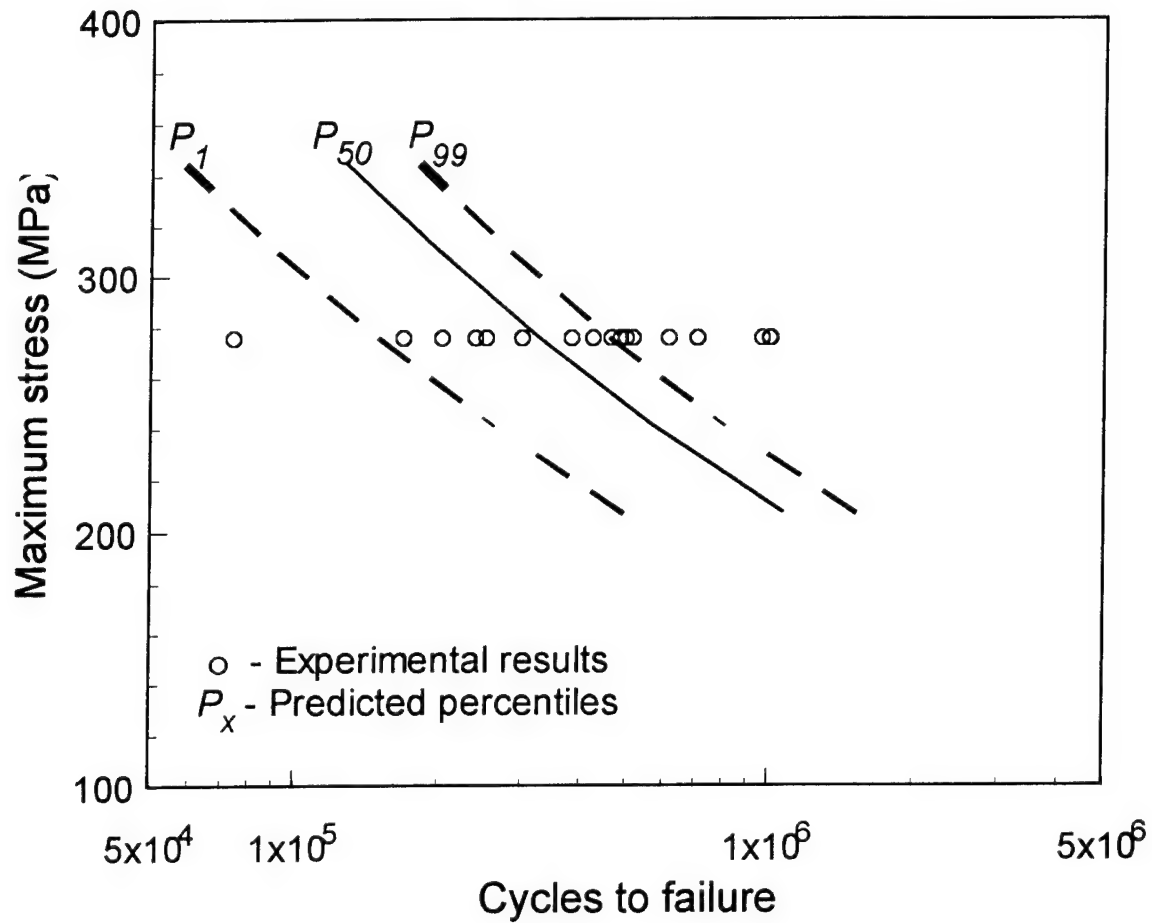


Figure 93. Comparison of the S-N fatigue curves obtained from the Monte-Carlo fatigue life predictions with experimental data for the open hole fatigue samples, low porosity 7050-T7451 plate alloy.

7050-T7451 Old Quality Alloy  
Open Hole Samples, 30 Hz, R = 0.1, LT Orientation

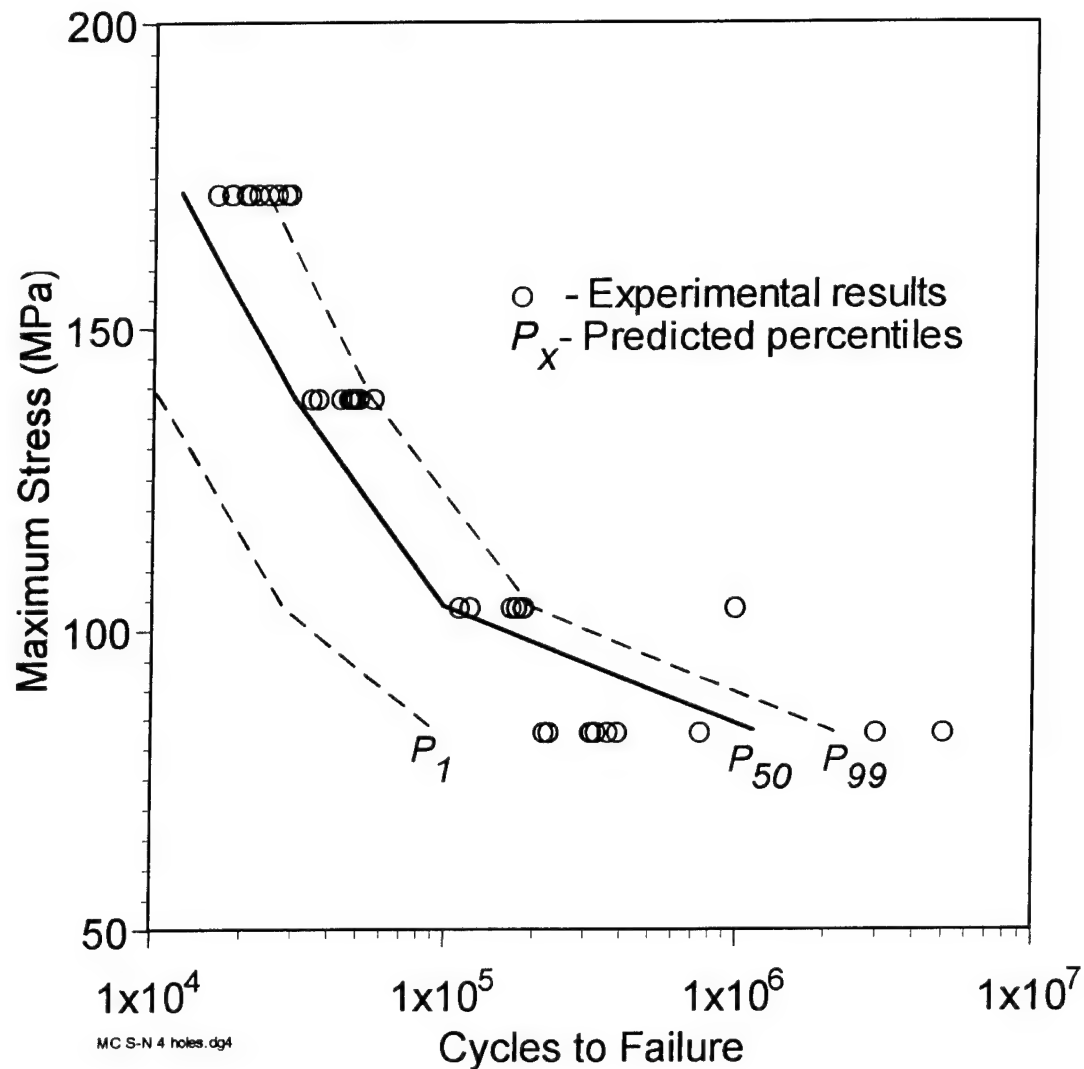


Figure 94. Comparison of the S-N fatigue curves obtained from the Monte-Carlo fatigue life predictions with experimental data for the open hole fatigue samples, old 7050-T7451 plate alloy.

7050-T7451 New Quality Alloy  
Open Hole Samples, 30 Hz, R = 0.1, LT Orientation

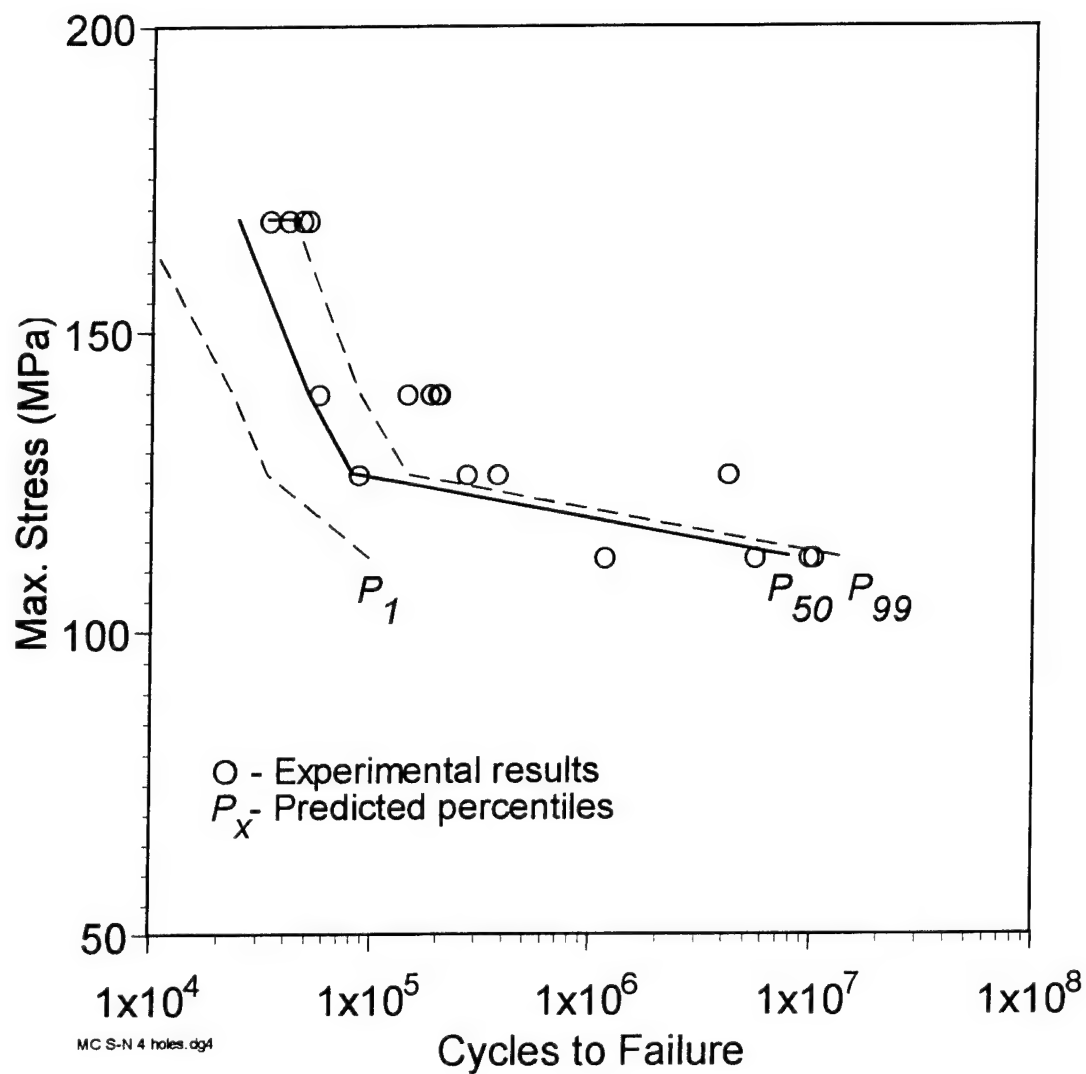


Figure 95. Comparison of the S-N fatigue curves obtained from the Monte-Carlo fatigue life predictions with experimental data for the open hole fatigue samples, new 7050-T7451 plate alloy.

7050-T7451 Low Porosity Plate Alloy  
Open Hole Samples, 30 Hz, R = 0.1, LT Orientation

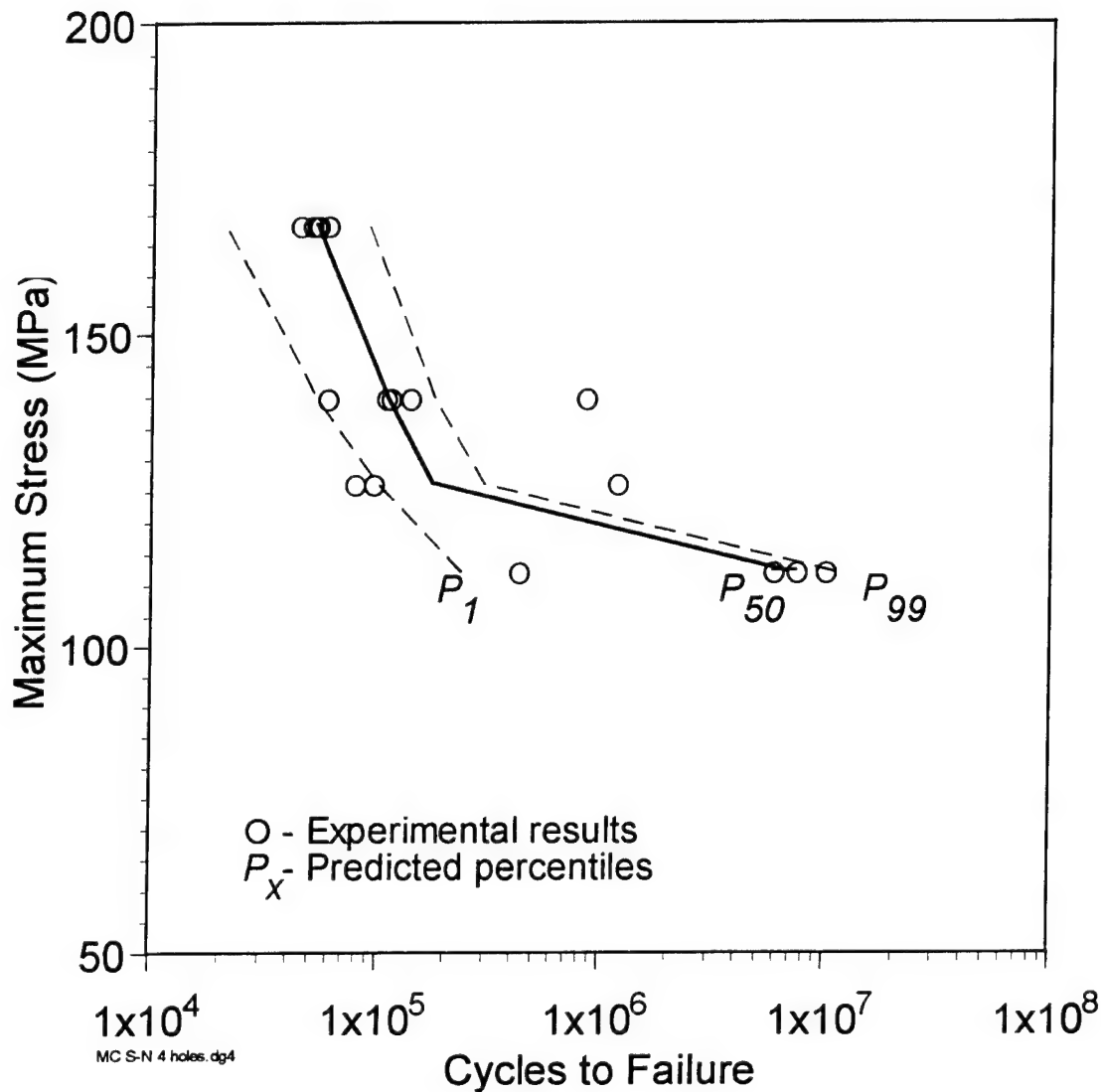


Figure 96. Comparison of the S-N fatigue curves obtained from the Monte-Carlo fatigue life predictions with experimental data for the open hole fatigue samples, low porosity 7050-T7451 plate alloy.

# 7050-T7451 Thin Plate Alloy Open Hole Samples, 30 Hz, R = 0.1, LT Orientation

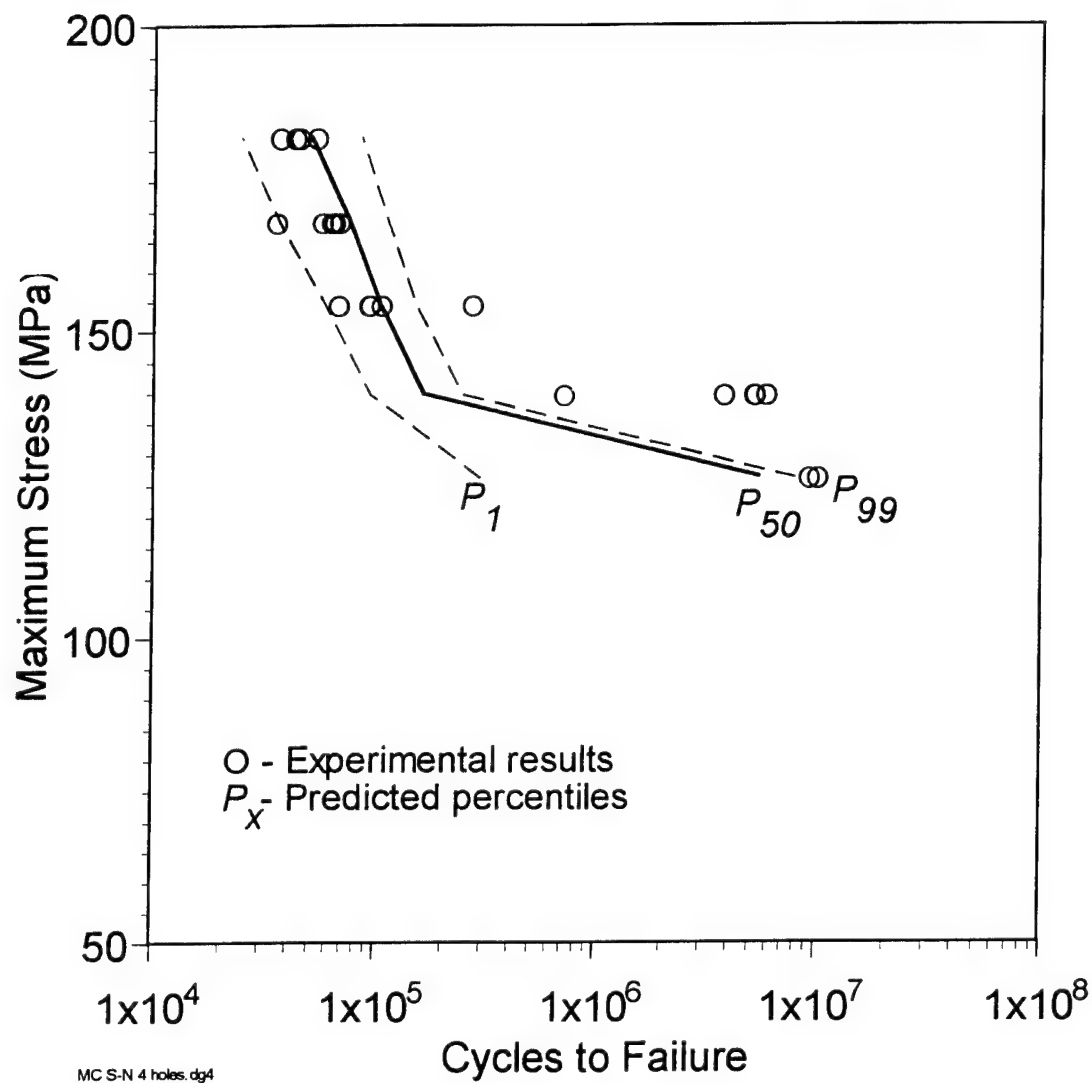
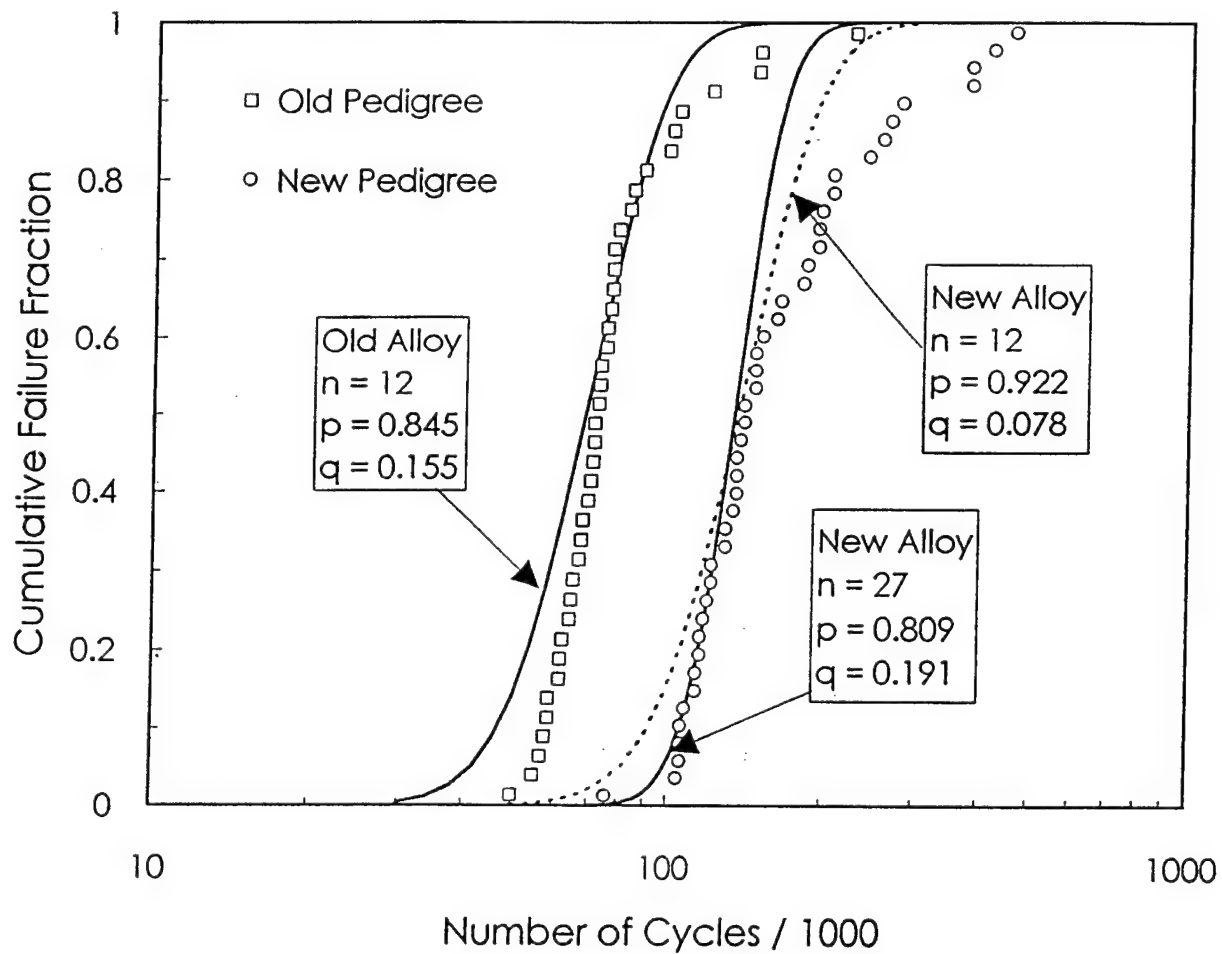


Figure 97. Comparison of the S-N fatigue curves obtained from the Monte-Carlo fatigue life predictions with experimental data for the open hole fatigue samples, thin plate 7050-T7451 alloy.

## Cumulative Fatigue Failure Distribution 7050 Alloy, Markov B-Models



Probability Vector  $v = (1, 0, 0, \dots)$

Figure 98 . Comparison of the fatigue data for old and new 7050 alloys with the predictions from the Markov B-model.  $\sigma_{\max}=240$  MPa,  $R = 0.1$ ,  $n$  is the size of the transition matrix,  $p$  is probability that crack does not grow during one duty cycle.

## Cumulative Fatigue Failure Distribution 7050 Alloy, Markov B-Model

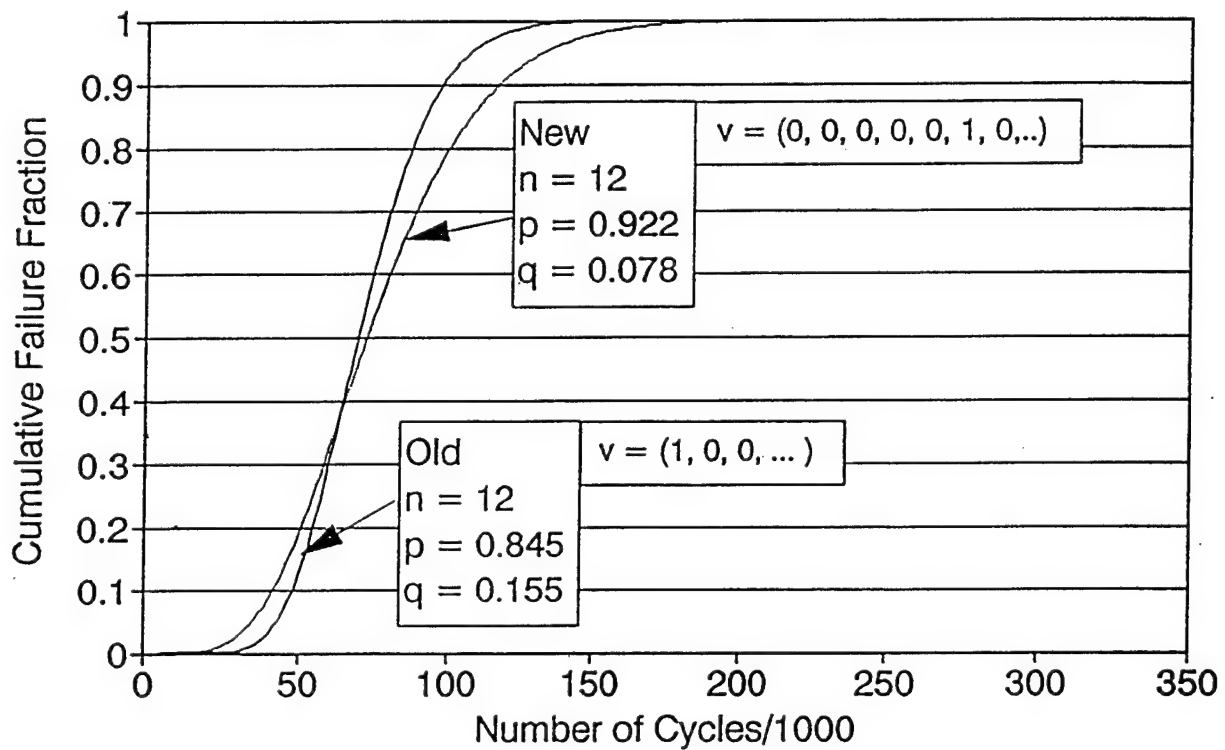


Figure 99 . Results of the simulation of the effect of the increase of the initial crack length on the Markov chain model prediction. Notation and loading the same as on the previous figure.

## Fatigue Failure Distribution 7050 Alloy, Markov B-Model

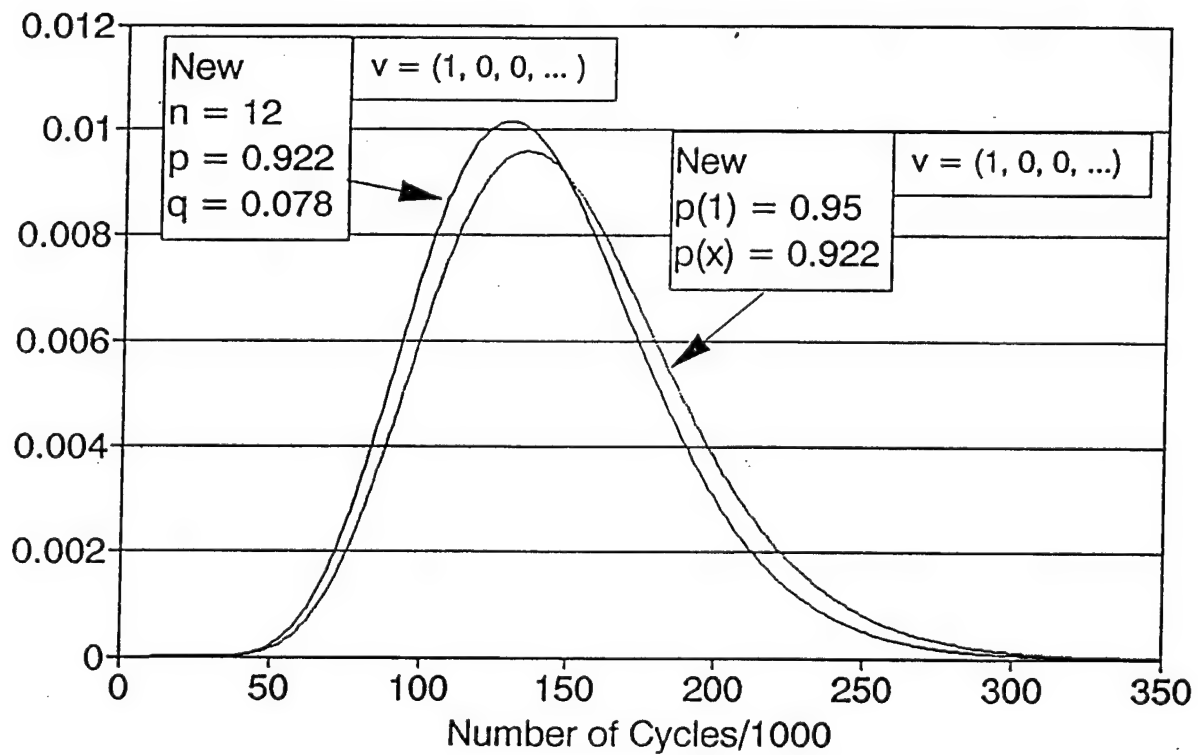


Figure 100 Effect of the change of the probability  $p$  in the first row of the transition matrix on the distribution of the fatigue life predicted by the Markov B-model.

# Fatigue Failure Distribution 7050 Alloy, Markov B-Model

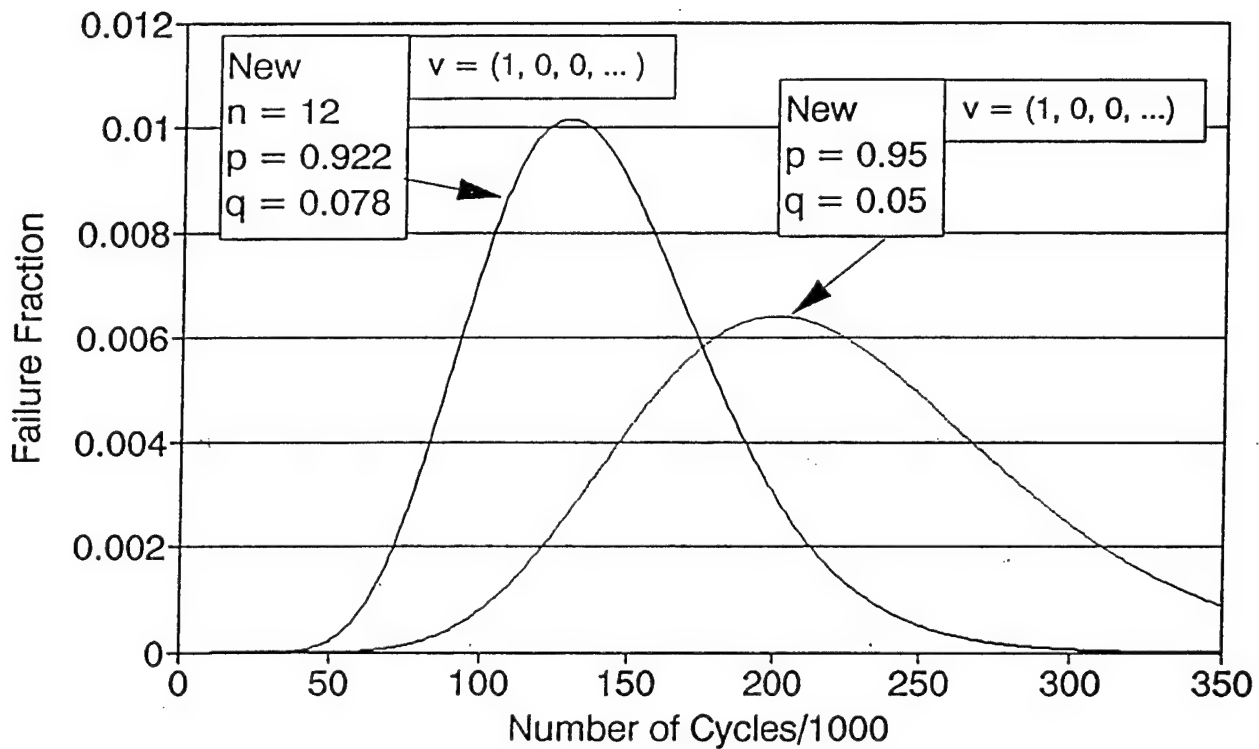


Figure 101 Effect of the change of all p-values in the entire transition matrix on the distribution of the fatigue life predicted by the Markov B-model.

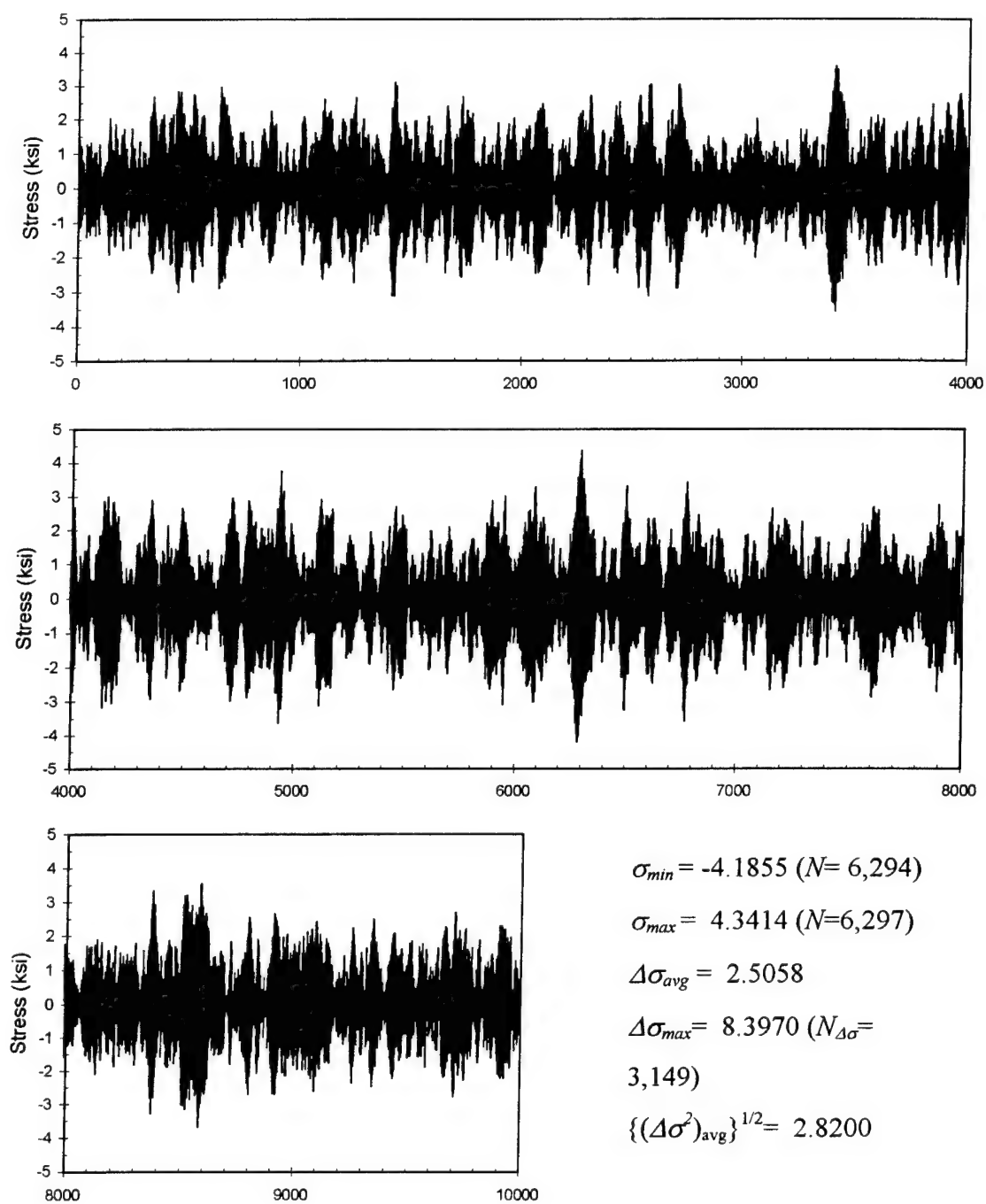
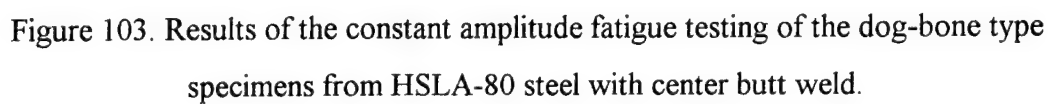


Figure 102. Unit *RMS* loading spectrum used in all variable amplitude fatigue testing of the HSLA-80 steel weldments.



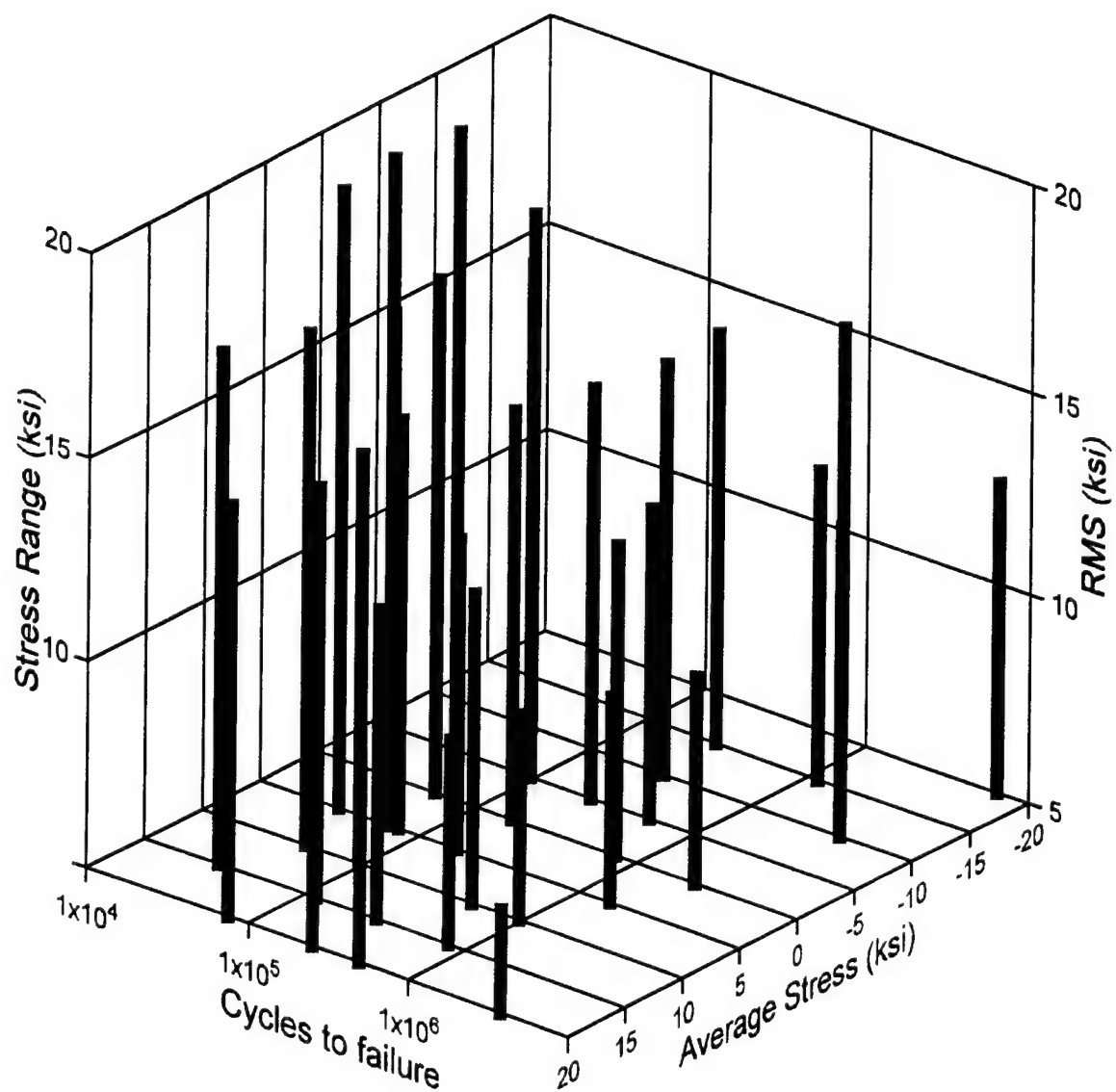


Figure 104. Results of the variable amplitude fatigue testing of the dog-bone type specimens from HSLA-80 steel with center butt weld.

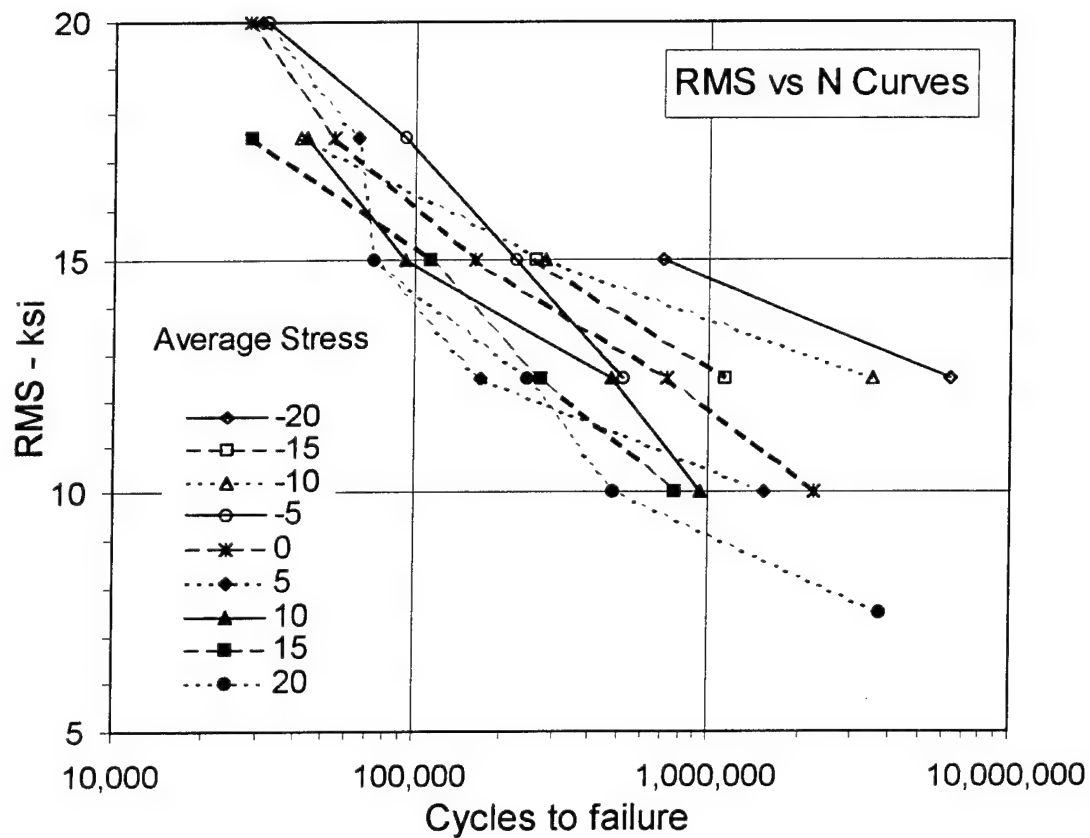


Figure 105. Fatigue curves for constant average stresses for the dog-bone specimens from HSLA-80 steel with center butt weld tested under variable loading conditions. The *RMS* values represent the multiplication factors applied to the unit spectrum loading shown in Figure 98 and  $\langle \Delta \sigma \rangle = 2.5058 \cdot RMS$ .

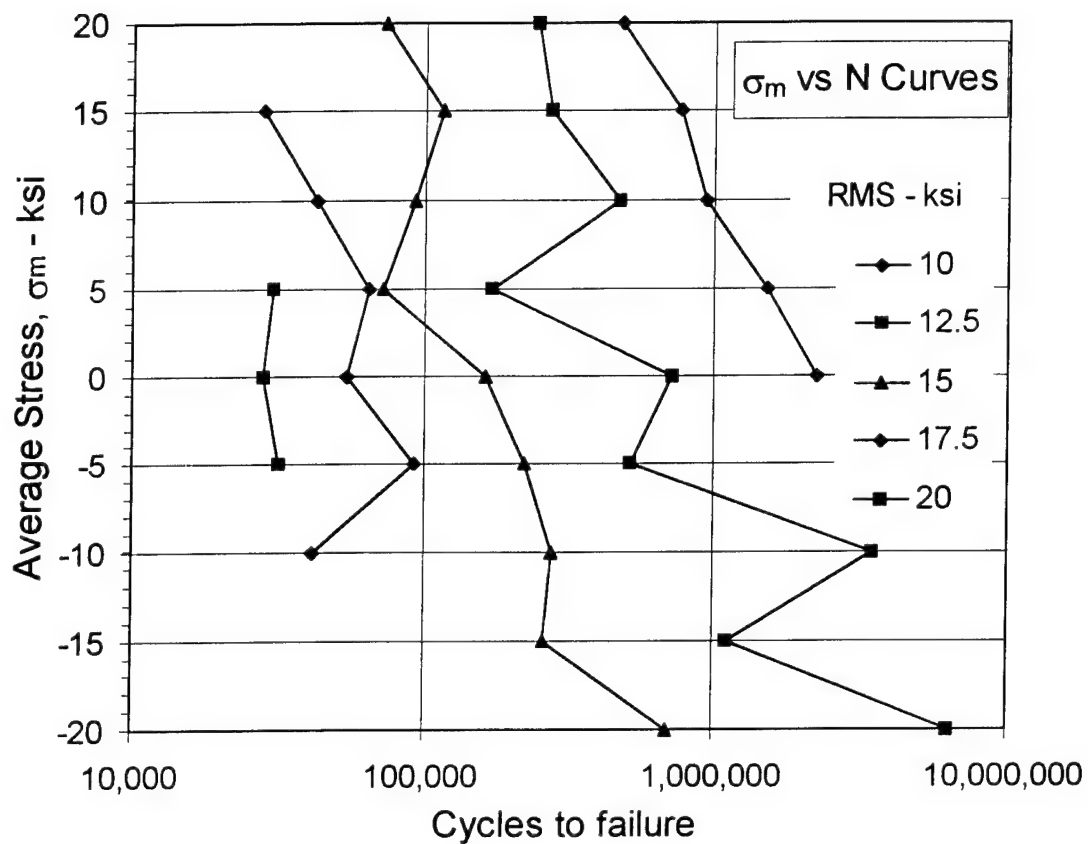
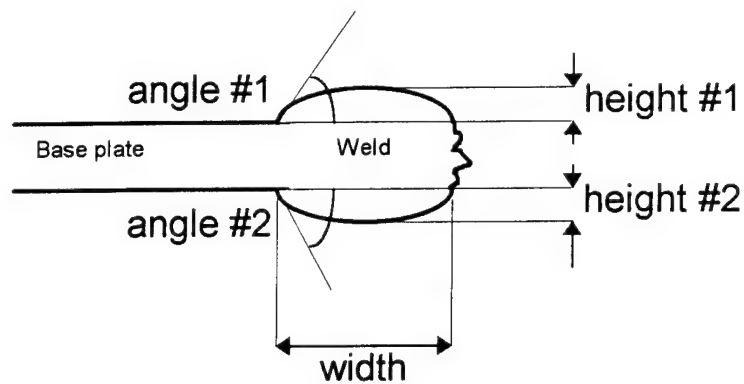


Figure 106. Fatigue curves for constant *RMS* stresses for the dog-bone specimens from HSLA-80 steel with center butt weld tested under variable loading conditions. The *RMS* values represent the multiplication factors applied to the unit spectrum loading shown in Figure 98 and  $\langle \Delta \sigma \rangle = 2.5058 \cdot RMS$ .

(a)



(b)

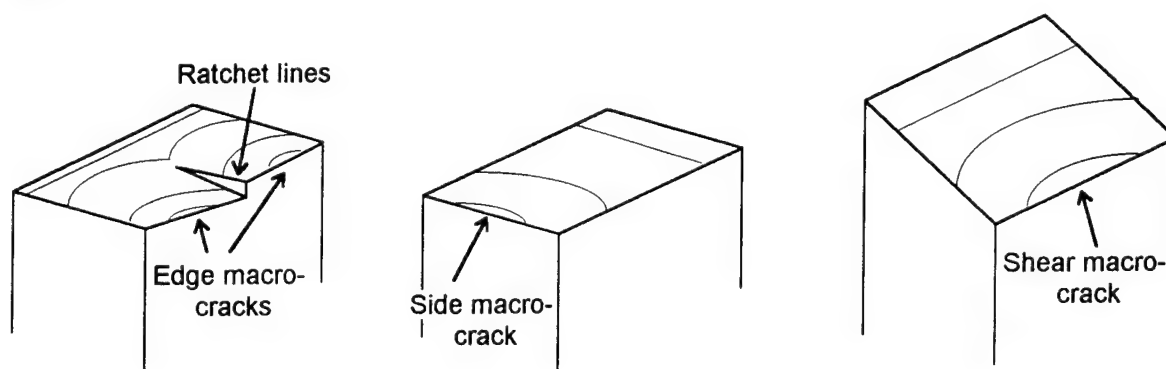


Figure 107. Schematics showing (a) geometrical parameters used for characterizing reinforcement and (b) crack types observed in the HSLA-80 weldments.

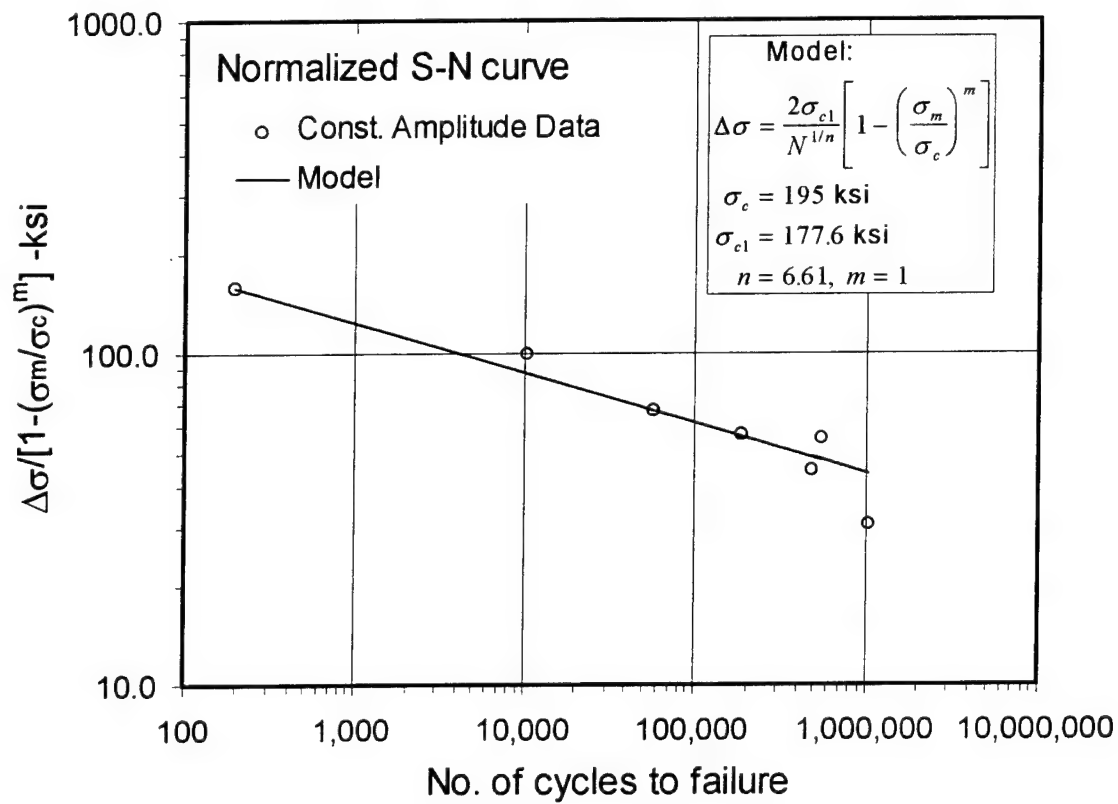


Figure 108. Normalized S-N curve illustrating goodness of fit of the model to the constant amplitude fatigue data for HSLA-80 weldments.

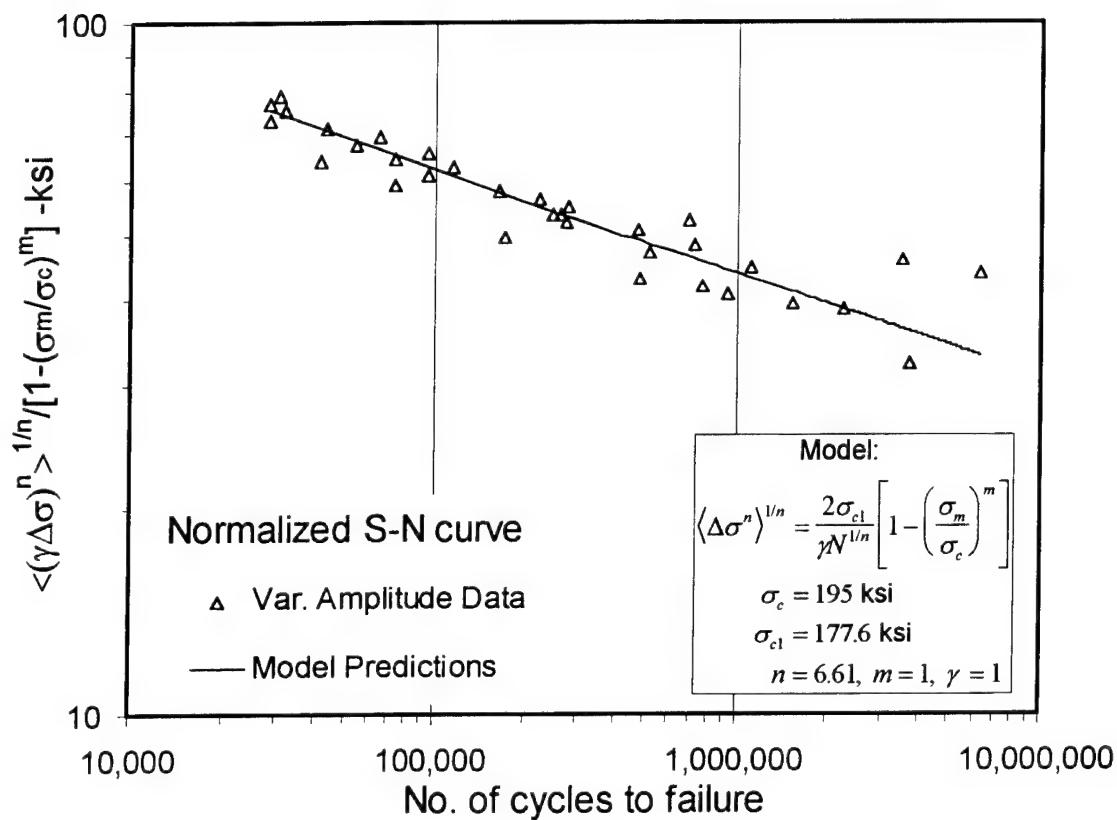


Figure 109. Normalized S-N curve showing comparison of the predictions with the experimental random fatigue data for HSLA-80 weldments. The model parameters estimated from the constant amplitude data.

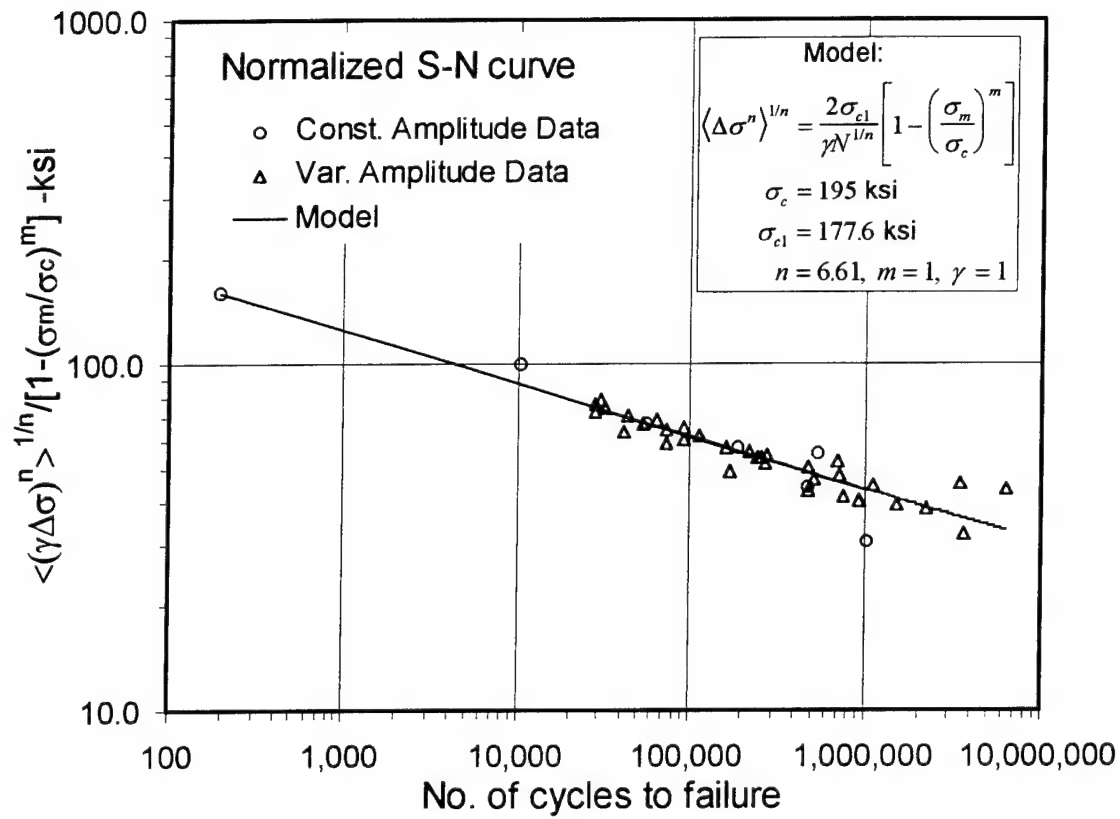


Figure 110. Normalized S-N curve showing comparison of the predictions with the constant and variable amplitude fatigue data for HSLA-80 weldments. The parameters of the model estimated using constant amplitude data.

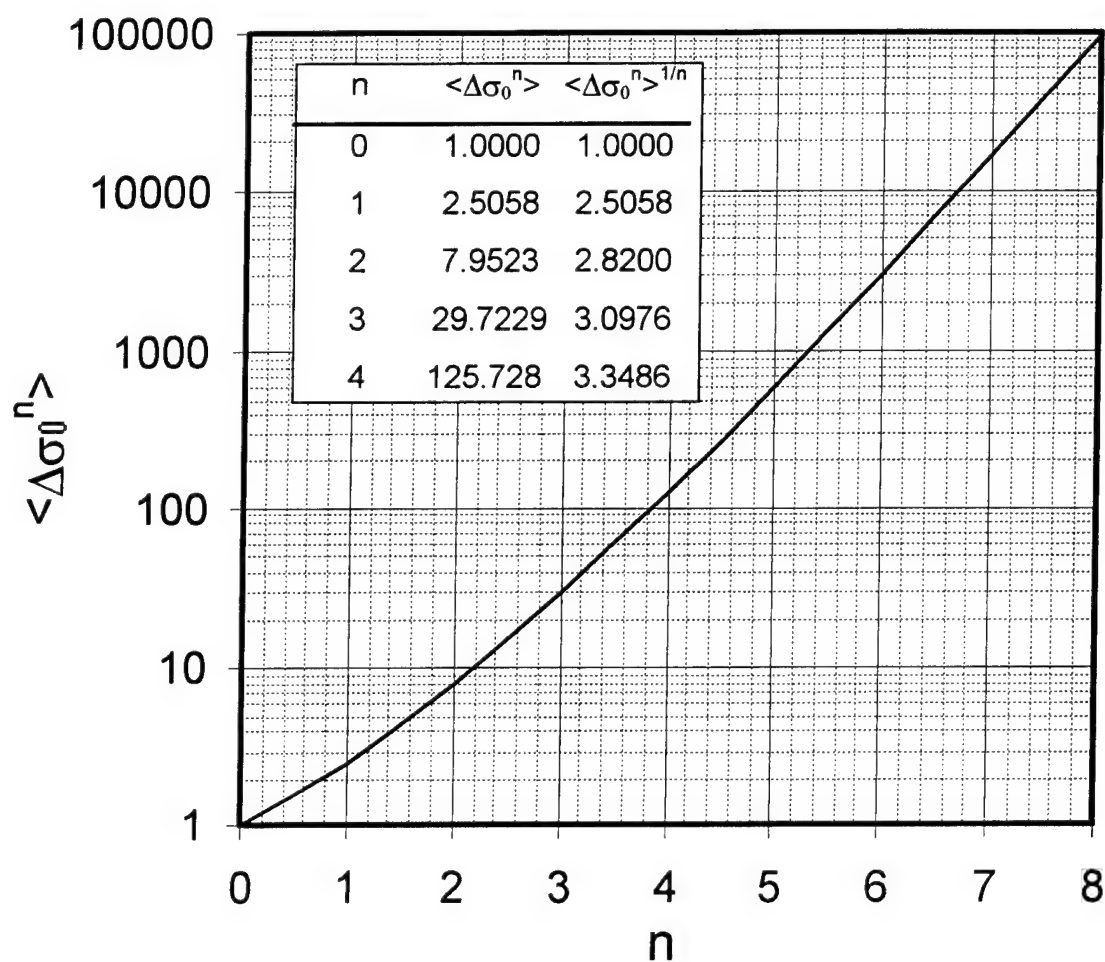


Figure 111. Values of the first eight moments of the stress ranges,  $\Delta\sigma_0$ , of the basic variable amplitude spectrum loading shown from Figure 98.

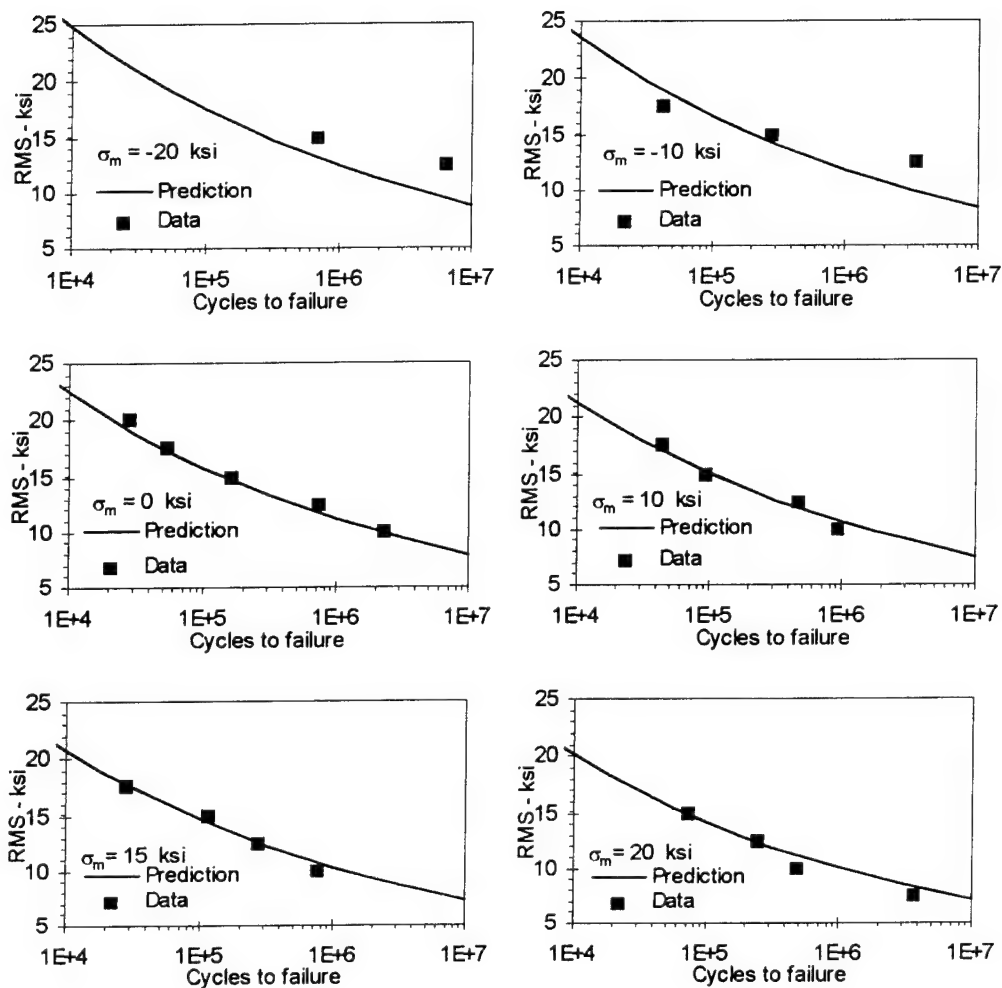


Figure 112. Comparison of the predicted *RMS* vs. *N* fatigue curves with experimental data for constant average stress for the HSLA-80 steel butt welds.

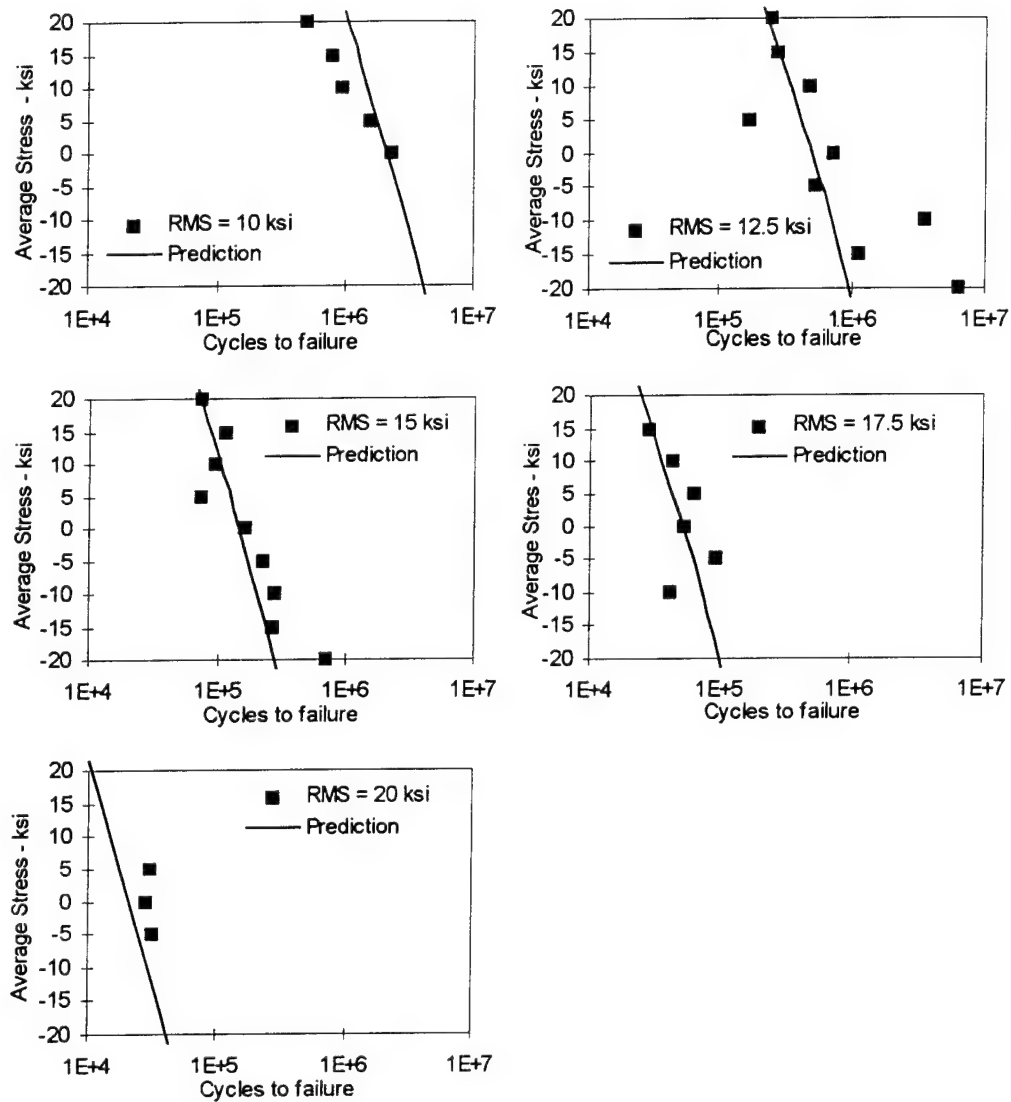


Figure 113. Comparison of the predicted  $\sigma_m$  vs. N fatigue curves with experimental data for constant *RMS* values for the HSLA-80 steel butt welds.

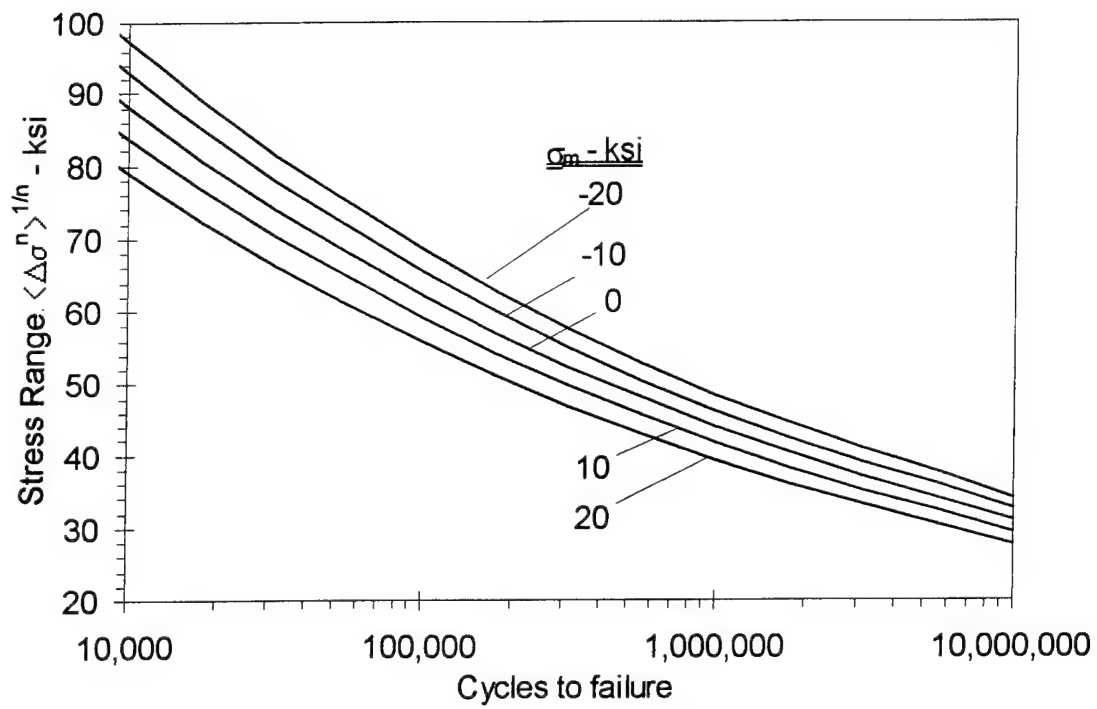


Figure 114. Predicted  $\Delta\sigma$  vs.  $N$  fatigue curves for constant average stresses for the HSLA-80 steel butt welds subjected to either constant or variable amplitude loading.

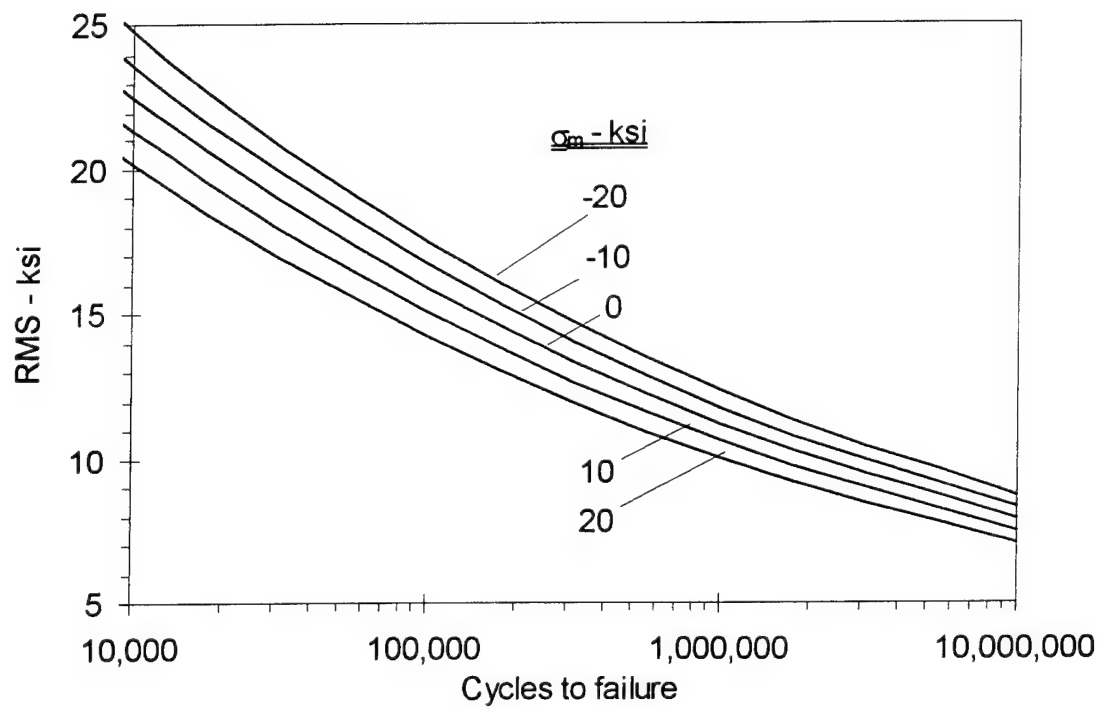


Figure 115. Predicted *RMS* vs. *N* fatigue curves for constant average stresses for the HSLA-80 steel butt welds subjected to either constant or variable amplitude loading.

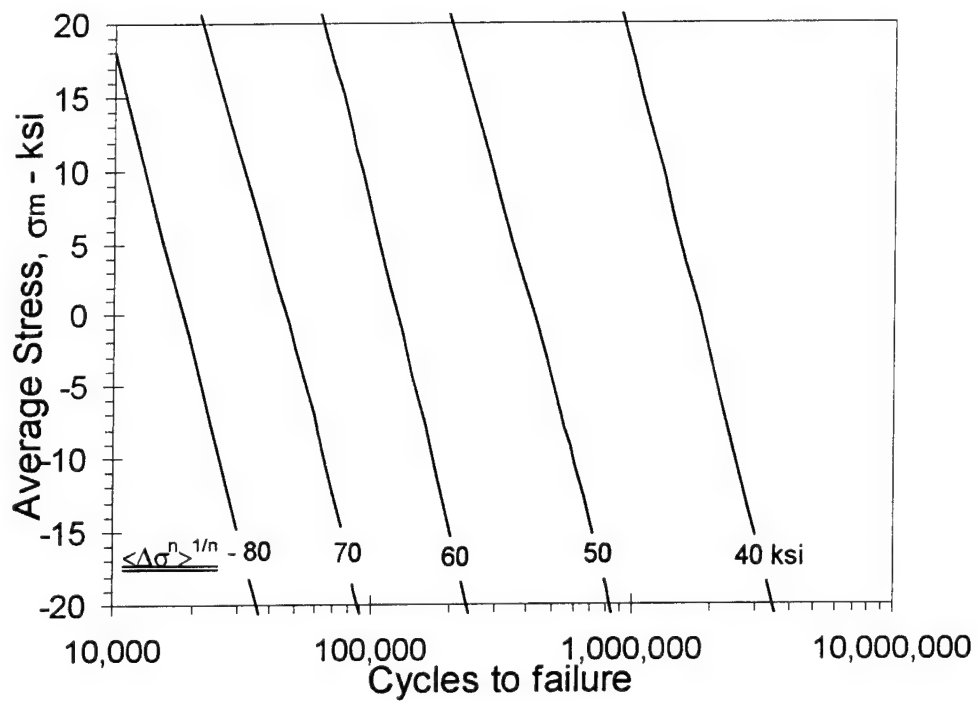


Figure 116. Predicted  $\sigma_m$  vs.  $N$  fatigue curves for constant average stress ranges for the HSLA-80 steel butt welds subjected to either constant or variable amplitude loading. Note that  $n=6.61$  and  $\langle \Delta \sigma^n \rangle^{1/n}$  reduces to  $\Delta \sigma$  for constant amplitude loading.

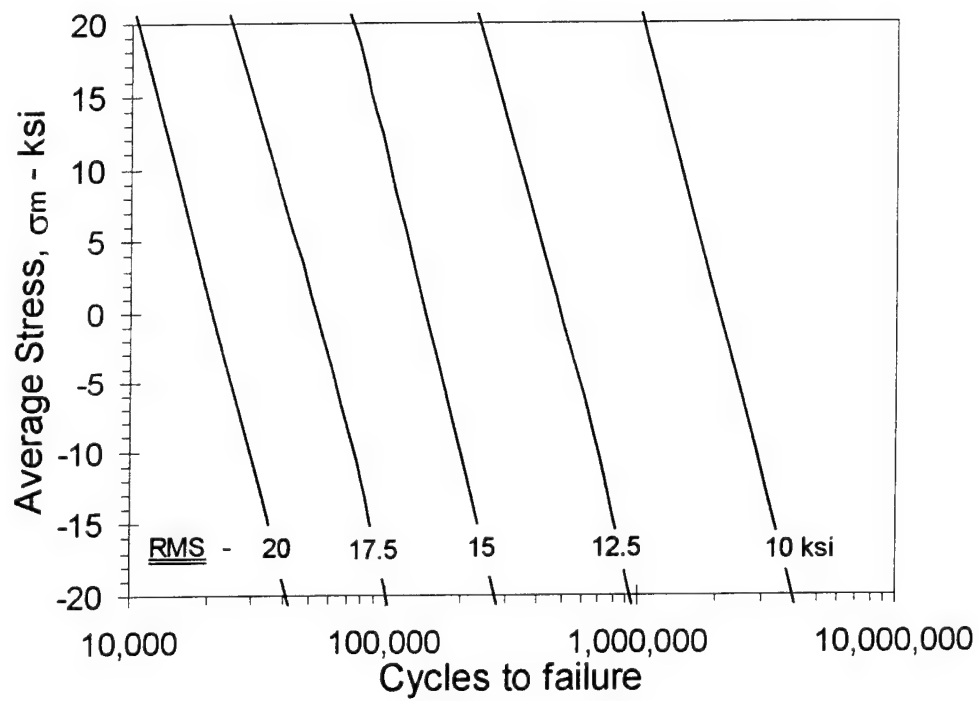


Figure 117. Predicted  $\sigma_m$  vs.  $N$  fatigue curves for constant  $RMS$  values for the HSLA-80 steel butt welds subjected to either constant or variable amplitude loading.

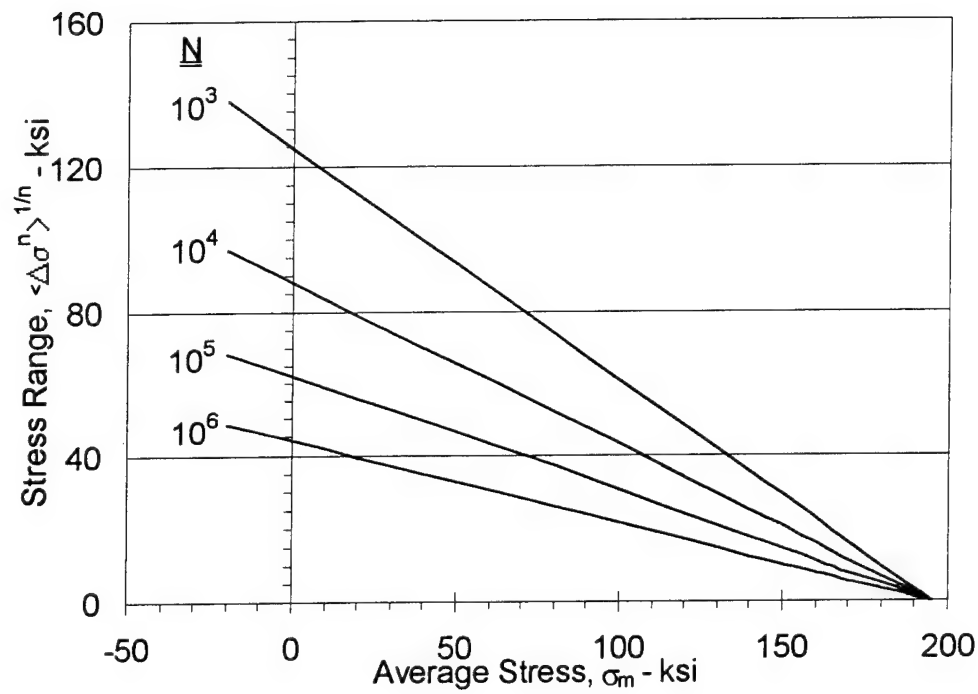


Figure 118. Predicted Goodman diagram in terms of the average stress range represented by  $\langle \Delta \sigma^n \rangle^{1/n}$  vs. average stress  $\sigma_m$  for the HSLA-80 steel butt welds subjected to either constant or variable amplitude loading.

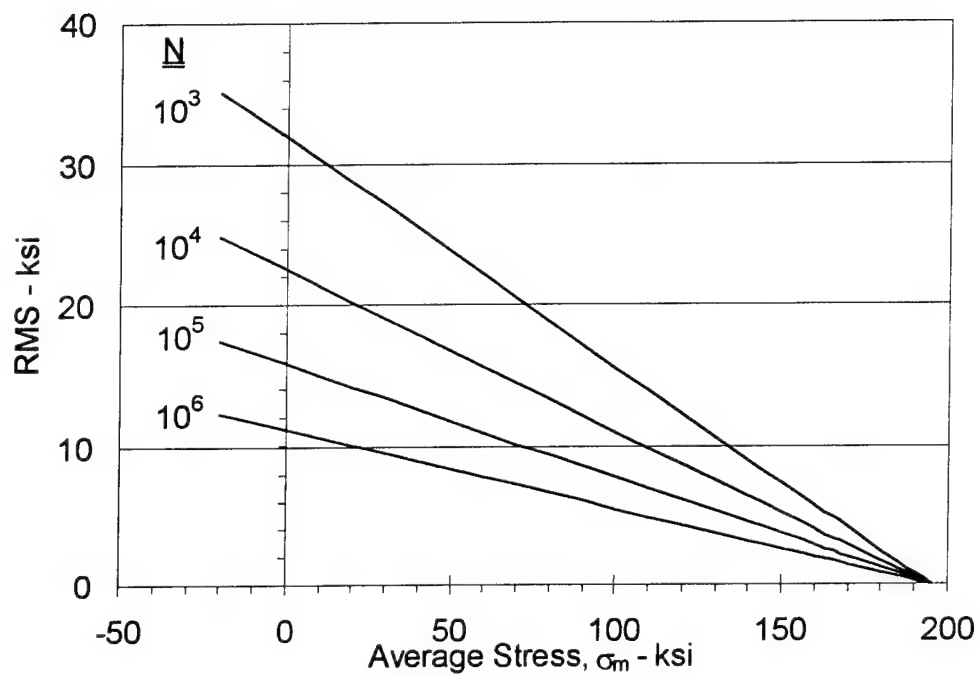


Figure 119. Predicted Goodman diagram in terms of the average stress range represented by  $RMS$  vs. average stress  $\sigma_m$  for the HSLA-80 steel butt welds subjected to either constant or variable amplitude loading.

*Appendix A. Fracture Surfaces of the Fatigue Failures of the HSLA-80 Steel Butt Weldments*

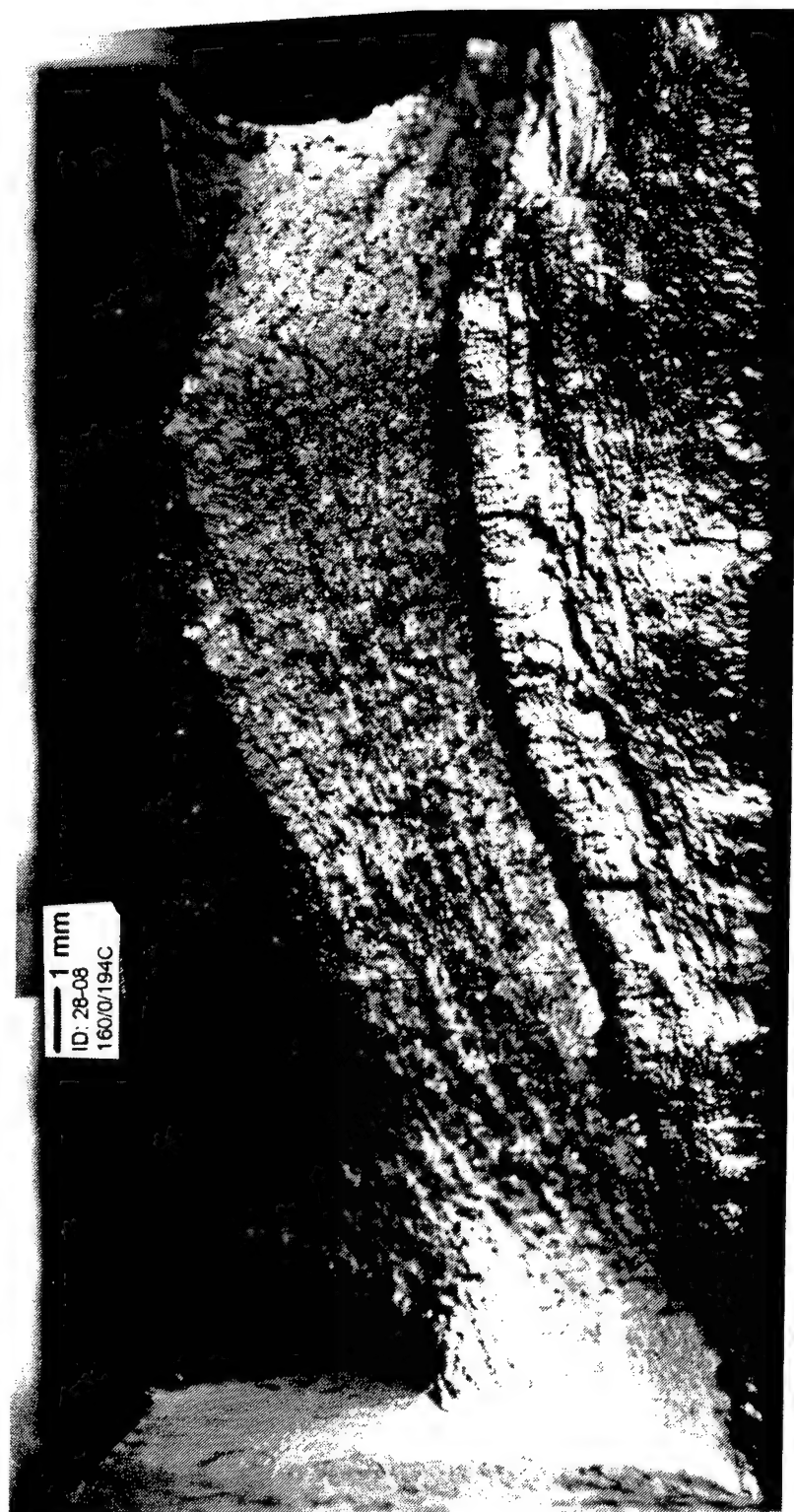


Figure A1. Fatigue fracture surface of the HSLA-80 but weld sample subjected to constant amplitude loading:  
 $\Delta\sigma = 160$  ksi,  $\sigma_m = 0$  ksi,  $R = -1$ ,  $N_f = 194$ .

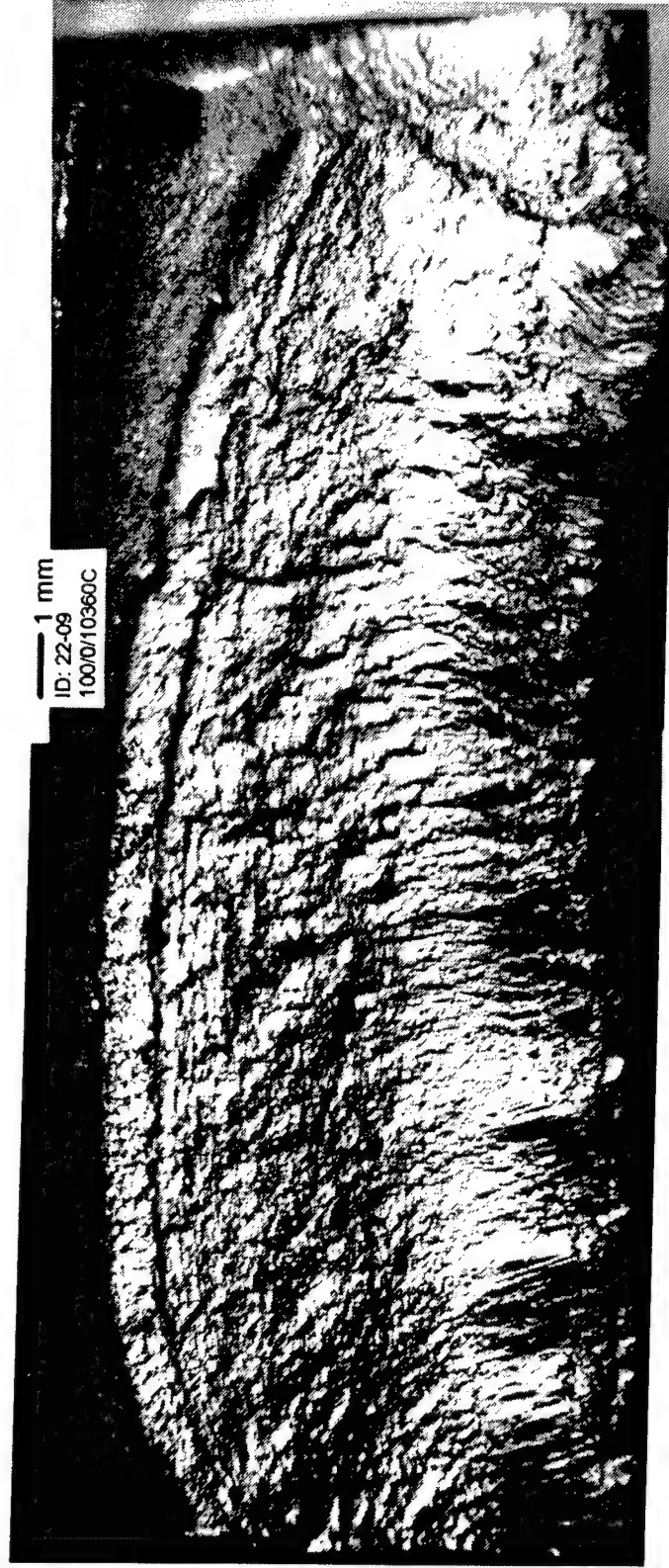


Figure A2. Fatigue fracture surface of the HSLA-80 but weld sample subjected to constant amplitude loading:  
 $\Delta\sigma = 100$  ksi,  $\sigma_m = 0$  ksi,  $R = -1$ ,  $N_f = 10,360$ .



Figure A3. Fatigue fracture surface of the HSLA-80 but weld sample subjected to constant amplitude loading:  
 $\Delta\sigma = 52.5$  ksi,  $\sigma_m = 43.75$  ksi,  $R = 0.25$ ,  $N_f = 56,960$ .



Figure A4. Fatigue fracture surface of the HSLA-80 but weld sample subjected to constant amplitude loading:  
 $\Delta\sigma = 50$  ksi,  $\sigma_m = 25$  ksi,  $R = 0$ ,  $N_f = 188,096$ .

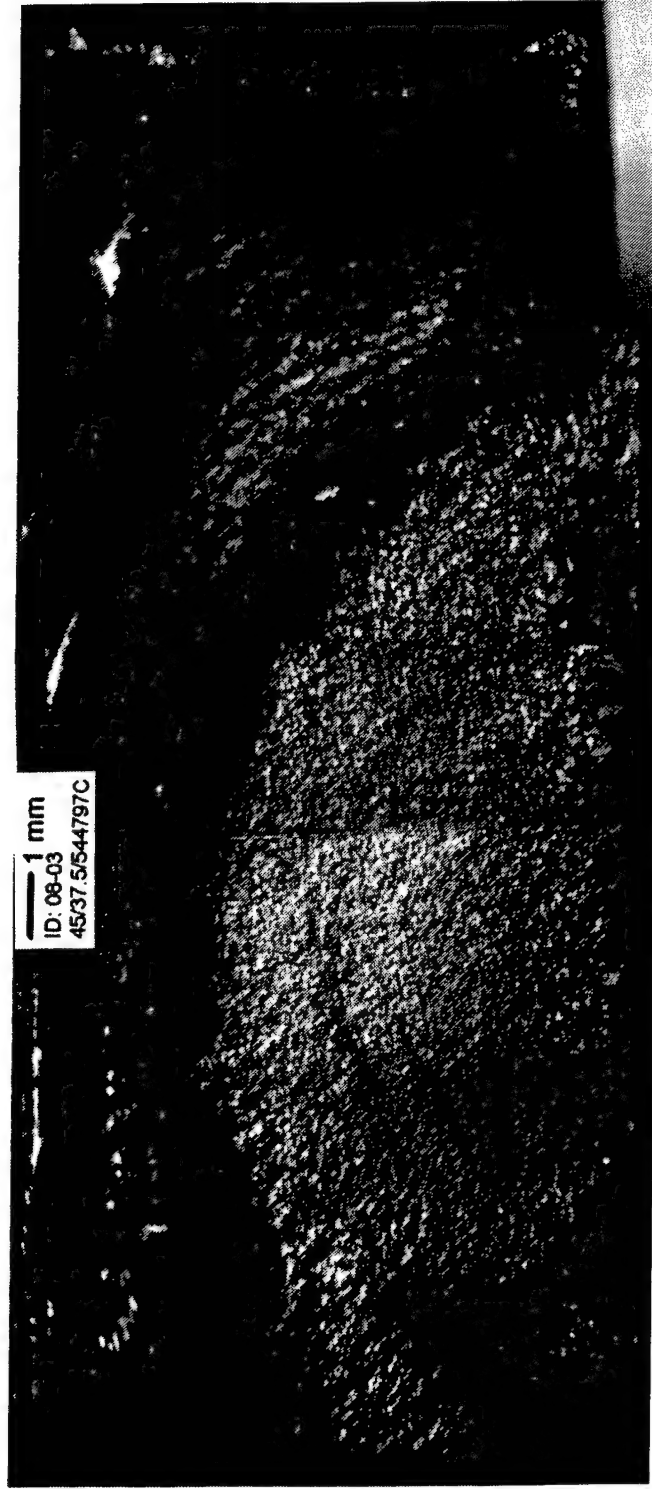


Figure A5. Fatigue fracture surface of the HSLA-80 but weld sample subjected to constant amplitude loading:  
 $\Delta\sigma = 45$  ksi,  $\sigma_m = 37.5$  ksi,  $R = 0.25$ ,  $N_f = 544,797$ .

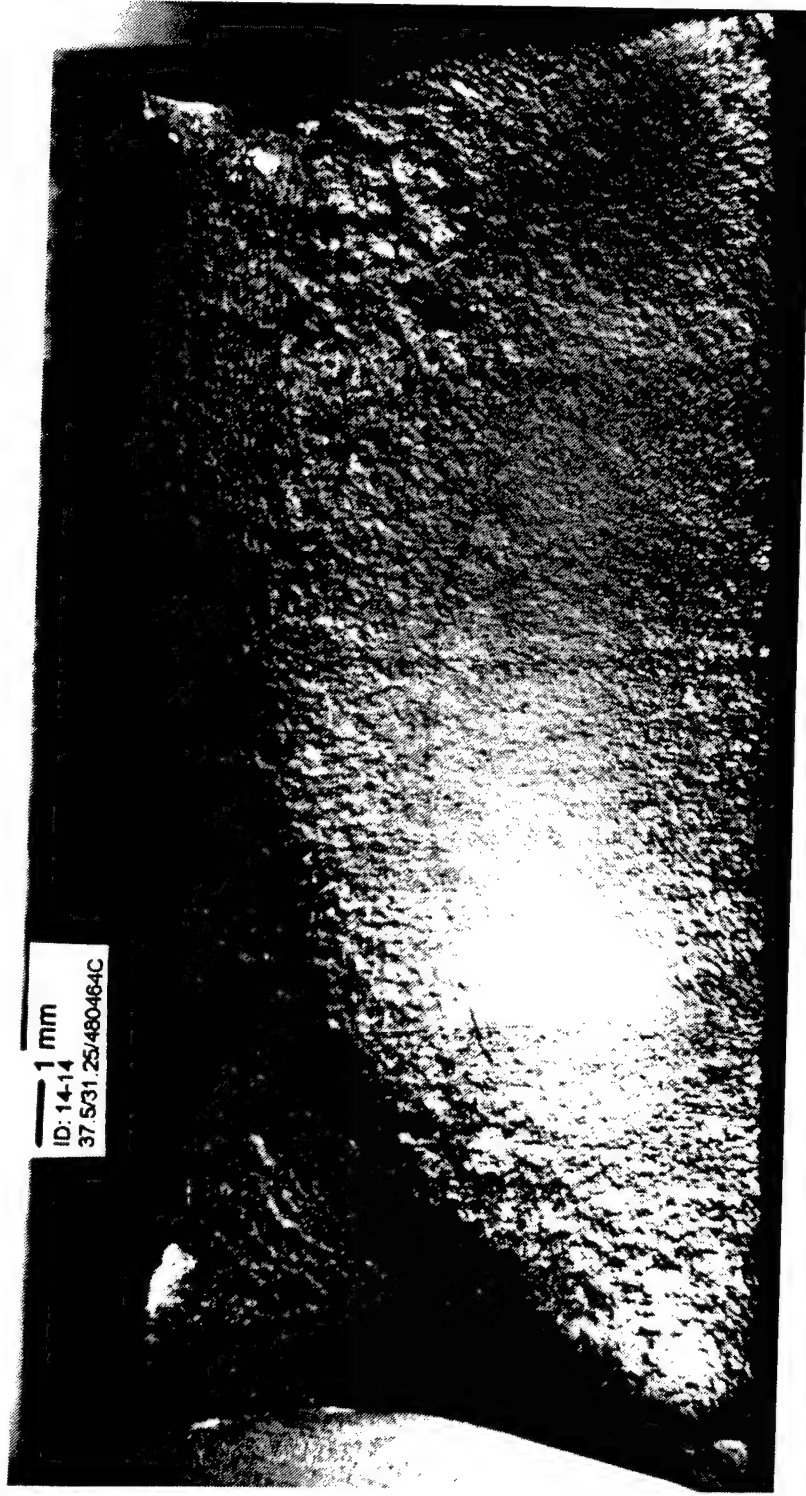


Figure A6. Fatigue fracture surface of the HSLA-80 but weld sample subjected to constant amplitude loading:  
 $\Delta\sigma = 37.5$  ksi,  $\sigma_m = 31.25$  ksi,  $R = 0.25$ ,  $N_f = 480,464$ .



1 mm  
ID: 10-06  
25/37 5/1049860C

Figure A7. Fatigue fracture surface of the HSLA-80 but weld sample subjected to constant amplitude loading:  
 $\Delta\sigma = 25$  ksi,  $\sigma_m = 37.5$  ksi,  $R = 0.5$ ,  $N_f = 1,049,860$ .

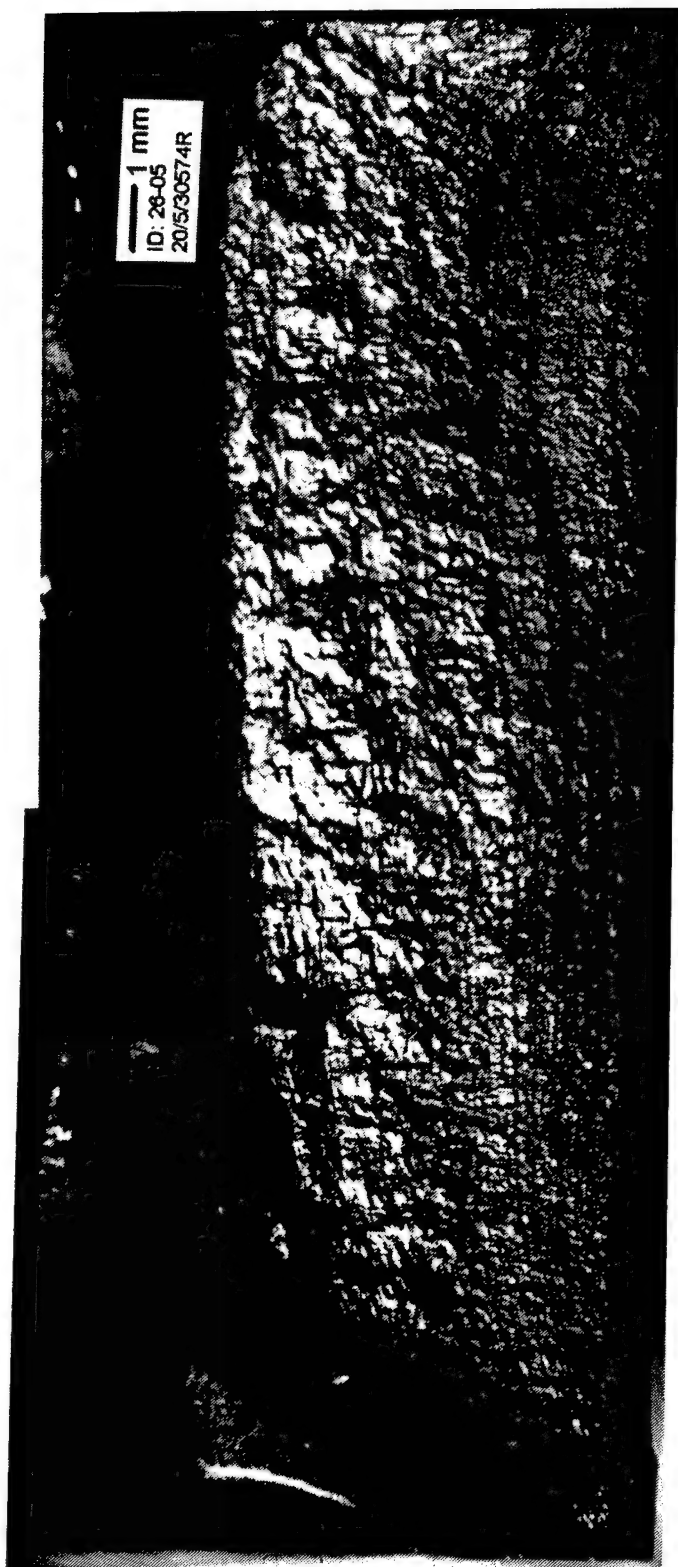


Figure A8. Fatigue fracture surface of the HSLA-80 but weld sample subjected to random loading:  
 $RMS = 20$  ksi,  $\sigma_m = 5$  ksi,  $N_f = 30,574$ .

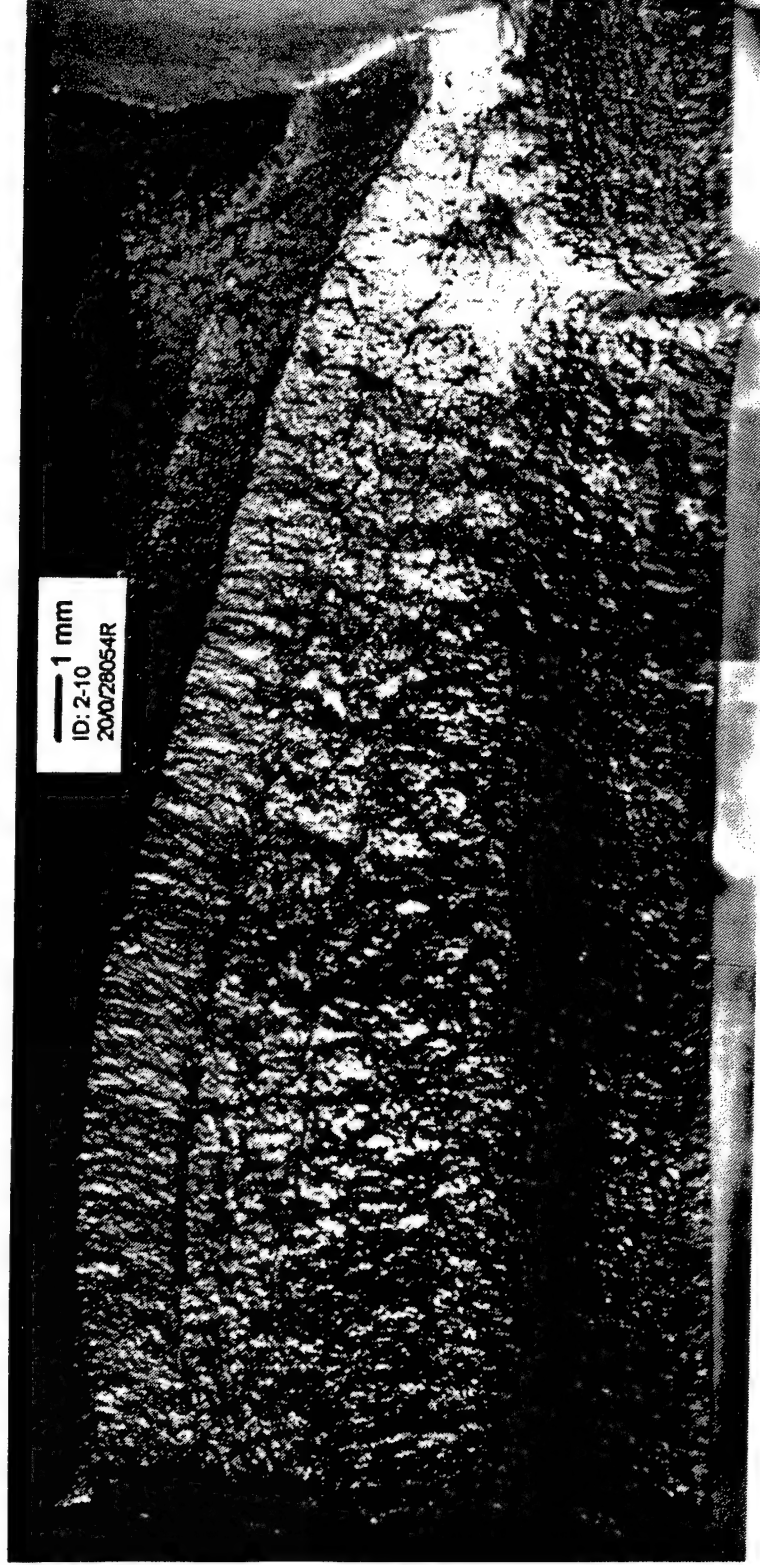


Figure A9. Fatigue fracture surface of the HSLA-80 but weld sample subjected to random loading:  
 $RMS = 20 \text{ ksi}$ ,  $\sigma_m = 0 \text{ ksi}$ ,  $N_f = 28,054$ .

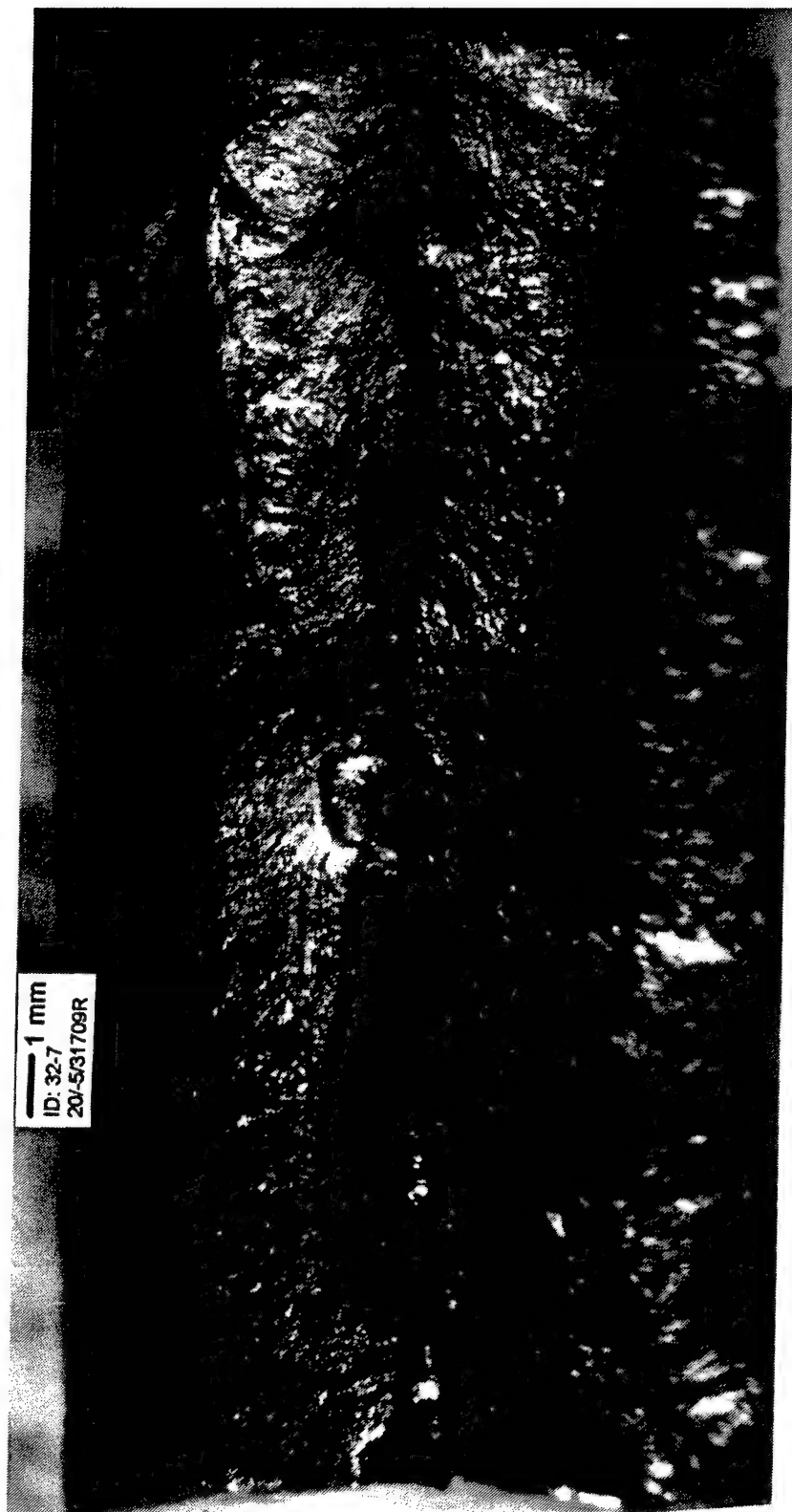


Figure A10. Fatigue fracture surface of the HSLA-80 but weld sample subjected to random loading:  
 $RMS = 20 \text{ ksi}$ ,  $\sigma_m = -5 \text{ ksi}$ ,  $N_f = 31,709$ .



Figure A11. Fatigue fracture surface of the HSLA-80 but weld sample subjected to random loading:  
 $RMS = 17.5$  ksi,  $\sigma_m = 15$  ksi,  $N_f = 28,149$ .

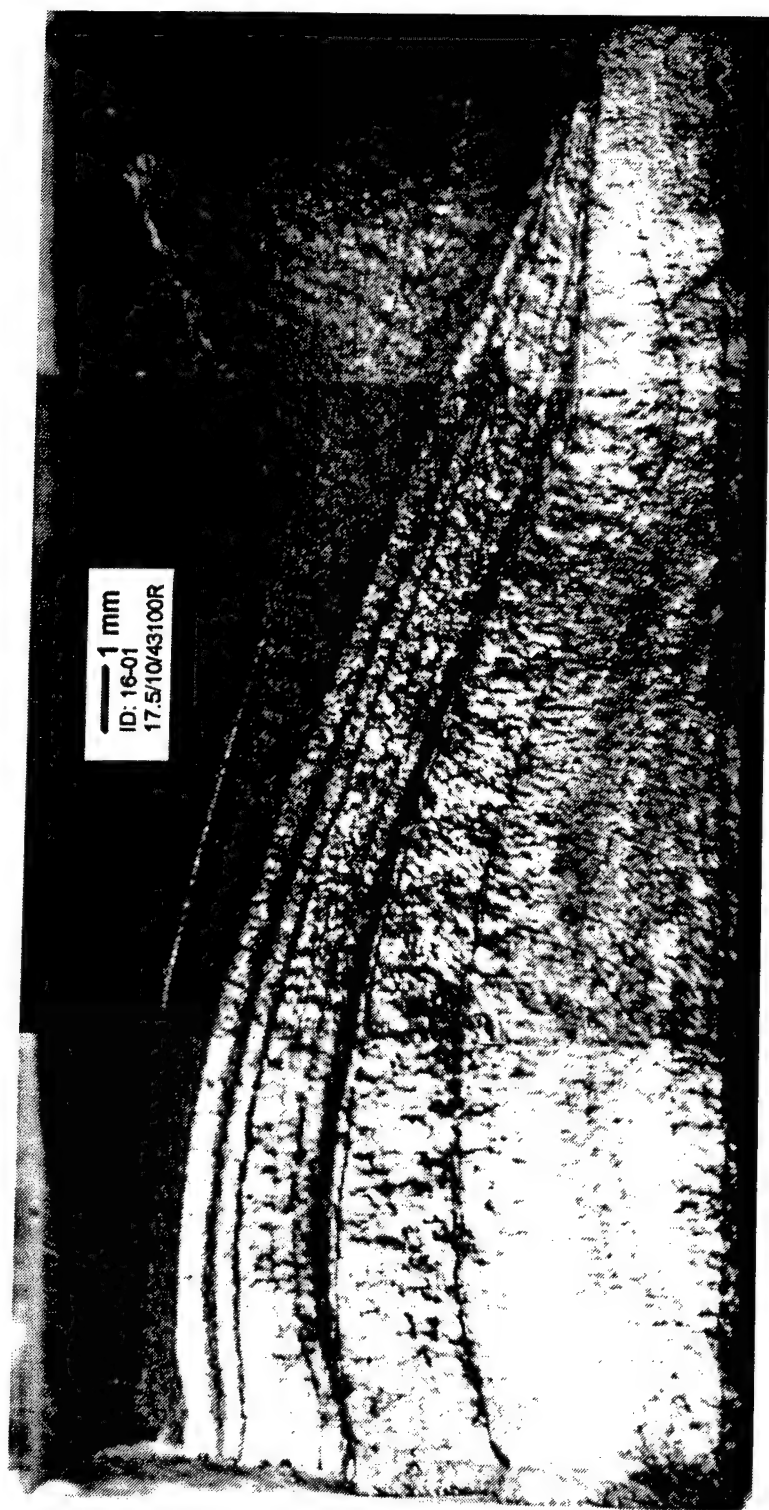


Figure A12. Fatigue fracture surface of the HSLA-80 but weld sample subjected to random loading:  
 $RMS = 17.5$  ksi,  $\sigma_m = 10$  ksi,  $N_f = 43,100$ .



Figure A13. Fatigue fracture surface of the HSLA-80 but weld sample subjected to random loading:  
 $RMS = 17.5$  ksi,  $\sigma_m = 5$  ksi,  $N_f = 64,298$ .

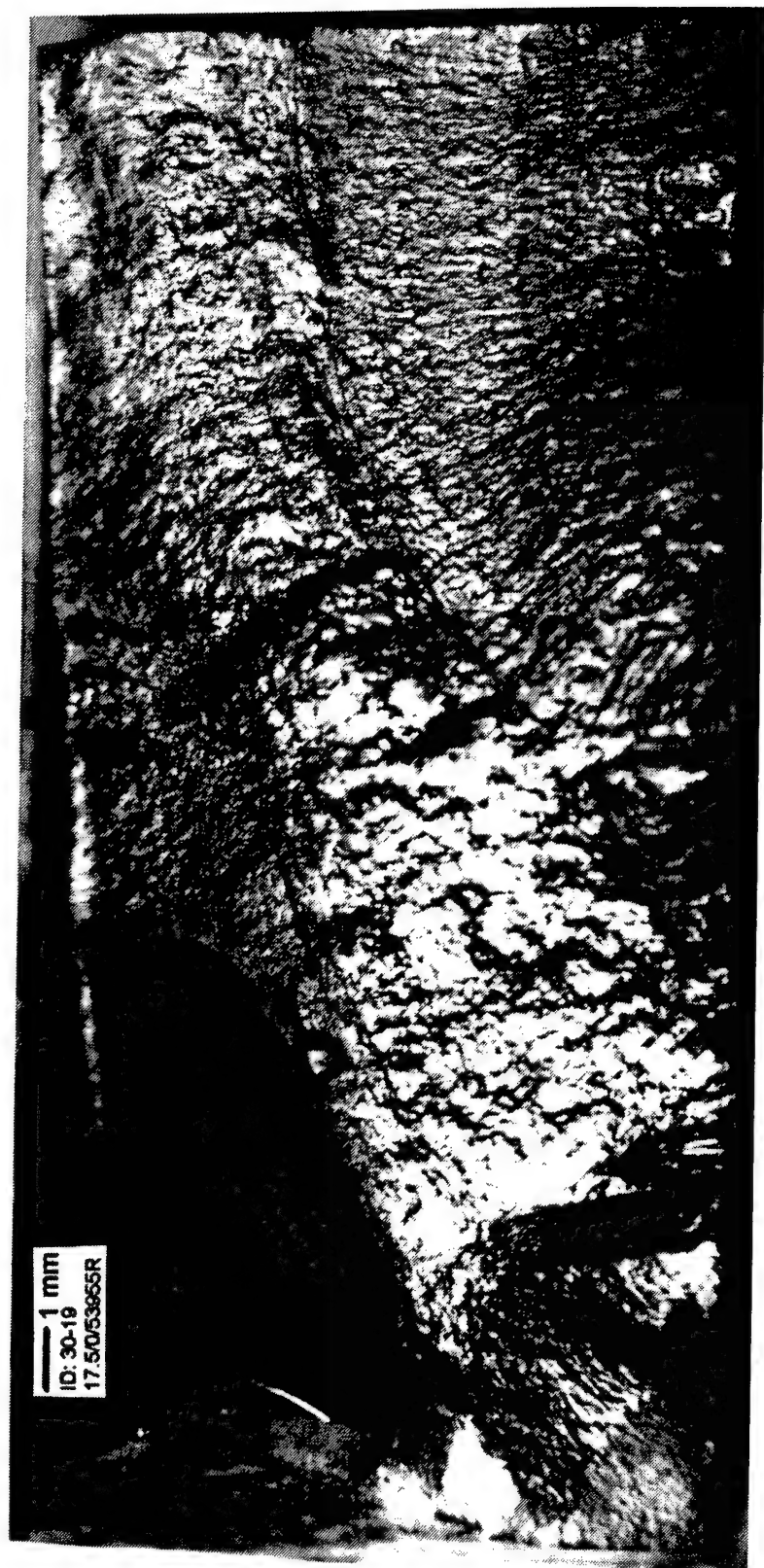


Figure A14. Fatigue fracture surface of the HSLA-80 but weld sample subjected to random loading:  
 $RMS = 17.5$  ksi,  $\sigma_m = 0$  ksi,  $N_f = 53,955$ .



Figure A15. Fatigue fracture surface of the HSLA-80 but weld sample subjected to random loading:  
 $RMS = 17.5$  ksi,  $\sigma_m = -5$  ksi,  $N_f = 93,147$ .

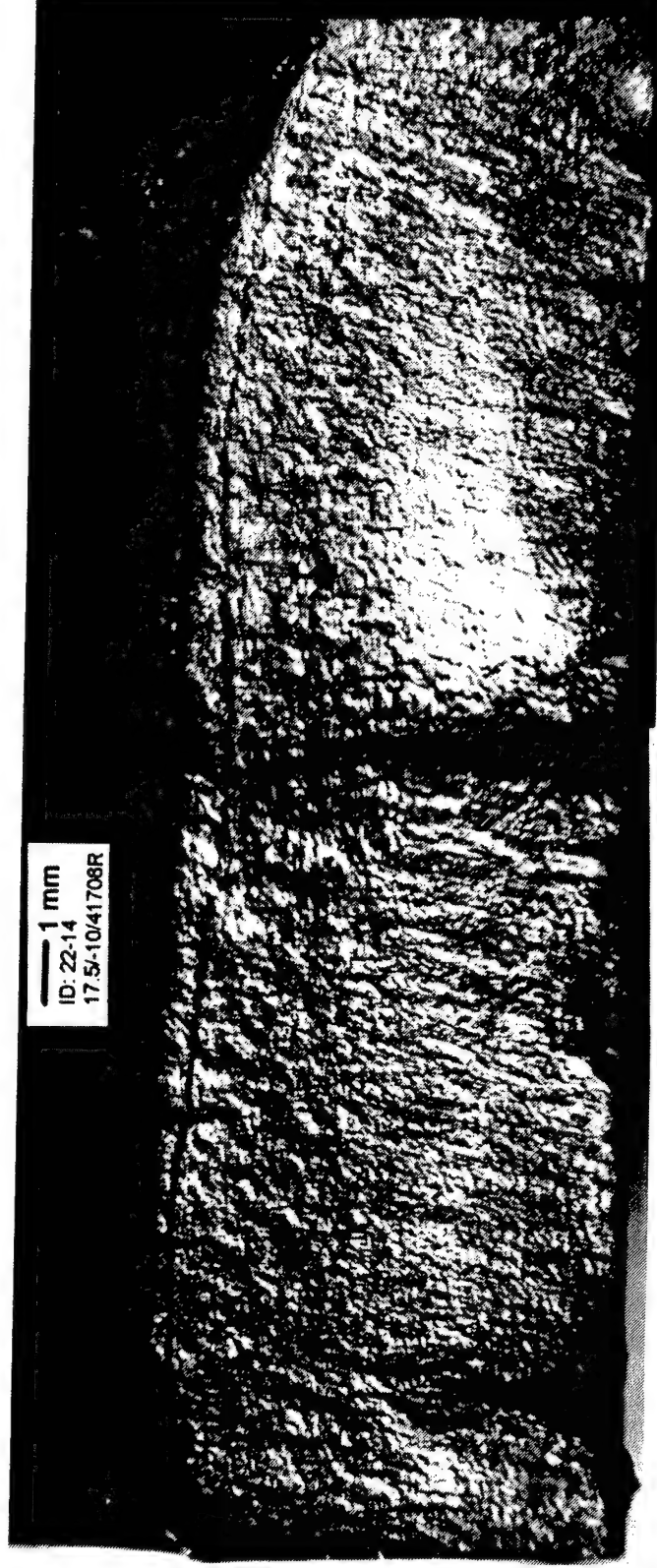


Figure A16. Fatigue fracture surface of the HSLA-80 but weld sample subjected to random loading:  
 $RMS = 17.5$  ksi,  $\sigma_m = -10$  ksi,  $N_f = 41,708$ .

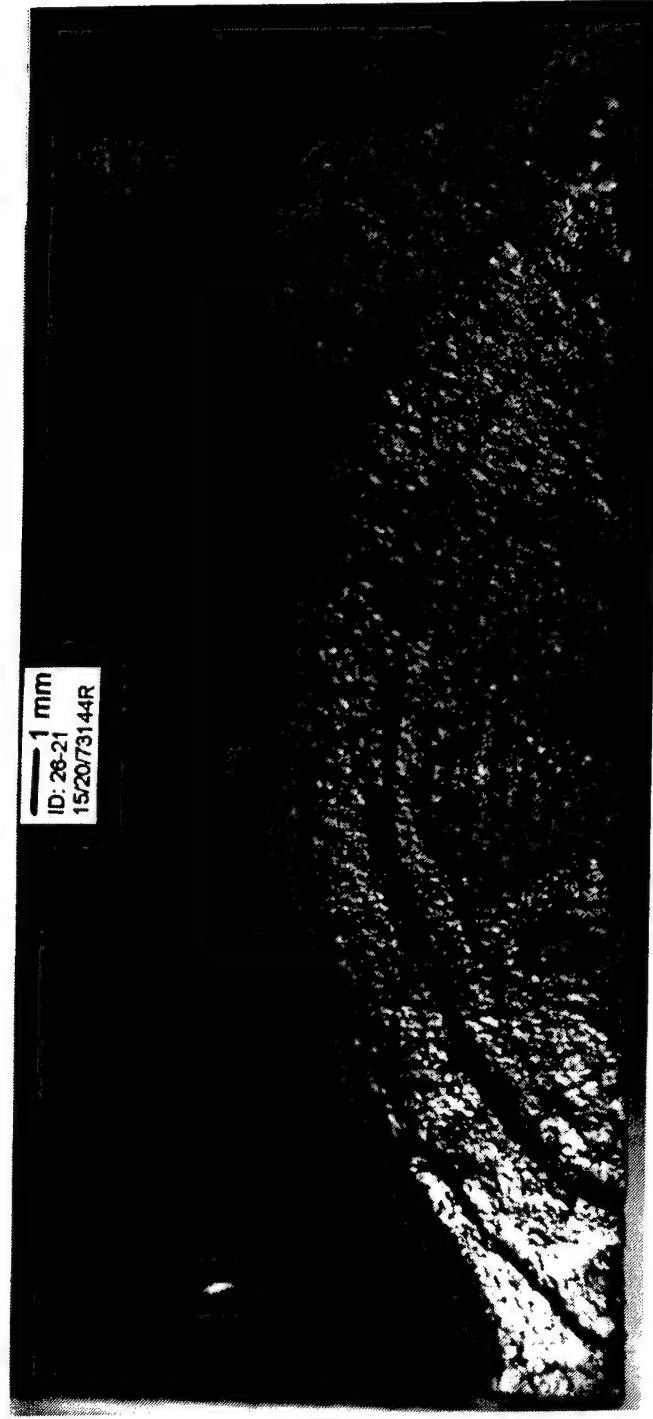


Figure A17. Fatigue fracture surface of the HSLA-80 but weld sample subjected to random loading:  
 $RMS = 15 \text{ ksi}$ ,  $\sigma_m = 20 \text{ ksi}$ ,  $N_f = 73,144$ .



Figure A18. Fatigue fracture surface of the HSLA-80 but weld sample subjected to random loading:  
 $RMS = 15 \text{ ksi}$ ,  $\sigma_m = 15 \text{ ksi}$ ,  $N_f = 114,309$ .



Figure A19. Fatigue fracture surface of the HSLA-80 but weld sample subjected to random loading:  
 $RMS = 15$  ksi,  $\sigma_m = 10$  ksi,  $N_f = 93,146$ .

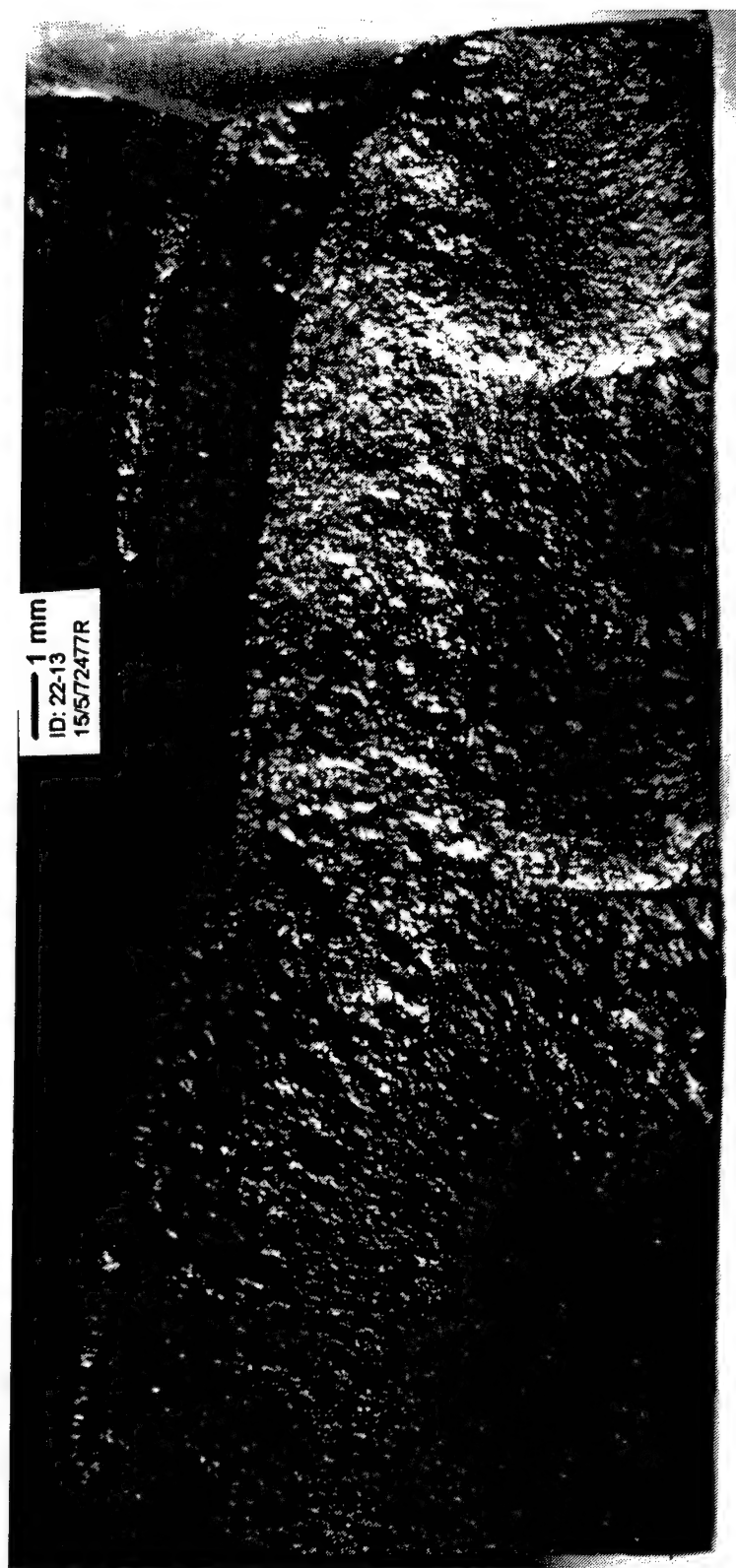


Figure A20. Fatigue fracture surface of the HSLA-80 butt weld sample subjected to random loading:  
 $RMS = 15 \text{ ksi}$ ,  $\sigma_m = 5 \text{ ksi}$ ,  $N_f = 72,477$ .



Figure A21. Fatigue fracture surface of the HSLA-80 but weld sample subjected to random loading:  
 $RMS = 15 \text{ ksi}$ ,  $\sigma_m = 0 \text{ ksi}$ ,  $N_f = 162,416$ .



Figure A22. Fatigue fracture surface of the HSLA-80 but weld sample subjected to random loading:  
 $RMS = 15 \text{ ksi}$ ,  $\sigma_m = -5 \text{ ksi}$ ,  $N_f = 222,468$ .



Figure A23. Fatigue fracture surface of the HSLA-80 but weld sample subjected to random loading:  
 $RMS = 15 \text{ ksi}$ ,  $\sigma_m = -10 \text{ ksi}$ ,  $N_f = 278,198$ .

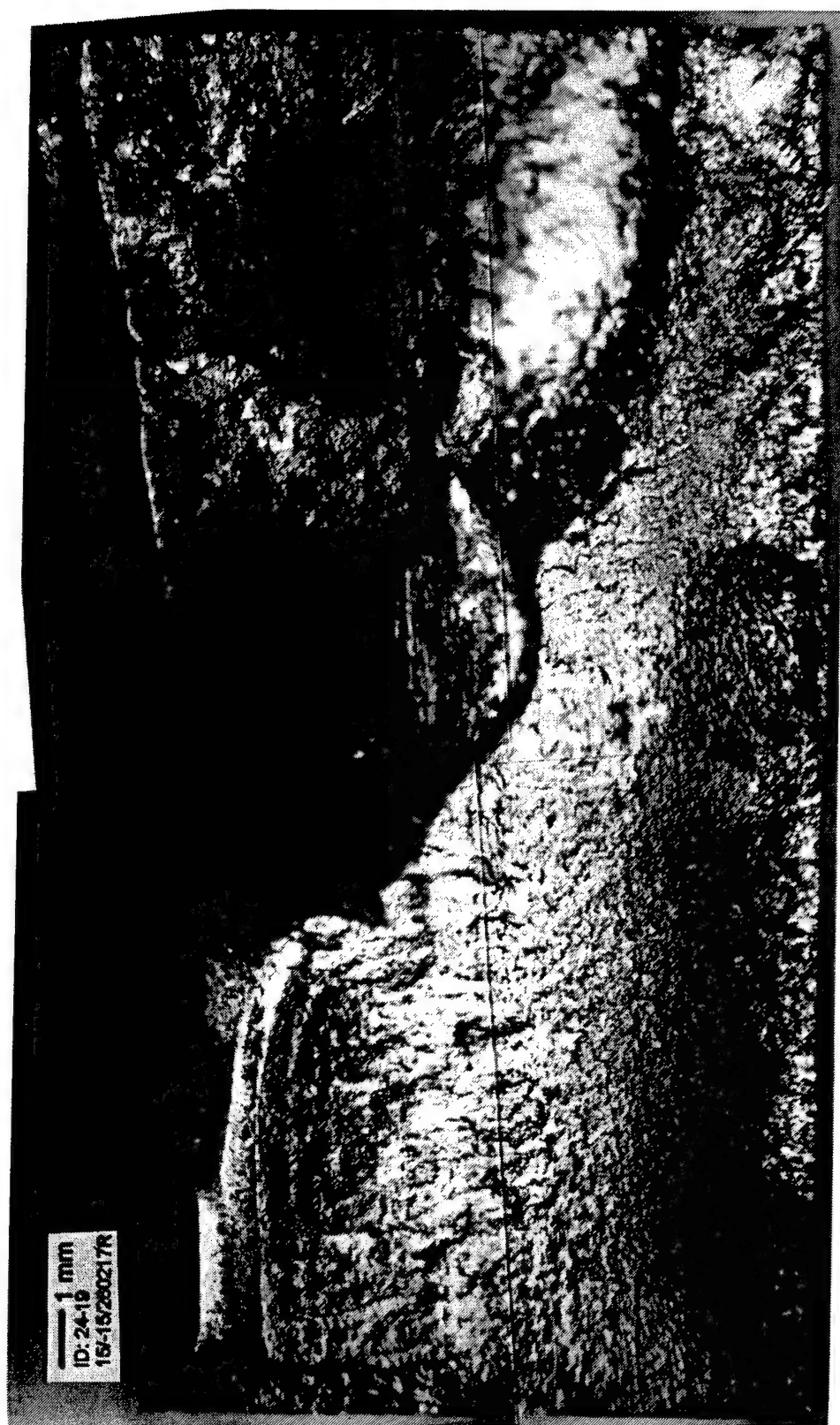


Figure A24. Fatigue fracture surface of the HSLA-80 but weld sample subjected to random loading:  
 $RMS = 15 \text{ ksi}$ ,  $\sigma_m = -15 \text{ ksi}$ ,  $N_f = 260,217$ .

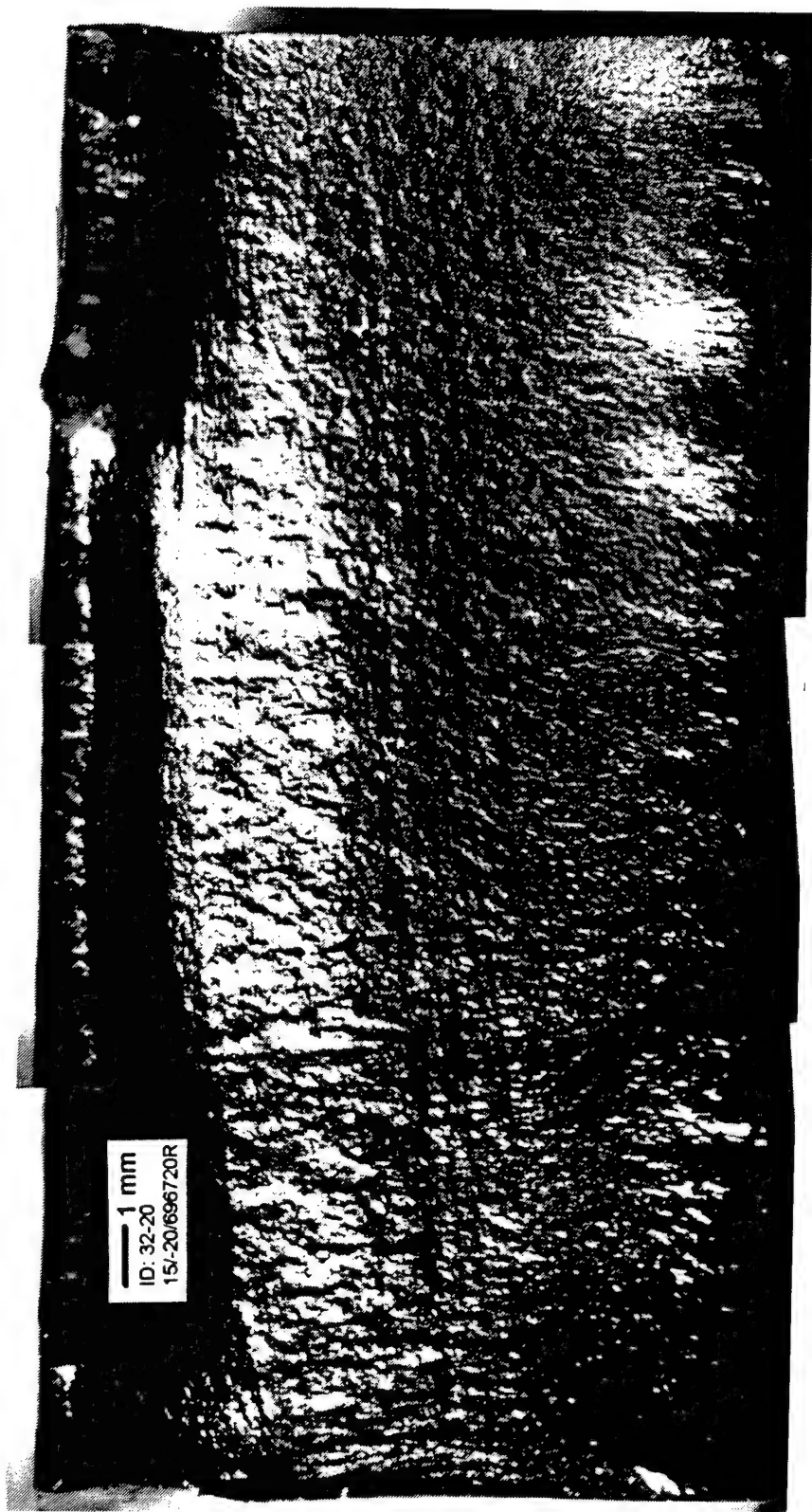


Figure A25. Fatigue fracture surface of the HSLA-80 but weld sample subjected to random loading:  
 $RMS = 15$  ksi,  $\sigma_m = -20$  ksi,  $N_f = 696,720$ .

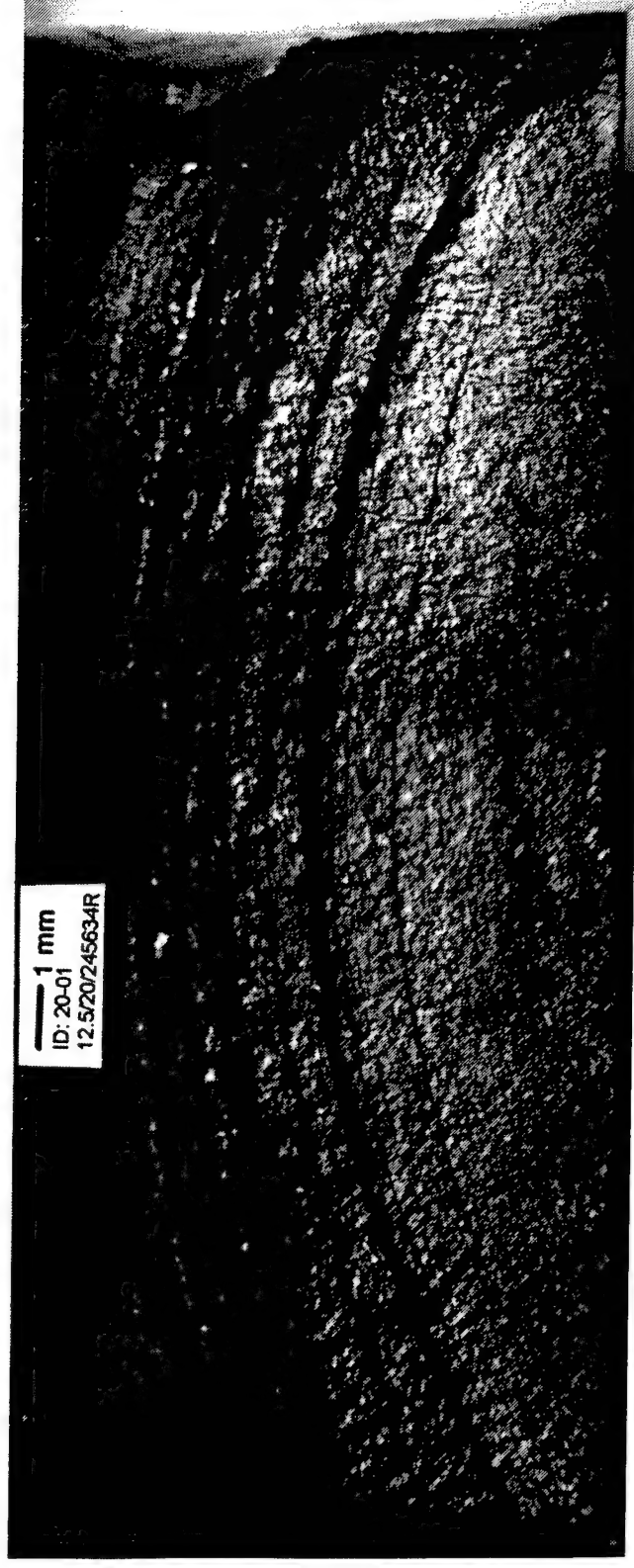


Figure A26. Fatigue fracture surface of the HSLA-80 but weld sample subjected to random loading:  
 $RMS = 12.5 \text{ ksi}$ ,  $\sigma_m = 20 \text{ ksi}$ ,  $N_f = 245,634$ .



Figure A27. Fatigue fracture surface of the HSLA-80 but weld sample subjected to random loading:  
 $RMS = 12.5$  ksi,  $\sigma_m = 15$  ksi,  $N_f = 271,993$ .

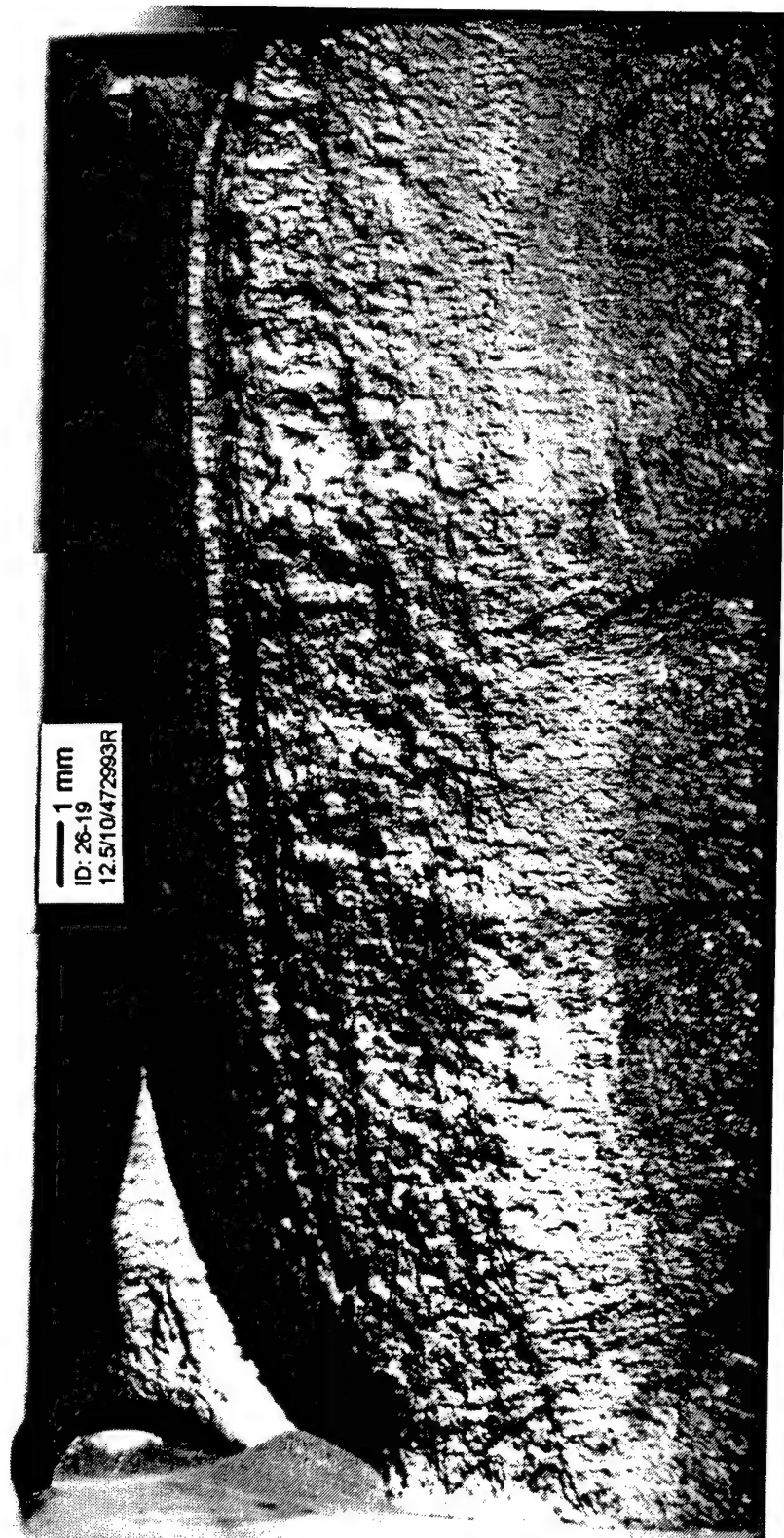


Figure A28. Fatigue fracture surface of the HSLA-80 but weld sample subjected to random loading:  
 $RMS = 12.5 \text{ ksi}$ ,  $\sigma_m = 10 \text{ ksi}$ ,  $N_f = 472,993$ .

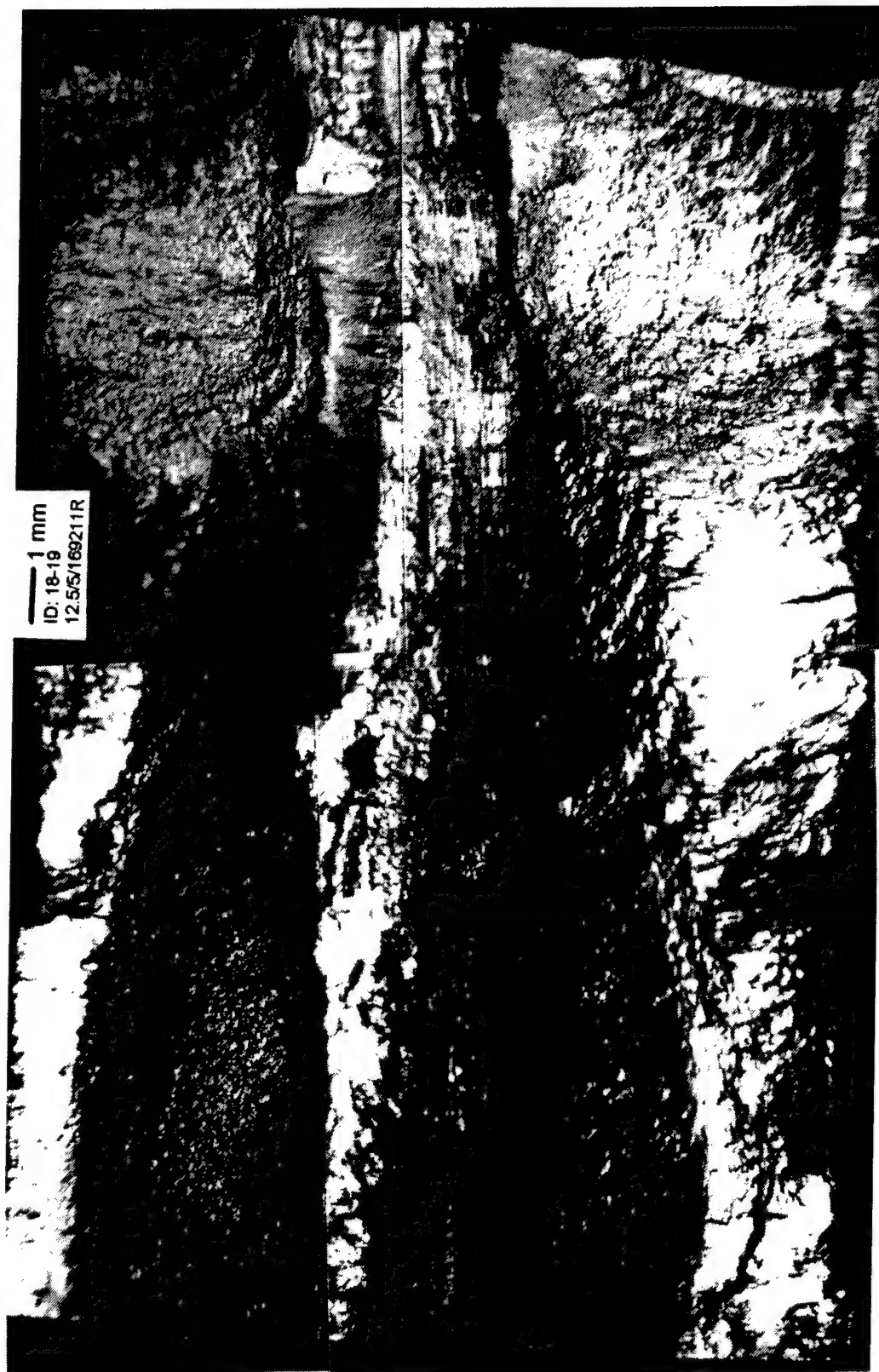


Figure A29. Fatigue fracture surface of the HSLA-80 but weld sample subjected to random loading:  
 $RMS = 12.5$  ksi,  $\sigma_m = 5$  ksi,  $N_f = 169,211$ .



Figure A30. Fatigue fracture surface of the HSLA-80 but weld sample subjected to random loading:  
 $RMS = 12.5$  ksi,  $\sigma_m = 0$  ksi,  $N_f = 725,230$ .

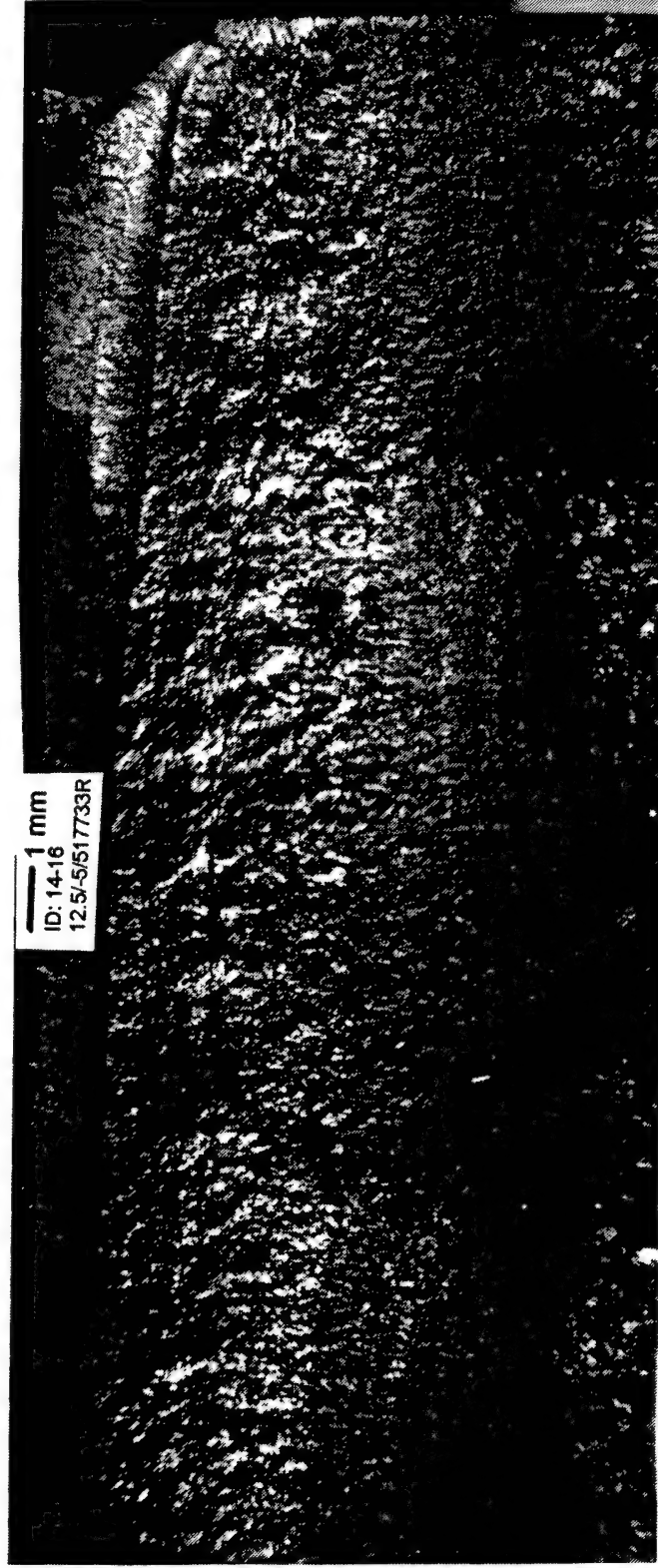


Figure A31. Fatigue fracture surface of the HSLA-80 but weld sample subjected to random loading:  
 $RMS = 12.5$  ksi,  $\sigma_m = -5$  ksi,  $N_f = 517,733$ .



Figure A32. Fatigue fracture surface of the HSLA-80 but weld sample subjected to random loading:  
 $RMS = 12.5$  ksi,  $\sigma_m = -10$  ksi,  $N_f = 3,490,091$ .



Figure A33. Fatigue fracture surface of the HSLA-80 but weld sample subjected to random loading:  
 $RMS = 12.5 \text{ ksi}$ ,  $\sigma_m = -15 \text{ ksi}$ ,  $N_f = 1,121,328$ .



Figure A34. Fatigue fracture surface of the HSLA-80 but weld sample subjected to random loading:  
 $RMS = 12.5$  ksi,  $\sigma_m = -20$  ksi,  $N_f = 6,305,613$ .

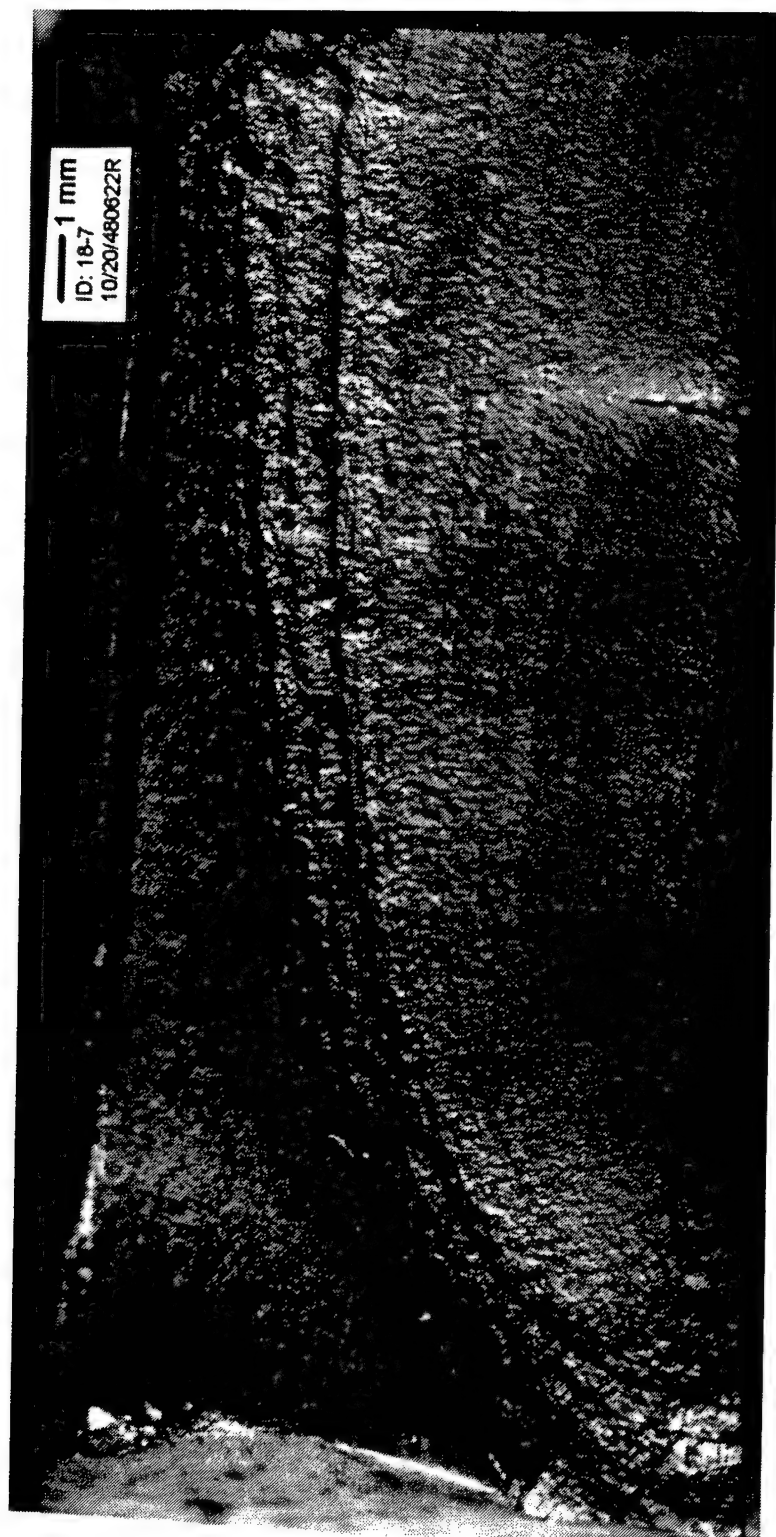


Figure A35. Fatigue fracture surface of the HSLA-80 but weld sample subjected to random loading:  
 $RMS = 10 \text{ ksi}$ ,  $\sigma_m = 20 \text{ ksi}$ ,  $N_f = 480,622$ .

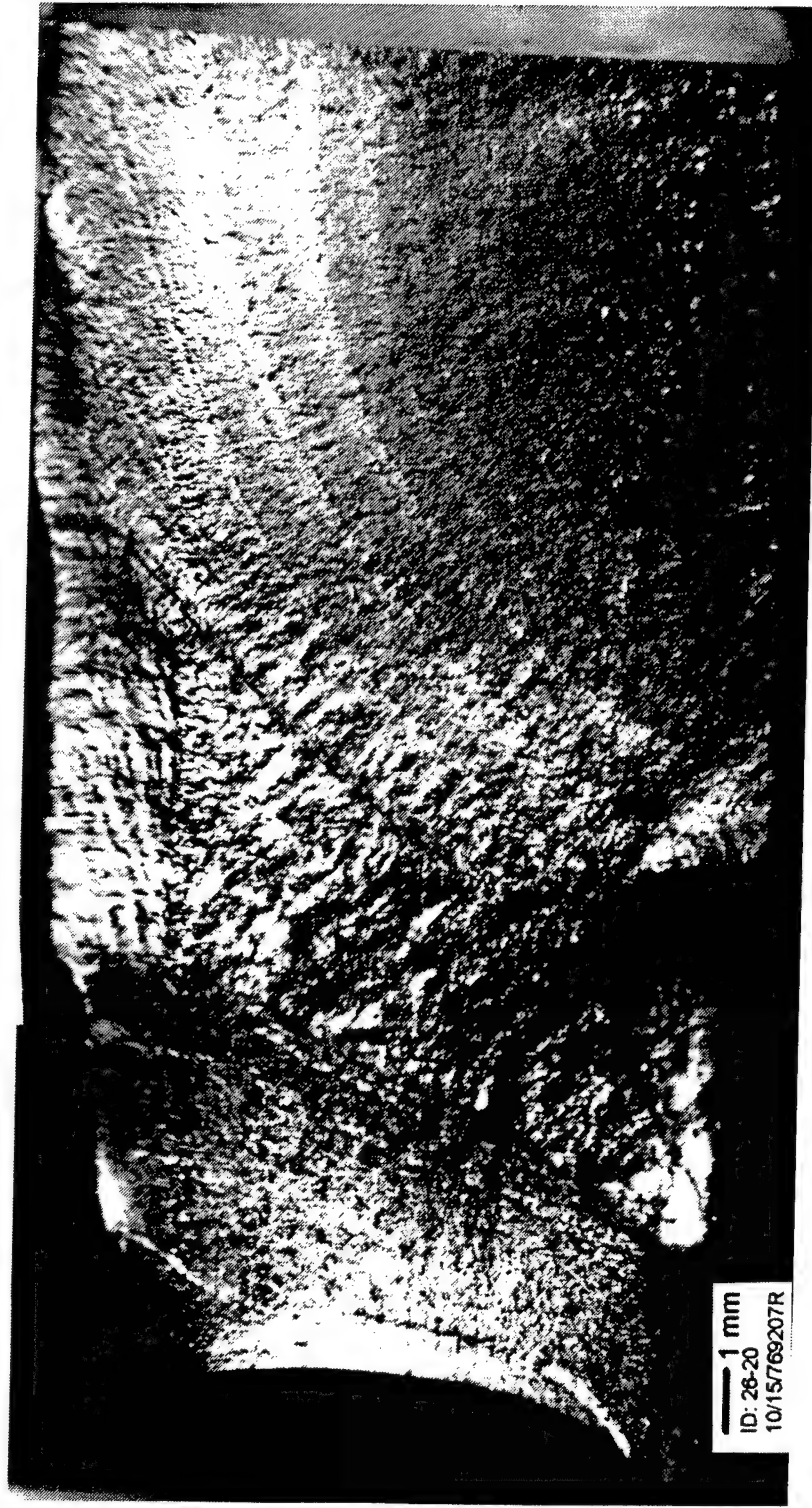


Figure A36. Fatigue fracture surface of the HSLA-80 but weld sample subjected to random loading:  
 $RMS = 10$  ksi,  $\sigma_m = 15$  ksi,  $N_f = 769,207$  .

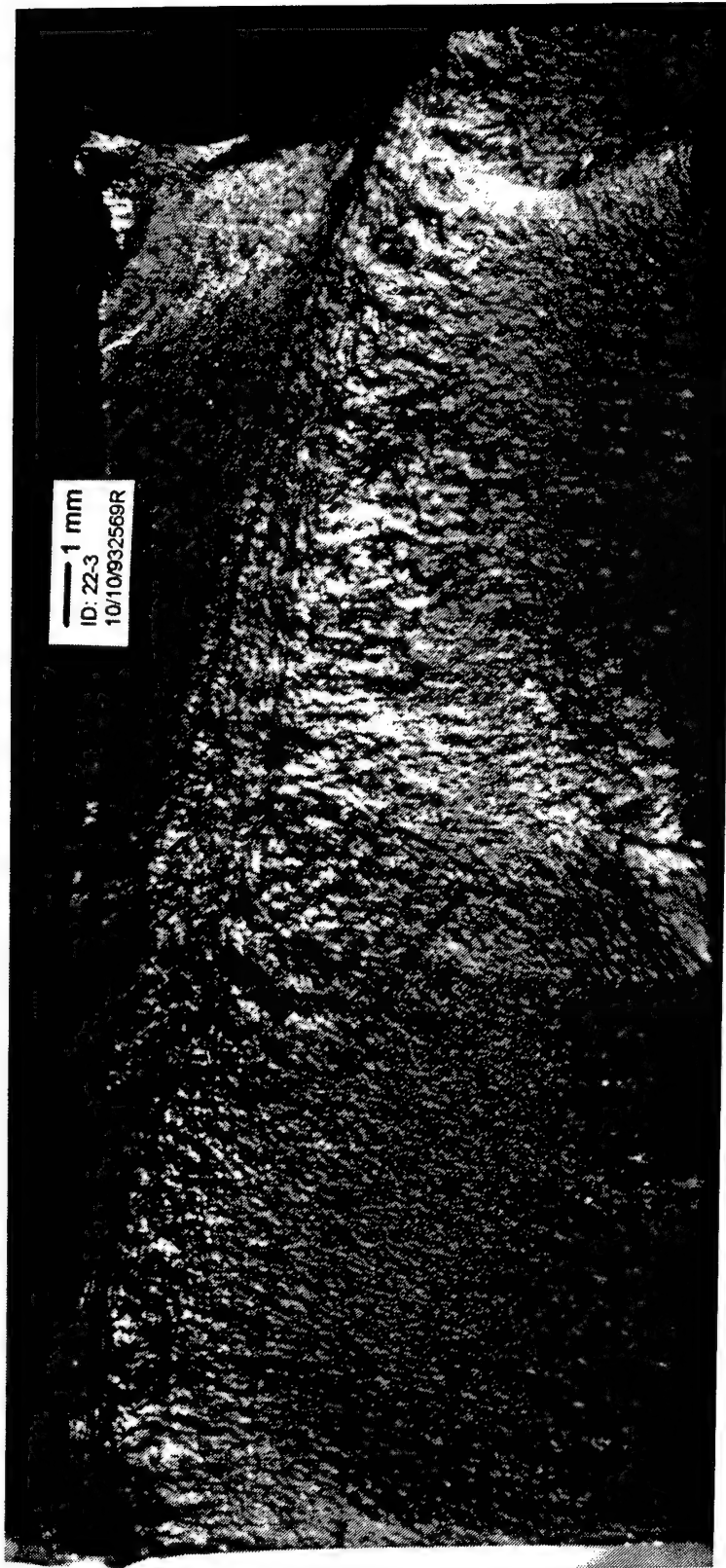


Figure A37. Fatigue fracture surface of the HSLA-80 but weld sample subjected to random loading:  
 $RMS = 10 \text{ ksi}$ ,  $\sigma_m = 10 \text{ ksi}$ ,  $N_f = 932,569$ .



Figure A38. Fatigue fracture surface of the HSLA-80 but weld sample subjected to random loading:  
 $RMS = 10 \text{ ksi}$ ,  $\sigma_m = 5 \text{ ksi}$ ,  $N_f = 1,515,599$ .



Figure A39. Fatigue fracture surface of the HSLA-80 but weld sample subjected to random loading:  
 $RMS = 10 \text{ ksi}$ ,  $\sigma_m = 0 \text{ ksi}$ ,  $N_f = 2,253,059$ .

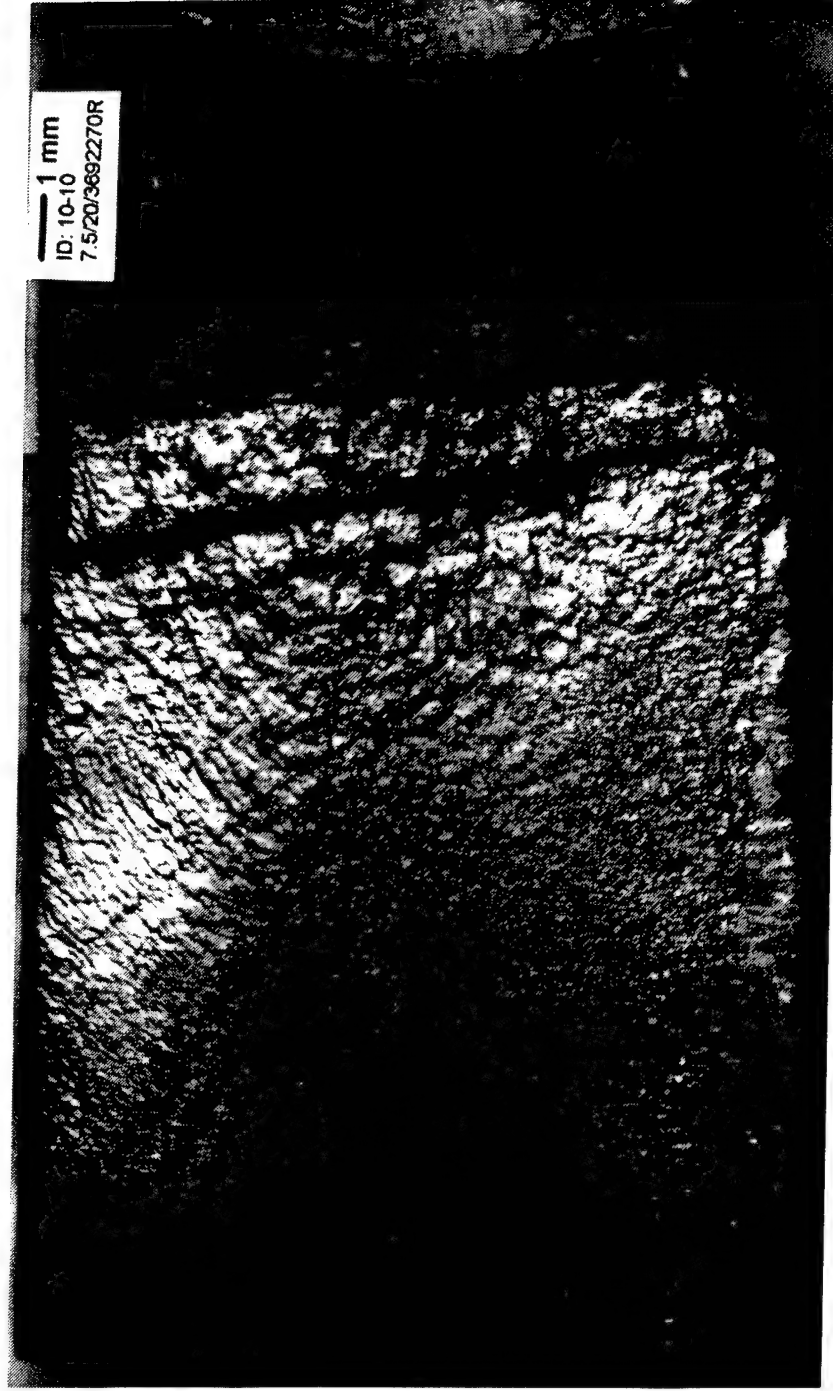


Figure A40. Fatigue fracture surface of the HSLA-80 but weld sample subjected to random loading:  
 $RMS = 7.5 \text{ ksi}$ ,  $\sigma_m = 20 \text{ ksi}$ ,  $N_f = 3,692,270$ .

*Appendix B. Quantitative Analysis of Heterogeneous Grain Structures on Plane  
Sections*

**J. Zhang, A. J. Luevano and M. A. Przystupa**

*Scripta Metallurgica et Materialia*, 26 (1992) pp. 1061-1066.

## QUANTITATIVE ANALYSIS OF HETEROGENEOUS GRAIN STRUCTURES ON PLANE SECTIONS

Jimin Zhang, Annetta J. Luévano and Marek A. Przystupa

Department of Materials Science and Engineering, University of California  
Los Angeles, CA 90024, USA

(Received September 27, 1991)  
(Revised February 4, 1992)

### Introduction

Since most of the engineering materials have heterogeneous grain structures, their complete quantitative description must include not only the average values of grain sizes but also contain some quantification of their shapes and orientations. The standard procedure used in these characterizations usually involves measurement of the linear intercepts on the plane sections and then conversion of the intercept values to the grain sizes, shape factors, etc. [1, 2]. Depending on the idealized grain model used in the conversion, one obtains either three or two dimensional grain descriptions, and the variation of the grain structure is described either by the standard deviations or by the distribution plots.

Among all grain characteristics the shape is the most elusive. The prevailing approach in its characterization is to use arbitrarily defined shape factors. The quantity most often used for this purpose is the ratio of the grain or particle area to the square of its perimeter [3]. Other definitions of shape factor include ratios of the feature area to the area of a circumscribed circle or rectangle, aspect ratios of the circumscribed rectangle and ratios of variously defined length and width values [4, 5]. All these descriptions have been extensively discussed by Underwood [1] and DeHoff et al. [2].

In this work we are concerned with the measurements of the characteristics of heterogeneous grain structures on the plane sections, that is with the measurement of the parameters which are important in the modeling of mechanical properties or in characterizing the extent and nature of the prior thermo-mechanical processing. Our approach is based on the measurement of the linear intercepts on the plane sections and uses plots of the average intercept length vs. intercept scan angle to characterize structural inhomogeneities. These plots have been already proven useful in characterizing oriented grain structures [6]. In what follows we first test the sensitivity of the method by deriving theoretical relationships between the average intercept length and the intercept scan angle for simple geometrical shapes. We then show how to obtain the information about the grain size, aspect ratio and shape from the intercept length vs. angle plots. Finally the versatility of the method is illustrated in the analysis of the grain structure of the 7050-T7 aluminum alloys with partially recrystallized structure.

### Theoretical Models

Let us start from defining an average intercept length,  $L_i(\alpha)$ , as an average of all intercepts obtained from a set of parallel test lines drawn at angle  $\alpha$  through a two dimensional object. The relations between these averages and the scan angles are easy to derive and they are compiled, for

simple geometrical shapes, in Table I [7]. Figure 1 shows variation of the normalized average intercept lengths,  $d (= L_i(\alpha)/L_{max})$  vs.  $\alpha$  for a circle, selected regular polygons and a rectangle ( $\alpha = 0$  for the direction corresponding to the maximum average intercept length,  $L_{max}$ ). The curves have some interesting features. First, the average intercept length is a periodic function of  $\alpha$  with a period  $2\pi/n$  ( $n$  is the number of sides of a regular polygon). Second, it is possible to show that the amplitudes of these curves decrease with  $n$  and that they are proportional to  $\cos(\pi/n)$  [7]. Finally, for a rectangle the value of  $d$  at  $90^\circ$  is equal to the aspect ratio. This property is further illustrated in Figure 2 which shows curves for rectangles with different aspect ratios, and in Figure 3 which shows similar plots for a circle and ellipses ( $b$  and  $a$  are either height and width or minor and major axes respectively). In the case of ellipses, as for rectangles, the normalized average intercept length  $d$  changes with the scan angle and the aspect ratios can be also deduced from the plots [7]. The  $d$  vs.  $\alpha$  curves are then ideal for finding about the average shape and the aspect ratios of the measured features.

Another useful property of the  $d$  vs.  $\alpha$  curves is that they can be used to calculate the global average of all intercept lengths for all angles,  $L_n$ , which is as a measure of the object size. This average is equal to:

$$L_n = \frac{\int_0^{\alpha_p} H(\alpha) L_i(\alpha) d\alpha}{\int_0^{\alpha_p} H(\alpha) d\alpha} \quad (1)$$

or, equivalently, to:

$$L_n = \frac{\pi A}{L_p} \quad (1a)$$

where  $\alpha_p$  is the curve period,  $H(\alpha)$  is a projection of the measured shape on the direction perpendicular to the scan lines,  $A$  is figure area and  $L_p$  its perimeter [1]. The  $d$  vs.  $\alpha$  plots also suggest that the shape index,  $SI$ , (defined as the normalized area under the curve):

$$SI = \frac{1}{\alpha_p} \int_0^{\alpha_p} d d\alpha \quad (2)$$

will be a sensitive measurement of the differences in the grain shapes. Indeed, it is equal to 1 for a circle and decreases to 0.9485 for regular octagon, to 0.9085 for hexagon and to 0.7936 for square. For the rectangles and ellipses  $SI$  increases with  $b/a$  and for  $b/a = 1$  it reaches the values for square and circle respectively. The  $d$  vs.  $\alpha$  curves for more complex shapes, such as elongated polygons with different number of sides, have identical properties and can be also used in the characterizations of grain structures [7].

Although thus far  $L_n$  and  $SI$  have been defined for specific shapes, they can be also used for characterizing either regular grids of simple figures or oriented grain structures modeled as polygons, ellipses, etc. In these cases the  $d$  vs.  $\alpha$  plots have the same characteristics as a plot for a single element if the structure is perfectly aligned. If grains have the same shapes but are not aligned, then their  $d$  vs.  $\alpha$  curves exhibit phase difference and integrations in Eqs. 1 and 2 have to be carried out from 0 to  $\pi$ . For such structures the value of  $L_n$  remains the same, but the  $SI$  will now reflect both the grain shape and the alignment and it will be greater than that for a corresponding perfectly aligned structure. In the limiting case of randomly oriented identical non-spherical

grains, the  $d$  vs.  $\alpha$  is a horizontal line and the  $S/\bar{L}$  is equal to one. For such random structures the grain shape characteristics have to be measured individually and they can not be obtained from the globally measured intercept values.

In order to fully characterize the grain structure, one also needs to quantify grain orientation or alignment. The simplest parameter for this purpose is the ratio of the average intercept lengths for 0 and 90°, i.e.  $L_2(\alpha=0)/L_2(\alpha=90)$ . A more precise parameter, which we are going to use in this work, is the ratio of the total length of oriented lines to the total length of all lines,  $\Omega_{1,2}$ . This ratio was introduced by Saltykov[6] and for our case is equal to [1, 6]:

$$\Omega_{1,2} = \frac{L_2(\alpha=0) - L_2(\alpha=90)}{L_2(\alpha=0) + 0.571 L_2(\alpha=90)} \quad (3)$$

The value of  $\Omega_{1,2}$  is zero for random structure and approaches one for structure with highly oriented and elongated grains.

### Experimental

The material used to test the proposed method was partially recrystallized aluminum 7050-T7 plate alloy. The metallographic specimens used in the analysis were prepared by grounding on 600 grit sandpaper, and then polished using 9  $\mu\text{m}$  alumina powders and finally 3  $\mu\text{m}$  diamond paste. All samples were etched using Keller's 3A etchant for 20 to 45 seconds to reveal grain and subgrain boundaries respectively. Several photographs at magnifications 100X and 500X have been taken to study the grain structures. These photographs were scanned and saved as computer image data files for the analysis by a linear intercept program. The program automatically measures intercept lengths using scan angles from 0 to 180° from the horizontal axis, and then calculate average intercept lengths, shape indices, aspect ratios, size distributions, etc. All calculations take several minutes on a PC-based system.

### Results and Discussion

The 7050-T7 alloy is an ideal material to test the proposed method. It has both recrystallized and unrecrystallized grains and in addition all unrecrystallized grains have networks of well defined subgrains. Although the alloy shows different grain structures on all three L, S and T sections, only grains and subgrains on longitudinal planes were characterized in this study. Figures 4 and 5 show representative microstructures used in the analysis. The micrographs were taken from the middle, Figure 4, and top, Figure 5, sections of the plate. Figure 4 shows evidences of partial recrystallization, while recrystallized grains are absent in Figure 5. This indicates that the fraction of the recrystallized grains changes from the top of the plate to the middle (Note that sample in Figure 5 was etched for a short time to reveal grain boundaries only).

Both recrystallized and unrecrystallized grains and subgrains have different characteristics and have been measured separately to evaluate the sensitivity of the proposed method. The measurements showed that the average intercept length,  $L_{\bar{p}}$ , was 97.6  $\mu\text{m}$  for the unrecrystallized grains, 72.6  $\mu\text{m}$  for the recrystallized grains and 6.9  $\mu\text{m}$  for the subgrains. Figure 6 shows distributions of the intercept lengths: they differ not only in their averages but also in the scatter. The distribution for the subgrains is very narrow and well defined while those for the recrystallized and unrecrystallized grains have considerable spread. The interesting feature of the distribution for unrecrystallized grains is presence of two diffused maxima which give rough estimate of the average grain width and length.

Figure 7 shows  $d$  vs.  $\alpha$  curves for all three types of grains. The shape indices,  $SI$ , are 0.811 and 0.886 for the unrecrystallized and recrystallized grains respectively and 0.920 for subgrains. As expected, the  $SI$  for the unrecrystallized grains is the smallest, which indicates that they are the most elongated. This is further supported by the lowest  $d_{90}$  value for these grains. A surprisingly high  $SI$  and  $45^\circ$  periodicity of the curve for subgrains can be attributed to the preferential alignment of subgrain boundaries at either  $0$  or  $45^\circ$ . This results in a structure which can be approximated as two arrays of squares rotated by  $45^\circ$ . Such a structure has shape factor 0.930, which is very close to the observed value. It should be again emphasized that in addition to representing the normalized average intercept lengths the  $SI$  values also characterize the randomness of the structure - the higher the value, the more random, or isometric, is the structure. Consequently, in order to characterize the orientation and average grain shape in the isometric microstructures, it is necessary to calculate the  $SI$  for each grain individually and then use obtained data to deconvolute the global  $SI$  into the orientation and shape components [7].

Also, the aspect ratio  $d_y/d_x$  was 1.324 for the unrecrystallized grains and 1.154 for the recrystallized ones. The reason for the difference is that the recrystallized grains are more equiaxed. The aspect ratio for subgrains was the smallest and equal to 1.054.

As to the grain alignment, the orientation parameter  $\Omega_{1,2}$  was 17.1% for the unrecrystallized grains, 8.9% for the recrystallized ones and 3.3% for the subgrains. These values again indicate that both subgrains and recrystallized grains had practically no preferred orientation while unrecrystallized grains were oriented only slightly. This is in agreement with the finding based on the  $d$  vs  $\alpha$  curves which further indicates the consistency of the method and its usefulness in precise characterization of the grain structures.

### Conclusions

1. Theoretical models for calculating the change of the average intercept lengths with the scan angles for simple geometrical shapes have been developed. These models can be used to study relations between various shapes and their average intercept lengths, aspect ratios and shape indices. They can be also applied to the characterization of the heterogeneities in the partially aligned microstructures of single or multiphase alloys and composites.
2. The grain structures of partially recrystallized aluminum 7050-T7 alloy have been characterized using proposed methodology. Both recrystallized and unrecrystallized grains and subgrains have been studied. The method allowed for the quantification of minute differences in sizes, shapes and preferred orientation of all grain and subgrain types.
3. The plots of average linear intercept vs. scan angle provide quantitative information on grain sizes, shapes and orientation needed in the modeling of mechanical properties and/or in the characterization of the extent of thermo-mechanical processing. Since these plots contain information about both grain shapes and orientation, they are most useful for quantifying differences between partially aligned structures. A more detailed description of the individual grain shapes is needed for the characterization of the structures of randomly oriented grains.

### Acknowledgment

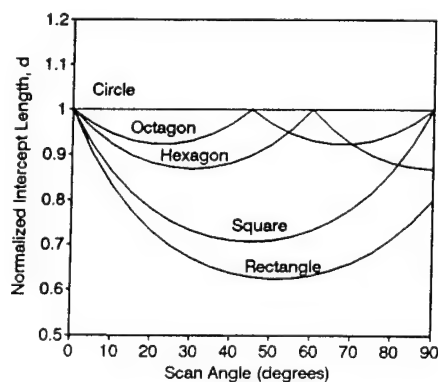
The authors are grateful to Alcoa Laboratories for providing us with the material and to the Office of Naval Research for their support under Grant No. N00014-91-J-1299 of which Dr. A. K. Vasudevan is the program manager.

## References

1. E. E. Underwood, *Quantitative Stereology*, Addison-Wesley Publishing Company, Reading, Massachusetts, pp196-197, 1970.
2. R. T. DeHoff and F. N. Rhines, editors. : *Quantitative Microscopy*, McGraw-Hill Book Company, New York, NY 10036, USA (1968).
3. S. Miyata and M. Kikuchi, "Quantitative Analysis of the Graphite Structure in Cast Iron by a Statistical Method," *Trans. Natl. Res. Inst. Met.*, vol. 16, No. 3, 1974, pp 25-31.
4. T. L. Capeletti and J. R. Hornaday, "Nodular Iron Shape Factor A New Approach to Quantifying Graphite Morphology," *Trans. Am. Foundrymen's Soc.*, vol. 82, 1974, pp59-64.
5. H. H. Hausner, "Characterization of the Powder Particle Shape," *Planseeber. Pulvermetall.*, vol. 14, 1966, pp75-84.
6. S. A. Saltykov, *Stereometric Metallography*, Second edition, Moscow: Metallurgizdat (1958).
7. J. Zhang, A. J. Luévano and M. A. Przystupa: "Theoretical Models for Quantitative Analysis of Grain and Particle Shapes" Submitted to *Materials Characterization*.

Table 1. Compilation of Expression for Average Intercept Lengths for Selected 2-D Figures

Form	Average Intercept Length $L_2(\alpha)$	Period
Circle:	$\frac{\pi a}{2}$	-----
Square:	$\frac{a}{\cos\alpha + \sin\alpha}$	$\pi/2$
Rectangle:	$\frac{a}{\cos\alpha + \frac{a \sin\alpha}{b}}$	$\pi/2$
Hexagon:	$\frac{\frac{3}{2}a \cos(\frac{\pi}{6})}{\cos(\frac{\pi}{6} - \alpha)}$	$\pi/3$
Octagon	$\frac{2a(1+\sqrt{2})}{\sin\alpha + (1+\sqrt{2})\cos\alpha}$	$\pi/4$

Fig. 1. Normalized intercept length  $d$  as a function of  $\alpha$  for circle, octagon, hexagon, square and rectangle.

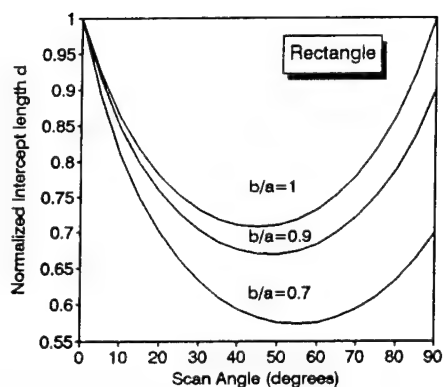


Fig. 2. Normalized intercept length  $d$  as a function of  $\alpha$  for rectangles with different aspect ratios  $b/a$ .

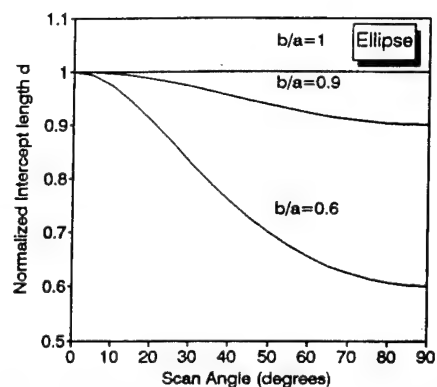


Fig. 3. Normalized intercept length  $d$  as a function of  $\alpha$  for ellipses with different major and minor axis ratios  $b/a$ : ( $a$  is constant for all three curves).

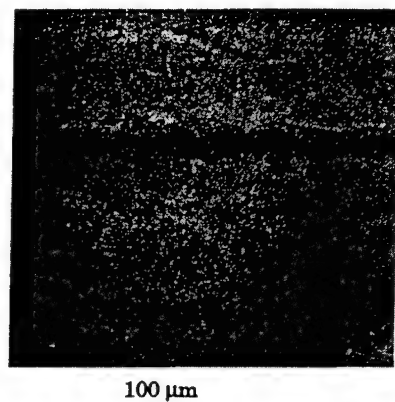


Fig. 4. Microstructure of Al 7050 near middle section of the plate showing a mixture of unrecrystallized and recrystallized grains.

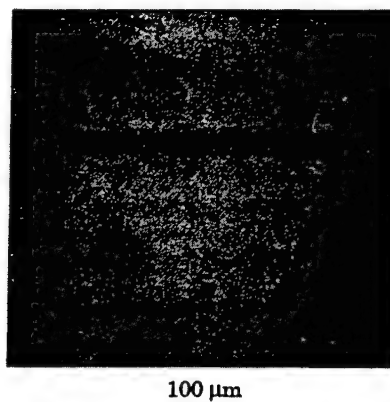


Fig. 5. Microstructure of Al 7050 near top section of the plate showing unrecrystallized grains only.

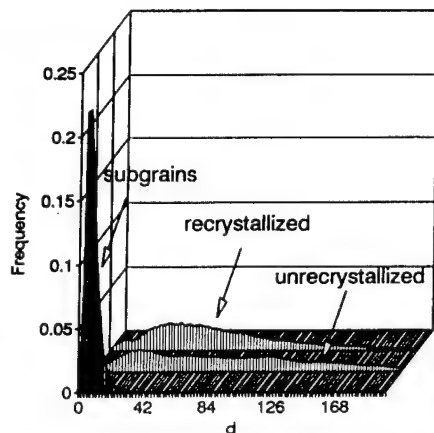


Fig. 6. Size distributions of different grains: recrystallized, unrecrystallized and their subgrains.

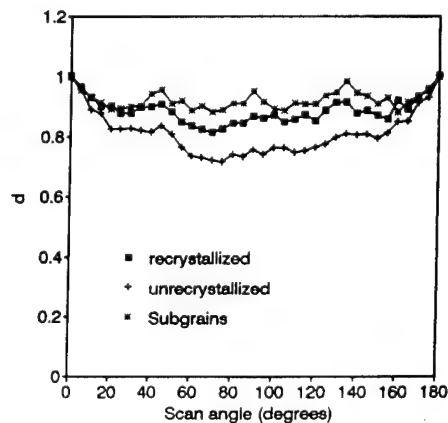


Fig. 7. Normalized intercept length vs. scan angle for the different grains. Overall shape indices are the areas under the curves.

*Appendix C. Microstructural Models for Quantitative Analysis of Grains and  
Second-Phase Particles*

J. Zhang, A. J. Luevano and M. A. Przystupa  
*Materials Characterization*, 33 (1994) pp. 175-185.

# Microstructural Models for Quantitative Analysis of Grains and Second-Phase Particles

Jimin Zhang, Annetta J. Luévano, and Marek A. Przystupa

*Department of Materials Science and Engineering, University of California, Los Angeles, CA 90024*

Microstructural models for quantitative analysis of shapes and orientations of grains and second-phase particles on plane sections have been proposed. The models use rectangle, ellipse, regular, and elongated polygons as idealized shapes. For each shape, a function describing the change of average linear intercept length with the scan angle has been derived. These functions are used in the identification of individual shapes as well as in the quantitative characterization of the collection of two-dimensional objects such as grains and particles. In addition, the shape index proposed in the authors' earlier work has now been extended to describe the conglomerates of grains or second phase particles. A new orientation factor describing an object's alignment has also been proposed. A simple method for constructing the normalized average intercept length versus scan angle plots using polar coordinates is also presented. The utility of the proposed methodology is illustrated in an example of the characterization of the size, shape, and degree of orientation of subgrains in the 7050 aluminum alloy.

## INTRODUCTION

To obtain any meaningful correlations between microstructure and mechanical properties, it is imperative to use not only information about the average sizes of grains and/or second-phase particles, but also information about their size, shape, and orientation distributions. The microstructural characterizations required to obtain the distributions are usually tedious and time-consuming; thus, they are performed very reluctantly. In this work, we develop two-dimensional microstructural models that simplify the measurement process for two-dimensional features on plane sections and allow for the characterization of those features precisely and automatically.

Among all quantitative parameters describing the grains or particles on plane sections, shape is the most difficult to define. The prevailing approach in its characteriza-

tion is to use shape factors or shape indices, such as those enumerated by Underwood [1], DeHoff and Rhines [2], and Vander Voort [3]. To make shape factors dimensionless, the proposed definitions involve ratios of either the areas or the linear dimensions. For example, the shape factor most commonly used is the one defined [4] as the ratio of the square of the particle circumference,  $L_p$ , to  $4\pi A$ , where  $A$  is the particle area. An alternative definition involves the ratio of the circumference of the equivalent circle to the actual perimeter [5]. Although shape factors are widely used, they do not always have one-to-one correspondence with the shapes they represent, that is, two different shapes can have the same value of the shape factor. This problem is particularly serious for concave and complex shapes where quantification of shape requires mathematical description of the feature's boundary lines using, for instance, Fourier series [6]. Other tech-

niques available for shape description include the spectral and the fractal analyses [7, 8].

Definitions of shape indices or factors that are directly related to the linear intercept method [5, 9, 10] are the most appealing because they can be easily incorporated into automatic measurements. There are two ways of characterizing shapes using the linear intercept method. The first one was developed by Saltykov [5] to characterize the angular dependence of the number of intercepts per unit length of test line,  $P_L$ , for systems of oriented straight lines. He constructed polar plots of  $P_L$  versus  $\alpha$ , where  $\alpha$  is the scan angle, for systems with one, two, and three orientation axes and named them "roses of the number of intersections." If one considers grids of rectangles and triangles as the systems of lines with two or three orientation axes, Saltykov's method is ideal for describing such two dimensional shapes. Hilliard [11] extended the method and proposed a general procedure for calculating  $P_L$  from the known angular orientations of lines. His method treats polygons or ellipses as special cases for which the expression for  $P_L$  has an integral form. The utility of the Saltykov-Hilliard method has been illustrated by Benes [12] in his characterizations of the degree of anisotropy of microstructure.

An alternative way of representing shapes based on the linear intercept method is to use the polar plot of the average intercept length,  $L_2$ , versus scanning angle,  $\alpha$ . The relationship between  $L_2$ - $\alpha$  polar plot and "Rose of Intersections" is straightforward because  $P_L$  is the reciprocal of the average intercept length,  $L_2$ . The  $L_2$ - $\alpha$  plots were used by Luo et al. [9] to study networks of straight lines with several oriented axes.

They showed that the polar plot of the average intercept length for a planar  $N$ -net system of straight lines was a convex  $2N$ -sided polygon and proposed a simple method for constructing such plots. However, the forms studied by both Luo et al. and Saltykov-Hilliard method were limited to only a few plane-filling polygons, and the

methods cannot be applied to the cases of collections of ellipses and circles.

This work fills some of the existing gaps in the analysis of two-dimensional features and extends the analysis of shapes introduced earlier by Zhang et al. [10]. In particular, the polar plots of the normalized average intercept length,  $d$ , versus scan angle ( $d$ - $\alpha$  curves) and the shape indices for regular polygons are treated here to complete the Zhang et al. [10] description. A simple method for constructing the polar  $d$ - $\alpha$  plots for polygons is also introduced. In addition, the paper proposes several models of elongated polygons that can be used to describe shapes commonly encountered in structural materials. It is also shown how the global shape index obtained from  $d$ - $\alpha$  curves can be deconvoluted into the shape and orientation components, and how the  $d$ - $\alpha$  curves can be used to obtain a new parameter describing grain orientation. The proposed methodology provides a theoretical basis for the automation of quantitative analyses of shapes, sizes, and orientations of grains and/or particles on the plane sections. An example of such an analysis is carried out for the subgrain structure of 7050 Al alloy.

## MICROSTRUCTURAL MODELS

### INTERCEPT LENGTH

To develop the theoretical microstructural models used in this work, we used the linear intercept method because of its simplicity and popularity in quantitative analysis. In this method, the average intercept length,  $L_2(\alpha)$ , of a two-dimensional object at a scan angle  $\alpha$  (Fig. 1) can be calculated as [10]:

$$L_2(\alpha) = \frac{A}{H_2(\alpha)}, \quad (1)$$

where  $L_2(\alpha)$  is the average of all intercept lengths at a given scan angle  $\alpha$ ,  $A$  is the object area, and  $H_2(\alpha)$  is its tangent height, defined as the projection of the object on the direction perpendicular to the scan lines. Because for a given object  $A$  is a constant,

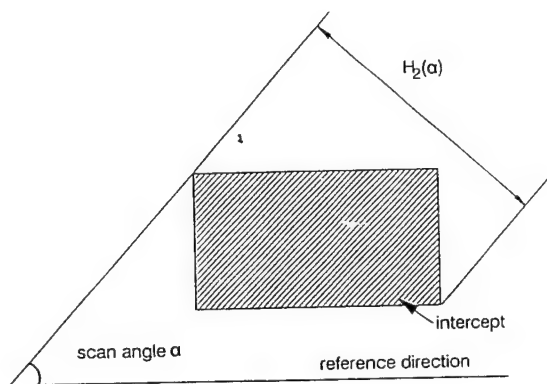


FIG. 1. Schematic defining the scan angle, intercept length, and tangent height  $H_2(\alpha)$  used in the text.

$L_2(\alpha)$  is only a function of the tangent height.

The average intercept length over all scan angles,  $L_{II}$ , is defined as:

$$L_{II} = \frac{1}{\pi} \int_0^\pi w_2(\alpha) L_2(\alpha) d\alpha, \quad (2)$$

where  $w_2(\alpha)$  is the weight factor that can be shown to be equal to:

$$w_2(\alpha) = \frac{H_2(\alpha)}{\frac{1}{\pi} \int_0^\pi H_2(\alpha) d\alpha}. \quad (3)$$

Combining Eqs. (2) and (3) gives

$$L_{II} = \frac{\pi A}{\int_0^\pi H_2(\alpha) d\alpha}, \quad (4a)$$

or, in the form amenable for computer usage,

$$L_{II} = \frac{\pi A}{\Delta\alpha \sum_{i=0}^n H_{2i}(\alpha_i)} \quad (4b)$$

where  $n = \pi/\Delta\alpha$ , and  $\Delta\alpha$  is the step size of the scan angle.

For convex shapes,  $\int_0^\pi H_2(\alpha) d\alpha$  is equal to  $L_p$ , the perimeter of the measured object. Thus, in this case

$$L_{II} = \frac{\pi A}{L_p}, \quad (5)$$

which is a standard equation used in the literature [13]. For convex shapes consisting of  $m$  simple ones, the formulae for the intercept lengths  $L_2(\alpha)$  and  $L_{II}$  are:

$$L_2(\alpha) = \frac{\sum_{i=0}^m A_i}{H_2(\alpha)} \quad (6)$$

and

$$L_{II} = \frac{\pi \sum_{i=0}^m A_i}{L_p}, \quad (7)$$

where  $A_i$ 's are areas of individual components. Equations (6) and (7) are quite general, and they can be used even for shapes formed by subtracting one shape from another, providing that the average intercept length is defined as the sum of the sections of straight lines inside the measured shape. As an example, a ring can be viewed as a larger circle minus a concentric smaller one; in this case the area of the inner circle is negative. The position of the inner negative shape has no effect on the value of  $L_2(\alpha)$  as  $H_2(\alpha)$  remains the same. Thus, if Eq. (6) is applied to a ring, the value of  $L_2(\alpha)$  would be the same whether the two circles are concentric or not.

### Rectangle, Ellipse, and Regular Polygons

To quantitatively characterize plane sections of grains and second-phase particles, the expressions for  $L_2(\alpha)$  and  $L_{II}$  for different shapes must be known. In this work, equations for  $H_2(\alpha)$ ,  $L_2(\alpha)$ , and  $L_{II}$  for rectangle, ellipse, regular polygons, and elongated polygons have been derived, and the results are listed in Table 1. Among these shapes, regular polygons represent the shapes spanning from a 3-fold symmetry triangle to a circle-like polygon. On the other hand, the rectangles, ellipses, and elongated polygons cover shapes with unrestricted aspect ratios. In all derivations, the major axes of all shapes have been set to be parallel to the scan line at  $\alpha = 0$ . This assures the simplest mathematical expressions for  $L_2(\alpha)$ . The expressions for a square are not listed in Table 1 because they are special cases of either a regular polygon with four sides or a rectangle with two sides of equal length. Similarly,

**Table 1** The Intercept Lengths for Selected Two-Dimensional Figures

Feature	$A$	$L_p$	$H_2(\alpha)$	$L_2(\alpha)$	$L_{II}$
Rectangle	$ab$	$2(a+b)$	$a \sin \alpha + b \cos \alpha$ $\alpha \left[0, \frac{\pi}{2}\right]$	$\frac{ab}{a \sin \alpha + b \cos \alpha}$	$\frac{\pi ab}{2(a+b)}$
Ellipse	$\pi ab$	$\pi \sqrt{2(a^2 + b^2)}$	$2\sqrt{\frac{b^2 + a^2 \tan^2 \alpha}{1 + \tan^2 \alpha}}$	$\frac{\pi ab}{2} \sqrt{\frac{1 + \tan^2 \alpha}{b^2 + a^2 \tan^2 \alpha}}$	$\frac{\pi ab}{\sqrt{2(a^2 + b^2)}}$
Regular polygon $n = \text{even}$	$\frac{na^2}{4 \tan(\frac{\pi}{n})}$	$na$	$a \frac{\cos(\frac{\pi}{n} - \alpha)}{\sin(\frac{\pi}{n})} \alpha \left[0, \frac{\pi}{n}\right]$	$\frac{na \cos(\frac{\pi}{n})}{4 \cos(\frac{\pi}{n} - \alpha)}$	$\frac{\pi a}{4 \tan(\frac{\pi}{n})}$
Regular polygon $n = \text{odd}$	$\frac{na^2}{4 \tan(\frac{\pi}{n})}$	$na$	$a \frac{\cos(\frac{\pi}{2n} - \alpha)}{\sin(\frac{\pi}{2n})} \alpha \left[0, \frac{\pi}{n}\right]$	$\frac{na \cos(\frac{\pi}{n})}{4 \cos(\frac{\pi}{2n}) \cos(\frac{\pi}{2n} - \alpha)}$	$\frac{\pi a}{4 \tan(\frac{\pi}{n})}$
Elongated pentagon	$b\left(a + \frac{b}{4\sqrt{3}}\right)$	$2a + b\left(1 + \frac{2}{\sqrt{3}}\right)$	$a \sin \alpha + b \cos \alpha$ $\alpha \left[0, \frac{\pi}{3}\right]$ $a \sin \alpha + b \cos \alpha + \frac{b}{\sqrt{3}} \sin\left(\alpha - \frac{\pi}{3}\right)$ $\alpha \left[\frac{\pi}{3}, \frac{\pi}{2}\right]$	$\frac{a + \frac{b}{4\sqrt{3}}}{\cos \alpha + \frac{a}{b} \sin \alpha}$ $\frac{a + \frac{b}{4\sqrt{3}}}{\cos \alpha + \frac{a}{b} \sin \alpha + \frac{\sin(\alpha - 60)}{\sqrt{3}}}$	$\frac{\pi b\left(a + \frac{b}{4\sqrt{3}}\right)}{2a + b\left(1 + \frac{2}{\sqrt{3}}\right)}$
Elongated hexagon	$ab + \frac{b^2}{2\sqrt{3}}$	$2\left(a + \frac{2b}{\sqrt{3}}\right)$	$a \sin \alpha + b \cos \alpha$ $\alpha \left[0, \frac{\pi}{3}\right]$ $a \sin \alpha + \frac{b \sin \alpha}{2 \cos(\frac{\pi}{6})}$ $\alpha \left[\frac{\pi}{3}, \frac{\pi}{2}\right]$	$\frac{a + \frac{b}{2\sqrt{3}}}{\cos \alpha + \frac{a}{b} \sin \alpha}$ $\frac{a + \frac{b}{2\sqrt{3}}}{\left(\frac{a}{b} + \frac{1}{\sqrt{3}}\right) \sin \alpha}$	$\frac{\pi b\left(a + \frac{b}{2\sqrt{3}}\right)}{2\left(a + \frac{2b}{\sqrt{3}}\right)}$
Elongated octagon	$b\left(a + \frac{b}{1 + \sqrt{2}}\right)$	$2a + \frac{6b}{1 + \sqrt{2}}$	$a \sin \alpha + b \cos \alpha$ $\alpha \left[0, \frac{\pi}{4}\right]$ $b \cos(\alpha - \alpha_1) \sqrt{\frac{1}{1 + \sqrt{2}} + \frac{(1 + \sqrt{2})^2 a^2}{b^2}}$ $\alpha_1 = 90 - \arctan\left(\frac{1}{\sqrt{2} + \frac{a}{b}(1 + \sqrt{2})}\right)$ $\alpha \left[\frac{\pi}{4}, \frac{\pi}{2}\right]$	$\frac{a + \frac{b}{1 + \sqrt{2}}}{\cos \alpha + \frac{a}{b} \sin \alpha}$ $\frac{a + \frac{b}{1 + \sqrt{2}}}{\cos(\alpha - \alpha_1) \sqrt{\frac{1}{1 + \sqrt{2}} + \frac{(1 + \sqrt{2})^2 a^2}{b^2}}}$ $\alpha_1 = 90 - \arctan\left(\frac{1}{\sqrt{2} + \frac{a}{b}(1 + \sqrt{2})}\right)$	$\frac{\pi b\left(a + \frac{b}{1 + \sqrt{2}}\right)}{2\left(a + \frac{3b}{1 + \sqrt{2}}\right)}$

equations for a circle can be obtained from those for an ellipse with  $a = b$  or a regular polygon when the number of sides is infinity. In calculating the  $L_{II}$  for an ellipse, the perimeter has been assumed to be equal  $\pi\sqrt{2(a^2 + b^2)}$ . Also, because of geometrical differences between regular polygons and even and odd numbers of sides, their expressions for  $H_2(\alpha)$  and  $L_2(\alpha)$  are listed separately in Table 1. However, the equations for the average intercept length over all the scan angles,  $L_{II}$ , are the same for both cases.

### Elongated Polygons

In real life, the aspect ratios of grains or particles are seldom equal to one and, for instance, grains in metals are usually elongated in certain directions as a result of plastic deformation. To describe such elongated shapes, we propose to use a series of elongated  $n$ -sided polygons. These polygons are formed by stretching the lengths of two parallel sides of a regular polygon. The resulting shapes can be classified as elongated pentagons, hexagons and octagons and their

formulae for  $L_2(\alpha)$  and  $L_{II}$  have been listed in Table 1. They all have rectangular cores with variable aspect ratios of height,  $a$ , to width,  $b$ . These model shapes can be readily used in the characterization of the grains or particles with various shapes by adjusting the values of  $a/b$  and  $n$ .

### Normalized Intercept Length versus Scan Angle Plots

The characteristics of the proposed model shapes can be explored by comparing their intercept length versus scan angle plots. It is convenient to use for this purpose a normalized intercept length in the plots,  $d_2(\alpha)$  or  $d$ , defined as:

$$d_2(\alpha) = d = \frac{L_2(\alpha)}{L_{2,\max}}, \quad (8)$$

where  $L_{2,\max}$  is the maximum intercept length. Such  $d$  versus scan angle,  $\alpha$ , plots for ellipses with different aspect ratios,  $b/a$ , are shown in Fig. 2. They clearly indicate that  $d$  is strongly dependent on both  $\alpha$  and  $b/a$ . Because for ellipses  $d_{\alpha=0} = \pi a/2$  and  $d_{\alpha=90} = \pi b/2$ , the aspect ratio defined as  $a/b$  is the same as the ratio of  $d_{\alpha=0}/d_{\alpha=90}$ . As expected, the  $d$  versus  $\alpha$  curve flattens out as the  $b/a$  ratio increases and becomes a horizontal line when the ellipse becomes a circle, that is, for  $b/a = 1$ .

Figure 3 shows the change of  $d$  versus  $\alpha$  for regular polygons with an even number of sides. Both the amplitudes and periods

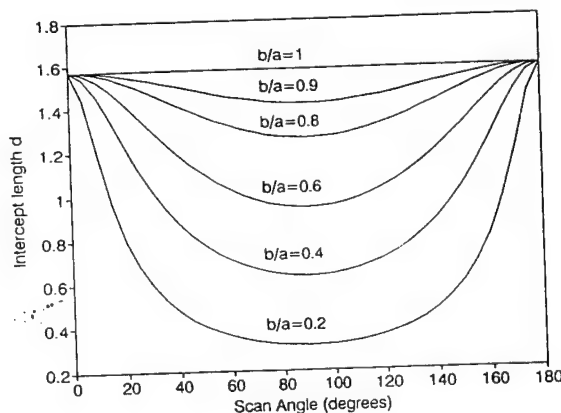


FIG. 2. Normalized intercept length,  $d$ , for ellipses with different  $b/a$  ratios.

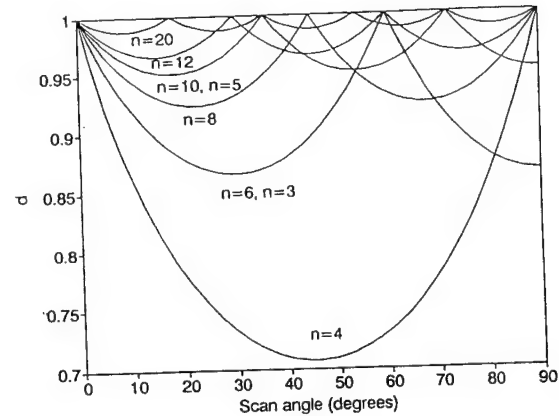


FIG. 3. Normalized intercept length,  $d$ , for regular  $n$ -sided polygons.

of the curves change as a function of the number of the sides,  $n$ . The larger the  $n$ , the smaller are the amplitude and the shorter the period. In the limit, when  $n$  goes to infinity, the polygon approximates a circle and the  $d$ - $\alpha$  curve is a horizontal line. This behavior is evident from the equation for the  $L_2(\alpha)$  in Table 1 that shows that for considered polygons the amplitudes of  $d$  versus  $\alpha$  curves should be proportional to  $\cos(\pi/n)$  and the period to  $2\pi/n$ .

For regular polygons with an odd number of sides, the  $d$ - $\alpha$  curves do not fall between the curves for their neighbors with an even number of sides. Instead, the  $d$ - $\alpha$  curve for the equilateral triangle is exactly the same as that for the regular hexagon, and the curve for a pentagon is identical to the one for a decagon, and so on. This coincidence results from the fact that the tangent heights (Table 1) of a regular polygon with an odd number of sides and a polygon with the number of sides twice that number are the same. Thus, the two formulae for  $L_2(\alpha)$  (Table 1) are also the same, except for the proportionality coefficients. Because these coefficients drop out during normalization, the  $d$ - $\alpha$  curves are exactly the same in both cases. Consequently, normalized  $L_2(\alpha)$  can be used for all the regular polygons regardless of the numbers of the sides. However, the standard deviation of  $L_2(\alpha)$  for any scan angle is always much larger for the polygons with an odd number of sides, because they are less "circular." This

property can be used as a distinguishing criterion.

The  $d$ - $\alpha$  curves for various elongated polygons have been compiled in Figs. 4-6. The figures illustrate the dependence of  $d$  on the number of the polygon sides and the aspect ratio,  $b/a$ , of the core rectangle. The length,  $a$ , in all polygons has been set to one to facilitate meaningful comparisons. Figure 4 shows how the curvature of the  $d$ - $\alpha$  curves for the elongated hexagons increases with decreasing  $b/a$  ratio. The reason for this change is that the polygons with smaller  $b/a$  have larger aspect ratios, hence, lower values of  $d$  at  $90^\circ$ . It is clear that a wide range of shapes can be represented by choosing different  $b/a$ . The local maxima on all curves correspond to the angular periods of the original regular hexagons, which is  $\pi/3$ . Similar maxima, and for the same reason, can be observed on the  $d$ - $\alpha$  curves for polygons with different numbers of sides but with  $b/a = 1$ , which are shown in Fig. 5. Note that although the curves are for polygons with different shapes, they all overlap in the region  $[0, \pi/4]$  due to the identical square cores. Figure 6 shows that the differences between  $d$ - $\alpha$  curves for the elongated polygons become quite small when  $b/a$  is below 0.5. Thus, it seems that for small  $b/a$  the effect of the core rectangle becomes dominant, and the elongated polygons can be approximated by that rectangle alone.

The  $d$ - $\alpha$  curves can also be presented in polar coordinates as shown, for a square and

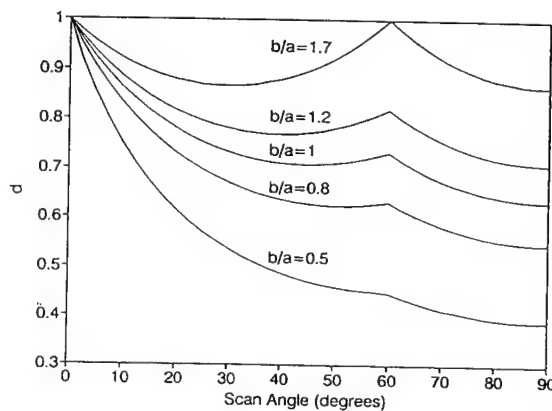


FIG. 4. Normalized intercept length,  $d$ , for elongated hexagons with different  $b/a$  ratios.

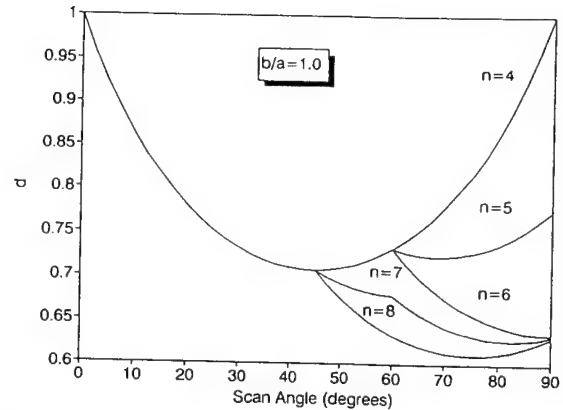


FIG. 5. Normalized intercept length,  $d$ , for elongated polygons with  $n$  sides.

hexagon, in Fig. 7. The main advantage of such plots is that they are similar to the original forms for all rotationally symmetrical shapes, for instance, regular polygons and circles. For nonrotationally symmetrical shapes, such as rectangles and ellipses, the polar  $d$ - $\alpha$  curves are slightly different from the originals, and they appear as a diamond and a quasi-ellipse, respectively (Fig. 8). All polar plots can, nevertheless, provide instant visual representations of the measured shapes and supplement the basic information obtained from the Cartesian plots. In addition, the polar plots for polygons are much easier to make than their Cartesian counterparts. This is because the expressions for  $L_2(\alpha)$  for polygons represent straight lines in the polar coordinates. As an example, the polar plot for a regular polygon

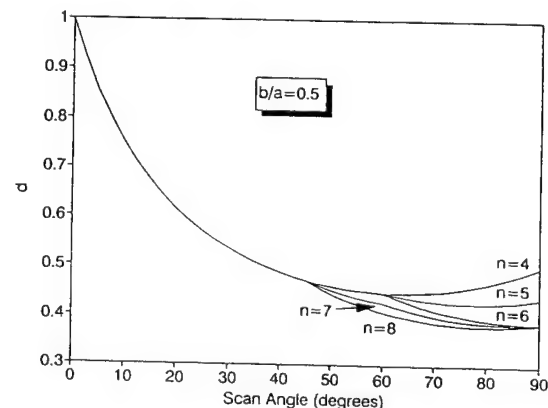


FIG. 6. Normalized intercept length,  $d$ , for elongated polygons with  $b/a = 0.5$ .

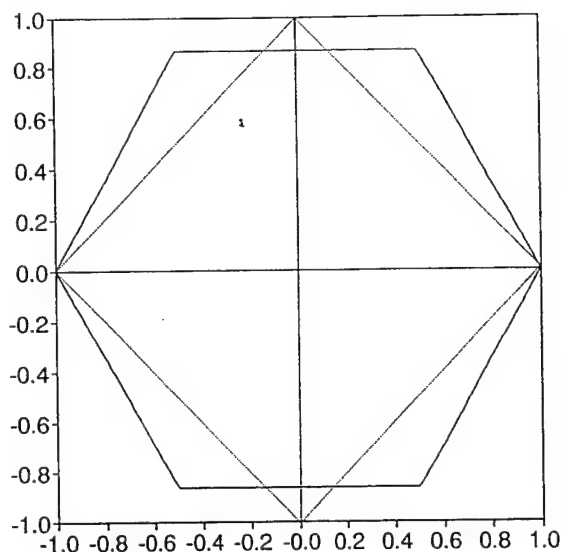


FIG. 7. Polar plot of  $d$ - $\alpha$  for a hexagon (solid line) and a square (dotted line).

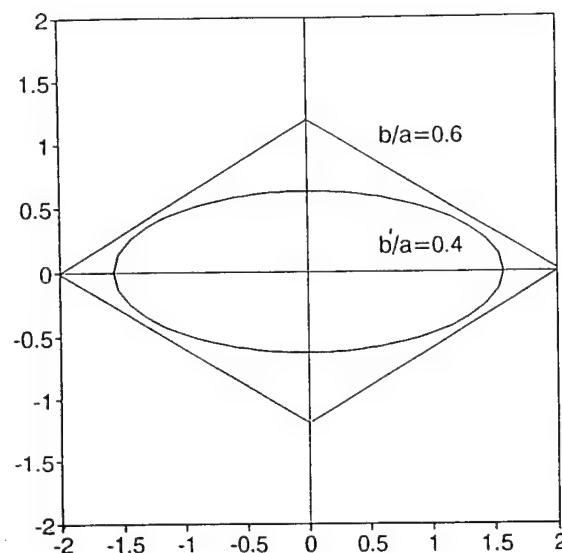


FIG. 8. Polar plot of  $d$ - $\alpha$  for an ellipse with  $b/a = 0.4$  and a rectangle with  $b/a = 0.6$ .

with twenty sides can be constructed by first dividing a unit circle on twenty  $18^\circ$  segments and then connecting the ends of segments with straight lines. For rotationally nonsymmetrical polygons, one only needs to know the  $d$  values for angles corresponding to the vertexes of the original polygons to draw the plots.

The proposed polar  $d$ - $\alpha$  plots are related to the  $P_L$ - $\alpha$  "rose" plots introduced by Saltykov [5] and Hilliard [11] because  $P_L$  is simply the reciprocal of the  $L_2(\alpha)$ . The advantage of our polar plots is that they provide direct information about the average intercept length and its directional variation. Also, in contrast to the plots of the roses of the number of intersections,  $P_L$ , the proposed plots can be constructed for any polygons without knowing the exact mathematical expressions for  $d(\alpha)$ .

The proposed polygonal model shapes and associated  $d$ - $\alpha$  curves are then very flexible. By changing the number of the polygon sides,  $n$ , and/or its core rectangle aspect ratio,  $a/b$ , one can cover all possible shapes expected of microstructural features. In addition, the  $d$ - $\alpha$  plots can be used in extracting information not only about the average length and aspect ratio but also, as will be shown in the next section, about the shapes of the two-dimensional objects.

### SHAPE INDEX

In order to quantify the shapes of the microstructural features, the authors defined a new shape index,  $SI$ , as the area under the  $d$ - $\alpha$  curve [10]. This index can be expressed as:

$$SI = \frac{1}{\alpha_p} \int_0^{\alpha_p} d \, d\alpha, \quad (9)$$

where  $\alpha_p$  is the angular period of the  $d$ - $\alpha$  curve. Some of the properties of such a defined shape index are obvious from its definition. First, because  $d$  is a normalized quantity, all two-dimensional shapes will have the  $SI$  between zero and one. Second, the normalization assures that the  $SI$  is independent of the actual sizes of the objects,  $L_{II}$ . Finally, the shape index is independent of the orientation of the object with respect to the scan lines. Different orientations of an object thus result in different initial shifts of the  $d$ - $\alpha$  curves but the areas under the curves, which are represented by the  $SI$ , stay the same.

Other characteristics of the shape index  $SI$  can be illustrated by example. The  $SI$  for regular polygons can be obtained by substituting  $L_{2,pol}(\alpha)$  (Table 1) after normalizing by  $L_{2,max}$  into Eq. (9). This gives:

$$SI = \frac{\cos \frac{\pi}{n}}{\frac{2\pi}{n}} \ln \left( \frac{\tan \left( \frac{\pi}{4} + \frac{\pi}{2n} \right)}{\tan \left( \frac{\pi}{4} - \frac{\pi}{2n} \right)} \right). \quad (10)$$

The last equation is plotted in Fig. 9. As expected, as  $n$  increases, the  $SI$  also increases because the polygon becomes more and more circular. Because for all practical purposes,  $SI$  is equal to one for  $n > 20$ , all polygons with the number of sides greater than 20 can be approximated by a circle. Similarly, for ellipses the shape indexes depend on the aspect ratios  $b/a$ , that is, not all the ellipses have the same shape index. As  $b/a$  decreases, the  $d$ - $\alpha$  curves shift downward, resulting in a smaller shape index. The same trends hold for other objects with variable aspect ratios such as rectangles and elongated polygons.

### ORIENTATION INDICES

So far we have only considered the characteristics of the individual objects. A problem associated with using the linear intercept method arises when dealing with a conglomerate of grains or particles as the average intercept length contains information about both orientations and shapes of the measured features. Because the real microstructures consist of a collection of objects, the relative orientations of them have to be also characterized. If two identical elongated grains are oriented at different angles with respect to the scan lines, their  $d$ - $\alpha$  curves will

have a phase difference, that is, they will be shifted relative to each other. If we now construct a  $d$ - $\alpha$  curve that is the average for all  $d$ - $\alpha$  curves for all grains, then the global shape index,  $SI_g$ , obtained from such an average curve will reflect both the shapes and the orientations of all grains. Consequently,  $SI_g$  will be a true representation of the grain shapes only if the grains are aligned. Because in most cases they are not,  $SI_g$  will increase with increasing grain misalignment, and it will approach unity for a statistically random grain structure.

The "true" average shape index for all grains can thus be found by artificially aligning grain directions in such a way that their axes corresponding to  $L_{2,\max}$  are all parallel. We shall call such shape index  $SI_{avg}$ . It is equal to:

$$SI_{avg} = \frac{1}{m\pi} \sum_{i=1}^m \int_0^\pi d_{2i}(\alpha) d\alpha, \quad (11)$$

where  $m$  is a number of measured grains, and the integration under the sum is carried from 0 to  $\pi$  to account for the different periodicities of the  $d$ - $\alpha$  curves for different grain shapes. Because  $SI_{avg}$  is the shape index without orientation component while  $SI_g$  contains information on both shape and orientation, one can deconvolute the shape and orientation effects by defining an orientation factor,  $\Omega$ , as:

$$\Omega = \frac{1 - SI_g}{1 - SI_{avg}}. \quad (12)$$

For randomly oriented features,  $SI_g$  will go to one and  $\Omega$  will be equal to zero. In a perfectly oriented structure, the  $SI_g$  and  $SI_{avg}$  are the same and  $\Omega$  is equal to one. The orientation factor,  $\Omega$ , is then a convenient factor that does not carry any information about the crystallographic orientation but that quantitatively describes the degree of grain alignment on a scale from zero to one.

### EXPERIMENTAL

The proposed methodology has been tested by characterizing the subgrain structure of a 7050-T7 Al plate alloy. The specimen used

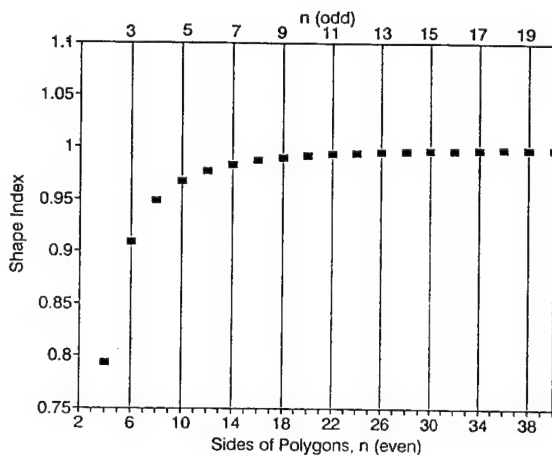


FIG. 9. Shape indices for  $n$ -sided regular polygons.

in the characterization was prepared using the technique described by Zhang et al. [10]. Several photographs at magnifications of  $\times 100$  and  $\times 500$  have been taken to assure good statistics. Figure 10 shows a typical micrograph with subgrain structure on the L section in the middle of the plate. All photographs were scanned and saved as computer image files for subsequent quantitative analysis. Because manual analysis of heterogeneous microstructures is normally very work intensive, a computer program based on the proposed methodology has been developed. The program automatically measured intercept lengths using scan angles from 0 to  $180^\circ$  from the horizontal axis, and then calculated the average intercept lengths, shape indices, aspect ratios, size distributions, etc. All calculations for one image usually take several minutes on a PC-based system.

## RESULTS AND DISCUSSION

Figure 11 shows the  $d$ - $\alpha$  curves for the subgrains in Fig. 10. They were obtained from both the global and individual characterization of subgrains to obtain  $L_2(\alpha)$ ,  $d$ ,  $SI$ , and  $\Omega$ . The global  $d$  curve clearly shows that the structure is anisotropic. This anisotropy can be quantified by using the global shape index,  $SI_g$ , which is the area under the global  $d$  versus  $\alpha$  curve—it is 0.8297. Information on the average shape of the grains is represented by the average  $d$  curve, and the  $SI_{avg}$

obtained from that curve is 0.6998. The 18% difference between the  $SI_g$  and  $SI_{avg}$  is due to the orientation effect that can be quantified with  $\Omega$ . In this case,  $\Omega$  is 0.568. In addition, the average subgrain aspect ratio can also be obtained from the plot in Fig. 11. It is equal to the ratio of  $d_{avg}$  at 0 and  $90^\circ$ , and for the subgrains in Fig. 10 it is 0.553.

To characterize the subgrain structure in the alloy studied, the models of the elongated polygons and the ellipse have been used. Because the shape index,  $SI_{avg}$ , of the studied subgrain structure is 0.6998, it is equivalent to that of an ellipse with  $b/a = 0.5222$  ( $SI_{avg} = 0.7120$ ), an elongated hexagon with  $b/a = 0.8352$  ( $SI_{avg} = 0.6908$ ), and an elongated octagon with  $b/a = 0.9072$  ( $SI_{avg} = 0.6947$ ). All three models gave good least-square fits to the experimental data with the octagon model having the best fit of the three. This seems to confirm that the elongated polygon models are versatile and very effective in the quantitative characterization of shapes. As seen in Fig. 10, the shapes of the subgrains on the plane section can be described as a conglomerate of polygons with different sizes and shapes. In such a case, the value of  $SI_{avg}$  can give an indication of how circular the grains are on average—the larger  $SI_{avg}$ , the more circular are the grains. Note that the actual sizes of the grains have no effect on  $SI_{avg}$  because it is obtained from the normalized intercept lengths.

A collection of plane-filling polygons is often described by an "average shape." Because the average number of corners per

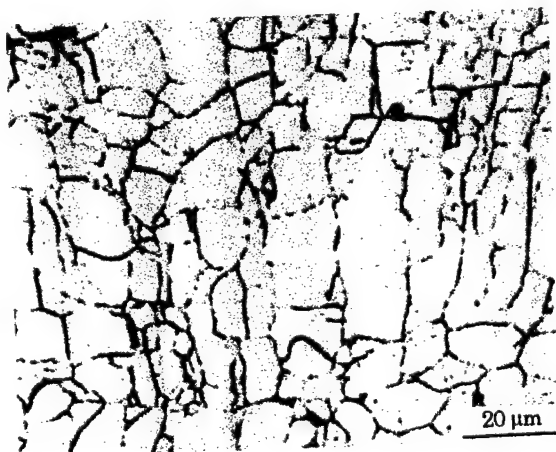


FIG. 10. Subgrain structure of the 7050 Aluminum alloy.

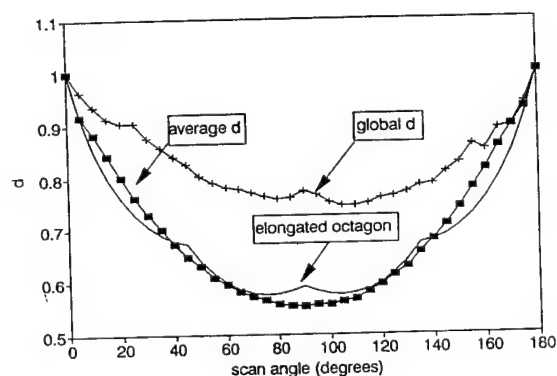


FIG. 11. Normalized intercept length,  $d$ , for the subgrain structure in Fig. 10.

polygon in such a collection is always equal to six [1], the average shape is always a hexagon. In this work, we propose to augment description of such structure with the shape index  $SI_{avg}$ , which depends not only on the number of sides but also on the aspect ratios of polygons. For regular hexagons,  $SI_{avg}$  has the highest value among all hexagons, and its value decreases with increasing hexagon aspect ratios. Therefore, even if the "average shape" of the polygons remains hexagonal, their  $SI_{avg}$  value does change as a function of the polygons' aspect ratios. For a collection of polygons, such as the subgrains analyzed in this study, the average shape and the shape index provide a complete set of information characterizing the structure.

To demonstrate the sensitivity of the proposed shape indices to the orientation effect, a hypothetical case of two identical rectangles perpendicular to each other has been studied. Figure 12 shows the  $d$ - $\alpha$  plots for each rectangle and for the overall structure. The shape indices are 0.56 for each rectangle and 0.74 for the whole structure, which gives a 32% change due to the orientation difference.

In addition, the grids of rectangles with the same orientation were analyzed to find the effects of sizes and aspect ratios of individual rectangles on  $SI$  and  $\Omega$ . As expected, for a grid with the rectangles of the same size, the  $d$ - $\alpha$  curve is exactly the same as for a single rectangle with  $SI_g = SI_{avg}$  and  $\Omega = 1$ . If the grid consists of rectangles with

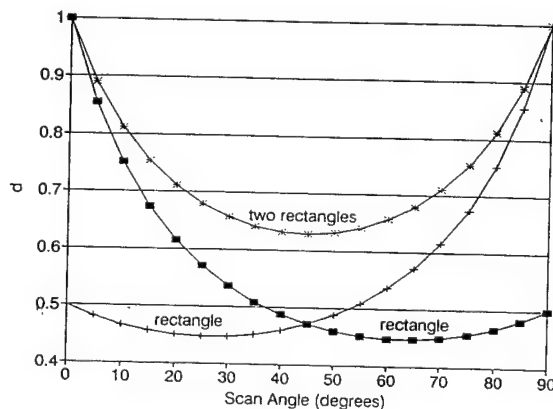


FIG. 12. Normalized intercept length,  $d$ , for a single rectangle and a structure with two rectangles perpendicular to each other.

different sizes but the same aspect ratios, the size difference affects only the average intercept length,  $L_2(\alpha)$ , and the  $d$  versus  $\alpha$  curve yield the same result as for the single element. Thus, the proposed shape indices are independent of both the average size and the size distribution of the grains.

The only restriction on the proposed microstructural models is that they can be applied only to two-dimensional structures even though the characterization of microstructural features is generally a three-dimensional problem. However, it is still the common practice in metallography today to characterize three-dimensional structures by the parameters of their plane section representations. In many cases, one plane section suitably chosen can be sufficient to represent the microstructure. Examples are an arbitrary chosen plane section for an isotropic structure, a plane section perpendicular to the fibers for a fiber-reinforced composite, and a plane of the propagation of a fatigue crack. In the case of the standard ASTM grain size method, it has even been possible to directly relate the total grain boundary area per unit volume to the mean intercept grain size obtained from measurements on plane sections in an assumption-free and unbiased manner [14]. In other cases, the three-dimensional microstructural information can be obtained using several plane sections. The longitudinal, transverse, and short transverse directions are commonly used for this purpose to obtain the grain sizes of metals after cold-working.

It should also be pointed out that the shape index,  $SI$ , defined here is not unique. Because it is equal to the area under the  $d$ - $\alpha$  curve, it is possible to imagine two different  $d$ - $\alpha$  curves with the same value of  $SI$ . To overcome this ambiguity, we suggest using the least-squares method to fit the experimentally measured  $d$ - $\alpha$  curve with the curve of a known shape, as demonstrated in this work.

The proposed microstructural models are then general, although they are applicable only to the two-dimensional objects. Because the models are independent of material, they can be used to characterize all possible en-

engineering materials and/or to any shape and orientation-related problems. Another potential application of the  $SI$ 's is in the study of the amount of local plastic deformation by comparing the shapes of individual grains or groups of grains before and after plastic deformation. Because the size of the analyzed area can be very small, the method should allow for the measurement of the local plastic deformation and deformation gradients.

### SUMMARY

The expressions for the change of the average intercept lengths as a function of scan angle for regular polygons, rectangles, and ellipses with different aspect ratios have been compiled. The curves of normalized average intercept lengths versus scan angles for these shapes have been used both to identify and to represent a variety of shapes commonly encountered in microstructural analysis.

Model structures of various elongated polygons have been proposed to complement the structures represented by the simple geometric shapes. These models have been tested in the analysis of the subgrain structure of the 7050 Al plate alloy. The results show that the sizes and the aspect ratios of the polygons can be easily adjusted to suit a variety of shapes of grains or second-phase particles.

The polar plots of normalized intercept lengths versus scan angles have been studied for their potential use in the direct graphic description of shapes. The polar plots for regular polygons with an even number of sides are the same as the polygons themselves. The polar plots for regular polygons with an odd number of sides are identical to those for regular polygons with twice the number of sides. A simple method for constructing these plots has been proposed.

The properties of the shape indices,  $SI$ , defined as the area under the plot of the normalized average intercept length versus scan angle have been analyzed and the formulas for their values for the regular polygons have been derived. These indices have been

proven useful in identifying the shapes of grains and second phase dispersions.

A new orientation factor,  $\Omega$ , has been proposed. This factor incorporates the shape indices of each object, and it can be used to quantitatively describe the degree of randomness of structures.

*The authors are grateful to Alcoa Laboratories for providing them with the material and to the Office of Naval Research for their support under Grant No. N00014-91-J-1299, for which Dr. A. K. Vasudevan is the program manager.*

### References

1. E. E. Underwood, *Quantitative Stereology*, Addison-Wesley Publishing Company, Reading, MA, pp. 196-197 (1970).
2. R. T. DeHoff and F. N. Rhines, editors, *Quantitative Microscopy*, McGraw-Hill Book Company, New York (1968).
3. G. F. Vander Voort, *Metallography Principles and Practice*, McGraw-Hill Book Company, New York (1984).
4. H. H. Hausner, Characterization of the Powder Particle Shape, *Planseeber. Pulvermetall.*, 14:75-84 (1966).
5. S. A. Saltykov, *Stereometric Metallography*, 2nd ed., Metallurgizdat, Moscow (1958).
6. T. Reti and I. Czinege, Shape characterization of particles via generalized Fourier analysis, *J. Microscopy* 156:15-32 (1989).
7. J. L. Chermant, M. Coster, and G. Gougeon, Shape analysis in  $R^2$  space using mathematical morphology, *J. Microscopy* 145:143-157 (1987).
8. E. Hornbogen, Fractals in microstructure of metals, *Int. Materials Rev.* 34:277-296 (1989).
9. G. M. Luo, A. M. Sadegh, and S. C. Cowin, The mean intercept length polygons for systems of planar nets, *J. Mat. Sci.* 26:2389-2396 (1991).
10. J. Zhang, A. J. Luévano, and M. A. Przystupa, Quantitative analysis of heterogeneous structures of aluminum 7050 alloy, *Scripta Metallurgia et Materialia* 26:1061-1066 (1992).
11. J. E. Hilliard, Specification and measurement of microstructural anisotropy, *Trans. Met. Soc. AIME* 224:1201-1207 (1962).
12. V. Benes, A practical approach to the stereology of anisotropic structures, *J. Microscopy* 154:165-175 (1988).
13. S. I. Tomkeieff, Linear intercepts, areas and volumes, *Nature* 155:24 (1945).
14. A. M. Gokhale, Interpretation of grain size descriptors, *Trans. Indian Inst. Metals* 35:595-600 (1982).

*Received March 1993; accepted February 1994.*

*Appendix D. Characterizations of Pore and Constituent Particle Populations in  
7050-T7451 Aluminum Plate Alloys.*

J. Zhang, M. A. Przystupa and A. J. Luevano

Submitted to *Mat. and Metall. Transactions A*.

Submitted for publication in Metallurgical and Materials Transactions A

## CHARACTERIZATIONS OF PORE AND CONSTITUENT PARTICLE POPULATIONS IN 7050-T7451 ALUMINUM PLATE ALLOYS

by

Jimin Zhang<sup>1</sup>, Marek A. Przystupa<sup>3</sup> and Annetta J. Luévano<sup>2</sup>

<sup>1</sup> Seagate Substrates, 3845 East Coronado Street, Anaheim, CA 92807

<sup>2</sup> TRW Space and Technology Division, 1 Space Park, Redondo Beach, CA 90278

<sup>3</sup> Department of Materials Science and Engineering, University of California, Los Angeles, Los Angeles, CA 90024, tel. (310) 825-6559, fax (310) 206-7353  
e-mail: amarek@ucla.edu

August 1996

## ABSTRACT

Although qualitative relationships between fatigue lifes and the sizes of the microstructural features such as pores and particles are well known, the quantitative models are lacking because of the unavailability of the required detailed microstructural data. The purpose of this work was to obtain such data for the two variants, old and new, of the aluminum 7050-T7451 thick-plate alloys. Both alloys had similar tensile and fracture properties but the new variant showed superior fatigue performance attributed to the smaller sizes of the fatigue crack initiating particles and pores. Those size differences, as well as the differences in the through-thickness size gradients, have been characterized in this work. The sizes, shapes, and orientations of particles and pores were analyzed first on the plane sections and then converted to the true 3-D characteristics using the moment method. In the conversions the particle and pore shapes have been assumed as triaxial ellipsoids and their size distributions as lognormal. The spatial distributions were quantified using the nearest neighbor spacing method. Results confirmed that the new alloy had smaller particles and pores than the old one. The size distributions in the former were also more confined. In both alloys the largest particles and pores were at the plate centers and the smallest at the surface. Their spatial distributions could be categorized as random with clusters.

## INTRODUCTION

Particles and pores are two of the most important microstructural features controlling fracture and fatigue of the engineering alloys, and aluminum alloys in particular. Since their sizes and spacing are usually non-uniform, the meaningful correlation of those dimensional characteristics with mechanical properties requires measurements of not only the average values, but also moments of the distributions. Such data are scarce in the literature, hence the purpose of this work was to perform microstructural characterizations of the 7050-T7451 Al plate alloys, keeping in mind specific needs of the microstructure based fatigue models.

All characterizations of the second phase features require two types of measurements: (1) those for obtaining the average characteristics of the individual features such as size, shape and orientation, and (2) those which give global properties, i.e. volume fraction, spatial distribution type, alignment, etc. The sizes are most conveniently measured on plane sections using either a linear intercept method or by measuring diameters of individual features [1-5]. The obtained distributions can be subsequently analyzed and converted to the true three dimensional (3-D) size distributions using one of the many available transformation methods [2-4]. To describe shapes, various arbitrarily defined shape factors can be used [1,2,6]. A common problem associated with those factors is that they have the same values for different shapes. However, since microstructural shapes in engineering materials are usually similar and relatively simple, their differences can be adequately captured with the shape factors. For complex shapes several more precise techniques, such as Fourier and spectral analysis, are also available [7-9].

As to the global properties, for both random and anisotropic microstructures the volume fractions can be adequately approximated by the area fractions on the appropriately

selected test planes. The pore and particle alignment can be quantified using one of the measures of the 'degree of orientation' [10, 6]. Their spatial distributions are usually classified as regular, random, clustered or random with clusters. The regular distribution is easy to recognize as the particles or pores are arranged in a distinct pattern. To characterize such distribution it is necessary to specify only the point density and to identify the pattern. The random distributions can be adequately characterized by the features' area density and the parameters of the Poisson distribution describing their spacing. Clusters are the most difficult to quantify. As recently reviewed by Vander Voort [11] the most popular methods include use of the number density [12], nearest neighbor spacing [13-15], Voronoi (Dirichlet) tessellation [12,16-19] and image amendments [11, 20]. Because of its simplicity, the nearest neighbor method has been preferred in this work. The spatial distribution types are in this case identified based on the differences between the average values and the variances of the nearest-neighbor distances for the real and the equivalent random microstructures.

The 7050-T7451 plate alloys are ideal materials for testing both the fatigue models and the microstructure characterizations techniques. These alloys have been recently extensively studied with the focus on the microstructural modifications leading to the improvement of their fatigue durability [21-24]. Results showed that although most of the mechanical properties of the slightly different alloy variants are practically the same, there are large differences in the fatigue lives between the variants [25,26]. It has been then postulated that the microstructural differences are responsible for the differences in the fatigue performance. These differences have been characterized in this work with emphasis on the constituent particle and pore size and spatial distributions. The basic measurements included determination of the pore and particle size distributions on various plane sections. Obtained 2-D data were then converted to the true 3-D size distributions. The

measurements also included estimations of the volume fractions, shapes, orientations and the types of the spatial distributions of both phases.

## BACKGROUND

The methodology used for converting pore and particle plane section measurements to the true 3-D size distributions depends primarily on their shape and alignment. The conversion problem has been studied extensively in the past and it has been shown that solution is possible if the shapes of all features are the same [2,27-29]. We will adopt the same-shape approximation in this work. It will be then assumed that all pores and particles in the 7050 alloys can be viewed as triaxial ellipsoids, Figure 1a, with different axial diameters  $D_{ci} < D_{bi} < D_{ai}$  but with identical aspect ratios, different for each feature type. A complete characterization of the particle and/or pore population will therefore require specification of the degree of alignment, characteristics of the size distribution of one of the major diameter and two aspect ratios.

### A. Alignment

The information about particle and pore alignment can be inferred from the orientations of their plane sections. The measure of alignment used in this work has been based on the comparison of the shape factors obtained from the measurements of the average intercept lengths obtained from the global microstructural scans with the scans of the individual features[1, 6]. The shapes are in this case characterized using a normalized intercept lengths,  $d(\alpha)$ :

$$d(\alpha) \equiv d = \frac{L_2(\alpha)}{L_{2,\max}} \quad \text{eq. 1}$$

where  $L_2(\alpha)$  is an average intercept length at a scan angle  $\alpha$  and  $L_{2,max}$  is the maximum average intercept length for scan angles from 0 to  $\pi$ . A corresponding shape index,  $SI$ , is defined as the area under the  $d$  vs.  $\alpha$  curve:

$$SI = \frac{1}{\alpha_p} \int_0^{\alpha_p} \frac{L_2(\alpha)}{L_{2,max}} d\alpha = \frac{1}{\alpha_p} \int_0^{\alpha_p} d d\alpha \quad \text{eq. 2}$$

where  $\alpha_p$  is the curve angular period. Such defined  $SI$  is independent of the measured object size and orientation and it varies between zero for a line and one for a circle. As demonstrated elsewhere [6], the shape of the  $d$ - $\alpha$  curves provide additional information about feature shape. For instance, for ellipses the reciprocal of  $d$  at  $90^\circ$  is equal to the aspect ratio.

To characterize particle and pore alignment one needs to define two additional normalized lengths, the average,  $d_{avg}$ , and the global,  $d_g$  [1,6]. The  $d_g$ -values are obtained by scanning all features without changing their orientations and  $d_{avg}$  by artificially aligning them along  $L_{2,max}$  direction. The area under the global  $d_g$ - $\alpha$  curve represents then a global shape index,  $SI_g$ , which increases with increasing particle misalignment and approaches unity for a statistically random structure. The true average shape index,  $SI_{avg}$ , can be obtained from the area under that the  $d_{avg}$ - $\alpha$  curve. Comparing  $SI_{avg}$  with  $SI_g$  allows for the quantification of the degree of alignment using an orientation factor,  $\Omega$  [6]:

$$\Omega = \frac{1 - SI_g}{1 - SI_{avg}} \quad \text{eq. 3}$$

For randomly oriented features,  $SI_g$  is then equal one and  $\Omega$  is zero. For a perfectly aligned structure  $SI_g$  is the same as  $SI_{avg}$  and  $\Omega$  is one. Comparing values of  $\Omega$  for particles and pores for the LS, TL and ST planes, Figure 1b, make then possible determination of the nature and the degree of their alignment.

## B. Size Distribution

Since fatigue models require as input continuous distribution functions[30], it will be assumed *a priori* that the 3-D distributions of the pore and particle sizes are lognormal, as supported by numerous experimental evidences [2-5,31]. To describe the lognormal distributions it will be then necessary to find only their first two moments. It is additionally expected that the particles and pores can be either randomly oriented or be partially aligned with one major axes parallel to the rolling plane normal, Figure 1a. Each of these cases require slightly different procedure for converting 2-D data to the 3-D size distributions, hence they will be dealt with separately.

### *Random Orientations*

The procedure for estimating moments of the lognormal size distributions of the same-shape randomly oriented features is well known. It was developed by DeHoff [2,31] and requires measurement of the three standard microstructural characteristics, namely

$N_A$  - the number of particles per unit area,

$N_L$  - the number of particle intercepts per unit length of a random test line,

$P_P$  - the fraction of random points within the phase of interest.

From them, the parameters of the true 3-D lognormal size distributions can be calculated from expressions:

$$\ln \mu_{D_a} = -2.5 \ln N_A + 4 \ln N_L - 1.5 \ln P_P + \ln \left( \frac{16 k_1^{2.5} k_3^{1.5}}{k_2^4} \right) \quad \text{eq. 4}$$

$$\ln^2 \sigma_{D_a} = \ln N_A - 2 \ln N_L + \ln P_P + \ln \left( \frac{2 k_2^2}{4 k_1 k_3} \right) \quad \text{eq. 5}$$

where  $\mu_{D_a}$  and  $\sigma_{D_a}$  are the geometric mean and geometric standard deviation of the 3-D maximum diameters and  $k_1$ ,  $k_2$  and  $k_3$  are the unitless shape factors, dependent on the

feature shape. As shown in the Appendix, for particles and pores approximated by triaxial ellipsoids these shape factors are

$$k_1 = \frac{1}{3} \left( 1 + \frac{1}{q_{ab}} + \frac{1}{q_{ac}} \right) \quad \text{eq. 6}$$

$$k_2 = \frac{\pi}{9} \left( 1 + \frac{1}{q_{ab}} + \frac{1}{q_{ac}} \right)^2 \quad \text{eq. 7}$$

$$k_3 = \frac{\pi}{6q_{ab}q_{ac}} \quad \text{eq. 8}$$

where  $q_{ab}$  and  $q_{ac}$  are the ellipsoid aspect ratios also defined in the Appendix. The ellipsoids average maximum diameter  $\bar{D}_a$ , volume density  $N_V$ , and volume fraction  $f$ , are in this case given by expressions:

$$\bar{D}_a = \mu_{D_a} \exp \left( \frac{1}{2} \ln^2 \sigma_{D_a} \right) \quad \text{eq. 9}$$

$$N_V = \frac{N_A^3 P_p}{N_L^3} \frac{k_2^3}{8k_1^3 k_3} \quad \text{eq. 10}$$

$$f = P_p \quad \text{eq. 11}$$

All that is required to find the characteristics of the randomly oriented same-shape triaxial ellipsoids are then the values of  $N_A$ ,  $N_L$  and  $P_p$  and the aspect ratios  $q_{ab}$  and  $q_{ac}$ . The first three quantities are readily available from the measurements on the random planes. The same holds for aspect ratio  $q_{ab}$ , equal to the largest aspect ratio observed for the plane sections. The second aspect ratio,  $q_{ac}$ , is not possible to ascertain directly from the plane section data. Possible ways to proceed have been discussed in details by DeHoff *et al* [28].

### ***One Axis Perpendicular to the Rolling Plane***

In this case the ellipsoids are aligned parallel to the rolling plane but have random rotations about the rolling plane normal, Figure 1a. Considering the nature of the rolling deformation, it is expected that for each ellipsoid its largest two diameters,  $D_a$  and  $D_b$ , will

be parallel to the rolling plane. The TL test planes will cut such ellipsoids parallel to the  $D_a$  -  $D_b$  plane and the obtained ellipsoidal cross-sections will have aspect ratios equal to  $q_{ab}$ . It is also possible to show that mathematically this case is equivalent to the one of the polydisperse spheres [27,32]. The first two moments of the maximum diameters of the ellipsoids, the parameters of their lognormal size distributions and their volume fraction are therefore given by relationships[2, 33]:

$$\overline{D_a} = \frac{\pi}{2} \left( \overline{\frac{1}{d_{aTS}}} \right)^{-1} \quad \text{eq. 12}$$

$$\overline{(D_a^2)} = 2 \overline{d_{aTS}} \left( \overline{\frac{1}{d_{aTS}}} \right)^{-1} \quad \text{eq. 13}$$

$$\ln \mu_{D_a} = 2 \ln \overline{D_a} - \frac{1}{2} \ln \overline{(D_a^2)} \quad \text{eq. 14}$$

$$\ln^2 \sigma_{D_a} = \ln \overline{(D_a^2)} - 2 \ln \overline{D_a} \quad \text{eq. 15}$$

$$f = \frac{\pi N_{A-TS}}{4 q_{ab}} \overline{(d_{aTS}^2)} \quad \text{eq. 16}$$

where  $\overline{d_{aTS}}$  is the average maximum diameter of the ellipsoidal cross-sections,  $\overline{(d_{aTS}^2)}$  average of their squares,  $\overline{(1/d_{aTS})}$  their harmonic mean and  $N_{A-TS}$  the number of cross-sections per unit area, all for the TS planes. This means that size distribution of the ellipsoids, their volume fraction and one of the aspect ratio can be obtained just from the measurements on the TS planes alone. Estimations of the volume density,  $N_V$ , and the second aspect ratio,  $q_{ac}$ , require additional measurements of the diameters  $d_{ci}$  on any of the planes perpendicular to the rolling plane, such as LS or TS. The average  $\overline{D_c}$  is then estimated using relation identical to eq. 12 [32, 33]:

$$\overline{D_c} = \frac{\pi}{2} \left( \overline{\frac{1}{d_c}} \right)^{-1} \quad \text{eq. 17}$$

The aspect ratio,  $q_{ac}$ , and  $N_V$  can be subsequently obtained from relations [2]:

$$q_{ac} = \frac{\overline{D_a}}{D_c} \quad \text{eq. 18}$$

$$N_V = \frac{N_{A-TS}}{D_c} \quad \text{eq. 19}$$

Characterization of the same-shape triaxial ellipsoids with one of the axes parallel to the rolling plane normal requires then measurements of:

- (1) major diameters, aspect ratios and area densities of the ellipsoidal cross-sections on the TS-planes,
- (2) diameters parallel to the rolling plane normal on the planes normal to the rolling plane.

## EXPERIMENTAL

The materials used in this study were two variants of the 15.24 cm thick 7050-T7451 plate alloys, designated as old and new, supplied by Alcoa Laboratories. Both alloys had almost identical tensile and fracture toughness properties, with the new alloys showing superior fatigue characteristics [22-26]. Samples for metallographic examinations were taken from the longitudinal (TL), transverse (ST) and short transverse (LS) planes at the surface, quarter depth and the center locations, as shown in Figure 1b. All samples were prepared by mechanical grinding to a surface finish of 600 grit using wet SiC paper, followed by polishing on a felt wheel with 1  $\mu\text{m}$  and then 0.25  $\mu\text{m}$  diamond pastes mixed with ethanol. This procedure provided a clean surface with no particle pull-outs. Measurements of the porosity and the constituent particles were made on the as-polished specimens to avoid distortions of shapes and number-densities by etching. All measurements were made from optical photographs taken at magnification 900X which was chosen as a compromise between efficiency and accuracy. All micrographs were digitized with a manual edge detection and analyzed using a custom-made image analysis program.

## RESULTS AND DISCUSSION

### A. Pores

Examples of typical pore cross-sections found on the LS planes at the center of the old alloy are shown in Figs. 2a. Their characteristics, as well as the characteristics of the pore sections on all other planes are summarized in Table 1. As expected, the area fractions were the highest at the center and the lowest near the surface. They were also, on average, 0.17% for the old and 0.11% for the new alloy variant. The pore sizes are represented in the Table 1 by the average intercept length over all scan angles,  $L_{II}$ . For the old alloy they were the smallest near the plate surface and increases toward the center. For the new, the smallest pores were also near the plate surface but there is almost no size difference between quarter-depth and the center. The average values of  $L_{II}$  were 4.42  $\mu\text{m}$  for the old and 4.65  $\mu\text{m}$  for the new alloy. Both alloys had largest pores and pore volume fractions at the center-plate locations.

The pore shapes have been characterized using the aforementioned  $d$ - $\alpha$  plots [1, 6]. Figure 3 shows typical  $d_g$  and  $d_{avg}$  vs. scan angle curves used in the analysis. The average shape indexes for pores on all test planes were 0.816 and 0.831 for the new and old alloys respectively conforming their ellipsoidal shapes[6]. The corresponding average pore aspect ratios, equal to the harmonic mean of the  $d$ -values at 90°, were 1.45 for the old and 1.51 for the new alloy. These values are in good agreement with aspect ratios obtained from the direct measurement listed in Table 1, again supporting assumption of the ellipsoidal shapes. Example of the changes of  $SI$ -values with location are in Figure 4a, showing that the changes were small. The shape factors were slightly smaller for the new alloy, suggesting more elongated pore shapes.

The orientation factors,  $\Omega$ , for pores on different test planes, Table 1, varied from 0.11, which corresponds to almost random structure, to 0.65 which indicates slight alignment. The average values were 0.40 for the new and 0.34 for the old alloy. Since  $\Omega$  increases to one as the pores become more and more elongated and aligned, pore alignment in the studied alloys can be considered as random. Examples of the change of the average orientation factor  $\Omega$  with location are shown in Figure 4b.

Since pore orientations could be approximated as random, their size distributions were estimated using the DeHoff's method [31]. The values of  $N_A$ ,  $N_L$  and  $P_p$  were in this case obtained by averaging the data obtained from the LS, TL and ST planes. The required average true pore aspect ratios  $q_{ab}$  and  $q_{ac}$  were estimated using a trial and error numerical method. The procedure used consisted of three steps: (1) generating a model 3-D specimen with identical ellipsoids randomly oriented and distributed in volume, (2) cutting model specimen with random planes to obtain distribution of the cross-section aspect ratios, and (3) comparing distributions of the generated aspect ratios with those from the measurements. The starting value of  $q_{ab}$  was always set equal to the largest observed plane-section aspect ratio. The shape of the model ellipsoids was then adjusted until the difference between the computer generated and the experimental aspect ratio distributions reached a local minimum closest to the starting values of  $q_{ab}$ . The final aspect ratios of the model ellipsoids were assumed equal to the true 3-D averages. Tests of the procedure showed that despite the differences between real and model microstructures, the obtained estimates have accuracy adequate for the 2-D to 3-D conversions.

Results from the numerical procedure and from the size conversions are summarized in Table III. For both alloys the calculated pore volume fractions were the largest at the plate centers and the smallest at the surface, Figure 5. The same trend was observed for the maximum pore diameters,  $D_a$ , in the old alloy. For the new alloy the pore sizes increased

slightly from the center to the quarter depth and were the smallest at the surface regions. However, as evident from the cumulative probability distributions shown in Figure 6, the center region of the new plate is expected to have higher number of the large pores.

Comparing pore size distributions for the old and new alloys it appears that new alloy has not only smaller pores but that their size distributions are more confined. This difference comes about from the smaller values of both  $\ln \mu_{Da}$ , representing average, and  $\ln^2 \sigma_{Da}$ , representing standard deviation. The large value of  $\ln^2 \sigma_{Da}$  for the center region of the old plate, compared to that for the new one, is of particular importance; it suggests that the old alloy has higher percentage of the largest pores. Since the largest pores act as the fatigue crack initiation sites, their size, hence also the size of the right tail of the distribution, is detrimental to the fatigue performance. For the plate centers the tail is longer for the old alloy, Figure 7a, suggesting presence of the larger number of big pores, hence shorter fatigue lives.

The obtain results for pores are then consistent with the inferior fatigue performance of the old alloy. They also illustrates the need for performing complete quantitative analysis to identify the relevant microstructural differences. The cumulative size distributions give in this case estimates of the expected maximum dimension of the 'initial flaws'. The orientation factor,  $\Omega$ , offers additional information on the relative orientations of the pore axis with respect to the axis of the applied stress. Both are important input parameters which, when use in the fatigue life prediction models, can substantially improve their predictive capabilities.

## B. Constituent Particles

The 7050-7451 plate alloys have two different types of constituent particles:  $\text{Al}_7\text{Cu}_2\text{Fe}$  and  $\text{Mg}_2\text{Si}$ . Since both serve as the fatigue crack initiation sites, their sections were characterized without distinction to their chemical compositions. A collection of the typical cross-sections of the constituent particles found on the LS plane at the center of the old plate alloy is shown in Figure 2b. Table II lists characteristics of the cross-sections obtained from all plane section measurements. The measured particle area fractions were 0.73% for the new and 0.72% for the old alloy which is about five times higher than for pores. The new alloy contained less particles than the old one at both center and quarter depth regions. The opposite was true at the surface. The 2-D constituent sizes, averaged over all nine sections, were  $4.86\ \mu\text{m}$  for the new and  $4.91\ \mu\text{m}$  for the old alloy. The particle sizes increased toward the plate center and were always larger than those for pores. The smallest sizes were observed on the ST planes, suggesting elongated shapes resulting from rolling.

Examples of typical  $d$ - $\alpha$  curves for constituent particles are in Figure 3. Analysis of such plots for the old alloy gave average  $SI$  of 0.76 and the aspect ratio 1.80. For the new alloy these values were 0.67 and 2.30 respectively. Examples of the changes of the shape indexes with test plane orientation are shown in Figure 4a. All obtained  $SI$  values, compiled in Table II, clearly support ellipsoidal approximation of the particle shapes. These values were lower than those for pores suggesting that particles had more elongated shapes. The average orientation factors,  $\Omega$ , for the constituents were 0.54 for the new and 0.41 for the old alloy. The values of  $\Omega$  for the old alloy are shown in Figure 4. Note that for the surface and quarter depth locations they are similar to those for pores. The particle orientations at those locations can be then assumed as random. For the plate center region, the orientation factors were high for the LS and ST planes and low for the TL sections.

This means the particles were aligned parallel to the rolling plane, but had random rotations about the rolling plane normal. In other words, one of the particles axes was parallel to the rolling plane normal. Based on the  $\Omega$ -values in Table II, the same type of particle alignment has been present throughout the new plate.

Since for the old alloy constituent particles had random orientations for both the surface and the quarter depth regions, their true size distributions, volume fractions and densities were calculated for those locations using the same procedure as for pores. For the new alloy and for the center-plate location of the old they were estimated using the procedure for one axis perpendicular to the TL plane described in the Background section. Results of the conversions are in Table III. As for pores, the particle sizes were the largest at the plate centers and the smallest at the surface, Figure 5b. The volume fractions for the old alloy were practically the same for all locations. In the new alloy they were the smallest at the quarter depth and the largest at the center, Figure 5b. The cumulative size distributions, Figure 6, show that the largest particles would be always expected at the plate center. At that region the average particle sizes were smaller for the old alloy which is the opposite to what was observed for the pores. However, the size distribution for the new alloy was much tighter, resulting in the higher probability of the larger particles in the old alloy, Figure 7b.

Comparing characteristics of the pores and the particles in both studied alloys it appears that the particles have higher volume fraction, larger sizes and that they are more elongated and aligned than pores. Despite those advantages, the fatigue cracks in the 7050 alloys have tendency to nucleate from pores rather than particles [22-26]. This apparent inconsistency can be attributed to the differences in the fatigue crack nucleation periods associated with each feature type. It has been observed that pores can act as cracks from the very first fatigue cycle, while formation of a crack at the particles require long

nucleation times [26]. As a consequence, a crack associated with the pore can grow to a critical size and cause fatigue failure before particle has enough time to nucleate a crack. This trend can be reversed in the presence of the stress concentrators, as has been indeed observed during fatigue of the 7050 samples with holes [22-24].

### C. Particle and Pore Spatial Distributions

Characterizations of the particle and pore populations for fatigue modeling purposes should also provide some information about the patterns describing their 3-D spatial distributions. Although such determinations are not possible without knowing 3-D coordinates of object centers, adequate information can be obtained from the plane section data. In this work such two-dimensional particle and pore spatial distributions have been quantified for the center regions of the studied alloys using the nearest neighbor spacing method [13]. The method utilizes two indexes, Q and R, defined as:

$$Q = \frac{\text{Observed Nearest Neighbor Distance}}{\text{Expected Nearest Neighbor Distance}} \quad \text{eq. 20}$$

$$R = \frac{\text{Observed Nearest Neighbor Distance Standard Deviation}}{\text{Expected Nearest Neighbor Distance Standard Deviation}} \quad \text{eq. 21}$$

where the expected values are calculated by assuming a random structure with the same feature density as the experimental one[14, 15]. To identify different types of spatial distribution the following guidelines, depicted on Figure 8, have been used [14, 15]:

- (1) clustered distribution,  $Q < 1$  and  $R < 1$ ;
- (2) regular distribution  $Q > 1$  and  $R > 1$ ;
- (3) random distribution with clusters  $Q < 1$  and  $R > 1$
- (4) random distribution  $Q = 1$  and  $R = 1$ .

Figure 9 shows an example of the Voronoi tessellation cell construction which were used to identify the neighbors [12-19]. The observed nearest neighbor distance was in this case 48.2  $\mu\text{m}$  with standard deviation of 33.2  $\mu\text{m}$ . The expected values for the random structure with the same point density are 51.86 and 27.18  $\mu\text{m}$  respectively. This gives  $Q = 0.93$  and  $R = 1.22$  which means that the spatial distribution of the pores in Figure 9 can be classified as random with clusters. The  $Q$  and  $R$  values and the identified spatial distribution types for the plates center regions are in Table 4 and in Figure 8. For all planes the spatial distributions were random with some tendency for clustering, higher for particles than for pores. It is therefore justifiable to assume that for the modeling purposes the cracks associated with particles and pores are non-interacting. We again emphasize that ideally one should use 3-D results to study the spatial distribution. However, as pointed out earlier, the main difficulty in this case is acquisition of the 3-D data on particle locations.

## CONCLUSIONS

- The true 3-D volume fractions, size distributions, shapes and orientations and 2-D spatial distributions of pores and constituent particles have been quantified for two variants of the 7050-T7451 Al plate alloy. The characterizations included measurements of all necessary quantities on the TL, ST and LS planes at the surface, quarter depth and at the center plate locations and converting them to the true 3-D characteristics.
- The true size distributions of particles and pores have been assumed *a priori* as lognormal and their shapes as triaxial ellipsoids. Both particle and pore average sizes were the largest at the plate centers and the smallest at the surface. Based on the size

distributions the center- regions were also expected the to have the highest percentages of the largest particles and pores.

- In both alloys the particles were about 1.5 times larger than pores, had larger aspect ratios and about five times larger volume fractions. The pores had random orientations while particles tend to be aligned parallel to the rolling plane, with random rotation about the rolling plane normal. The spatial distributions of both features could be classified as random with clusters.
- The new variant of the 7050-T7451 plate alloy had tighter particle and pore size distributions than the old one, particularly in the plate center region. As a result, the new alloy is expected to have smaller percentage of large particles and pores which explains its superior fatigue performance.

## APPENDIX

The shape factors  $k_1$ ,  $k_2$  and  $k_3$  in the DeHoff's method represent proportionality constants in the relations [31]:

$$D_v = k_1 a \quad \text{eq. A 1}$$

$$S = k_2 a^2 \quad \text{eq. A 2}$$

$$V = k_3 a^3 \quad \text{eq. A 3}$$

where  $D_v$ ,  $S$  and  $V$  are the average feature caliper diameter, surface area and volume, respectively and  $a$  is a measure of feature size. To find these shape factors for triaxial ellipsoids one needs explicit forms of relations A 1 to A 3. From the three, only the ellipsoid volume can be expressed in a close form:

$$V = \frac{\pi}{6} D_a D_b D_c = \frac{\pi}{6} \frac{D_a^3}{q_{ab} q_{ac}} \quad \text{eq. A 4}$$

where  $D_a$ ,  $D_b$  and  $D_c$ , are ellipsoid diameters, Figure 1a, and  $q_{ab}$  and  $q_{ac}$  are aspect ratios

$$q_{ab} = \frac{D_a}{D_b} \quad \text{eq. A 5}$$

$$q_{ac} = \frac{D_a}{D_c} \quad \text{eq. A 6}$$

Comparing equations A 3 and A 4, assuming  $a \equiv D_a$ , gives:

$$k_3 = \frac{\pi}{6 q_{ab} q_{bc}} \quad \text{eq. A 7}$$

The caliper diameter,  $D_V$ , can be calculated precisely only from the integral form.

However, a good approximation of that integral is a formula [34, 35]:

$$D_V \cong \frac{1}{3} (D_a + D_b + D_c) = \frac{D_a}{3} \left( 1 + \frac{1}{q_{ab}} + \frac{1}{q_{ac}} \right) \quad \text{eq. A 8}$$

which gives an error of the order of only 3%. Consequently,

$$k_1 \cong \frac{1}{3} \left( 1 + \frac{1}{q_{ab}} + \frac{1}{q_{ac}} \right) \quad \text{eq. A 9}$$

The expression for the triaxial ellipsoid surface area is also implicit, but the following formula:

$$S \cong \pi \left( \frac{D_a + D_b + D_c}{3} \right)^2 = \frac{\pi D_a^2}{9} \left( 1 + \frac{1}{q_{ab}} + \frac{1}{q_{ac}} \right)^2 \quad \text{eq. A 10}$$

is recommend by us as an adequate approximation. The last shape factor is then equal:

$$k_2 \cong \frac{\pi}{9} \left( 1 + \frac{1}{q_{ab}} + \frac{1}{q_{ac}} \right)^2 \quad \text{eq. A 11}$$

## ACKNOWLEDGMENTS

The authors would like to thank the Office of Naval Research for their support under Grant No. N00014-91-J-1299. Thanks are also due to Drs. R. J. Bucci, A. J. Hinkle and P. E. Magnusen from Alcoa Laboratories for providing the material used in this study and for valuable discussions.

## REFERENCES

1. J. Zhang, A. J. Luévano and M. A. Przystupa: *Scripta Metall. Mater.*, 1992, vol. 26, pp. 1061-66.
2. E. E. Underwood: *Quantitative Stereology*, Addison-Wesley Publishing Co., Reading, MA, 1970.
3. *Quantitative Microscopy*, R. T. DeHoff and F. N. Rhines, eds., McGraw-Hill, NY, 1968.
4. G. F. Vander Voort: *Metallography Principles and Practice*, McGraw-Hill, NY, 1984.
5. P. Louis and A. M. Goghale: *Metall. Mater. Trans. A*, 1995, vol. 26A, pp. 1741-44.
6. J. Zhang, A. J. Luévano and M. A. Przystupa: *Mater. Characterization*, 1994, vol. 33, pp. 175-85.
7. J. E. Hilliard: *Trans. Metall. Soc. AIME*, 1962, vol. 224, pp. 1201-7.
8. T. Reti and I. Czinege: *J. Microscopy*, 1989, vol. 156, pp. 15-32.
9. J. L. Chermant, M. Coster and G. Gougeon: *J. Microscopy*, 1987, vol. 145, pp. 143-57.
10. S. A. Saltykov: *Stereometric Metallography*, 2nd Edition, Metallurgizdat, Moscow, 1958.
11. G. F. Vander Voort: *Mater. Characterization*, 1991, vol. 27, pp. 241-60.
12. M. T. Shehata and J. D. Boyd: in *Inclusions and Their Influence on Material Behavior*, R. Rungta ed., ASM International, Metals Park, OH, 1988, pp. 123-31.
13. H. Schwarz and H. E. Exner: *J. Microscopy*, 1983, vol. 131, pp. 129-55.
14. P. J. Wray, O. Richmond, H. L. Morrison: *Metallography*, 1983, vol. 16, pp. 39-58.
15. W. A. Spitzig, J. F. Kelly and O. Richmond: *Metallography*, 1985, vol. 18, pp. 235-61.
16. H. Hermann, H. Wendrock and D. Stoyan: *Metallography*, 1989, vol. 23, pp. 189-200.

17. T. N. Ronus, J. M. Fridy, K. B. Lippert and O. Richmond: in *Simulation and Theory of Evolving Microstructures*, M. P. Anderson and A. D. Rollett, eds., TMS, Warrendale, PA, 1990, pp. 269-75.
18. J. R. Brockenbrough, W. H. Hunt Jr. and O. Richmond: *Scripta Metall. Mater.*, 1992, vol. 27, pp. 385-90.
19. R. K. Everett: *Scripta Metall. Mater.*, 1993, vol. 28, pp. 663-68.
20. W. B. James: in *Practical Applications of Quantitative Metallography*, ASTM STP 839, J. L. McCall and J. H. Steele, Jr., eds., ASTM, Philadelphia, PA, 1984, pp. 132-45.
21. *Aluminum Alloys - Contemporary Research and Applications*, A. K. Vasudevan and R. D. Doherty, eds., Academic Press, Inc., San Diego, CA, 1989.
22. P. E. Magnusen, A. J. Hinkle, R. J. Bucci, R. L. Rolf and D. A. Lukasak: in *Fatigue 90*, Proc. Fourth Int. Conf. on Fatigue and Fatigue Thresholds, Materials and Engineering Publications, Ltd, Honolulu, HA, 1990, vol. 2, pp. 2239-44.
23. P. E. Magnusen, A. J. Hinkle, W. Kaiser, R. J. Bucci and R. L. Rolf: *J. of Testing and Evaluation*, 1990, vol. 18, pp. 439-45.
24. P. E. Magnusen, R. J. Bucci, A. J. Hinkle, M. E. Artley and R. L. Rolf: in *Advances in Fracture Research*, Salama et al eds., Proc. ICF7, 1989, vol. 2, pp. 999-1006.
25. A. J. Luévano, M. A. Przystupa, J. Zhang: *J. Mater. Eng. and Performance*, 1994, vol. 3, pp. 47-54.
26. J. R. Brockenbrough, A. J. Hinkle, P. E. Magnusen and R. J. Bucci: in *FAA/NASA Int. Symposium on Advanced Structural Integrity Methods for Airframe Durability and Damage Tolerance*, NASA Conference Publication 3274, Part 1, September 1994, pp. 71-84.
27. S. D. Wicksell: *Biometrika*, 1926, vol. 18, pp. 151-72.
28. R. T. DeHoff and P. Bousquet: *J. Microscopy*, 1970, vol. 92, pp. 110-35.

29. L-M. Cruz Orive: *J. Microscopy*, 1976, vol. 107, pp. 235-53.
30. K. Sobczyk and B. F. Spencer, Jr., *Random Fatigue: From Data to Theory*, Academic Press, Inc., San Diego, CA, 1992.
31. R. T. DeHoff: *Trans. Metall. Soc. AIME*, 1965, vol. 233, pp. 25-29.
32. G. M. Tallis: *Biometrics*, 1970, vol. 26, pp. 87-103.
33. M. G. Kendall and P. A. P. Moran: *Geometrical Probability*, Hafner Publishing Company, NY, 1963, pp. 86-89.
34. D. Greeley, J. D. Crapo and R. T. Vollmer: *J. Microscopy*, 1978, vol. 114, pp. 31-39.
35. J. D. Crapo and D. Greeley: *J. Microscopy*, 1978, vol. 114, pp. 41-48.

## TABLES

Table I. Average Sizes, Shapes and Orientations of the Pore Cross-Sections in the 7050-T7451 Plate Alloys

Alloy	Location	Test Plane	$L_{II}$ $\mu\text{m}$	Area Fract. %	Aspect Ratio	Shape Index $SI$	Orient. Factor $\Omega$	Area Density $\text{mm}^{-2}$
OLD	Center	TL	4.4	0.12	1.50	0.811	0.35	95.7
		LS	5.4	0.37	1.45	0.834	0.30	158.7
		ST	5.8	0.29	1.51	0.820	0.46	92.9
	Quarter	TL	3.9	0.14	1.45	0.834	0.41	130.6
		LS	3.5	0.04	1.42	0.839	0.35	50.8
		ST	4.1	0.08	1.41	0.843	0.30	68.7
	Surface	TL	4.1	0.07	1.50	0.813	0.15	65.3
		LS	3.5	0.06	1.40	0.845	0.36	76.0
		ST	3.3	0.04	1.41	0.842	0.24	50.7
NEW	Center	TL	4.9	0.11	1.55	0.809	0.11	69.4
		LS	4.4	0.20	1.49	0.800	0.48	89.4
		ST	5.4	0.14	1.56	0.805	0.39	69.4
	Quarter	TL	5.3	0.08	1.52	0.815	0.16	41.6
		LS	4.9	0.08	1.52	0.823	0.46	54.1
		ST	4.6	0.09	1.46	0.829	0.27	54.9
	Surface	TL	4.2	0.07	1.47	0.831	0.35	64.3
		LS	4.1	0.08	1.52	0.815	0.65	77.2
		ST	4.4	0.07	1.53	0.815	0.55	63.1

$L_{II}$  - average intercept length

Table II. Average Sizes, Shapes and Orientations of the Constituent Particle Cross-Sections in the 7050-T7451 Plate Alloys

Alloy	Location	Test Plane	$L_{II}$ $\mu\text{m}$	Area Fract. %	Aspect Ratio	Shape Index $SI$	Orient. Factor $\Omega$	Area Density $\text{mm}^{-2}$
OLD	Center	TL	9.9	0.63	2.06	0.704	0.41	94.3
		LS	5.8	0.52	2.36	0.655	0.70	66.9
		ST	3.8	0.91	1.62	0.790	0.56	327.4
	Quarter	TL	8.1	0.84	1.78	0.761	0.15	186.8
		LS	4.2	0.71	1.77	0.761	0.29	249.7
		ST	4.5	0.93	1.87	0.747	0.45	252.1
	Surface	TL	6.2	0.75	1.71	0.769	0.32	328.0
		LS	3.5	0.55	1.90	0.736	0.63	254.4
		ST	3.1	0.45	1.76	0.760	0.35	303.8
NEW	Center	TL	9.1	0.54	1.78	0.748	0.22	94.3
		LS	4.9	0.48	2.35	0.663	0.75	69.3
		ST	4.0	0.85	2.27	0.663	0.59	297.8
	Quarter	TL	7.5	0.35	2.33	0.671	0.17	140.8
		LS	3.9	0.64	2.48	0.659	0.71	216.4
		ST	3.4	0.35	2.53	0.646	0.55	135.7
	Surface	TL	6.9	1.12	2.34	0.674	0.43	509.8
		LS	3.3	0.74	2.41	0.652	0.74	371.2
		ST	2.9	0.46	2.05	0.712	0.53	295.5

$L_{II}$  - average intercept length

Table III. True 3-D Characteristics of the Porosity and Constituent Particles in the 7050-T7451 Plate Alloys

Feature	Alloy	Location	$\overline{D}_a$ $\mu\text{m}$	Aspect Ratios		Vol. Fract. %	Vol. Density $\text{mm}^{-3}$	Parameters of Lognorm. Distr.	
				$q_{ab}$	$q_{ac}$			$\ln \mu_{Da}$	$\ln^2 \sigma_{Da}$
Pores	NEW	Center	6.7	1.50	1.61	0.15	$1.5 \times 10^4$	1.823	0.149
		Quarter	6.9	1.51	1.90	0.09	$1.0 \times 10^4$	1.871	0.121
		Surface	5.6	1.34	1.68	0.07	$1.6 \times 10^4$	1.696	0.051
	OLD	Center	7.3	1.56	1.79	0.28	$2.2 \times 10^4$	1.888	0.188
		Quarter	5.5	1.47	1.65	0.09	$2.0 \times 10^4$	1.664	0.074
		Surface	5.3	1.45	1.85	0.09	$1.6 \times 10^4$	1.556	0.223
Const. Part.	NEW	Center	10.2	1.66	2.10	0.41	$1.2 \times 10^4$	2.264	0.125
		Quarter	9.2	2.08	1.96	0.32	$2.7 \times 10^4$	2.205	0.032
		Surface	8.1	2.11	1.85	0.62	$7.7 \times 10^4$	2.057	0.080
	OLD	Center	9.5	1.78	1.78	0.56	$2.5 \times 10^4$	2.112	0.279
		Quarter	7.8	1.61	1.43	0.64	$3.8 \times 10^4$	1.912	0.282
		Surface	8.1	1.71	2.08	0.59	$5.3 \times 10^4$	2.025	0.123

$\overline{D}_a$  - average maximum diameter

Table IV. Parameters of the Pore and Constituent Particles Spatial Distribution in the Old  
and New 7050-T7451 Plate Alloys, Center Section.

Alloy	Feature	Plane	Q	R	Observed		Equiv. Random		Spatial Distribution type
					$\Delta_{NN}[\mu\text{m}]$	Std $[\mu\text{m}]$	$\Delta_{NN}(\mu\text{m})$	Std $[\mu\text{m}]$	
OLD	Pores	TL	0.867	1.303	44.3	34.8	51.1	26.7	Rand. with clust.
		LS	0.892	1.016	33.1	19.7	37.1	19.4	Rand. with clust.
		ST	0.929	1.225	48.2	33.2	51.9	27.1	Rand. with clust.
	Const. Part.	TL	0.572	1.079	29.3	28.9	51.2	26.8	Rand. with clust.
		LS	0.739	1.333	45.5	42.9	61.6	32.2	Rand. with clust.
		ST	0.912	1.329	25.2	19.2	27.6	14.6	Rand. with clust.
NEW	Pores	TL	0.923	1.264	55.2	39.5	59.8	31.3	Rand. with clust.
		LS	0.857	1.461	45.8	40.8	53.4	27.9	Rand. with clust.
		ST	0.933	1.210	57.5	39.0	61.6	32.2	Rand. with clust.
	Const. Part.	TL	0.679	1.273	35.3	34.6	52.0	27.2	Rand. with clust.
		LS	0.663	1.160	39.9	36.5	60.2	31.5	Rand. with clust.
		ST	0.814	1.138	23.0	16.8	28.3	14.8	Rand. with clust.

$\Delta_{NN}$  - Average nearest-neighbor distance

Std - Standard deviation of  $\Delta_{NN}$ .

## FIGURES

Figure 1. Schematic showing (a) assumed triaxial ellipsoidal shapes of particles and pores and (b) designations of the test planes used in the characterizations of the 7050-T7451 plate alloys.

Figure 2. Examples of typical cross-sections of (a) micropores and (b) constituent particles found on the LS-planes in the center region of the old 7050-T7451 plate alloy.

Figure 3. Angular variation of the normalized average intercept lengths of the pore and constituent particle sections on the LS-planes for the old 7050-T7451 alloy variant, plate center. (See text for definitions of  $d_g$  and  $d_{avg}$ )

Figure 4. Average (a) shape indexes,  $SI$ , and (b) orientation factors,  $\Omega$ , of the pore and particle sections on indicated test planes at different locations in the old variant of the 7050-T7451 plate alloy.

Figure 5. Calculated (a) pore and (b) constituent particle size and volume fraction gradients in the old and new variants of the 7050-T7451 plate alloys.

Figure 6. Estimated cumulative probability distributions of the pore and constituent particle sizes at indicated locations within the old and new variants of the 7050-T7451 plates.

Figure 7. Calculated size distributions of (a) pores and (b) constituent particles in the old and new variants of the 7050-T7451 alloys, plate center region.

Figure 8. Results of the characterizations of the pore and constituent particle spatial distributions; old and new variants of the 7050-T7451 alloy, plate center regions.

Figure 9. Example of the Voronoi tessellation cells constructed on the pore centers used in the identifications of the nearest neighbors. Points represent locations of the pore centers; ST-plane, center plate region, old 7050-T7451 alloy.

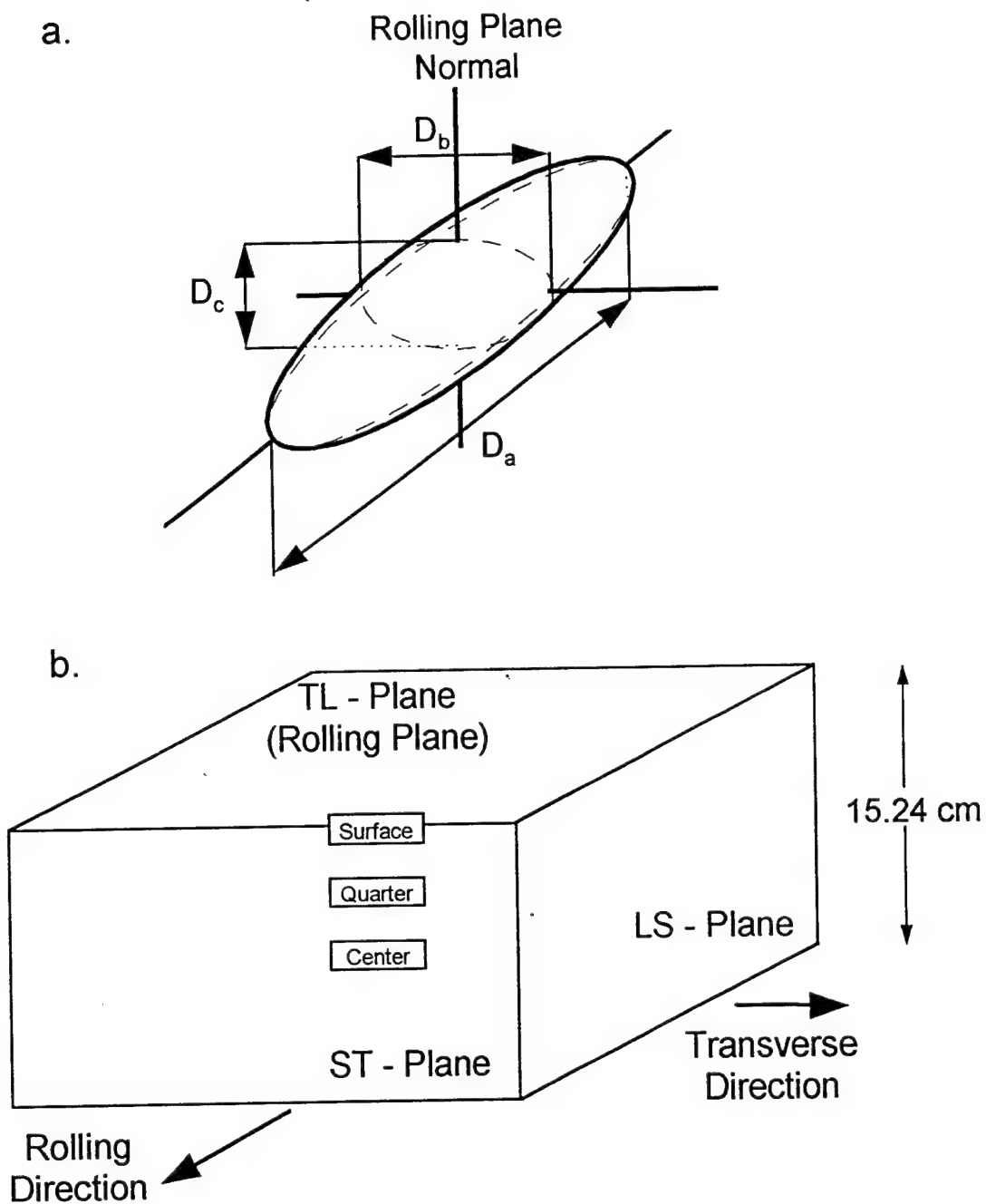


Figure 1. Schematics showing (a) assumed triaxial ellipsoidal shapes of particles and pores and (b) designations of the test planes used in the characterizations of the 7050-T7451 plate alloys.

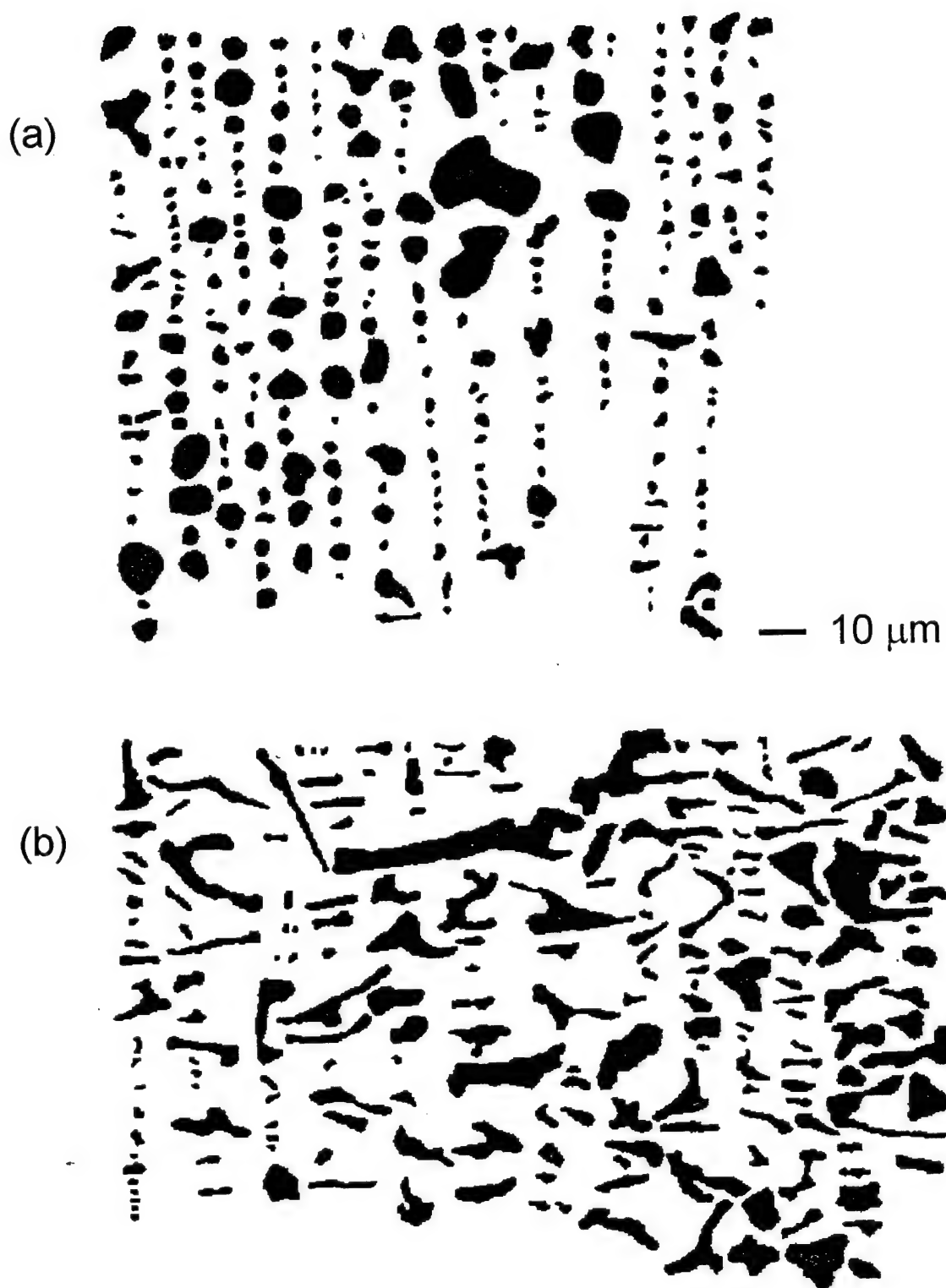


Figure 2. Examples of typical cross-sections of (a) micropores and (b) constituent particles found on the LS-planes in the center region of the old 7050-T7451 plate alloy.

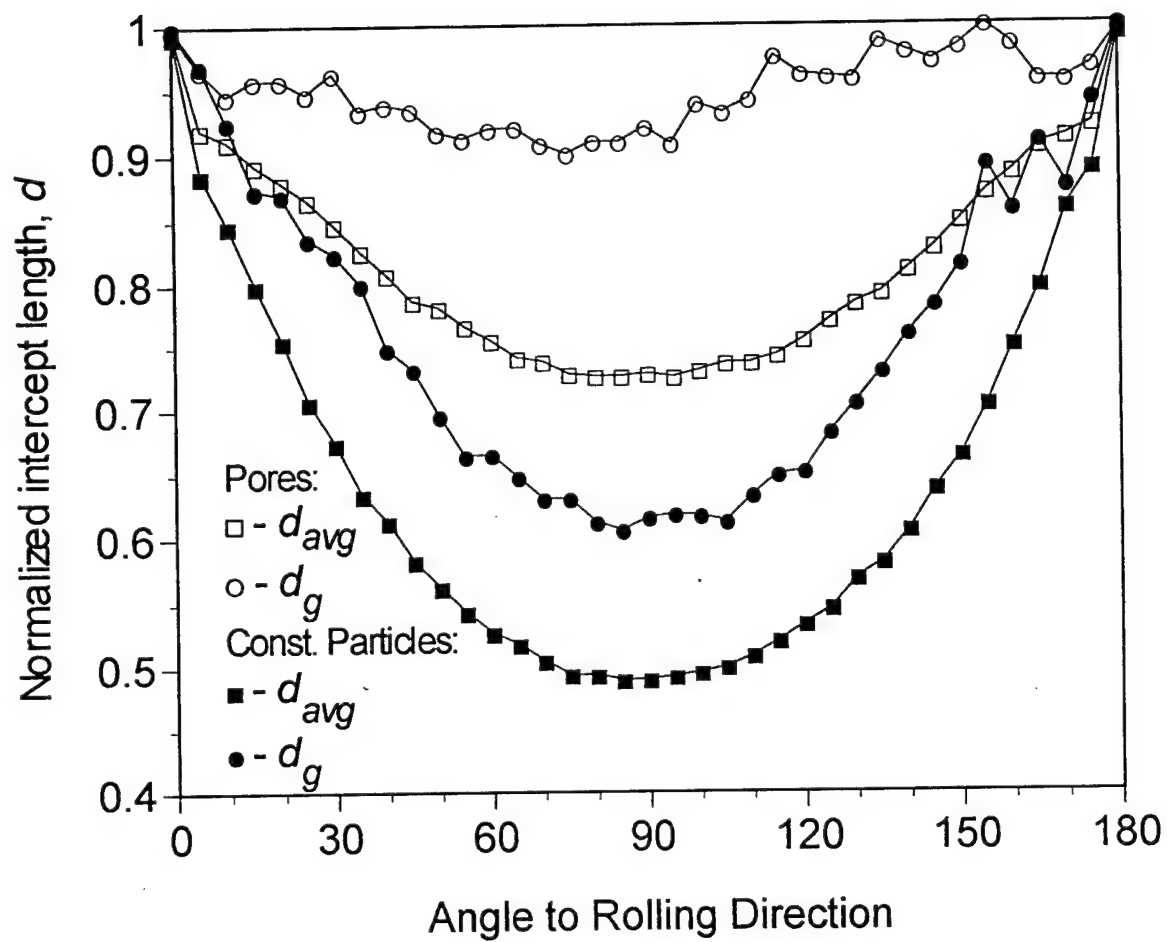


Figure 3. Angular variation of the normalized average intercept lengths of the pore and constituent particle sections on the LS-planes for the old 7050-T7451 alloy variant, plate center. (See text for definitions of  $d_g$  and  $d_{avg}$ )

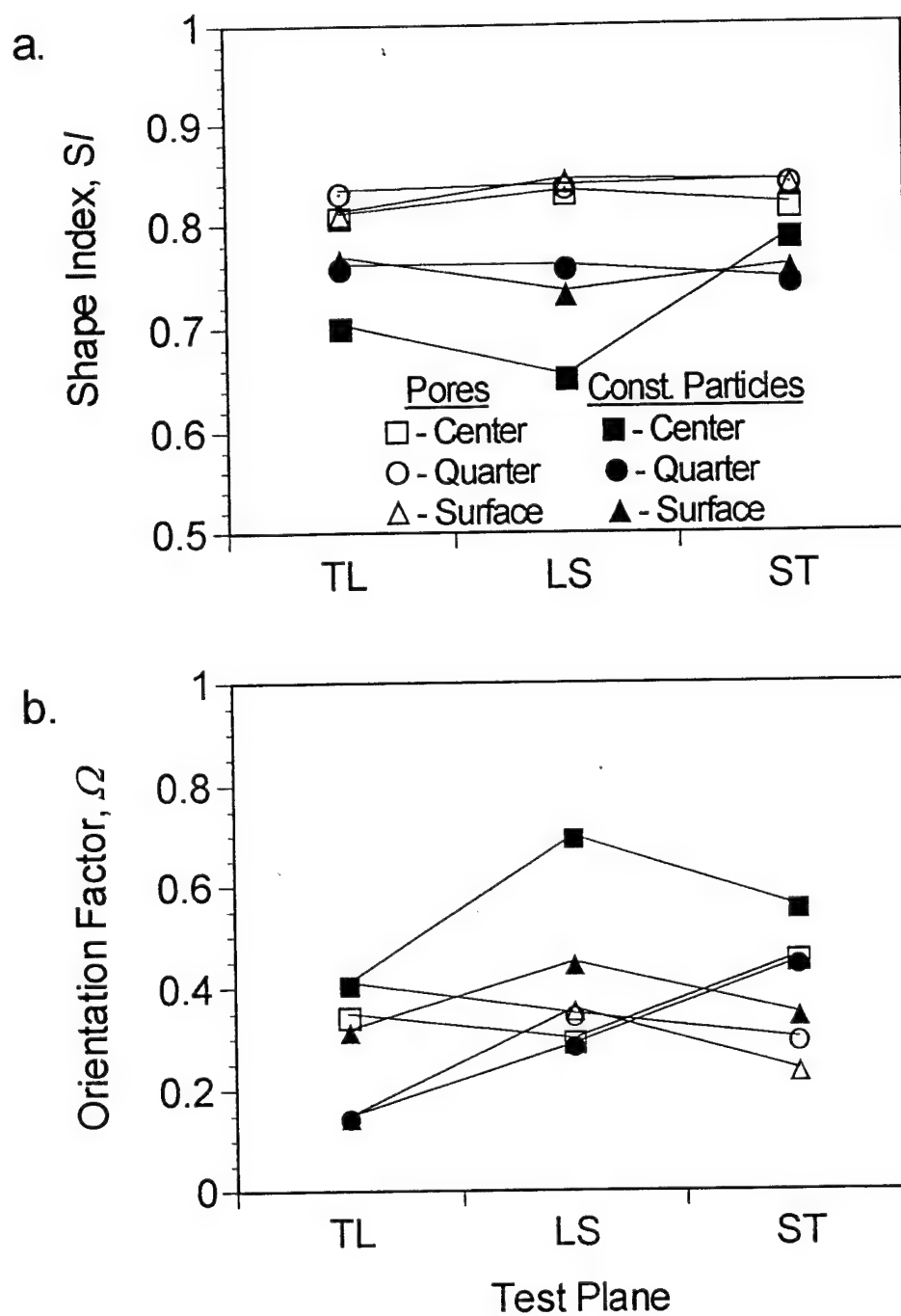


Figure 4. Average (a) shape indexes,  $SI$ , and (b) orientation factors,  $\Omega$ , of the pore and particle sections on indicated test planes at different locations in the old variant of the 7050-T7451 plate alloy.

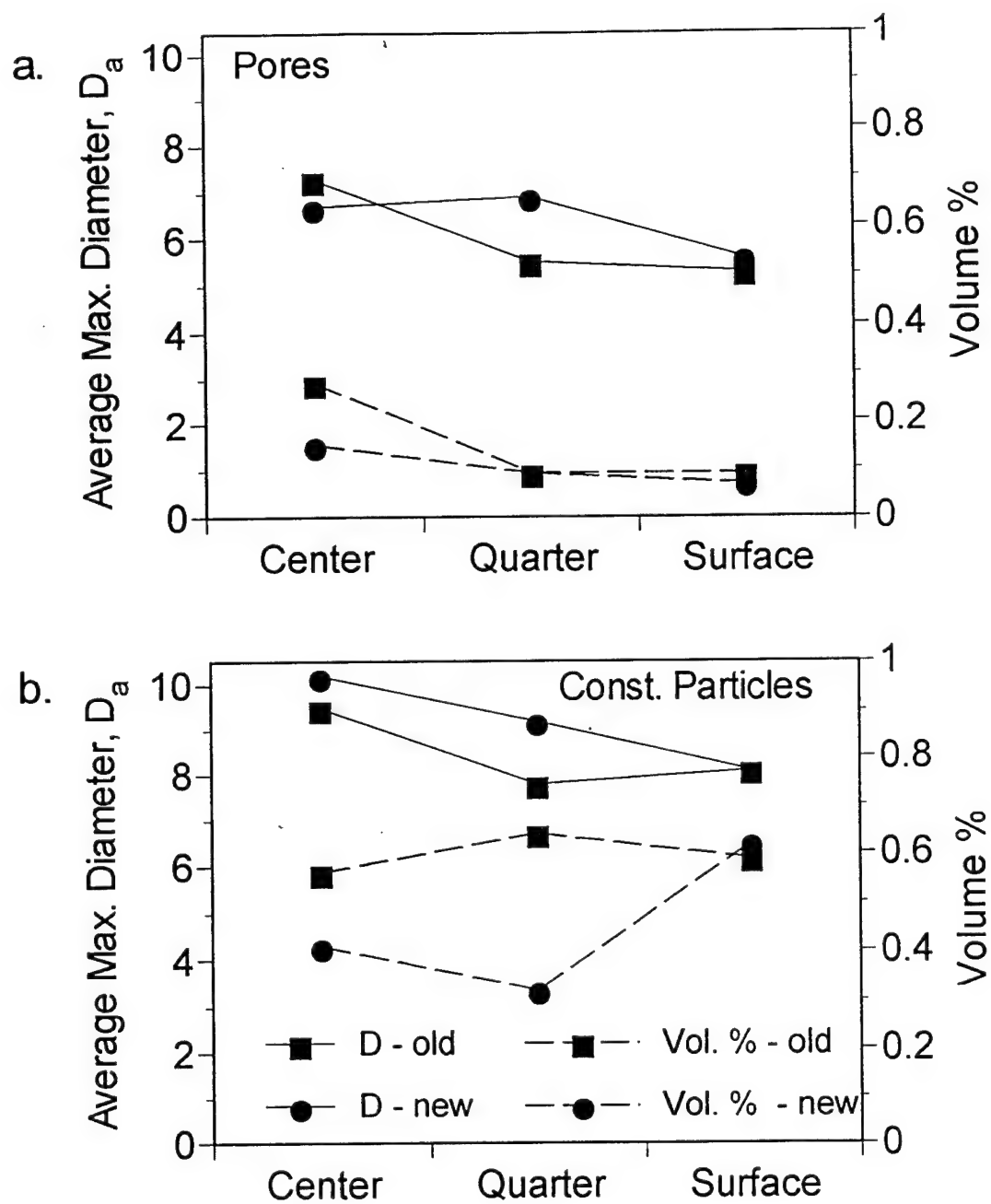
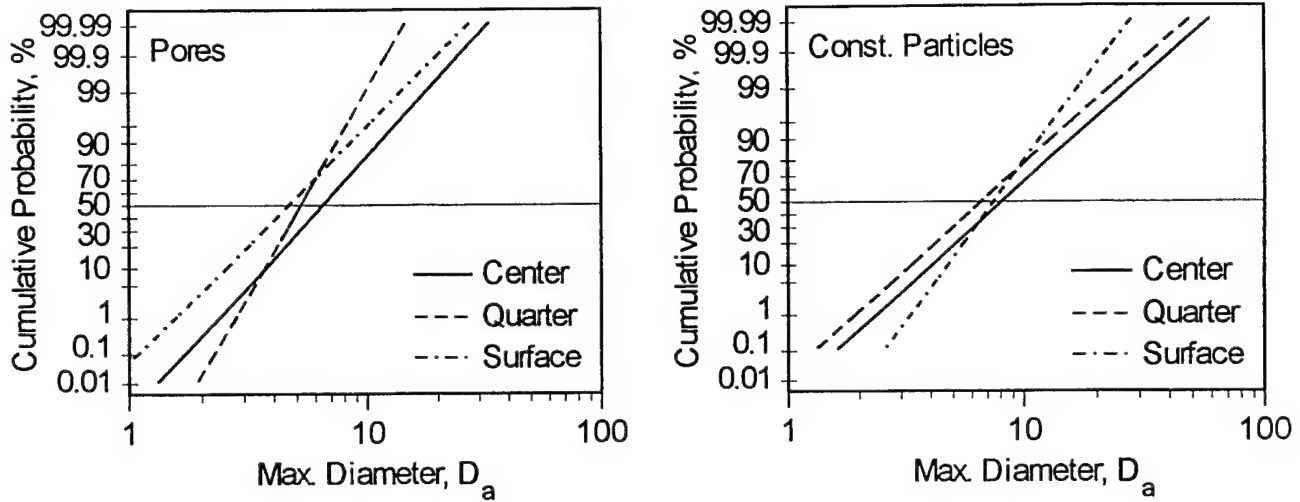


Figure 5. Calculated (a) pore and (b) constituent particle size and volume fraction gradients in the old and new variants of the 7050-T7451 plate alloys.

Old 7050-T7451 Plate Alloy



New 7050-T7451 Plate Alloy

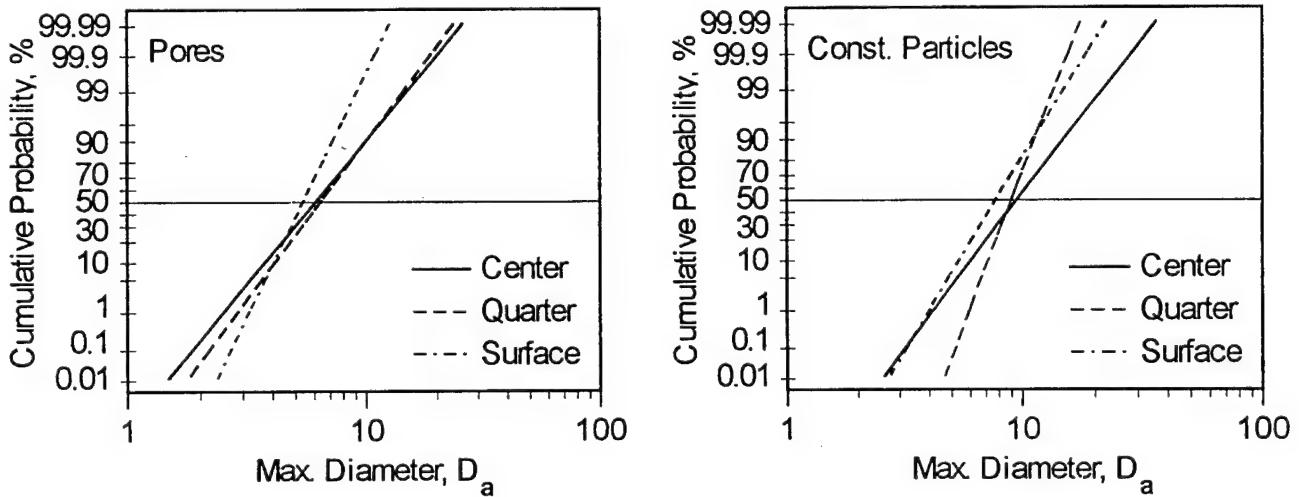


Figure 6. Estimated cumulative probability distributions of the pore and constituent particle sizes at indicated locations within the old and new variants of the 7050-T7451 plates.

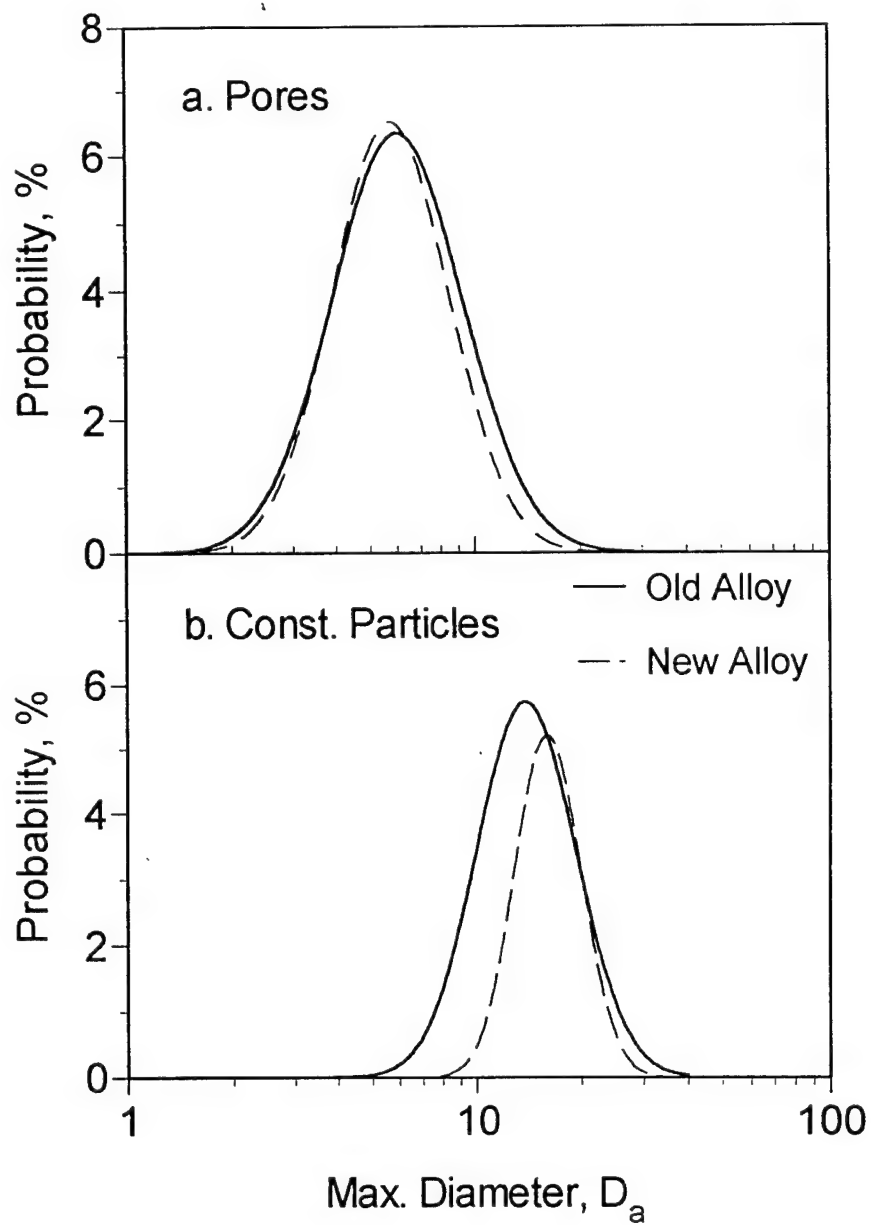


Figure 7. Calculated size distributions of (a) pores and (b) constituent particles in the old and new variants of the 7050-T7451 alloys, plate center region.

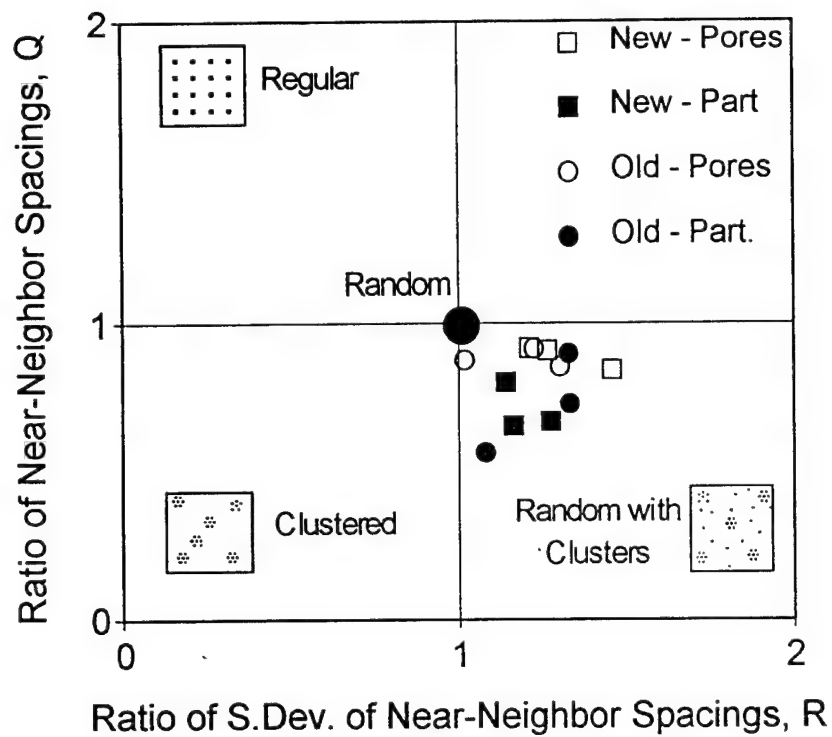


Figure 8. Results of the characterizations of the pore and constituent particles spatial distributions; old and new variants of the 7050-T7451 alloy, plate center regions.

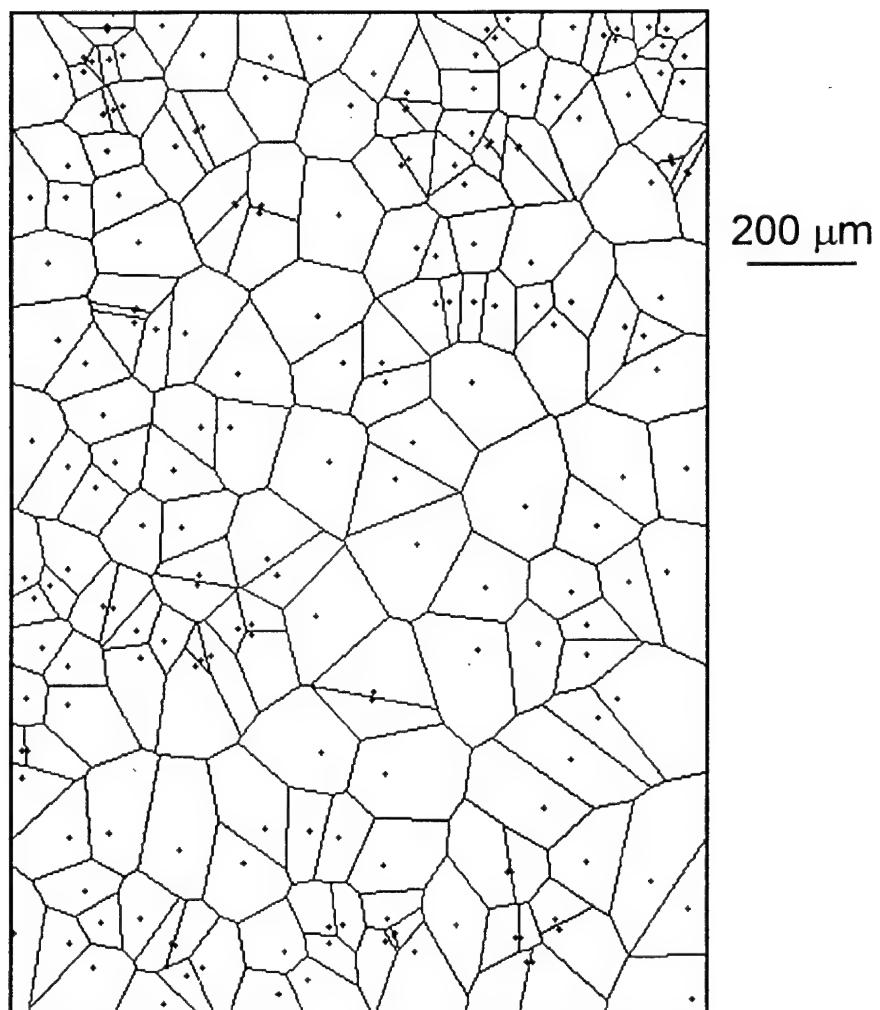


Figure 9. Example of the Voronoi tessellation cells constructed on the pore centers used in the identifications of the nearest neighbors. Points represent locations of the pore centers; ST-plane, center plate region, old 7050-T7451 alloy.

*Appendix E. Estimation of True Size Distribution of Partially Aligned Same-Shape  
Ellipsoidal Particles*

M. A. Przystupa

Accepted for publication in *Scripta Materialia*.

# ESTIMATION OF TRUE SIZE DISTRIBUTION OF PARTIALLY ALIGNED SAME-SHAPE ELLIPSOIDAL PARTICLES

Marek A. Przystupa

Department Materials Science and Engineering, University of California, Los Angeles,  
Los Angeles, CA 90095-1595, E-mail: amarek@ucla.edu

## INTRODUCTION

The purpose of this note is to present relations for estimating true size distributions, from the plane section data, of the same-shape triaxial ellipsoidal particles which have one of the axes aligned. This case is of practical importance to composites and alloys with ellipsoidal dispersions aligned parallel to for instance rolling plane but with random orientations about that plane normal, figure 1. The problem of obtaining true size distribution of such particles is not new and it has been treated extensively over the past seventy years [1,2]. The first comprehensive solutions were due to Wicks [3,4], followed by the solutions for specialized cases of prolate and oblate ellipsoids [5-7] and randomly oriented triaxial ellipsoids [8]. However, the explicit expressions for the considered case are lacking and this note is intended to fill that gap.

## THEORETICAL CONSIDERATIONS

The considered spatial distribution of particles is illustrated in figure 1. All ellipsoids are assumed to have different major semi-axes  $A_i > B_i > C_i$ , with  $C_i$ -semi-axes aligned and parallel to  $z$  and with random orientations of  $A_i$  and  $B_i$  in the  $x$ - $y$  plane. The aspect ratios of all ellipsoids are the same and equal to

$$q_{ab} = \frac{A_i}{B_i} = \frac{\bar{A}}{\bar{B}}, \quad q_{ac} = \frac{A_i}{C_i} = \frac{\bar{A}}{\bar{C}}, \quad q_{bc} = \frac{B_i}{C_i} = \frac{\bar{B}}{\bar{C}} \quad (1)$$

where bars indicate average values. Although only two of the three aspect ratios are independent, all three are easy to find: all cross-sections on planes perpendicular to  $z$  have aspect ratios  $q_{ab}$  and  $q_{ac}$  and  $q_{bc}$  can be determined, respectively, as the largest and the smallest aspect ratios of the sections on planes parallel to  $z$ , figure 2. These two types of planes offer the maximum information and it is assumed that they are going to be used to obtain all input data.

The size distribution of the same-shape ellipsoids can be fully described by the size distribution of one of their semi-axes. What is needed is a relationship between the true size distribution of that particular semi-axes and the size distribution of the ellipsoid two dimensional sections on the test planes. To find that relation let us start by defining a true size probability distribution functions  $F(D)$  such that  $F(D)\delta D$  is a fraction of ellipsoids in size interval  $[D, D+\delta D]$  with  $D$  representing one of the semi-axes. A test plane with a vector normal  $\mathbf{n}$  will then have area density of particle cross-sections equal to [1,9,10]:

$$N_{A\mathbf{n}} = N_V \int_0^\infty P_{\mathbf{n}}(D) F(D) dD \quad (2)$$

where  $N_V$  is the number of ellipsoids per unit volume and  $P_{\mathbf{n}}(D)$  is the probability of intersecting an ellipsoid of size  $D$  with test plane  $\mathbf{n}$ .  $P_{\mathbf{n}}(D)$  can be expressed as [9,10]:

$$P_{\mathbf{n}}(D) = \int_0^\pi \int_0^{2\pi} H_{\mathbf{n}}(D, \varphi, \theta) \frac{\sin \varphi}{4\pi} d\varphi d\theta = \bar{H}_{\mathbf{n}}(D) \quad (3)$$

where  $H_{\mathbf{n}}(D, \varphi, \theta)$  is the ellipsoid tangent height for test plane longitude and azimuth angles (measured from  $x$ )  $\varphi$  and  $\theta$ , respectively, and where  $\bar{H}_{\mathbf{n}}(D)$  is the ellipsoid's average tangent height. Combining equations (2) and (3) gives a well known relationships [1]:

$$N_{An} = N_V \overline{H_n} \quad (4)$$

where  $\overline{H_n}$  is average height of all ellipsoids. We now introduce an ancillary distribution of cross section sizes,  $\phi_n(d)$ , on test plane  $n$  with  $d$  representing either of the semiaxes. The fraction of sections with sizes in the interval  $[d, d+\delta d]$  is then equal to:

$$\phi_n(d)\delta d = \frac{N_V}{N_{An}} \int_0^\infty \int_0^\pi \int_0^{2\pi} \frac{2\delta h(D, d, \varphi, \theta)}{H_n(D, \varphi, \theta)} \cdot H_n(D, \varphi, \theta) F(D) \frac{\sin \varphi}{2\pi} dD d\varphi d\theta \quad (5)$$

where  $h(D, d, \varphi, \theta)$  is the distance from the ellipsoid center to the test plane which gives a cross-section of size  $d$  and where the first term under the integral represents the probability of such intersection. Combining eq. (5) with (3) and (4) results in the following relation between true and plane section size distributions:

$$\phi_n(d) = \frac{2}{\overline{H_n}} \int_0^\infty \int_0^\pi \int_0^{2\pi} \left| \frac{dh(D, d, \varphi, \theta)}{dd} \right| \cdot \frac{\sin \varphi}{4\pi} F(D) dD d\varphi d\theta \quad (6)$$

Since  $\phi_n(d)$  can be measured experimentally, eq. (6) can be solved for  $F(D)$  provided that the expressions for the average tangent height,  $\overline{H_n}$ , and the derivative are known. As will be shown below, those expressions are different for the two types of considered test planes.

#### Test planes perpendicular to $z$

In this case the ellipsoids are cut parallel to the  $x$ - $y$  plane, figure 2, and it is convenient to assume that  $D = A$ , and that  $d = a$ , the major semiaxes of the intersection. For such assumptions  $\phi = \pi/2$ ,  $0 < \theta < 2\pi$  and tangent height is equal to

$$H_{nz}(A, \varphi, \theta) = 2C = \frac{2A}{q_{ac}} \Rightarrow \overline{H_{nz}} = \frac{2\overline{A}}{q_{ac}} \quad (7)$$

It is also easy to show that the distance from the center of the ellipsoid to the test plane is independent of  $\phi$  and  $\theta$  and equal to:

$$h(A, a) = \frac{1}{q_{ac}} \sqrt{A^2 - a^2} \Rightarrow \left| \frac{dh}{da} \right| = \frac{a}{q_{ac} \sqrt{A^2 - a^2}} \quad (8)$$

Substituting eqs. (7) and (8) to eq. (6) gives:

$$\phi_{nz}(a) = \frac{a}{\overline{A}} \int_a^\infty \frac{F(A)}{\sqrt{A^2 - a^2}} dA \quad (9)$$

which is an Abel type integral identical to that describing 2-D to 3-D conversion for polydisperse spheres. Finding the distribution of  $F(A)$  requires then measurements of the distribution of the major semiaxes of the particle sections on  $z$ -planes  $\phi_{nz}(a)$  and then solving equation (8) using any of the well known methods devised for spheres [1]. As for spheres, the first three moments of the true size distribution can be recovered without the need for solving equation (9) from relationships [1, 9, 11]:

$$\overline{A} = \frac{\pi}{2} \left( \frac{1}{a} \right)^{-1}, \quad \overline{A^2} = 2a \left( \frac{1}{a} \right)^{-1}, \quad \overline{A^3} = \frac{3\pi}{4} a^2 \left( \frac{1}{a} \right)^{-1} \quad (10)$$

where  $(1/a)$  is a harmonic mean and  $\overline{a^2}$  average of squares of the sections major semiaxes. Knowledge of the moments is sufficient for estimating the number of ellipsoids per unit volume,  $N_V$ , and their volume fraction,  $f$ . From eqs. (4) and (7) they are:

$$N_v = \frac{q_{ac} N_{An_z}}{2\bar{A}} = \frac{q_{ac} N_{An_z}}{\pi} \left( \frac{1}{a} \right) \quad (11)$$

$$f = N_v \frac{4\pi}{3} \overline{(ABC)} = N_v \frac{4\pi}{3q_{ab}q_{ac}} \bar{A}^3 = \frac{\pi N_{An_z}}{q_{ab}} \bar{a}^2 \quad (12)$$

The measurements of the sections area density  $N_{An_z}$ , half-axes  $a$  and aspect ratios  $q_{ab}$  on  $n_z$  planes allows then for estimation of the ellipsoids:

- true size distribution from eq. (9)
- moments of the true size distributions from eqs. (10)
- volume fraction from eq. (12)

Finding volume density via eq. (11) requires additional measurement of the aspect ratio  $q_{ac}$  on any of the plane parallel to  $z$ .

*Test planes parallel to  $z$*

As shown in figure 2, the ellipsoids are now sectioned perpendicular to  $x$ - $y$  plane. Assuming  $D \equiv C$  and  $d \equiv c$ , the semi-axes parallel to  $z$ -axis, gives  $\phi = 0$  and  $0 < \theta < 2\pi$ . It is easy to show that the tangent height is now given by relation:

$$H_{n_z}(C, 0, \theta) \equiv H_{n_z}(C, \theta) = 2Cq_{ac} \sqrt{\cos^2 \theta + \left( \frac{\sin \theta}{q_{ab}} \right)^2} \quad (13)$$

which results in the average tangent height equal:

$$\overline{H_{n_z}} = 2\bar{C}q_{ac} \int_0^{2\pi} \sqrt{\cos^2 \theta + \left( \frac{\sin \theta}{q_{ab}} \right)^2} \frac{d\theta}{2\pi} = 2q_{ac} \bar{C}E(q_{ab}) \quad (14)$$

where  $E(q_{ac})$  is a shape function, plotted in figure 3, related to a complete elliptic integral of the second kind [12]. The relation between the distance to the ellipsoid center,  $h(C, c)$ , and the minor half axes of the section,  $c$ , is now given by

$$h(C, c, \theta) = \frac{H_{n_z}(C, \theta)}{2} \sqrt{1 - \left( \frac{c}{C} \right)^2} \Rightarrow \left| \frac{dh}{dc} \right| = \frac{H_{n_z}(C, \theta)c}{2C\sqrt{C^2 - c^2}} \quad (15)$$

Substituting eqs. (14) and (15) to (6) gives:

$$\phi_{n_z}(c) = \frac{1}{q_{ac} \bar{C}E(q_{ab})} \int_c^\infty \int_0^{2\pi} \frac{H_{n_z}(C, \theta)c}{2C\sqrt{C^2 - c^2}} F(C) dC \frac{d\theta}{2\pi} = \frac{c}{\bar{C}} \int_c^\infty \frac{F(C)}{\sqrt{C^2 - c^2}} dC \quad (16)$$

The result is identical to eq. (9) with  $A$  replaced by  $C$  and  $a$  by  $c$ . The size distribution  $F(C)$  and the moments can be then obtained using the aforementioned procedures, except that now the measured quantities are sections half-axes parallel to  $z$ . The expressions for the ellipsoids volume densities and volume fraction are, however, different as from eqs. (4), (10) and (14) we have:

$$N_v = \frac{N_{An_z}}{2q_{ac} \bar{C}E(q_{ab})} = \frac{N_{An_z}}{\pi q_{ac} E(q_{ac}/q_{bc})} \left( \frac{1}{c} \right) \quad (17)$$

while from eqs. (1), (10) and (12) the volume fraction will be equal

$$f = N_v \frac{4\pi}{3} q_{ac} q_{bc} \bar{C}^3 = \frac{\pi q_{bc} N_{An_z}}{E(q_{ac}/q_{bc})} \bar{c}^2 \quad (18)$$

Since all quantities in eq. (16)-(18) can be measured on planes parallel to  $z$ , these planes alone are sufficient for finding all true characteristics of the ellipsoids. Hence, by measuring area density  $N_{An_z}$ ,

half-axes  $c$  and the aspect ratios of sections on those planes one can obtain:

- the aspect ratios  $q_{ac}$  and  $q_{bc}$  as the maximum and minimum observed aspect ratios

- true size distribution from eq. (16)
- moments of the size distribution from eqs. (10) with  $A$  replaced by  $C$  and  $a$  by  $c$
- volume density and volume fraction of ellipsoids from eq. (17) and (18)

## PRACTICAL COMMENTS

The derived expressions allows for the use of two different sets of planes for characterizing partially aligned triaxial ellipsoids. Planes parallel to  $z$  are sufficient to obtain all characteristics, while planes perpendicular to  $z$  allow for the measurement of only the size distribution and volume fractions. Since in reality the same-shape approximation may not be entirely true, the errors in estimating aspect ratios from single measurement can contribute significantly to the errors in estimates of  $N_V$  and  $f$ . It would be then advisable to obtain estimates of the average aspect ratios based on the large number of data. Fortunately such estimate are possible for all the ratios. As already discussed,  $q_{ab}$  is the easiest to find: it is the average aspect ratio of the cross-sections on  $z$  planes. The same holds for average value of  $q_{ac}$  which can be obtained from:

$$q_{ac} = \frac{\bar{A}}{\bar{C}} = \frac{\overline{(1/c)}}{\overline{(1/a)}} \quad (19)$$

which requires measurement on both planes parallel and perpendicular to  $z$ . As for  $q_{bc}$ , it is possible to show that it is related to the aspect ratios  $q_{bcm_x}$  on planes parallel to  $z$  through relation:

$$q_{bcm_x} = q_{bc} \left( \cos^2 \theta + \left( \frac{\sin \theta}{q_{ab}} \right)^2 \right)^{-1/2} \quad (20)$$

which averaged over  $0 < \theta < 2\pi$  results in

$$\overline{q_{bc}} = q_{bc} \int_0^{2\pi} \left( \cos^2 \theta + \left( \frac{\sin \theta}{q_{ab}} \right)^2 \right)^{-1/2} \frac{d\theta}{2\pi} \Rightarrow q_{bc} = \frac{\overline{q_{bcm_x}}}{E_1(q_{ab})} \quad (21)$$

where  $E_1(q_{ab})$  represents the integral, plotted in figure 3, related to the hypogeometric function. Hence, finding  $q_{bc}$  also necessitates measurements on both sets of the test planes.

## SUMMARY

- The relations for estimating true size characteristics, volume fractions and volume densities of the same-shape in-plane aligned triaxial ellipsoidal have been compiled.
- The measurements on planes perpendicular to the plane of alignment allow for estimations of all true size characteristics. The two necessary aspect ratios are the largest and the smallest observed aspect ratios and the true size distribution can be obtained from the measured distribution of the section diameters.
- Measurements on planes parallel to the plane of alignment are not sufficient for finding all true characteristics. They allow however for the estimation of the true size distribution, volume fraction and one of the true aspect ratios.
- Alternative expressions for estimating average aspect ratios were also derived. They should be useful for finding aspect ratios when triaxial-ellipsoid is an approximation of the particle shapes.

## ACKNOWLEDGMENTS

The author would like to thank ONR for financial support under Grant N00014-91-J-1299. Thanks are also due to Dr. J. Zhang from Seagate and Ms. A. J. Luévano from TRW for valuable discussions.

## REFERENCES

1. E. E. Underwood, Quantitative Stereology, Addison-Wesley, Reading, MA (1970).
2. H. J. G. Gundersen and E. B. Jensen, J. Microsc. 131, 291 (1983).
3. S. D. Wicksell, Biometrika, 17, 84 (1925).
4. S. D. Wicksell, Biometrika, 18, 152 (1926).
5. R. T. DeHoff and F. N. Rhines, AIME Trans. 221, 975 (1961).
6. R. T. DeHoff, AIME Trans. 224, 474 (1962).
7. L-M. Cruz Orive, J. Microsc. 107, 235 (1976).
8. R. T. DeHoff and P. Bousquet, J. Microsc. 92, 119, (1970).
9. G. M. Tallis, Biometrics, 26, 87 (1970).
10. L. Karlsson and R. Sandstrom, Metallography, 19, 143 (1986)
11. M. G. Kendall and P. A. P. Moran, Geometrical Probability, p. 86, Hafner Publishing Company, New York (1963).
12. Handbook of Mathematical Functions, edited by M. Abramowitz and A. Stegun, Dover Publications, Inc., New York (1972).

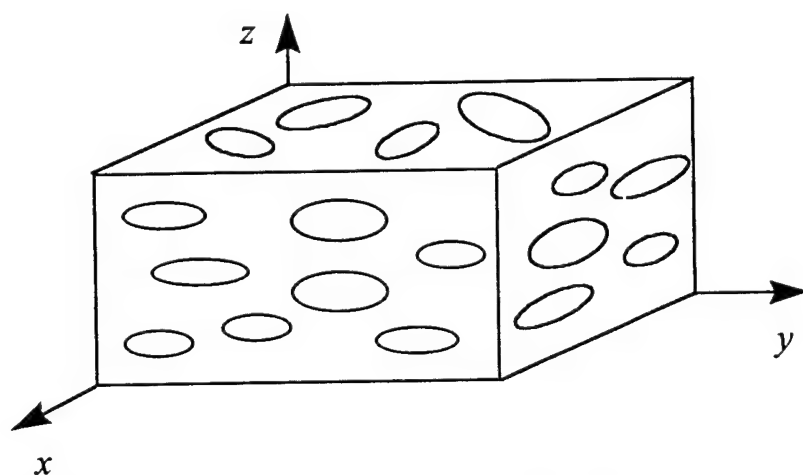


Figure 1. Schematic showing observed cross-sections of triaxial ellipsoidal particles aligned parallel to the  $x$ - $y$  plane with random rotations about  $z$ -axis, the case considered in the paper.

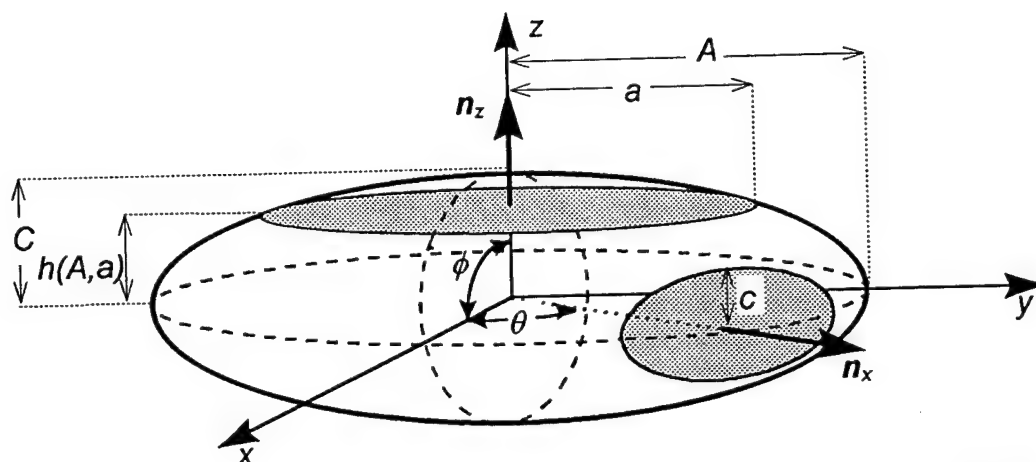


Figure 2. Example of particle sections observed on planes  $n_z$  normal to  $z$  and planes  $n_x$  parallel to  $z$ .

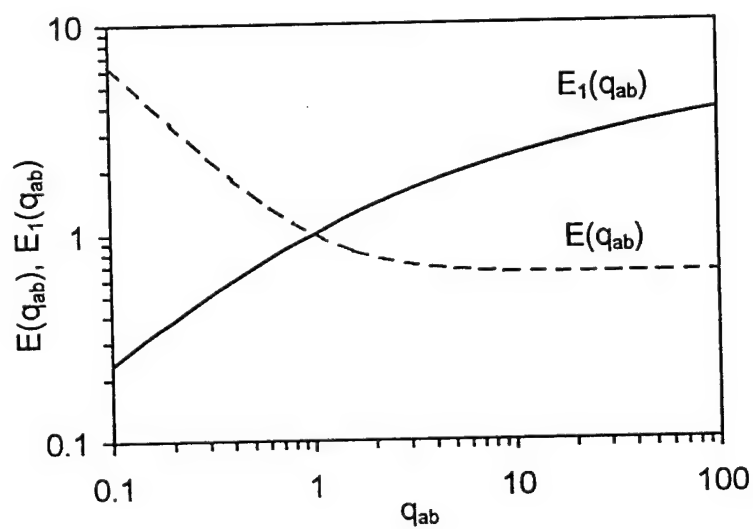


Figure 3. Change of shape functions  $E(q_{ab})$  and  $E_1(q_{ab})$  with the triaxial ellipsoid aspect ratio  $q_{ab}$ .

*Appendix F. Accumulation of Microstructural Damage Due to Fatigue of High-Strength Aluminum Alloys*

A. J. Luevano J. Zhang, and M. A. Przystupa  
*J. of Materials and Performance*, 3 (1994) pp. 47-54.

# Accumulation of Microstructural Damage Due to Fatigue of High-Strength Aluminum Alloys

A. J. Luévano, M. A. Przystupa, and J. Zhang

The microstructural features of aluminum alloy 7050-T7451 in the vicinity of fatigue cracks and on the crack path were studied to determine which of these features influence fatigue crack propagation. The studies included characterization of the full spectrum of microstructural and fracture surface features—from the largest (e.g., roughness and grain type) to the smallest (e.g., second-phase particles and dislocations). Of all the features studied, only the second-phase particles were shown to have a definite influence by causing crack deflection. The number of particles encountered by the fatigue cracks were significantly higher than the expected average. The fatigue crack path was predominately transgranular, and there was no change in the dislocation and precipitation structures in the crack-affected zone.

## Keywords

Aluminum alloys, cracks: propagation, fatigue

## 1. Introduction

FATIGUE failures in metals and alloys are always preceded by the accumulation of microstructural damage. Such damage manifests itself as microcracking, debonding, development of slip bands, formation of dislocation cell structures, and, ultimately, nucleation and growth of a fatigue crack. The sequence of damage accumulation events leading to the fatigue crack nucleation and growth is debatable, but there is no doubt that fatigue resistance is low in alloys susceptible to large amounts of microstructural damage (Ref 1). In order to design alloys for improved fatigue resistance and/or to formulate realistic life-prediction models, it is thus necessary to determine which forms of damage occur in different alloys and to rank their importance.

The purpose of this work was to identify microstructural damage processes taking place during fatigue in a typical precipitation-hardened aluminum aerospace plate alloy and to assess the importance of these processes in controlling crack propagation rates. Aluminum alloys were chosen because of their prominence in aerospace applications. These alloys also have very complex structures consisting of unrecrystallized or partially recrystallized grains with matrix and grain-boundary precipitates, constituent particles, microporosities, and, in many instances, precipitation-free zones (Ref 2-5). The dominant fatigue crack usually initiates at the largest surface micropore and propagates tortuously through the matrix. Crack deflections results from the linking up of the main crack with microcracks in the damage zone preceding it or from preferred intergranular fracture, cracking along slip planes, and so on. Each of these factors constitutes a different type of microstructural damage mechanism. The mechanism that is actually active can be identified through metallographic and fractographic examinations. The results of such an analysis, for the 7050-T7451 plate alloy, are reported here. Included is information

about the crack geometry, the distribution of different features on the crack path, and the microstructural damage inflicted during fatigue.

## 2. Experimental Procedure

The material used in this study was from the center of a batch of 14.5 cm thick 7050-T7451 plate alloy designated as "old quality" by Alcoa. This alloy (Fig. 1) is 20% recrystallized and contains, by volume, about 0.1% of porosities and 0.65% constituent particles in the form of stringers (Ref 6). Their average sizes are 3.4 and 4.5  $\mu\text{m}$ , respectively (Ref 6). The precipitate microstructure consists of grain-boundary and matrix precipitates (Fig. 2).

The precipitate phases present were identified by comparing the diffraction patterns of the examined alloy with patterns of other 7xxx alloys. The patterns were identical to those taken by Park and Andrell (Ref 7) of overaged 7075. They identified the matrix phases as  $\eta'$  and  $\eta$  variants (predominantly  $\eta$ 1,  $\eta$ 2, and  $\eta$ 4) and the grain-boundary precipitates as predominantly  $\eta$ . Because the alloy had been partially recrystallized, the dislocations were not apparent in these microstructures.

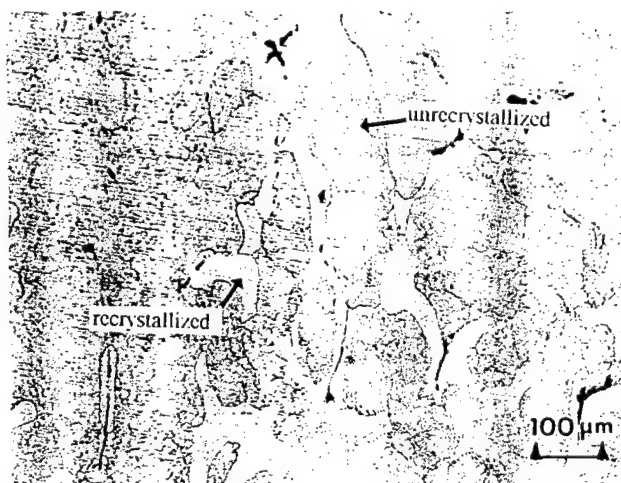
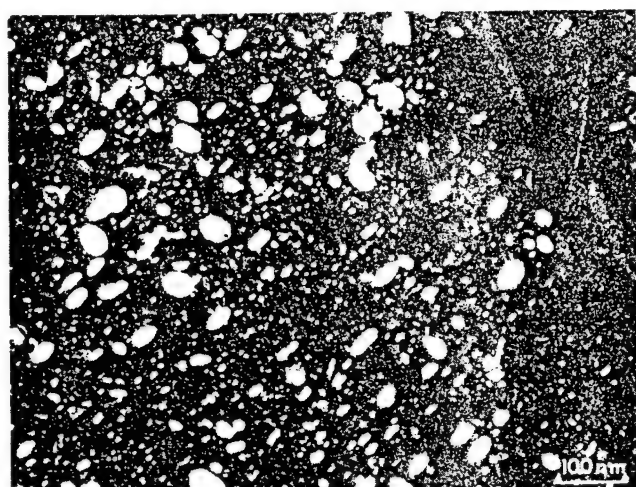
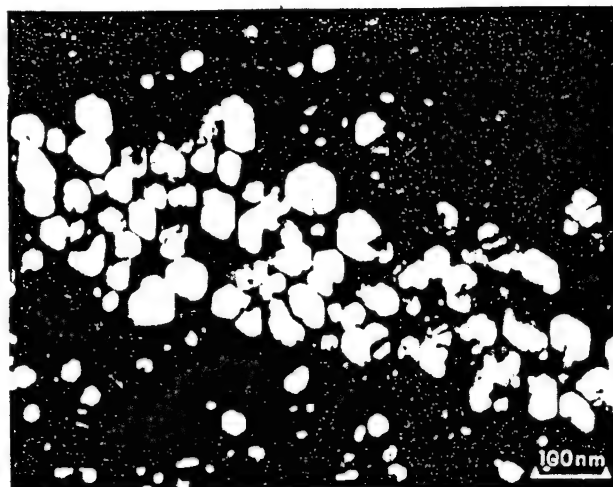


Fig. 1 Micrograph showing recrystallized and unrecrystallized grains in aluminum alloy 7050-T7451

A.J. Luévano, M.A. Przystupa, and J. Zhang, Department of Materials Science and Engineering, University of California, Los Angeles, Los Angeles, CA 90024



(a)



(b)

Fig. 2 Microstructure of 7050-T7451 grain-boundary precipitates (a) and matrix precipitates (b)

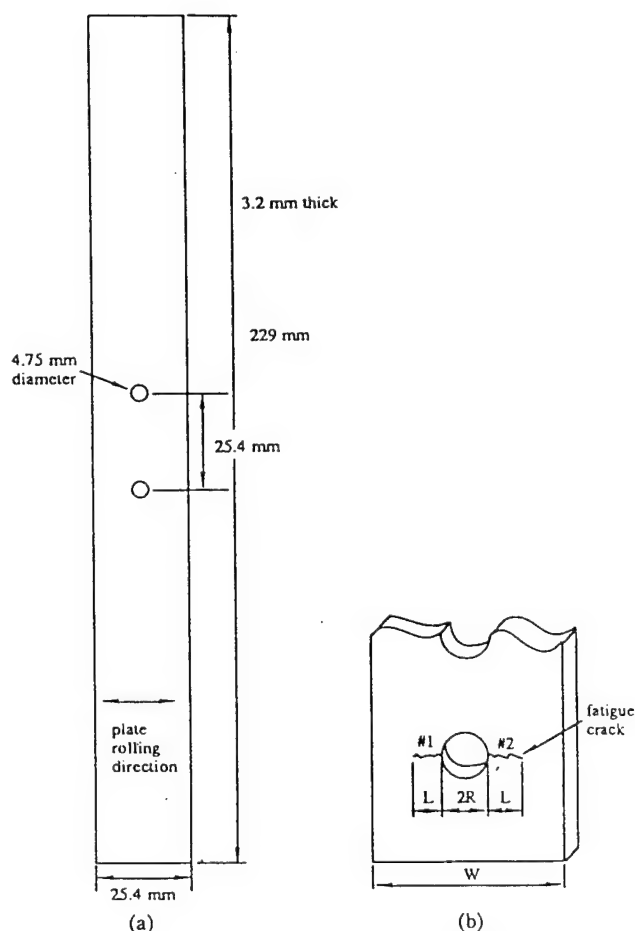


Fig. 3 (a) Two-hole fatigue sample. (b) Schematic of secondary fatigue cracks

The samples for damage assessment used in this investigation were cut from two-hole fatigue specimens (Fig. 3a). Two-hole specimens were used to simulate the loading condition of bolt holes in an aircraft part (Ref 3-5). The specimens were cut from the center section of a plate, with the long axis normal to the rolling direction. They were then fatigued to failure under the conditions of  $\sigma_{\max} = 170$  MPa,  $R = 0.1$ , and a frequency of 10 Hz. In all cases, the cracking started from large surface micropores (Ref 5). Some of the failed samples contained secondary fatigue cracks at the unfailed hole (Fig. 3b). These cracks are ideal for identifying the microstructural features on both sides of the fatigue crack path. The microstructures in the vicinity of two such cracks that formed on opposite sides of the same hole were studied in this investigation, which employed both scanning electron microscopy (SEM) and transmission electron microscopy (TEM).

The SEM examinations were used to determine the crack roughness, the relationship of the crack path to grain structure, the number of second-phase particle intercepts, and the severity of microcracking. The microstructures were characterized along two crack paths (Fig. 3b) at the surface sections and at the one-third and two-thirds thicknesses of the sample. Scanning electron microscopy photographs of specimens in both the etched and unetched conditions were used for all measurements. Actual crack lengths and the fractions of the crack paths through various regions (i.e., unrecrystallized grains, recrystallized grains, and grain boundaries) were measured on the micrographs using a digitizer.

One of the cracks was analyzed using a computerized system for fractographic analysis (Ref 8). This system allows automatic estimation of the actual and projected crack lengths, roughness parameters, distribution of the angles describing orientations of crack segments, and fractal dimension. The general concept of the fractal analysis is based on the principle that the number of ruler lengths,  $N$ , required to measure the length

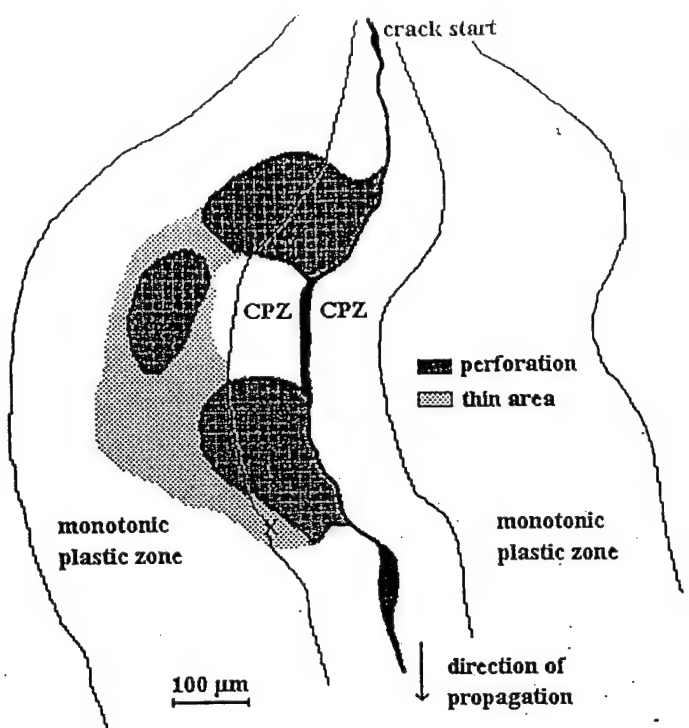


Fig. 4 Schematic of thin foil used for dislocation study. The thinned area examined is marked with an X

of a curve depends on the size of the ruler,  $\rho$ , used in the measurement (Ref 9). A small ruler resolves finer details than a large one, but at the same time requires a disproportionately greater number of steps to cover the analyzed curve. A plot of  $\log(N)$  versus  $\log(1/\rho)$  for a fractal curve yields a straight line that can be described by:

$$N = k \left( \frac{1}{\rho} \right)^d$$

where  $d$  is the fractal dimension and  $k$  is a constant. Such a defined fractal dimension gives an indication of the roughness of a surface: The closer the number is to 1, the smoother the surface. This method of defining a fractal has been proposed by Mandelbrot (Ref 9).

To determine whether a fatigue crack deflects toward constituent particles, the average number of particles per unit length of a straight line was compared with the actual number of particles per unit crack length. For both measurements, enlarged photographs of the entire crack length were used. The expected number of particles for a straight crack was measured using a scan grid of parallel lines spaced 0.5 cm apart. Because of the anisotropy of constituent particle spatial distribution, the grid was always aligned with the average direction of crack propagation. The number of constituent particle intercepts per unit length along the actual crack path was calculated from measurements of the actual crack lengths and total number of particles intersected by the crack.

Table 1 Crack lengths and roughness parameters

Crack No.	Section	Projected length, $\mu\text{m}$	Actual length, $\mu\text{m}$	Profile roughness parameter
1	Surface	1937	2400	1.24
	$1/3$ thickness	2771	3277	1.18
	$2/3$ thickness	2773	3307	1.19
2	Surface	3292	3635	1.10
	$1/3$ thickness	3600	4037	1.12
	$2/3$ thickness	3433	4171	1.22

The SEM studies were supplemented by TEM examination to determine whether any change in dislocation structure occurred in the vicinity of the crack path. Specifically, evidence of dislocation activities in or near the cyclic plastic zone was sought. Samples for this purpose were cut from various sections along the fatigue crack path. Each TEM sample contained either starting, middle, or end regions of the fatigue crack. The samples were dimpled using a solution of 10% nitric acid and 90% water at room temperature and a voltage of 25 V. Final polish and perforation were done with a solution of 30% nitric acid and 70% methanol at a temperature of  $-30^\circ\text{C}$  and a voltage of 15 to 18 V.

All TEM samples were examined in the scanning (STEM) mode to determine the position of the perforations in relation to the fatigue crack. The thinned area around the perforation chosen for examination was always the one closest to the crack. Because little control over the position of the perforation is possible, we were unsuccessful in obtaining samples with suitable thinned area next to the crack. The location of the thinned area closest to the fatigue crack used in this study is shown schematically in Fig. 4. As indicated in Fig. 4 and explained in the following section, this area was on the border between the cyclic and the monotonic plastic zones. All other TEM samples were from the monotonic plastic zone.

### 3. Results and Discussion

#### 3.1 Roughness and Crack Geometry

The results of the crack length measurements and the profile roughness parameters, defined as the ratios of the actual to the projected crack lengths, are summarized in Table 1. As expected, the projected crack lengths in the interiors of the samples were longer than those at the surface due to the curved crack front profile. The roughness parameters varied between 1.1 and 1.24, which is in agreement with the average roughness parameter of 1.2 obtained in the parallel studies for the actual fatigue fracture surfaces of the investigated sample using fractal analysis (Ref 6).

Profiles of crack 2 at the surface section opposite that used in Table 1 were analyzed using an automated fractographic and fractal analysis system. Both the upper and the lower surfaces of the crack were examined. The crack length for the upper profile was 3128  $\mu\text{m}$ ; for the lower surface profile, 3028  $\mu\text{m}$ . Roughness parameters were 1.27 and 1.25, respectively (a difference of only 1.35%). Results of the fractal analysis for the upper surface profile of crack 2 are shown in Fig. 5. The slopes

of the curve is 1.041, which represents the fractal dimension. The fractal dimension for the lower profile was a comparable 1.037. The results indicated only one of the profiles required study.

The distribution of the crack segment orientations for the upper profile of crack 2 is shown in Fig. 6. As expected, the most frequent angle for the upper profile is at about 90°, which is the general crack propagation direction. The lower profile exhibited a similar symmetrical trend. Both distributions were relatively flat, indicating a considerable amount of crack deflection in both profiles.

In addition to the main fatigue cracks, two other types of cracks were observed in the studied specimens. The more common type was crack branching. The branches often grew toward and into constituent particles (Fig. 7a). Microcracks were also observed near, but separate from, the main crack. Two ex-

amples of such microcracks are shown in Fig. 8. Both were located near the end of the fatigue crack, and the crack shown in Fig. 8(a) originated at a constituent particle. This means that the growth of a fatigue crack in 7050-T7451 alloy is preceded by the microcracking ahead of the crack tip, with the constituent particles serving as the potential microcrack nucleation sites. The crack then propagates toward the microcracks, resulting in a noticeable amount of crack deflection.

### 3.2 Grain Structure

The interaction of the fatigue crack with grains was evaluated based on measurements of the fractions of the length of the crack that passed through the various types of grains and/or grain boundaries. Because the material was partially recrystal-

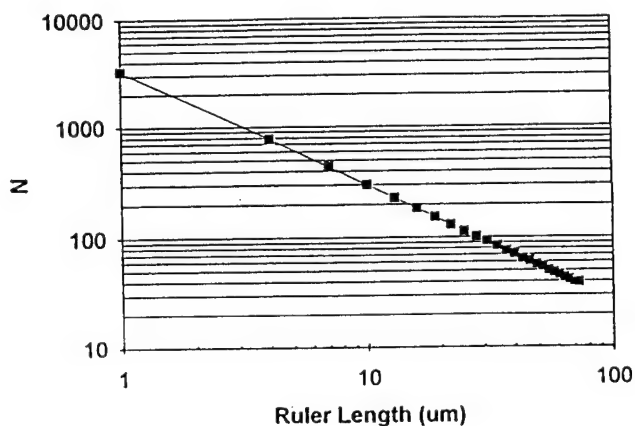


Fig. 5 Plot for determining fractal dimensions of fatigue crack 2, upper profile, surface region

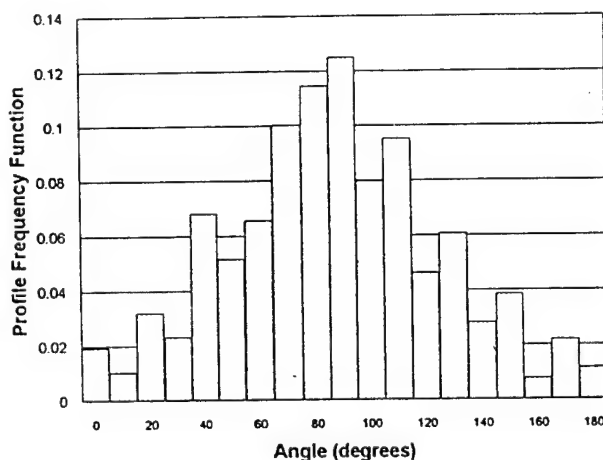
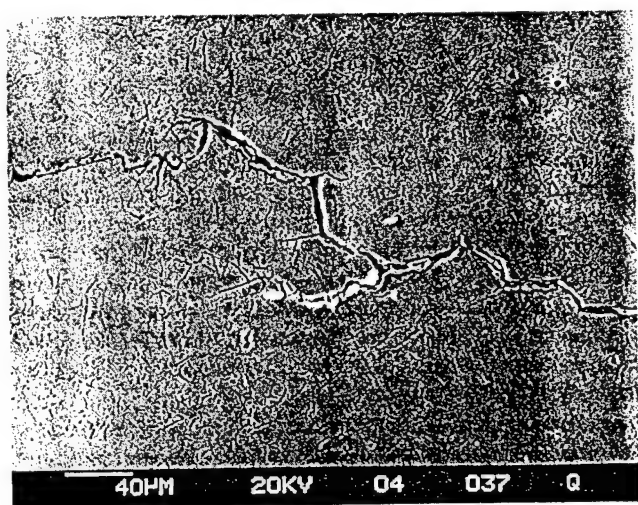
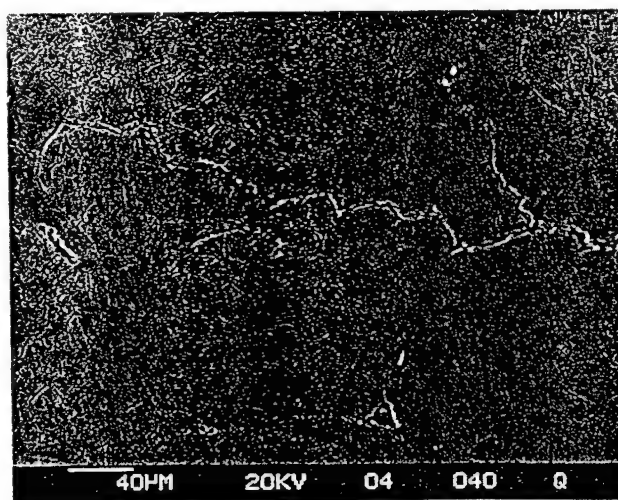


Fig. 6 Distribution of angular orientation of crack segment, crack 2, surface section



(a)



(b)

Fig. 7 Branching of fatigue cracks in 7050-T7451 alloy. (a) Branches propagating through constituent particles. (b) Branches propagating along grain boundaries

lized, the grains encountered by the crack were either recrystallized or unrecrystallized with subgrains. The lengths of the crack path along boundaries and through each type of grains were measured from micrographs and used in the calculation of the percentages. Intergranular portions of the crack path were separated into the following categories, depending on the types of grains on either side of the crack: (1) unrecrystallized/recrystallized, (2) recrystallized/recrystallized, and (3) unrecrystallized/unrecrystallized. The results (Table 2) indicate that the crack propagated both transgranularly and intergranularly, with the preferred fracture mode being transgranular. The transgranular portion of the crack was primarily through the unrecrystallized grains which is not unexpected as the material is only 20% recrystallized. The fractions of the recrystallized grains encountered by the crack varied widely, but generally were lower than the recrystallization levels.

Intergranular failures constituted between 6 and 40% of the total fatigue crack path. From the possible combinations, the boundaries between unrecrystallized and recrystallized grains were most frequently chosen by the crack. This implies that such boundaries are most susceptible to fatigue damage. It was

also observed that some of the transgranular cracks in the unrecrystallized grains propagated along subgrain boundaries. The percentages of crack path along subgrain boundaries in the unrecrystallized grains, also given in Table 2, indicate that only a small portion of the crack path followed subgrain boundaries. In the case of crack 2, the crack was too wide to allow accurate determination of its path.

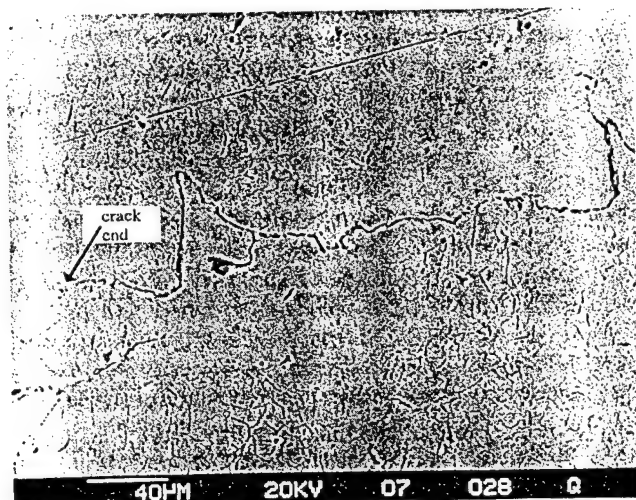
### 3.3 Second-Phase Particles

To determine the influence of the constituent particles on the crack path deflections, the expected number of particle intercepts along a straight line through a sample were compared with the number of particles intercepted by the actual crack path. As described earlier, the measurements were taken from enlarged photographs (e.g., Fig. 9) that enhanced the details. The results are summarized in Table 3. For each section the number of particle intercepted by the crack was always greater than the expected average for the straight line. To determine whether the values were significantly different, the null hypothesis that they were the same was tested using Student's t-distribution (Ref 10). In all cases the null hypothesis

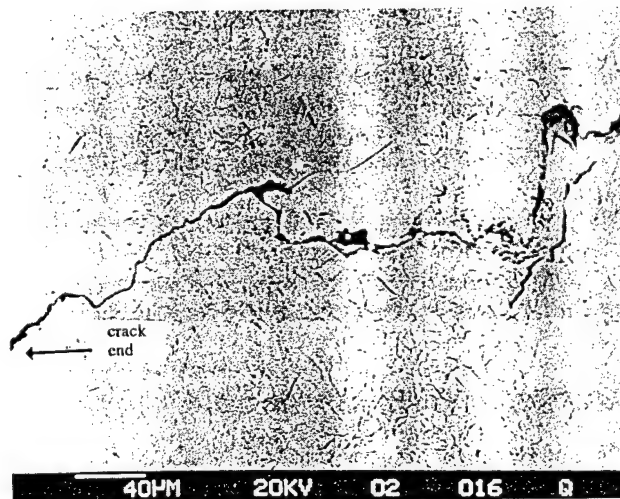
Table 2 Percentage of crack length in various regions of grain structure

Crack No.	Sample Section	Transgranular crack path			Intergranular crack path (a)				
		Unrecrystallized, %	Recrystallized, %	Total, %	U/R boundaries, %	R/R boundaries, %	U/U boundaries, %	Subgrain, %	Total, %
1	Front surface	76.1	12.3	88.4	2.2	1.5	...	7.9	11.6
	1/3 thickness	54.3	5.9	60.2	25.8	7.2	5.1	1.7	39.8
	2/3 thickness	63.4	22.4	85.8	12.6	...	1.5	...	14.2
	Back surface	65.6	12.8	78.4	12.8	8.8	...	...	21.6
2	Surface	65.8	26.2	92.0	8.0	...	...	...	8.0
	1/3 thickness	75.7	18.5	94.2	5.8	...	...	...	5.8

(a) U/R, unrecrystallized/recrystallized; R/R, recrystallized/recrystallized; U/U, unrecrystallized/unrecrystallized



(a)



(b)

Fig. 8 Microcracks in the vicinity of the main crack. Arrows indicate the end of the fatigue crack.

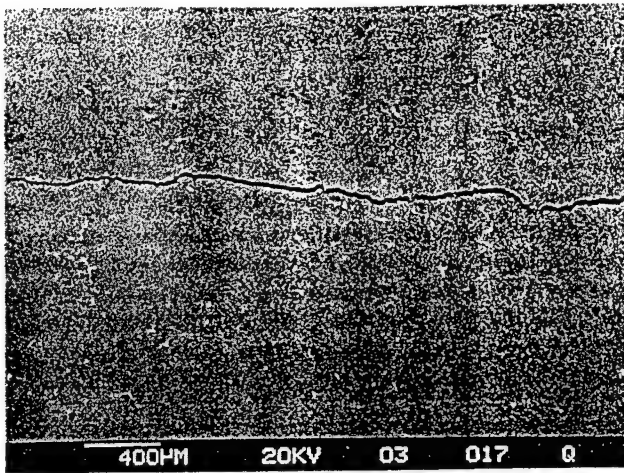


Fig. 9 Example of the type of micrograph used to calculate the number of particles intercepted by scan lines and the crack

Table 3 Number of intercepts of scan lines and crack path with second phase particles.

Crack No.	Section	Straight line No./ $\mu\text{m}$	Crack path No./ $\mu\text{m}$	Significance level (%)
1	surface	$9.9 \times 10^{-4} + 6.5 \times 10^{-4}$	$2.0 \times 10^{-3}$	<0.1
	1/3 thickness	$8.7 \times 10^{-4} + 4.5 \times 10^{-4}$	$2.1 \times 10^{-3}$	<0.1
	2/3 thickness	$9.4 \times 10^{-4} + 5.8 \times 10^{-4}$	$1.6 \times 10^{-3}$	<0.1
2	surface	$8.0 \times 10^{-4} + 5.8 \times 10^{-4}$	$1.3 \times 10^{-3}$	<0.1
	1/3 thickness	$1.2 \times 10^{-4} + 5.8 \times 10^{-4}$	$1.9 \times 10^{-3}$	<0.1
	2/3 thickness	$1.0 \times 10^{-3} + 4.1 \times 10^{-4}$	$2.2 \times 10^{-3}$	<0.1

had to be rejected at a significance level of less than 0.1%. This means that there was a less than 0.1% chance that the number of particles intercepted by the crack was the same as that for the straight line; the actual calculated probability was even smaller (in the  $1 \times 10^{-10}\%$  range).

It is thus justifiable to conclude that the constituent particles affected the crack path by causing crack deflections. The most likely reason for this behavior is particle cracking. As shown in Fig. 7, some of the particles in the vicinity of the fatigue crack path had microcracks. Such particles always attract the main fatigue crack, causing crack deflections. Because the investigated 7050-T7451 alloy originally contained broken constituents (Ref 11, 12), it is impossible to tell which of the particles fractured as a result of fatigue. However, the number of particles intersected by the fatigue crack was significantly larger than the number of broken particles observed in the starting material. This means that fatigue resulted in constituent particle cracking in the crack-affected zone of the alloy.

### 3.4 Precipitates and Dislocations

Both precipitate and dislocation microstructures in the vicinity of the crack were examined and compared to that of the bulk material to establish whether fatigue-related damage occurred. Because the studied material was subjected to high-cycle fatigue, the most probable region of damage was the cyclic plastic zone (CPZ). To determine the size of that zone and thus

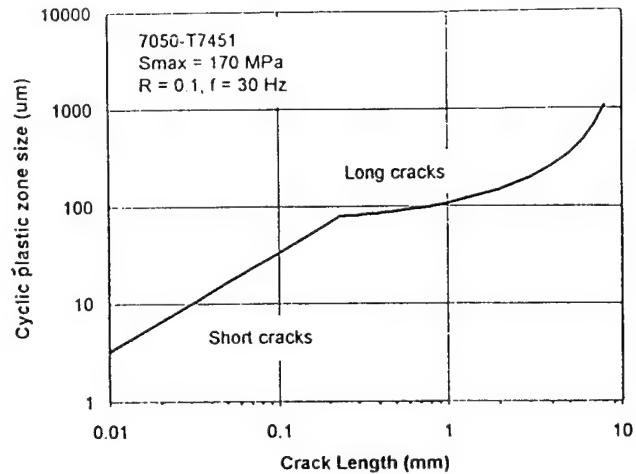


Fig. 10 Changes in CPZ size with crack length

how close to the fatigue crack the TEM sample had to be perforated, Eq 1 was used (Ref 1):

$$r_c = \frac{1}{\pi} \left( \frac{\Delta K}{2\sigma_y} \right)^2 \quad (\text{Eq 1})$$

where  $\Delta K$  is the stress-intensity factor amplitude and  $\sigma_y$  is the yield strength, equal to 450 MPa for 7050-T7451 alloy.

The change in the CPZ size,  $r_c$ , with crack length using Eq 1 is shown in Fig. 10. Two cases had to be considered. The first involved small through-thickness cracks, each of length  $L$ , emanating from the fasten hole of radius  $R$ . In this case, the stress-intensity factor can be approximated as (Ref 13, 14):

$$\Delta K = 3.36 \Delta \sigma \sqrt{\pi L} \sqrt{\frac{2R + 2L}{2R + L}} \quad (\text{Eq 2})$$

where  $\Delta \sigma$  is stress amplitude, which was equal to 153 MPa. Another expression for  $\Delta K$  must be used for large cracks. In this case, both cracks and the hole can be approximated as a through-thickness center crack of length  $2(R+L)$  (Fig. 3b), and  $\Delta K$  is equal to (Ref 13):

$$\Delta K = \Delta \sigma \sqrt{\pi(R+L)} \left( \sec \frac{\pi(R+L)}{W} \right)^{1/2} \quad (\text{Eq 3})$$

where  $W$  is the double-hole specimen width. As Fig. 10 shows, the size of the plastic zone at the crack initiation site was about 10  $\mu\text{m}$ . At the termination point, when the cracks were 2.5 to 3.5 mm long, the zone increased to about 250  $\mu\text{m}$ . This is comparable to the typical grain size, which for the studied 7050-T7451 alloy is 138  $\mu\text{m}$  for unrecrystallized grains. Thus, to observe any possible damage due to fatigue, the TEM sample had to be perforated in a grain adjacent to the fatigue crack. Such accuracy is difficult to achieve. However, as shown in Fig.

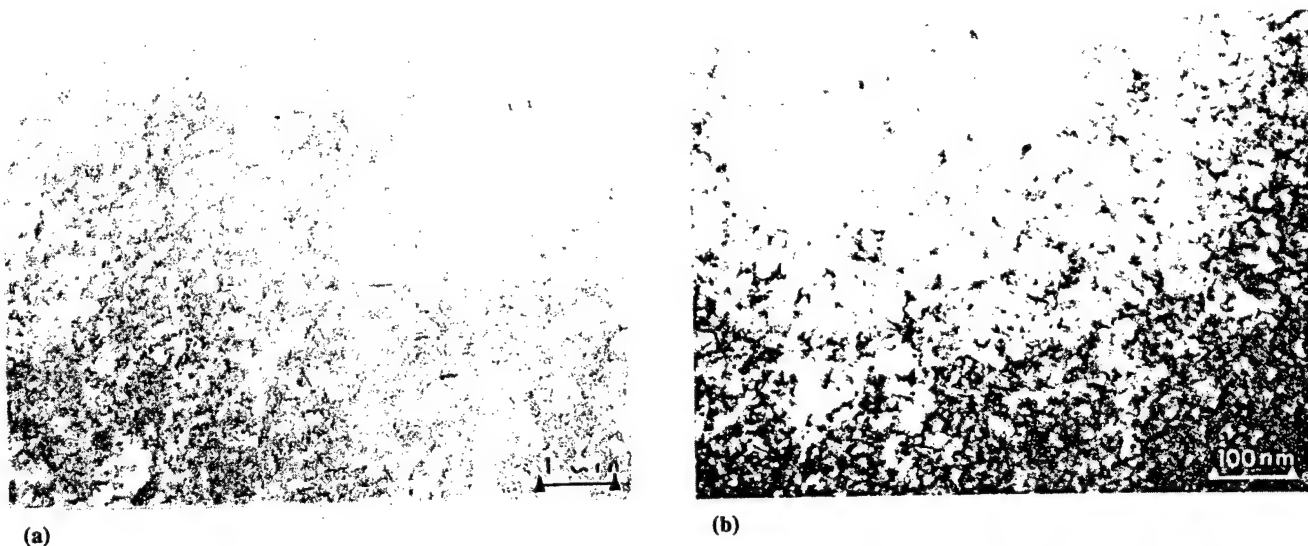


Fig. 11 Microstructure of the matrix in (a) bulk 7050-T7451 and (b) thin foil closest to the crack shown

4, we were able to obtain a foil with perforation approximately 0.7 mm from the crack initiation site and 100  $\mu\text{m}$  from the crack surface. The CPZ in this area was about 100  $\mu\text{m}$  (Fig. 10). Hence, the area examined was not in the CPZ, but on the border between the CPZ and the monotonic plastic zone. Examination of that particular sample revealed no evidence of changes in the precipitate structure or debonding at the grain boundaries. Also, the dislocation structure was no different from that of the bulk material. Figure 11 compares the microstructure of the matrix in the bulk 7050-T7451 material and in the area indicated in Fig. 4. Although the dislocations are difficult to locate, there clearly are no tendencies to grouping and/or banding in the area nearest the CPZ.

The above findings are consistent with other studies of dislocation structure in 7xxx alloys in low-cycle fatigue. For instance, it was reported that even at low strain amplitudes the grouping of dislocations can be seen after only a few fatigue cycles (Ref 16). The studied sample was exposed to 47,812 fatigue cycles, so some dislocation activities should be expected to occur. The fact that none was observed can be attributed to the low maximum stress (only 38% of the yield strength) and to the partially recrystallized polygonized structure with stable subgrains. The material had few free dislocations to begin with, and thus the amount of fatigue-related dislocation damage would be confined to the CPZ and would be much less than that for unrecrystallized, cold-worked alloys. Moreover, the slip in 7xxx aluminum alloys is affected by both temper and the percentage of copper present in the alloy. In the T7 stabilized temper, these alloys have more unshearable precipitates than in the T6 condition. Therefore, the slip is more homogeneous (Ref 17) and crack-tip deformation can be absorbed in the CPZ area. The affect of aging on the dislocation structure of 7050 alloy fatigued under low-cycle, low-strain-amplitude conditions was investigated by Coyne and Starke (Ref 18). They reported that going from underaged to peak aged to overaged conditions resulted in decreased dislocation banding and lower dislocation

densities within the bands. The effect of copper on slip is similar. As the copper content increases, slip becomes more homogeneous and slip bands are not observed. Lin and Starke (Ref 19), observed this phenomenon in 7xxx alloys with 2.1% Cu. Our alloy contained 2.3% Cu. and was in the overaged condition. The lack of dislocation activities is consistent with the Lin and Starke findings. However, some dislocation activities had to have taken place to facilitate fracture. The fact that none was observed can be explained by the location of the TEM examination areas. All areas examined were on the border outside the CPZ and thus in the region where plastic deformation would be small. As reported by Wilkins and Smith (Ref 20), moving away from the crack tip from the cyclic to the monotonic plastic zone, the dislocation structure changes from one characteristic of high-strain fatigue to one of low-strain fatigue. Results of our study confirm this and indicate that no visible dislocation activities occurred in the monotonic plastic zone in the investigated 7050-T7451 alloy.

## 4. Conclusions

The microstructure in and adjacent to fatigue cracks in aluminum alloy 7050-T7451 has been characterized to assess the amount of fatigue damage on the grain structure, second-phase particle and dislocation levels. The following conclusions have been reached:

- The fatigue crack path is 60 to 95% transgranular, with no preference toward unrecrystallized or recrystallized grains.
- The intergranular portion of the crack path occurs preferentially between unrecrystallized and recrystallized grains.
- Deflection of crack paths is controlled by the second-phase particles. The number of particles on the crack path is significantly higher than the expected average.

- No change in dislocation structure and no alterations of the precipitate structure was observed in the vicinity of the fatigue cracks.

## Acknowledgements

The funding for this program was provided by the Office of Naval Research under contract N00014-91-J-1299. The authors are indebted to Dr. A.K. Vasudévan, the program manager, for valuable discussions and to Drs. P.E. Magnusen and R.J. Bucci from Alcoa Laboratories for providing the fatigue samples.

## References

1. S. Suresh, *Fatigue of Materials*, Cambridge University Press, 1991
2. A.K. Vasudévan, R.D. Doherty, and S. Suresh, Fracture and Fatigue Characteristics in Aluminum Alloys, *Aluminum Alloys—Contemporary Research and Applications*, Treatise on Materials Science and Technology, Vol 31, A.K. Vasudévan and R.D. Doherty, Ed., Academic Press, 1989, p 446
3. C.R. Owen, R.J. Bucci, and R.J. Kegarise, Aluminum Quality Breakthrough for Aircraft Structural Reliability, *J. Aircraft*, Vol 26, 1989, p 178-184
4. A.J. Hinkle, P.E. Magnusen, R.L. Rolf, and R.J. Bucci, Effect of Microporosity on Notched Specimen Fatigue Life, *Proceedings of 5th International Conference on Structure Safety and Reliability*, A. H-S. Ang., M. Shinozuka, and G.I. Schueller, Ed., American Society of Civil Engineers, 1989, p 1467-1474
5. J.R. Brockenbrough, R.J. Bucci, A.J. Hinkle, J. Liu, P.E. Magnusen, and S.M. Miyasato, "Role of Microstructure on Fatigue Durability of Aluminum Aircraft Alloys," F33615-92-C-5915, Alcoa, 1993
6. M.A. Przystupa, J. Zhang, and A.J. Luévano, "Development of the Microstructure Based Stochastic Life Prediction Models," N00014-91-J-1299, University of California Los Angeles, 1992—(available from Defense Technical Information Center, Bldg. 5, Cameron Station, Alexandria, VA 22304-6145)
7. J.K. Park and A.J. Ardell, Microstructures of the Commercial 7075 Al Alloy in the T651 and T7 Temper, *Metall. Trans. A*, Vol 14A, 1983, p 1957-1965
8. M.A. Przystupa, J. Zhang, and A.J. Luévano, "Development of the Microstructure Based Stochastic Life Prediction Models," N00014-J-1299, University of California—Los Angeles, 1993 (available from Defense Technical Information Center, Buld. 5, Cameron Station, Alexandria, VA 22304-6145).
9. B.B. Mandelbrot: *Fractal Geometry of Nature*, W.H. Freeman, 1982.
10. E.L. Crow, F.A. Davis, and M.W. Maxfield, in *Statistical Manual*, Dover Publications, 1960, p 37
11. M.A. Przystupa, J. Zhang, and A.J. Luévano, "Development of the Microstructure Based Stochastic Life Prediction Models," N00014-J-1299, University of California—Los Angeles, 1991 (available from Defense Technical Information Center, Buld. 5, Cameron Station, Alexandria, VA 22304-6145).
12. J. Zhang, A.J. Luévano, and M.A. Przystupa, Quantitative Analysis of Heterogeneous Grain Structure on Plane Sections, *Scr. Metall. Mater.*, Vol 26, 1992, p 1061-1066
13. R.C. Shah, Stress Intensity Factors for Through and Part-Through Cracks Originating at Fastener Holes, in *Mechanics of Crack Growth*, STP 590, ASTM, 1976, p 429-459
14. O.L. Bowie, *J. Math. Phys.*, Vol 35, 1956, p 60-71
15. D. Broek, in *Elementary Engineering Fracture Mechanics*, 4th ed., Kluwer Academic Publishers, 1991, p 85
16. C. Laird, Mechanisms and Theories of Fatigue, in *Fatigue and Microstructure*, American Society for Metals, 1978, p 149-204
17. F.-S. Lin and E.A. Starke, Jr., The Effect of Copper Content and Deformation Mode of the Fatigue Crack Propagation of Al-6Zn-2Mg-xCu Alloys at Low Stress Intensities, *Mater. Sci. Eng.*, Vol 45, 1980, p 153-165
18. E.J. Coyne, Jr. and E.A. Starke, Jr., The Effect of Microstructure on the Fatigue Crack Growth Behaviour of an Al-Zn-Mg-(Zr) Alloy, *Int. J. Fract.*, Vol 15(No. 5), 1979, p 405-417
19. F.-S. Lin and E.A. Starke, Jr., The Effect of Copper Content and Degree of Recrystallization on the Fatigue Resistance of 7XXX-type Aluminum Alloy, *Mater. Sci. Eng.*, Vol 43, 1980, p 65-76
20. M.A. Wilkins and G.C. Smith, Dislocation Structures Near a Propagating Crack in an Al/2% Mg Alloy, *Acta Metall.*, Vol 18, 1970, p 1035-1043

*APPENDIX G. Microstructure Based Fatigue Life Predictions for Thick Plate  
7050-T7451 Airframe Alloys*

M. A. Przystupa, R. J. Bucci, P. E. Magnusen and A. J. Hinkle

Accepted for publication in *International J. of Fatigue*

## MICROSTRUCTURE BASED FATIGUE LIFE PREDICTIONS FOR THICK PLATE 7050-T7451 AIRFRAME ALLOYS

Marek A. Przystupa<sup>1</sup>, Robert J. Bucci<sup>2</sup>, Paul E. Magnusen<sup>2</sup> and Andrew J. Hinkle<sup>2</sup>

<sup>1</sup>Dept of Materials Science and Engineering, Univ. of California, Los Angeles, Los Angeles, CA 90095-1595, e-mail: amarek@ucla.edu, tel. (310) 825-6559, fax (310) 206-7353

<sup>2</sup>Alcoa Technical Center, 100 Technical Drive Alcoa Center, PA 15069

### ABSTRACT

The purpose of this work was to test a microstructure based fatigue life prediction Monte-Carlo model for potential use in quantifying fatigue quality and reliability of metallic structural alloys. The model used was of the crack growth type with the sizes of crack initiating pores, local crack geometry and crack tip texture as random variables. The model was verified using data for 7050-T7451 plate alloy fatigue tested in smooth sample configuration at  $\sigma_{\max}$  of 241 and 276 MPa and  $R=0.1$ . The mechanical testing was supplemented with characterizations of the size distributions of the fatigue performance limiting bulk porosity and measurements of the actual sizes of the fatigue crack initiating pores. Predicted fatigue lives were in good agreement with the experimental results and the model identified the size distribution of the crack initiating pores as the dominant variable controlling fatigue performance. The distributions of those pores were predicted from the bulk pore size data using the statistics of extremes. The developed approach proved effective in incorporating microstructural information in modeling fatigue and could be used in ranking fatigue quality and reliability of materials based on microstructural data.

### Introduction

Most of the existing crack growth life prediction models are based on the Paris/Erdogan type growth laws. Since such laws are deterministic, these models are suitable for predicting the average fatigue life. The statistical variability can be introduced into them either

through the stochastic multiplication factor or by replacing all parameters with stochastic variables[1]. The later approach allows for dynamic change of the crack tip environment with crack length, hence it is ideal for investigation the microstructural effects using a Monte-Carlo (MC) method[2]. The MC model used in this work incorporates microstructural changes on the crack path through the following crack growth law[3,4]:

$$\frac{da}{dN} = C \Delta K^m = \mathcal{D} \frac{C'}{M^n} \Delta K^m \quad (1)$$

where  $C$ ,  $C'$ ,  $m$  and  $n$  are material constants,  $\mathcal{D}$  is crack deflection correction coefficient and  $M$  is a Taylor factor dependent on material crystallographic texture [5]. Integrating eq. 1 gives fatigue life equal:

$$N = N_o + \int_{a_o}^{a_{crit}} \frac{M^n}{\mathcal{D} C' \Delta K^m} \cdot da \quad (2)$$

where  $N_o$  is number of nucleation cycles,  $a_o$  is an initial and  $a_{crit}$  final crack lengths. The microstructure enters the model through (1) initial crack size  $a_o$  equal to the size of the microstructural crack initiating flaws, (2) Taylor factor  $M$  controlled by crystallographic texture and (3) crack deflection correction  $\mathcal{D}$  related to the spatial distribution of the microstructural features. During MC simulations eq. 2 can be integrated numerically with random values of  $N_o$ ,  $a_o$  and  $a_{crit}$  as input and with randomly selected values of  $M$  and  $\mathcal{D}$  for each integration steps. The calculations are then repeated for various combinations of all variables, giving the distribution of fatigue lives. The model is extremely flexible and it allows for simulation of the effects from each individual variable and from their combinations. In this work we investigated only the effects of the initial crack sizes  $a_o$ , texture and crack deflections on fatigue lives of the 7050-T7451 plate alloys. In these alloys the cracks initiate preferentially from large pores and it can be assumed that the nucleation stage is insignificant, e.g.  $N_o = 0$ [6].

## Experimental Results

The test material used was 7050-T7451 thick (145 mm) plate alloy with yield strength of 455 MPa, tensile strength 515 MPa, fracture toughness  $32.3 \text{ MPa m}^{1/2}$  and fatigue crack growth rate given by relation[7]:

$$\frac{da}{dN} = 7.5 \times 10^{-12} \Delta K^{4.175} \quad (3)$$

(results in m/cycle for  $\Delta K$  in  $\text{MPa m}^{1/2}$ ). The L-T smooth fatigue samples used in testing were cut from the plate center and had gauge length 50.8 mm and diameter 12.7 mm. All tests were conducted at ambient atmosphere under constant amplitude loading with maximum stresses 241 MPa (45 samples) and 276 MPa (23 samples),  $R = 0.1$  and at frequency 10 Hz. The results are summarized in figure 1.

The microstructural characterizations included both metallography and fractography. The metallography focused on the measurement of the size distribution of the bulk porosity at the center of the plate. The magnification used was 900X and the data were collected from the LS, TL and ST planes. Obtained cumulative size distribution of pore maximum dimensions is shown in figure 2. The average bulk pore maximum dimension was  $23.8 \mu\text{m}$ , aspect ratio 1.52 and area density  $76.1 \text{ mm}^{-2}$ . Additional microstructural data on the same material have been reported in [8]. The fractographic examinations were limited to twenty samples tested at  $\sigma_{\text{max}}=241 \text{ MPa}$ . In all cases cracks initiated from large pores which had average max. length of  $153.2 \mu\text{m}$  and average aspect ratio of 1.80. The cumulative size distribution of the pore maximum dimensions are also shown in figure 2.

## Results and Discussion

The obtained results were used in estimating both the magnitudes of the microstructural contributions to the scatter in fatigue lives and in testing the predictive capabilities of the microstructure based fatigue MC model. The former can be obtained from eq. 2 by inte-

grating it with the upper and lower bound values of the microstructural variables and the later by changing microstructural variables with crack length. To obtain bounds on the initial crack sizes, it was assumed that each pore acts as microcrack and that the initial crack size is equal to the size of the largest pore intersecting fatigue sample surface. The size distribution of such pores, one from each sample, constitutes an extreme value distribution of bulk pores (parent distribution) with the sample size,  $N_G$ , equal to the number of pores intersecting sample surface [9]. To obtain the extreme value distribution, the bulk pore sizes were fitted with a Gumbel parent

$$F(\log d) = \exp\left(-\exp\left(-\frac{\log d - \mu}{\sigma}\right)\right) \quad (4)$$

where  $d$  is pore size and  $\mu$  and  $\sigma$  are distribution parameters, utilizing recommended weight function:

$$w_i = \frac{1}{1 - p_i} \quad (5)$$

where  $i$  is the ordered pore size number and  $p_i$  its empirical probability[9]. The Gumbel distribution was chosen because it described the best the right tail of the parent and because of its utility in the extreme value calculations. For a Gumbel parent the extreme value distribution is also given by eq. (4), with the same dispersion  $\sigma$  and with  $\mu$  equal to:

$$\mu_N = \mu + \sigma \ln N_G \quad (6)$$

The investigated alloy had pore area density  $76.1 \text{ mm}^{-2}$ , hence sample size,  $N_G$ , was  $1.54 \times 10^5$ . The parameters of the parent and extreme distribution are compiled in Table I and both distributions are compared with the experimental data in figure 2. The predicted sizes of the crack initiating pores are in very good agreement with the actual fractographic data indicating the correctness of the approach. The predicted crack initiating pore sizes corresponding to the 1 and 99 percentiles were 87.4 and 517  $\mu\text{m}$  respectively. They were used as the initial crack sizes in eq. 2 to estimate the variability in fatigue life attributable to pores. Obtained crack growth curves, for  $\sigma_{\max} = 240 \text{ MPa}$ , are in figure 3a. They were

generated using stress intensities from Raju and Newman [10] and assuming initial thumb-nail crack with depth equal to the pore size and with aspect ratio of the bulk pores. The predicted dispersion was 150,000 cycles which is comparable to that of the experimental results.

The effects of the changes of the crystallographic texture along the crack path on fatigue life have been estimated from the expected changes of the resulting Taylor factors ( $M$ ). For fcc metals and alloys those changes can lead to the local  $M$  between 2.5 and 4.5[5]. The crack growth curves obtained using these values are shown in Figure 3c. They were simulated for initial crack size 172  $\mu\text{m}$ , the predicted extreme average,  $n$  equal 2 [3] and using the same loading conditions as for the pore size effect. The obtained range of fatigue lives was 165,000 cycles. It should be however kept in mind that this represents the maximum one-sided effects. In reality the scatter will be smaller because the extreme conditions are not going to persist throughout the entire fatigue life. The realistic estimate of texture effect was obtained by varying  $M$  with crack length. For small cracks with plastic zone of the order of few grains  $M$  was assumed to be uniformly distributed between 2.5 and 4.5. Since for longer cracks the plastic zone penetrates increasing number of grains, the range of local  $M$ -values can be progressively decreased. Eventually, for a critical number of grains,  $N_{\text{crit}}$ , of about twenty five the crack tip samples the average texture, hence  $M$  can be assumed constant and equal to the average value [11], figure 4a. Such changes of  $M$  used in 1,000 MC simulations resulted in the predicted fatigue life range of only 5,200 cycles, figure 3c.

To evaluate the contribution from the changes of microstructural crack geometry on scatter, the reported fracture surface roughness data for 7050-T7451 alloy have been used [12]. The profile roughness was incorporated into the crack growth model by assuming

that the crack had idealized periodic profile shown in figure 4b. For such profile the deflection correction factor in eq. (2) is equal to [3,13]:

$$\mathcal{D} = \frac{1}{R_L} \quad (7)$$

where  $R_L$  is the profile roughness parameter equal to the ratio of the crack true and projected lengths. The maximum reported value of the profile roughness for 7050-T7451 alloy is 1.54 [12]; it gives the lower limit for  $\mathcal{D}$ . The upper limit corresponds to the straight crack without deflections i.e. when both  $R_L$  and  $\mathcal{D}$  are one. Crack growth curves obtained for those limits are in figure 3b. The estimated fatigue life variability was 61,000 cycles which is less than that for texture. This is again a one-sided overestimation. To obtain a realistic estimate of the range, the  $\mathcal{D}$ -values were varied along the crack path uniformly between the upper and lower bounds. The resulting spread of fatigue lives was only 2,200 cycles, figure 3b.

The fatigue lives in the 7050-T7451 plate alloys would be then expected to be controlled primarily by the size distribution of crack initiating pores, with other microstructural factors playing secondary role. Figures 1 and 5 show comparison of the experimental S-N fatigue data with the MC results simulated with initial crack size, yield strength and crack deflections as random variables. The initial crack sizes were generated according to the predicted extreme value distribution, with aspect ratios equal to the bulk pore average. The yield strength and crack geometry fluctuations were incorporated into the model using the aforementioned distributions of Taylor factors and deflection corrections  $\mathcal{D}$ . The predictions compare favorably with the experimental data for both short and mid-range fatigue lives. For long lives the model underestimates the experimental results. Although this is desirable from the point of view of the safe design, the underestimation is substan-

tial. This error is due the overestimation of the small crack initiating pore sizes by the extreme value procedure.

### Summary

- A Monte-Carlo crack growth model was used to estimates the magnitudes of microstructural effects on fatigue life of the 7050-T7451 thick plate alloys. The random variables used included crack initiating pore size, crystallographic texture and crack deflections.
- The model, with the initial crack sizes predicted from the bulk pore size distribution using statistics of extreme, show good predictive capabilities for the low and mid range fatigue lives.
- The size distributions of microstructural flaws, such as porosity, has been identified as the dominant variable controlling fatigue lives in 7050-T7451 plate alloys.

### Acknowledgments

Work supported by ONR under Grant N00014-91-J-1299 (UCLA) and Contract N00014-91-C-0128 (Alcoa). The authors would like to thank Dr. J. Zhang and Ms. A. J. Luévano, formerly from UCLA, for performing some of the metallographic and fractographic examinations.

### References

1. Provan, J. W. (ed.) *Probabilistic Fracture Mechanics and Reliability* (Martinus Nijhoff Publishers, Dordrecht, Netherlands, 1987)
2. Ang A. H-S. and Tang, W. H. *Probability Concepts in Engineering* vol. 2 (Copyright by authors, 1990) pp 274-325.
3. Suresh, S. *Fatigue of Materials* (Cambridge Unicersity Press, Cambridge, 1991)

4. Vasudevan, A. K., Sadananda, K. and Louat, N. 'A Review of Crack Closure, Fatigue Crack Threshold and Related Phenomena' *Mater. Sc. And Eng A* 188 (1994) pp 1-22.
5. Bunge, H. J. 'Some Applications of the Taylor Theory of Crystal Plasticity' *Kristall und Technik* 5 (1970) pp 145-175.
6. Grandt, A. F. et al 'Modeling the Influence of Initial Material Inhomogeneities on the Fatigue Life of Notched Components' *Fatigue Fract. Engng Mater. Struct.* 16 2 (1993) pp 199-213.
7. Magnusen, P. E. et al 'The Role of Microstructure on the Fatigue Durability of Aluminum Aircraft Alloys' *Final Report ONR Contract N00014-91-C-0128* (Alcoa Technical Center, Alcoa Center, PA, 1995)
8. Przystupa, M. A. et al 'Development of the Microstructure Based Stochastic Fatigue Life Prediction Models' *Progress Report ONR Grant N00014-91-J-1299* (UCLA, Los Angeles, 1993).
9. Castillo, E. *Extreme Value Theory in Engineering* (Academic Press, San Diego, 1988)
10. Raju, I. S. and Newman, J. C. 'Stress-Intensity Factors for Circumferential Surface Cracks in Pipes and Rods Under Tension and Bending Loads' *ASTM STP 905* (ASTM, Philadelphia, PA, 1986) pp 789-805.
11. Chan, K. S. and Lankford, J. 'The Role of Microstructural Dissimilitude in Fatigue and Fracture of Small Cracks' *Acta Met.* 36 (1988) pp 193-206.
12. Luévano, A. J., Przystupa, M. A. and Zhang, J. 'Accumulation of Microstructural Damage Due to Fatigue of High-Strength Aluminum Alloys' *J of Matr. Eng and Performance* 3 (1994) pp 47-54.
13. Vasudevan, A. K. and Suresh, S. 'Lithium-Containing Aluminum Alloys: Cyclic Fracture' *Met. Trans.* 16A (1985) pp 475-477.

## Tables

TABLE I. Parameters of the Gumbel Distributions of Pore Largest Dimensions

	$\mu$	$\sigma$
Bulk Pores (weighted fit)	1.450	0.290
Crack Initiating Pores ( $N_G=1.54 \times 10^5$ )	4.913	0.290

### List of Figures:

Figure 1. Comparison of the experimental S-N results with the predictions from the Monte-Carlo simulations for indicated  $\sigma_{\max}$  levels : 7050-T7451 plate alloy, L-T smooth fatigue samples,  $R = 0.1$ , 10 Hz.

Figure 2. Distributions of the largest dimensions of the bulk and the actual crack initiating pores for 7050-T7451 plate alloy. Predicted crack initiating pore size distribution was obtained from the weighted Gumbel distribution fitted to the bulk data using sample size of  $1.54 \times 10^5$ .

Figure 3. Effects of the extreme variation of (a) flaw sizes, (b) crack deflections and (c) texture on fatigue life of the 7050-T7451 plate alloy fatigued  $\sigma_{\max}=241$  MPa and  $R = 0.1$ . Random curves correspond to the random variations of deflections and texture along the crack path.

Figure 4. Schematics showing (a) change of the range of Taylor factor values with number of grains intersected by the crack tip and (b) idealized crack profile assumed during Monte-Carlo simulations.

Figure 5. Comparison of the S-N fatigue data for the 7050-T7451 plate alloys with the Monte-Carlo predictions obtained with initial crack sizes, texture and crack deflections as random variables.

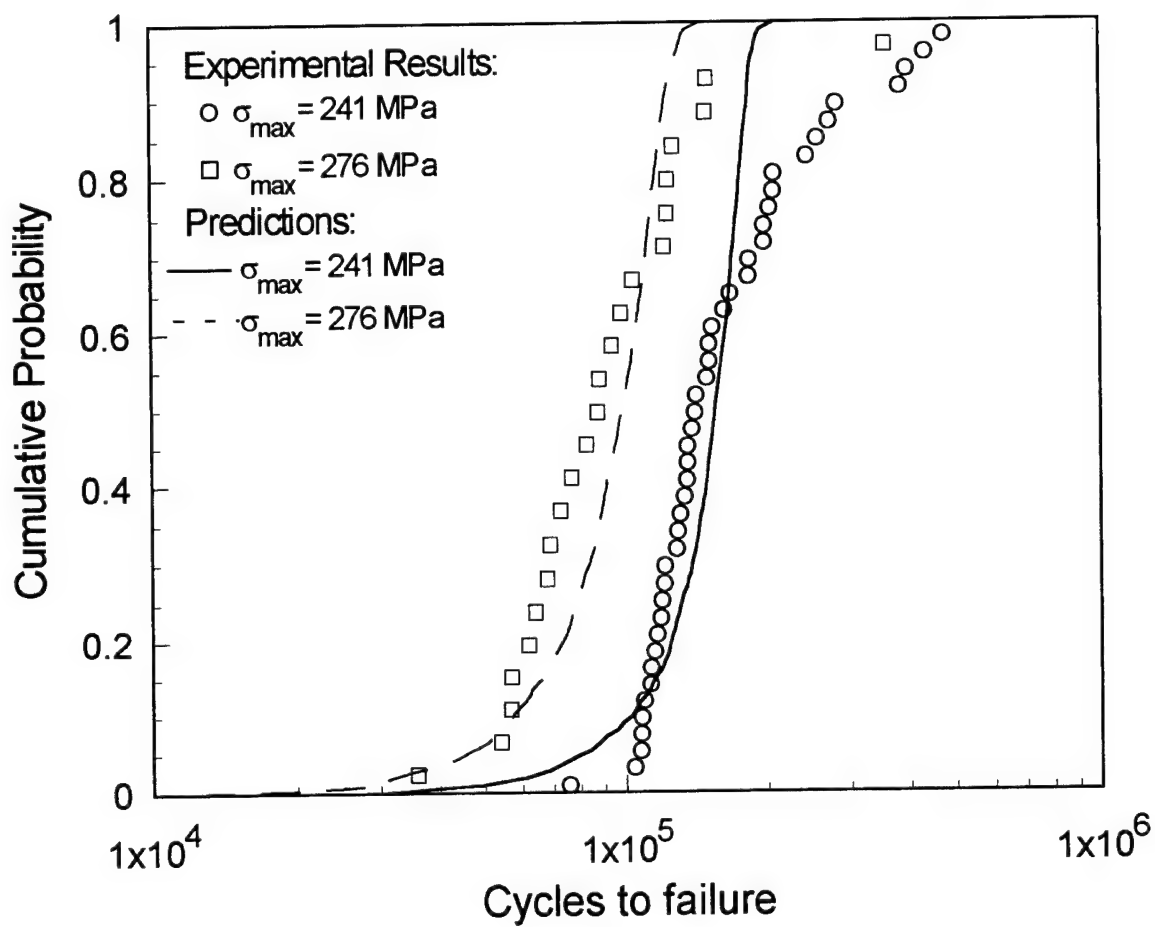


Figure 1. Comparison of the experimental S-N results with the predictions from the Monte-Carlo simulations for indicated  $\sigma_{\max}$  levels : 7050-T7451 plate alloy, L-T smooth fatigue samples,  $R = 0.1$ , 10 Hz.

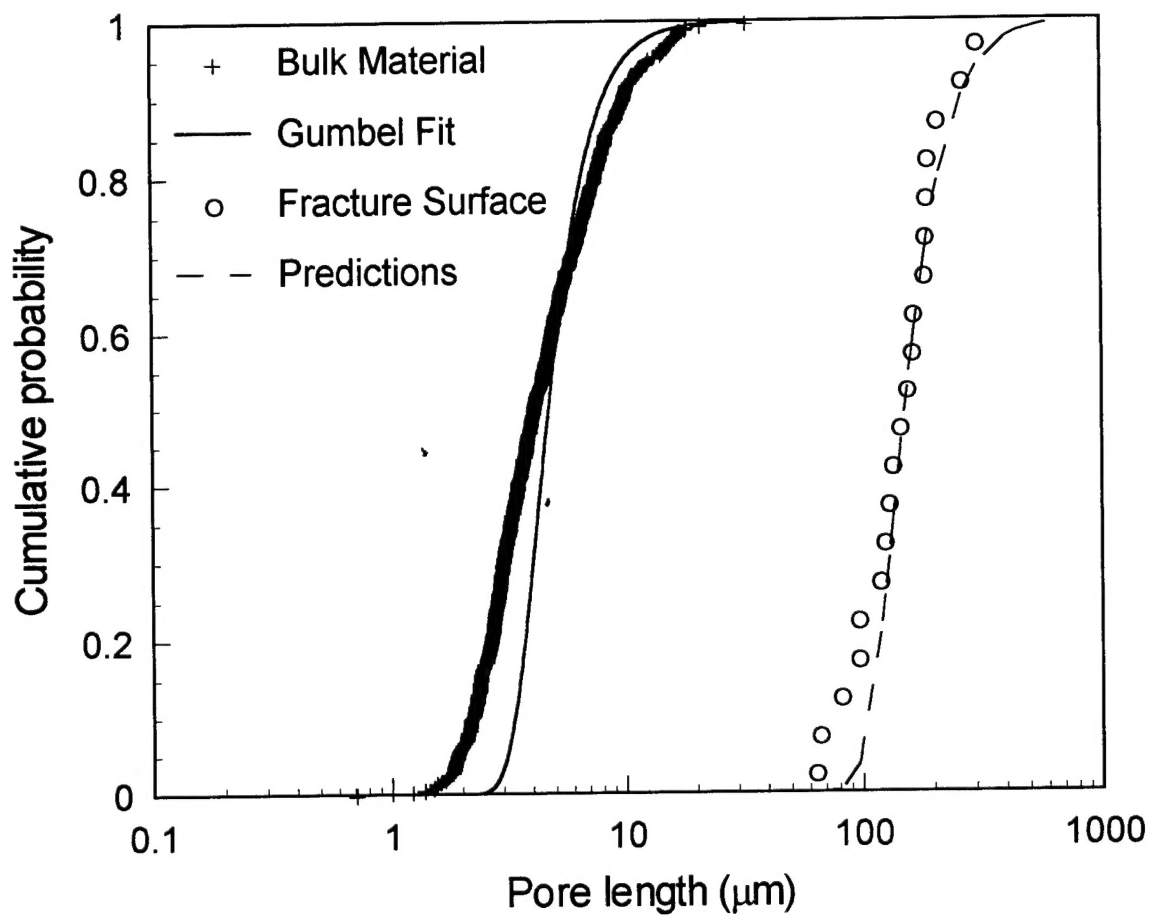


Figure 2. Distributions of the largest dimensions of the bulk and the actual crack initiating pores for 7050-T7451 plate alloy. Predicted crack initiating pore size distribution was obtained from the weighted Gumbel distribution fitted to the bulk data using sample size of  $1.54 \times 10^5$ .

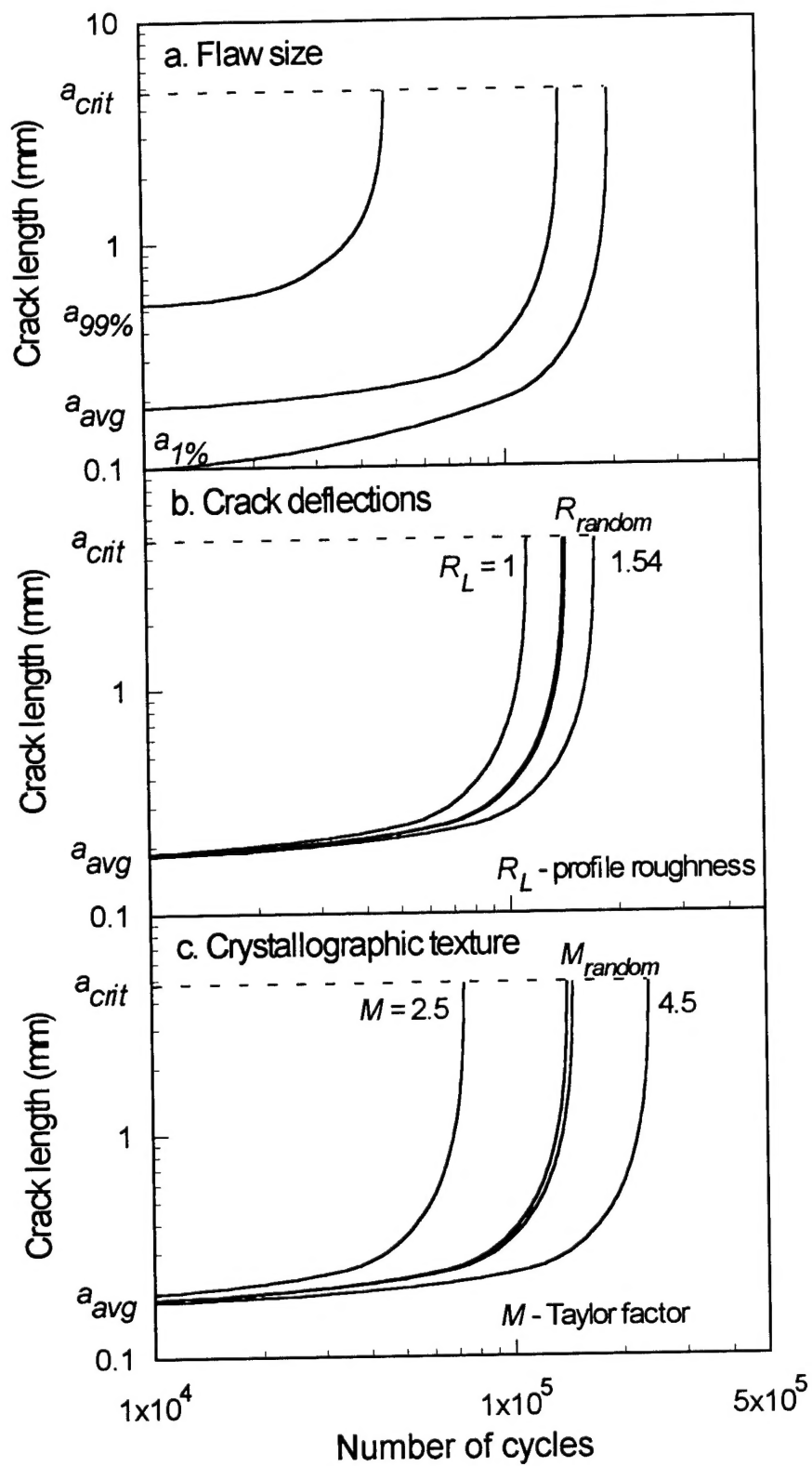


Figure 3. Effects of the extreme variation of (a) flaw sizes, (b) crack deflections and (c) texture on fatigue life of the 7050-T7451 plate alloy fatigued at  $\sigma_{\max}=241$  MPa and  $R = 0.1$ . Random curves correspond to the random variations of deflections and texture along the crack path.

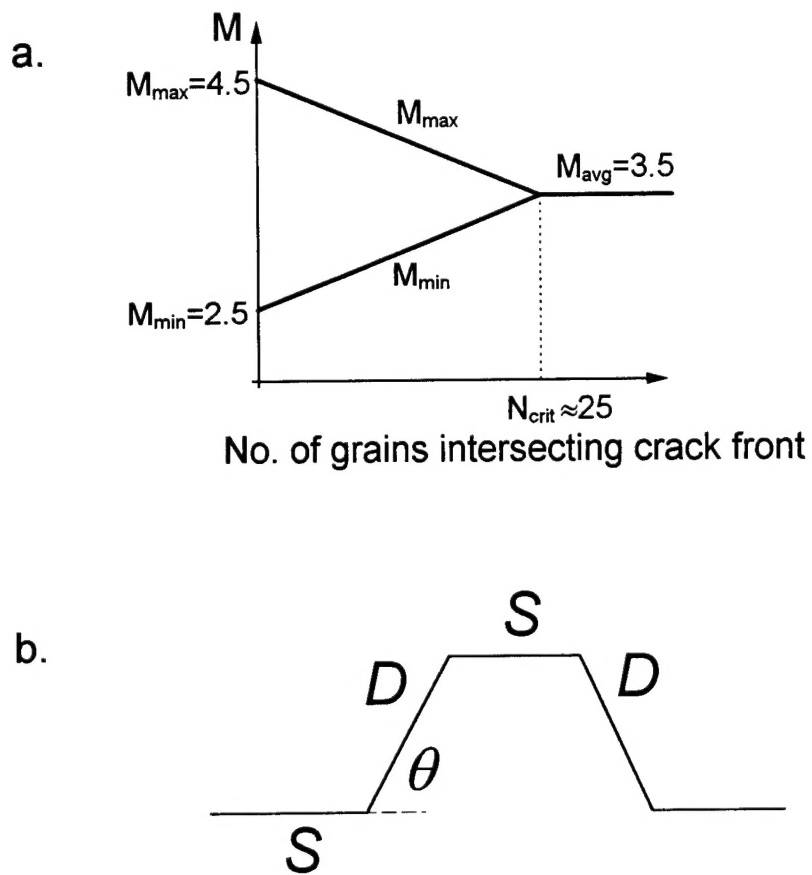


Figure 4. Schematics showing (a) change of the range of Taylor factor values with number of grains intersected by the crack tip and (b) idealized crack profile assumed during Monte-Carlo simulations.

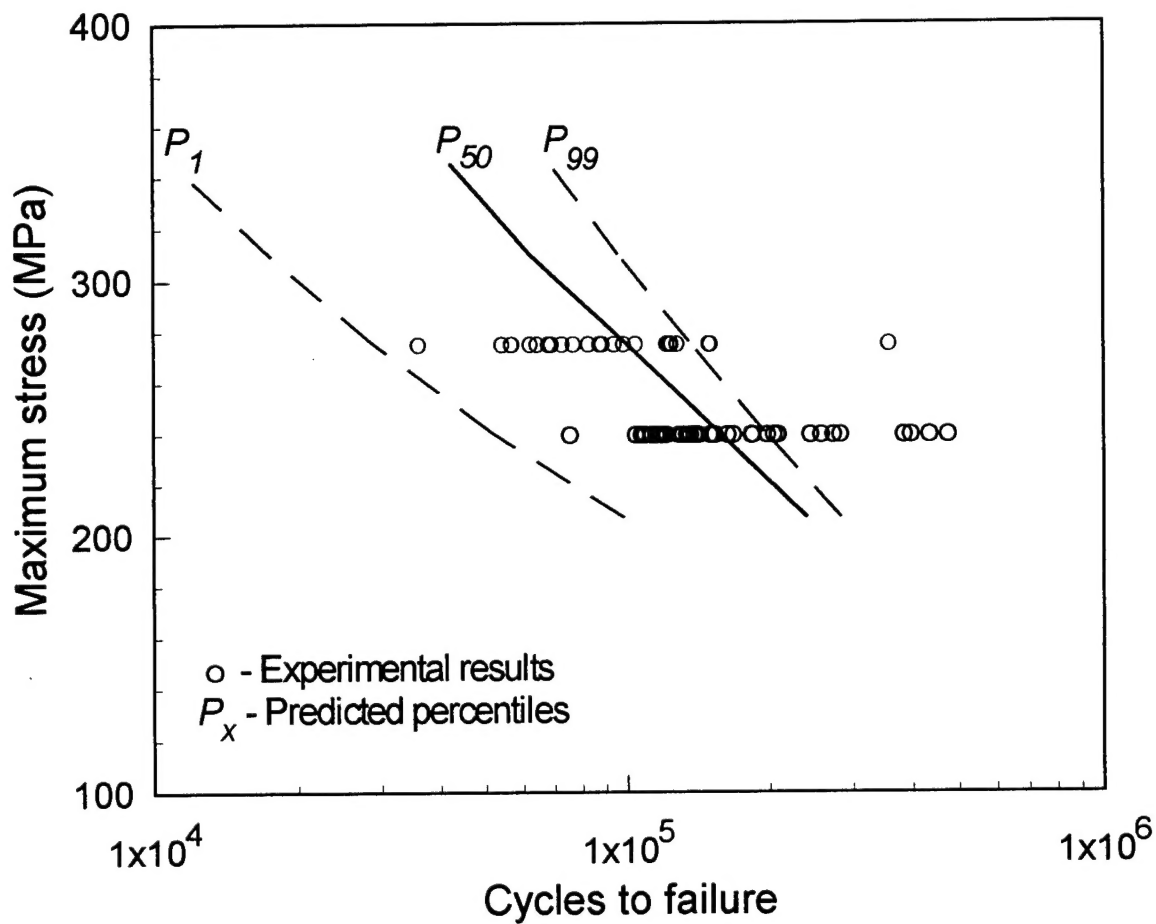


Figure 5. Comparison of the S-N fatigue data for the 7050-T7451 plate alloys with the Monte-Carlo predictions obtained with initial crack sizes, texture and crack deflections as random variables.